Faculty of Sciences
Department of Analytical Chemistry
Research group of Electrochemistry and Surface Analysis (ESA)

The development of an environmentally friendly coating for the corrosion inhibition of lead objects

by

Michel **De Keersmaecker**

Promotors: Prof. Dr. A. Adriaens, Prof. Dr. F. Du Prez

Doctoral thesis submitted in fulfillment of the requirements for the degree of Doctor in Sciences

Academic year 2015-2016

Electrochemistry and Surface Analysis

Contents

I General introduction 1

1 Short history of lead 3

1.1 First indications of lead usage . . . 3

1.2 Egyptian civilization . . . 4

1.3 Cupellation . . . 4

1.4 Greek and Roman civilization . . . 5

1.4.1 Military . . . 5

1.4.2 Monetary . . . 6

1.4.3 Water supply . . . 7

1.4.4 Food and drinks . . . 7

1.4.5 Household and art . . . 8

1.4.6 Poison and medicine . . . 8

1.5 The middle ages . . . 9

1.6 The industrial revolution: an increase in lead production . . . 12

1.7 Lead in the 20^{th} century . . . 13

2 Protection and preservation of lead archaeological objects 19

2.1 Composition of lead artifacts . . . 19

2.1.1 Lead and its alloys . . . 19

2.2 Deterioration of lead and lead artifacts . . . 21

2.2.1 Basic principles . . . 21

2.2.2 Uniform corrosion . . . 23

2.2.3 Localized corrosion . . . 28

2.2.4 Overview of lead corrosion products . . . 31

2.3 Treatment of lead artifacts . . . 32

2.3.1 Preventive conservation . . . 32

2.3.2 Interventive conservation . . . 32

2.4 Ethical challenges in conservation . . . 37

3 Objectives and strategy **47**

3.1 Objectives . . . 47

3.2 Strategy . . . 47

3.3 Short outline . . . 48

4 Surface analysis techniques **49**

4.1 Materials . . . 49

4.2 The pre-treatment of the lead samples . . . 49

4.3 pH measurements . . . 51

4.4 Microscopy . . . 51

4.4.1 Optical microscopy . . . 52

4.4.2 Scanning electron microscopy . . . 52

4.5 Scattering techniques . . . 57

4.5.1 Laboratory powder X-ray diffraction . . . 57

4.5.2 Synchrotron X-ray diffraction . . . 61

4.5.3 Setup and instrumentation . . . 63

4.6 X-ray photoelectron spectroscopy . . . 64

4.6.1 X-ray photoelectron spectrometer . . . 65

4.6.2 Data analysis . . . 66

4.7 Attenuated total reflection infrared spectroscopy . . . 68

4.7.1 Infrared spectroscopy: basics . . . 68

4.7.2 Attenuated total reflection . . . 69

4.7.3 Infrared spectroscopy: instrumentation . . . 70

4.7.4 Infrared spectroscopy: analysis . . . 71

5 Polymer characterization techniques **77**

5.1 Nuclear magnetic resonance spectroscopy . . . 77

5.2 Differential scanning calorimetry . . . 78

5.3 Thermogravimetric analysis . . . 79

II Lead carboxylate coatings **81**

6 Kinetic description of corrosion reactions **83**

6.1 Polarization . . . 83

6.1.1 Activation polarization . . . 83

6.1.2 Concentration polarization . . . 84

6.2 The symmetry factor . . . 85

6.2.1 Outer sphere electron transfer . . . 85

6.2.2 Metal dissolution and deposition . . . 86

6.2.3 Charge transfer to or from a species adsorbed to the surface . . . 86

6.3 The transfer coefficient . . . 87

6.4 Mixed potential theory . . . 88

7 Electrochemical deposition of a lead dodecanoate coating **91**

7.1 The development of lead carboxylate coatings . . . 91

7.2 Voltammetric techniques . . . 92

7.2.1 The voltammetric cell . . . 92

7.2.2 Cyclic voltammetry . . . 92

7.2.3 Linear polarization . . . 93

7.3 Experimental . . . 95

7.3.1 Solutions . . . 95

7.3.2 Instruments . . . 95

7.4 Electrochemical behavior of lead . . . 96

7.4.1 Electrochemical behavior of lead in an alkaline solution . . . 96

7.4.2 Electrochemical behavior of lead in a sodium dodecanoate solution . . . 97

7.4.3 Tafel analysis . . . 98

7.5 Spectroscopic characterization of the dodecanoate film . . . 99

7.6 Conclusions . . . 102

8 Deposition method comparison for a lead dodecanoate coating **105**

8.1 Single-sine electrochemical impedance spectroscopy . . . 105

8.1.1 Basic concepts . . . 105

8.1.2 Data validation . . . 106

8.1.3 Data modeling . . . 108

8.1.4 Fitting procedure . . . 113

8.1.5 The complex nonlinear least squares fit algorithm . . . 113

8.2 Deposition techniques . . . 115

8.3 Electrochemical evaluation of lead dodecanoate coatings . . . 116

8.3.1 Influence of the initial reduction step . . . 116

8.3.2 Fitting of the impedance data . . . 116

8.3.3 Evaluation of the potentiodynamic polarization data . . . 119

8.4 Visual comparison of the coatings . . . 121

8.5 Reproducibility of the lead dodecanoate coating . . . 121

8.6 Conclusions . . . 121

9 Influence of time, method and temperature on the deposition of a $Pb(C_{12})_2$ coating **125**

9.1 Deposition procedures . . . 125

9.2 Factorial design approach . . . 126

9.3 Electrochemical evaluation of the lead dodecanoate coatings . . . 126

9.3.1 Influence of the temperature and the deposition method . . . 126

9.3.2 Influence of the temperature and the deposition method on the surface structure . . . 129

9.3.3 Influence of the deposition time on coatings produced using the immersion method . . . 130

9.3.4 Reproducibility of the coating deposited at room temperature . . . 132

9.4 Summary and conclusions . . . 133

10 Electrochemical and surface study of NaC_{12} on lead **135**

10.1 Experimental procedures . . . 135

10.1.1 Electrochemical tests . . . 135

10.1.2 Surface analysis techniques . . . 135

10.2 Corrosion inhibition study using sodium dodecanoate . . . 136

10.3 Adsorption study: chemisorption or physisorption? . . . 140

10.4 Surface and cross-sectional analysis . . . 143

10.5 Mechanistic model of the deposition of the lead dodecanoate coating . . . 144

10.6 XPS analysis of the corrosion and passive layers . . . 145

10.6.1 Analysis of an atmospherically corroded lead sample . . . 145

10.6.2 Analysis of a coated lead sample using the cyclic voltammetry (CV) procedure . . . 146

10.6.3 Analysis of a coated lead sample using the IMM procedure . . . 149

10.6.4 Influence of reduction step on the XPS data . . . 150

10.7 Summary and conclusions . . . 151

11 Lead dodecanoate coatings for the protection of organ samples **155**

11.1 Description and treatment of the organ samples . . . 155

11.2 Experimental procedures . . . 156

11.2.1 Deposition procedure . . . 156

11.2.2 Corrosion test procedure . . . 156

11.2.3 Surface analysis techniques . . . 156

11.3 Microscopic examination . . . 157

11.4 EDS-analysis . . . 158

11.5 XRD-analysis . . . 159

11.6 Corrosion testing . . . 161

11.6.1 Organ plate samples . . . 161

11.6.2 English organ sample . . . 163

11.7 Conclusions . . . 164

III Time lapse studies **167**

12 Time-lapse multisine impedance study of lead in acetic acid **169**

12.1 Odd random phase electrochemical impedance spectroscopy . . . 169

12.1.1 The excitation signal . . . 169

12.1.2 Data analysis . . . 170

12.2 ORP-EIS: A case study on lead immersed in acetic acid . . . 174

12.2.1 Experimental procedures . . . 174

12.2.2 Time-lapse impedance study . . . 174

12.2.3 Instantaneous impedance values . . . 175

12.2.4 Impedance model . . . 180

12.2.5 Fitting results . . . 180

12.2.6 Scanning electron images . . . 182
12.2.7 Discussion using fitted parameters . . . 183
12.3 Conclusions . . . 188

13 Spectroelectrochemical characterization of a $Pb(C_{12})_2$ coating 191
13.1 In-situ X-ray diffraction measurements . . . 191
13.2 Growth of a coating on lead using cyclic voltammetry . . . 192
13.3 Corrosion test of the lead dodecanoate coated lead coupon . . . 198
13.4 Summary and conclusions . . . 202

IV Polymer coatings 205

14 Hydrogenated dimer acids as a coating for lead substrates 207
14.1 Experimental . . . 207
14.1.1 Oligomer analysis . . . 207
14.1.2 Neutralization of the hydrogenated dimer acid . . . 207
14.1.3 Inhibitor solutions . . . 207
14.1.4 Electrochemical procedure . . . 208
14.1.5 Deposition techniques . . . 208
14.1.6 Surface analysis techniques . . . 208
14.2 Thermal properties of DA and NaDA . . . 209
14.3 SEM-EDS analysis . . . 209
14.4 ATR-IR analysis . . . 210
14.5 XPS analysis . . . 212
14.6 Electrochemical impedance spectroscopy . . . 215
14.6.1 Bare lead sample . . . 215
14.6.2 DA-coated sample . . . 218
14.6.3 NaDA-coated sample . . . 219
14.7 Potentiodynamic polarization curves . . . 220
14.7.1 Bare lead sample . . . 220
14.7.2 Coatings . . . 221
14.8 Conclusions . . . 222

15 Acrylate-based coatings to protect lead substrates 225
15.1 Polymer preparation . . . 225
15.1.1 Synthesis of 1-ethoxyethyl acrylate . . . 225
15.1.2 Synthesis of the RAFT reagent . . . 226
15.1.3 Synthesis of the acrylate copolymers: RAFT polymerization . . . 226
15.1.4 Deprotection of the acrylate polymer . . . 230
15.2 Experimental . . . 230
15.2.1 Inhibitor solutions . . . 230
15.2.2 Surface analysis techniques . . . 231

15.3 Infrared analysis . . . 231
15.4 Corrosion protection of acrylate coatings . . . 233
15.4.1 Corrosion experiment . . . 233
15.4.2 Bare lead sample . . . 233
15.4.3 Time lapse EIS study of the polymer coatings . . . 234
15.5 SEM-EDS analysis . . . 241
15.6 Conclusions . . . 245

V Conclusions and future work 249

16 Summary of the results and conclusions 251
16.1 Lead carboxylate coatings . . . 251
16.1.1 Influence of the deposition method and reduction treatment . . . 251
16.1.2 Influence of the deposition temperature . . . 252
16.1.3 Influence of the deposition time . . . 253
16.1.4 Adsorption considerations . . . 253
16.1.5 Lead corrosion in an acetic acid environment . . . 253
16.2 Polymer coatings . . . 253
16.2.1 Dimer acid coatings . . . 254
16.2.2 Acrylate-based coatings . . . 254
16.3 General summary . . . 254
16.4 Perspectives . . . 255
16.4.1 Future improvements . . . 255
16.4.2 Future tests . . . 256
16.4.3 Final remarks . . . 257
16.5 Publications in international peer-reviewed journals . . . 271
16.6 Oral and poster presentations on national and international conferences . . . 272
16.7 European search reports . . . 273

Het is gelukt. Het is zover. Klaar. Finished! Vijf jaar lang heb ik gewerkt aan dit lijvige werk. Om dit werk te kunnen schrijven heb ik veel geleerd, gewerkt, gereisd, gevloekt, me geërgerd, geschreven, gevraagd, verbeterd maar ook en vooral gelachen, gebabbeld en me geamuseerd. Plezante en minder plezante momenten beleefd, maar dit gelukkig nooit alleen. Ik zou graag alle mensen willen bedanken die hebben bijgedragen tot het afwerken van dit manuscript. Vandaar deze waslijst aan dankbetuigingen voor enkele bijzondere mensen ···

Allereerst zou ik graag mijn promotor Annemie Adriaens willen bedanken. Mieke, op alle mogelijke vlakken heb ik een eigen inbreng mogen tonen en mogen bewijzen dat ik aan wetenschappelijk onderzoek kan doen. Je hebt me steeds weten te motiveren en bij te staan daar waar nodig. Het is ook jouw verdienste dat dit werk tot een goed einde gekomen is. Verder, wil ik je ook bedanken voor de verschillende uitstappen die ik heb mogen maken naar DESY in Hamburg en het ESRF in Grenoble. Het toont een zeer groot vertrouwen in mijn kennis en vaardigheden. Ook bedankt om mij elk jaar de kans te geven om mijn onderzoek te delen op verschillende internationale conferenties. Om in de voorbije vijf jaren zo vele kansen te krijgen, moet je wel een gemotiveerde promotor hebben. Mieke, bedankt voor het helpen aanvragen van de o zo belangrijke fondsen.

Verder wil ook mijn copromotor Filip Du Prez in deze lijst op nemen. Bedankt om mij te willen begeleiden gedurende mijn tijd op S12. Gedurende de vergaderingen hebben we verschillende waardevolle discussies gevoerd waardoor ik weer met duizend en één nieuwe ideeën kon verder werken. Ook wil ik je bedanken om mij op te nemen in de groep op S4. Om mij te helpen bij het bereiden van de polymeren en nieuwe ideeën uit te werken, heb ik ook kunnen rekenen op Sanne, Otto en Stef.

I certainly also would like to thank professor Mark Dowsett for helping me decipher all recorded XRD-spectra using the esaProject software. Thank you for the efforts for the further development of the eCell so that we could perform all in-situ electrochemical measurements at the ESRF. I really enjoyed learning and working during several beam times. Even after your retirement, passionate as always, you have been a crucial help in finishing and completing this manuscript.

Pieter-Jan, jou wil ik bedanken om de voorbije jaren, de perfecte collega te zijn. We hebben veel gelachen samen, niet alleen op S12, maar ook de verschillende beam times die we samen gedaan hebben, waar we ook talloze afleveringen van The Big Bang Theory gezien hebben. Ook in moeilijke tijden of bij problemen konden we altijd op elkaar rekenen om zo de volgende keer er terug met volle moed tegenaan te gaan. Hierbij wil ik je ook succes wensen met het schrijven van jouw manuscript.

I also would like to thank Rosie, Victoria and Alice for all the conversations in the lab and during the beam time. We could always share our ideas about our work and help each other to look for new experiments. Furthermore, all of us enjoyed a chat and a drink during conferences and beam times. To me work and after work activities seem equally important.

Ik wil ook, in het bijzonder enkele mensen bedanken op de VUB voor de hulp met de impedantiemetingen. Ik heb enorm veel bijgeleerd over de basis van de techniek, wat mij toeliet betere beslissingen in mijn doctoraat. Ik wil vooral Tom Hauffman bedanken om mij wegwijs te maken in het labo op de VUB en te helpen met een zeer interessante publicatie op basis van de op de VUB ontwikkelde ORP-EIS techniek. Ook Thibault Muselle was een enorme hulp voor het werken met de Matlabsoftware. Verder wil ik Annick Hubin en Herman Terryn om mij op te nemen in de groep en mij alle kansen te geven om mijn onderzoek te verbeteren. Voor de wiskundige benadering van de ORP-EIS analyse wil ik ook John Latiare bedanken. The book 'Electrochemical impedance spectroscopy' of Mark E. Orazem and Bernard Tribollet is mentioned and recommended for its clear mathematical interpretations and background on the impedance technique.

Karolien, ik wil ook jou bedanken voor de enorme hulp in het begin van mijn doctoraat. Bedankt om mijn onderzoek mee op weg te helpen en te sturen in de juiste richting. Daarnaast wil ik je ook bedanken voor de gezellige babbels.

Voor een probleem met de elektronica of met één of ander toestel, kon ik altijd op Jorge rekenen. Het is makkelijk samen te werken met iemand die altijd bereid is om eender welk probleem op te lossen. Bedankt ook om mij dingen bij te leren en voor alle gezellige babbels. Verder wil ook Davy bedanken voor het maken van de elektrodehouders en het ponsen van de loodcoupons.

Als assistenten bouw je gedurende de jaren een speciale band op. We kunnen altijd op elkaar rekenen en we helpen elkaar waar nodig. Jolien, Lien en Sylvia, het was fijn om al die jaren samen met jullie het practicum te begeleiden en voor de vele babbels in het assistentenlokaal tijdens de practica. Ik heb veel bijgeleerd over de verzorging en opvoeding van kinderen, het organiseren van conferenties en feestjes en het bouwen van energiezuinige woningen. Een speciale dank gaat ook uit naar Tine, Chantal en Philip die mij altijd geholpen en bijgestaan hebben tijdens mijn jaren op S12. In dit opzicht, wil ik ook Prof. Frank Vanhaecke bedanken om mij te helpen bij mijn eerste ervaringen bij het geven van zijn werkcolleges.

Uiteraard wil ik ook alle andere collega's, op S12 en daarbuiten, uitdrukkelijk bedanken voor alle hulp die ieder van hen me op zijn eigen manier heeft geboden. Ik denk hierbij in het bijzonder aan Tom, Brecht, Pieter, Peter, Stijn, Annelies, Elbeshary, Debbie, Anastasia, Alessia, Farzin, Matt, Lana, James, Joen, Didier, Andrei. Aan allen die ik vergeten ben: ook bedankt!

Naast al het volk op de werkvloer, zou ik graag mijn ouders, grootouders, mijn zus en mijn broer willen bedanken voor de steun niet deze vijf jaar alleen, maar gedurende mijn volledige universitaire carrière. Dit werd voornamelijk op prijs gesteld op momenten dat het mij soms aan motivatie en goesting ontbrak, en het nodig was mij terug op het juiste spoor te brengen. Zonder hun toeverlaat zou ik nooit zo ver geraakt zijn!

Tot slot zou ik nog graag mijn nummer één willen bedanken. Voor mij, verdient zij toch een heel speciale plaats in dit dankwoord. Tineke, schat, het zou te simpel zijn om je gewoon te bedanken voor alle hulp de laatste jaren. Je bent ondertussen een veel belangrijker deel van mijn leven geworden. De voorbije jaren was je mijn steun en toeverlaat. Ik ben zeker dat zonder je goede zorgen en je geduld, het nooit gelukt was om dit doctoraat af te ronden! Ik beloof je dat ik in de toekomst meer tijd ga vrijmaken voor de belangrijkere dingen in het leven waarvoor we tot nu toe de tijd nog niet gevonden hebben.

Michel

9 oktober 2015

Summary

Despite all the efforts, our cultural heritage is being destroyed faster today than at any time in the past. Therefore, an understanding of these basic 'corrosion' processes causing deterioration - the breaking up and the aging of ancient artifacts - is urgently needed. Extensive research towards an intervention to protect and preserve our cultural heritage has become essential for the cultural and social development of present and future generations. In general, the research activities proceed in two directions: (1) try to reduce the corrosive substances in the environment and/or (2) apply a surface protection treatment. The aim of this work focuses on the second pathway, namely developing a protective coating which is stable, reversible, corrosion protective and aesthetically justified. The global strategy on lead-rich artifacts can be divided into three stages: (i) to assess the effects of corrosive atmospheres on lead, (ii) to study the deposition of potential protective layers and (iii) to observe the direct effects of VOCs on protected surfaces. The microscopic features, morphology, composition, crystal structure of all deposited coatings are analyzed using attenuated total reflection infrared spectrosopy (ATR-IR), optical (OM) and secondary electron microscopy (SEM), X-ray diffraction (XRD) and X-ray photoelectron spectroscopy (XPS).

Based on preliminary studies on carboxylate inhibitors because of their complexation reaction with the lead oxide, this work starts with the use of an aqueous sodium dodecanoate solution to form a coating using three deposition methods such as cyclic voltammetry, immersion and amperometry. To increase reproducibility and the protective behavior, a reduction pretreatment is tested. Along with the investigation towards the ideal deposition method, also the influence of the deposition time and temperature are examined using a multivariate statistical analysis. Basically, a longer deposition time and a lower temperature seem beneficial for the corrosion protective properties of the deposited coating investigated using impedance measurements. The use of cyclic voltammetry or immersion with reduction pretreatment shows no significant difference.

In order to get a view on the basics of the deposition reaction, electrochemical treatments are used to investigate the adsorption and corrosion inhibition characteristics of sodium dodecanoate inhibitors on lead. Clearly, the sodium dodecanoate inhibitor concentration has an important effect on the coating's adsorption properties. The critical micelle concentration forms a transition between monolayer adsorption occurring at low concentrations and multilayer formation following the dissolution-precipitation mechanism at high concentrations. Additionally, a time lapse in-situ spectroelectrochemical study of the growth of lead dodecanoate coatings on a lead substrate using synchrotron radiation X-ray diffraction gives us more information about the speed of deposition and the coating's crystal structure.

To understand the corrosive and morphological characteristics of lead dodecanoate protective coatings on real samples,

three pipe organ samples were studied. The results indicate that the three pipe organ samples are made of an alloy composed mainly of lead and tin. After immersion and the deposition of the coating, only lead and no tin is detected, which indicates the formation of a thick coating containing lead dodecanoate complexes because of a reaction with the corrosion products on the artifact's surface. Impedance studies show that the coating deposited using the immersion technique protects the artifact against corrosion.

A logical step towards a new coating on lead is the use of organic compounds with more than one carboxylic functional group. Dimer acids, neutralized or not, form a relatively stable metal-coordinated polymer where the lead ions form links between the carboxylic groups of the dimer acid in a metal-coordinated physical network with self-healing properties. Both coatings show a different appearance explained by the reaction mechanism, the inhibitor reactivity and the used solvent. The neutralized compound provided a better barrier against corrosion and showed a link between the immersion time, the coating thickness, the rate of water uptake and the degree of polymer entanglements.
Adding more carboxylic groups, a random acrylate copolymer is prepared using a controlled radical polymerization using a RAFT agent. During the deposition some of the carboxylic groups chemically react with lead metal ions to protect the lead substrate. The coating thickness and porosity, the profile of the water uptake, the diffusion and delamination processes and the corrosion product formation were studied depending on the acrylic acid content and the molecular weight of the prepared polymer using impedance measurements. Based on the electron images and the odd random phase impedance measurements, the acrylate random copolymers are promising materials to be used as a coating on lead substrates.

Nederlandstalige samenvatting

Ondanks al onze inspanningen, wordt ons cultureel erfgoed vandaag sneller vernield dan in om het even welke periode in het verleden. Daarom is het nodig om een volledig zicht te krijgen op de basischemie van de corrosieprocessen die het vervalproces - de afbraak en het verouderen van de artefacten - veroorzaken. Een uitgebreid onderzoek naar een ingreep om ons cultureel erfgoed te beschermen en te bewaren is essentieel geworden voor de culturele en sociale ontwikkeling van de huidige en toekomstige generaties. In het algemeen verlopen alle onderzoeksactiviteiten in twee richtingen: (1) het proberen om de hoeveelheid corrosieve stoffen in de omgeving te verminderen en/of (2) het behandelen van het artefact met een beschermende deklaag. Het doel van dit werk focust zich volledig op de tweede route door een beschermende deklaag te ontwikkelen die zowel stabiel, reversibel, corrosiebeschermend en esthetisch verantwoord is. De globale strategie voor loodrijke artefacten kan verdeeld worden in drie fases: (i) het beoordelen van de effecten van de corrosieve atmosfeer op lood, (ii) het bestuderen van de afzetting van potentieel beschermende lagen en (iii) het observeren van de directe effecten van vluchtige organische stoffen op de beschermende oppervlakken. De microscopische kenmerken, de morfologie, de compositie en de kristalstructuur van alle afgezette deklagen wordt geanalyseerd door gebruik te maken van attenuatie van de totale reflectie infrarood spectroscopie, optische en secundaire electron microscopie, X-straal diffractie en X-straal photoelektron spectroscopie.

De eerste studies maken gebruik van inhibitoren gebaseerd op geneutraliseerde lineare monocarbonzuren met lange koolstofketens als gevolg van hun complexeringsreactie met het loodoxide aanwezig op het oppervlak van loden voorwerpen. Uitgaande van deze basis, wordt een waterige oplossing van natrium dodecanoaat gebruikt om een deklaag te vormen, gebruik makend van drie verschillende afzettingsmethodes namelijk cyclische voltammetrie, onderdompeling en amperometrie. Om de reproduceerbaarheid en de inhibitie-efficiëntie te verhogen, wordt een voorbehandeling op basis van een reductieproces getest. Naast het onderzoek naar de ideale afzettingsmethode wordt ook de invloed van de afzettingstijd en -temperatuur onderzocht door gebruik te maken van multivariate statistische analyse. In principe zijn een langere afzettingstijd en een lagere afzettingstemperatuur gunstig voor de corrosiebeschermende eigenschappen van de afgezette deklaag welke onderzocht werden aan de hand van impedantiemetingen. Het gebruik van cyclische voltammetrie of onderdompeling met een voorbehandeling blijkt geen significant verschil te vertonen in de corrosiebeschermende eigenschappen.

Om een zicht te krijgen op de basis van de afzettingsreactie, worden elektrochemische metingen uitgevoerd om de adsorptie en corrosie-inhiberende eigenschappen van de natrium dodecanoaat inhibitormoleculen te achterhalen. Het is duidelijk dat de concentratie aan inhibitormoleculen hier een grote invloed op heeft. De kritisch micellaire concentratie

vormt een transitie tussen de adsorptie van een monolaag welke plaatsvindt bij lage concentraties en de adsorptie van een multilaag welke plaatsvindt bij hogere concentraties als gevolg van een oplossing-neerslag mechanisme. Gebruik makend van synchrotronstraling, hebben we ook een in situ spectroelektrochemische meting uitgevoerd om de groei van looddodecanoaat deklagen in functie van de tijd te analyseren. Deze meting geeft ons meer informatie over de afzettingsnelheid en de kristalstructuur van de deklaag.
Om de corrosiebeschermende en morfologische eigenschappen van de looddecanoaat deklaag na te gaan op echte artefacten, hebben we de deklaag ook getest op drie orgelstalen. De resultaten tonen aan dat de drie stalen vooral bestaan uit een legering van tin en lood. Na de onderdompeling en de afzetting van de deklaag zien we een grotere aanwezigheid van lood wat wijst op de vorming van een dikke beschermlaag bestaande uit looddodecanoaat complexen door de reactie met de corrosieproducten op het oppervlak. Impedantiemetingen tonen aan dat de deklaag, afgezet gebruik makend van de onderdompelingmethode, het artefact beschermt tegen corrosie.

Een logische stap in het onderzoek naar een nieuwe deklaag is het gebruik van organische verbindingen met meer dan één carbonzure functionele groep. Dimeerzuren, geneutraliseerd of niet, vormen een relatief stabiel metaal gecoördineerd polymeer waarbij de loodionen dienen als een link tussen de carbonzure groepen van het dimeerzuur in een fysisch netwerk met zelfherstellende eigenschappen. Beide deklagen vertonen een verschillend uitzicht wat kan verklaard worden door het reactiemechanisme, de reactiviteit van de inhibitor en het gebruikte solvent. De geneutraliseerde verbinding vormt een betere barrière tegen corrosie en toont een link tussen de onderdompelingstijd, de dikte van de deklaag, de wateropnamesnelheid en de polymeerverstrengelingsgraad.
Om verbindingen met meer carbonzure groepen te kunnen gebruiken, wordt een random acrylaat copolymeer bereid met behulp van een gecontroleerde radicale polymerisatie met een RAFT reagens. Tijdens de afzetting reageren sommige van de carbonzure groepen met de loodionen om het loodoppervlak te beschermen. Aan de hand van impedantiemetingen, worden de dikte en de porositeit van de deklaag, het wateropnameprofiel, de diffusie- en delaminatieprocessen en de vorming van corrosieproducten bestudeerd als functie van de hoeveelheid acrylzure groepen en het moleculair gewicht van het gebruikte polymeer. Op basis van de elektronbeelden en de impedantiemetingen kunnen we besluiten dat de random acrylaat copolymeren veelbelovende materialen zijn voor de productie van een deklaag op loodoppervlakken.

List of symbols

List of Latin symbols

A	area, in [cm^2]
A_{eff}	effective area, in [cm^2]
B	the magnetic field strength, in [T]
B.E.	binding energy, in [eV]
C	capacitance, in [F]
C	concentration, in [M] or [mol L^{-1}]
C_{coat}	coating capacitance, in [F]
C_{dl}	capacitance element of the double layer in the electric equivalent circuit, in [F]
C_{eff}	effective capacitance, in [F]
C_{ox}	capacitance of the oxide layer, in [F]
d	thickness, in [m] or [μm]
d	lattice spacing between the different layers of atoms, in [nm]
D	diffusion coefficient, in [m^2 s^{-1}]
D_{eff}	effective diffusion coefficient, in [m^2 s^{-1}]
e	charge of the electron [$1.6021766 \times 10^{-19}$ C]
E	potential, in [V]
E_{corr}	corrosion potential, in [V]
E_e	potential at equilibrium, in [V]
E_F	Fermi energy, in [eV]
E_V	energy of the vacuum level, in [eV]
E_W	work function, in [eV]
E_0	standard cell potential, in [V]
f	frequency of the multisine excitation signal, in [Hz]
f	($= \frac{F}{RT} = 25.693$ mV)
f_{max}	maximum excited frequency of the multisine excitation signal, in [Hz]
F	Faraday constant [9.64853399×10^4 C mol^{-1}]

$\mathcal{F}()$	Fourier transform function
ΔG	Gibbs free energy change, in [J mol^{-1}]
$\Delta G^{\neq}$	Gibbs free energy of activation, in [J mol^{-1}]
h	Planck's contant [6.626069 $\times$ 10^{-34} m^2 kg s^{-1} or J s]
$\bar{h}$	Dirac constant [$\frac{h}{2\pi}$]
i	current density, in [A cm^{-2}]
i_0	exchange current density, in [A cm^{-2}]
i_{corr}	corrosion current density, in [A cm^{-2}]
i_L	limiting current density, in [A cm^{-2}]
i_{net}	net current density, in [A cm^{-2}]
I	current, in [A]
I	intensity, in [a.u.]
I_a	anodic current, in [A]
I_c	cathodic current, in [A]
I_B	backscattered electron current, in [A]
I_S	secondary electron current, in [A]
j	the imaginary number
J	the coupling constant
k	refers to the kth frequency of the harmonic grid of the multisine excitation signal
k_b	rate constant of the reverse reaction, in [depends on order of the reaction]
k_f	rate constant of the forward reaction, in [depends on order of the reaction]
k_a	anodic rate constant, in [depends on order of the reaction]
k_c	cathodic rate constant, in [depends on order of the reaction]
k_B	Boltzmann constant [1.3806488 $\times$ 10^{-23} m^2 kg s^{-2} K^{-1} or J K^{-1}]
K	equilibrium constant
K_{ads}	equilibrium constant of an adsorption process
K_{sp}	solubility product
L	electrical inductance, in [H] (Henry)
L_{ads}	electrical inductance due to an adsorption reaction, in [H] (Henry)
n	number of electrons involved in the electrode reaction
n	CPE exponent ($0 < n < 1$)
N	number of harmonic related sine waves in the multisine excitation signal
N_A	Avogadro constant [6.022141 $\times$ 10^{23} mol^{-1}]
N_0(E)	number of electrons per unit volume of metal
P	number of periods
q	q-space value, in [Å^{-1}]
Q	the reaction quotient
r	ion radius, in [Å]
R	resistance, in [Ω]
R	universal gas constant [8.3144621 J mol^{-1} K^{-1}]

R_{ct}	charge-transfer resistance, in [Ω]
R_{ox}	resistance of the oxide layer, in [Ω]
R_{pore}	pore resistance, in [Ω]
R_u	uncompensated resistance or electrolyte resistance, in [Ω]
s	variable of Laplace transform, in [s^{-1}]
t	absolute time, in [s] or [h] or [d]
$t^\star$	instant time, in [s]
T	absolute temperature, in [K]
T_0	onset temperature, in [K]
$T_{d,max}$	temperature of maximum decomposition rate, in [K]
$U(k)$	amplitude of the sine waves in the multisine, in [V]
$U(t)$	multisine excitation signal in the time domain, in [V]
v	rate of the reaction, in [mol L^{-1} s^{-1}]
v	scan rate, in [V^{-1}]
$Z_{W,corr}$	Warburg constant of the corrosion process due to mass transfer, in [Ω $s^{-1/2}$]
wt% or w%	weight percentage, in [%]
Y_0	admittance of the constant phase element, in [$s^n\Omega^{-1}$]
Y	the admittance or reciprocal of the impedance, in [S]
Z	atomic number
$\|Z\|$	modulus of the complex impedance Z, in [Ω]
$Z_{real}(\omega)$	real part of the complex impedance Z at the angular frequency ω, in [Ω]
$Z_{imaginary}(\omega)$	imaginary part of the complex impedance Z at the angular frequency ω, in [Ω]
Z_W	diffusion impedance, in [Ω]

List of Greek symbols

α	symmetry factor [between 0 and 1, generally range around 0.5]
α_a	dimensionless anodic transfer coefficient
α_c	dimensionless cathodic transfer coefficient
β_a	anodic Tafel slope, in [V] or [V dec^{-1}]
β_c	cathodic Tafel slope, in [V] or [V dec^{-1}]
δ()	Dirac-delta function
δ	chemical shift, in [ppm]
δ_f	coating thickness, in [m]
δ_s	scissoring vibration, in [cm^{-1}]
δ_N	Nernst diffusion layer, in [m]
ϵ[]	the expected value
ϵ_0	permittivity of the vacuum [8.85×10^{-12} F m^{-1}]
ϵ_r	relative permittivity
η	the overvoltage or overpotential, defined as (E - E_e), in [V]
η_{IE}	the inhibition efficiency, in [%]

θ	diffraction angle between the incident rays and the surface of the crystal, in [°]
θ	surface coverage
θ_i	incident angle, in [°]
θ_s	scattered angle, in [°]
λ	wavelength of the used light, in [m^{-1}]
ν_{as}	asymmetric stretch, in [cm^{-1}]
ν_s	symmetric stretch, in [cm^{-1}]
σ	nuclear screening constant
ϕ	angle which describes the phase shift, in [°]
ϕ_k	k^{th} random phase in the multisine excitation signal between [0, 2π] such that E[ejϕk] = 0 with E[] the expected value
ρ	rocking vibration, in [cm^{-1}]
τ	relaxation time, in [s]
τ	time constant, in [s]
ω	wagging vibration, in [cm^{-1}]
ω	angular frequency (= 2πf), in [rad s^{-1}]
ω_k	k^{th} frequency, in [Hz]
ω_{k_e}	excited k^{th} frequency, in [Hz]
$\omega_{k_{even}}$	even k^{th} frequency, in [Hz]
$\omega_{k_{ne}}$	non-excited k^{th} frequency, in [Hz]
$\omega_{k_{odd}}$	odd k^{th} frequency, in [Hz]

List of abbreviations

ASTM	American society for testing and materials, is an international standard organization
ATR-IR	attenuated total reflection infrared spectroscopy
COLLAPSE	Corrosion of Lead and Lead-Tin Alloys of Organ Pipes in Europe
CV	cyclic voltammetry
EA	electron acceptor
EC	European Commission
EDAX Inc.	an instrumentation company providing energy-dispersive X-ray spectroscopy microanalysis detectors
EDS (or EDX)	energy dispersive X-ray spectroscopy
EEC	equivalent electric circuit
EIS	electrochemical impedance spectroscopy
FEG	field emission gun
FEI	an instrumentation company providing equipment for materials science
FRF	frequency response function
FT-IR	Fourier transform infrared spectroscopy
IHP	inner Helmholtz plane
IUPAC	International Union of Pure and Applied Chemistry
JEOL	an instrumentation company providing electron microscopes
LSV	linear sweep voltammetry

OCP	open current potential
OHP	outer Helmholtz plane
OXFORD	an instrumentation company providing energy-dispersive X-ray spectroscopy microanalysis detectors
RH	relative humidity
SCE	saturated calomel reference electrode
SDD	silicon drift detector
SEM	scanning electron microscopy
SHE	standard hydrogen electrode
VOC	volatile organic acids
UHV	ultra high vacuum
XPS	X-ray photoelectron spectroscopy
XRD	X-ray diffraction

PART I

GENERAL INTRODUCTION

1 Short history of lead

Lead was one of the first metals discovered by the human race [1]. Since 3500 B.C., this metal has been used for different applications in diverse civilizations on various locations on our planet [2]. So, for what purposes was lead used? Which cultures used lead and to what extent? In what follows, we give a short overview of the use of lead in the Middle East, Egypt and Europe. To help, a complete time line is given of important events and periods in Figure 1.1.

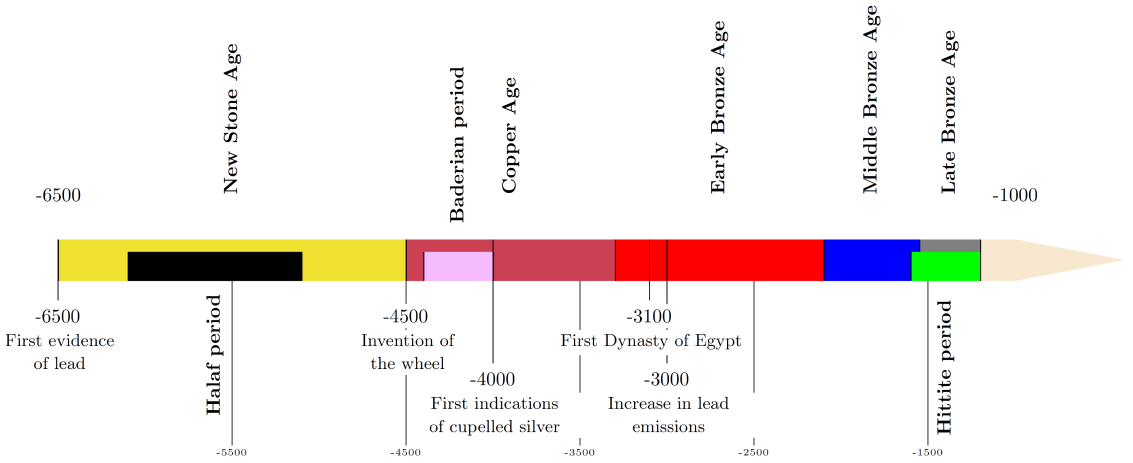


Figure. 1.1 – Overview of the periods and events from 6500 B.C. to 1000 B.C.

1.1 First indications of lead usage

In graves close to the ancient Hittite city of Çatal Hüyük, a settlement with a population of at least 5,000 people in what is now south-central Turkey, many lead and copper objects have been found including metal objects like beads, tubes, tools and small man-made statues, dated ca. 6500 years B.C. [3]. These suggest the presence of part-time craft workshops in the area [4, 5]. Lead metal has also been uncovered at Yarum Tepe in northern Iraq in the form of a 6th millennium B.C. bangle. Moreover, there is evidence of a conical lead piece from the Halaf period (6100 - 5100 B.C.) at the Arpachiyah site, near what is now Mosul in Iraq [6]. Furthermore, lead objects have been excavated at the 4th millennium B.C. site of Anau in Turkmenistan, where the mined metal probably originated in some part of central Asia [7]. As a last example, several litharge (PbO) fragments dated from 3600 B.C. to 2000 B.C. [8] have been revealed at the ancient Tappeh Hissar site in Iraq [9].

Another way of proving the early use of lead is conducted by Shotyk et al. [1]. The discovery of a Swiss peat bog in the Jura mountains has allowed his team to construct atmospheric lead profiles going back 14500 years. Their data suggests

that the atmospheric lead release increased over natural levels about 6000 years ago due to forest clearing for agriculture. Starting from 3000 B.C., however, mining, melting as well as anthropogenic sources have dominated lead emissions till the present. Large observed fluctuations coincide with major historical events such as the rise and fall of the Roman empire and the industrial revolution in Europe [10]. Indeed, according to manuscripts of Xenophon (434 - 359 B.C.) and Lucretius (98 - 55 B.C.), lead mines produced smoke that was harmful to people's health because of the high lead emissions [11].

Native lead is extremely rare, but is melted relatively easy from galena (PbS) using a simple wood fire [12]. The readily attractive metallic appearance and the easy smelting process, though on a small scale, began at least as early as 9000 years ago [13]. The smelting of lead is assumed to be the inception of metallurgy [14]. The early use of lead is explained by its physical and chemical properties. First, its softness, low melting point and inert nature explain why the metal is relatively easily refined from its ores and shaped into useful forms [15]. Secondly, the multiple uses of lead metal in history can also be explained by means of its existence on earth. Lead is extremely widely distributed in the earth's crust ($\pm$ 0.0013% lead), not as a pure metal, but as lead ores in mineral deposits [16].

1.2 Egyptian civilization

Garland and Bannister [17], as well as Lucas [18], talk about an ancient Egyptian lead source called the Gebel Rosas or 'lead mountain' situated south of Quseir on the Red Sea coast. Also many other mine locations in Egypt have been published by Stos-Gale and Gale [19] and Hassan and Hassan [20]. Popular uses for the mined and refined lead, although not extensively worked by the ancient Egyptians, were weights on fishing nets, jewelry, beads, solder, various domestic utensils, in glazes for pottery, construction, and casting into ornaments and decorations [21, 22]. Furthermore, lead was used in different types of glass and enamels as well. As an example, work of Brill et al. [23] showed that yellow glass produced during the reign of Amentotep II (the 18^{th} Dynasty, 1427 - 1400 B.C.) contains lead of Egyptian origin. Moreover, two excavated fishing weights from the Uluburun wreck, dated ca. 1300 B.C., were found to be made of lead from ores of the Taurus mountains [24]. Lead is also used in pigments like lead white ($2Pb(CO_3)_2 \cdot Pb(OH)_2$) and chrome yellow ($PbCrO_4$) as described by Ambers et al. [25] in his study of the Gayer-Anderson cat dating to the Egyptian Late Period (around 600 B.C.). Galena was used as eye-paint in Egypt during the prehistoric Baderian period, about 5000 years B.C. [18]. In fact, the practice of using galena for eye-paint survives to the present day, particularly in India, where it is known as surma, and among Asian immigrants [26]. As a last example, a carved metal statue, from the Osiris Temple at Abydos in Egypt, preserved in the British Museum, is believed to date from the First Dynasty about 3400 B.C. [27]. Due to importance of lead in their daily life, the Egyptian word *dḥty* or *ḏḥty* was used to denote the metal [28, 29].

Other well-known examples are lead plumb bobs widely used by Egyptian architects [30] and hollow cast bronze weights, often in the shape of animals, filled with lead to the prescribed weight in connection with balances [31]. In the Uluburun wreck weights belonging to the merchants aboard the ship were also excavated, together with three sets of balances. From the 149 weights found on the ship, 78 contained iron, 38 were made of bronze and 8 were pure lead [32].

1.3 Cupellation

In pre-Roman times, there were only two possibilities of obtaining silver from ores, either (1) by direct smelting or (2) by cupellation using argentiferous lead ores (i.e. PbS) [33]. The cupellation (selective oxidation) process, the oldest metallurgical process known to mankind, is usually performed in a shallow bowl, called a cupel, charged with lead ore

and fuel [9, 34].

$$Pb(l) + O_2(g) \rightarrow PbO\ (l) + Pb(Ag)(l) \tag{1.1}$$

During the heating stage, lead is easily oxidized to litharge by blasting air over it. At the same time, the silver impurities in the argentiferous galena are reduced [6]. The cupellation process relies on the fact that the produced lead oxides absorb the other metal impurities [34] and that the noble metals coalesce into a small pool on top of the litharge cake [6]. These cakes are then removed by skimming or by adsorption to the cupel walls [35–37].

As native silver is rare, silver objects in the ancient world were commonly produced by cupellation characterized by lead concentrations above 0.05 per cent [38]. In addition to the lead/silver ore mines in Egypt, others are present in the North Caucasus [39], Spain [40], the Laurion mine in Attica (Greece) [41], the Augustan-Tiberian deposits in Germania [42] and Rio Tinto in Carthage [43]. The best known remains from this technique are so-called litharge cakes [9]. As mentioned in section 1.1, archaeological investigations on the ancient of site of Tappeh Hissar have revealed litharge fragments. Also slag cake containing arsenic, lead, nickel and antimony has been found at the 4^{th} millennium B.C. Arslantepe site in Turkey [39]. It is clear that such smelting industries arose in several places in the ancient world, particularly in Asia Minor (Turkey) [44]. It did not take long, however, to find ways to use this 'by-product' of silver mining. Indeed, the widespread production of lead is a consequence of the use of the cupellation process [45].

1.4 Greek and Roman civilization

In Greek and Roman civilizations, lead metal artifacts were an essential part of the community and society [46], where it became the most important metal in their daily life [47]. Most of the objects excavated from this period appear to consist of highly pure lead, which indicates that the cupellation procedure had been updated over the years [48]. Evidence for the extensive use of lead could be found in the elevated lead pollution and the extensive lead poisoning of humans [49]. Nriagu et al. [50] even suggested that lead poisoning was one of the causes for the fall of the Roman Empire. In the following part, different aspects of the Greek and Roman daily life are discussed in terms of the use of lead. Additionally, a time line is given for the Greek and Roman period showing the important events and people described in the text in Figure 1.2.

1.4.1 Military

Because of its weight, lead was not useful for the production of short-range weapons [42]. However, projectiles used by the Greeks and the Romans during military campaigns, such as sling bullets and shots were made of lead [51, 52]. Greep [53] published the recovery of 64 lead bullets near Verulamium (St Albans, UK), which were used by the Roman army in Britannia. Bode et al. [42] and Durali-Müller [54] studied the provenance of ca. 150 lead objects collected from several Augustan Roman military camps in Germania east of the river Rhine. During these excavations not only amorphous casting debris, but also lead weights, pipe fragments, plumbs and slingshots were found. Also a Roman medical writer Aulus Cornelius Celsus talks about finding

"Plumbea glans, aut lapis, aut simile aliquid" (Medicinae, VII, V, 4)

which translates to "a leaden bullet, or stone or something similar" in a body [55].

Under the direction of Daniels et al. [56] excavations have been conducted in the Housesteads Roman fort, one of the best preserved forts along Hadrian's Wall. A profound analysis of the debris with energy-dispersive X-ray fluorescence (ED-XRF) and scanning electron microscopy with an attached X-ray spectrometer (SEM-EDS) insured the presence of

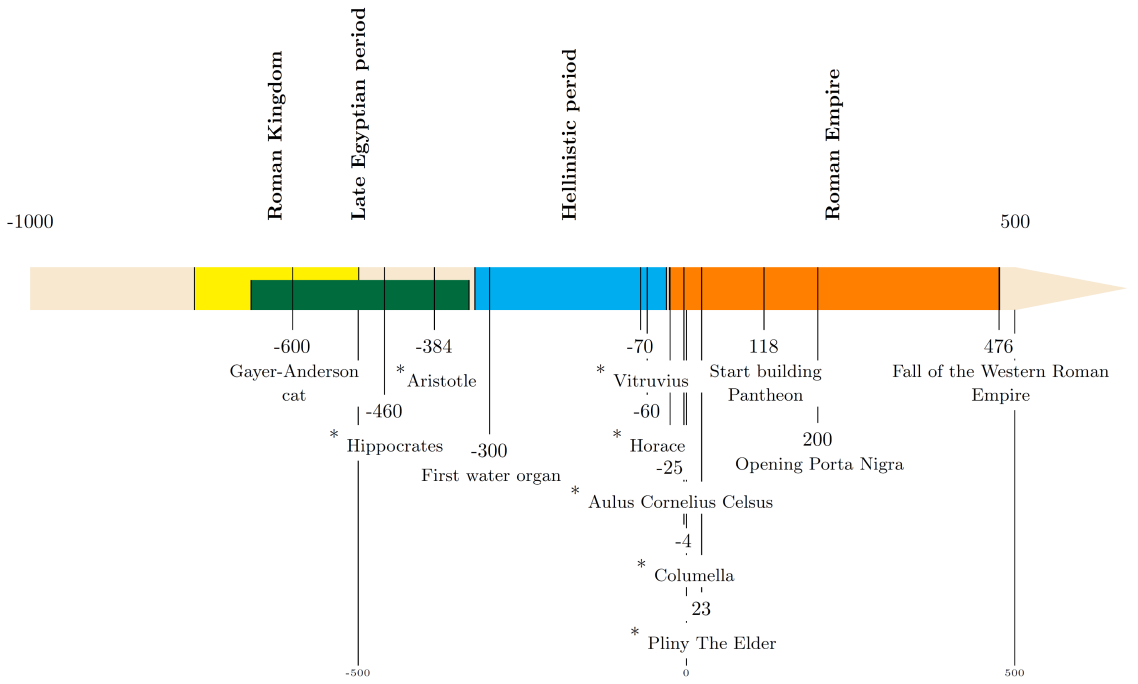


Figure. 1.2 – Overview of the periods, events and people from the Greek and Roman period

predominantly copper alloys. However, the alloys consist of fairly high levels of lead which means that in the Late Roman period, many military fittings (in particular legionary and cavalry equipment) were made from leaded bronzes [57]. Lead metal was also used by the Romans to construct their warships. The part of the ship touching the water was covered with lead sheathing to protect the ship from corroding [58]. For the anchor, Romans used a massive lead block to add weight [59]. Roman galleys were filled with lead braziers, probably the only devices on board for cooking [60], lead containers for storing liquids, and other lead kitchenware [61]. Also other massive lead items such as seaming seals, lead cooking pots and parts of a bilge-pump system like pipes and joints have been recovered along the coast of Israel from Roman shipwrecks [62]. Additionally, because of the intensive use of lead, lead cargo was often carried in the form of ingots which have been recovered from some wrecks [61]. Lots of these Roman lead ingots produced in Augustan-Tiberian Germania were discovered in two Roman shipwrecks in the Mediterranean [63]. On some of the ingots, the inscriptions cited the manufacturer and the provenance of the lead [64].

"Flavi Veruclae plumb(um) Germ(anicum)" or "Augusti Caesaris Germanicum"

1.4.2 Monetary

In general, the use of lead for the production of coins was rare. In the Hellinistic period (323 B.C. - 31 B.C.), however, lead currency became more popular [65]. By Roman law, lead coins were actually forbidden, but in some places in the Roman Empire like Egypt, Roman Gaul and North Africa, lead coins were issued. Lead metal was often used to debase gold or silver coins, and as a component of alloys, particularly bronze, where it often constituted 1 - 20 percent of the metal [66]. For example, the coin cabinet of the Kunsthistorisches Museum in Vienna holds a large collection of ancient Greek bronze coins with a high lead content produced in the Greek speaking provinces of the Roman Empire up to ca. 280 A.D. [67]. Also in the Greek and Roman period lead *tesserae* or tokens, coin-shaped objects that were minted on one side, circulated in various regions and cities and acquired monetary status [68, 69]. Lead coin-shaped artifacts were found by Burachkov [70] in Tauric Chersonesos during excavations and were labeled as 'lead medals'. Only later on, a discussion by Kovalenko [71] regarded them as coins.

1.4.3 Water supply

Often Roman and Greek cities were supplied with water from a nearby source using aqueducts built with a downhill gradient [72]. To cross a valley, ancient engineers predominantly built bridges to transport the water in lead pipes [73]. Another method was the construction of inverted siphons to convey water across valleys using Archimedes' understanding of hydrostatics and the water and air pressure [74]. The aqueduct of Pergamon (Turkey) consisted of lead pipes and was the first one to use this principle of communicating vessels [75]. The main aqueduct ends at the distribution tank called the *castellum divisorium*, which is the junction where the urban distribution system begins. Lead pipes were used to transport the water to a water tower or *secondary castellum* from where lead pipes branched the supply to individual customers [76]. In Nîmes (France), for example, the water was distributed through 13 large lead pipes. To distribute water to houses and baths in the city, pipes of lead, ceramic, wood or leather have been used [72]. The Roman architect, Vitruvius, mentioned the use of lead pipes to Pompeii and Herculaneum [77]. The supply system was mainly used to provide large quantities of water for public baths and fountains, but also for drinking water and private bath houses [72]. This way of transporting water, however, leads to a high lead concentration in the drinking water due to the corrosion of the lead plumbing. Exposure to these high lead concentrations is considered dangerous [49]. The hardness of Rome's water (320 ppm $CaCO_3$), however, tells us that it is unlikely that enough lead was dissolved to produce lead poisoning, which means other lead sources were more harmful [78]. A famous Roman writer, Horace (1st century B.C.), mentions the purity of water in relation to lead piping. In a letter to an old friend, he compared the purity of town water to fresh countryside water [79].

"Purior in vicis aqua tendit rumpere plumbum quam quae per pronum trepidat cum murmure rivum?"
(Horace Epistulae I, X, 20-21).

Additionally Vitruvius recognized the health risk and proposed using earthenware pipes [77]. As seen in the text, the Romans used the Latin word *Plumbum* to denote lead. A person who joins and mends pipes is called a plumber or *plumbarious*, which literally translates to 'A person working with lead' [80]. *Plumbum* is also the reason for the chemical symbol for lead, Pb. Another way of getting water was the use of leaden cisterns, which allowed rain water storage. A Roman cylindrical lead cistern was excavated close to Roman settlement in Lickfold (UK) [81].

1.4.4 Food and drinks

In the daily food and drinks of the Romans and Greeks extremely high lead levels were found [82]. Food poisoning causing sterility, infertility and stillbirths, is a consequence of the use of lead as a building material for their food-storage containers, as preservative (lead is a microbicide) [83] or as food colorant [49]. Romans used, among others, an artificial sweetener, sugar of lead or lead(II)acetate ($Pb(CH_3COO)_2$), a poisonous crystalline solid, to sweeten and preserve their foods [84]. They made this by adding acetic acid (vinegar) to litharge [85]. Looking at the 450 recipes in the Roman Apician Cookbook, a collection of fifth century recipes attributed to gastrophiles associated with Apicius, the famous Roman gourmet, one notices that one-fifth of the recipes contains lead products [85]. Moreover to make wine, the Romans only used lead vessels or lead-lined copper kettles to boil the grapes [86]. In copper pots, the formation of copper acetate (verdigris) ensures a caustic astringent taste [87]. This is described in the book 'De Re Rustica' written by the Roman winemaker Columella, where he writes

"Ipsa autem vasa, quibus sapa aut defrutum coquitur, plumbea potius quam aenea esse debent. Nam in coctura aeruginem remittunt aenea, medicaminis saporem vitiant."
(De re rustica VII, XX, 3-4 [88]).

which freely translates to "[t]he vessels themselves in which the thickened and boiled-down must is boiled should be of lead rather than of brass; for, in the boiling, brazen vessels throw off copper rust, and spoil the flavor of the preservative" [89]. Actually Romans only used lead because they had the habit to drinking their wine as sweet as possible to add more flavor [90]. In this case, lead acetate seeps out of the lead and forms poisonous crystals at the bottom of the lead pot [89].

1.4.5 Household and art

The Greeks and Romans also used lead to manufacture items for household or decorative purposes [49]. Roman domestic equipment is usually divided into wares and fine wares, where the former indicates everyday earthenware (such as terracotta) jars, dishes and bowls used for cooking or storage and transport of foods or other goods [91]. The more decorative and elegant fine wares were used for formal dining [92]. The most common late Hellinistic and early Roman period fine ware was a lead-glazed hemispherical bowl or *skyphos* [93]. Also Roman *amphorae*, used as storage vessels, were glazed using lead compounds [89]. Chemical analyses of five sherds of green glazed pottery excavated in the Canosa area (Italy) contained 70% of PbO in the glaze layer [94]. At a Roman cemetery near Zadar (Croatia), 900 pieces of Roman glass vessels were found in good condition. A fast XRF analysis showed the use of litharge as an additive to the glass [95].



Figure. 1.3 – The roof of the Pantheon in Rome is made out of lead sheets. © M. De Keersmaecker

[3]

Jewelry was worn by both Roman and Greek women to show how wealthy their family was. Wealthy families could afford jewelry made of gold or silver, while ordinary jewelry was made of cheaper metals like lead, tin or copper [96]. Kuleff et al. [97] investigated 53 lead artifacts including finger rings, earrings and some cult figures dated around the Hellinistic period (Thracia) using inductively coupled plasma atomic emission spectroscopy (ICP-AES), atomic absorption spectroscopy (AAS) and inductively coupled plasma mass spectrostrometry (ICP-MS).

Oxidized lead products were used frequently as paints and white pigment in make-up powders and other cosmetics by the women in the Greco-Roman period [98]. X-ray diffraction (XRD) analysis conducted by Welcomme et al. [98] made clear that the white pigments consist of hydrocerussite ($2\,PbCO_3 \cdot Pb(OH)_2$) and cerussite ($PbCO_3$). The analyses of Roman cosmetics from Pompeii, Gaul and Germany indicate the use of gypsum ($CaSO_4 \cdot 2\,H_2O$) or calcite. Using Raman spectroscopy, Aliatis et al. [99] acknowledged that pigments used in Roman wall paintings preserved in the Vesuvian area contained cerussite, minium and litharge.

In history lead sheets are used as roof coverings for buildings, but also as statue sockets [42]. A well-known example is the exterior of the Hadriatic concrete dome of the Pantheon (Rome), which is covered with lead roofing by Emperor Constans II in 663 (see Figure 1.3) [100]. Also the Porta Nigra in Trier (Germany) contains seven tons of lead [101]. Closer to home, the outside of cultural center of Bonheiden, built in the 20st century, is covered with lead plates [102].

1.4.6 Poison and medicine

One of the earliest occupational diseases contracted by mankind was lead poisoning due to exposure to lead [103]. During the time of Roman occupation about 80,000 workers engaged in the mining and smelting of lead were occupationally

exposed to lead each year [104]. Furthermore, generations of artisans throughout antiquity worked with this dangerous metal [103]. In ancient times, other people were constantly exposed to lead contaminated fermented beverages, food and drinking water [105]. As a preservative, 20 mg of lead was added to one liter of wine [106], which is 10 times the dose sufficient to produce lead poisoning [107]. Still, the skeletal lead content in the Roman era peaked at a level only 41 - 47% of that of modern Europeans [83]. Eventually, as mysterious maladies became more common, some Romans and Greeks began to suspect a connection between the metal and these illnesses [108]. The Greek physician Hippocrates (460 - 377 B.C.) described the symptoms of lead poisoning as appetite loss, colic, pallor, weight loss, fatigue, irritability, and nervous spasms [109]. The Romans called the disease *saturnine gout* or saturnism, because they noticed similarities between symptoms of this disorder and the irritable god [110]. Of the Romans, Vitruvius (1st century B.C.) mentions that water impregnated with lead was injurious in his book 'De Architectura'

"Etiamque multo salubrior est ex tubulis aqua quam per fistulas, quod plumbum videtur esse ideo vitiosum, quod ex eo cerussa nascitur; haec autem dicitur esse nocens corporibus humanis."
(De Architectura IIX, VI, 10-11) [111]

which translates to "[w]ater conducted through earthen pipes is more wholesome than that through lead; indeed that conveyed in lead must be injurious, because from it white lead is obtained, and this is said to be injurious to the human system." [112, 113]

Sometimes lead was also used to treat diseases. Even in ancient times, the effects of lead on various functions of the human reproductive system were known [105]. Lead is, for example, known to be a very effective spermicide [114]. In his text *Historia Animalium*, Aristotle [115] mentions that women used a lead ointment as contraceptive. A Greek physician, Soranus of Ephesus, writes about a contraceptive ointment recipe based on lead in his book *Gynaecology* [116]: "Conception is prevented by smearing the mouth of the womb with old (sour) oil or honey or cedar gum or opobalsam, either alone or mixed with cerussite (white lead), or with ointment which is prepared with myrtle oil and cerussite." In his encyclopedia, published ca. 77 - 79 A.D., Pliny explains the use of lead plates for cooling the heat of fleshly lust [117]. Lead salts were also used to treat ulcers, abscesses and indurations of the breast as described by Celsus [105]. Hippocrates mentions the use of leaden tubes for intra-uterine medication and Celsus discusses using them for insertion in the rectum and vagina to prevent postoperative cicatricial contractions and adhesions [105]. The ancient Greeks emptied the bladder by inserting a lead or copper tube through the urethra, which is now called a *catheter* [118]. There is also evidence for the use of leaden (or lead-tainted) mortars, pestles, medicament jars, and dispensatories [89].



Figure. 1.4 – The lead glass window of the Ste Croix Cathedral in Orléans. © M. De Keersmaecker

1.5 The middle ages

First of all, an overview of the events and periods described in the following sections from the beginning of the Middle Ages is given in Figure 1.5. In medieval times, lead was used for ammunition, roofing, coffins, cisterns, tanks, and

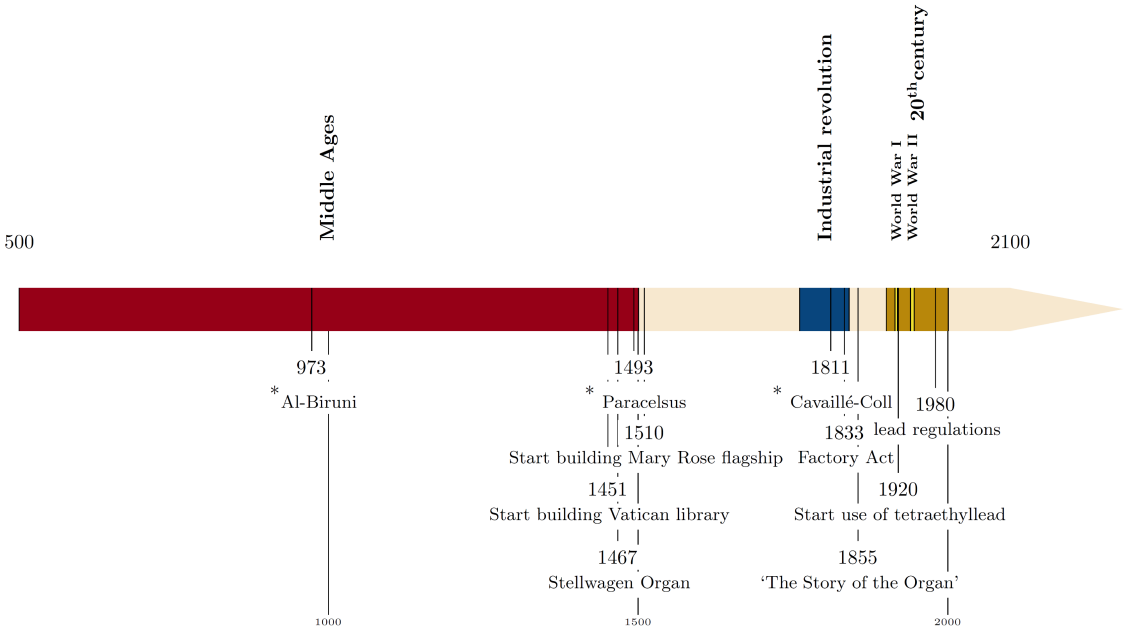


Figure. 1.5 – Overview of the periods and events starting from the begin of the Middle Ages.

gutters, and for statues, ornaments, coins, medallions and paints. An important paleo-metallurgical site of Europe for lead smelting is found at the Mont-Lozére, testifying to mining activities in this area during medieval times [119]. Spier [120] also cataloged a collection of medieval Byzantine lead pendants and amulets circulating in museums around the world. Furthermore, lead pigments such as lead-tin yellow and lead antimonate were used in medieval paintings and manuscripts [121, 122]. In the Middle Ages, lead was frequently used to treat several diseases [105]. A Swiss-German physician, Paracelsus, was known to be the first toxicologist and recommended the use of lead acetate for the treatment of gonorrhea [123]. Al-Biruni, a Persian scholar, suggests a treatment of ulcers, testicular wounds and inflammations with lead oxides [124]. Additionally lead found a new use in the greatest advancement of the 15th century, the printing press [125]. In the world of fashion, white lead is used as a cosmetic to give woman a white pallor to the face in 15th - 16th century [126].



Figure. 1.6 – Wall paintings from the Bibliotheca Apostolica Vaticana in Rome. © M. De Keersmaecker

Furthermore, in the 16th century, lead was wrapped around a rough cube of cast iron to be used as a shot on the Mary Rose, the flagship of King Henry VIII [127]. During the same period, stained glass windows held together by lead frames decorated medieval churches (see Figure 1.4) [128], and architects used lead to seal spaces between stone blocks and to frame roof installations [129]. Wedepohl and Baumann [130] examined the composition of 26 lead medieval glass samples, made in the 13th - 14th century, retrieved from various locations in Europe. All samples contained between 65 to 74% PbO. In addition to glass, lead was also used in paints. A beautiful example, shown in Figure 1.6, are the wall paintings from the Bibliotheca Apostolica Vaticana in Rome filled with 'lead white' containing cerussite, hydrocerussite and also minium Pb_3O_4 [131].

Another very important application of lead in this period is the production of lead-tin pipe organs in churches because

of their good sound characteristics [132]. Indeed, pipe organs have always played an important role in the world of music. Often, for example, prayers are accompanied by organ music [133]. The term 'organ' comes from the Greek word 'organon' and Latin word 'organum', which basically means 'tool' or 'instrument' [134]. Ctesibius of Alexandria, a musician and engineer who lived around 200 B.C., is generally credited with building the first pipe organ, the hydraulis [134], which Charles Francis Abdy Williams described as follows in 'The Story of The Organ' (1903) [135].

"About 284 to 246 B.C. there lived at Alexandria, under Ptolemy Euergetes, a man named Ctesibius, who followed his father's trade of barber. Being of a mechanical turn of mind, he observed that the counterweight of a movable mirror, used for the purposes of his trade, produced a musical sound by the force with which it drove the air out of the tube in which it moved. Experimenting with the principle thus noticed, he succeeded in making a machine consisting of a hollow vase inverted, with an opening on the top, to which was attached a trumpet, and, on water being pumped into the vase the air was driven forcibly through the trumpet, producing a very powerful sound; and the machine caused so much admiration that it was consecrated in the temple of Venus."



Figure. 1.7 – The romantic grand Cavaillé-Coll organ in the Ste Croix Cathedral of Orléans. © M. De Keersmaecker

Perrot [136] defines that a pipe organ consists of one or more ranks of sounding pipes, a wind chest to store air, a mechanical blower and a keyboard to direct the air into its various pipes. When playing the organ, the pressurized air is stored in a wooden wind chest until the player causes it to be released by operating a sliding mechanism that allows the air to be forced into selected pipes resulting in sound [137]. Normally, a pipe organ consists of hundreds to thousands of pipes which can be selected together or individually [138]. The sound emanates from an assemblage of pipes made of metal such as tin, lead, antimony, zinc and sometimes copper or various kinds of wood [139]. The form of the pipes, which can be round, square, long, short, broad or narrow, depends on the sound the organ builder wants to create. Of all the materials mentioned, the organ builders preferred to use tin because of its great durability, silver color, lightness and flexibility. Furthermore, tin is less susceptible to temperature changes and tarnishing [140]. The only disadvantage of tin was its price [141]. The romantic grand organ, of the French organ builder Cavaillé-Coll, in the Ste Croix cathedral of Orléans, depicted in Figure 1.7, is an organ composed of four keyboards, a pedal for a total of 54 sets and more than 3700 pipes made of first choice tin [142]. Aristide Cavaillé-Coll and other famous organ builders such as Eberhard Friedrich Walcker and Henry Willis are responsible for many innovations that revolutionized organ building, performance and composition [143, 144]. Most of the time, however, organ pipes are manufactured using a wide range of lead-tin alloys, from nearly pure lead to nearly pure tin sheets [145]. The tin content varies usually from about 30% to 90% [146]. For example, German organ builders distinguished between *pure tin* and *tin*. *Pure tin* explains itself; but *tin* indicates that no more than $\frac{1}{4}$th of the total weight is alloyed metal, which is the most highly prized metal for making organ pipes [146]. Often, the front pipes of an organ were made from an alloy with a higher tin content [147]. In England, the tin concentrations in the organ pipes were higher because the English tin mined in Cornwall, the favorite material of most organ builders, was cheaper [148, 149]. A well-known example is John Loosemore's organ located at the Exeter Cathedral in Devon close to Cornwall, which consists of pure tin pipes [150]. Mostly organ builders use a mixture of $\frac{1}{2}$ tin and $\frac{1}{2}$ lead, a compromise between price and quality of the pipe, which

they call (spotted) *metal* [100]. It is also worth mentioning that the amount of tin defines the pipe's tone, since tin is the most tonally resonant of all metals [140]. Lead, on the other hand, gives a more 'hollow' sound [151]. Therefore, the composition of the pipe also depends on the tone the organ builder wants to obtain [152]. Pure lead or lead with a slight admixture of tin is considered worthless as a material for metal organ pipes [153].

Often the material can affect the geometry depending on the pipe type (see Figure 1.8) [141]. Thicker sheets are necessary to compensate the lead's natural softness and render bodies of flue pipes so heavy that they are easily deformed from the weight [140]. Especially deformations around the mouth area change the formed sound oscillations. The tubes of reed pipes are very vulnerable around the vibrating copper tongue at the narrow end [154]. However, pipes with a high lead concentration are frequently used for the production of organs. All the pipes of the old organ of the Nicolai church in Utrecht have been replaced by lead pipes [155]. Furthermore, the 1467 Stellwagen organ in the Ste Jakobi church in Lübeck (Germany) is made of lead with low tin concentrations [154].

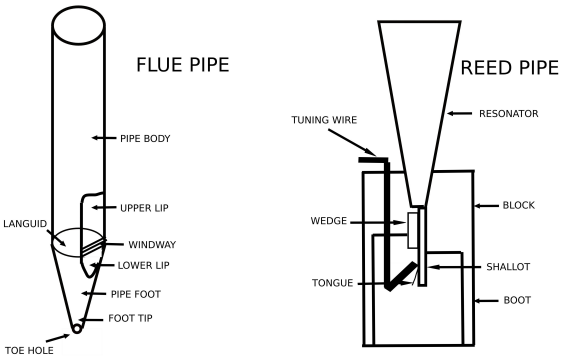


Figure. 1.8 – Mechanism of flue and reed pipe. © Cavasant Frères

We can conclude that the production of the pipe organs combines skills in woodworking and metallurgy with knowledge of mechanics and pneumatics [100]. The organ is therefore a costly and unique inheritance that forms an important part of our common sounding cultural heritage [156]. Today, more than 10,000 historical pipe organs, some of which were built more than 500 years ago, can be found in churches all over Europe [145]. Despite the pipe organ's enormous importance, most of these organs are corroding in the churches. Most of them are in need restoration and conservation as soon as possible [157].

1.6 The industrial revolution: an increase in lead production

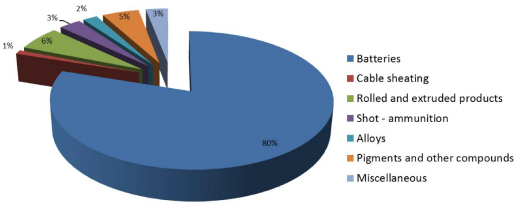


Figure. 1.9 – Different end uses of lead. ©Gravita Engineering & Technology

The start of the industrial revolution in Europe accelerated the use of lead, which resulted in an elevated amount of lead in the environment and the ecosystem [158]. Indeed, a clear increase in the lead isotope concentrations was measured in peat bogs by Shotyk et al. [1] and Weiss et al. [159]. This increase was a consequence of some new uses of lead during the industrial revolution, such as the manufacturing of ammunition and glassware and the advances in printing processes [160]. Around 1750, European and British lead smelting operations also started flourishing [161]. Often, women and children were also employed indiscriminately in lead processes such as pottery glazing and lead compounds manufacturing [162].

The huge increase in lead demand caused by the industrial revolution caused various industrial diseases, of which the most widespread was lead poisoning [163]. For example, the production of lead white, $2\,PbCO_3{\cdot}Pb(OH)_2$, by exposing lead metal to acetic acid vapors, was very hazardous because of the continuous handling of the metal [164]. Starting from the 1830s, prescribed standards were bundled in the Factory Act to protect the factory workers [165], after which

the pigment was shaken and ground mechanically [164]. Lead white paints obtain up to 50% lead [166].

1.7 Lead in the 20th century

Prior to the early 1900s, lead was used primarily in ammunition, burial vault liners, ceramic glazes, leaded glasses, crystals, paints or other protective coatings, pewter, water lines and pipes. Following World War I, the demand for lead increased because of the growth in the production of motorized vehicles, many of which require lead-acid batteries to start their engines [167]. Around the 1920s, lead was added to gasoline in the form of tetraethyllead, $(CH_3CH_2)_4Pb$, to boost the octane levels and reduce the sound of engine-knocking [168]. The combustion of this leaded gasoline turned out to be responsible for a large part of the air-polluting lead by-products, causing a considerable international alarm [158]. According to the Agency for Toxic Substances and Disease Registry, environmental levels of lead have increased more than a 1,000-fold over the past three centuries as a result of the human activity on earth [169]. Consequently, governments all over the world established federal regulations and made recommendations to limit lead emissions to protect public health.

By the mid-1980s, a significant shift in the uses of lead had taken place as a result of compliance with environmental regulations and the substitution of other materials for lead in non-battery products, such as gasoline, paints, solders, and water systems. Even today, despite its toxic properties, lead in various forms is one of the four most extensively exploited metals. To clarify, a list of potential uses is given (see reference graph in Figure 1.9) [80, 100, 170].

- the ballast keel of sailboats and scuba diving weight belts, due to its high density
- glazing bars for stained glass
- white lead, which is used in the production of lead crystal glass
- projectiles for fishing sinkers and firearms (ammunition)
- white lead, lead sulfate and lead chromate, which are used as coloring elements in paints and ceramic glazes
- sheets utilized in the construction industry for weathering, roofing and cladding to prevent water penetration
- sheets for the lining of chemical treatment baths, acid plants and storage vessels
- sheets for sound insulation and radiation shielding (in medical applications using X-rays)
- organ pipes with variable amounts of tin to control the tone of the pipe
- soldering and as electrodes in the process of electrolysis
- high voltage power cables as a sheathing material to prevent water diffusion into insulation
- statues, sculptures and their moldings are used as decorative motifs
- tetra-ethyl lead, which is utilized as an anti-knock additive for aviation fuel
- lead based semiconductors are used in photo voltaic (solar energy) cells and infrared detectors
- construction of roofing materials
- molten lead, which is used to cool certain types of nuclear reactors
- lead isotopes are used for medical and scientific purposes.

References for Chapter 1

[1] W. SHOTYK et al., History of atmospheric lead deposition since 12,370 ^{14}C yr BP from a peat bog, Jura mountains, Switzerland, *Science* **281** (5383) (1998), 1635–1640.

[2] H. WALDRON, Lead poisoning in the ancient world, *Med. Hist.* **17** (4) (1973), 391–399.

[3] D. HESKEL, A model for the adoption of metallurgy in the ancient Middle East, *Curr. Anthropol.* **24** (3) (1983), 362–366.

[4] N. GALE and Z. STOS-GALE, Lead isotope studies in the Aegean, *Proc. Br. Acad.* **77** (1991), 63–108.

[5] N. GALE and Z. STOS-GALE, Lead and silver in the ancient Aegean, *Sci. Amer.* **244** (1981), 176–192.

[6] D. POTTS, *A companion to the archaeology of the ancient Near East*, John Wiley & Sons, 2012, 303.

[7] R. PUMPELLY, *Explorations in Turkestan: Prehistoric civilizations of Anau*, Carnegie Institution of Washington, 1908, 239.

[8] H. MATTHEWS, R AND FAZELI NASHI, *The neolithization of Iran*, Oxbow Books, 2013, 235.

[9] N. NEZAFATI and E. PERNICKA, Early silver production in Iran, *Iran. Archaeol.* **3** (2012), 37–45.

[10] E. BORSOS et al., Anthropogenic air pollution in the ancient times, *Acta Climatol. Chronol.* **36-37** (2003), 5–15.

[11] K. WEEBER, *Smog über Attika: Umveltverhalten im Altertum*, Artemis-Verlag, 1990.

[12] P. MOOREY, *Materials and manufacture in ancient Mesopotamia: The evidence of archaeolgy and art. Metals and metalwork, glazed materials and industries*, Clarendon Press, 1985, 125.

[13] G. LE ROUX et al., Recent atmospheric Pb deposition at a rural site in southern Germany assessed using a peat core and snowpack, and comparison with other archives, *Atmos. Environ.* **39** (36) (2005), 6790–6801.

[14] R. FORBES, *Metallurgy in antiquity: A notebook for archaeologists and technologists*, Brill Archive, 1964, 172–173.

[15] V. COSTA and F. URBAN, Lead and its alloys: Metallurgy, deterioration and conservation, *Rev. Conserv.* **6** (2005), 48–62.

[16] R. ALPHER and R. HERMAN, The primeval lead isotopic abundances and the age of the earth's crust, *Phys. Rev.* **84** (6) (1951), 1111–1114.

[17] H. GARLAND and C. BANNISTER, *Ancient Egyptian metallurgy*, Charles Griffin & Company, 1927, 32.

[18] A. LUCAS and J. HARRIS, *Ancient Egyptian materials and industries*, Dover Publications, 2012, 243.

[19] Z. STOS-GALE and N. GALE, Sources of galena, lead and silver in predynastic Egypt, *Rev. d'Archéométrie* **1** (1981), 285–296.

[20] A. HASSAN and F. HASSAN, Sources of galena in predynastic Egypt at Nagada, *Archaeometry* **23** (1) (1981), 77–82.

[21] W. PETRIE and LONDON UNIVERSITY COLLEGE, *Objects of daily use*, Aris & Philips, 1927, 1–74.

[22] J. WILKINSON, *A popular account of the ancient Egyptians*. Oxford University Press, 1854, 162.

[23] R. BRILL et al., *Lead-isotope analyses of some objects from Egypt and the Near East, in studies in early Egyptian glass*, ed. by C. LILYQUIST, R. BRILL, and M. WYPYSKI, Metropolitan Museum of Art, 1993, 59–76.

[24] K. YENER et al., Stable lead isotope studies of central Taurus ore sources and related artifacts from eastern Mediterranean Chalcolithic and Bronze Age sites, *J. Archaeol. Sci.* **18** (5) (1991), 541–577.

[25] J. AMBERS et al., A new look at an old cat: A technical investigation of the Gayer-Anderson cat, *Tech. Res. Bull.* **2** (2008), 1–12.

[26] A. ATTENBURROW et al., Surma and blood lead levels in Asian children in Glasgow, *Lancet* **315** (8163) (1980), 323.

[27] R. FAULK and J. GRAY, Getting the lead out? The misuse of public nuisance litigation by public authorities and private counsel, in: *Toxics law reporter*, The Bureau of National Affairs, 2006, 7.

[28] C. GORDON et al., *Boundaries of the ancient Near Eastern world*, A&C Black, 1998.

[29] L. LESKO, *A dictionary of Late Egyptian*, Scribe Publications, 1982, 260.

[30] E. GORING et al., *Chief of Seers: Egyptian studies*, Routledge, 1997, 292.

[31] W. HAYES, *The scepter of Egypt*, Plantin Press, 1959, 297.

[32] C. PULAK, The balance weights from the Late Bronze Age shipwreck at Uluburun, in: *Metals Make the World Go Round*, Oxford University Press, 2000, 247–266.

[33] N. WILSON, *Encyclopedia of ancient Greece*, Routledge, 2013, 661.

[34] W. HENDERSON, *Main group chemistry*, Royal Society of Chemistry, 2000, 79–80.

[35] Z. STOS-GALE and N. GALE, The sources of Mycenaean silver and lead, *J. Field Archaeol.* **9** (4) (1982), 467–485.

[36] N. GALE, W. GENTNER, and G. WAGNER, The minerogical and geographical silver sources for archaic Greek coinage, *Metall. Numis.* **1** (1980), 3–49.

[37] N. GALE and Z. STOS-GALE, Ancient Egyptian silver, *J. Egypt. Archaeol.* **67** (1981), 103–115.

[38] P. CRADDOCK, *Early metal mining and production*, Edinburgh University Press, 1995, 213.

[39] M. IVANOVA, *The Black Sea and the early civilizations of Europe, the near East and Asia*, Cambridge University Press, 2013, 90.

[40] G. RAPP, *Archaeomineralogy*, Springer, 2009, 153.

[41] J. HUGHES, *Environmental problems of the Greeks and Romans: Ecology in the ancient Mediterranean*, John Hokins University Press, 2014, 139.

[42] M. BODE, A. HAUPTMANN, and K. MEZGER, Tracing Roman lead sources using lead isotope analyses in conjunction with archaeological and epigraphic evidence - a case study from Augustan/Tiberian Germania, *Archaeol. Anthropol. Sci.* **1** (2009), 177–194.

[43] J. HENDERSON, *The science and archaeology of materials: An investigation of inorganic materials*, Routledge, 2013, 238.

[44] P. MUSHAK, *Lead and public health: Science, risk and regulation*, Elsevier, 2011, 900.

[45] D. SETTLE and C. PATTERSON, Lead in albacore: Guide to lead pollution in Americans, *Science* **207** (4436) (1980), 1167–1176.

[46] J. TSCHEN-EMMONS, Artifacts from ancient Rome, PhD thesis, University of California, 2014, 161.

[47] J. EMSLEY, *Molecules at an exhibition: Portraits of intriguing materials in everyday life*, Oxford University Press, 1998, 216–218.

[48] A. CINCOTTI, L. MASSIDDA, and U. SANNA, Chemical and isotope characterization of lead finds at the Santa Barbara nuraghe (Bauladu, Sardinia), *J. Cult. Herit.* **4** (4) (2003), 263–268.

[49] S. CHEW, *World ecological degradation: Accumulation, urbanization and deforestation*, Altamira Press, 2001, 91.

[50] J. NRIAGU, Saturnine gout among Roman aristocrats. Did lead poisoning contribute to the fall of the Empire?, *N. Engl. J. Med.* **308** (1983), 660–663.

[51] M. GUARUCCI, *L'epigrafia greca dalle origini al tardo impero*, Libreria dello Stato, 1987, 238.

[52] W. PRITCHETT, *The Greek state at war*, University of California Press, 1974, 43–49.

[53] S. GREEP, Lead sling-shot from Windridge farm, St Albans and the use of the sling by the Roman army in Britain, *Brittania* **18** (1987), 183–200.

[54] DURALI-MÜLLER, Roman lead and copper mining in Germany, PhD thesis, University of Frankfurt/Main, 2005, 1–147.

[55] A. CELSUS, L. TARGA, and J. RODE, *Aulus Cornelius Celsus on medicine: In eight books*, ed. by A. LEE, Harold E. Cox, 1831, 238.

[56] S. BLACKSHAW and V. DANIELS, The testing of materials for use in storage and display in museums, *Conserv.* **3** (1) (1979), 16–19.

[57] A. RUSHWORTH, *Housesteads Roman fort - thre grandest station: Excavation and survey at housesteads*, English Heritage Publishing, 2014, 583.

[58] Y. KAHANOV, Some aspects of lead sheathing in ancient ship construction, in: *Tropis V*, ed. by H. TZALAS, Hellenic Institute for the Preservation of Nautical Tradition, 1999, 197–206.

[59] KAPITÄN, Greco-Roman anchors and the evidence for the one-armed wooden anchor in antiquity, in: *Marine Archaeology*, Archon Books, 1973, 383–396.

[60] E. GALILI and J. SHARVIT, Ship fittings and devices used by ancient mariners: Finds from underwater surveys off the Israeli coast, in: *Tropis V*, Hellenic Institute for the Preservation of Nautical Tradition, 1993, 167–183.

[61] S. KINGSLEY and K. RAVEH, *The ancient harbor and anchorage at Dor, Israel (Results of underwater surveys 1976-1991)*, Tempus Reparatum, 1996, 28.

[62] B. ROSEN and E. GALILI, Lead use on Roman ships and its environmental effects, *Int. J. Naut. Archaeol.* **36** (2) (2007), 300–307.

[63] L. LONG and C. DOMERGUE, Le véritable plomb de L. Flavius Verucla et autre lingots, *MEFRA* **107** (1995), 801–867.

[64] P. ROTHENHÖFER, Geschäfte in Germanien. Zur Ausbeutung von Erzlagerstätten unter Augustus in Germanien, *Z. Papyrol. Epigr.* **143** (2003), 277–286.

[65] O. MØRKHOLM, P. GRIERSON, and U. WESTERMARK, *Early Hellenistic coinage from the accession of Alexander to the peace of Apamaea (336-188 B.C.)* Schocken Books, 1991, 371–374.

[66] J. BOULAKIA, Lead in the Roman World, *Am. J. Archaeol.* **76** (2) (1972), 139–144.

[67] M. GRIESSER et al., Application of X-ray and neutron tomography to study antique Greek bronze coins with a high lead content, *Mater. Sci. Eng.* **37** (2012), 1–5.

[68] Y. FARHI, City coins from Roman Palestine made of lead and comparable materials, in: *Israel Numismatic Journal*, Old City Press, 2010, 177–186.

[69] P. MATTIAS, G. MAURA, and G. RINALDI, The degradation of lead antiquities from Italy, *Stud. Conserv.* **29** (1984), 87–92.

[70] P. BURACHKOV, *General catalogue of the coins of the ancient Hellinistic colonies of the Northern Black Sea coast*, Odessa, 1884, 118.

[71] S. KOVALENKO, Struck lead pieces from Tauric chersonesos: Coins or tesserae, *The Numastic Chronicle* **162** (2002), 33–58.

[72] L. ADKINS and R. ADKINS, *Handbook to life in ancient Rome*, Infobase Publishing, 2004, 144.

[73] S. MITHEN, *Thirst: For water and power in the ancient world*, Harvard University Press, 2012, 133.

[74] L. MAYS, *Ancient water technologies*, Springer, 2010, 16.

[75] J. ADAM, *Roman building: Materials and techniques*, Routledge, 2005, 490.

[76] L. MAYS, D. KOUTSOYIANNIS, and A. ANGELAKIS, A brief history of urban water supply in the antiquity, *Water Sci. Technol. Water Supply* **7** (1) (2007), 1–12.

[77] W. JASHEMSKI and F. MEYER, *The natural history of Pompeii*, Cambridge University Press, 2002, 34–35.

[78] L. AMULREE, Hygienic conditions in ancient Rome and modern London, *Med. Hist.* **17** (1973), 244–255.

[79] A. DE PRETIS, *Epistolarity in the first book of Horace's epistles*, Gorgias Press, 2004, 241.

[80] S. WATT, *Lead*, Marshall Cavendish, 2001, 5 / 26.

[81] E. CURWEN, Roman lead cistern from Pullborough, Sussex, *Ant. J.* **23** (3-4) (1943), 155–157.

[82] R. CORNELIS, *Handbook of elemental speciation*, John Wiley & Sons, 2005, 252–271.

[83] F. RETIEF and L. CILLIERS, Lead poisoning in ancient Rome, *Acta Theol.* **26** (2) (2006), 147–164.

[84] L. HOUGH and J. EMSLEY, The shape of sweeteners to come, *New Scientist* **1513** (1986), 48–51.

[85] J. EMSLEY, *The elements of murder: A history of poison*, Elsevier, 2006, 286.

[86] H. JOHNSON, *The story of wine*, Touchstone, 1992, 297.

[87] H. WATTS, *A dictionary of chemistry and the allied branches of other sciences*, Van Nostrand Reinhold, 1872, 716.

[88] L. COLUMELLA and J. GESNER, *L. Junii Moderati Columella: De re rustica*, Cura & Sumptibus Societatis Literatae, 1781, 338.

[89] J. NRIAGU, *Lead and lead poisoning in antiquity*, John Wiley & Sons, 1983, 334 / 437.

[90] L. COLUMELLA, E. FORSTER, and E. HEFFNER, *On agriculture: Books X-XII*, Harvard University Press, 1955, 233.

[91] P. ARTHUR and G. MARSH, Early fine wares in Roman Britain, *Archaeol. J.* **137** (1) (1980), 482–483.

[92] I. HANSEN, R. HODGES, and S. LEPPARD, *Butrint 4: The archaeology and histories of an Ionian town*, Oxbow Books, 2013, 32.

[93] K. GREENE, Late Hellinistic and early Roman invention and innovation: The case of lead-glazed pottery, *Am. J. Archaeol.* **111** (4) (2007), 653–671.

[94] G. DE BENEDETTO et al., Investifation on Roman lead glaze from Canosa: Results of chemical analyses, *Archaeometry* **46** (4) (2004), 615–624.

[95] K. TANTRAKARN et al., Archaeological analysis of Roman glass excavated from Zadar, Croatia, by a newly developed portable XRF spectrometer for glass, *X-ray Spectrom.* **38** (2009), 121–127.

[96] C. HYNSON, *How people lived in ancient Greece*, Rosen Publishing Group, 2008, 30.

[97] I. KULEFF et al., Chemical and lead isotope compositions of lead artifacts from ancient Thracia (Bulgaria), *J. Cult. Herit.* **7** (4) (2006), 244–256.

[98] E. WELCOMME et al., Investigation of white pigments used as make-up during the Greco-Roman period, *Appl. Phys. A* **83** (4) (2006), 551–556.

[99] I. ALIATIS et al., Pigments used in Roman wall paintings in the Vesuvian area, *J. Raman Spectrosc.* **41** (2010), 1537–1542.

[100] S. GURUSWAMY, *Engeneering properties and applications of lead alloys*, CRC Press, 1999, 483.

[101] L. SCHWINDEN, Die Porta Nigra, in: *Das römantische Trier*, Theiss, 2001, 143–187.

[102] E. VAN EYCKEN, *Problemen met loden wandplaten van 't Blikveld*, Antwerp, 2009.

[103] B. LEVY, *Preventing occupational disease and injury*, American Public Health Association, 2005, 302.

[104] A. LANSDOWN, *The carcinogenicity of metals: Human risk through occupational and environmental exposure*, Royal Society of Chemistry, 2013, 429.

[105] H. NEEDLEMAN, *Human lead exposure*, CRC Press, 1991, 30.

[106] C. PATTERSON, H. SHIRAHATA, and J. ERICSON, Lead in ancient human bones and its relevance to historical developments of social problems with lead, *Sci. Total. Environ.* **61** (1987), 167–200.

[107] R. DREISBACH and W. ROBERTSON, *Handbook of poisoning: Prevention, diagnosis and treatment*, Appleton & Lange, 1987, 632.

[108] J. ERMATINGER, *The decline and fall of the Roman empire*, Greenwood Publishing, 2004, 60.

[109] M. LESSLER, Lead and lead poisoning from antiquity to modern times, *Ohio J. Sci.* **88** (3) (1988), 78–84.

[110] S. DALVI and M. PILLINGER, Saturnine gout, redux: a review, *Am. J. Med.* **126** (5) (2013), 450e1–480.e8.

[111] V. POLLIO and F. GRANGER, *Vitruvius, On architecture*, Harvard University Press, 1934, 188.

[112] I. ROWLAND and T. HOWE, *Vitruvius. Ten Books on Architecture*, Cambridge University Press, 1999, 352.

[113] M. POLLIO and J. GWILT, *The architecture of M. Vitruvius Pollio in ten books*, Woodfall, 1826, 255.

[114] N. HIMES, *Medical history of contraception*, Schocken Books, 1970, 553.

[115] R. SALLARES, *The ecology of the ancient Greek world*, Cornell University Press, 1991, 156.

[116] SORANUS and O. TEMKIN, *Soranus' gynecology*, John Hokins University Press, 1956, 258.

[117] H. PLINY THE ELDER, *Natural history*, Harvard University Press, 1938, 31.

[118] E. STRAUS and A. STRAUS, *Medical marvels: The 100 greatest advances in medicine*, Prometheus Books, 2006, 234.

[119] S. BARON et al., Medieval lead making on Mont-Lozère Massif (Cévennes-France): Tracing ore sources using Pb isotopes, *Appl. Geochem.* **21** (2006), 241–252.

[120] J. SPIER, Medieval Byzantine magical amulets and their tradition, *J. Warburg Courtauld Inst.* **56** (1993), 25–62.

[121] R. CLARK et al., Synthesis, structural characterisation and Raman spectroscopy of the inorganic pigments lead tin yellow types I and II and lead antimonate yellow: their identification on medieval paintings and manuscripts, *J. Chem. Soc., Dalton Trans.* **16** (1995), 2577–2582.

[122] P. VANDENABEELE et al., Pigment investigation of a late-medieval manuscript with total reflection X-ray fluorescence and micro-Raman spectroscopy, *Analyst* **124** (2) (1999), 169–172.

[123] L. STEVENSON, History of lead poisoning, PhD thesis, John Hopkins University, 1949.

[124] H. SAID, *Al-Biruni's book on pharmacy and materia medica*, Hamdard National Foundation, 1973, 376.

[125] E. RINGWALT, *American encyclopaedia of printing*, Menamin & Ringwalt, 1871, 311.

[126] S. DOWNING, *Beauty and cosmetics 1550-1950*, Shire Books, 2012, 13.

[127] R. WALKER and A. HILDRED, Manufacture and corrosion of lead shot from the flagship Mary Rose, *Stud. Conserv.* **45** (4) (2000), 217–225.

[128] O. MECKING, Medieval lead glass in central Europe, *Archaeometry* **55** (4) (2013), 640–662.

[129] J. BLAIR, W. BLAIR, and N. RAMSAY, *English medieval industries: Craftsmen, techniques, products*, A&C Black, 1991, 191.

[130] K. WEDEPOHL and A. BAUMANN, Isotope composition of Medieval lead glasses reflecting early silver prodcution in central Europe, *Miner. Deposita* **32** (1997), 292–295.

[131] G. CHIARI and R. LANZA, Remanent magnetization of mural paintings from the Bibliotheca Apostolica (Vatican, Rome), *J. Appl. Geophys.* **41** (1999), 137–143.

[132] T. CLARKE, Music and chemistry: Organ failure, *Nature* **427** (6969) (2004), 8–9.

[133] J. RICE, *Prayer: asking and receiving*, Sword of the Lord Publishers, 2000, 283.

[134] M. KHOSROW-POUR, *Systems and software development, modeling, and analysis: New perspectives*, IGI Global, 2014, 35–38.

[135] C. ABDY WILLIAMS, *The story of the organ*, Walter Scott Publishing, 1903, 316.

[136] J. PERROT, *The organ, from its invention in the Hellenistic period to the end of the 13th century*, Oxford University Press, 1971, xix.

[137] C. CAGLE, The pipe organ in early modern England, PhD thesis, Virginia Polytechnic Institute and State University, 2002.

[138] E. VANGUNDY, *How to start a organ tuning business*, MicJames, 2014, 3.

[139] J. SHANNON, *Understanding the pipe organ: A guide for students, teachers and lovers of the instrument*, McFarland Incorporated Publishers, 2009, 129–130.

[140] E. HOPKINS and E. RIMBAULT, *The organ, its history and construction*, Robert Cocks & Co., 1870, 98.

[141] N. FLETCHER and T. ROSSING, *The physics of musical instruments*, Springer, 1998, 571.

[142] RÉPUBLIQUE FRANÇAISE, *Orléans grand orgue Cavaillé-Coll cathédrale Sainte-Croix*, tech. rep., 2008.

[143] F. DOUGLASS, *Cavaillé-Coll and the French romantic tradition*, Yale University Press, 1999, 235.

[144] L. SCHMADEL, *Dictionary of minor planet names*, Springer, 2012, 422.

[145] C. CHIAVARI et al., Conservation of organ pipes: protective treatments of lead exposed to acetic acid vapours, in: *Metal 04: Proceedings of the international conference on metals conservation*, ed. by J. ASHTON and D. HALLAM, National Museum of Australia Canberra, 2004, 281–293.

[146] M. CAMPBELL, C. GREATED, and A. MYERS, *Musical instruments: History, technology, and performance of instruments of western music*, Oxford University Press, 2004, 416.

[147] P. WILLIAMS, *The organ yearbook*, Laaber-Verlag, 2009, 39.

[148] C. KNIGHT, *Popular history of England*, Evand Bradbury, 1859, 308.

[149] G. AUDSLEY, *The art of organ building*, Courier Corporation, 2013, 503.

[150] M. WALKER and D. DAVIES, *Heavenly harmony: Organs and organists of Exeter cathedral*, Impress Books, 2014, 228.

[151] D. RUMSEY, *Materials used in medieval pipe making*, tech. rep., 2012, 2.

[152] H. ALDERSEY-WILLIAMS, *Periodic tales: The curious lives of the elements*, Penguin, 2011.

[153] O. FAUST, *The pipe organ and player piano*, Merchant Books, 2003, 45.

[154] C. BERGSTEN et al., *The Collapse project: Corrosion of organ pipes - causes and recommendations*, University of Gothenburg, Göteborg Organ Art Center, 2011, 136–140.

[155] H. VERHOEF, ed., *Het oude orgel van de Nicolaikerk te Utrecht: Kroongetuige van de Nederlandse muziekgeschiedenis*, Walburg Pers, 2009, 208.

[156] C. MARTINI, A. NIKLASSON, and J. BERGSTEN, Collapse project: Europees onderzoek naar corrosie bij pijpwerk, *Orgelkunst* **28** (1) (2005), 30–43.

[157] A. NIKLASSON, Atmospheric corrosion of historic lead organ pipes, PhD thesis, Chalmers University of Technology, 2007.

[158] M. YU, H. TSUNODA, and M. TSUNODA, *Environmental toxicology: Biological and health effects of pollutants*, CRC Press, 2011, 197.

[159] D. WEISS et al., Atmospheric Pb deposition since the Industrial Revolution recorded by five Swiss peat profiles: Enrichment factors, fluxes, isotopic composition, and sources, *Environ. Sci. Technol.* **33** (1999), 1340–1352.

[160] D. ADRIANO, *Trace elements in terrestrial environments: Biogeochemistry, bioavailability, and risks of metals*, Springer, 2001, 399.

[161] R. EISLER, *Handbook of chemical risk assessment: Health hazards to humans*, CRC Press, 2010, 205.

[162] S. HERNBERG, Lead poisoning in a historical perspective, *Am. J. Ind. Med.* **38** (3) (2000), 244–254.

[163] T. LEGGE and K. GOADBY, *Lead poisoning and lead adsorption: The symptoms, pathology, prevention (1912)*, Kessinger Publishing, 2010, 340.

[164] S. FLEMING, Science detects the forgeries, *New Scientist* **68** (978) (1975), 567–569.

[165] J. LIPPITT, P. WEBB, and W. MARTIN, *Hazardous waste handbook*, Butterworth-Heinemann, 2000, 248.

[166] U. KINDESJÖ, Phasing out lead in solders, PhD thesis, Lund University, 2002.

[167] D. PAVLOV, *Lead-acid batteries: science and technology: Science and technology*, Elsevier, 2011, 151.

[168] K. KELLY, *Medicine today: 2000 to the present*, Infobase Publishing, 2010, 32.

[169] S. SHIVANI, *Handbook of research on diverse applications of nanotechnology in biomedicine, chemistry, and engineering*, IGI Global, 2014, 521.

[170] UNITED NATIONS, *Final review of scientific information on lead*, tech. rep., 2010, 16.

2

Protection and preservation of lead archaeological objects

2.1 Composition of lead artifacts

2.1.1 Lead and its alloys

Post-transition metals like lead are known for their low smelting and boiling points, poor electrical conductivity, and high electronegativity values compared to transition metals [1, 2]. Moreover, lead is a lustrous, solid, silver-blue heavy metal presenting some extreme properties such as its high density, softness, malleability and ductility, which are ideal for the production of lead artifacts [3]. Another interesting property is the immediate formation of an oxide film protecting the metal from further corrosion [4]. Table 2.1 sums up the most important physical properties of lead.

PHYSICAL PROPERTY	LEAD
COLOR	silvery
SMELTING POINT	327 °C
BOILING POINT	1749 °C
MOHS HARDNESS	1.5 (scratch with a fingernail)
DENSITY	11.3 g cm^{-3}
CONDUCTIVITY	$4.8 \cdot 10^6$ S m^{-1}
CRYSTAL STRUCTURE	face cubic centered (fcc)
OXIDATION STEPS	II +, IV +
PAULING ELECTRONEGATIVITY	2.33

Table 2.1 – Important physical properties of the lead metal [1, 5, 6].

Lead metal is easily alloyed with other metals in order to form metal alloys with low melting points [7]. These lead alloys are easily forged into a usable object and easily recycled [8]. The properties of these alloys mainly depend on their chemical composition, distribution and morphology. Regarding composition, antiquities are generally made of very impure lead [3]. The most frequently associated elements, such as antimony ($< 0.01\%$) [9], silver (0.02%) and copper (0.005%), have a very limited solid solubility in the lead metal matrix at room temperature [10]. This means that even with a very small concentration of foreign elements, the solubility limit is easily exceeded, which leads to the formation of new crystalline phase, changing the metal's properties [11]. One of the exceptions is tin, which is soluble in lead till 19.5% [12].

Knowing this, it is interesting to examine general tendencies in the lead content of old lead artifacts. Figure 2.1 shows

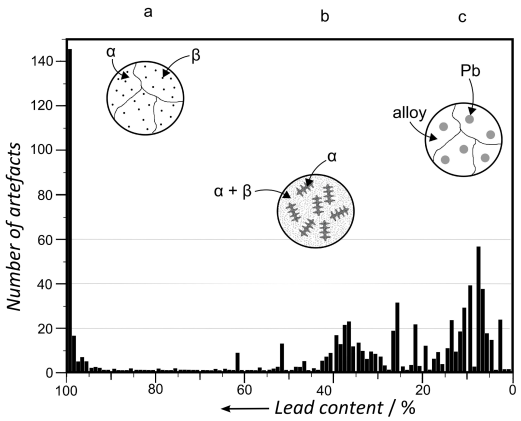


Figure. 2.1 – Distribution of lead artifacts according to lead content based on Figure in [3]. Three compositional groups: (a) high lead content, the structure of which consists of a lead-rich matrix (α) with precipitates of a second phase, minor-element-rich (β); (b) intermediate lead content, corresponding to low melting-point alloys, used in the as-cast condition, revealing lead-rich (α) dendrites in an eutectic matrix (α + β); (c) low lead content, exemplified by copper-based leaded alloys, where lead is segregated in the form of fine globules.

the statistical distribution of lead artifacts according to their lead content. Three main groups are discerned. Most of the objects are considered 'pure lead' because they have a lead content higher than 80%. Most of the artifacts contain other elements including copper, antimony and silver precipitating as a second phase (see phase β in Figure 2.1a). A second group with artifacts containing about 40% lead are characterized by a low melting point. The metal is composed of dendrites of a lead-rich α phase surrounded by the eutectic α + β phase, rich in an other element (see Figure 2.1b). The last group contains alloys with lead quantities lower than 30% [3]. The lead is added in low quantities to improve properties for casting and machine manipulation [13]. Once again, the immiscibility between the elements ensures the dispersion of lead rich fine globules in the alloy matrix (see Figure 2.1c) [3]. In the following part, two frequently alloys are discussed.

2.1.1.1 Lead-tin alloys

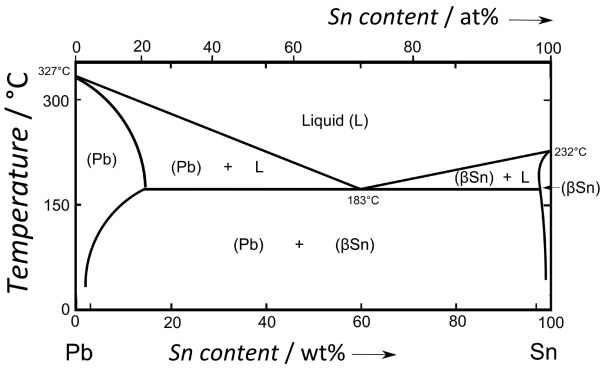


Figure. 2.2 – Phase diagram of lead and tin based on Figure in [12].

Often lead is alloyed with tin to improve its corrosion and resonant properties [14]. In Figure 2.2, the Pb-Sn phase diagram shows three one phase systems (α, β and L) and three two phase systems (α + L, β + L and α + β). Phase α is a solid alloy of tin in lead and phase β is a solid alloy of lead in tin [12]. The strength and the hardness of the material shows a maximum at an eutectic mixture of both metals [6]. In ancient times, the alloying of lead and tin was used for the building of organ pipes. The addition of tin protects the pipes better against corrosion because of the formation of a SnO layer [6, 15, 16]. However, only when high concentrations of tin are added, no corrosion is noticed [17]. A large amount of impurities in the lead metal such as copper, bismuth and antimony influence the size and arrangement of the crystal grains, so that holes are created in the metal's microstructure and the corrosion is promoted [4]. Adding tin is an option, but this changes the color and the sound characteristics of the

pipes. Thus, another solution is necessary [18].

2.1.1.2 Lead-antimony alloys

The lead-antimony alloy is known for its high corrosion resistance in most environments forming a protective and impermeable patina even faster than pure lead [19]. Furthermore, the mechanical properties such as hardness and strength are affected even at very low concentrations. For example, adding 0.1% of antimony doubles the tensile strength of the lead-tin alloy [20].

Hardening lead was necessary depending on the end use. For example, a huge amount of lead alloyed printing letters, containing a high amount of antimony, are kept at the Museum Plantin-Moretus in Antwerp [21]. Sometimes antimony was also considered to be an impurity due to the old-fashioned lead smelting process [22, 23]. However, these antimony impurities could have a considerable effect on the corrosion and mechanical properties [24]. The Egyptians and the Romans used lead(II)antimonate, $Pb_2Sb_2O_7$, to produce opaque yellow glasses [25]. Moreover, the compound was used as a pigment called *Naples yellow* in paints and cosmetics [26, 27].

Nowadays, lead-antimony alloys with maximum 3.5 wt% antimony are more frequently used for grids of the plates of lead-acid batteries among other things [28]. The use of these alloys as ammunition, cable sheathing and anodes is also well-known [29]. Like lead, antimony is also a cumulative poison [30].

2.1.1.3 Copper-lead alloys

Starting from the Bronze Age (3300 - 1200 B.C.) so-called *bronzes*, alloys made of copper and tin from separate ore sources, were made [31]. Another major binary alloy of copper is *brass* or *calamine brass*, which contains various amounts of zinc mostly under 40 wt% depending on the period [32]. Especially in the Roman period, 30% of the copper artifacts was made of *brass* [33]. A brass artifact dated 4700 - 4000 B.C. was found at the Jiangzhai site in China and suggests that brass was known even before bronze [34]. Moreover, copper-antimony and copper-arsenic alloys were found [35]. A cast arsenical copper axe described by Scott [36] and a Nahal Mishmar hoard described by Shalev and Northover [37] clearly evidences the use of these alloys.

During the Greaco–Roman Age, 6 to 8% lead was added to copper and bronze (lead bronze), improving the fluidity of the metal for casting coins and statues [38]. Furthermore, adding lead to bronze, copper or brass (2%) improves the machinability and castability of the alloy [13]. The corrosion resistance of the alloy depends largely on its microstructure, which depends on different properties such as mechanical working, hardness, smelting point and cooling rate [39]. Alloying copper was meant to improve its physical and mechanical properties depending on the end use and is still used today [40].

2.2 Deterioration of lead and lead artifacts

2.2.1 Basic principles

The primary cause of the deterioration of lead metal is corrosion. Corrosion is defined by the IUPAC as “An irreversible interfacial reaction of a material (metal, ceramic, polymer) with its environment which results in consumption of the material or in dissolution into the material of a component of the environment. Often, but not necessarily, corrosion results in effects detrimental to the usage of the material considered. Exclusively physical or mechanical processes such as smelting or evaporation, abrasion or mechanical fracture are not included in the term corrosion” [41, 42]. Interaction with compounds in the environment can be devastating for all lead objects [43]. The most important factors are the relative humidity and air pollution [44]. Furthermore, corrosion depends on a variety of factors such as inclusions, surface imperfections, differences in the orientation of grains, lack of chemical homogeneity, localized stresses, and

external variation in environment [39]. In next two sections we briefly discuss the corrosion processes based on two parameters: the thermodynamic properties and the kinetic properties.

2.2.1.1 Thermodynamic properties

Using the basic principles of thermodynamics, it is possible to calculate the spontaneity of the corrosion reactions of lead metal objects in a chosen environment based on the principles of the electrochemical cell [45]. When the free energy change, or Gibbs free energy ΔG, which is related to the equilibrium potential E^0_{cell} of the corrosion cell reaction through

$$\Delta G = -nFE^0_{\text{cell}}, \tag{2.1}$$

is smaller than 0, we are dealing with a spontaneous corrosion process. In the equation, n is the number electrons transferred in the reaction and F is Faraday's constant (96485 C mol^{-1}). Standard electrode potentials of the most frequent electrochemical reactions where lead is involved are given in Table 2.2. Reactions with more positive standard potentials than the oxidation of lead, can drive the lead corrosion process. However, this discussion only makes it possible to look at the tendency for corrosion. Indeed, these values are standard values and do not include external factors [46].
To include these external factors, Pourbaix-diagrams are used based on the Nernst equation of the corrosion cell [46, 47],

$$E_{\text{cell}} = E^0_{\text{cell}} - \frac{RT}{nF}\ln Q, \tag{2.2}$$

where R is the universal gas constant (8.31446 J K^{-1} mol^{-1}), T is the absolute temperature and Q is the reaction quotient represented by $\frac{(a_{\text{ox}})^{\text{a}}}{(a_{\text{red}})^{\text{b}}}$ with a and b the stoichiometric constants of the half-reaction. These diagrams show the stability of all lead corrosion products as a function of the potential and the pH depending on the environment. A disadvantage of the Pourbaix diagrams is the lack of information concerning the kinetics of the corrosion reactions. Furthermore, these diagrams only take into account pure materials at a certain temperature and pressure [48]. A Pourbaix study on lead in alkaline solutions is given in [49] showing areas where the metal is stable (immunity), a soluble metal component is stable (corrosion) and a slightly soluble metal component is stable (passivation).

ELECTRODE REACTION	E_0 (vs SHE)
Pb^{4+} (aq) + $2e^-$ $\rightleftharpoons$ Pb^{2+} (aq)	1.67
O_2 (g) + $4H^+$ + $4e^-$ $\rightleftharpoons$ $2H_2O$ (l) (i)	1.23
$2H^+$ (aq) + $2e^-$ $\rightleftharpoons$ H_2 (g) (ii)	0
Pb^{2+} (aq) + $2e^-$ $\rightleftharpoons$ Pb (s)	-0.13
PbCl (s) + $2e^-$ $\rightleftharpoons$ Pb (s) + $2Cl^-$	-0.27
$PbSO_4$ (s) + $2e^-$ $\rightleftharpoons$ Pb (s) + $2SO_4^{2-}$	-0.36
$Pb(OH)_2$ (s) + $2H^+$ + $2e^-$ $\rightleftharpoons$ Pb (s) + $2H_2O$	-0.41
$PbCO_3$ (s) + $2e^-$ $\rightleftharpoons$ Pb (s) + $2CO_3^{2-}$	-0.51

Table 2.2 – Standard electrode potential in H_2O at 25°C (298 K) [46].

2.2.1.2 Kinetic description

A full description of the kinetic properties of a lead corrosion reaction is given in section 6. In the following sections, we give an overview of the known types of corrosion mechanisms for lead in different environments. Furthermore, it is important to mention the difference between the corrosion types observed on pure lead samples or artifacts.

2.2.2 Uniform corrosion

An exposed pure metal is completely corroded in specified environments, which can be a liquid, gaseous or hybrid electrolyte (such as biological organisms) [50]. In general, we distinguish two types of volatile compounds corrosive towards lead: inorganic and organic compounds.

2.2.2.1 Atmospheric corrosion in the presence of inorganic compounds

Studies on the degradation of pure lead were initiated by Vernon in the 1920s [51]. It was established that moist air forms a native oxide following a reaction with atmospheric oxygen [52]. A water layer on top of the metal surface, serving as an electrolyte, plays a crucial role in this lead corrosion process, because it provides a medium for the dissolution of a whole range of atmospheric gasses [53]. The amount of water is particularly humidity-dependent, indicating that the corrosion rate depends on the temperature and relative humidity of the environment [54]. These statements indicate that moist air, where air dissolves in water, initiates corrosion mostly by creating hydroxides considering the following cathodic reactions [55],

$$O_2(g) + 2H_2O(l) + 4e^- \rightleftharpoons 4OH^-, \tag{2.3a}$$

$$O_2(g) + 2H_2O(l) + 2e^- \rightleftharpoons H_2O_2 + 2OH^-. \tag{2.3b}$$

Simultaneously, these hydroxides form soluble lead hydroxides using the anodic reaction with the formation of intermediate adsorbed species as explained by reactions [56–58],

$$Pb(s) + OH^-(aq) \rightleftharpoons PbOH_{ads} + e^-, \tag{2.4a}$$

$$PbOH_{ads} + OH^-(aq) \rightleftharpoons Pb(OH)_2(s) + e^-. \tag{2.4b}$$

This means that at any given time, multiple cathodic and anodic areas on the metal surface form local corrosion-cells, resulting in a general attack of the sample surface. It is clear that most of the time atmospheric exposure results in this type of corrosion [59]. The unstable lead hydroxides undergo a chemical reaction based on a kind of decomposition explained by the dehydratation reaction [56, 60],

$$PbOH_{ads} + OH^-(aq) \rightleftharpoons PbO^-_{ads} + H_2O(l), \tag{2.5a}$$

$$PbO^-_{ads} \rightleftharpoons PbO(s) + e^-, \tag{2.5b}$$

forming a tightly adherent lead oxide layer [61–63]. The potential-pH diagram is given in [64]. Next to the formation of lead oxides, as a consequence of the dissolution of the atmospheric gas CO_2 forming bicarbonate-ions,

$$CO_2(g) + H_2O(l) \rightleftharpoons HCO_3^-(aq) + H^+(aq), \tag{2.6a}$$

$$HCO_3{}^-(aq) + H_2O \rightleftharpoons CO_3{}^{2-}(aq) + H^+(aq). \tag{2.6b}$$

other lead corrosion products like cerussite ($PbCO_3$), hydrocerussite ($Pb_3(CO_3)_2(OH)_2$), plumbonacrite ($Pb_{10}O(OH)_6(CO_3)_6$), litharge (PbO) and plattnerite (PbO_2) are formed [6, 53, 65]. As an example, we show the reaction to form plumbonacrite starting from PbO,

$$6HCO_3{}^-(aq) + 10PbO(s) + 6H^+(aq) \rightleftharpoons Pb_{10}O(OH)_6(CO_3)_6(s) + 3H_2O(g). \tag{2.7}$$

This atmospheric corrosion process is explained in Figure 2.3 and ensures that lead passivation gently sets in over time [61]. A porous coating of corrosion products gradually protects the underlying bulk lead metal against further corrosion, which means that the corrosion process is anodically controlled [42]. This protective layer is the main reason why, in general, lead artifacts are preserved so well through the ages [66].

For all metals, depending on the composition of the environment, other atmospheric corrosion reactions are possible [67]. For example, hydrogen sulfide (H_2S) and sulfur dioxide (SO_2) gasses are dissolved in water [61], forming lead sulphate crystals (anglesite) following the thermodynamic association reaction [68],

$$Pb^{2+}(aq) + SO_4{}^{2-}(aq) \rightarrow PbSO_4(s)\downarrow, \qquad (2.8)$$

together with traces of PbS. In this case, the rate of atmospheric lead corrosion is considerably limited because of a lead sulphate patina preventing further corrosion [69]. The formation of these insoluble compounds is often very important. Discharging the lead-acid battery, for example, ensures the formation of stable lead sulphates on the lead plates so that the sulfuric acid electrolyte becomes diluted [70].

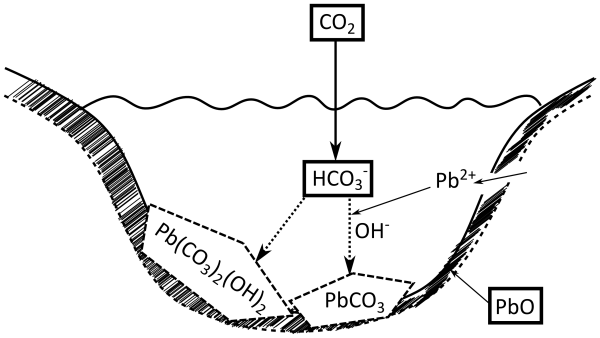


Figure. 2.3 – A schematic representation of the atmospheric corrosion processes on lead involved in the formation of carbon containing compounds based on Figure in [61].

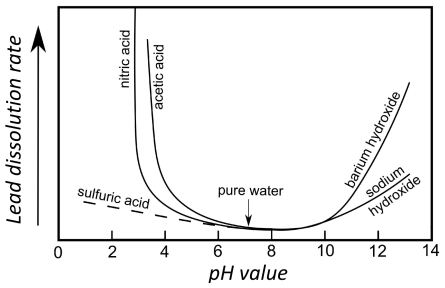


Figure. 2.4 – The rate of lead solubility as a function of different inorganic acids and hydroxides from Figure in [3].

Looking at the atmospheric corrosion of lead in a marine environment, consisting of mainly chlorides, we see the formation of lead chlorides (cotunnite) together with traces of moderately to poorly soluble lead hydroxychloride corrosion products [4, 61]. An example are lead shots covered with protective layers of various insoluble salts found on the Mary Rose (see section 1.5), considered to be complex mixed basic salts, impure and/or compounds [71]. Industrial waste gas emissions containing nitrogen oxides [72], NO_X, yield mainly nitric acid due to a disproportionation reaction with water as presented by a [73–75]

$$2NO_2(g) + H_2O(g) \rightleftharpoons HNO_3(g) + HNO_2(g). \qquad (2.9)$$

Its presence in the atmosphere is the main culprit for acid rain, which is corrosive for most metals. The lead nitrate corrosion product film is not found as a consequence of its high solubility in water [19, 76–78]. To conclude, we can state that lead is quite actively corroded by corrosive gases and that many different lead salts are formed depending on the characteristics of the environment. In our case, the corrosion rate is a very important factor to decide which products will arrest the destruction of lead metal samples. In this respect, we show in Figure 2.4 the rate of lead solubility as a function of different inorganic acids and hydroxides. It is clear that the solubility and stability of the corrosion product play a crucial role, which means that environments containing nitrates and organic acids are most corrosive towards lead [3]. Next to the environment, the composition of the metal is important, as more impurities ensure a faster corrosion process, which is described further in section 2.2.3.

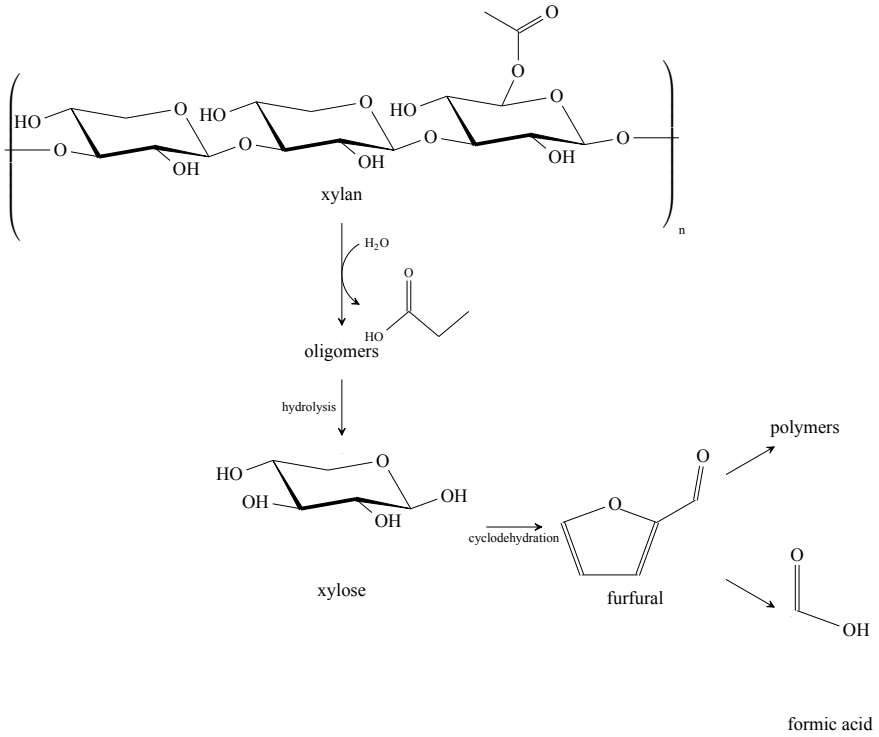


Figure. 2.5 – Scheme of the hydrolysis of hemicelluloses

It is noticeable that the lead crystals in the Pb^{II} oxidation state are favored over the Pb^{IV} oxidation state, because Pb^{IV} species do not exist in solution [61]. Furthermore, all formed lead salts are toxic [79] and should be handled with care. This is the reason for abandoning lead for handling drinking water, which contained many dissolved lead corrosion products [4].

2.2.2.2 Atmospheric corrosion in the presence of organic compounds

VERY HARMFUL		
unseasoned oak (white and red)	sweet chestnut	plywood and chipboard
fire-proofed woods	teak	rot-proofed woods
MODERATELY HARMFUL		
seasoned oak	birch	larch
beech	ash	red cedar
LESS HARMFUL		
Honduras and African mahogany	elm	douglas fir
ramin	pine	obeche

Table 2.3 – Wood types harmful for lead metal artifacts [80–84].

Volatile organic acids have long been known to be corrosive to lead. The most aggressive are acetic acid and formic acid, which form readily soluble lead acetates and lead formiates. In section 1.6, we describe the formation of this ‘white lead’ by readily oxidizing lead disks using acetic acid vapor. The lead metal is continuously attacked by organic acids, creating a uniform corrosion pattern [3]. Often, this kind of atmospheric corrosion is noticed when lead is in the presence of wood, but also varnish and/or paint [80]. In the following part, we provide a more detailed view on the corrosion process and associated environments.

A group of hemicelluloses found in the plant cell walls of wood are called xylans, which are polysaccharides made from xylose units. Depending on the type of wood, the xylan content differs from 10 - 35% in hardwoods and from 10 - 15% in softwoods. Moreover, on average every second xylose unit is acetylated in hardwoods [85], which is not the case for softwoods. Deacetylation of these hemicellulose xylan acetyl side chains produces acetic acid [86, 87]. Formic acid, on the other hand, arises from the degradation of furfural derived from the dehydration of xylose [88, 89]. As a conclusion, we can state that the kinetics of this degradation depend on the relative humidity and temperature, and that the amount of corrosion depends on the wood type used. Table 2.3 mentions different wood types according to their harmfulness towards lead metal artifacts. Is is clear that some wood types are more corrosive towards lead depending on the emission of a variety of acids, aldehydes and other degradation products [81]. Oak often is used to make windchests or wooden organ pipes. Hence, based on Table 2.3, it is easy to explain why our organ pipes deteriorate so rapidly [90].

	FORMIC ACID	ACETIC ACID
$K_H{}^*$	$3600\ M \cdot atm^{-1}$	$7800\ M \cdot atm^{-1}$
K_a	$10^{-3.75}$ M	$10^{-4.76}$ M
complex formation	$K_1 = 10^{1.23}\ M^{-1}$	$K_1 = 10^{2.33}\ M^{-1}$
	$K_2 = 10^{2.01}\ M^{-1}$	$K_2 = 10^{3.60}\ M^{-1}$
Water solubility (g/100 mL)	$Pb(HCOO)_2$	$Pb(CH_3COO)_2$
	1.6	44.3
	$Pb(HCOO)(OH)$	$Pb(CH_3COO)_2 \cdot 2\ Pb(OH)_2$
	[a]	6.3

[*] Henry's law constant

[a] not known in literature

Table 2.4 – Different properties of acetic acid and formic acid: comparative study [91].

Even low concentrations (170 - 1100 ppb) of acetic acid in moist air are extremely corrosive to lead as stated by Niklasson et al. [65], explaining the rapid lead deterioration. The acidity and the high solubility in water of gaseous organic acids are interpreted as their most important properties for lead corrosion. Dissolving into the aqueous electrolyte, acetic acid ensures a decrease of the pH value, which result in the dissolution of the native basic PbO layer [92] explained by,

$$PbO(s) + 2CH_3COOH(aq) \rightleftharpoons Pb^{2+}(aq) + 2CH_3COO^-(aq) + H_2O(g). \tag{2.10}$$

This simple acid-base reaction actually triggers the electrochemical corrosion process that generates ions for the production of new solid lead corrosion products as shown in Figure 2.6. First, the formation of lead acetate trihydrate is explained by reaction [65],

$$2PbO(s) + Pb^{2+}(aq) + 2CH_3COO^-(aq) + H_2O(g) \rightleftharpoons Pb(CH_3COO)_2 \cdot 2PbO \cdot H_2O(s). \tag{2.11}$$

This compound turns into basic lead carbonates explained by the following equilibria [93–95],

$$2Pb(CH_3COO)_2 \cdot 2PbO \cdot H_2O(s) + 2H_2O(g) + 2CO_2(g) \rightleftharpoons Pb_3(OH)_2(CO_3)_2(s) + 2CH_3COOH(g), \tag{2.12a}$$

$$3Pb_3(OH)_2(CO_3)_2(s) + PbO \rightleftharpoons Pb_{10}O(OH)_6(CO_3)_6(s). \tag{2.12b}$$

This liberation of acetic acid causes a continuous metal corrosion in an auto-catalytic way explaining the large amount

of corrosion by small amounts of acetic acid [3].

Low formic acid concentrations (160 ppb) are also very corrosive towards lead, but less effective than acetic acid. Nevertheless, formic acid is a stronger acid than acetic acid as seen in Table 2.4. The lower effectiveness of lead formate to dissolve in water and the difficulty to form lead complexes explain why this acid is less aggressive compared to acetic acid [91]. Just like acetic acid, formic acid dissolves the native oxide in the acidified aqueous electrolyte [96],

$$PbO(s) + 2HCOOH(aq) \rightleftharpoons Pb^{2+}(aq) + 2HCOO^{-}(aq) + H_2O(l), \tag{2.13}$$

to form lead formiates and lead formiate hydroxides. The combination of formic and acetic acid seems to have a synergistic effect on the corrosion of lead [91, 97]. To demonstrate the combination of lead metal with wood, varnish and/or paint is very common, two examples are briefly discussed below.

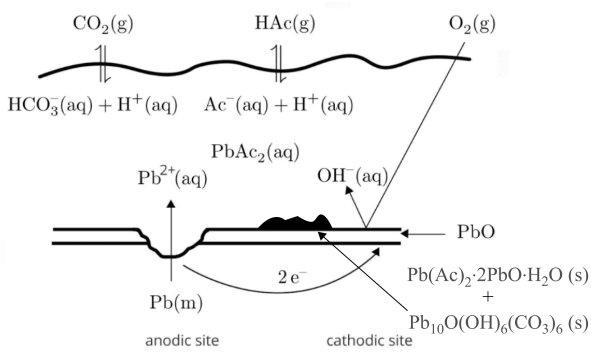


Figure. 2.6 – A schematic representation of the atmospheric corrosion processes on lead in moist air containing acetic acid vapor based on Figure in [65].

Organ pipes

In the nineties, some organs made in the 15th - 17th century which originated from different European churches started to lose their specific sounds [15]. Metal conservators established that the air escaped through small holes in the metal organ pipes [98]. Furthermore, they discovered the sudden appearance of white chalky residue all over the pipes' interior that eventually worked its way through the outside in small localized spots [15]. Mostly, this type of corrosion takes place on the inside and outside of the foot of the organ pipe where the pipe is in contact with the wooden windchest (see Figure 2.7). When the corrosion moves upwards along the pipe, the mouth of the organ pipe is damaged. First, the sound quality will change, and after a long exposure the pipe will not produce any more sound [17]. At this point, the damage is irreversible and untreatable.

To help solve the widespread problem, a team of metallurgists, chemists, organ makers and music historians started the European (EC 5th Framework Programme: Energy, environment and sustainable development) research program COLLAPSE (Corrosion of Lead and Lead-Tin Alloys of Organ Pipes in Europe) to monitor and study the climate conditions close to the pipes [53, 91, 99]. As a conclusion two causes for the corrosion were [100–102] the

- central heating increases the temperature and relative humidity and favors the conditions for corrosion.
- the separation of organic acids by the hydrolysis of wood in the organ's wind chest is a consequence of changes in the churches' atmospheric air.

In reality, both causes are part of the problem, but the second one has a higher impact on the corrosion process, as been described by T. Clarke [15]. Conservation scientists believe that close to the wooden parts, an acidic microclimate is created in the windchest [103]. The acetic acid concentrations can range from 0.04 to 2.4 ppm in pipe organ wind chests [104]. It is important to mention that organ pipes alloyed with tin showed less corrosion [99].

Museum storage and display cases

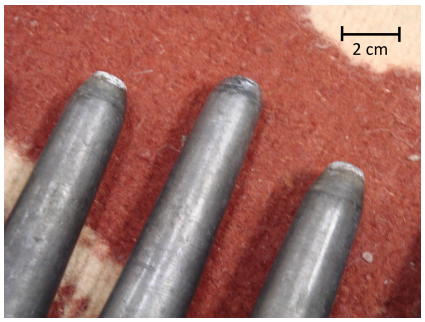
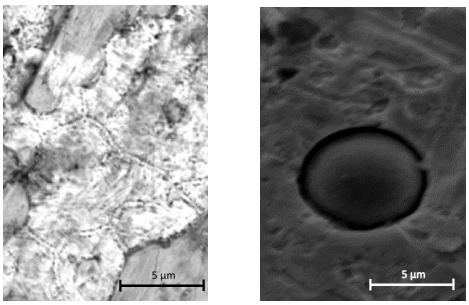


Figure. 2.7 – Lead corrosion of the foot of the organ pipe ©Lapon.

Often, wooden construction materials are used for building storage and display cases, both of which are, as explained, detrimental towards artifacts stored inside [105–108]. It is also possible that two artifacts stored in one case are corrosive towards one another [109–111]. The fact that the artifacts are stored in a closed environment without ventilation, allowing the organic acid concentration to rise quickly, increases the corrosion rate. High concentrations in the range of 0.05 to 40 ppb can attack and corrode the lead artifacts [97, 112]. Trying to prevent the release of organics or the development of rot, coatings are applied to seal and protect the wood surfaces of case interiors [113]. However, many problems have been reported using this 'solution', depending on the choice of sealant or paint [114–116]. Due to their own volatile content, many coatings are themselves dangerous to the artifacts [81]. In Table 2.5, we sum up possible destructive coating materials for pure lead and lead-alloyed artifacts. Browsing conservation literature indicates that many myths and contradictions regarding the choice of sealant are still prevalent [81]. Mainly metal artifacts are susceptible to this kind of corrosion. However, paintings filled with metal-containing pigments clearly show the same problems [117–119]. To be complete, the organic acids produced by the museum visitors also have to be taken into account. Due to these practices in museums, to the present day much of our cultural heritage has disappeared or deteriorated. It is therefore a necessity to find protection against the formation of lead corrosion products, which promote the destruction of lead organ pipes [6].

2.2.3 Localized corrosion



(a) **(b)**

Figure. 2.8 – (a) Intergranular corrosion and (b) Copper inclusion in lead matrix. ©M. De Keersmaecker.

Lead artifacts do not suffer uniform attack in many cases [120]. The microstructure and composition of lead artifacts create active and passive regions on the surface, which have an enormous effect on the corrosion behavior. For example, a formed passive layer (due to atmospheric corrosion) can be locally disrupted, making locally exposed areas more vulnerable for specific types of corrosion. Below, we will briefly discuss three types of this localized corrosion on lead artifacts: intergranular, pitting and selective corrosion [3, 50].

2.2.3.1 Intergranular corrosion

In a polycrystalline material, intergranular corrosion starts at preferred sites along the interface between crystallites, called the grain boundaries [121]. These grain boundaries show a higher density of imperfections in the crystal structure, ensuring a higher disordered and more irregular system. Therefore, these local places have a higher entropy and thus a higher energy [122], which means that these grain boundaries become more anodically reactive than the core of the grains in certain environments [123]. This kind of local corrosion attack creates electrolyte penetration and excess corrosion products along isolated boundaries, which can cause weakening of the metal structure [3]. There is almost no perceptible

destruction, but the metal's properties such as the decrease of the ductility, the strength of the metal and the production of debris change very rapidly [123, 124]. The corrosion rate of this type of corrosion depends on the morphology or shapes and size of the grains, as well as the impurities and their distribution in the matrix of the grains [125].

PVA glue	some types of wallpaper	contact cement
velvet	plastic wood	burlap
some types of polyesters	rust inhibitors	some types of varnishes
some types of plastics	some types of dyes	jute
some types of paints	flame-proofed fabrics and wood	products to treat rot and/or insects
products containing ammonia	vinegar-based products	low quality paper and cardboard
oil-based stain	vermiculite	some kinds of wool
unwashed pebbles and sand	some types of silicone adhesives	vinyl

Table 2.5 – Paints, glues and other materials destructive to lead metal artifacts [80–82, 126].

Observations of lead-tin organ pipes by Chiavari et al. [127] reveal the formation of intergranular corrosion along the grain or dentrite boundaries forming cracks and very local pustules. When the pipe alloy consists of smaller grains and is more homogeneous due to extensive hammering, the corrosion resistance is improved, yet results in a loss of the strength of the bulk material [128, 129]. Bigger grains, indeed, promote corrosion along cracks in the bulk metal [3]. The same is seen when investigating Roman water pipes [130]. In general, fine-grained alloy structures are more easily deformed than corroded.

An interesting example of preferential intergranular attack is seen on lead-antimony alloys in the range of 0.5% to about 6% antimony [131]. Furthermore, there exists the interaction in pipe organ metals between low solubility impurities such as copper and the lead matrix [132] as seen in Figure 2.8. Impurities along the boundaries locally disrupt the native lead oxide film, allowing atmospheric gases easier access to the bulk metal [3]. However, no general tendencies are reported. In trying to predict intergranular corrosion, it is important to look at the nature of the alloy (impurity or element, metallic or non-metallic) [133], and its solubility and distribution (homogenous or segregated) in the lead matrix [134, 135]. When in an organic acid environment, for example, tin-alloyed organ pipes have a higher corrosion resistance compared to pure lead pipes, which can be attributed to the protective behavior of tin in these media [16]. To conclude, we can state that the microstructure and composition of lead and its alloys have an important influence on their corrosion behavior [136].

2.2.3.2 Selective leaching corrosion

Selective leaching corrosion, also called dealloying, is a type of corrosion where one metal component is preferentially leached from an alloyed material [4]. The rate of the process depends on the distance between the alloyed metals in the galvanic series. The less noble or more active metal is selectively removed from the alloy [137]. After the process, the metal is spongy and porous and has lost strength, hardness and ductility [59].

Often this kind of corrosion is seen in copper alloyed artifacts where lead is added to enhance its castibility and machinability properties. First of all, dezincification of brass is a well-known phenomenon in conservation studies [138–140] and can be recognized by a change in color (yellow to orange) [137]. Secondly, the addition of lead ensures the formation of isolated globules due to its insolubility in the copper-rich matrix [3], so that the lead metal that will preferentially corrode. The corrosion products are often referred to as 'lead worms' [141]. Other examples are the extensive selective leaching of copper-lead alloys [142] and lead-antimony alloys, even in low concentrations [143].

2.2.3.3 Pitting corrosion

Pitting is the most unexpected form of corrosion [137]. The process can be split into three different time frames: pit formation, pit growth and degradation.

Pit formation

The lead metal readily forms a relatively impenetrable passive layer as described in section 2.2.2.1 and shown in Figure 2.10 (step 1). However, discontinuities in the passive layer expose the bulk lead metal to the environment [144]. On the one hand, weak spots in the film can be a consequence of the lead metal's microstructure and impurities. Examples are galvanic contacts due to heterogeneous distribution of micro-segregations, selective corrosion or crevice corrosion [145]. On the other hand, pits are formed due to local chemical or mechanical damage. In this case, the localized corrosion starts because of coating failure, local condensation of moist, momentary change in concentration, erosion-corrosion, scratches or thermal expansion [137]. This step is shown in Figure 2.10 (step 2).

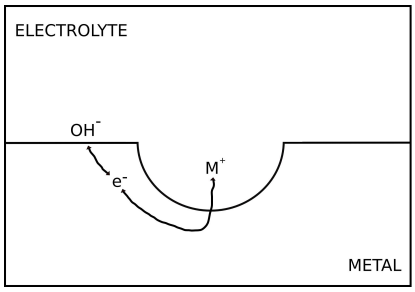


Figure. 2.9 – Active pit on a passive metal surface. ©M. De Keersmaecker.

Depending on the nature of the film, a rapid repair of the film at the breakdown site can stop the corrosion process before it starts [146]. However, in many cases, the damaging conditions persist and a cavity is formed [137]. A reason for this is the formation of soluble and bulky lead corrosion products [147]. At this moment, an active pit exists on a completely passivated lead metal surface, which allows the formation of a potential gradient (as shown in Figure 2.9) [148]. Indeed, the initiation of the corrosion process is a result of a change in the local anodic behavior of the lead material [149].

Pit growth

When an opening is formed in the passivated layer (such as a coating or a patina), the pits start to form crevices [144]. Typically these cracks are filled with the surrounding electrolyte [150] when they are a few micrometers wide, as shown in Figure 2.10 (step 3) [151]. However, the small dimensions of the fissures prevent circulation of the electrolyte in the surrounding environment, which causes the conditions to become more aggressive inside the crevice. This more severe environment causes local active lead metal dissolution and tends to accelerate the corrosion process [152]. The migration of hydrated acetates (or nitrates) forms an acidic environment in crevices formed on the lead substrate, which permits the continuous production of lead salts due to the formation bulky porous precipitates. The lead acetates (or nitrates) formed (see reaction 2.10) dissolve into the aqueous electrolyte and migrate away from the crevice [153]. A reaction with CO_2 (see reaction 2.12a) forms white powdery precipitates far from the corrosion pit. At his point, new acetic acid molecules are also formed, ensuring a continuous attack of the lead substrate [6].

Degradation

The crevices become deeper and inside them the lead metal is slowly eaten away. After a long time, depending on the thickness of the material, perforations are observed. It is clear that these holes can have destructive consequences for the object. Some important examples for lead are summed up below.

- Perforations of lead sheets around the base of organ pipes make sure the sound is distorted or vanishes [3]
- Degradation of lead artifacts makes it difficult to read ancient inscriptions [154]
- Lead roofing corrodes in the presence of wood beams, creating leaks [155, 156]

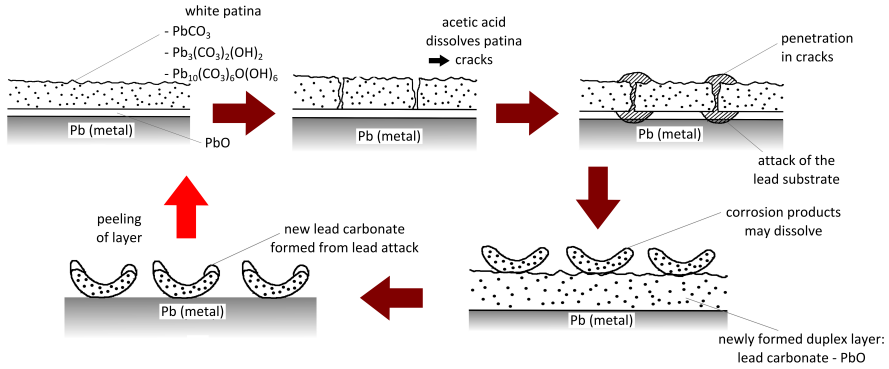


Figure. 2.10 – Schematic mechanism of 'active' lead corrosion in the proximity of organic acids based on Figure in [65].

- Lead sculptures are deformed at places in direct contact with more noble metals and sealing products [3]
- Localized corrosion produces holes on excavated lead artifacts or lead pipes buried in an acidic environment [3]
- High nitrate concentrations in drinking water slowly degrade copper-lead solder pipes [157]
- Antique wooden display cases are used to store artifacts and cause pitting and cracking issues on lead objects [158]
- Gibson and Watt [110] conducted simulations proofing the pitting corrosion of lead due to acetic and formic acid

2.2.4 Overview of lead corrosion products

Table 2.6 shows all mentioned lead corrosion products with the most important characteristics and with the indication of some references for more information.

CHEMICAL NAME	MINERAL	CHEMICAL FORMULA	COLOR	CRYSTAL	REF
lead(II)carbonate	cerussite	$PbCO_3$	colorless	orthorhombic	[159–161]
lead(II)carbonate hydroxide	hydrocerussite	$Pb_3(CO_3)_2(OH)_2$	white	rhombicuboctahedral	[161]
α-lead(II)oxide	litharge	α-PbO	red	tetragonal	[162, 163]
β-lead(II)oxide	massicot	β-PbO	yellow	orthorhombic	
lead(II,IV)oxide	minium	Pb_3O_4	light red	tetragonal	[160]
lead(II)sulphate	anglesite	$PbSO_4$	colorless	orthorhombic	[164]
lead(II)sulfide	galena	PbS	gray	cubic and octahedral	[165]
lead(II)nitrate	-	$Pb(NO_3)_2$	white	cubic	[166]
basic lead(II)acetate	-	$Pb_3O_2(CH_3COO)_2 \cdot 0.5H_2O$	white	triclinic	[167]
lead(II)formate	-	$Pb(HCOO)_2$	white	-	[168]
basic lead(II)formate	-	$Pb_2O(CHOO)_2$	white	orthorhombic	[167]
lead(II)acetate trihydrate	lead sugar	$Pb(C_2H_3O_2)_2.3H_2O$	white	monoclinic	[168, 169]
lead(II)formate hydroxide	-	Pb(HCOO)(OH)	white	orthorhombic	[6]
lead(II)carbonate hydroxide oxide	plumbonacrite	$Pb_{10}O(OH)_6(CO_3)_6$	gray	hexagonal	[170]

Table 2.6 – Characteristics of the lead corrosion products.

2.3 Treatment of lead artifacts

As established in the previous section, lead metal objects are under constant attack and decay. It is important to note that the treatments used on lead artifacts depend on the aims of the conservator. For example, different treatments are needed to improve the readability of the surface such as inscriptions, repairing mechanical problems and conserving purposes depending on the environment [3]. In what follows, we focus on the prevention of the deterioration process [171]. To do this, conservators have to preserve the artifact's cultural, historical and technological identity in the best possible way [172]. Furthermore, conservators have to consider treatments with minimal intervention, which are preferably reversible and repeatable. Recently, only materials with a non-toxic nature towards both the objects, conservator and environment are considered to be used in conservation procedures [173]. Taking into account all these philosophies, two types of conservation are known: preventive and interventive conservation. Both will be briefly discussed below.

2.3.1 Preventive conservation

The changing indoor environmental conditions determined by factors such as temperature, light, humidity and air pollution (also from human beings) are crucial factors in the research towards the conservation of lead artifacts [174]. Mainly seasonal changes and the build-up of pollutants in sealed off showcases have a deteriorating effect on the lead metal collections [81]. Trying to limit these degradation phenomena, it is possible to keep the lead artifacts in a controlled environment in which all variables can be regulated [175].
Preventive corrosion, known as 'collections care', depends on the museum's policy and resources. When possible, climate control equipment is installed in museums [176, 177]. In the following list, several possible interventions are summed up, all of which can be combined.

- Dehumidification [178]
- Installation of air conditioning [179]
- Airflow system using filters (activated carbon filter) [180]
- Do not use potentially dangerous woods such as fibreboard and hardboards [3]

Of all these summed up problems, the change in relative humidity (RH) seems to be the most common one, as stated in an overall study of Thomson [181]. Indeed, the RH has an influence on the shape of the exhibits, the rate of the chemical corrosion reactions and the biological deterioration sources [43]. Preventing changes in RH could already solve a major part of the corrosion problem. Furthermore, some effort is needed to avoid temperature changes and to keep an acceptable exposure level of pollutants [112].
Museum conservators must also consider the fact that the ideal environmental conditions differ for the preservation of artifacts and the preservation of the building or display case [182]. Additionally, sometimes one artifact is constructed using different materials requiring different preventive conditions [183]. It is clear that a lot of preparations are necessary before considering a certain controlled environment. Often, for example, lead artifacts are stored in sealed containers or plastic bags [184, 185].

2.3.2 Interventive conservation

Often treatment methods are developed using an experimental set up using artificially prepared lead samples. In general, alloys, impurities, and the structure and presence of surface products are not taken into account [3]. Therefore, applying approved treatments on 'real' objects must be done with care. For this reason, it is important to know the limits and

consequences of the approved treatments or to contact specialists [186]. In what follows, we describe different possible treatment methods for lead metal samples and their limits.

2.3.2.1 Cleaning of lead artifacts

The first process in the conservation and restoration of lead objects is the cleaning process. Cleaning includes tasks like the removal of dirt and the dissolution of corrosion product crust [187]. There are, however, different possibilities to clean the lead artifact's surfaces.

Mechanical cleaning

Often the process of mechanical cleaning is used for the removal of the dirt and corrosion products from the surface of the artifact. To remove the top part of the thick crusts, archaeological objects have to be cleaned mechanically, at least in a first step [188]. In the case of lead, it is difficult to visually identify the original surface, which means a trained eye is required. Furthermore, conservators have to be careful using invasive equipment such as scalpels and power-driven tools [189]. These tools may smear or scratch the underlying sample due to the softness of the lead metal [190]. Considering that the dust is poisonous, handling lead artifacts using mechanical cleaning could be hazardous. It is recommended to use the appropriate safety measures [191]. Overall, the mechanical cleaning of lead is considered difficult.

Chemical treatment

After a first rough cleaning, lead artifacts can be cleaned chemically by using acids, alkalis, sequestering agents and ion-exchange resins to remove the lead corrosion products [192]. In what follows, we evaluate one of each agents for lead cleaning.

Different acids, such as nitric and sulfuric acid were abandoned very early in conservation history due to the serious damage caused. Around the 1940's, an interesting method was developed using dilute hydrochloric acid, which does not attack the lead metal, but forms a thin protective $PbCl_2$ crust. After that, one needs to immerse the artifact in diluted ammonium acetate, which is the only lead oxide dissolving reagent [185]. The procedure is called Caley's method because he cleaned 56 stable objects from the Athens Agora using this method [193]. Furthermore, the resulting film leaves a nice appearance, which does not change over a long period of time. Ideally this treatment is used for lightly corroded specimens. In other cases, electrolytic reduction, as described in section 2.3.2.2, is more appropriate [185]. The method also requires careful attention to avoid dissolution of the artifact, especially when using alloys.

Another possible electrochemical method, known as 'Krefting's method', is the use of dilute nitric acid as described by Rathgen [194] or an aqueous caustic soda solution with some metallic zinc powder to dissolve the crust [195] as described by Plenderleith [196], who used the following reaction [197]

$$Zn + 2NaOH \leftrightharpoons Na_2ZnO_2 + H_2. \tag{2.14}$$

This powder, in the form of granules, provides a homogeneous current distribution along the artifact. After washing the artifact with tap water, the artifact looks clean, but often residues of metal salts remain on the surface. In the work of Brown [192], an example is mentioned where a seal of Pope Paul III is treated using this method. However, the lack of selectivity and reaction control makes this method problematic for stabilization purposes (see section 2.3.2.2) [197].

A frequently reported method involves the immersion of the lead and lead alloyed artifacts in a solution of a sequestering agent [198]. Often a 4-10 % aqueous ethylenediaminetetracetic acid (EDTA) disodium salt solution is used, following the procedure developed by Kuhn [199]. In a publication of Van den Abeele et al. [200], EDTA was tested on artificially corroded metal plates (copper, brass and lead). Working on artifacts, Lane [201] warns us that the sequestering agents creep under the crust and start attacking the bare lead. Also, when using EDTA, it is recommended to put the sample in

a bath of ammonium acetate to remove the lead oxides [3].

Another example is described by Brown et al. [192] where a lead metal medal is cleaned by using hot-distilled water and a ion-exchange resin in the acid form, which has the advantage of avoiding chemicals and multiple rinsing steps. During the procedure, the resin beads absorb Pb^{2+} ions from the corrosion products while at the same time the CO_2 and organic acids are boiled off [202]. However, for heavily corroded artifacts this method is often less effective. In some cases, conservators even have seen damage of the artifacts [203].

Looking at all treatments mentioned, most of the chemicals used are corrosive towards lead. Therefore, treated lead artifacts have to be rinsed thoroughly. However, experience has taught us that rinsing is never entirely effective, which means corrosion easily starts again [204].

Laser cleaning

Cleaning lead artifacts using pulsed lasers is a feasible option, in spite of lead's low melting temperature. Indeed, a short pulse duration and a low repetition frequency or the use of a water bath avoid local heat accumulation. Thick crusts can be easily removed, preserving a thin protective patina [205]. Drakaki et al. [206] successfully used this method for the cleaning of Roman coins.

2.3.2.2 Stabilization of lead artifacts

Whereas stabilization processes are characterized by maintaining the details of the corrosion crust, cleaning processes dissolve the entire corrosion layer. Stabilization methods are often used on artifacts with thick corrosion crusts.

Plasma cleaning

A plasma treatment converts corrosion products of the artifact's crust to metallic lead by using a hydrogen plasma following the reaction [207]

$$2PbCO_3 \cdot Pb(OH)_2 + 2H^{\cdot} \rightleftharpoons 3Pb + 2CO_2 + 4H_2O, \tag{2.15}$$

with the production of water and carbon dioxide. Depending on the procedure's characteristics, such as the concentration of the gas mixture, the pressure and the type of electrical discharge, the treatment's performance changes. The limiting factor is that the converted lead obstructs further reduction of underlying layers [3]. As a result, the penetration depth of the method is limited to a thickness of 0.1 to 0.2 mm, which means this method can only be used for lightly corroded artifacts. Also, in the case of lead, the temperature has to be kept as low as possible [208]. More on the plasma treatment of lead is found in [207, 209, 210].

Electrolytic treatment

For the conservation of lead artifacts, two processes are considered based on reduction reactions. The easiest way is (1) the direct reduction of lead corrosion products or otherwise (2) we use the decomposition of water (reaction (ii) in Table 2.2) for the production of H_2 bubbles to generate a mechanical action at the metal surface to remove crust deposits very effectively. This process can be applied locally or in solution [3].

The use of zinc granules in Krefting's method was inconvenient because of the lack of control over the electrochemical reaction, which inevitably led to the loss of the corrosion crust. A possible solution is the use of a power supply to generate the necessary electron flux. Now, the metal artifact is immersed in a conductive salt (such as sodium carbonate) solution and put into contact with the power supply using conductive wires. The artifact is connected to the cathode (negative pole) and the counter-electrode to the anode (positive pole). The counter-electrode is often made of stainless steel when used in alkalis, lead when used in acidic electrolytes or platinum. The latter is usually recommended due to its inertness

in all conditions. However, this set-up uses high current densities (around 2 - 5 A dm^{-2}), indicating a mechanical stripping of the corrosion crust due to hydrogen bubbling [211] (see Table 2.7).

A less invasive treatment was proposed in the 1960s by Lane [212]. In this case, the current density is kept low to avoid hydrogen bubbling and to allow the reduction of only the corrosion crust (see Table 2.7). The poor cohesion and adherence of the newly produced lead metal, make it difficult to consolidate the artifact. Therefore, often the use of ion exchange resins in intimate contact with the artifact is recommended. Three electrolyte solutions have been tested, dilute sulphuric acid (2 to 10% H_2SO_4 v/v), sodium carbonate (5% Na_2CO_3 w/v) and sodium hydroxide (5% NaOH w/v). Each of these solutions has its advantages and disadvantages, as discussed in recent literature [213].

Later, in the 1990s, a potentiostatic method, based on a three-electrode system, was designed to control the potential applied to the artifact [213]. To start, a polarization plot is recorded to identify all possible electrochemical processes by identifying peaks in the voltammogram. Afterwards, the actual treatment can be executed by applying a constant potential and monitoring the current to check the reaction progress (see Table 2.7). When using the treatment on composite or fragile objects, it is recommended to perform it locally by using an electrolytic stainless steel pencil wrapped in cotton, known as an *electrolytic pencil* [3].

METHOD	MATERIALS	EFFECTS	REFERENCE
Krefting's method	Zn granules and dilute HNO_3	mechanical stripping	[192, 194, 197, 202]
	Zn granules and NaOH	mechanical stripping	[196]
cathodic polarization	NaOH	mechanical stripping	[203, 211]
2 to 5 A dm^{-2}	H_2SO_4	mechanical stripping	[211, 213, 214]
	Na_2CO_3	mechanical stripping	[215]
consolidative reduction	dilute H_2SO_4	reduction of corrosion crust	[194, 216, 217]
(galvanostatic)	Na_2CO_3	reduction of corrosion crust	[218, 219]
6 to 300 mA dm^{-2}	NaOH	reduction of corrosion crust	[220, 221]
consolidative reduction	Na_2SO_4	reduction of corrosion crust	[222–224]
(potentiostatic)	H_2SO_4	reduction of corrosion crust	[225]
	$NaHCO_3$	reduction of corrosion crust	[92]

Table 2.7 – Summary of the presented electrochemical treatments [3].

Often, authors of publications on the subject of metal cleaning forget to mention the stability of the artifacts after treatment. In most cases, however, the treatments are not successful in stopping the corrosion progression. In what follows, we try to give an overview of the methods used to decrease the surface reactivity after the treatment of lead artifacts.

Fast post-treatments

Early work by Organ [192] talks about rinsing the artifact in a diluted sulfuric acid solution so that a sulfate film is formed. This method does not offer a complete protection, but can be helpful in certain conditions. Another, more general, method is anodic polarization. It is used in different media such as sulfuric acid [226], sodium sulfate and potassium iodide [227]. This technique can also produce lead oxide films [212]. Most of these treatments have been tested on laboratory scale, in specific conditions and often on pure metal samples. It is clear that science cannot guarantee the complete harmlessness of the treatments in very specific cases. For example, treating an artifact, the chances of changing the structure and the surface chemistry are quite high.

2.3.2.3 Preservation

As established, lead and its alloys are under constant attack by their surroundings. As proposed, eliminating organic vapors, high humidity environments, mechanical disturbances and galvanic-cell formations makes it easy to preserve lead artifacts. However, in some situations this is impossible and we need to protect the artifact using inhibitors or barrier coatings. In the last part, we give an overview of the possibilities.

Inhibitors

Corrosion inhibitors are defined by Gräfen et al. [228] as "substances that reduce or eliminate the aggressiveness of a corrosive medium and are either already contained in the corrosive medium or are specifically added to it. A distinction is made between electrochemical, chemical, and physical inhibitors." The use of inhibitors for lead is rare due to its resistance to atmospheric corrosion [229]. However, organic corrosion inhibitors, that mainly contain nitrogen, sulfur or oxygen atoms, are able to adsorb onto the metal surface to protect the underlying bulk material against corrosion [230]. For example, volatile amines can be used in closed museum humidification systems to decrease the corrosion rate of lead metal artifacts [231], which is probably due to self-assembly [232]. Several amino acids have also been tested to inhibit lead corrosion [233].

However, surfactant inhibitors with a polar hydrophilic *head* and a non-polar hydrophobic *tail* are often used, because of their many advantages such as high inhibition efficiency, low price, low toxicity, and easy production [230]. To illustrate, Sharma et al. [234] used benzotriazole for the protection of ancient and historic leaded bronzes due to the formation of crystalline polymeric Pb-BTA and PbO-BTA complex film [235]. Brunoro et al. [236] suggested that alloys showed a lower inhibition efficiency because of a weaker metal-triazole bond. Rocca et al. [92, 237–239] worked extensively on the ability of sodium monocarboxylates to slow down lead corrosion. In this case, the passivation was a consequence of the formation of a crystalline metallic soap layer [240]. Other examples are shown in Table 2.8. Often these inhibitors are often used during the treatments to minimize attack from some reactants.

INHIBITOR	EXAMPLE COMPOUNDS	REFERENCE
volatile amines	diethylaminoethanol (DEAE)	[231]
amino acids	alanine, valine, histidine, glutamic and cysteine	[233, 241]
pyrazole derivatives	3-amino-5-phenylpyrazole and 5-amino-3-(4-methylphenyl)pyrazole	[242]
benzotriazole (BTA)		[234, 235, 239, 243]
carboxylates	sodium decanoate and sodium dodecanoate	[92, 237–239, 244]
phosphates	poly- or orthophosphates	[245–248]
sodium dodecyl sulfate (SDS)		[249]
hydrazine derivatives	hydrazine, phenyl hydrazine, 2,4- dinitrophenyl hydrazine, 4-nitrobenzoyl hydrazine and tosyl hydrazine	[250, 251]

Table 2.8 – Summary of the presented corrosion inhibitors on lead and lead alloys.

Barrier protection

As an alternative, a coating is applied to lead artifacts to protect them from corrosive environment gasses. In literature, lead metal artifacts are often coated by using paraffin wax, microcrystalline waxes or a mixture of both, such as the Renaissance wax by rubbing the sample with a cloth [252]. Important disadvantages of this method are the susceptibility to the accumulation of dust and reversibility problems [253]. Sometimes, acrylic varnishes or polyvinyl resins are also considered for treating lead artifacts [254]. However, when these treated artifacts are kept in very humid environments, it is very likely the coating will decompose to form acetic acid [22]. Another example is a linseed oil to form a *varnish*

like layer, which allows normal patination on lead roof surfaces or outdoor statues [255].

These examples show it is important to consider the particular conditions and the corresponding corrosion mechanisms to which the sample will be exposed after treatment. Next to the material choice, however, other important factors are needed to provide definitive conclusions about the coating's degree of protection [3]. These include the application method, number of coats, the aging and decomposition properties, the composition of the artifact and the thickness of the coating. In addition, laboratory experiments conducted using accelerated corrosion or electrochemical tests on clean or coated lead samples do not always agree with artifacts, whether or not they are placed in the same environment. Even coatings which show no corrosion to the naked eye, can allow localized attacks, which indicates that the coating is susceptible to long-term corrosion [256].

COATING MATERIAL	SPECIFICS	REFERENCE
natural wax	beeswax, carnauba	[252]
paraffines	polyethylene wax, paraffin wax	[193, 218, 257]
microcrystalline wax	Cosmolloid 80H	[220, 257, 258]
mixture of paraffin and microcrystalline wax	Renaissance wax	[252, 257, 259]
acrylic varnish	Paraloid B-72	[254, 258]
polyvinyl resin	Butvar B-98	[254]
oil coating	linseed oil	[260]
hydrophobic silicon		[221]
carboxylates	sodium decanoate and sodium undecanoate	[261]

Table 2.9 – Summary of coatings used on lead and lead alloys.

In conclusion, we state that it is difficult to produce a coating which is capable of preventing lead corrosion in atmospheres with organic acid vapor traces. At this moment, several research groups are still working on a solution for this problem.

Restoration

Polyvinyl acetate was once used as a glue for repairing lead artifacts [221]. However, this kind of adhesive was abandoned because of its emission of organic acid vapors [22]. Moreover, sometimes epoxy resins are used as an embedding or restoring material [221].

2.4 Ethical challenges in conservation

As in other fields of conservation and restoration, the work of the metal conservators, such as choosing a treatment or cleaning procedure, is guided by ethical standards. Over the years, a set of universal intervention guidelines has been (inter)nationally established and written down in different codes. All these documents are based on the fact that "the conservation process is governed by absolute respect for the aesthetic, historic, and physical integrity of the work, and requires a high sense of moral responsibility" [262]. The two most interesting examples are the *Code of Ethics and Guidelines for Practice of the American Institute for Conservation* [263] and the professional guidelines from the European Confederation of Conservator-restorers' Organizations [264].

Specifically, in the case of metal conservation, the main concern is the destruction of valuable scientific data using specific treatments. At first sight, the patina of metallic historical objects simulates the long-lost state of artifacts. However, for technical and architectural reasons it is occasionally necessary to remove the object's patina thereby changing its appearance, allowing misjudgment. Indeed, because of these treatments museum visitors or even professionals have

often problems to distinguish between fakes, originals, copies or forgeries [265].

When possible, endangered and damaged historical objects must be preserved. However, a general agreement states that "one must intervene as little as possible and avoid any structural and decorative falsification" [266]. To decide which treatments should be used on valuable artifacts, it is advised and generally accepted to ask opinions of as many experts as possible including archaeologists, art historians, historians, scientists and conservators [267].

References for Chapter 2

[1] K. LEW, *Lead*, Rosen Publishing Group, 2008, 10–12.

[2] A. DE, *A text book of inorganic chemistry*, New Age International Limited, 2007.

[3] V. COSTA and F. URBAN, Lead and its alloys: Metallurgy, deterioration and conservation, *Rev. Conserv.* **6** (2005), 48–62.

[4] ASTM INTERNATIONAL, *Corrosion tests and standards*, ed. by R. BABOIAN, 2005, 533.

[5] UNITED NATIONS, *Final review of scientific information on lead*, tech. rep., 2010, 16.

[6] A. NIKLASSON, Atmospheric corrosion of historic lead organ pipes, PhD thesis, Chalmers University of Technology, 2007.

[7] C. DI MARTINI, Lead and lead alloys, in: *Metallography and microstructures*, ASM International, 2002, 415–424.

[8] N. GALE and Z. STOS-GALE, Lead and silver in the ancient Aegean, *Sci. Amer.* **244** (1981), 176–192.

[9] B. PREDEL, Pb-Pt (Lead - Platinum), in: *Ni-Np - Pt-Zr*, Springer, 1998, 1–4.

[10] R. PRENGAMAN, Lead alloys, in: *Ullmann's Encyclopedia of Industrial Chemistry*, John Wiley & Sons, 2000, 1–12.

[11] H. BAKER and ASM INTERNATIONAL, *Properties and selection: Nonferrous alloys and special-purpose materials*, ASM International, 1990.

[12] B. SIVASANKAR, *Engineering chemistry*, McGraw-Hill Book Company, 2008, 40–41.

[13] G. JOSEPH and K. KUNDIG, *Copper: Its trade, manufacture, use, and environmental status*, ASM International, 1998, 72.

[14] L. SELWYN and CANADIAN CONSERVATION INSTITUTE, *Metals and corrosion: A handbook for the conservation professional*, Canadian Conservation Institute, 2004, 223.

[15] T. CLARKE, Music and chemistry: Organ failure, *Nature* **427** (6969) (2004), 8–9.

[16] C. OERTEL et al., Acetic acid vapor corrosion of lead-tin alloys containing 3.4 and 15 % tin, *J. Electrochem. Soc.* **156** (12) (2009), C414–C421.

[17] C. BERGSTEN et al., *The Collapse project: Corrosion of organ pipes - causes and recommendations*, University of Gothenburg, Göteborg Organ Art Center, 2011, 136–140.

[18] D. HAMILTON, U.S. NAVAL HISTORICAL CENTER, and NAUTICAL ARCHAEOLOGY PROGRAM, *Basic methods of conserving underwater archaeological material culture*, tech. rep., Texas A&M University, 1998, 1–110.

[19] S. GURUSWAMY, *Engeneering properties and applications of lead alloys*, CRC Press, 1999, 483.

[20] I. KALPAKIDIS, *Effects of heating and load history on the behavior of lead-rubber bearings*, ProQuest, 2008, 10.

[21] P. STORME, M. JACOBS, and E. LIETEN, Research on corrosion of lead printing letters from the Museum Plantin-Moretus, Antwerp, *Proc. Chem.* **8** (2013), 307–316.

[22] C. PEARSON, *Conservation of marine archaeological objects*, Butterworth-Heinemann, 1987, 90.

[23] I. KULEFF et al., Chemical and lead isotope compositions of lead artifacts from ancient Thracia (Bulgaria), *J. Cult. Herit.* **7** (4) (2006), 244–256.

[24] A. ALESSANDRELLO et al., Measurements on radioactivity of ancient roman lead to be used as shield in searches for rare events, *Nucl. Methods Phys. Res.* **B61** (1991), 106–117.

[25] G. MOLINA et al., Production technology and replication of lead antimonate yellow glass from New Kingdom Egypt and the Roman Empire, *J. Archaeol. Sci.* **41** (2014), 171–184.

[26] J. DIK et al., Early prodcution recipes for lead antimonate yellow in Italian art, *Archaeometry* **47** (3) (2005), 593–607.

[27] A. SHORTLAND, P. NICHOLSON, and C. JACKSON, Lead isotopic analysis of 18th-dynasty Egyptian eyepaints and lead antimonate colorants, *Archaeometry* **42** (1) (2000), 153–157.

[28] A. UEBERSCHAER, U. HEUBNER, and M. REINERT, *Lead-antimony alloy*, 1976.

[29] F. HABASHI, *Alloys: Preparation, properties, applications*, John Wiley & Sons, 1998, 111–112.

[30] A. SIGEL, H. SIGEL, and R. SIGEL, eds., *Metal ions in biological systems*, CRC Press, 2005, 172.

[31] M. HARTWIG, *A companion to ancient Egyptian art*, John Wiley & Sons, 2014, 511.

[32] K. EHRHARDT, *European metals in native hands: Rethinking technological change 1640-1683*, University of Alabama Press, 2005, 143.

[33] P. CRADDOCK, The composition of the copper alloys used by the Greek, Etruscan and Roman civilizations, *J. Archaeol. Sci.* **5** (1) (1978), 1–16.

[34] X. FAN et al., Brass before bronze? Early copper-alloy metallurgy in China, *J. Anal. At. Spectrom.* **27** (5) (2012), 821–826.

[35] D. SCOTT, J. PODANY, and B. CONSIDINE, *Ancient & historic metals: Conservation and scientific research*, Getty Publications, 1994, 272–275.

[36] D. SCOTT, *Metallography and microstructure in ancient and historic metals*, Getty Publications, 1991, 92.

[37] S. SHALEV and J. NORTHOVER, The metallurgy of the Nahal Mishmar hoard reconsidered, *Archaeometry* **35** (1) (1993), 35–47.

[38] J. CASAS and J. SORDO, *Lead: Chemistry, analytical aspects, environmental impact and health effects*, Elsevier, 2011, 3.

[39] M. MEGAHED, Electrochemical study of (lead bronze) alloy in 3.5% NaCl solution and testing two protective coatings, applied on some selected archaeological objects, in: *Proc. 4th International Congress on Science and technology for the safeguard of cultural heritage in the Mediterranean basin*, ed. by A. FERRARI, Institute of Chemical Methodologies, 2009, 3–12.

[40] J. FRICK, *Woldman's engineering alloys*, ASM International, 2000, 290–291.

[41] IUPAC, *Compendium of chemical terminology (the 'Gold Book')*, ed. by A. MCNAUGHT and A. WILKINSON, 2nd, Blackwell Scientific Publications, 2014, 340.

[42] B. SHAW and R. KELLY, What is corrosion?, *Electrochem. Soc. Interf.* **15** (1) (2006), 24–26.

[43] G. PAVLOGEORGATOS, Environmental parameters in museums, *Build. Environ.* **38** (12) (2003), 1457–1462.

[44] S. OESCH and M. FALLER, Environmental effects on materials: The effect of the air pollutants SO_2, NO_2, NO and O_3 on the corrosion of copper, zinc and aluminium. A short literature survey and results of laboratory exposures, *Corros. Sci.* **39** (9) (1997), 1505–1530.

[45] J. WARNER, Thermodynamic considerations in the corrosion of metals, *J. Electrochem. Soc.* **83** (1) (1943), 319–333.

[46] P. ATKINS, *Physical chemistry*, 10th, Oxford University Press, 2010, 227–233.

[47] A. BOND et al., *Electroanalytical methods*, ed. by F. SCHOLZ, 2nd, Springer, 2010, 137.

[48] M. POURBAIX, *Atlas of electrochemical equilibria in aqueous solutions*, NACE International, 1974, 489.

[49] V. BIRSS and M. SHEVALIER, The lead anode in alkaline solutions, *Electrochem. Sci. Technol.* **134** (4) (1987), 802–808.

[50] N. PEREZ, *Electrochemistry and corrosion science*, Springer Science, 2004, 3.

[51] W. VERNON, Second experimental report to the atmospheric corrosion research committee (British non-ferrous metals research association), *Trans. Faraday Soc.* **23** (1927), 113–183.

[52] H. TOMPKINS, The interaction of some atmospheric gases with a tin-lead alloy, *J. Electrochem. Soc.* **120** (5) (1973), 651–654.

[53] A. NIKLASSON et al., Air pollutant concentrations and atmospheric corrosion of organ pipes in European church environments, *Stud. Conserv.* **53** (1) (2008), 24–40.

[54] N. LEBOZEC, M. JÖNSSON, and D. THIERRY, Atmospheric corrosion of magnesium alloys: Influence of temperature, relative humidity, and chloride deposition, *Corros.* **60** (4) (2004), 356–361.

[55] K. KINOSHITA, *Electrochemical oxygen technology*, John Wiley & Sons, 1992, 1–4.

[56] E. ABD EL AAL, S. ABD EL WANEES, and A. ABD EL AAL, Anodic behavior and passivation of a lead electrode in sodium carbonate solutions, *J. Mater. Sci.* **28** (10) (1993), 2607–2614.

[57] S. ABD EL-REHIM et al., Potentiodynamic and cyclic voltammetric behavior of a lead electrode in NaOH solution, *Monatsh. Chem. Chem. Mon.* **128** (1997), 245–254.

[58] N. DAHOTRE and T. SUDARSHAN, *Intermetallic and ceramic coatings*, CRC Press, 1999, 111–113.

[59] J. DAVIS, *Surface engineering for corrosion and wear resistance*, ASM International, 2001, 16–26.

[60] I. ZHITOMIRSKY et al., Electrochemical preparation of PbO films, *J. Mater. Sci. Lett.* **14** (11) (1995), 807–810.

[61] T. GRAEDEL, Chemical mechanisms for the atmospheric corrosion of lead, *J. Electrochem. Soc.* **141** (4) (1994), 922–927.

[62] A. DOMÉNECH-CARBÓ, M. DOMÉNECH-CARBÓ, and M. PEIRÓ-RONDA, Dating archeological lead artifacts from measurement of the corrosion content using the voltammetry of microparticles, *Anal. Chem.* **83** (14) (2011), 5639–5644.

[63] E. KIM and J. HERRERA, Characteristics of lead corrosion scales formed during drinking water distribution and their potential influence on the release of Lead and Other Contaminants, *Environ. Sci. Technol.* **44** (2010), 6054–6061.

[64] P. DELAHAY, M. POURBAIX, and P. VAN RYSSELBERGHE, Potential-pH diagram of lead and its applications to the study of lead corrosion and to the lead storage battery, *J. Electrochem. Soc.* **98** (2) (1951), 57–64.

[65] A. NIKLASSON, L. JOHANSSON, and J. SVENSSON, Influence of acetic acid vapor on the atmospheric corrosion of lead, *J. Electrochem. Soc.* **152** (12) (2005), B519–B525.

[66] B. SCHOTTE, A study of the electrolytic reduction of corroded lead objects and the application, characterization and testing of a protective lead carboxylate coating, PhD thesis, Ghent University, 2007, 12–13.

[67] F. MANSFELD, *Corrosion mechanisms*, CRC Press, 1986, 211–284.

[68] G. GARDNER and G. NANCOLLAS, Complex formation in lead sulfate solutions, *Anal. Chem.* **42** (7) (1970), 794–795.

[69] B. SHARMA, *Objective question bank in chemistry*, Krishna Prakashan Media, 1997, 221.

[70] P. MOSELEY et al., *Valve-regulated lead-acid batteries*, Elsevier, 2004, 3–5.

[71] R. WALKER and A. HILDRED, Manufacture and corrosion of lead shot from the flagship Mary Rose, *Stud. Conserv.* **45** (4) (2000), 217–225.

[72] T. STERNER and B. TURNHEIM, Innovation and diffusion of environmental technology: Industrial NO_x abatement in Sweden under refunded emission payments, *Ecol. Econom.* **68** (12) (2009), 2996–3006.

[73] A. RUSSELL, G. MCRAE, and G. CASS, The dynamics of nitric acid production and the fate of nitrogen oxides, *Atmos. Environ.* **19** (6) (1985), 893–903.

[74] J. HOUSE, *Inorganic chemistry*, Academic Press, 2012, 470.

[75] M. FONTANA, *Corrosion Engineering*, 3rd, McGraw-Hill Book Company, 1986.

[76] L. FERRIS, Lead nitrate-nitric acid-water system, *J. Chem. Eng. Data* **5** (3) (1960), 242–242.

[77] E. ABD EL AAL, S. ABD EL WANEES, and A. ABD EL AAL, Autocatalytic dissolution of Pb in HNO_3, *J. Mater. Sci.* **27** (2) (1992), 365–373.

[78] M. EL-NAGGAR, Effects of HNO_3 concentration on the electrochemical behavior of lead, *Monatsh. Chem. Chem. Mon.* **132** (10) (2001), 1189–1200.

[79] R. POHANISH, *Sittig's handbook of toxic and hazardous chemicals and carcinogens*, William Andrew, 2012, 1572–1615.

[80] S. BLACKSHAW and V. DANIELS, Selecting safe materials for use in the display and storage of antiquities, in: *ICOM Conserv. Comm. Conf. 5th Trienn. Meet.* 1978, 1–9.

[81] C. MILES, Wood coatings for display and storage cases, *Stud. Conserv.* **31** (3) (1986), 114–124.

[82] INTER-SERVICE METALLURGICAL RESEARCH COUNCIL, V. RANCE, and H. COLE, *Corrosion of metals by vapors from organic materials: A survey*, 1958, 1–25.

[83] S. BLACKSHAW and V. DANIELS, The testing of materials for use in storage and display in museums, *Conserv.* **3** (1) (1979), 16–19.

[84] S. CLARKE and E. LONGHURST, The corrosion of metals by acid vapors from wood, *J. Appl. Chem.* **11** (11) (1961), 435–443.

[85] L. CHRISTOPHER, Adding value prior to pulping: Bioproduts from hemicellulose, in: *Global Perspectives on Sustainable Forest Management*, ed. by C. OKIA, InTech, 2012, 225–246.

[86] S. DAVIES et al., Rapid analysis of formic acid, acetic acid, and furfural in pretreated wheat straw hydrolysates and ethanol in a bioethanol fermentation using atmospheric pressure chemical ionisation mass spectrometry, *Biotechnol. Biofuels* **4** (28) (2011), 1–8.

[87] P. ARNI, G. COCHRANE, and J. GRAY, The emission of corrosive vapours by wood. I. Survey of the acid-release properties of certain freshly felled hardwoods and softwoods, *J. Appl. Chem.* **15** (7) (1965), 305–313.

[88] E. PALMQVIST and B. HÄHN-HÄGERDAL, Fermentation of lignocellulosic hydrolysates. II: inhibitors and mechanisms of inhibition, *Bioresour. Technol.* **74** (2000), 25–33.

[89] J. ALMEIDA et al., Increased tolerance and conversion of inhibitors in lignocellulosic hydrolysates by *Saccharomyces cerevisiae*, *J. Chem. Technol. Biotechnol.* **82** (2007), 340–349.

[90] J. SEIDEL, *The organ and its construction*, Ewer, 1852, 52.

[91] A. NIKLASSON, L. JOHANSSON, and J. SVENSSON, Atmospheric corrosion of historical organ pipes: influence of acetic and formic acid vapor and water leaching on lead, in: *Metal 04: Proc. International conference on metals conservation*, National Museum of Australia Canberra, 2004, 273–280.

[92] E. ROCCA, C. RAPIN, and F. MIRAMBET, Inhibition treatment of the corrosion of lead artefacts in atmospheric conditions and by acetic acid vapor: use of sodium decanoate, *Corros. Sci.* **46** (3) (2004), 653–665.

[93] A. NIKLASSON, L. JOHANSSON, and J. SVENSSON, The influence of relative humidity and temperature on the acetic acid vapor-induced atmospheric corrosion of lead, *Corros. Sci.* **50** (11) (2008), 3031–3037.

[94] N. FLEMMING et al., Thermal decomposition of basic lead carbonates: A comparison of hydrocerussite and plumbonacrite, *Thermochim. Acta* **81** (1984), 1–8.

[95] E. ROCCA, F. MIRAMBET, and J. STEINMETZ, Study of ancient lead materials: A gallo-roman sarcophagus - contribution of the electrolytic treatment to its restoration, *J. Mater. Sci.* **39** (2004), 2767–2774.

[96] A. NIKLASSON, L. JOHANSSON, and J. SVENSSON, Atmospheric corrosion of lead: The influence of formic acid and acetic acid vapors, *J. Electrochem. Soc.* **154** (11) (2007), C618–C625.

[97] J. TÉTREAULT et al., Corrosion of copper and lead by formaldehyde, formic and acetic acid vapors, *Stud. Conserv.* **48** (4) (2003), 237–250.

[98] C. MARTINI, A. NIKLASSON, and J. BERGSTEN, Collapse project: Europees onderzoek naar corrosie bij pijpwerk, *Orgelkunst* **28** (1) (2005), 30–43.

[99] C. CHIAVARI et al., Atmospheric corrosion of historical organ pipes: The influence of environment and materials, *Corros. Sci.* **50** (9) (2008), 2444–2455.

[100] L. SELWYN, D. RENNIE-BISAILLION, and N. BINNIE, Metal corrosion rates in aqueous treatments for waterlogged wood-metal composites, *Stud. Conserv.* **38** (3) (1993), 180–197.

[101] Y. LU and N. MOSIER, Kinetic modeling analysis of maleic acid-catalyzed hemicellulose hydrolysis in corn stover, *Biotechnol. Bioeng.* **101** (6) (2008), 1170–1181.

[102] L. BRATASZ et al., Impact of indoor heating on painted wood: monitoring the mediaeval altar in the church of Santa Maria Maddalena in Rocca Pietore, Italy, *Stud. Conserv.* **52** (2007), 199–210.

[103] M. DE KEERSMAECKER et al., In-situ spectroelectrochemical characterization of the electrochemical growth and breakdown of a lead dodecanoate coating on a lead substrate, *Talanta* **132** (2015), 760–768.

[104] V. KONTOZOVA-DEUTSCH, Characterization of indoor gaseous and particulate pollutants for conservation in museums and churches, PhD thesis, University of Antwerp, 2007.

[105] H. HODGES, Showcases made of chemically unstable materials, *Museum* **34** (1982), 56–58.

[106] W. ODDY, An unsuspected danger in display, *Museums J.* **73** (1973), 27–28.

[107] A. WERNER, Conservation and display (i) Environmental control, *Museums J.* **72** (1972), 58–62.

[108] T. OIKAWA et al., Volatile organic compounds from wood and their influences on museum artifact materials I. Differences in wood species and analyses of causal substances of deterioration, *J. Wood Sci.* **51** (4) (2005), 363–369.

[109] E. GALILI, B. ROSEN, and J. SHARVIT, Artifact assemblages from two Roman shipwrecks off the Carmel coast, *'Atiqot* **63** (2010), 61–110.

[110] L. GIBSON and C. WATT, Acetic and formic acids emitted from wood samples and their effect on selected materials in museum environments, *Corros. Sci.* **52** (1) (2010), 172–178.

[111] M. RYHL-SVENDSEN, Corrosivity measurements of indoor museum environments using lead coupons as dosimeters, *J. Cult. Herit.* **9** (3) (2008), 285–293.

[112] J. TÉTREAULT, J. SIROIS, and E. STAMATOPOULOU, Studies of lead corrosion in acetic acid environments, *Stud. Conserv.* **43** (1) (1998), 17–32.

[113] P. SPECTRE, *Painting and varnishing*, WoodenBoat Books, 1995, 28–29.

[114] SCOTTISH MUSEUMS COUNCIL, *The effects of storage and display materials onmuseum objects*, tech. rep., 2003, 1–5.

[115] D. THICKETT and L. LEE, *Selection of materials for the storage or display of museum objects*, British Museum Press, 2004, 6–26.

[116] J. TÉTREAULT, Sustainable use of coatings in museums and archives - some critical observations, *Coatings in Museums and Archives* **8** (2011), 39–48.

[117] C. HIGGITT, M. SPRING, and D. SAUNDERS, Pigment-medium interactions in oil paint films containing lead-based pigments, *WAAC Newsletter* **27** (2) (2005), 12–16.

[118] K. KEUNE, Binding medium, pigments and metal soaps characterised and localised in paint cross-sections, PhD thesis, Swammerdam Institute for Life Sciences, 2005, 113–169.

[119] L. ROBINET and M. CORBEIL, The characterization of metal soaps, *Stud. Conserv.* **48** (1) (2003), 23–40.

[120] E. COLES, J. GIBSON, and R. HINDE, The corrosion of lead by dilute aqueous organics, *J. Appl. Chem.* **8** (1958), 341–348.

[121] R. LESAR, *Introduction to computational materials science*, Cambridge University Press, 2013, 303.

[122] H. FECHT, Intrinsic instability and entropy stabilization of grain boundaries, *Phys. Rev. Lett.* **65** (5) (1990), 610–613.

[123] B. SYRETT and A. ACHARYA, *Corrosion and degradation of implant materials*, ASTM, 1979, 123.

[124] E. LEHOCKEY et al., On the relationship between grain boundary character distribution and intergranular corrosion, *Scr. Mater.* **36** (10) (1997), 1211–1218.

[125] W. ROSTOKER and J. DVORAK, *Interpretation of metallographic structures*, Elsevier, 2012, 270.

[126] K. HNATIUK, Effects of display materials on metal artifacts. Effets des materiaux d'etalage sur les objets de metal, *Gaz. - Q. Can. Museums Assoc.* **14** (3-4) (1981), 42–50.

[127] C. CHIAVARI and C. MARTINI, Deterioration of tin-rich organ pipes, *J. Mater. Sci.* **41** (2006), 1819–1826.

[128] Advances in localized corrosion, in: *Proc. 2nd International Conference on localized corrosion*, ed. by H. ISAACS et al., National association of corrosion engineers, 1990, 474.

[129] L. SHREIR, G. BURSTEIN, and R. JARMAN, *Corrosion*, Butterworth-Heinemann, 1994, 1409.

[130] R. TYLECOTE, The behavior of lead as corrosion resistant medium undersea and in soils, *J. Archaeol. Sci.* **10** (1983), 397–409.

[131] J. BURBANK and A. SIMON, The relation of the anodic corrosion of lead and lead-antimony alloys to microstructure, *J. Electrochem. Soc.* **100** (1) (1953), 11–14.

[132] C. CHIAVARI et al., Influence of microstructure and composition on corrosion of lead-rich organ pipes, in: *Corrosion of metallic heritage artifacts*, ed. by P. DILMANN et al., Elsevier, 2014, 352–365.

[133] K. RALSTON and N. BIRBILIS, Effect of grain size on corrosion: A review, *Corros.* **66** (7) (2010), 1–13.

[134] T. HIRASAWA et al., Electrochemical characteristics of Pb-Sb alloys in sulphuric acid solutions, *J. Power Sources* **85** (2000), 44–48.

[135] D. KELLY, P. NIESSEN, and E. VALERIOTE, The influence of composition and microstructure on the corrosion behavior of Pb-Ca-Sn alloys in sulfuric acid solutions, *J. Electrochem. Soc.* **132** (1985), 2533–2538.

[136] M. TERADA et al., Microstructure and intergranular corrosion of the austenitic stainless steel 1.4970, *J. Nucl. Mater.* **358** (2006), 40–46.

[137] S. BRADFORD, *Corrosion control*, Springer Science, 2012, 61.

[138] K. ZOHDY, M. SADAWY, and M. GHANEM, Corrosion behavior of leaded-bronze alloys in sea water, *Mater. Chem. Phys.* **147** (3) (2014), 878–883.

[139] C. LIANG et al., Corrosion behavior of brass coinage in synthetic sweat solution, *T. Nonferr. Metal Soc.* **25** (2) (2015), 654–660.

[140] L. CAMPANELLA et al., The effect of tin on dezincification of archaeological copper alloys, *Corros. Sci.* **51** (9) (2009), 2183–2191.

[141] K. TRENTELMAN et al., A comparative study of the composition and corrosion of branches from Eastern Han dynasty money trees, *Stud. Conserv.* **44** (1999), 170–183.

[142] S. SHAH, R. GRUGEL, and B. LICHTER, Corrosion behavior of lead-copper alloys in sulfuric-acid for battery applications, *J. Appl. Electrochem.* **21** (11) (1991), 1013–1022.

[143] A. ALLAH et al., Effect of alloying with antimony on the dissolution behavior of lead in H_2SO_4 solution - further investigation, *B. Soc. Chim. Fr.* **5** (1991), 635–640.

[144] J. DAVIS, *Alloying: Understanding the basics*, ASM International, 2001, 271.

[145] C. DEGRIGNY, *Étude des processus de corrosion développés sur des poids en plomb du musée du CNAM de Paris: proposition d'un mécanisme de corrosion*, tech. rep., Arc'Antique, Nantes, 1995.

[146] N. SATO, Basics of corrosion chemistry, in: *Green corrosion chemistry and engineering: Opportunities and challenges*, ed. by S. SHARMA, 1st, Wiley, 2012, 1–32.

[147] N. TENNENT, J. TATE, and L. CANNON, The corrosion of lead artifacts in wooden storage cabinets, *SSCR Journal* **4** (1) (1993), 8–11.

[148] R. WOLFE et al., Measurement of pH gradients in the crevice corrosion of iron using a palladium hydride microelectrode, *J. Electrochem. Soc.* **152** (2) (2005), B82–B88.

[149] F. WALL et al., Does anything pin the pitting behavior of aluminum?, in: *Proc. International Symposium on corrosion and protection of light metal alloys*, ed. by R. BUCHHEIT, The Electrochemical Society, 2004, 1–11.

[150] P. JAKOBSEN and E. MAAHN, Temperature and potential dependence of crevice corrosion of AISI 316 stainless steel, *Corros. Sci.* **43** (9) (2001), 1693–1709.

[151] S. TSUJIKAWA, Y. SONO, and Y. HISAMATSU, *Corrosion Chemistry within Pits*, ed. by A. TURNBULL, National Physical Laboratory, 1987, 171.

[152] P. MARCUS, *Corrosion mechanisms in theory and practice*, CRC Press, 2011, 451–453.

[153] A. PATERAKIS, The formation of acetate corrosion on bronze antiquities: Characterisation and conservation, PhD thesis, University College London, 2010, 99.

[154] D. SCOTT, *Ancient metals: Microstructure and metallurgy*, Conservation Science Press, 2010, 129.

[155] P. DONOVAN and J. STRINGER, Corrosion of metals and their protection in atmospheres containing organic acid vapors, *Br. Corr. J.* **6** (3) (1971), 132–138.

[156] M. AMIN and S. ADBEL REHIM, Pitting corrosion of lead in sodium carbonate solutions containing NO_3^- ions, *Electrochim. Acta* **49** (2004), 2415–2424.

[157] C. NGUYEN, K. STONE, and M. EDWARDS, Nitrate accelerated corrosion of lead solder in potable water systems, *Corros. Sci.* **53** (2011), 1044–1049.

[158] R. GRAYBURN et al., Time-lapse synchrotron X-ray diffraction to monitor conservation coatings for heritage lead in atmospheres polluted with oak-emitted volatile organic compounds, *Corros. Sci.* **82** (2014), 280–289.

[159] S. HILLIER, K. SUZUKI, and J. COTTER-HOWELLS, Quantitative determination of cerussite by X-ray powder diffraction and inferences for lead speciation and transport in stream sediments from a former lead mining area in Scotland, *Appl. Geochem.* **16** (6) (2001), 597–608.

[160] J. RALPH and I. CHAU, *Mindat database*, 2014.

[161] J. OLBY, The basic lead carbonates, *J. Inorg. Nucl. Chem.* **28** (1966), 2507–2512.

[162] A. MONTASER, P. VELUCHAMY, and H. MINOURA, Structure, morphology and photoelectrochemical responses of anodic PbO films formed on Pb electrodes in various concentrations of alkaline solution, *J. Electroanal. Chem.* **419** (1) (1996), 47–53.

[163] P. VELUCHAMY and H. MINOURA, Selective formation of α-PbO and β-PbO films on Pb electrodes by potentiostatic anodisation in alkaline solutions, *J. Electroanal. Chem.* **396** (1995), 211–217.

[164] C. BLOUNT, Synthesis of berite, celestite, anglesite, witherite and strontianite from aqueous solutions, *Am. Mineral.* **59** (1974), 1209–1219.

[165] R. SIMMONS, N. AHSIAN, and H. RAVEN, *The book of stones*, North Atlantic Books, 2007, 164–165.

[166] H. NOWOTNY and G. HEGER, Structure refinement of lead nitrate, *Acta Crystallogr. C* **42** (2) (1986), 133–135.

[167] C. MAUCK et al., Synthesis and structures of $Pb_3O_2(CH_3COO)_2 \cdot 0.5H_2O$ and $Pb_2O(HCOO)_2$: two corrosion products revisited. *Inorg. Chem.* **49** (22) (2010), 10736–10743.

[168] P. HARRISON and A. STEEL, Lead(II) carboxylate structures, *J. Organomet. Chem.* **239** (1) (1982), 105–113.

[169] R. RAJARAM and J. MOHANA ROA, Crystal structure of lead acetate trihydrate, *Z. Kristallogr.* **160** (3-4) (1982), 225–233.

[170] S. KRIVOVICHEV and P. BURNS, Crystal chemistry of basic lead carbonates. II. Crystal structure of synthetic plumbonacrite, *Mineral. Mag.* **64** (6) (2000), 1069–1075.

[171] D. WATKINSON, *Conserving cultural material: ethical challenges for the conservator*, tech. rep., Cardiff University, 2014, 1–10.

[172] S. OGDEN, Understanding, respect, and collaboration in cultural heritage preservation: A conservator's developing perspective, *Libr. Trends* **56** (1) (2007), 275–287.

[173] B. RODGERS, *The archaeologist's manual for conservation: A guide to non-toxic, minimal intervention artifact stabilization*, Springer, 2004, 5.

[174] K. GYSELS et al., Indoor environment and conservation in the Royal Museum of Fine Arts, Antwerp, Belgium, *J. Cult. Herit.* **5** (2) (2004), 221–230.

[175] F. ASCIONE et al., Energy saving strategies in air-conditioning for museums, *Appl. Therm. Eng.* **29** (4) (2009), 676–686.

[176] M. SVENDSEN et al., *Ultra low energy museum storage*, tech. rep., National Museum of Denmark, 2011, 1–8.

[177] D. LAFUENTE, E. CANO, and E. MARTIN, Science and technology for the conservation of cultural heritage, in: *Science and technology for the conservation of cultural heritage*, ed. by M. ROGERIO-CANDELERA, M. LAZZARI, and E. CANO, CRC Press, 2013, 99–102.

[178] W. BOUSTEAD, Dehumidification in museum storage areas, *Stud. Conserv.* **12** (1) (1967), 103–107.

[179] M. HISHAM and D. GROSJEAN, Air pollution in southern California museums: indoor and outdoor levels of nitrogen dioxide, peroxyacetyl nitrate, nitric acid, and chlorinated hydrocarbons, *Environ. Sci. Technol.* **25** (5) (1991), 857–862.

[180] THE GETTY CONSERVATION INSTITUTE, *Airborne particles in museums*, Getty Publications, 1993, 104.

[181] G. THOMSON, *The museum environment*, Elsevier, 2013, 66–124/207.

[182] R. KERSCHNER, A practical approach to environmental requirements for collections in historic buildings, *J. Am. Inst. Conserv.* **31** (1) (1992), 65–76.

[183] B. RODGERS, Archaeological composites, in: *The archaeologist's manual for conservation: A guide to non-Toxic, minimal intervention artifact stabilization*, Springer, 2007, 187–200.

[184] P. MATTIAS, G. MAURA, and G. RINALDI, The degradation of lead antiquities from Italy, *Stud. Conserv.* **29** (1984), 87–92.

[185] R. WILLIAMSON and P. NICKENS, *Science and technology in historic preservation*, Springer, 2000, 207.

[186] P. DILLMAN et al., *Corrosion of metallic heritage artifacts: Investigation, conservation and prediction of long term behavior*, Elsevier, 2013, 5.

[187] C. EWEN, *Artifacts*, Altamira Press, 2003, 24–26.

[188] P. CRIDLEBAUGH, *Formulating ethics and standards in archaeology*, Chicora Foundation, 1990, 33.

[189] G. MONGER, Treatment of a Roman child's lead coffin liner, *UKIC Conservation News* **77** (2002), 36–37.

[190] J. CRONYN, *Elements of archaeological conservation*, Routledge, 2003, 207.

[191] L. SELWYN, Health and safety concerns relating to lead and lead compounds in conservation, *Journal of the Canadian Association for Conservation* **30** (2005), 18–37.

[192] NATIONAL BUREAU OF STANDARDS, *Corrosion and metal artifacts: A dialogue between conservators and archaeologists and corrosion scientists*, ed. by B. BROWN et al., National Bureau of Standards, 1977, 133–137.

[193] E. CALEY, Coatings and incrustations on lead objects from the Agora and the method used for their removal, *Stud. Conserv.* **2** (2) (1955), 49–54.

[194] F. RATHGEN, G. AUDEN, and H. AUDEN, *The preservation of antiquities*, Cambridge University Press, 1905, 150.

[195] R. ORGAN, Book review: The conservation of antiquities and works of art: treatment, repair and restoration by H. Plenderleith and A. Werner, *Stud. Conserv.* **18** (4) (1973), 189–194.

[196] H. PLENDERLEITH, Plomb, étain et alliages, in: *La conservation des antiquités et oeuvres d'art*, Éditions Eyrolles, 1966, 278–290.

[197] D. SCOTT and THE GETTY CONSERVATION INSTITUTE, *Copper and bronze in art: Corrosion, colorants and conservation*, Getty Publications, 2002, 354.

[198] J. WATSON, Conservation of lead and lead alloys using EDTA solutions, in: *Lead and tin: Studies in conservation and technology*, ed. by S. POLLARD and G. MILES, vol. 3, United Kingdom Institute for Conservation, 1985, 44–45.

[199] H. KUHN, Neue Reinigungsmethode für korrodierte Bleigegenstande, *Museumskunde* **29** (1960), 156–161.

[200] W. VAN DEN ABEELE et al., De reiniging en bescherming van metalen: oderzoek van verschillende chemische reinigingsmethoden voor koper, messing en lood, *Interdisciplinair vakblad voor conservering en restauratie* **3** (2) (2002), 25–33.

[201] H. LANE, The reduction of lead, in: *Conservation in archaeology and the applied arts*, International Institute for Conservation, 1975, 215–217.

[202] R. ORGAN, Use of ion-exchange resin in the treatment of lead objects, *Museums J.* **53** (2) (1953), 49–52.

[203] N. HARINARAYANA, Some observations on the treatment of a hoard of lead coins from Andipatti, *Archaeol. Stud.* **2** (1977), 65–70.

[204] R. BERTHOLON and C. RELIER, La conservation des métaux archéologiques, in: *La conservation en Archéologie*, Paris: Masson, 1990, 163–270.

[205] R. PINI et al., Tests of laser cleaning on archeological metal artifacts, *J. Cult. Herit.* **1** (1) (2000), S129–S137.

[206] E. DRAKAKI et al., Laser cleaning on Roman coins, *Appl. Phys. A* **79** (4-6) (2004), 1111–1115.

[207] V. DANIELS, L. HOLLAND, and M. PASCOE, Gas plasma reactions for the conservation of antiquities, *Stud. Conserv.* **24** (1979), 85–92.

[208] B. GOTTLIEB et al., A new method for cleaning and conservation of lead objects using hydrogen and oxygen plasma, in: *ICOM Committee for Conservation 10th triennial meeting*, ed. by J. BRIDGLAND, International Council of Museums Committee for Conservation, 1993, 767–771.

[209] F. DHOOGHE, Studie van het elektrochemisch reductieproces van gecorrodeerde loden voorwerpen en fundamenteel onderzoek naar de applicatie van loodzepen als beschermende laag, PhD thesis, Ghent University, 2006, 27.

[210] B. SCHOTTE, A study of the electrolytic reduction of corroded lead objects and the application, characterization and testing of a protective lead carboxylate coating, PhD thesis, Ghent University, 2007, 26–27.

[211] A. DOMÉNECH-CARBÓ, Electrochemistry in treatment and conservation of metal artifacts, in: *Electrochemical methods in archaeometry, conservation and restoration*, Springer, 2009, chap. 6, 135–140.

[212] H. LANE, Consolidative reduction of lead, in: *Recent advances in conservation*, UK Institute for Conservation, 1967, 1–3.

[213] C. DEGRIGNY and R. LE GALL, Conservation of ancient lead artifacts corroded in organic acid environments: Electrolytic stabilization/consolidation, *Stud. Conserv.* **44** (3) (1999), 157–169.

[214] T. SKINNER, The treatment of lead objects from a marine site, in: *The Laboratories of the National Museum of Antiquities of Scotland*, ed. by T. BRYCE and J. TATE, National Museum of Antiquities of Edinburgh, 1980, 46–50.

[215] H. LANE, Some comparisons of lead conservation methods, including consolidative reduction, in: *Proc. Symposium on the Conservation and Restoration of Metals*, Scottish Society for Conservation and Restoration, 1980, 48–58.

[216] H. GUIDA, M. MARABELLI, and I. REINDELL, Restoration and storage of lead artifacts, *Restaurator* **4** (1980), 227–237.

[217] C. ENDERLY and H. LANE, The conservation of the lead figure from Toprakal, in: *Lead and tin: Studies in conservation and technology*, ed. by C. MILES and S. POLLARD, UK Institute for Conservation, 1985, 47–51.

[218] L. GREEN and J. MÁRTA, A re-evaluation of lead conservation techniques at the British Museum, in: *Conservation of metals: Problems in the treatment of metal-organic and metal-inorganic composite objects: International restorer seminar*, 1989, 121–130.

[219] R. BERTHOLON, *Conservation des métaux archéologiques*, tech. rep., Université de Paris, 1985, unpublished.

[220] R. ORGAN, The consolidation of fragile metallic objects, in: *Recent advances in conservation*, ed. by G. THOMSON, Butterworth-Heinemann, 1963, 128–134.

[221] E. NOSEK, The investigation and conservation of a lead paten from the 11th century, *Stud. Conserv.* **30** (1985), 19–22.

[222] B. SCHOTTE et al., Chemical and morphological changes of historical lead objects as a result of the use of electrolytic reduction as a stabilization treatment, *Anal. Chem.* **78** (2006), 8319–8323.

[223] B. SCHOTTE and A. ADRIAENS, Treatments of corroded lead artifacts, *Stud. Conserv.* **51** (2006), 1–8.

[224] C. DEGRIGNY, Use of electrochemical techniques for the conservation of metal artefacts: a review, *J. Solid State Electrochem.* **14** (3) (2010), 353–361.

[225] A. CARRADICE and S. CAMPBELL, The conservation of lead communion tokens by potentiostatic reduction, *Stud. Conserv.* **39** (1994), 100–106.

[226] C. DEGRIGNY, *Etude de la dégradation des objets en plomb dans les collections publiques et des moyens de les stabiliser et de les conserver à long terme*, tech. rep., Arc' Antique, 1996, unpublished.

[227] T. STAMBOLOV, *The corrosion and conservation of metallic antiquities and works of art*, C.L. Publication, 1985, 137–146.

[228] H. GRÄFEN et al., *Corrosion*, Wiley, 2005, 68–69.

[229] E. CANO and D. LAFUENTE, Corrosion inhibitors for the preservation of metallic heritage artefacts, in: *Corrosion and conservation of cultural heritage artifacts*, ed. by P. DILLMAN et al., Woodheat Publishing, 2013, 570–594.

[230] M. MALIK et al., Anti-corrosion ability of surfactants: A review, *Int. J. Electrochem. Sci.* **6** (2011), 1927–1948.

[231] P. VOLENT and N. BAER, Volatile amines used as corrosion inhibitors in museum humidification systems, *Int. J. Museum Manag. Curat.* **4** (4) (1985), 359–364.

[232] I. GALLARDO, J. PINSON, and N. VILÀ, Spontaneous attachment of amines to carbon and metallic surfaces, *J. Phys. Chem. B* **110** (2006), 19521–19529.

[233] N. HELAL et al., Environmentally safe corrosion inhibition of Pb in aqueous solutions, *J. Alloys Compd.* **456** (1-2) (2008), 372–378.

[234] V. SHARMA, U. SHANKAR LAL, and T. SINGH, Method for stabilization of leaded bronzes affected by corrosion of lead, *Stud. Conserv.* **48** (3) (2003), 203–209.

[235] K. RAHMOUNI et al., Protection of ancient and historic bronzes by triazole derivatives, *Electrochim. Acta* **54** (22) (2009), 5206–5215.

[236] G. BRUNORO et al., Organic films for protection of copper and bronze against acid rain corrosion, *Corros. Sci.* **45** (10) (2003), 2219–2231.

[237] E. ROCCA and J. STEINMETZ, Inhibition of lead corrosion with saturated linear aliphatic chain monocarboxylates of sodium, *Corros. Sci.* **43** (5) (2001), 891–902.

[238] E. ROCCA and F. MIRAMBET, The electrochemical techniques for the diagnosis and restoration treatments of technical and industrial heritage: three examples of metallic artifacts, *J. Solid State Electrochem.* **14** (3) (2010), 415–423.

[239] E. ROCCA, Corrosion inhibitors for metallic artifacts: temporary protection, in: *Corrosion of metallic heritage artifacts: Investigation, conservation and prediction of long term behavior*, 2014, 308–335.

[240] F. LACOUTRE et al., Anhydrous lead(II)heptanoate, *Acta Crystallogr. C* **57** (5) (2001), 530–531.

[241] M. KIANI et al., Inhibitory effect of some amino acids on corrosion of Pb-Ca-Sn alloy in sulfuric acid solution, *Corros. Sci.* **50** (4) (2008), 1035–1045.

[242] W. BADAWY, M. HEFNY, and S. EL-EGAMY, Effect of some organic amines as corrosion inhibitors for lead in 0.3 M HCl solution, *Corros.* **46** (12) (1990), 978–982.

[243] A. GALTAYRIES et al., Surface characterization of corrosion inhibitors on bronzes for artistic casting, in: *Corrosion of metallic heritage artifacts: Investigation, conservation and prediction of long term behavior*, ed. by P. DILLMAN et al., Woodhead Publishing, 2014, 335–352.

[244] M. DE KEERSMAECKER et al., Electrochemical and surface study of neutralized dodecanoic acid on a lead substrate, *J. Electrochem. Soc.* **161** (3) (2014), C126–C137.

[245] B. BOFFARDI, Minimization of lead corrosion in drinking water, *Mater. Performance* **29** (8) (1990), 45–49.

[246] B. BOFFARDI and A. SHERBONDY, Control of lead corrosion by chemical treatment, *Corros.* **47** (12) (1991), 966–975.

[247] T. HOLM and M. SCHOCK, Potential effects of polyphosphate products on lead solubility in plumbing systems, *J. Am. Water Works Ass.* **83** (7) (1991), 76–82.

[248] M. EDWARDS and L. MCNEILL, Effect of phosphate inhibitors on lead release from pipes, *Journal / American Water Works Association* **94** (3) (2002), 79–90.

[249] A. TIZPAR and Z. GHASEMI, The corrosion inhibition and gas evolution studies of some surfactants and citric acid on lead alloy in 12.5 M H_2SO_4 solution, *Appl. Surf. Sci.* **252** (24) (2006), 8630–8634.

[250] S. SANKARAPAPAVINASAM, F. PUSHPANADEN, and M. AHMED, Hydrazine and substituted hydrazines as corrosion inhibitors for lead in acetic acid, *Br. Corr. J.* **24** (1) (1989), 39–42.

[251] S. SANKARAPAPAVINASAM and M. AHMED, Tosylhydrazine as protector for lead in acetic acid vapor, *J. Electrochem. Soc. of India* **39** (4) (1990), 255–256.

[252] D. HEATH and G. MARTIN, The corrosion of lead and lead/tin alloys occurring on Japanese lacquer objects, *Stud. Conserv.* **33** (1) (1988), 137–141.

[253] D. MOFFETT, Wax coatings on ethnographic metal objects: Justifications for allowing a tradition to wane, *J. Am. Inst. Conserv.* **35** (1) (1996), 1–7.

[254] M. DAVIS, F. HUNTER, and A. LIVINGSTONE, The corrosion, conservation and analysis of a lead can cannel coal necklace from the Early Bronze Age, *Stud. Conserv.* **40** (4) (1995), 257–264.

[255] B. BORDASS, Underside corrosion of lead roofs and its prevention, *EHRT* **1** (1998), 21–71.

[256] P. DILLMAN et al., Introduction: conservation versus laboratory investigation in the preservation of metallic heritage artifact, in: *Corrosion and conservation of cultural heritage artifacts*, 2013, 1–5.

[257] V. HORIE, *Materials for conservation: Organic consolidants, adhesives and coatings*, 2nd, Butterworth-Heinemann, 2010, 128–190.

[258] E. CANO, D. LAFUENTE, and D. BASTIDAS, Use of EIS for the evaluation of the protective properties of coatings for metallic cultural heritage: a review, *J. Solid State Electrochem.* **14** (3) (2010), 381–391.

[259] V. FLEXER et al., A new strategy for corrosion inhibition coatings for lead heritage metal objects, *Electrochim. Acta* (2015).

[260] D. HALLAM et al., An EIS method for assessing thin oil films used in museums, in: *Proc. International conference on metal conservation*, 2004, 379–387.

[261] C. CHIAVARI et al., Conservation of organ pipes: protective treatments of lead exposed to acetic acid vapours, in: *Metal 04: Proceedings of the international conference on metals conservation*, ed. by J. ASHTON and D. HALLAM, National Museum of Australia Canberra, 2004, 281–293.

[262] F. MATERO, Ethics and policy in conservation, *Getty Conservation Institute Newsletter* **15** (1) (2000), 5–8.

[263] AMERICAN INSTITUTE FOR CONSERVATION, *AIC Code of ethics and guidelines for practice*, tech. rep., American Institute for Conservation, 1994, 1–11.

[264] EUROPEAN CONFEDERATION OF CONSERVATOR-RESTORERS' ORGANIZATIONS, *Practical guidelines*, tech. rep., 2002, 1–5.

[265] J. ASHLEY-SMITH, The ethics of conservation, *The Conservator* **6** (1) (1982), 1–5.

[266] J. ASHMAN, Ethics in conservation, *J. Soc. Arch.* **14** (1) (1993), 15–24.

[267] Ancient and historic metals: Conservation and scientific research, in: *Proc. of a Symposium organized by the J. Paul Getty Museum and the Getty Conservation Institute*, ed. by D. SCOTT, J. PODANY, and B. CONSIDINE, Getty Publications, 2007, 72.

3 Objectives and strategy

3.1 Objectives

From the discussion in chapter 2 it is clear that lead corrosion is an important problem in conservation. Results of experiments from the research project COLLAPSE (Corrosion of Lead and Lead-Tin Alloys of Organ Pipes in Europe), supported by the European Commission under the 5th framework program, have shown signs of accelerated lead corrosion and degradation. This 'active' corrosion is caused by the emission of different organic acids from the wooden parts in the nearby environment. **The main goal is to prevent the corrosion of lead artifacts. Research concerning the protection of objects proceeds in two directions: (1) try to reduce the corrosive substances in the nearby environment and/or (2) perform a surface protection treatment. The aim of this work focuses on the development of a complete procedure for the production of a protective coating which is stable, reproducible, reversible, corrosion resistant and aesthetically justified. This methodology can then be used by conservators to protect lead artifacts in museums and churches. To reach this goal, we require the collection of reliable experimental results using powerful electrochemical techniques to determine possible organic compounds suitable for the formation of a protective coating.** Based on previous experiments, we concluded that lead reacts with carboxylic groups, forming lead carboxylate complexes. In this work, the coating deposition will make use of this lead carboxylate reaction to form organic coatings on lead substrates. The innovative element will be the use of new organic compounds and more advanced electrochemical techniques.

3.2 Strategy

The global strategy of this work can be divided into three stages: (i) to assess the effects of corrosive atmospheres on lead, (ii) to study the deposition of potential protective layers and (iii) to observe the direct effects of VOCs on protected surfaces. From this point of view, the use of long chain carboxylic acids and its salts, dicarboxylic acids and its salt and homemade polymers are tested as a protective layer on lead substrates. The use of dicarboxylic acids and polymers has a few advantages over the use of monocarboxylic acids

- more active groups per chain producing a more stable layer
- a larger modularity
- more functional groups on one larger macromolecule
- the possibility to change the properties of the molecule

This thesis focusses on the formation of a protective coating on lead and lead alloy artifacts. First, we will continue the work on carboxylic acids and their salts. Then, the use of dicarboxylic acids and their salts is checked using a hydrophobic hydrogenated dimer acid (C36). After that, the use of polymers will be tested using the same strategy as before by working with carboxylic functional groups which react with the substrate. New polymers can then be synthesized and characterized. Furthermore, we will need to develop a technique for the formation of polymer coating on the lead substrate. This method will depend, of course, on the polymer used, keeping in mind the end-users, the conservators. The work is complementary to the EU projects SENSORGAN and TRUESOUND as both try to protect cultural heritage made of lead.

Next to the development of new coatings, we will look at the stability of the lead-substrate coating system and the corrosion resistance of the coating. To do this, we will use different electrochemical methods dependending on what we want to know about the coating. In the different case studies a lot of important issues, like adsorption behavior of the carboxylic groups, mechanism of coating deposition, electrochemical deposition, characterization of the coating, corrosion resistance, etc., will be addressed.

3.3 Short outline

Part II will be dedicated entirely to different studies of producing a lead carboxylate coating. Two electrochemical methods called cyclic voltammetry (CV) and amperometry (AMP) are used to form a coating on a lead sample in carboxylate inhibitor solution. Furthermore, the immersion method is tried to produce a coating. Next to the well-known linear polarization method, electrochemical impedance spectroscopy is introduced to test the protective behavior of the coating against corrosion using a standard corrosive environment for lead. On the basis of a statistical study, different methods, the temperature and the deposition time are tested to find the best protective coating. As to identify the adsorption characteristics of the inhibitor on the lead substrate, a new electrochemical study is done adding an inhibitor to a chosen standard corrosion environment. Besides looking at the inhibition characteristics of the coating, we also did a spectroscopic characterization of the crystalline layer using different analytical techniques, mostly based X-rays. As a last study, we tried to apply our carboxylate coating on a real organ sample. In this case, we changed the corrosive environment to a solution with a low acetic acid concentration.

Next, part III will study the corrosion performance of a lead metal in an acetic acid environment over time. We will use one specific in-situ measuring technique (ORP-EIS), which makes it easier to deal with unreliable experimental data (= an easy data validation approach). Moreover, we can correct the raw data before proceeding to the subsequent modeling step. For example in this case, we analyze our raw non-stationary data trying to process them and split them up in different consecutive stationary data files.

Another in-situ experiment, based on synchrotron XRD analysis, allows us to study the growth of a lead carboxylate coating and to study the inhibition performance of coated lead sample over time. Using synchrotron X-rays and an electrochemical cell, developed by our research group in collaboration with Warwick University, we are able to immerse a lead sample in an inhibitor solution to study the formation of our coating. The coated sample is then immersed into an acetic acid corrosive solution to have a look at the protective behavior of the produced coating.

Part IV will focus on the research of a polymer coating for the protection of the lead sample. Again using a combination of electrochemical and spectroscopic measurements, we will link the protective behavior of our coating to its appearance and its reaction with the metal surface.

4 Surface analysis techniques

4.1 Materials

The products and chemicals used are summarized in Table 4.1 together with a number of their standard characteristics.

4.2 The pre-treatment of the lead samples

The pre-treatment of the lead samples consists of two important stages: the cutting of the samples and the polishing of the substrate surface. The lead samples are stamped from a lead plate (20.0 cm × 20.0 cm; thickness = 2.0 mm). The result is individual circular coupons with diameter 12.5 - 12.6 mm and thickness 2.0 mm.
The polishing of the coupons is carried out by means of a polishing machine, a Minimet 1000 Grinder-Polisher (Buehler, USA). The cut coupons are clamped in a round plastic holder (diameter = 40.0 mm; thickness = 16.0 mm), in which four holes (diameter = 12.65 mm; depth = 1.55-1.6 mm) are cut symmetrically. In this way four coupons can be polished at the same time and following the same protocol. The polishing process consists of different steps following the metallographic guidelines:

1. The coupons are polished by hand with a rough abrasive paper (400 grit SiC) to eliminate all major irregularities at the surface of the substrate; the polishing of lead metal should always be done WET, because lead is toxic when small particles are inhaled.
2. When the surface shows no more pits and scratches, the sample is further polished by hand with abrasive paper with 1200 grit SiC. It is preferred to polish 5 to 10 minutes with 1200 grit SiC abrasive paper [1].
3. The polished coupons are washed with deionized water in an ultrasonic bath for only 1 minute (ultrasonic baths could damage the lead surface).
4. The surface is now fine-polished for 20 minutes using a polishing cloth (12” micro cloth PSA 10/PK, Buehler, USA) with diamond polish dissolved in oil with a particle size of 6 μm first, and then 1 μm (MetaDi Diamond Suspension, Buehler, USA).
5. To be sure all diamond has been removed from the polished lead surface, the substrate is cleaned in an ultrasonic bath no longer than 1 minute.
6. The cleaned lead substrates are pressed hard on a bare polishing cloth with a small amount of isopropanol, so that a smooth and glossy surface is obtained.
7. At the end, a shiny blue-white surface is obtained [2].

IUPAC[a] NAME	CAS NUMBER	CHEMICAL FORMULA	SHORT NOT.	PURITY	SOL IN WATER[b]	SOL IN ETH[b]	COMPANY	HAZARD SYMBOLS	MW[c] /g mol^{-1}
2-propanol	67-63-0	C_3H_7OH	iPA	> 99.5%	***	***	VWR	flammable	60.1
ethanol	64-17-5	C_2H_5OH	EtOH	> 99.5%	***	***	VWR	flammable	46.1
decanoic acid	334-48-5	$C_{10}H_{20}O_2$	HC10	> 98%	0.00015 g/mL	soluble	Fluka	-	172.3
dodecanoic acid	143-07-7	$C_{12}H_{24}O_2$	HC12	> 98%	± soluble	1 g/mL	Sigma-Aldrich	-	200.32
ethanoic acid	64-19-7	$C_2H_4O_2$	HAc	> 99%	***	***	Vel NV	corrosive	60.1
lead	7439-92-1	Pb	-	99.75%	***	***	Goodfellow	toxic	207.2
sodium hydroxide	1310-73-2	NaOH	-	> 99%	***	***	Merck	corrosive	40.0
dimer acid	61788-89-4		DA	> 99%	not soluble	± soluble	Sigma-Aldrich	-	≈ 570.0
2,2'-azobis(2-methyl-propionitrile)	78-67-1	$C_8H_{12}N_4$	AIBN	98%	***	***	Jansen Chemica	-	164.2
toluene	108-88-3	C_7H_8	-	> 99.9%	***	***	Sigma Aldrich	flammable	92.1
tetrahydrofuran	109-99-9	C_4H_8O	THF	> 99.9%	***	***	Sigma Aldrich	flammable	72.1
2-ethylhexyl acrylate	103-11-7	$C_{11}H_{20}O_2$	EHA	98%	not soluble	***	Sigma Aldrich	irritant	184.2
lauryl acrylate	2156-97-0	$C_{15}H_{28}O_2$	LA	90%	not soluble	***	Sigma Aldrich	irritant	240.4
acrylic acid	79-10-7	$C_3H_4O_2$	AA	99.5%	***	***	Acros Organics	-	72.1
etoxyethylene	109-92-2	C_4H_8O	-	99%	***	***	Aldrich Chemistry	lightly flammable	72.1
carbon disulfide	75-15-0	CS_2	-	> 99%	***	***	Sigma Aldrich	highly flammable, toxic irritant	76.4
1-butanethiol	109-79-5	$C_4H_{10}S$	-	99%	***	***	Sigma Aldrich	-	90.2
2-bromopropanoic acid	598-72-1	$C_3H_5BrO_2$	-	> 99%	***	***	Sigma Aldrich	corrosive, danger	153.0

[a] IUPAC = International Union of Pure and Applied Chemistry

[b] Data from Merck Index, 12th Edition

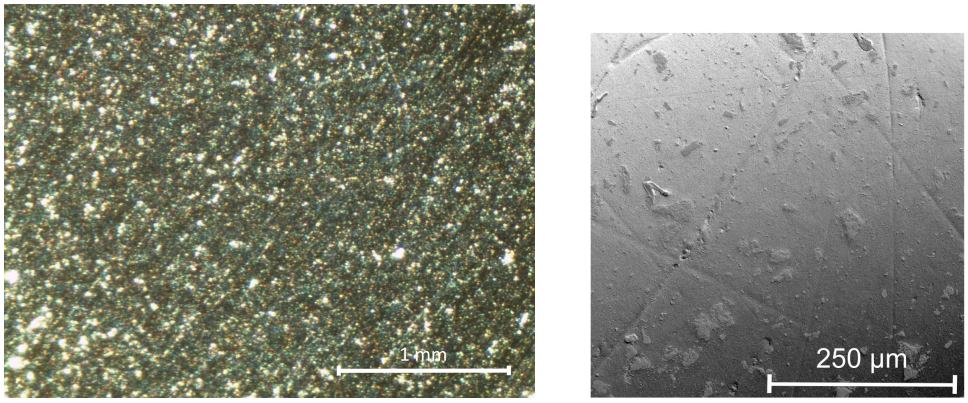
[c] MW = Molecular weight

Table 4.1 – List of the chemicals used.

ABRASIVE PAPER POLISHING CLOTH	TIME	PRESSURE (POUND)	SPEED (RPM)
P400	first pits disappear	-	-
P600	smooth surface without scratches	-	-
P1200	smooth surface without scratches	1	10
polishing cloth with 6 μm diamond polish	shiny surface	5	20
polishing cloth with 1 μm diamond polish	shiny surface	5	20

Table 4.2 – Instructions for the use of the Mimimet 1000 Grinder-Polisher (Buehler, USA) to polish lead substrates.

An ideally polished sample must be shiny and contain no more irregularities visible to the naked eye. Figure 4.1 shows a clear image of the appearance of an ideally polished lead sample. To have a complete view, optical (Nikon SMZ800 microscope, Nikon, Japan) and electron images (Phenom, Phenom-World, The Netherlands) are presented.



(a) **(b)**

Figure. 4.1 – (a) Optical image (6.3 x) and (b) electron image (500 μm x 500 μm) of an ideally polished lead sample.

4.3 pH measurements

The pH of all the solutions in water was measured using a pH-meter (Orion model 420A) connected to a pH-electrode (Metrohm). Prior to each use the pH-electrode was calibrated using standard buffer solutions with a pH of 4 (Merck, Germany, citric acid, NaOH and NaCl) and a pH of 7 (Merck, Germany, $Na_2HPO_4/KHPO_4^-$ buffer solution).

4.4 Microscopy

To have a visual image of the sample surface at various magnifications, electromagnetic radiation or electron beams are used to illuminate the specimen. Interactions with the sample involve diffraction, reflection, or refraction processes. The collection of the scattered radiation or another signal allows the creation of an image. Depending on the incident particles, two types of microscopy were used, namely optical and scanning electron microscopy.

4.4.1 Optical microscopy

Optical microscopy is based on the interaction of visible light with the specimen. The interacted visible light is processed and magnified by a lens system to produce an image. The images are taken using a Nikon SMZ800 microscope with magnifications of 1x, 2x, 3x, 4x, 5x and 6.3x. In this case, it is possible to make direct visual images using a camera of the type Nikon DSFi1, which is coupled to directly to the microscope. Using the camera software (Elements D, Nikon), the camera can be controlled by means of a computer.

4.4.2 Scanning electron microscopy

Electron microscopy is based on the interaction of electrons, which have shorter wavelengths than visible light, with the surface of the sample. This explains why electron microscopes have a higher resolving power, achieve a better resolution and higher magnifications. Afterwards, the electrons produced during interaction with the sample are processed and directly detected. The detector depends on the type of electrons to be analyzed.

4.4.2.1 Electron gun design

All electron microscopes have an electron gun to illuminate the sample. The design of the electron source is based on the principle of removing electrons from metallic solids. Electrons with enough energy to overcome the metal's work function tail out beyond the surface with the result that the electrons are emitted. The statistics are calculated according to the Fermi-Dirac distribution [3–5]. Furthermore, the emitted electrons need a momentum directed normal to the emission surface, which is described by the de Broglie equation depending on the accelerating voltage [6]. These stringent requirements for the electron beam are best met by thermionic and field emission sources.

Thermionic sources

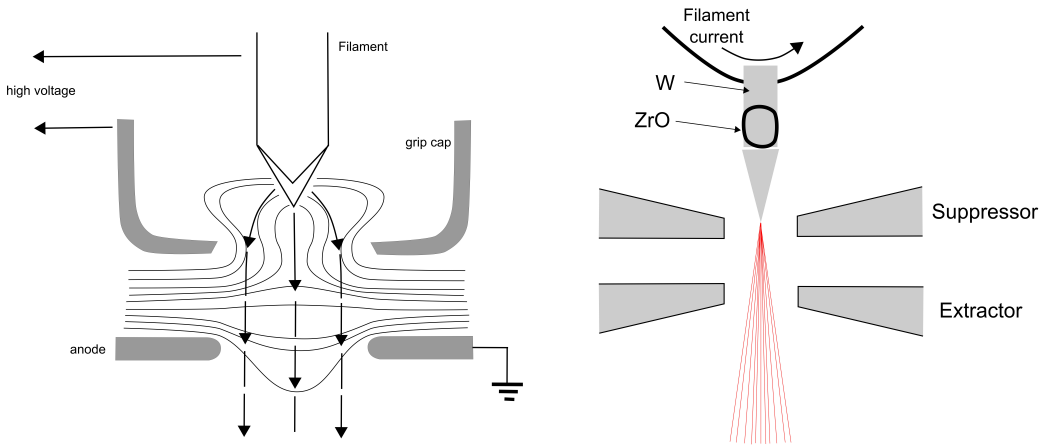


Figure. 4.2 – The relative appearance of (a) a traditional thermionic electron gun and (b) a thermal field emission gun. The suppressor is negatively biased with respect to the cathode, while the extractor is positively biased. These figures are based on [7]

Thermionic emission uses heat to provide energy for the electrons to overcome the potential-energy barrier [8]. The first microscope with a thermionic source was developed by Knoll, Houtermans and Schulze [9], which is used as a basis of modern instruments. Figure 4.2a illustrates the appearance of a traditional thermionic electron gun. Often, the filament is operated at 10 to 300 kV, which ensures a stable high emission electron beam. Thermionic emission specimens are usually polycrystalline metals or alloys. Lafferty [10] demonstrated that materials such as lanthanum hexaboride, LaB_6, possessed superior thermionic properties, and Broers [11] later described an electron source using a pointed LaB_6 rod in a scanning electron microscope. The advantages of LaB_6 include its much lower operating temperature and significantly

higher emission current than tungsten.

Field emission sources

Field emission removes electrons from a metal surface by applying an electrostatic field. The field-emission microscope was invented by Müller at the Siemens research laboratory in Berlin around 1936 [12]. In the 1970's, Crewe and co-workers [13, 14] developed a field emission source for commercial scanning electron microscopy. However, one must take into account that field emission is very sensitive to contamination and to flux and direction fluctuation.
In general, two types of field emission electron guns are known. The cold type, whose cathode is used at room temperature, and the thermal type (or Schottky field emission gun), whose cathode is heated to about 1800 K. The advantages of the Schottky field emission (mostly used in modern SEM instruments) are

- the higher degree of tolerance of the vacuum during operation
- the angular current density is larger than for the cold type
- the necessary field intensity is relatively low
- the electron beam is highly stable

The field emission gun is made of a needle-shaped tungsten crystal coated with zirconium dioxide (ZrO) at the tip to reduce the potential barrier [15]. The higher the acceleration voltage, the finer the patterns. Any fluctuation in the acceleration voltage, however, directly affects the electron beam. Figure 4.2b shows the structure of a thermal field emission gun.

4.4.2.2 The electron optical system

Bruche and Scherzer [17] were among the first to apply Hamilton's analogy between light optics and dynamics to electrons. The refractive index of the electrons depends on the strength of the electric and magnetic field. Based on the kind of field used, two lens types are known: an electrostatic and an electromagnetic lens. In the case of electrostatic lenses, an electron passes from a low potential V_1 to a higher potential V_2 where the equipotentials of the electric field are shaped by the electrodes used. At this point, the electron undergoes refraction defined by Snell's law

$$\frac{\sin r}{\sin i} = \sqrt{\frac{V_1}{V_2}}. \tag{4.1}$$

As a consequence, the electron beam is focused by what is called an *immersion lens*. However, in present electron microscopes, a series of two immersion lenses is used, called *Einzel lenses*. These lenses consist of three colinear tubes, with the middle tube at an elevated potential so that electrons pass from low to high potential and back to low potential [18]. A magnetic lens, on the other hand, consists of a soft iron pole piece and a coil to provide the flux. The flux lines run from the top to the bottom of the lens. The vector component, however, is orthogonal to the original trajectory of the electrons causing a helical spiral trajectory of the electrons. As a consequence, the image is rotated and the electrons are focused. Most electron microscope *only* use magnetic lenses.

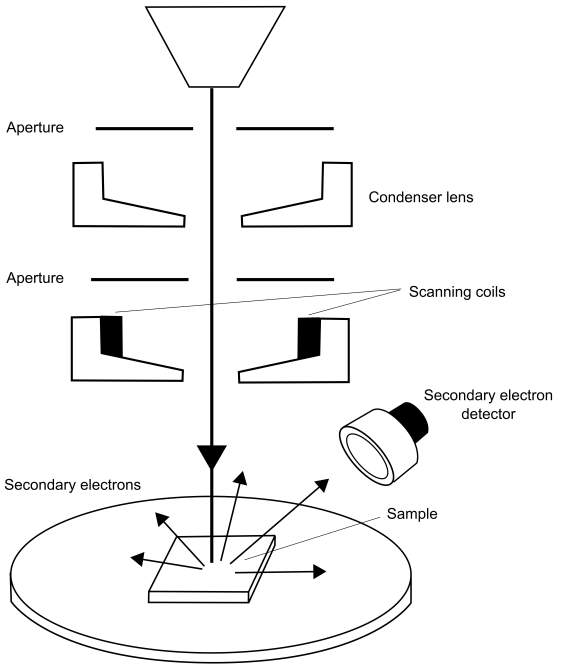


Figure. 4.3 – Schematic diagram of an SEM set-up [16].

The design of the electron microscope lens system is depicted schematically in Figure 4.3. The condenser lens, at the top, forms an intermediate image of the source behind the aperture and thus controls the angle at which the electron beam diverges into the final lens. This means that the condenser lens has a profound effect on the current and the final achievable spot size. The objective lens forms the final spot on the specimen surface so indeed focuses its object which is the intermediate image of the source formed by the condenser lens.

4.4.2.3 Secondary and backscattered electrons

Postwar developments of McMullan [19], Smith and Oatley [20, 21] ensure that commercial SEM instrument became available starting from the 1960's. The basic SEM is probably the most versatile instrument in materials science to non-destructively visualize surface topography and morphology.

When a conducting solid sample is bombarded with an incident (primary) electron beam as shown in Figure 4.4, a portion of the emitted radiation consists of low-energy electrons as a result of atomic excitation. These electrons are termed secondary electrons, and are characterized by their relatively low energy as compared with the incident electron energy. As a general rule, electrons are classified as secondary electrons if their energy is less than 50 eV [7]. The secondary emission yield depends on the primary electron energy (the accelerating potential), the density (the atomic number Z), topography, local surface-charge accumulation and to a small extent, the crystallography of the emission surface as the work function is altered [22, 23]. Auger and secondary electrons are excited along the primary beam path, but one must take into account that only those excited in the top 0.5 nm (secondary electrons) and 1 - 2 nm (Auger electrons) can escape through the surface. Elastically scattered electrons called backscattered electrons are higher in energy and can escape from deeper in the sample. Palluel [24] stated that the backscattered electron yield is proportional to the atomic number of the sample's elements. This means that depending on the electron type, information of different parts of the sample is obtained (see Figure 4.4). Everhart and Thornley [25] developed the most efficient electron collection device for secondary electrons based on a scintillator photo-multiplier system using the photoelectric effect. For the detection of backscattered electrons, a silicon planar Li drifted Si diode is positioned above the sample [26].

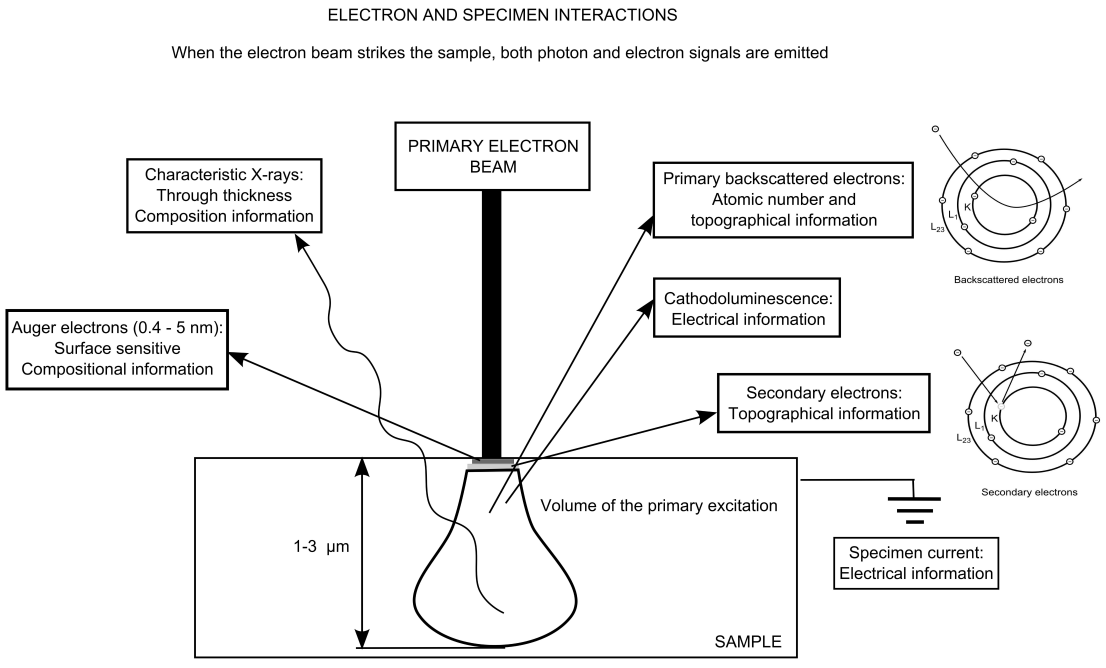


Figure. 4.4 – The interaction volume at the sample illuminated with the incident electron beam. The schematic process for the production of secondary and backscattered electrons is shown as well [27].

4.4.2.4 Image formation

The images recorded using a secondary electron microscope depend on the position of the detector(s). First of all, the incident beam is rapidly swept across the surface to be able to analyze the whole sample. The current measured by the secondary electron detector will change continuously and cause brightness variations depending on the surface morphology and dimensions.

The use of a backscatter detector, mounted between the sample and the objective lens, renders an image with bright portions indicating a higher atomic number and with darker portions indicating a lower atomic number depending on the chemical composition and surface orientation [28]. One of the instruments used, the Phenom (Phenom-World, The Netherlands) contains only a backscatter detector, which is split up in four quadrants from which the opposite quadrants are electronically coupled (see Figure 4.5) [29]. This allows the user to get both compositional and topographical information. Indeed, by adding the signals compositional information is recorded, while the signals are subtracted to get topograpical information [29].

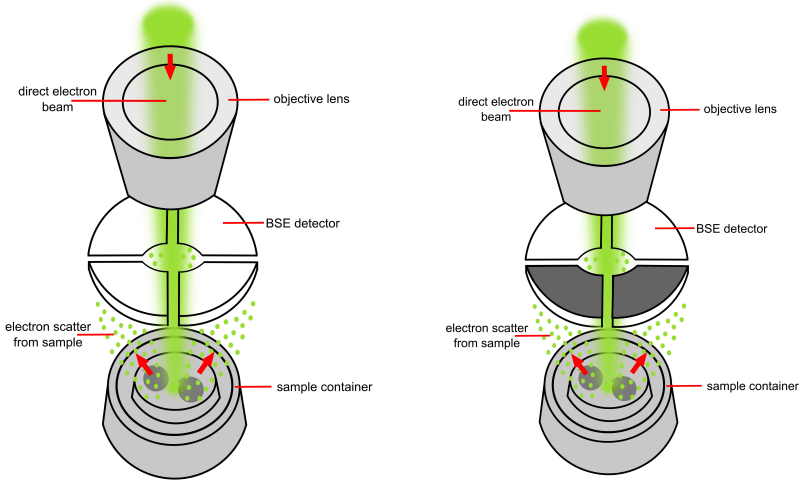


Figure. 4.5 – Schematic representation of the Phenom detection system for the detection of backscattered electrons for (a) information about the composition of the sample and (b) information about the topography of the sample [30].

A new type of low-angle backscatter detector is able to collect backscattered electrons that leave the sample at lower angles allowing a higher surface sensitivity, resolution and atomic number contrast [31].

4.4.2.5 Image quality

The performance of the microscope's lens system that we described in section 4.4.2.2 is limited by spherical aberration, chromatic aberration and astigmatism [32]. The first term describes the lens effect on off-axis rays. The second term is a consequence of the focus change in the lens depending on the energy spread of the incident beam. Finally, astigmatism is caused by the different focus of the lens for different orientations of the image [33]. However, many researchers try to correct these problems [34]. Secondly, the imaging system's resolution is limited by diffraction depending on the finite aperture causing blurring of the image. An estimate of the theoretical lateral resolution in optical microscopy is proposed, based on the Rayleigh criterion [35]

$$\Delta l \approx \frac{1.22\lambda}{2\mathrm{NA}} \tag{4.2}$$

where λ is the incident wavelength and NA is the numerical aperture of the lens. In the case of scanning electron

microscopy, the resolution depends on the beam diameter (which depends on the beam energy). However, also sample drift and noise can cause image imperfections [36].

4.4.2.6 EDS spectra

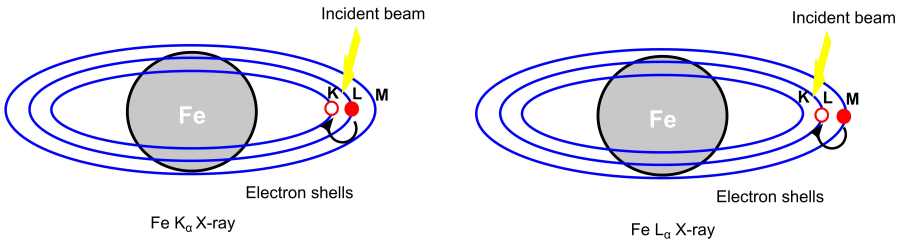


Figure. 4.6 – Schematic representation of the X-ray formation [37].

As seen in Figure 4.4, the interaction of an incident electron beam also produces specific X-rays. A build-in silicon drift detector allows the detection of these X-rays with very high count rates (high sensitivity) and lowest X-ray energies, but low resolution (about 100 eV) [38]. It was Moseley [39] who proposed that atoms irradiated with energetic electrons are excited to energy levels dependent on the quantum state of the bound electrons energized. If these 'holes' are in inner shells, the atoms are not in a stable state. In Figure 4.6 is shown that the atoms are stabilized when the atom loses energy in the form of X-rays [37]. This return of a bound electron from state i to j is expressed as Moseley's law [40],

$$E_{\mathrm{i}} - E_{\mathrm{j}} = \Delta E = \mathrm{C}(\mathrm{Z} - \sigma)^2, \tag{4.3}$$

where C is a constant for any discrete transition and σ is a nuclear screening constant which adjusts for the effective charge of the nucleus. Figure 4.7 shows this relationship.

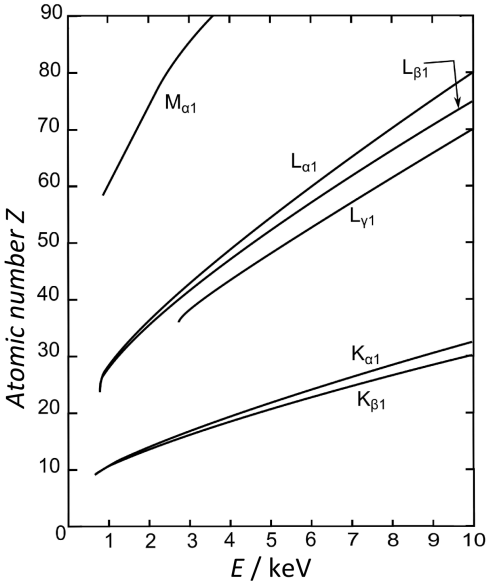


Figure. 4.7 – Energies of major X-ray emission lines observed below 10 keV [27, 41].

The characteristic X-ray lines are named according to the shell in which the initial vacancy occurs and the shell from which an electron drops to fill that vacancy. For instance, if the initial vacancy occurs in the K shell and the vacancy filling electron drops from the adjacent L shell, a K_α X-ray is emitted. Within a given shell, there may be electrons in orbitals differing in energy due to bonding effects. Thus, the K_α peak actually comprises the $K_{\alpha 1}$ and $K_{\alpha 2}$ X-rays. To ionize an atom, the incoming radiation must possess a minimum amount of energy called the binding energy, which is a specific and characteristic for each electron in the atom. The binding energy for a K-shell electron, for example, is greater than that of an L-shell electron, since the K-shell electron is closer to the nucleus and more tightly bound. Therefore, if sufficient energy exists in the incident beam to excite the K level, L and M X-rays will also be excited if these shells and the one above them are occupied. Figure 4.7 assures that measuring a spectral range of 0 - 20 keV allows the user to detect all elements from boron to uranium. Essentially, each element has characteristic X-ray line(s)

summarized in a database that allow a sample's elemental composition to be identified by a 'non-destructive' technique [41]. However, in some cases, sample damage is possible which means one always has to take care.
Since the X-rays are formed by the electron beam interaction with the sample surface, a chosen sample area being imaged is analyzed. The software allows the user to do point and line measurements together with elemental mappings of a selected area. For example, it is possible to take an image and, at same time, measure the elemental composition. Depending on the sample density and accelerating voltage of the incident beam, the depth of an EDS-analysis is usually 0.5 to 2 μm [42] and the detection limits are as low as 0.1% for the higher atomic number elements [43]. The qualitative analysis consists of different phases: background removal, deconvolution of overlapped peaks, and the calculation of elemental concentration. Often, this is done automatically using the software package.

4.4.2.7 Instrumentation

(i) The Phenom (Phenom-World, The Netherlands) electron microscope used for taking basic pictures of the surfaces studied in this thesis is equipped with a LaB_6 thermionic source. This source has an optimal resolution and a signal-to-noise ratio during an acceleration under a standard electric field of 5 kV. The Phenom instrument has a magnification range of 250 - 20,000x with a resolution around 50 nm. The use of the build-in backscatter detector is explained in section 4.4.2.4.

(ii) A Schottky field emission gun (FEG) is used in the JEOL JSM-7600F Field Emission Scanning Electron Microscope (JEOL, USA). The accelerating voltage could be set from 0.1 to 30 kV. The instrument has been build-up with a full set of detectors for secondary electrons and backscattered electrons and offers a 25 - 1,000,000x magnification with 1 nm (at 15 kV) resolution. Furthermore, the instrument has a build-in X-MAX^N SDD-detector (OXFORD Instruments, UK) operated by the INCA software.

(iii) The FEG SEM Quanta-450 (FEI, USA) uses a FEG with an accelerating voltage from 0.1 to 30 kV. The instrument has three types of secondary electron detectors and offers a 6 - 1,000,000x magnification with 1 nm (at 15 kV) resolution. The instrument is equipped with build-in EDAX SDD detector (EDAX, USA) operated by the TEAM software.

(iv) A SEM XL30 (Philips, The Netherlands) instrument with a zirconated tungsten FEG, equipped with both a secondary electron and backscattered electron detector. The electron beam source was operated at 20 kV (1 - 30 kV).The magnification of the instrument is 20 - 1,000,000x and the resolution is 2 nm at 30 kV. Furthermore, an EDAX energy dispersive x-ray detector with an ultra thin window is mounted using the EDAX software.

4.5 Scattering techniques

In the first part of this section, we briefly explain the principles of basic laboratory X-ray diffraction. In a second part, we describe the set-up and advantages of synchrotron radiation X-ray diffraction.

4.5.1 Laboratory powder X-ray diffraction

4.5.1.1 Crystalline structures

Most of the time, X-ray diffraction (XRD) is used to provide information on solid crystalline samples namely single crystals and polycrystalline materials. However, XRD can also provide valuable information on amorphous solids [44]. Crystals are defined by Barrett [45] as "a composition of atoms arranged in a regular ordered pattern or point lattice in three dimensions." In a single crystal the order is maintained over the whole volume of the material, while in a polycrystalline

material small single-crystal regions are observed, separated by grain boundaries [46]. The smallest repeating unit stacked in three dimensions is known as the unit cell. In Figure 4.8a, this small volume is described by the interrelationship between the lengths (**a**,**b**,**c**) of its sides and the interaxial angles (α,β,γ) between them, called the lattice parameters [47]. One of the requirements for the unit cell is that it can be stacked to fill the three-dimensional space. Seven unit-cell shapes meet this requirement and are known as the 7 crystal systems [48]. In 1848, Auguste Bravais demonstrated that these crystal systems provide 14 possible point lattices [49]. In a real crystal, a lattice point may be occupied by one atom or by a group of atoms known as the basis [50]. An important difference between lattice points and atoms is that the lattice points tell us nothing about the chemistry of the bonding within the crystal; for that we need to include the identity of the atoms and their positions. So, the relationship is described as [50]

$$\text{BRAVAIS LATTICE} + \text{BASIS} \rightarrow \text{CRYSTAL STRUCTURE} \tag{4.4}$$

All this information is summarized in the International Tables for Crystallography [51]. Furthermore, Miller indices (hkl) have been proposed to provide a way of uniquely describing crystal planes in a lattice [52] and are determined following a procedure described by Masel [53] using reciprocal values of multiples of the lattice length parameters. As an example a (210) plane is shown in Figure 4.8b.

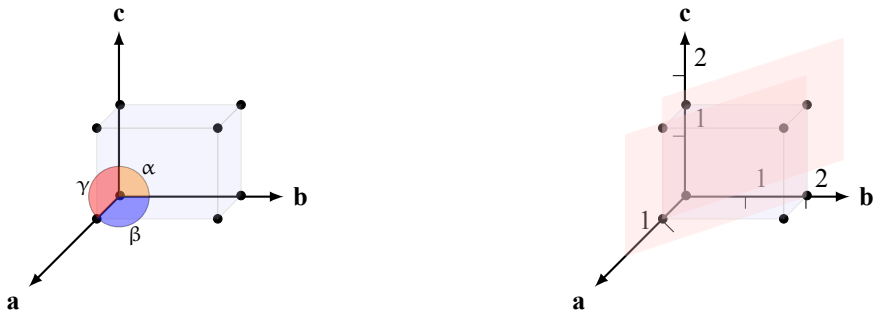


Figure. 4.8 – (a) A primitive unit cell described by lattice parameters (**a**,**b**,**c**) and (α,β,γ). (b) An example of the determination of Miller indices (hkl) of a crystal plane (210). The black dots represent the basis. This figure is based on [54].

4.5.1.2 Diffraction of crystalline structures - Bragg's law

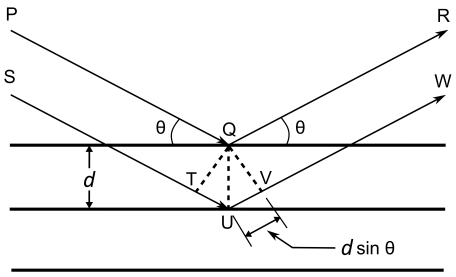


Figure. 4.9 – Bragg's reflections [54].

When a beam of X-rays interacts with an isolated atom, two processes may occur as stated by Guinier [44]: "(1) the beam may be *absorbed* with an ejection of electrons from the atom, or the beam may be *scattered*". The scattering process is caused by the oscillation of free or bound electrons in the electric field of the incident wave. In the case of a crystal (or closely packed solid) these scattered X-rays start to interfere if there is some regularity to the structure on the same scale as the X-ray wavelength. If the waves are in phase, then constructive *interference* occurs and when the waves are 180°out of phase, destructive interference occurs. As a conclusion, *diffraction* is defined by Guinier [44] as "the result of the combination of two different phenomena: (a) scattering by each individual atom, and (b) interference between the waves scattered by these atoms."

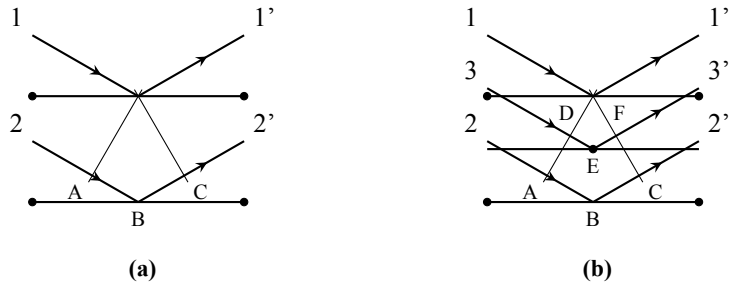


Figure. 4.10 – Diffraction from the (001) planes of (a) base-centered and (b) body-centered orthorhombic unit cells

In 1913, Bragg developed a simple theory around X-ray diffraction [55]. To derive Bragg's law, we consider a diffracted wave which makes the same angle, θ, with the atomic planes and the incident wave as pointed out in Figure 4.9. Constructive interference only takes place when the path length difference between QR and UW is exactly a number (n) of wavelengths λ. Using elementary trigonometry, the total path difference $\delta = n\lambda$ is written as

$$n\lambda = 2d \sin\theta, \tag{4.5}$$

where λ is the wavelength of the incident beam, θ is the diffraction angle between the incident rays and the surface of the crystal, d is the inter-planar spacing and n is an integer presenting the order of reflection. This equation is known as Bragg's law [56]. The distance between the adjacent planes for a certain crystal system, d, can be calculated using simple analytical geometry based on the Miller indices (hkl) and the Bravais lattice [54]. For example, the orthorhombic crystal system returns d using

$$\frac{1}{d_{hkl}^2} = \frac{h^2}{\mathbf{a}^2} + \frac{k^2}{\mathbf{b}^2} + \frac{l^2}{\mathbf{c}^2} \tag{4.6}$$

Furthermore, the integer n describes the parallel planes of the form (nh,nk,nl). The Bragg's reflection and diffraction pattern is possible because the inter-planar spacing is of the order of few angstroms and wavelength of X-rays is of the same order.

4.5.1.3 Diffraction of crystalline structures - Structure factor

The structure factor, F, describes the effect of the crystal structure on the relative intensity of the diffracted beam. In Figure 4.10, we consider the diffraction from the (001) planes of (a) a base-centered orthorhombic unit cell and (b) a body-centered orthorhombic unit cell. For the base-centered lattice, if the Bragg law is satisfied, this means that the path difference ABC is λ and diffraction will occur. For the body-centered lattice, if waves 1' and 2' are in phase, their path difference is λ. However, the other plane of atoms midway produces a wave 3' where the path difference with wave 1' is $\frac{\lambda}{2}$. These waves are completely out of phase, destructive interference will occur, and no diffracted beam will be measured. This means that for some structures some reflections are absent, called forbidden reflections [57]. To calculate F, we use the following formula derived in [58],

$$F = \sum_{\mathrm{i}} f_{\mathrm{i}} \exp\ \left(2\pi \mathrm{i}(\mathrm{h}\mathbf{u}_{\mathrm{i}} + \mathrm{k}\mathbf{v}_{\mathrm{i}} + \mathrm{l}\mathbf{w}_{\mathrm{i}})\right), \tag{4.7}$$

where f is the atomic scattering factor, **u**, **v** and **w** are the atom positions in the unit cell, and h, k and l are the Miller indices of the reflection. The summation is performed over all atoms in the unit cell. This equation tell us which reflections hkl

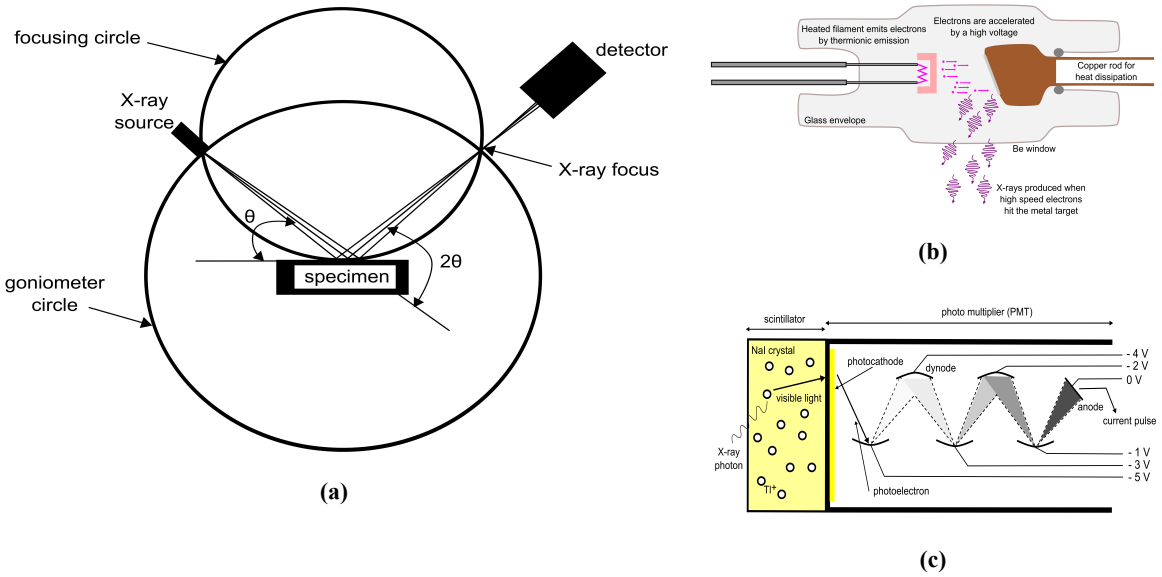


Figure. 4.11 – Schematic of a (a) Bragg-Brentano geometry, (b) modern X-ray tube and (c) scintillation detector [54].

to expect in the diffraction pattern for a given crystal structure with atoms located at positions **u**, **v** and **w** (called selection rules) and applies on all Bravais lattices [54]. In what follows, we discuss the actual X-ray diffraction measurements based on two principles of X-ray generation: laboratory powder X-ray diffraction and synchrotron X-ray diffraction.

4.5.1.4 Instrumentation

In a laboratory X-ray instrument, an X-ray tube, a sample and a scintillation detector are placed on the circumference of a goniometer circle as shown in Figure 4.11a. Mostly this diffractometer uses a Bragg-Brentano or θ - 2θ geometry in which case the X-ray source is fixed, the sample scans a range of θ while the detector moves through a range of 2θ angles. The range depends on the measuring time.

The X-ray tube used, as shown in Figure 4.11b, consists of a heated tungsten filament cathode at a highly negative potential, which produces electrons that collide with the water-cooled anode at ground potential. The energy loss of the electrons because of the impact with the metal anode is manifested in a small percentage (less than 1%) of X-rays [48]. Therefore, based on this process, the tube produces characteristic lines of the target metal superimposed on a continuous X-ray spectrum, called Bremsstrahlung. Using a monochromator, the sample is eventually only bombarded with characteristic lines of the target element (often Cu or Mo). Furthermore, the beam size can be adjusted using slits. Actually, in this work, diffractometers with both tubes are used. A basic and conventional powder Siemens D5000 X-ray diffractometer is equipped with a Ge focusing monochromator to produce $MoK_{\alpha 1}$ radiation ($\lambda = 0.711$ Å). The instrument is configured to use the Bragg-Brentano geometry as described above and is equipped with a scintillation detector shown in Figure 4.11c. The incident X-rays cause a crystal (NaI crystal doped with 1% Tl) to fluoresce depending on the amount of absorbed X-ray photon. The light is measured with a photomultiplier. Although, the scintillation detector is very efficient, problems are seen with the energy resolution [59].

Another more advanced instrument is the Panalytical X'Pert Pro Multipurpose Diffractometer equipped with a curved Ge focusing monochromator to produce $CuK_{\alpha 1}$ radiation ($\lambda = 1.5405$ Å). In this case, the X-ray radiation is filtered using a Ni beta filter, which is often done to reduce the intensity of the CuK_{β} ($\lambda = 1.387$ Å) and W radiation. Indeed, the Ni absorption (with an edge around 1.488 Å) of for a Cu tube is 50% for CuK_{α} and 99% for CuK_{β} radiation [60]. One advantage is that at higher 2θ-values, filtering only one diffraction peak appears, instead of two as a consequence of CuK_{α}

and CuK_β diffraction [61]. This way we avoid peak splitting phenomena in the diffraction spectra. Furthermore, it also helps narrowing the diffraction peaks in the spectrum [62]. The instrument is equipped with a solid-state detector, where the incident X-rays create an electron-hole pair in a p-i-n diode. The number of electrons is measured and is directly proportional to the energy of the incoming X-ray [63]. The latest generation of solid-state detectors (like the PIXcel detector) is based on compound semiconductors characterized by a large band gap and can be used without cooling. Next to XRD, the instrument can also be used in X-ray reflectivity (XRR) mode, to analyze thin films on samples using lower incident angles [64].

4.5.1.5 Data analysis

These laboratory instruments can produce excellent resolution diffraction patterns, which display the counts per second from the detector in function of the corresponding 2θ value. The recorded diffraction patterns have a background, which is usually subtracted using the processing software EsaProject (© 2008 Mark Dowsett, EVA Surface Analysis). To compare peaks on a common scale, we convert the 2θ-space to Q-space using Bragg's law and the relation [65]

$$Q = \frac{2\pi}{d} = \frac{4\pi \sin\theta}{\lambda} \tag{4.8}$$

Most commercial software allows you to compare standard patterns with experimentally observed patterns, allowing rapid matching of patterns and material identification. The identification in this work is done using reference structures in the ICDD database (at http://www.icdd.com) and the Mincryst database (at http://database.iem.ac.ru/mincryst/index.php). The identification of the measured structure is carried out based on both the peak positions (2θ) and their intensities [66].

4.5.2 Synchrotron X-ray diffraction

Before explaining our experiment setup, we start with the basics for the production of monochromatic synchrotron radiation on a beamline.

4.5.2.1 Synchrotron radiation

Synchrotron radiation is the result of a charged particle moving with relativistic speed in a curved path. The electrons are forced to follow circular paths under the effect of magnetic fields (perpendicular to the direction of their motion) using bending magnets build into the storage ring [67]. To able to get enough speed, the electrons are accelerated by a linear accelerator or Linac (MeV energy range) and by a booster ring (GeV energy range) before they enter the storage ring. During each turn, the electrons loose part of their energy in a pencil-like beam tangential to their orbital path, producing synchrotron radiation utilized at different so-called beamlines. Afterwards, this lost energy is regained in passing through radio frequency electric field cavities build into the linear sections of the ring [68].

Bending magnets were the main elements in the early 1970s synchrotron facilities (such as the one in Daresbury, UK) to produce extremely intense radiation. Later on, trying to increase the radiation's brightness and quality and produce narrow and parallel beams of X-rays, also other magnetic structures, such as wigglers and undulators, were placed in the ring's linear sections [69–72]. Indeed, synchrotron radiation has a high natural collimation and a very polarized character (linear polarization factor P $\sim$ 99%), which is important for most analytical applications [73].

A schematic of a modern synchrotron source is shown in Figure 4.12 together with the most important elements. These improvements are demonstrated in the European Synchrotron Radiation Facility (ESRF) in Grenoble (France) which produces electrons with an energy of 6 GeV. Basically, there are more than 40 beamlines at the ESRF, all performing different types of experiments. In this work, all the experiments were performed at the Belgian-Dutch CRG beamline DUBBLE (BM26A) of the ESRF [74].

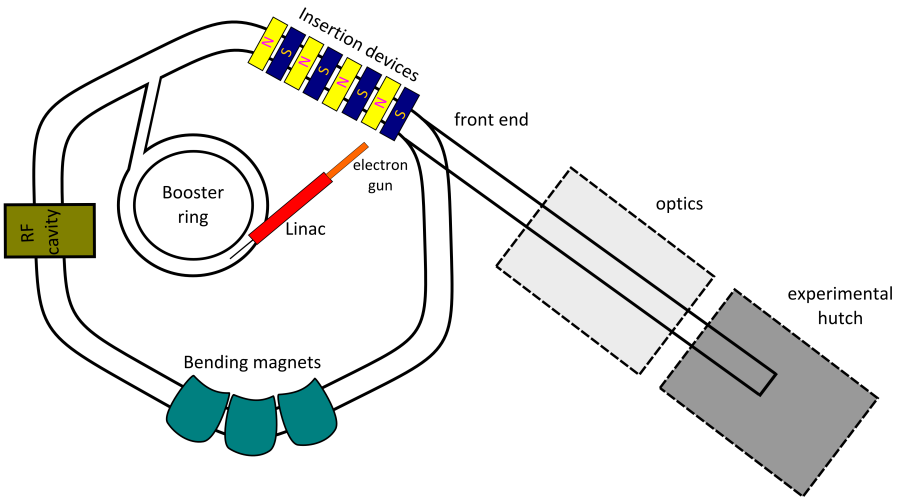


Figure. 4.12 – A schematic of the most important components of a third generation synchrotron source [68].

The DUBBLE beamline is placed at a bending magnet with a magnetic field strength of around 0.4 T. The bending-magnet radiation is produced in the form of a flattened cone and is defined by a critical energy of 9.8 keV [74]. Figure 4.13 shows the theoretical bending magnet spectrum of the DUBBLE beamline based on the given values defining clearly the critical energy. One has to take into account that at low- and medium-energy facilities, it is difficult to achieve high energy beams because of hardware limitations.

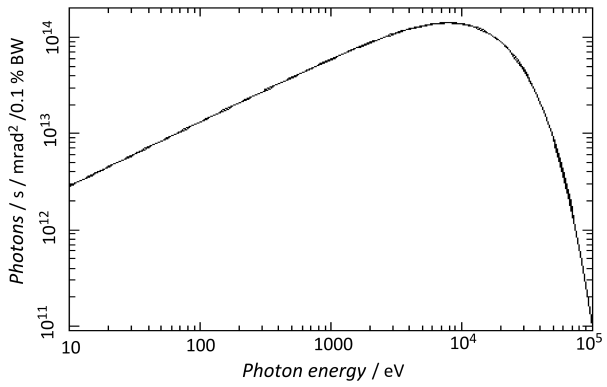


Figure. 4.13 – Bending magnet spectrum of the DUBBLE BM26A beamline.

Before entering the experimental hutch, where the actual experiments are carried out, the beam is send through the optics hutch as seen in Figure 4.12. At beamline BM26A, the polychromatic beam coming from the ring is diffracted using a double-crystal monochromator consisting of highly perfect Si(111) single crystals (d_{111} = 3.1356Å) in a vacuum vessel as shown in Figure 4.14a. The first water cooled crystal absorbs 99.9% of the radiation, because this part does not satisfy the Bragg condition explained in section 4.5.1.2. Depending on the use of a nondispersive or dispersive mode, the second crystal is used for further focusing of the reduced flux beam. Depending on the relative geometries, crystallographic orientation, and/or crystal types, the monochromator's radiation can be more or less monochromatic. This is further explained in [75]. In this case, the second crystal is used for horizontal focusing, called *sagittal focusing* [76]. However, an increase of the beam monochromaticity always implies a beam flux decrease. Figure 4.14b shows that the optics of the DUBBLE BM26A beamline is equipped with a vertical focusing mirror (1200 × 150 × 50 mm) after the monochromator and to enhance the angular and energy resolution, a cooled collimating mirror with a Si coating is added in front of the monochromator [74, 77]. Using these optics, a typical beam size at the sample is 10.0 × 10.0 μm^2 to 2.0 × 0.3 mm^2 [77]. At this point, it is clear that synchrotron X-rays are much higher flux compared to the X-ray tubes used in laboratory instruments. This high flux allows us to record patterns much faster (in the order of seconds), which enables us to collect time-lapse data in quick succession.

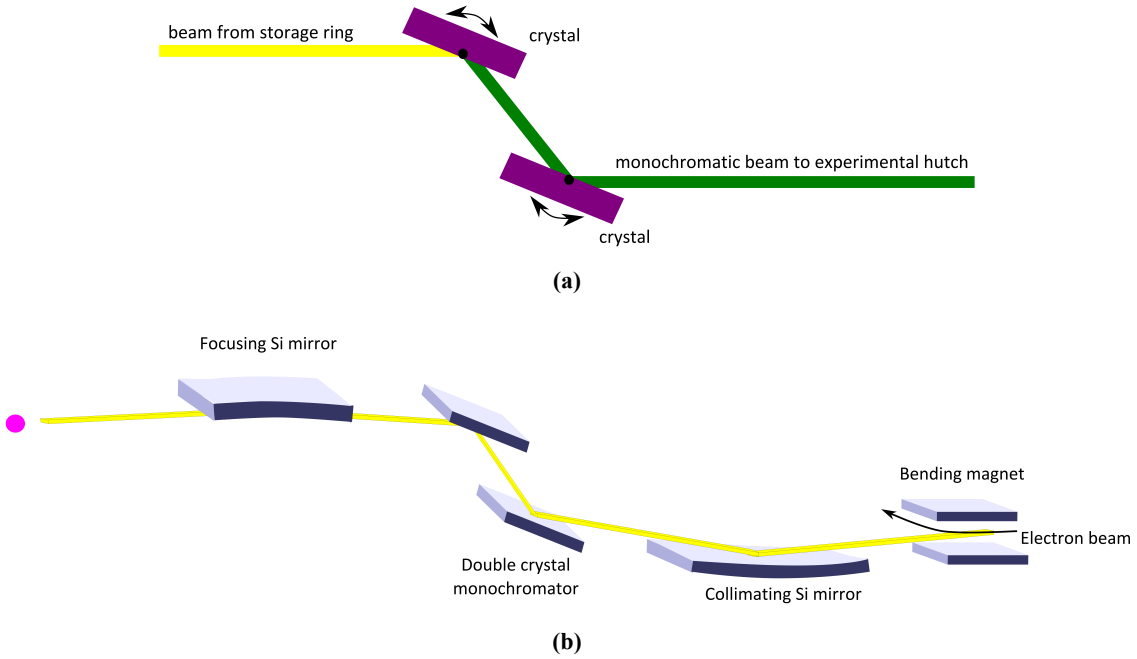


Figure. 4.14 – X-ray optics: (a) Basic geometry of the double-crystal monochromator and (b) Schematic of the X-ray optical system at DUBBLE [75].

To be able to record data, it is important the user knows the intensity of the incident beam coming into the experimental hutch. For this reason, the incoming beam's fluctuations are monitored using an ionization chamber [75]. X-ray photons entering the chamber are absorbed by a gas (often N_2) and therefore ionize the gas. An electric field ensures the produced photoelectrons and ions are accelerated towards the poles. This way collisions start to ionize other gas particles. The amount of charged particles produced by this avalanche process, which is proportional to the X-ray flux, is measured as counts per second. The given beam monitor value is used to normalize the data.

4.5.3 Setup and instrumentation

The XRD setup using synchrotron radiation in this work is completely different from laboratory experiments. The use of an X-ray tube during laboratory experiments ensures that the incident X-rays diverge from the source [78]. In synchrotron radiation diffractometry, however, storage rings naturally provide well-defined, monochromatic and parallel X-ray beams with a cross section large enough to illuminate a large part of the specimen [79]. The X-ray beam is kept on a constant energy of 8 keV with dimensions of 1 mm $\times$ 200 µm. This means it is possible to collect diffraction patterns from a fixed two-dimensional CCD camera using a fixed X-ray incident angle to increase the amount of data, which in the end improves the analysis [80]. Furthermore, a Mar CCD 165 detector (Mar USA Inc., USA), consisting of 2048 $\times$ 2048 individual elements with a pixel size of 79 mm, was used to record the two-dimensional diffraction patterns of the deposited layers [81]. In this thesis, we choose an incident angle of 10° to be sure we are not scattering from our sample holder. The camera axis is then positioned to collect as much diffraction bands as possible in the desired 2θ-range depending on the sample to be analyzed. The setup was designed to place the camera face 130 mm from the intersection between the beam axis and the surface. For our samples, the camera axis was placed at 40.5° in order to obtain a final 2θ-range of 8° to 70°. The complete setup and geometry of the experiment is shown in Figure 4.15. A fast shutter was also mounted to shield the sample from X-ray damage between exposures. After exposure to the monochromatic beam, the camera is actually intersecting with the diffraction cones forming elliptical rings on the camera face showing the diffraction pattern of the measured polycrystalline sample [82]. A fast shutter was to shield the sample from X-ray damage between exposures.

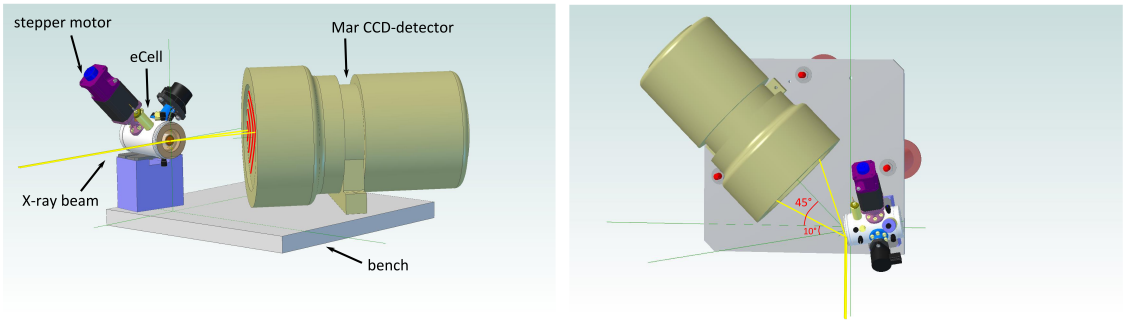


Figure. 4.15 – The setup and geometry of the experiment at BM26A (DUBBLE) for time-lapse XRD measurements ©Mark Dowsett.

4.5.3.1 Data analysis

All recorded two-dimensional diffraction patterns were processed using the esaProject 2012 software (©EVA Surface Analysis) [83–85]. It is analytical software package, which handles and analyzes both two dimensional XRD powder diffractograms in different data formats, as well as a huge range of spectra, all in native format, and provides an acquisition to publishing capability for XRD, X-ray absorption spectroscopy (XAS), X-ray emitted optical luminescence (XEOL), and other spectroscopic data with a rapidly developing image. Furthermore, diffraction image stacks can be batch processed using esaProject through a reprojection algorithm to transform two-dimensional images to line spectra, which makes it possible to integrate by summing image rows. Then, the line spectrum shows the total intensity at all recorded 2θ values esaProject software. The software also has a feature for data plotting and formatting to get publishable graphs and images.

4.6 X-ray photoelectron spectroscopy

It was established by Siegbahn and co-workers [86] that sharp peaks could be observed in energy-analyzed photoemitted electrons using monochromatic X-rays. Indeed, X-ray photoelectron spectroscopy is based on measuring the element-specific binding energy of electrons in the atomic shell as a result of a single-step photoemission process shown in Figure 4.16 [87]. A detected photoelectron is attributed to one electron level nl_J with a principal quantum number (n = 1, 2, 3, ...), an angular quantum number (l = 0, 1, 2, ... or s, p, d, ...), and finally the total angular momentum given by the absolute value of the sum of angular and spin momentum ($J = |\mathbf{l} + \mathbf{s}|$ in the so-called j-j coupling) [88]. In Figure 4.16b, the de-excitation process (the Auger process) that follows photoelectron emission is shown. It is clear that peaks from both photoelectrons and Auger electrons are observed in XPS spectra. Knowing that the emitted photons are massless and chargeless energy packages, indicates these are annihilated during photon-electron interaction with complete energy transfer. The measured experimental quantity is the kinetic energy (E_{kin}) of the emitted photoelectrons, which depends on the energy $h\nu$ of the primary monochromatic X-ray source. The characteristic parameter for the electron is the binding energy (E_{b}) (with reference to the Fermi level, E_{F}). The relation between these parameters is given by [89]

$$E_{\text{b}} = h\nu - E_{\text{kin}} - \phi, \tag{4.9}$$

where E_{b} and E_{kin} are respectively the binding and the kinetic energy of the emitted photoelectron, $h\nu$ is the photon energy, and ϕ is the spectrometer work function determined by calibration of the spectrometer. The measured binding energies depend on the valence of the respective atom, which means that different oxidation states of one atom can be

treated like different elements [87].

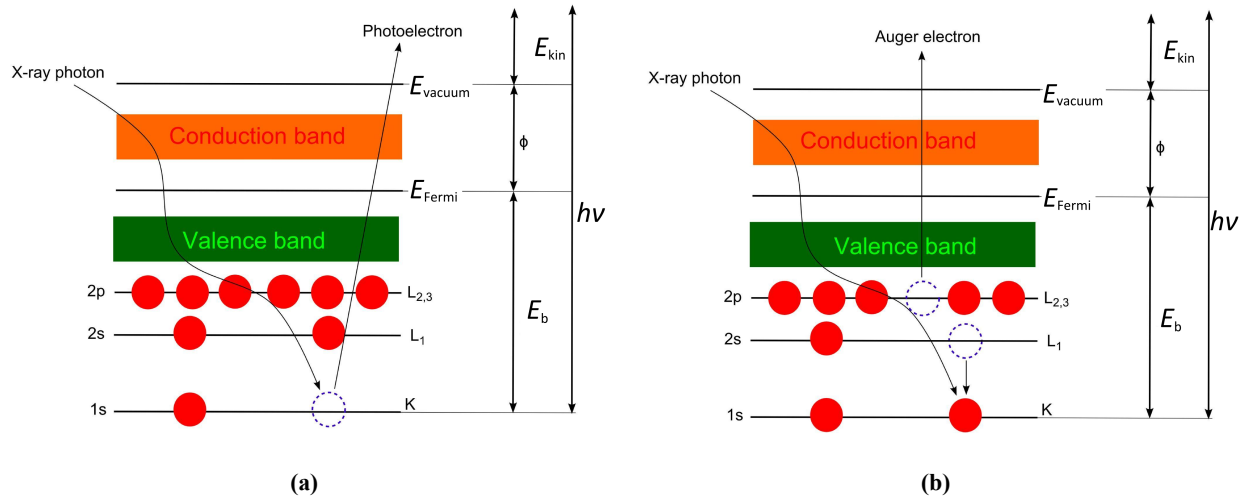


Figure. 4.16 – Schematic representation of (a) the photoelectron emission process and (b) the Auger de-excitation process [90].

The XPS technique is often used because of its high sensitivity and surface specificity. Indeed, the yield of photoelectrons exiting the surface is very high compared to number of atoms in the sample. The surface specificity, however, is a consequence of the low escape depth of the formed photoelectrons is no more than a few atomic planes ($<$ 1 - 5 nm) [91]. In what follows, the instrument parts are described and explained.

4.6.1 X-ray photoelectron spectrometer

In this work, all measurements were carried out using a S-Probe monochromatized XPS spectrometer from Surface Science Instruments (VG) consisting of a vacuum vessel routinely operative in the UHV regime (2×10^{-9} mbar) using a cryopump, an X-ray tube, a concentric hemisperical analyzer with associated lenses and an electron detection system. The scheme is shown in Figure 4.17

The X-ray tube consists of an aluminum target anode (also Mg is possible). The Al K_α X-ray (1486.6 eV) radiation satisfies a number of important criteria like the narrow line width to minimize contribution to photoelectron line width, a sufficient energy to excite photoemission from at least one core level, the ease of fabrication of anode and the high thermal conductivity [92]. The source is operated at a voltage of 10 kV and power of 200 W. Furthermore, quartz crystal monochromators are added to the system to minimize the contribution of Bremsstrahlung, satellite and ghost radiation, which reduces the background and significantly improves the S/N ratio [93]. Using this set-up, the X-rays are focused into a spot of 150 µm $\times$ 800 µm on the sample.

An concentric hemisperical analyzer illustrated in Figure 4.17 measures the energy distribution of electrons emitted from the sample at a take-off angle of 45°. Two concentric hemispheres with radii R_1 and R_2 have a mean equipotential surface between them of radius R_0. Potentials -V_1 and -V_2 are applied to the hemispheres with $V_2 > V_1$, so that the pass energy is 107.5 eV. If electrons of energy E_0 are injected tangentially to the equipotential surface they are brought to a focus, irrespective of the plane of their circular trajectory, according to [87]

$$e\Delta V = e(V_2 - V_1) = E_0 \left(\frac{R_2}{R_1} - \frac{R_1}{R_2} \right). \tag{4.10}$$

Since the analyzer dimensions are fixed, it is clear from Eq. 4.10 that by ramping the deflection voltage, electrons of

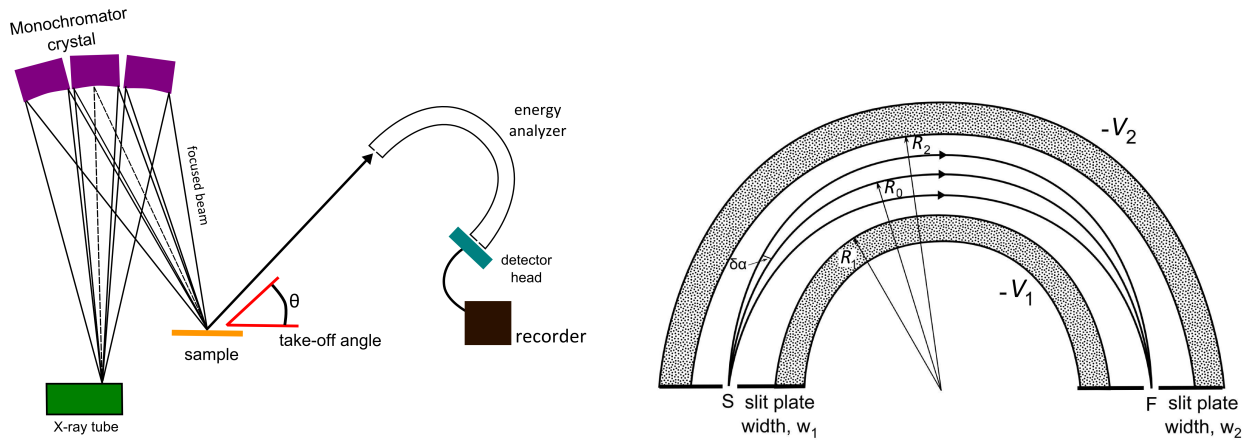


Figure. 4.17 – Schematic of the XPS instrument with a magnification of the hemispherical electron analyzer [87].

progressively higher energy are focused. Only electrons with a given energy, called the pass energy, are allowed to pass through the detector slits. As the energy range is scanned, the intensity is measured and plotted in a photoelectron spectrum. As a conclusion we state that the energy resolution depends on different parameters such as the diameter of the analyzer, the pass energy and the spread of energies in the X-ray source [93].

Photoelectrons are measured using a SSI position-sensitive detector of 40 mm $\times$ 40 mm with a width of 13.70 eV [94]. The detector consists of an array of channel multipliers a few tens of microns in diameter fused into a thin disc, so that electrons can be detected as a function of position explained in Figure 4.17 [93]. The XPS spectra show the counts per second of the detector as a function of the binding energy. Because E_b and E_kin have a different sign, the E_b scale is plotted with increasing energy from right to left.

4.6.2 Data analysis

After recording an XPS measurement, still a profound data analysis is required to be able to make assumptions about the present elements and their oxidation states.

4.6.2.1 Qualitative analysis

To start, the photoelectron core level peaks, valence band peaks and Auger electron peaks are characterized based on element spectra compiled in relevant handbooks [95–99]. The interpretation of the elemental peaks involves also the characterization of satellite peaks in the vicinity of XPS core lines, especially for transition-element compounds [100, 101], lanthanides [102] and actinides [103], which are generally called ‘shakeup’ peaks. For the analysis, it is also important to identify the doublet peaks for certain elements given by the ratio of their degeneracy ($2J + 1$), as compiled in Table 4.3.

SUBSHELL	J VALUES	INTENSITY RATIO OF PEAK AREAS
s	1/2	-
p	1/2, 3/2	1:2
d	3/2, 5/2	2:3
f	5/2, 7/2	3:4

Table 4.3 – Spin-orbit splitting intensities [87].

The core-level binding energy shifts provide a local probe of the changes in the electronic structure of an atom in different

environments in molecules and solids [104]. A simplified model predicts that when an atom is bonded to another one with higher electronegativity, a charge transfer to the latter occurs, thus increasing the E_b. To demonstrate the power of the XPS technique, a typical example is given in Figure 4.18. The total shift between XPS core levels for carbon atoms in different chemical environments are sometimes 10 eV or more [105, 106].

In practice, references to standard spectra of compounds are used to interpret binding energy shifts providing information on the chemical state of a material. For example, the NIST X-ray Photoelectron Spectroscopy (XPS) Database (http://srdata.nist.gov/xps/) gives easy access to the energies of many photoelectron and Auger-electron spectral lines. Furthermore, software packages exist (like CasaXPS © Casa Software Ltd.), which run automatic peak identification tools.

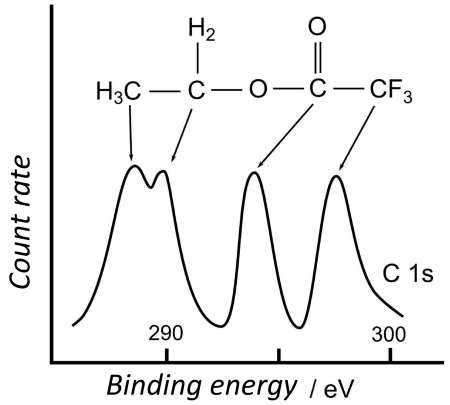


Figure. 4.18 – Chemical shifts for the C 1s levels in ethyl trifluoroacetate. The chemical shifts are related to the electronegativity differences: The known [107] electronegativity differences (ΔE) are C - H: 0.4; C - O: 1.0; C - F: 1.5, which rationalize the chemical shifts in ethylfluoroacetate [108].

However, before analysis, raw XPS spectra have to be checked for charge compensation and peak broadening phenomena. Indeed, an insulating sample will charge relative to the instrument causing a retarding electric field at the sample surface [109]. Peak broadening arises from the resolution of the energy analyzer, from the energy distribution of the incident photon flux and from charging of the material. Other sources of broadening are beyond the scope of this thesis, but, in general, the peaks are fitted using a Gaussian broadening [110].

4.6.2.2 Quantitative analysis

Another interesting property of XPS measurements is that the number of electrons recorded for a given transition is proportional to the number of atoms at the surface. In practice, however, to produce accurate atomic concentrations from XPS spectra is not straightforward. An accuracy of 10% is typically quoted for routinely performed XPS atomic concentrations.

First, we construct a background sensitive to change in the data. Often, the Shirley algorithm [111] is used, which is based on an iterative procedure. For routine XPS analysis, the most popular functional forms for the data fitting are based on the Gaussian and Lorentzian functions. Accepted practices in the literature [112] show that the best fit was obtained using a weighting of 85% Gaussian and 15% Lorentzian curve shape. From the fitting, we calculate the peak area and the peak position, which gives quantitative information on relative atomic concentrations. However, the proportion between the peak intensity and the relative concentration of the emitting element depends in a complex manner on the intensity of the primary beam, the ionization cross section, on the probability of Auger transition in the case of AES, on the attenuation length, on the spectrometer transmission efficiency and on the detector efficiency [113]. The exact term for the absolute signal intensity, I_A, of a core-level electron, A, in XPS is [114]

$$I_{\mathrm{A}} = \sigma_{\mathrm{A}}(h\nu)D(E_{\mathrm{b}}) \int_{\gamma=0}^{\pi} \int_{\phi=0}^{2\pi} L_{\mathrm{A}}(\gamma) \int_{y=-\infty}^{\infty} \int_{x=-\infty}^{\infty} J_0(xy)T(wy\gamma\phi E_{\mathrm{b}}) \int_{z=0}^{\infty} N_{\mathrm{A}}(xyz) \mathrm{e}^{\frac{-z}{\lambda_{\mathrm{A}}(E_{\mathrm{b}})\cos\theta}} \,\mathrm{d}x\,\mathrm{d}y\,\mathrm{d}z\,\mathrm{d}\phi\,\mathrm{d}\gamma \quad (4.11)$$

where $\sigma_{\mathrm{A}}(h\nu)$ is the photoionization cross-section, $D(E_{\mathrm{b}})$ is the detection efficiency of photoelectrons, $L_{\mathrm{A}}(\gamma)$ is the angular asymmetry of the photoelectron intensity, J_0 is a factor combining the properties of the X-ray line in the detection plane, T is the transmission function of the energy analyzer, N_{A} is the atomic density at position xyz, γ is the angle between incident beam and analyzer aperture, ϕ is the azimuth angle, $\lambda_{\mathrm{A}}(E_{\mathrm{b}})$ is the attenuation length as a function of binding energy and θ is the emission angle of the photoelectron.

Since a numerical solution of this term is too complex a good approximation is needed. A more practical approach uses the concept of sensitivity factors [115–118]. The intensity of a signal from an element A, I_{A}, in a solid is proportional to its molar fraction x_{A} [92],

$$x_{\mathrm{A}} = \frac{I_{\mathrm{A}}}{I_{\mathrm{A}}^0}, \quad (4.12)$$

where I_{A}^0 is the intensity from a pure A sample, and may be considered as a sensitivity factor. In general what is used in the commercial data treatment software is a set of relative sensitivity factors, normalized to a reference element. For this reference, the sensitivity factor is set to unity. The molar fraction x_{A} in a homogeneous specimen composed of i elements, is then given by [92]

$$x_{\mathrm{A}} = \frac{N_{\mathrm{A}}}{\sum N_{\mathrm{i}}} = \frac{I_{\mathrm{A}}/S_{\mathrm{A}}}{\sum I_{\mathrm{i}}/S_{\mathrm{i}}}, \quad (4.13)$$

where I_{i} is the area of the peak generated by constituent i, N_{i} its number of moles and S_{i} its relative sensitivity factor. Since the sensitivity factors include instrumental parameters, they need to be determined on each spectrometer, and for each primary beam intensity. Moreover, since the escape depth is matrix and surface roughness dependent, using the values of sensitivity factors included in the data treatment software introduces errors [113]. For example, the CasaXPS library contains relative sensitivity factors based on the Scofield ionization cross-sections related to the Al monochromatic source [119]. These Scofield cross-sections were computed using Hartree-Fock theory to determine the relative intensity of the transitions throughout the periodic table for a given photon energy. The cross-sections are relative to the C 1s transition.

4.7 Attenuated total reflection infrared spectroscopy

First, the basics of infrared spectroscopy and attenuated total reflection is explained. Next, we describe the instrumentation and the data analysis.

4.7.1 Infrared spectroscopy: basics

When infrared radiation interacts with matter, it can be absorbed, causing the chemical bonds in the material to vibrate. Specific functional groups in molecules tend to absorb infrared radiation in the same wavenumber range regardless of the rest of the molecule's structure, which means a correlation exists between the absorbing wavenumbers and its structure. This makes infrared spectroscopy a useful chemical analysis tool [120].

The most interesting spectral IR range for chemical analysis is the mid-IR region. Mid-infrared spectroscopy is based on the absorption of radiation in the range of approximately 4000 - 400 cm^{-1}, which enables excitation of vibrational

or vibrational-rotational transitions of molecules involving transitions from/to rotational and/or vibrational levels in the same ground electronic state [121–123]. In the case of diatomic molecules, the vibration levels are based on the principle of harmonic oscillators or more precise the Morse oscillator which takes into account the possibility of bond breakage [124]. When looking at polyatomic molecules, we have to look at the degrees of freedom describing the movements relative to each other. Table 4.4 shows the different degrees of freedom for linear and non-linear molecules [125]. These movements or vibrations have to leave the mass' center unmoved, move all the atoms in phase and transform as an irreducible representation of the molecular point group, meaning either a change in bond length (stretching) or bond angle (bending) [126].

However, not every vibration is infrared active. Indeed, it is the polarity of the electric vector which changes from positive to negative over time and interacts with the molecule. Therefore, it is important that the molecule contains two opposite charges separated by a distance, which is called a dipole moment. The studied vibration must have a change in dipole moment or it will not be detected using infrared radiation. This condition is summarized as [127]

$$\frac{\partial \mu}{\partial x} \neq 0 \tag{4.14}$$

where $\partial\mu$ is the change in dipole moment and ∂x is the change in bond distance. Vibrations that satisfy this equation are infrared active, others are infrared inactive. Eq. 4.14 is also important because the size of $\left(\frac{\partial \mu}{\partial x}\right)^2$ is directly related to the intensity of infrared absorbance. This intensity is plotted as an absorbance or a transmittance as a function of the incident wave's wavenumber [127].

DEGREES OF FREEDOM	LINEAR	NON-LINEAR
translational	3	3
rotational	2	3
vibrational	3N - 5	3N - 6
total	3N	3N

Table 4.4 – Degrees of freedom for polyatomic molecules.

4.7.2 Attenuated total reflection

Attenuated total reflection (ATR) spectroscopy derives from internal reflection spectroscopy, and was independently pioneered by Fahrenfort [128] and Harrick [129] in the early 1960s. When radiation propagates from an optically denser medium (refractive index n_1) toward an optically rarer medium (refractive index n_2 with $n_1 > n_2$), total internal reflection will occur at the interface of the two media, if the incidence angle (θ) is exceeding the critical angle, which is defined as a function of both refractive indices

$$\theta_c = \sin^{-1}\left(\frac{n_2}{n_1}\right). \tag{4.15}$$

At each reflection, an evanescent field is extending into the adjacent optically rarer medium. This evanescent field may be described as a standing electric wave normal to the interface of the two media, and results from the superposition of the electric fields of the incident and reflected waves [130]. The amplitude of this standing electric wave exponentially decays with distance from the interface following [129]

$$E = E_0 \mathrm{e}^{-\left(\frac{z}{d_\mathrm{p}}\right)}, \tag{4.16}$$

where E_0 is the amplitude of the electric field at the interface ($z = 0$), z is the distance from the interface, and d_p is the penetration depth, which is defined as the distance where the amplitude of the electric field is $\frac{1}{\mathrm{e}}$ of E_0. This means that d_p is a function of both refractive indices n_1 and n_2, the incidence angle θ, and the wavelength of the radiation λ [130]

$$d_\mathrm{p} = \frac{\lambda}{2\pi\sqrt{n_1^2 \sin^2\theta - n_2^2}}. \tag{4.17}$$

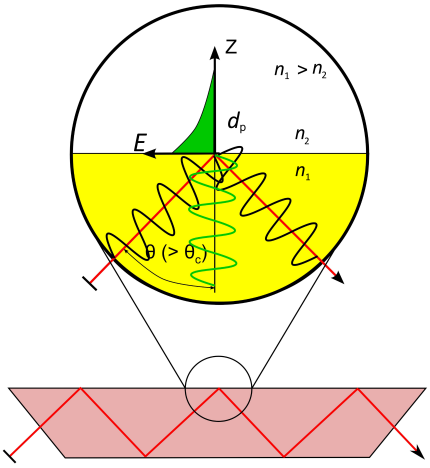


Figure. 4.19 – Total reflection of an infrared beam in an ATR-crystal [131].

A schematic of the principle of total internal reflection is schematically shown in Figure 4.19. If the optically rarer medium (the substrate) - or constituents therein - is absorbing IR radiation, attenuated total reflection (ATR) is resulting at characteristic wavelengths corresponding to the vibrational resonant frequency [132]. One of the main advantages of ATR spectroscopy is the fact that absorption spectra can be obtained at highly absorptive and/or scattering samples, such as turbid liquids or powder samples, given the minimal penetration into an otherwise opaque medium. This technique is mostly used together with FTIR spectroscopy, because of favorable penetration depth of the IR beam in the substrate [130]. Typically the ATR crystals are made of zinc selenide (ZnSe), zinc sulfide (ZnS), Germanium (Ge), and silicon (Si) [133, 134]. In this thesis, a Spectrum 100 Series Universal and a "Golden Gate" ATR accessory with a diamond crystal are used.

4.7.3 Infrared spectroscopy: instrumentation

In this work, all measurements were recorded using a Perkin Elmer Spectrum 1000 FTIR Infrared spectrometer, which is based on the old idea of the radiation interference between two beams to yield an interferogram. The basic components of the so-called FTIR spectrometer are shown schematically in Figure 4.20a.

The most ubiquitous IR source used in FTIR is a resistively heated silicon carbide rod (Globar). An electric current is passed through the bar which becomes very hot, producing at the same time large amounts of IR radiation. Next to the IR source, most FTIR's use a HeNe laser to measure the optical path difference of the interferometer as a reference [136, 137].

The core of the instrument is the interferometer, named after Michelson, who did lots of important optical discoveries. His interferometer shown in Figure 4.20b consists of two perpendicularly plane mirrors, one of which can travel in a direction perpendicular to the plane. A semi-reflecting film, the beamsplitter, bisects the planes of these two mirrors, causing 50% of the incident radiation to be reflected to one mirror and 50% to be transmitted to the other mirror. Both beams are reflected returning to the beamsplitter where they recombine and interfere. This way the moving mirror produces an optical path difference between the two arms of the interferometer. For path differences of $\left(n + \frac{1}{2}\right)\lambda$, the transmitted beam interferes destructively and the reflected beam constructively. The resultant interference pattern is produced by

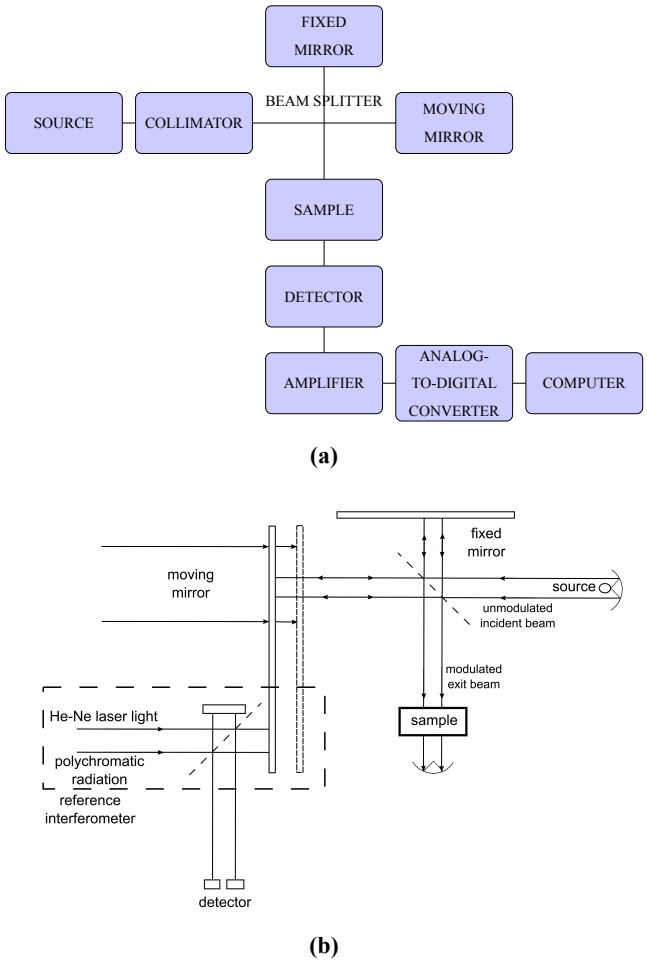


Figure. 4.20 – Schematic of (a) the (ATR-)FTIR spectrometer and (b) the Michelson interferometer [135].

scanning the moving mirror through a distance of $\frac{\delta}{2}$. It was then Michelson himself who realized that the polychromatic interference pattern contained all spectral information.

Unfortunately, there is not a perfect detector for the entire infrared region. In the mid-infrared region, these so called high throughput ($>$ 20% of the beam reaches the detector) experiments are run using a thermal detector, such as deuterated triglycine sulfate (DTGS), because it gives full, specific detectivity in high-flux environments. When equipped with a KBr window, DTGS detectors are sensitive from 400 cm^{-1} to beyond 4000 cm^{-1} and cover the complete mid-infrared region [120, 136]. However, one must take into account three significant disadvantages of DGTS detectors are (1) the speed of the detector, (2) the high noise level and (3) the lower sensitivity [138].

4.7.4 Infrared spectroscopy: analysis

The analysis of IR data starts with the conversion of the interference pattern to an IR spectra using a Fourier transformation. To enhance the signal-to-noise ratio, it is recommended that multiple spectra are averaged. Finally, we can start analyzing the data using reference tables. In what follows, each part is explained.

4.7.4.1 Fourier transformation

The mathematics of the conversion of an interference pattern into a spectrum is beyond the scope of this thesis. However, we will have a look at the process of Fourier transformation. The essential equations relate the intensity falling on the detector, I(δ), to the spectral power density at a particular wavenumber, $\bar{\nu}$, given by $B(\bar{\nu})$ are as follows [135]

$$I(\delta) = \int_0^{+\infty} B(\bar{\nu}) \cos 2\pi\, \bar{\nu}\delta \, \mathrm{d}\bar{\nu}, \tag{4.18a}$$

$$B(\bar{\nu}) = \int_{-\infty}^{+\infty} I(\delta) \cos 2\pi\, \bar{\nu}\delta \, \mathrm{d}\delta. \tag{4.18b}$$

The domains of distance and frequency are interconvertible by the mathematical method of Fourier transformation and are known as a Fourier transform pair. The first equation shows the variation in power density as a function of difference in pathlength, which is an interference pattern. The second shows the variation in intensity as a function of the wavenumber, which is an infrared spectrum. During an experiment, one obtains an interferogram with and without a sample in the beam and transforming the interferograms into spectra of (a) the source with the sample adsorptions and (b) the source without the sample adsorptions. The ratio corresponds to a double beam dispersive spectrum. The major advance towards routine FTIR analysis came with a new mathematical method devised by Cooley and Turkey [139] in 1965 for fast Fourier transformation. This was combined with advances in microcomputers which enabled these calculations to be carried out rapidly on-line rather than off-line.

4.7.4.2 Signal averaging

The main advantage of rapid scanning instruments is the ability to increase the signal-to-noise ratio by signal averaging, which leads to an increase of the signal-to-noise proportional to the square root of time as described in [123]

$$\frac{\mathrm{S}}{\mathrm{N}} \propto n^{0.5} \tag{4.19}$$

A diminishing return for signal averaging is that it takes an increasingly longer time to achieve improvement. The accumulation of a large number of repeat scans makes greater demands on the instrument if it is to exactly reproduce the conditions [123].

4.7.4.3 Absorption band identification

For identification purposes, the mid-IR region is often subdivided into the group frequency region from 4000 cm^{-1} to 1300 cm^{-1} and the fingerprint region from 1300 cm^{-1} to 400 cm^{-1}. The first region contains the main adsorption bands of the vibrational modes of functional groups such as [140]:

- Alcohols and amines (4000 - 3000 cm^{-1})
- Saturated aliphatic stretches (3000 - 2800 cm^{-1})
- Thiol compounds (2300 cm - 1600 cm^{-1})
- Carbonyl compounds (1800 - 1500 cm^{-1})

These bands are important for the characterization of the molecular structure of the compound [132].
The fingerprint region, on the other hand, contains bending and skeletal vibrations of polyatomic systems. The presence of multiple absorptions makes it difficult to analyze individual bands, but the total pattern is very characteristic and reproducible to be matched to reference spectra [132].

References for Chapter 4

[1] D. SCOTT, A note on the metallographic preparation of ancient lead, *Stud. Conserv.* **41** (1) (1996), 60–62.

[2] K. EDNIE, Metallographic preparation of soft materials: Lead alloys, *Mater. Charact.* **36** (4-5) (1996), 243–255.

[3] E. FERMI, Zur Quantelung des idealen einatomigen Gases, *Eur. Phys. J. A.* **36** (11) (1926), 902–912.

[4] P. DIRAC, On the theory of quantum mechanics, *Proc. Roy. Soc. A* **112** (762) (1926), 661–677.

[5] A. SOMMERFELD and H. BETHE, *Handbuch der Physik*, vol. 24, Berlin: Springer, 1933, 333.

[6] S. DUSHMAN, Thermionic emission, *Rev. Mod. Phys.* **2** (1930), 381–476.

[7] L. MURR, *Electron and ion microscopy and microanalysis*, Marcel Dekker, 1982, 180.

[8] O. RICHARDSON, *Thermionic emission from hot bodies*, Wexford College Press, 2003, 196.

[9] M. KNOLL, F. HOUTERMANS, and W. SCHULZE, Untersuchung der Emissionsverteilung an Glühkathoden mit dem magnetischen Elektronenmikroskop, *Z. Phys.* **78** (5-6) (1932), 340–362.

[10] J. LAFFERTY, Boride cathodes, *J. Appl. Phys.* **22** (3) (1951), 299–309.

[11] A. BROERS, Some experimental and estimated characteristics of the lanthanum hexaboride rod cathode electron gun, *J. Phys. E* **2** (3) (1969), 273.

[12] E. MÜLLER, Das Feldionenmikroskop, *Z. Phys.* **131** (1) (1951), 136–142.

[13] A. CREWE, The current state of high resolution scanning electron microscopy, *Q. Rev. Biophys.* **3** (01) (1970), 137–175.

[14] A. CREWE, J. WALL, and J. LANGMORE, Visibility of single atoms, *Science* **168** (3937) (1970), 1338–1340.

[15] C. WU, Y. MAKIUCHI, and C. CHEN, High-energy electron beam lithography for nanoscale fabrication, in: *Lithography*, ed. by M. WANG, InTech, 2010, chap. 13, 241–266.

[16] B. KOUROSH KALANTAR-ZADEH and F. BENJAMIN, *Nanotechnology-enabled sensors*, 1st, Springer, 2008, 250–255.

[17] E. BRÜCHE and O. SCHERZER, *Geometrische Elektronenoptik*, Berlin: Springer, 1934, 348.

[18] J. HUMPHRIES, *Principles of charged particle acceleration*, Dover Publications, 1986, 124.

[19] D. MCMULLAN, An improved scanning electron microscope for opaque specimens, *Proc. Inst. Electr. Engr.* **100** (1953), 245–259.

[20] K. SMITH and C. OATLEY, The scanning electron microscope and its fields of application, *Br. J. Appl. Phys.* **6** (1955), 391–399.

[21] C. OATLEY, W. NIXON, and R. PEASE, Scanning electron microscopy, *Adv. Electron. Electron Phys.* **21** (1965), 181–247.

[22] H. SEILER, Secondary electron emission in the scanning electron microscope, *J. Appl. Phys.* **54** (11) (1983), R1–R18.

[23] R. WARNECKE, Secondary emission of pure metals, *J. Phys. Rad.* **7** (6) (1936), 270–280.

[24] P. PALLUEL, The backscattered component of secondary electron emission of metals, *Comptes Rendus* **224** (1947), 1492–1551.

[25] T. EVERHART and R. THORNLEY, Wide-band detector for micro-microampere low-energy electron currents, *J. Sci. Instrum.* **37** (7) (1960), 246.

[26] Failure analysis, in: *Electronic Materials Handbook*, ed. by K. ZWILSKY, E. LANGER, and M. MINGES, ASM International, 1989, chap. 9, 957–1117.

[27] J. GOLDSTEIN et al., *The SEM and its modes of operation*, ed. by J. GOLDSTEIN et al., 3rd, Springer, 2003, 21–60.

[28] D. PRIOR et al., The application of electron backscatter diffraction and orientation contrast imaging in the SEM to textural problems in rocks, *Am. Mineral.* **84** (1999), 1741–1759.

[29] C. THIEL, *An introduction to semiconductor radiation detectors*, Montana State University, 1999, 1–5.

[30] PHENOM-WORLD, *Application note: Topography imaging with Phenom*, Phenom-World, 2007, 1–2.

[31] C. SCHWANDT, Characterizing nanometer-scale materials using a low-angle backscattered electron detector, *Am. Lab.* **42** (11) (2010), 13–17.

[32] D. WILLIAMS and C. CARTER, *Transmission electron microscopy: A textbook for materials science*, 2nd, Springer, 2009, 103–112.

[33] I. WATT, *The principles and practice of electron microscopy*, 2nd, Cambridge University Press, 1997, 199–201.

[34] R. ERNI, Aberration correction, in: *Aberration-corrected imaging in transmission electron microscopy*, Imperial College Press, 2010, 187–313.

[35] LORD RAYLEIGH, On the theory of optical images, with special reference to the microscope, *Phil. Mag.* **42** (255) (1896), 167–195.

[36] Y. ZHU, *Modern techniques for characterizing magnetic materials*, Springer, 2005, 333.

[37] J. GOLDSTEIN et al., *Introduction*, Plenum Press, 1981, chap. 1, 1–19.

[38] P. LECHNER et al., Silicon drift detectors for high resolution room temperature X-ray spectroscopy, *Nucl. Iunstrum. Meth. A* **377** (2–3) (1996), 346–351.

[39] M. MOSELEY, The high frequency spectra of the elements, *Phil Mag.* **26** (1913), 1024–1034.

[40] D. BELL and A. GARRATT-REED, *Energy dispersive X-ray analysis in the electron microscope*, Microscopy handbooks, Garland Science, 2003, 160.

[41] K. HEINRICH, *Electron beam X-ray microanalysis*, New York: Van Nostrand Reinhold, 1981, 60–70.

[42] E. REID et al., Characterization of African dust transported to Puerto Rico by individual particle and size segregated bulk analysis, *J. Geophys. Res.* **108** (D19) (2003), 2156–2202.

[43] L. GIANNUZZI and F. STEVIE, *Introduction to focused ion beams*, Springer Science, 2005, 272.

[44] A. GUINIER, *X-ray diffraction in crystals, imperfact crystals and amorphous bodies*, Dover Publications, 1994, 41.

[45] C. BARRETT, *Structure of metals*, 1st, New York: McGraw-Hill Book Company, 1943, 592.

[46] D. SANDS, *Crystals and lattices*, Dover Publications, 1969, chap. 1, 1–12.

[47] R. TILLEY, *Understanding solids: The science of materials*, vol. 209, John Wiley & Sons, 2004, 593.

[48] J. DAINTITH, ed., *A dictionary of physics*, Oxford University Press, 2009, 110.

[49] A. BRAVAIS, Mémoire sur les systèmes formés par les points distribués régulièrement sur un plan ou dans l'espace, *J. Ecole Polytech.* **19** (1850), 1–128.

[50] D. ASKELAND and P. FULAY, *The science and engineering of materials*, 5th, Cengage Learning, 2005, 888.

[51] INTERNATIONAL UNION OF CRYSTALLOGRAPHY, *International tables for crystallography*, ed. by S. HALL, T. HAHN, and B. MCMAHON, 5th, Springer, 2005, 1–594.

[52] M. ALLABY, ed., *A dictionary of geology and earth sciences*, 4th, Oxford University Press, 2013, 376.

[53] R. MASEL, *Principles of adsorption and reaction on solid surfaces*, John Wiley & Sons, 1996, 33–37.

[54] C. SURYANARAYANA and M. GRANT NORTON, *X-ray diffraction: A practical approach*, Plenum Press, 1998, 14–15.

[55] W. BRAGG and W. BRAGG, The reflection of X-rays by crystals, *Proc. Roy. Soc. A* **88** (605) (1913), 428–438.

[56] C. HAMMOND, *The basics of crystallography and diffraction*, 3rd, International Union of Crystallography texts on crystallography, Oxford University Press, 2009, 448.

[57] M. DE GRAEF and M. MCHENRY, *What is a crystal structure?*, 2nd, Cambridge University Press, 2012, chap. 3, 55–78.

[58] C. BARRETT and T. MASSALSKI, *Structure of metals, crystallographic methods, principles and data*, 3rd, Pergamon, 1980, 654.

[59] B. HE, *Two-dimensional X-Ray diffraction*, John Wiley & Sons, 2011, 426.

[60] M. KHAN et al., Structural and thermal studies of silver nanoparticles and electrical transport study of their thin films, *Nanoscale Res. Lett.* **6** (2011), 434–442.

[61] M. CERRO-ALARCÓN et al., Surface study of graphite-supported Ru-Co and Ru-Ni bimetallic catalysts, *Appl. Catal. A* **275** (2004), 257–269.

[62] B. FULTZ and J. HOWE, Diffraction and the X-ray powder diffractometer, in: *Transmission electron microscopy and diffractometry of materials*, 2013, chap. 1, 1–57.

[63] E. KAUFMANN, *Characterization of materials*, Characterization of Materials, Wiley, 2003, 1392.

[64] L. PARRATT, Surface studies of solids by total reflection of X-rays, *Phys. Rev.* **95** (2) (1954), 359–369.

[65] M. DE KEERSMAECKER et al., In-situ spectroelectrochemical characterization of the electrochemical growth and breakdown of a lead dodecanoate coating on a lead substrate, *Talanta* **132** (2015), 760–768.

[66] M. CHE and J. VÉDRINE, *Characterization of solid materials and heterogeneous catalysts: From structure to surface reactivity*, Wiley, 2012, 902.

[67] Basics of synchrotron radiation, in: *Synchrotron radiation: Basics, methods and applications*, ed. by S. MOBILIO, C. MENEGHINI, and F. BOSCHERINI, Springer, 2015, 3–28.

[68] P. WILLMOTT, Synchrotron physics, in: *An introduction to synchrotron radiation*, John Wiley & Sons, 2011, chap. 3, 39–85.

[69] Z. HUANG, Brightness and coherence of synchrotron radiation and FELs, in: *Proc. 4th International Particle Accelerator Conference*, 2013, 1–5.

[70] K. KIM, Brightness, coherence and propagation characteristics of synchrotron radiation, *Nucl. Methods Phys. Res. A* **246** (1-3) (1986), 71–76.

[71] A. SCHLACHTER, ed., *New directions in research with third-generation soft X-ray synchrotron radiation sources*, Kluwer Academic Publishers, 1994, 257–258.

[72] R. CLARKE, Incoherent sources: synchrotrons, in: *Encyclopedia of Modern Optics*, Elsevier, 2005, 217–224.

[73] R. CACIUFFO et al., Monochromators for X-ray synchrotron radiation, *Phys. Rep.* **152** (1) (1987), 1–71.

[74] M. BORSBOOM et al., The Dutch-Belgian beamline at the ESRF, *J. Synchrotron Radiat.* **5** (1998), 518–520.

[75] P. WILLMOTT, Beamlines, in: *An introduction to synchrotron radiation*, John Wiley & Sons, 2011, chap. 4, 87–130.

[76] G. SILVERSMIT et al., Polycapillary based μ-XAS and confocal μ-XANES at a bending magnet source of the ESRF, *JPCS* **190** (2009), 1–6.

[77] S. NIKITENKO et al., Implementation of a combined SAXS/WAXS/QEXAFS set-up fot time-resolved in-situ experiments, *J. Synchrotron Radiat.* **15** (2008), 632–640.

[78] T. SHAM, ed., *Chemical applications of synchrotron radiation: X-ray applications*, World Scientific, 2002, 802.

[79] L. ZEVIN and G. KIMMEL, *Quantitative X-ray diffractometry*, Springer, 2012, 53.

[80] J. BÖHM et al., Tensile testing of ultrathin polycrystalline films: A new synchrotron based method, *Rev. Sci. Instrum.* **75** (2004), 1110–1119.

[81] R. DOYLE, *MarCCD v 0.10.17 software manual*, Mar USA, 2006, 1–160.

[82] GUINEBRETIÈRE, Instrumentation used for X-ray diffraction, in: *X-ray diffraction by polycrystalline materials*, ISTE, 2007, 39–126.

[83] A. ADRIAENS and M. DOWSETT, Time resolved spectroelectrochemistry studies for protection of heritage metals, *Surf. Eng.* **24** (2) (2008), 84–89.

[84] A. ADRIAENS et al., Insights into electrolytic stabilization with weak polarization as treatment for archaeological copper objects, *Anal. Bioanal. Chem.* **387** (2007), 861–868.

[85] M. DOWSETT et al., In-situ spectroelectrochemical study of the growth process of a lead decanoate coating as corrosion inhibitor for lead surfaces, *Surf. Interface Anal.* **41** (7) (2009), 565–572.

[86] K. SIEGBAHN et al., Atomic, molecular and solid-state structure studied by means of electron spectroscopy, *Nova Acta Regiae Soc. Sci. Ups.* **282** (1967).

[87] S. HOFMANN, *Auger- and X-ray photoelectron spectroscopy in materials science: A user-oriented guide*, Springer Series in Surface Sciences, Springer, 2012, 528.

[88] D. WOODRUFF and T. DELCHAR, *Modern techniques of surface science*, 2nd, Cambridge University Press, 1994, 139–145.

[89] J. WATTS and J. WOLSTENHOLME, Electron spectroscopy: Some basic concepts, in: *An introduction to surface analysis by XPS and AES*, John Wiley & Sons, 2003, chap. 1, 1–15.

[90] S. AMELINCKX et al., eds., *Handbook of microscopy: Methods II: Applications in materials science, solid-state physics and chemistry*, vol. 2, Wiley, 2008, 621–640.

[91] C. POWELL and A. JABLONSKI, Electron effective attenuation lengths for applications in Auger electron spectroscopy and X-ray photoelectron spectroscopy, *Surf. Interface Anal.* **33** (3) (2002), 211–229.

[92] D. BRIGGS, *Handbook of X-ray and ultraviolet photoelectron spectroscopy*, ed. by D. BRIGGS, Heyden, 1977, 398.

[93] D. BRIGGS, *Surface analysis of polymers by XPS and static SIMS*, Cambridge Solid State Science Series, Cambridge University Press, 1998, 198.

[94] K. PEIPONEN, R. MYLLYLÄ, and A. PRIEZZHEV, *Optical measurement techniques: Innovations for industry and the life sciences*, Springer Series in Optical Sciences, New York: Springer Science, 2009, 158.

[95] B. CRIST, *Handbook of monochromatic XPS spectra, semiconductors*, Wiley, 2000, 1–568.

[96] B. CRIST, *Handbook of monochromatic XPS spectra, polymers and polymers damaged by X-rays*, Wiley, 2000, 1–454.

[97] B. CRIST, *Handbook of monochromatic XPS spectra, the elements of native oxides*, Wiley, 2000, 1–548.

[98] J. MOULDER and J. CHASTAIN, *Handbook of X-ray photoelectron spectroscopy: A reference book of standard spectra for identification and interpretation of XPS data*, Physical Electronics Division, Perkin-Elmer Corporation, 1992, 1–262.

[99] K. CHILDS and C. HEDBERG, *Handbook of Auger electron spectroscopy: A book of reference data for identification and interpretation in Auger electron spectroscopy*, Physical Electronics, 1995, 1–135.

[100] K. KIM and N. WINOGRAD, Charge transfer shake-up satellites in X-ray photoelectron spectra of cations and anions of SrTiO3, TiO2 and Sc2O3, *Chem. Phys. Lett.* **31** (2) (1975), 312–317.

[101] H. CHERMETTE, P. PERTOSA, and F. MICHEL-CALENDINI, Molecular orbital study of satellites in XPS spectra of BaTiO3 and TiO2, *Chem. Phys. Lett.* **69** (2) (1980), 240–245.

[102] C. JØRGENSEN and H. BERTHOU, Split photo-electron signals from the unique closed-shell cation lanthanum(III), *Chem. Phys. Lett.* **13** (3) (1972), 186–189.

[103] W. HOWNG and R. THORN, The multicomponent structure of the 4d orbital in X-ray photoelectron spectra of the lanthanum(III) ion, *Chem. Phys. Lett.* **56** (3) (1978), 463–465.

[104] Z. ZENG et al., First-principles calculation of core-level binding energy shift in surface chemical processes, English, *Science China Chemistry* **53** (2) (2010), 402–410.

[105] C. WAGNER et al., *Handbook of X-ray photoelectron spectroscopy*, ed. by E. MUILENBERG, Eden Prairie: Perkin Elmer Corporation, 1979, 1–190.

[106] C. FADLEY, *Electron emission spectroscopy*, ed. by W. DEKEYSER et al., Boston: Reidel Publishing Company, 1973, 151.

[107] W. HENDERSON, *Main group chemistry*, Royal Society of Chemistry, 2000, 79–80.

[108] W. PRICE, *Electron spectroscopy: Theory, techniques and applications*, ed. by C. BRUNDLE and A. BAKER, New York: Academic Press, 1977, 384.

[109] J. CAZAUX, About the charge compensation of insulating samples in XPS, *J. Electron Spectrosc. Relat. Phenom.* **113** (1) (2000), 15–33.

[110] P. BAGUS, E. ILTON, and C. NELIN, The interpretation of XPS spectra: Insights into materials properties, *Surf. Sci. Rep.* **68** (2) (2013), 273–304.

[111] D. SHIRLEY, High-resolution X-ray photoemission spectrum of the valence bands of gold, *Phys. Rev. B* **5** (12) (1972), 4709–4714.

[112] Q. BHATIA, M. BURRELL, and J. CHERA, XPS surface studies of injection-molded poly(phenylene ether)/nylon 6,6 and poly(phenylene ether)/HIPS blends, *J. Appl. Polym. Sci.* **46** (11) (1992), 1915–1925.

[113] K. JANSSENS and R. VAN GRIEKEN, *Non-destructive micro analysis of cultural heritage materials*, Elsevier Science, 2004, 828.

[114] T. BARR, *Modern ESCA: The principles and practice of X-ray photoelectron spectroscopy*, Boca Raton FL USA: CRC Press, 1994, 73.

[115] M. SEAH, I. GILMORE, and S. SPENCER, Quantitative XPS: I. Analysis of X-ray photoelectron intensities from elemental data in a digital photoelectron database, *J. Electron Spectrosc. Relat. Phenom.* **120** (1–3) (2001), 93–111.

[116] V. NEFEDOV et al., Relative intensities in X-ray photoelectron spectra. I, *J. Electron Spectrosc. Relat. Phenom.* **2** (4) (1973), 383–403.

[117] V. NEFEDOV et al., Relative intensities in X-ray photoelectron spectra. II, *J. Electron Spectrosc. Relat. Phenom.* **7** (2) (1975), 175–185.

[118] J. CASTLE and R. WEST, Sensitivity factors, cross-section and resolution data for use with the Si Kα X-ray source, *J. Electron Spectrosc. Relat. Phenom.* **19** (3) (1980), 409–428.

[119] J. SCOFIELD, Hartree-Slater subshell photoionization cross-sections at 1254 and 1487 eV, *J. Electron Spectrosc. Relat. Phenom.* **8** (2) (1976), 129–137.

[120] P. GRIFFITHS and J. DE HASETH, *Fourier transform infrared spectroscopy*, John Wiley & Sons, 2007, 360.

[121] M. AVRAM and G. MATEESCU, *Infrared spectroscopy: Applications in organic chemistry*, New York: Wiley, 1972, 479.

[122] T. THEOPHANIDES, *Fourier transform infrared spectroscopy: Industrial chemical and biochemical applications*, Springer, 1984, 19–20.

[123] B. STUART, *Infrared spectroscopy: Fundamentals and applications*, John Wiley & Sons, 2004, 12.

[124] J. ZHANG, *Theory and application of quantum molecular dynamics*, World Scientific, 1999, 27–29.

[125] D. FERTIS, *Mechanical and structural vibrations*, Wiley, 1995, 12–29.

[126] A. ALVAREZ-ORDÓNEZ and M. PRIETO, *Fourier transform infrared spectroscopy in food microbiology*, Springer, 2012, 3–4.

[127] B. SMITH, *Infrared spectral interpretation: A systematic approach*, Taylor & Francis, 1998, 10.

[128] J. FAHRENFORT, Attenuated total reflection: A new principle for the production of useful infra-red reflection spectra of organic compounds, *Spectrochim. Acta* **17** (7) (1961), 698–709.

[129] N. HARRICK, *Internal reflection spectroscopy*, Interscience, 1967, 36.

[130] V. TOLSTOY, I. CHERNYSHOVA, and V. SKRYSHEVSKY, *Handbook of infrared spectroscopy of ultrathin films*, Wiley, 2003, 27–56.

[131] T. CROMPTON, *Polymer reference book*, Rapra Technology Limited, 2006, 171–172.

[132] M. DERRICK, D. STULIK, and J. LANDRY, *Infrared spectroscopy in conservation science*, ed. by T. BALL and S. TIDWELL, Getty Publications, 1999, 13–61.

[133] C. MENDIVE et al., ATR-FTIR measurements and quantum chemical calculations concerning the adsorption and photoreaction of oxalic acid on TiO_2, *Phys. Chem. Chem. Phys.* **8** (27) (2006), 3232–3247.

[134] M. LARSSON, A. HOLMGREN, and W. FORSLING, Xanthate adsorbed on ZnS studied by polarized FTIR-ATR spectroscopy, *Langmuir* **16** (21) (2000), 8129–8133.

[135] B. STUART and D. ANDO, eds., *Biological applications of infrared spectroscopy*, John Wiley & Sons, 1997, 191.

[136] B. SMITH, *Fundamentals of Fourier transform infrared spectroscopy*, 2nd, CRC Press, 2011, 207.

[137] J. SMITH and V. HINSON-SMITH, Product review: The endearing FTIR spectrophotometer, *Anal. Chem.* **75** (1) (2003), 37A–39A.

[138] K. KEMPFERT et al., *Application note: Detectors for Fourier transform spectroscopy*, tech. rep., Thermo Nicolet Corporation, 2001, 1–4.

[139] J. COOLEY and J. TUKEY, An algorithm for the machine calculation of complex Fourier series, *Math. Comp.* **19** (1965), 297–301.

[140] J. COATES, Interpretation of infrared spectra: A practical approach, in: *Encyclopedia of Analytical Chemistry*, ed. by R. MEYERS, John Wiley & Sons, 2000, 10815–10837.

5

Polymer characterization techniques

5.1 Nuclear magnetic resonance spectroscopy

Many nuclei in molecules possess a spin angular momentum, including ^{1}H, ^{13}C, ^{15}F and ^{31}P. They have a clear energy state difference between $m_{\mathrm{I}} = +\frac{1}{2}(\uparrow)$, which is denoted α or spin up and $m_{\mathrm{I}} = -\frac{1}{2}(\downarrow)$, which is denoted β or spin down, when a magnetic field is applied. It is worth mentioning that common nuclei like ^{12}C and ^{16}O have zero spin, and so are invisible in magnetic resonance [1].

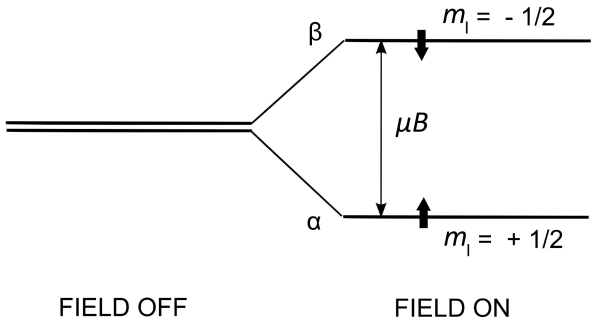


Figure. 5.1 – The nuclear spin energy levels of a spin-$\frac{1}{2}$ nucleus in a magnetic field. Resonance occurs when the energy separation of the levels matches the energy of the photons in the electromagnetic field [2]. μ is the magnetic moment.

Based on Figure 5.1, the energy separation of two states of spin-$\frac{1}{2}$ nuclei is [2]

$$\Delta E = E_{\beta} - E_{\alpha} = \frac{1}{2}\gamma\bar{h}B - (-\frac{1}{2}\gamma\bar{h}B) = \gamma\bar{h}B \tag{5.1}$$

with γ the gyromagnetic ratio. When at the same time, a radiation of frequency ν is used, the resonance condition $h\nu = \gamma\bar{h}B$ is satisfied.

Next to the applied magnetic field, a local magnetic field dB is induced by the electronic orbital angular momentum at the nuclei, which is proportional to the applied field [2],

$$\mathrm{d}B = -\sigma B, \tag{5.2}$$

where the dimensionless quantity σ is called the shielding constant, which depends on the details of the electronic structure near the magnetic nucleus of interest. The total energy difference is then calculated using [2],

$$\Delta E = \gamma \bar{h}(1-\sigma)B. \tag{5.3}$$

Instead of reporting the frequencies in terms of the shielding constant, it is more convenient to express them in terms of the chemical shift. The chemical shift of a nucleus is the difference between the resonance frequency of the nucleus in question and that of a reference standard. The standard for protons is the proton resonance in tetramethylsilane ($Si(CH_3)_4$, commonly referred to as TMS). Chemical shifts are reported on the δ scale, which is defined as [2]

$$\delta = \frac{\nu - \nu_0}{\nu_0} \times 10^6. \tag{5.4}$$

In this expression, ν_0 is the resonance frequency of the standard. The advantage of this scale is the independence of the applied field.

Depending on the surrounding atoms of the nucleus, the resonance splits into individual lines, called the *fine structure*. Indeed, each magnetic nucleus can contribute to the local field experienced by the other nuclei. The strength of this interaction is expressed in terms of the scalar coupling constant J in Hz. Suppose the spin of an X nucleus is α; then the spin of A will have a Larmor frequency of a combined effect of the external field, the shielding constant and the spin-spin interaction of the nucleus A with X. The spin-spin coupling will result in one line in the spectrum of A being shifted by -$\frac{1}{2}J$ from the frequency it would have had in the absence of the coupling. If the spin of X is β, then the spin of A will have a Larmor frequency shifted by $\frac{1}{2}J$. So, instead of a single line from A, we get a doublet of lines separated by J and centered on the chemical shift characteristic for X as shown in Figure 5.2a [1].

As explained in Figure5.2b, the A resonance in an AX_n species is split into a doublet of separation J by one X, and each line of that doublet is split again by the same amount by the second X. This results in three lines in the intensity ratio 1:2:1 (because the central frequency can be obtained in two ways). In general, N equivalent spin-$\frac{1}{2}$ nuclei split the resonance of a nearby spin into n + 1 lines with an intensity distribution given by Pascal's triangle in Figure 5.2c [3].

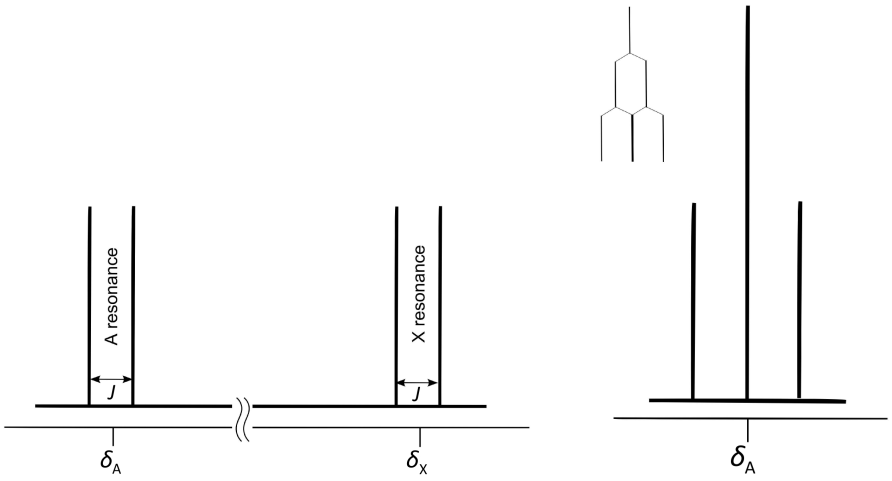
The ^{1}H NMR spectra were recorded in $CDCl_3$ at room temperature, with a Avance 300 spectrometer (Bruker, USA). This spectrometer is a wide bore (89 mm), high resolution, solid NMR spectrometer operating at a magnetic field strength of 7 T (^{1}H frequency is 300 MHz).

5.2 Differential scanning calorimetry

To determine melting points, purity, and glass transition temperatures (T_g) of polymer compounds, differential scanning calorimetry (DSC) is used. Qualitative and quantitative information is gained from the enthalpy changes depending on the physical and chemical changes of the sample, which are measured as a function of time and temperature [4–6].

The DSC instrument is a closed system where the internal energy cannot be created or destroyed, and is based on the first law of thermodynamics. As the change in volume can be neglected, the total heat flow measured in the instrument is equal to a change in enthalpy, which is further related to the heat capacity of the sample. This indicates that the change in enthalpy is a consequence of the physical and chemical sample changes, which are grouped into exothermic and endothermic transitions [7].

In this work, we used a DSC1/700 instrument (Mettler-Toledo Inc., Switzerland), which is based on the heat flux technique or heat-exchanging calorimetry. The heat flow from the furnace to the samples passes symmetrically through a metal disk of medium thermal conductivity. To keep the measurement uncertainties as small as possible, the arrangement of the sample, the reference sample and the temperature sensor in relation to one another and to the support must always be



(a) (b)

n	intensity distribution
0	1
1	1 1
2	1 2 1
3	1 3 3 1
4	1 4 6 4 1

(c)

Figure. 5.2 – (a) The effect of spin-spin coupling on an AX spectrum. (b) The origin of the 1:2:1 triplet in the A resonance of an AX_2 species. (c) Pascal's triangle [2].

the same [8].

5.3 Thermogravimetric analysis

Thermogravimetric analysis (TGA) is a technique in which the mass of a substance is monitored as a function of temperature as the sample specimen is subjected to a controlled temperature program in a controlled atmosphere. The weight change of a material is plotted as a function of increasing temperature in an atmosphere of nitrogen, helium, air, other gas, or in vacuum. Using nitrogen or another relatively inert atmosphere as opposed to air will delay the onset of decomposition and may change the shape of the entire thermogram. The measurements are used to make determinations about composition, purity and thermal stability of different compounds such as inorganic materials, metals, polymers and plastics, ceramics, glasses, and composite materials [9–11]. The technique allows the determination of the temperature, water content and weight change of decomposition reactions [12].

In this thesis, the analysis is done using a TGA/SDTA851e (Mettler Toledo Inc., Switzerland) instrument with an easily programmable furnace and a precision balance with a readability down to 1 μg. The sample is loaded into an aluminum oxide crucible, which is placed in a sealed chamber to allow full control [13]. In this case, a heating rate of 10 °C min^{-1} from 25 °C - 800 °C is used under a nitrogen atmosphere.

References for Chapter 5

[1] H. GUNTHER, The proton magnetic resonance spectra of organic molecules - Chemical shift and spin-spin coupling, in: *NMR spectroscopy: Basic principles, concepts and applications in chemistry*, ed. by WILEY, 3rd, 2013, chap. 2, 29–67.

[2] P. ATKINS, Nuclear magnetic resonance, in: *Physical chemistry*, 5th, Oxford University Press, 1994, 623–633.

[3] J. KEELER, Setting the scene, in: *Understanding NMR spectroscopy*, 2nd, Wiley, 2010, 5–23.

[4] S. PRATI, G. CHIAVARI, and D. CAM, DSC application in the conservation field, *J. Therm. Anal. Calorim.* **66** (1) (2001), 315–327.

[5] W. BRENNAN, Some applications of differential scanning calorimetry for the analysis of polymers, *Thermochim. Acta* **17** (3) (1976), 285–293.

[6] J. WEN et al., Applications of differential scanning calorimetry for thermal stability analysis of proteins: Qualification of DSC, *J. Pharm. Sci.* **101** (3) (2012), 955–964.

[7] P. COLLINGS and M. HIRD, Differential scanning calorimetry, in: *Introdcuction to liquid crystals: Chemistry and physics*, Taylor & Francis, 2009, chap. 9.4, 196–198.

[8] R. DANLEY, New heat flux DSC measurement technique, *Thermochim. Acta* **395** (1-2) (2002), 201–208.

[9] P. SEPE and RAPRA TECHNOLOGY LIMITED, *Thermal analysis of polymers*, Rapra Technology Limited, 1997.

[10] T. OZAWA, Thermal analysis — review and prospect, *Thermochim. Acta* **355** (1-2) (2000), 35–42.

[11] M. RAMIAH, Thermogravimetric and differential thermal analysis of cellulose, hemicellulose, and lignin, *J. Appl. Polym. Sci.* **14** (5) (1970), 1323–1337.

[12] R. PRIME et al., *Thermogravimetric analysis*, ed. by J. MENCZEL and P. BRUCE, Wiley, 2009, chap. 3, 241–317.

[13] R. RIESEN, K. VOGEL, and M. SCHUBNELL, DSC by the TGA/SDTA851 considering mass changes, *J. Therm. Anal. Calorim.* **64** (2001), 243–252.

PART II

LEAD CARBOXYLATE COATINGS

6

Kinetic description of corrosion reactions

To understand the kinetics of corrosion processes, first the concept of polarization is explained. As explained in the introduction, corrosion is a multi-electron process, however, to explain the different relevant parameters, we start with the explanation of a single electron process.

6.1 Polarization

When cell electrodes are connected by a low impedance path, current starts flowing through the circuit, indicating that net oxidation and reduction reactions are taking place. As a consequence, the electrode potentials start to deviate from their equilibrium values, which is called polarization. In what follows, two principal forms of polarization are described: activation and concentration polarization [1].

6.1.1 Activation polarization

Activation polarization arises out of a slow step in the electrode reaction for which an activation energy in the form of an increment in potential is required for the reaction to proceed [1]. To clarify, the free energy profile of single electron-transfer is shown schematically in Figure 6.1, where the electrode is assumed to be anodically polarized with an overpotential $\eta = E - E_0$, where E_0 is the equilibrium potential.

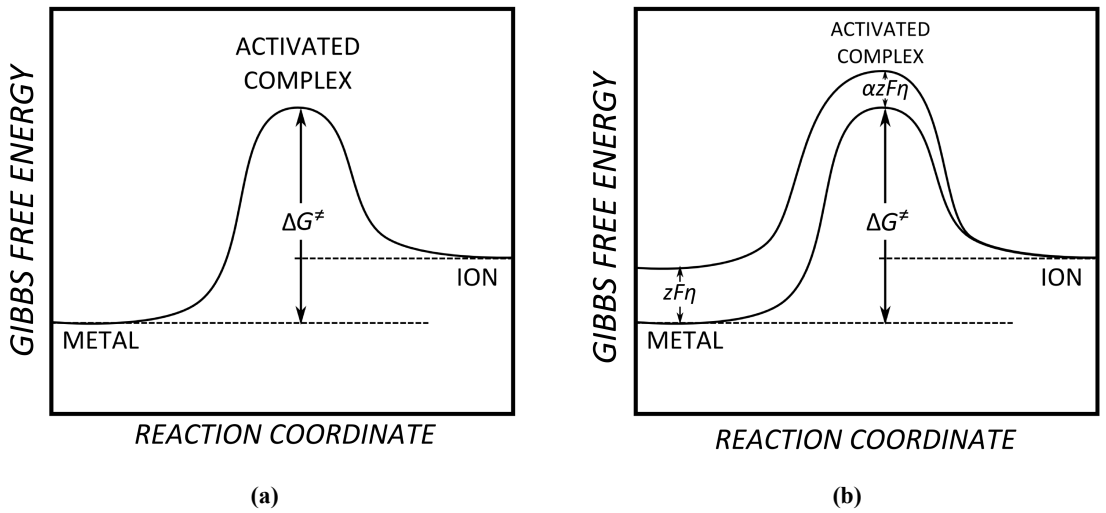


Figure. 6.1 – Schematic energy profile for activation polarization (a) at equilibrium and (b) at an anodic overpotential η [2, 3].

Since Eq. 2.1 states that $\Delta G = -nFE$, the polarization process has increased the metal's energy by $nF\eta$ and that of

the activated complex by $\alpha nF\eta$, relative to that of the produced ions. The symmetry factor α defines the position of the maximum in the profile relative to the minima shown in Figure 6.1 [3].

At equilibrium, the dissolution and deposition activation energy are both equal to ΔG^*, but for the polarized electrode the equilibrium changes. The dissolution activation energy decreases to $[\Delta G^* - (1-\alpha)nF\eta]$ and the deposition activation energy increases to $[\Delta G^* + \alpha nF\eta]$ based on the geometry of the profile in Figure 6.1. Using the transition state theory and the Arrhenius equation, the anodic current i_a can be defined as [3]

$$i_\text{a} = k \cdot \exp \frac{-[\Delta G^* - (1-\alpha)nF\eta]}{RT}, \tag{6.1a}$$

$$= k \cdot \exp \frac{-\Delta G^*}{RT} \cdot \exp \frac{(1-\alpha)nF\eta}{RT}, \tag{6.1b}$$

$$= i_0 \exp \frac{(1-\alpha)nF\eta}{RT}, \tag{6.1c}$$

and using a similar reasoning, the cathodic current i_c is

$$i_\text{a} = i_0 \exp \frac{-\alpha nF\eta}{RT}. \tag{6.2}$$

The difference between both currents is called the net current and is given by [4]

$$i_\text{net} = i_0 \left[\exp \frac{(1-\alpha)nF\eta}{RT} - \exp \frac{-\alpha nF\eta}{RT} \right]. \tag{6.3}$$

This is called the *Butler-Volmer* equation expressing the relationship between the current and the overpotential. A much more user-friendly version for Eq. 6.3 can be made using an approximation. At high positive overpotentials, the value of the cathodic current is insignificant, so that the equation can be reduced to [4]

$$i_\text{net} = i_0 \left[\exp \frac{(1-\alpha)nF\eta}{RT} \right], \tag{6.4a}$$

$$\eta = \frac{RT}{(1-\alpha)nF} \ln \frac{i_\text{net}}{i_0}. \tag{6.4b}$$

where η is the overpotential and $\frac{RT}{(1-\alpha)nF}$ is the anodic Tafel constant (expressed in V). Sometimes, $(1-\alpha)$ is replaced by β. In a similar way, the cathodic Tafel constant can be calculated at high negative overpotentials. Corrosion reactions (= anodic dissolution) are usually controlled by activation polarization where the ion dissolution is the probable rate-controlling step [1].

6.1.2 Concentration polarization

Concentration polarization is a result of diffusion-limiting effects close to the electrode surface. Clearly, the reaction rate is no longer dependent on the potential, but rather on the mass transport of the reagents and products. The magnitude of this current, known as the limiting current density i_L (in A cm^{-2}) is described by [5]

$$i_\text{L} = \frac{DnFc}{\delta}, \tag{6.5}$$

where D is the reagent diffusion coefficient, n is the number of electrons transferred, F is the Faraday constant, c is the reagent bulk concentration in the solution and δ is the thickness of the diffusion layer. As evident from equation 6.5, the i_L value increases when increasing the velocity (smaller δ), the temperature (higher D), and the concentrations. In the case of a hydrogen evolution reaction, for example, concentration polarization becomes significantly important in solutions

with low proton concentrations [1].

6.2 The symmetry factor

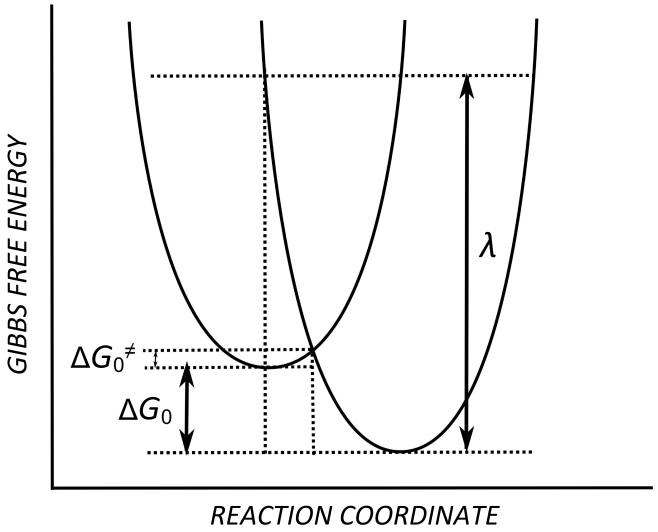


Figure. 6.2 – Representation of the electron transfer, without movement of the nuclei, according to the Born-Oppenheimer approximation. λ is the solvent reorganization energy.

The meaning of the symmetry factor has been interpreted on the basis of different models, without reaching a general consensus. Butler [6, 7] considered α to represent the fraction of the potential-distance profile across the electrical double layer (with exclusion of the diffusion layer) that enhances the electron transfer rate by bringing the reactant on top of the potential-energy barrier, where the transition state complex is located. If the potential barrier is symmetric and symmetrically located within the double layer, then α equals 0.5. Hush [8] considered α to be the fractional charge on the reacting ion in the transition state distinguishing three types of reactions: (i) outer-sphere electron transfer, (ii) metal dissolution and deposition and (iii) charge transfer to and from species adsorbed on the surface.

6.2.1 Outer sphere electron transfer

A single-electron transfer reaction always occurs at the solution side of the electrode's interface called the outer-Helmholtz plane (OHP). A rearrangement of the water molecules, due to the influence of the charge of the ion, changes the 'outer sphere' configuration. The 'inner sphere' around the central atom stays intact. The development of this theory is based on the Born-Oppenheimer approximation, which indicates that the electronic and nuclear motions are separable in time, as shown in Figure 6.2. Following this model, the standard Gibbs energy of activation ΔG^0 for an outer-sphere charge-transfer process is defined by the solvent reorganization energy, which plays an important role in determining the rate of outer-sphere electrons processes. This means that also the symmetry factor becomes a function of the solvent reorganization energy λ and the standard electrochemical Gibbs free energy ΔG_0 given by

$$\alpha = \frac{1}{2} + \frac{\Delta G_0}{2\lambda} - \frac{F|\eta|}{4\lambda}, \tag{6.6}$$

which leads to $\alpha \approx 0.5$ for high solvent reorganization energies. Moreover, according to Eq. 6.6, this model predicts a potential-dependent symmetry factor, which leads to a deviation from linearity of the Tafel slope.

6.2.2 Metal dissolution and deposition

Metal deposition is evidently a very different process than outer-sphere electron transfer, because both charge and mass cross the interface. This immediately raises the question regarding the identity of the particle that carries the charge across the interface: is it the electron, as in outer-sphere electron transfer, or is it the metal ion? Moreover, several bonds need to be broken in the process of depositing a hydrated metal ion, in contrast with the outer-sphere charge transfer, where no bonds are broken.

It has been stated by several leading electrochemists [9–11] that in metal deposition the charge is carried across the interface by the metal cation, although no proof is presented. It would seem obvious that the mechanism of charge transfer for metal deposition must be entirely different from that developed for outer-sphere electron transfer, because transfer of electrons and heavy ions represents an entirely different physical phenomena. A possible mechanism is presented in [12].

6.2.3 Charge transfer to or from a species adsorbed to the surface

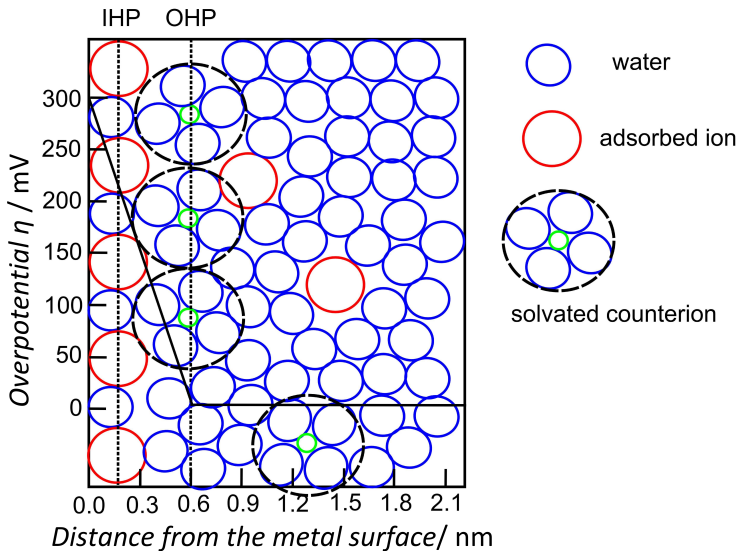


Figure. 6.3 – Schematic representation of the positions of the ion and counterion in the double layer [12].

A yet different situation presents itself when charge transfer occurs between the electrode and a species already adsorbed to the surface [12]. This is shown schematically for the oxidation of an adsorbed ion in Figure 6.3. When an overpotential η is applied across the interface, only a fraction is applied between the metal surface and the inner Helmholtz plane. This fraction is given by the ratio between the thicknesses of the inner and outer Helmholtz planes as $\frac{\delta_{\text{IHP}}}{\delta_{\text{OHP}}}$. The activated state lies somewhere between the initial and final states, the range of values of the symmetry factor is given by [12]

$$0 \leq \alpha \leq \frac{\delta_{\text{IHP}}}{\delta_{\text{OHP}}}, \tag{6.7}$$

The charge is carried from the adsorbed species to the electrode by electrons, not by ions. The movement of an electron from the adsorbed ion at the IHP to the metal occurs very quickly, with no activation energy. This means there is no symmetry factor as such, and the Tafel slope is determined by the transfer coefficient given by the ratio of thicknesses of the inner and outer Helmholtz planes. A complete theory around this topic has not been treated in the literature. This theory also applies to metal deposition, when the metal ion being deposited is adsorbed on the surface. Actually, this theory applies to all electrode processes in which both mass and charge are transferred across the interface, such as corrosion. In conclusion, assuming that the symmetry factor is 0.5 has some important implications when considering

the reaction mechanism.

6.3 The transfer coefficient

So far we assumed that the electrode process is simply the addition of one electron to a single molecule of O to produce a single molecule of R. Now we consider a process with the stoichiometric half-cell reaction,

$$\nu_{\mathrm{O}}\mathrm{O} + \mathrm{ne}^{-} \leftrightharpoons \nu_{\mathrm{R}}\mathrm{R}. \tag{6.8}$$

Using the Butler-Volmer equation for a single elementary step in Eq. 6.3, we expect the following relationship between the cathodic current density i_{c} and the applied potential,

$$i_{\mathrm{c}} \propto \exp\left(\frac{\alpha_{\mathrm{c}} nFE}{RT}\right). \tag{6.9}$$

This expression holds in the absence of depletion and diffuse-layer effects that may alter the reactant concentration at the electrode surface with respect to its bulk value. The dimensionless cathodic transfer coefficient α_{c} is immediately obtained from the slope of the plot of ln $|i_{\mathrm{c}}|$ against E [13],

$$\alpha_{\mathrm{c}} = -\left(\frac{RT}{nF}\right)\left(\frac{\partial \ln |i_{\mathrm{c}}|}{\partial E}\right), \tag{6.10}$$

with the derivative $\frac{\partial \ln |i_{\mathrm{c}}|}{\partial E}$ is referred to as the cathodic Tafel slope. The same calculation is done for the anodic Tafel slope with the anodic transfer coefficient α_{a}.

The concerted addition of two or more electrons in a single step is highly unlikely in view of Marcus' rate theory of electron transfer [14–16] based on the outer sphere electron transfer reaction model. We expect that any multi-electron electrode process necessarily involves two or more elementary steps, called multistep mechanisms. The aim is to identify the rate-determining step, which involves (1) evaluation of the reaction orders of the various participating reactants, taking into account chemisorption effects when the process is heterogeneous; (2) characterization of the reaction intermediates, their adsorption behavior and double-layer effects; (3) measurement of steady-state potential versus logarithmic current relations, and (4) the determination, where possible, of the reaction's stoichiometric number [17]. In the frequent case in which the multistep electrode reaction consists of a sequence of elementary one-electron transfer steps and chemical steps, the transfer coefficient can be estimated by the quasi-equilibrium method, which assumes that all steps are in equilibrium, with only the exception of the *rate-determining step* (rds). In general, this assumption holds when the rate constant of the rds is at least 100 times smaller than those of all steps that precede the rds [13].

Alternatively, the steady-state method can be adopted, where the effective concentrations of all intermediates are assumed to reach a steady-state; this implies that the rates of their concentrations changes can be neglected. Usually, this approach makes assumptions about relative magnitudes of some rate constants. An exhaustive treatment of the transfer coefficient for multistep electrode reactions, including adsorption of intermediates and combination or dissociation rate-determining steps, can be found in Lefebvre's monograph [17]. In his book on electrode processes [18], Conway treated some examples of consecutive elementary one-electron transfer steps by both the steady-state and the quasi-equilibrium method. The effect of reactant adsorption on Tafel slopes was also considered. In his comprehensive book on electrochemical kinetics [10], Vetter adopted a similar approach, which he applied on metal/metal ion electrode reactions. A practically identical approach was adopted by Brenet and Traore in their monograph on transfer coefficients in electrode kinetics [19]. Furthermore, Erdey-Gruz's textbook [20] reported the following expression of the 'overall transfer coefficient' for

a sequence of consecutive elementary electron transfer steps and chemical steps characterized by a single rds, as derived by Bockris and Reddy [21], based on the steady-state and equilibrium method,

$$\alpha_c = \frac{n_f}{\nu} + n_r\alpha, \tag{6.11a}$$

$$\alpha_a = \frac{n_b}{\nu} + n_r(1-\alpha), \tag{6.11b}$$

where n_f is the number of electrons released by the electrode before the rds, ν is the number of occurrences of the rds in the electrode reaction, n_r is the number of electrons involved in the rds, n_b is the number of electrons taken up by the electrode before the rds, and α is the symmetry factor with $0 \leq \alpha \leq 1$ [12]. Since the sum $n_f + n_r + n_b$ is equal to the number of electrons in the overall reaction, summing α_c and α_a, yields

$$\alpha_c + \alpha_a = \frac{n}{\nu}. \tag{6.12}$$

It must be stressed that Eq. 6.12 only holds if the forward and backward electrode reactions are characterized by the same rds, a situation that is not necessarily encountered [22].

6.4 Mixed potential theory

The Butler-Volmer equations for a system with one corroding metal, an electron donor, and one electron acceptor (EA) are given by [23, 24]

$$i_M = i_{0,M}\left[e^{\alpha_{a,M}} - e^{-\alpha_{c,M} f \eta_M}\right], \tag{6.13a}$$

$$i_{EA} = i_{0,EA}\left[e^{\alpha_{a,EA}} - e^{-\alpha_{c,EA} f \eta_{EA}}\right], \tag{6.13b}$$

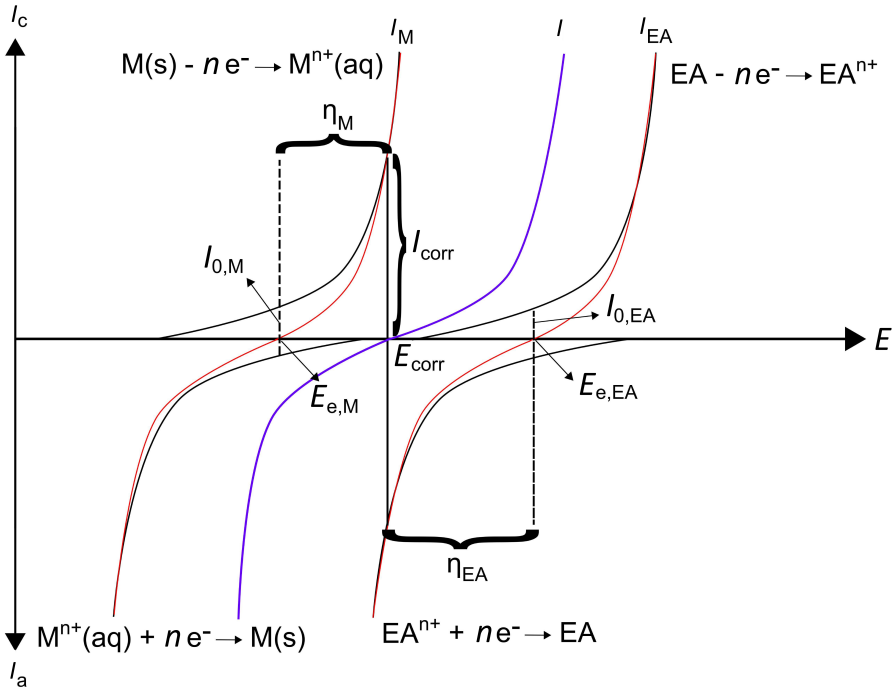


Figure. 6.4 – Current-potential curve of the corrosion behavior starting from the partial Butler-Volmer curves of M and EA. The corrosion potential E_{corr} is presented [25].

where $i_{\mathrm{M/EA}}$ is the current density, $i_{0,\mathrm{M/EA}}$ is the exchange current density, $\alpha_{\mathrm{a,M/EA}}$ is the anodic transfer coefficient, $f = \frac{F}{RT}$, $\alpha_{\mathrm{c,M/EA}}$ is the cathodic transfer coefficient and $\eta_{\mathrm{M/EA}}$ = overpotential of the metal and electronacceptor. Both equations are shown in Figure 6.4. At the intersection point, the potential of the corroding metal is represented by the corrosion potential or E_{corr}. This corrosion potential is not the equilibrium potential of either of the constituent partial reactions, but rather some intermediate potential determined by simultaneous occurrence of these partial oxidation and reduction reactions at the same rate. Furthermore, at the intersection point, the rate of the anodic reaction is equal to the rate of the cathodic reaction, which corresponds to the corrosion current density i_{corr} measured at the corrosion potential written as [25]

$$i_{\mathrm{corr}} = i_{\mathrm{M}} = -i_{\mathrm{EA}}, \tag{6.14a}$$

$$i_{\mathrm{corr}} = i_{0,\mathrm{M}} \exp\left[\alpha_{\mathrm{a,M}} f(E_{\mathrm{corr}} - E_{\mathrm{e,M}})\right] = -i_{0,\mathrm{EA}} \exp\left[-\alpha_{\mathrm{c,EA}} f(E_{\mathrm{corr}} - E_{\mathrm{e,EA}})\right]. \tag{6.14b}$$

This theory, propounded by Wagner and Traud in 1938 [26], is known as the *mixed-potential theory* of corrosion. From this point of view, it is clear that for corrosion to occur, spatially separated anodic and cathodic sites on the electrode are required.

References for Chapter 6

[1] U. CHATTERJEE, S. BOSE, and S. ROY, *Environmental degradation of metals*, Corrosion Technology, Taylor & Francis, 2001, 25–32.

[2] E. MCCAFFERTY, *Introduction to corrosion science*, Springer, 2010, 131–132.

[3] D. TALBOT and J. TALBOT, *Corrosion science and technology*, CRC Press, 1998, 97–102.

[4] C. BAMFORD and R. COMPTON, eds., *Electrode kinetics: Principles and methodology*, Elsevier, 1986, 26–31.

[5] J. DAVIS, *Corrosion: Understanding the basics*, 1st, ASM International, 2000, 82–88.

[6] J. BUTLER, Studies in heterogeneous equilibria. II. The kinetic interpretation of the Nernst theory of electromotive force, *Trans. Faraday Soc.* **19** (March) (1924), 729–733.

[7] J. BUTLER, Studies in heterogeneous equilibria. III. A kinetic theory of reversible oxidation potentials at inert electrodes, *Trans. Faraday Soc.* **19** (March) (1924), 734–739.

[8] N. HUSH, Adiabatic rate processes at electrodes. I. Energy-charge relationships, *J. Chem. Phys.* **28** (5) (1958), 962–972.

[9] N. SATO, *Electrode reactions in ion transfer*, Elsevier, 1998, 289–323.

[10] K. VETTER, *The theory of overvoltage*, Academic Press, 1967, chap. 2, 104–396.

[11] D. GRAHAME, Electrode processes and the electrical double layer, *Ann. Rev. Phys. Chem.* **6** (1) (1955), 337–358.

[12] E. GILEADI, The enigma of metal deposition, *J. Electroanal. Chem.* **660** (2) (2011), 247–253.

[13] R. GUIDELLI et al., Defining the transfer coefficient in electrochemistry: An assessment (IUPAC technical report), *Pure Appl. Chem.* **86** (2) (2014), 245–258.

[14] R. MARCUS, On the theory of oxidation-reduction reactions involving electron transfer, *J. Chem. Phys.* **24** (5) (1956), 966–978.

[15] R. MARCUS, On the theory of oxidation-reduction reactions involving electron transfer. II. Applications to data on the rates of isotopic exchange reactions, *J. Chem. Phys.* **26** (4) (1957), 867–871.

[16] R. MARCUS, On the theory of oxidation-reduction reactions involving electron transfer. III. Applications to data on the rates of organic redox reactions, *J. Chem. Phys.* **26** (4) (1957), 872–877.

[17] M. LEFEBVRE, Establishing the link between multistep electrochemical reaction mechanisms and experimental Tafel slopes, in: *Modern Aspects of Electrochemistry*, ed. by B. E. CONWAY, J. BOCKRIS, and R. WHITE, vol. 32, Modern Aspects of Electrochemistry, Springer US, 2002, 249–300.

[18] B. CONWAY, *Theory and principles of electrode processes*, New York: Ronald Press, 1965, 1–303.

[19] J. BRENET and K. TRAORE, *Attempts at a theoretical interpretation of the transfer coefficient*, Academic Press, 1971, chap. 4, 56–70.

[20] T. ERDEY-GRÚZ, *Kinetics of electrode processes*, Wiley, 1972, 68.

[21] J. BOCKRIS and A. REDDY, *Electrochemistry in materials science*, 2nd, Springer, 2000, chap. 12, 1637–1788.

[22] R. HURD, Polarization curves of redox systems involving consecutive electron transfers: Some theoretical aspects, *J. Electrochem. Soc.* **109** (4) (1962), 327–332.

[23] F. ROPITAL and Y. CHAUVIN, Fundamentals on metallic alloys and corrosion, in: *Corrosion and degradation of metallic materials*, IFP Publications, 2010, chap. 3, 147–259.

[24] M. PAUNOVIC and M. SCHLESINGER, *Fundamentals of electrochemical deposition*, The ECS Series of Texts and Monographs, Wiley, 2006, 79–92.

[25] A. ADRIAENS, *Corrosie*, Leuven: Acco, 2008.

[26] C. WAGNER and W. TRAUD, Concerning the evaluation of corrosion reactions by superposition of electrochemical partial reactions and concerning the potential formation on mixed electrodes, *Z. Electrochem.* **44** (1938), 391–402.

7

Electrochemical deposition of a lead dodecanoate coating

Reprinted from J. Solid State Electrochem., 14 (3), K. De Wael, M. De Keersmaecker, M. Dowsett, D. Walker, P. Thomas and A. Adriaens, Electrochemical deposition of dodecanoate on lead in view of an environmentally safe corrosion inhibition, 407-413, 2010, with permission from Springer.

7.1 The development of lead carboxylate coatings

In this first chapter, we describe one of the latest developments in the search towards a coating on lead artifacts namely the deposition of lead carboxylate coatings. Recent strategies, developed for the conservation of organ pipes and published by Chiavari et al. [1], try to deposit a protective coating using thiourea, sulfuric acid, phosphoric acid and monocarboxylates on lead samples. To test the coating's protectivity, the samples are corroded in an acetic environment to study the production of lead corrosion products. As a conclusion, Chiavari et al. [1] postulated that non-toxic linear sodium monocarboxylates form the most protective coating for the active acetic acid corrosion.

In 2001, the protective coating for lead using aqueous solutions of sodium linear monocarboxylates was already proposed by Rocca et al. [2]. Investigations focused on the neutralized acids with growing carbon chains with chemical formula: $CH_3(CH_2)_{n\text{-}2}COONa$ with n = 7 - 11, referred to as 'NaC_n'. Next to the efficient lead corrosion reduction, the authors also stated that the inhibition efficiency of the sodium monocarboxylates mainly depends on the length of the carbon chains and the concentration used. From these results, a dissolution-precipitation mechanism for the reaction of lead with the sodium linear monocarboxylates is suggested. In a first phase, the lead metal will oxidize in the presence of oxygen dissolved in the aqueous solution [2],

$$Pb(s) + 2H^+(aq) + \frac{1}{2}O_2(g) \rightleftharpoons Pb^{2+}(aq) + H_2O(l). \tag{7.1}$$

In a next step, the lead carboxylate will precipitate when the solubility product is reached [2],

$$Pb^{2+}(aq) + 2CH_3(CH_2)_{n-2}COO^-(aq) \rightleftharpoons Pb(CH_3(CH_2)_{n-2}COO)_2(s), \tag{7.2}$$

with the formation of lead carboxylate crystals [3]. The proposed mechanism is in good agreement with thermodynamic data and the dissolution-precipitation mechanism is applicable to other carboxylic acids [4]. The high inhibition efficiency of these lead carboxylate soaps is understood, based on their insolubility in water, their hydrophobic character, their drastic change to the morphology of the corrosion layer and their ability to locally neutralize the acidity of the water film filled with acetic acid [5],

$$Pb(C_{10})_2(s) + 2CH_3COOH(aq) \rightleftharpoons 2CH_3COO^-(aq) + Pb^{2+}(aq) + 2HC_{10}(aq). \quad (7.3)$$

The $Pb(C_{10})_2/HC_{10}$-equilibrium maintains a high pH, preventing the formation of local acidic sites which lead to the lead dissolution. Furthermore, their easiness to use, their environmentally friendly character and their ability to be removed using ethanol make the sodium linear monocarboxylates solutions ideal for the preservation of metallic cultural heritage [5].

7.2 Voltammetric techniques

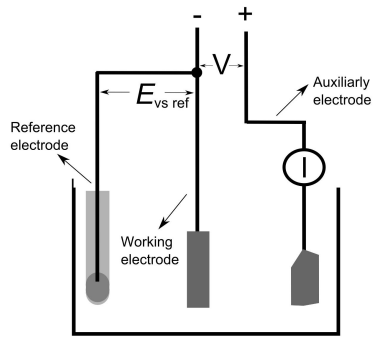


Figure. 7.1 – General set-up for voltammetric measurements.

Knowing the deposition mechanism of the carboxylates, different voltammetric techniques are used to produce and analyze corrosion protective lead carboxylate coatings. These methods observe the relationship between potential and current to identify electrochemical processes. Basically, the electrode potential is varied and the resulting current is recorded [6]. Using this collected electrochemical information, the protective properties of the coatings are rated. To start, we will give a brief explanation about the set-up and the techniques used for deposition and corrosion testing in a voltammetric cell.

7.2.1 The voltammetric cell

A voltammetric cell consists of the working electrode, the auxiliary electrode and a reference electrode connected to a potentiostat, which is used to control the potential. The current of the working electrode is recorded as a function of its potential measured against the reference electrode, but the voltage is applied between and the current passes between the working and the auxiliary electrode, as seen in Figure 7.1 [7]. In this manner, the solution resistance, which creates an iR drop, is kept low [8].

7.2.2 Cyclic voltammetry

In cyclic voltammetry, a triangular waveform shown in Figure 7.2a is applied to the working electrode. After applying a linear voltage ramp between times t_0 and t_1, the ramp is reversed to bring the potential back to its initial value at time t_2. Obviously, this cycle can be repeated. As a function of the applied potential, the current is plotted in a current-potential curve known as a *voltammogram* [9].

A typical cyclic voltammogram in Figure 7.2b shows an increase in the anodic current. After that, the current starts to decrease with the formation of a peak. The decrease is a consequence of analyte depletion near the electrode surface and diffusion limitations from the bulk solution. It is clear that each individual peak represents an electrochemical process. When the potential is reversed, an anodic current continues to flow because of the ongoing oxidation processes. When the potential becomes sufficiently less positive, the oxidized product near the electrode begins to reduce, which gives rise to a cathodic peak. Finally, as the reduced product is depleted, the cathodic current decays back towards its initial value [9]. The blue curve in Figure 7.2b illustrates a *reversible* reaction, which means the electron transfer is fast enough to maintain equilibrium concentrations at the electrode surface. Different criteria are used to define reversible behavior based on recorded voltammograms such as the Tomes criterion, the peak potential is independent of the scan rate, both peak heights are equal and the Randles-Sevcik equation described as [10–12]

$$I_{\mathrm{p}} = 0.4463\, nFAc\sqrt{\frac{nFD\nu}{RT}}, \tag{7.4}$$

where I_{p} is the peak height, A is the area of the working electrode, c is the concentration, D is the diffusion coefficient and ν is the scan rate, is valid. In general, it is very important to know whether or not an electrochemical process is reversible. It is observed experimentally that reversibility is greatest at slow scan rates [12]. If, however, the electron transfer rate is slow compared to the time scale of the experiment, we will see non-Nernstian behavior (i.e. contrary to equation 2.2) at the electrode surface creating an *irreversible behavior*. In Figure 7.2b, the orange curve shows that the cathodic and anodic peaks are drawn out and become more separated. At the limit of irreversibility, where the reduction is very slow, no cathodic peak is seen [13]. The intermediate region is '*quasi-reversible*' [9, 12].

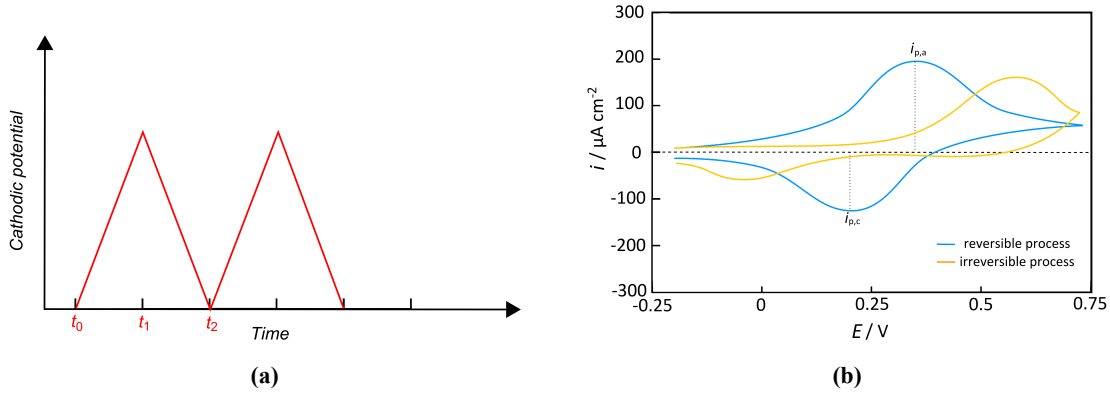


Figure. 7.2 – (a) Potential waveform in cyclic volammetry [9]. (b) Effect of the heterogenous rate constants on the process reversibility. The transfer coefficient are set to 0.5 [12].

7.2.3 Linear polarization

The Butler-Volmer equation, Eq. 6.3, is often used in a strictly empirical way to analyze data. Experimentally, the interesting kinetic information is expressed in two parameters, the exchange current density and the transfer coefficients. Based on a voltammogram, two ways exist for determining the corrosion rates namely (i) the Tafel extrapolation [14] and (ii) the determination of the polarization resistance.

7.2.3.1 Tafel extrapolation

When the potential η is sufficiently large, $|\frac{F\eta}{RT}| > 1$ and one of the exponential terms in Eq. 6.3 can be neglected. When the overpotential is large and positive, the cathodic component of the current is negligible and we have

$$\ln\left(\frac{i}{i_0}\right) = \frac{\alpha_{\mathrm{a}} F\eta}{RT}, \tag{7.5}$$

where α_{a} has been substituted for $(1-\alpha)n$. In the case, the overpotential is large and negative, the anodic component of the current is negligible to give

$$\ln\left(\frac{i}{i_0}\right) = \left|\frac{\alpha_{\mathrm{c}} F\eta}{RT}\right|, \tag{7.6}$$

where α_{c} has been substituted for αn. Both equations are known as the Tafel equations [15, 16]. This logarithmic current-potential relationship was discovered empirically by J. Tafel in 1906 [17]. The Tafel equations predict that when

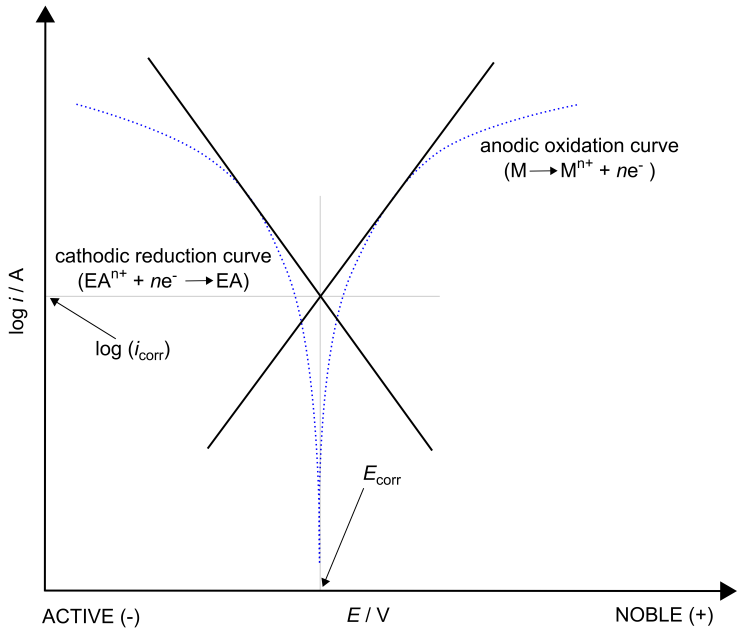


Figure. 7.3 – The extrapolation of the two Tafel slopes for the determination of the corrosion current i_{corr}

the current is measured as a function of overpotential and then plotted as log i vs. η, a linear region should be found. Extrapolation of these linear portions to zero overpotential yields the exchange current as the intercept; the slopes are -16.90 α_{c} and 16.90 α_{a}. Such a plot is shown in Figure 7.3 [18]. Increasing the measurement range, show us that the electrochemical process is limited by the transport rate causing the plot to flatten out. This limitation depends on the efficiency of stirring, the diffusion coefficients of the electroactive species and the electron-transfer rate. Slow electron-transfer processes show a too small exchange current, where faster processes show no Tafel region because the transport limitation sets in before. The potential range to be used will depend on the electrode material, the solvent, the supporting electrolyte, and the acidity of the solution [19].

7.2.3.2 Polarization resistance

When the electron-transfer rate is too fast to be measured by the Tafel approach, all is not lost. When considering the limiting case of a small overpotential using the Butler-Volmer equation, the exponential terms can be expanded in a power series [19]

$$i = i_0 \left[1 + \frac{\alpha_{\text{a}} F\eta}{RT} + ... - \left(1 - \frac{\alpha_{\text{c}} F\eta}{RT} + ...\right)\right] = i_0 \left[1 + \frac{\alpha_{\text{a}} F\eta}{RT} - 1 + \frac{\alpha_{\text{c}} F\eta}{RT}\right] = i_0 \frac{(\alpha_{\text{a}} + \alpha_{\text{c}}) F\eta}{RT}. \tag{7.7}$$

Retaining only the first non-vanishing term, the current is approximately linear in η and the electrode behaves as an ohmic resistance given by [19]

$$R_{\text{p}} = \frac{RT}{Fi_0}, \tag{7.8}$$

This resistance is called the polarization resistance. Using the Nernst equation 2.2, we see that the exchange current varies with the equilibrium potential according to the partial derivatives [20]

$$\left[\frac{\partial \ln i_0}{\partial E_\mathrm{e}}\right]_{[\mathrm{R}]} = \frac{F}{RT}\alpha_\mathrm{a}, \tag{7.9a}$$

$$\left[\frac{\partial \ln i_0}{\partial E_\mathrm{e}}\right]_{[\mathrm{O}]} = -\frac{F}{RT}\alpha_\mathrm{c}. \tag{7.9b}$$

This indicates that a R_p measurement of a series of solutions with constant $[\mathrm{O}]^*$ and variable $[\mathrm{R}]^*$ allows the evaluation of cathodic transfer coefficient.

7.3 Experimental

7.3.1 Solutions

Inhibitor solutions of different carboxylic acids (see Table 4.1) neutralized using a standardized 0.25 mol L^{-1} NaOH solution are made using the protocol in the doctoral thesis of Schotte [21]:

1. The suspensions are prepared by adding the calculated amount of carboxylic acid in a 100 mL-flask.
2. Add the calculated volume of the NaOH solution.
3. Stir the suspensions until a turbulent solution is obtained and the soap is completely dissolved (about 8 hours).
4. Measure the pH, which should be around 9

To test the corrosion properties of a coating, we need a mixture that represents an environment that simulates typical atmospheric corrosion on lead objects [22]. For testing lead, we use the ASTM D 1384-87 solution, which contains 148 mg L^{-1} Na_2SO_4 (Sigma–Aldrich, USA), 138 mg L^{-1} $NaHCO_3$ (Sigma–Aldrich, USA) and 165 mg L^{-1} NaCl (Sigma–Aldrich, USA) [23].

7.3.2 Instruments

All electrochemical measurements are performed in an electrochemical cell provided with a saturated calomel reference electrode (SCE) containing two compartments (Radiometer Analytical, France), a carbon counter electrode and a polished (see procedure in section 4.2) lead (diameter = 6.0 mm; purity = $>$ 99.99%; Goodfellow, Cambridge, UK) working electrode embedded in an epoxy resin. The surface area of the working electrode was 0.2827 cm^2.

A PGSTAT20 potentiostat controlled by GPES 4.9 005 software package running (ECO Chemie, The Netherlands) was used to record voltammetric curves. The modification of a lead electrode was performed by recording successive cyclic voltammetric scans (five or 30 scans) in a potential window from −1.3 to 1.5 V vs. SCE with a scan rate of 50 mV s^{-1} in a 0.025 mol L^{-1} NaC_{12} solution. The polarization experiments were carried out at a scan rate of 1 mV s^{-1} from -0.25 to 1.3 V vs. E_corr. The corrosion potential, E_corr, was determined by a potentiometric measurement during 1,000 s.

Reflectance spectra were acquired using a Perkin Elmer Spectrum 1000 FTIR Infrared spectrometer equipped with Spectrum 100 Series' Universal ATR accessory. The spectra were recorded over the range 3,200 – 400 cm^{-1} and averaged over 16 scans.

The XRD spectrum was recorded using a Panalytical XPert Pro Multipurpose Diffractometer equipped with a curved germanium focusing monochromator to produce $CuK_{\alpha 1}$ radiation and a PIXcel detector described in section 4.5.1.4. Data were collected by means of a conventional $\theta - 2\theta$ scan in the 2θ range 2 – 40° with a step-size of 0.0263° 2θ over a period of 80 min.

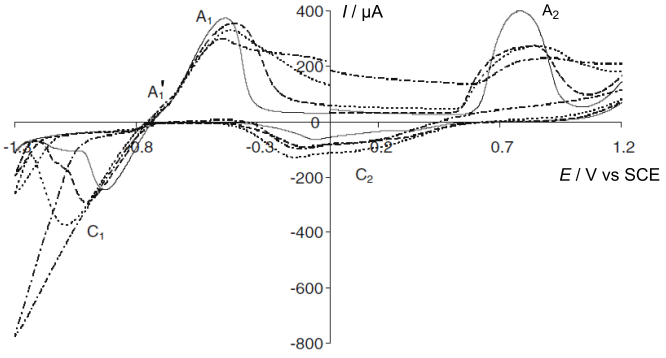


Figure. 7.4 – Current-potential curves recorded at a lead electrode in a 0.025 mol L^{-1} NaOH solution in the absence of dodecanoic acid at a scan rate of 50 mV s^{-1} and a temperature of 298 K as a function of scan number. The first four scans are shown (scan 1: solid line, scan 2: broken line, scan 3: dotted line and scan 4: dash-and-dot line).

7.4 Electrochemical behavior of lead

7.4.1 Electrochemical behavior of lead in an alkaline solution

Figure 7.4 shows the first four scans recorded at a bare lead electrode in the alkaline non-corrosive reference solution (without carboxylates). The first voltammogram (scan 1) shows two well-defined oxidation peaks labeled A_1 (in the potential region from -620 to -300 mV) and A_2 (600 to 1000 mV) due to PbO and PbO_2 formation, respectively. In addition, a small shoulder A_1' is observed on the cathodic side of the first anodic process. This process can be explained as the formation of a thin $Pb(OH)_2$ film according to the following mechanism [24, 25],

$$Pb + OH^- \rightleftharpoons PbOH_{ads} + e^-, \tag{7.10a}$$

$$PbOH_{ads} + OH^- \rightleftharpoons PbOH_2 + e^-. \tag{7.10b}$$

The $Pb(OH)_2$ film formed mostly dissolves, yielding $Pb(OH)_3^-$ ions, whereas the remaining $Pb(OH)_2$ transforms into PbO at a more positive potential than that required for the formation of $Pb(OH)_2$. The mechanism corresponding to this reaction is given below [24]

$$PbOH_{ads} + OH^- \rightleftharpoons PbO^-_{ads} + H_2O, \tag{7.11a}$$

$$PbO^-_{ads} \rightleftharpoons PbO + e^-. \tag{7.11b}$$

The oxidation process A_1 is called the lead dissolution process. The same reaction is seen in the lead-water Pourbaix diagram [26]. After this process, the electrode becomes passive and the current drops to a lower value and extends over a wide potential range. Within this region, the value of $I_{passivation}$ is nearly constant and, to some extent, independent of the applied potential. The second oxidation peak A_2 can be explained as the transformation of PbO to PbO_2 according to [24]

$$3PbO + 2OH^- \rightleftharpoons Pb_3O_4 + H_2O + 2e^-, \tag{7.12a}$$

$$Pb_3O_4 + 4OH^- \rightleftharpoons 3PbO_2 + 2H_2O + 2e^-. \tag{7.12b}$$

When the anodic potential is reversed after process A_2, two reduction processes appear (C_2 in the potential region from

400 to -400 mV and C_1 from -760 to -1300 mV). It is clear that the process in the potential region from 400 to -400 mV encloses several reduction reactions. This separation could be explained by the fact that PbO_2 would be reduced first to Pb_3O_4 and the latter to PbO [24],

$$3PbO_2 + 2H_2O + 2e^- \leftrightharpoons Pb_3O_4 + 4OH^-, \tag{7.13a}$$

$$5Pb_3O_4 + 11H_2O + 10e^- \leftrightharpoons 3[5PbO \cdot 2H_2O] + 10OH^-. \tag{7.13b}$$

Process C_1 occurs in the region of the PbO/Pb potential [24, 25, 27]. This process corresponds to the lead deposition phenomenon. A change of the voltammetric behavior is observed during the consecutive scans. This phenomenon can be explained by the fact that the products formed during the potential cycling are adsorbed particles and thus have an influence on the electron transfer at the electrode. The passivation between process A_1 and A_2 no longer remains constant but increases slightly as a function of scan number, indicating the growth and thickening of the oxide surface film. After four scans, a layer of higher lead oxides is formed, blocking the lead surface. Figure 7.5 shows optical images from the lead surface at various stages in the experiment. The first two are before (a) and after (b) potential cycling in the alkaline reference solution. The red–brown-colored adsorbed species is a mixture of lead oxides, Pb_3O_4 and PbO_2 [28].

7.4.2 Electrochemical behavior of lead in a sodium dodecanoate solution

When dodecanoic acid is added to the alkaline reference solution, it is expected that sodium hydroxide neutralizes the acid, resulting in the formation of sodium dodecanoate. Figure 7.6 shows the cyclic voltammetry behavior of 0.025 mol L^{-1} NaC_{12} at a lead electrode in the potential window from −1.3 to 1.5 V vs SCE at a scan rate of 50 mV s^{-1}. In the first scan, three redox processes are observed, i.e. A_1, A_1' and C_1. In comparison with the electrochemical behavior of lead in the reference solution, A_1 and A_1' represent the dissolution of lead. The reduction process C_1 represents the lead deposition process. From scan 2, a stable voltammetric signal is observed, and from this until scan 30 only the processes A_1' and C_1 are observed. There is no further oxidation process after peak A_1'.

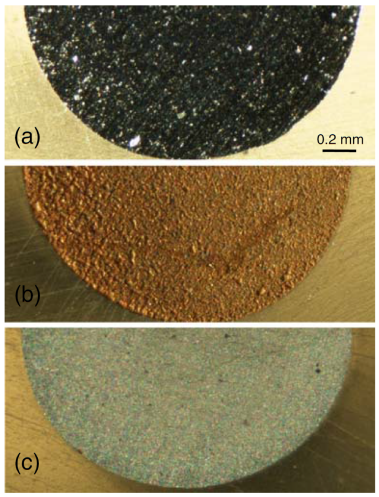


Figure. 7.5 – Optical images of a bare lead electrode (a), a lead electrode after potential cycling in an alkaline reference solution (b) and a lead electrode coated with dodecanoate (c).

The shoulder A_1' has already been described as the dissolution of lead and the formation of a thin $Pb(OH)_2$ film according to eqs. 1 and 2 in the absence of NaC_{12} (see above). It is at this corresponding potential that, in the presence of NaC_{12}, the formation of the dodecanoate film occurs during the next scans. The dodecanoate ion acts as a ligand for complexation with lead ions, instead of hydroxide in the reference solution. In addition, further oxide formation (A_1 and A_2) is inhibited in the next scans. Scan 2 only shows a well-defined oxidation peak A_1' and a reduction process C_1. In contrast, in the first scan, there is still a competition between hydroxide and dodecanoate adsorption as process A_1' as well as A_1 appears. This ties in very nicely with our real-time XRD observations of the growth of lead decanoate, where we see the oxidation essentially stop after a couple of hours, after which it decreases as it is

masked by the decanoate growth [29]. Following the addition of NaC_{12}, the oxidation A_1' and reduction C_1 reactions represent the lead dissolution/deposition respectively. The carboxylate is adsorbed onto the lead, resulting in a blocking of the surface for further oxidation. A first indication of adsorption is the decrease of the lead related redox reactions compared with corresponding processes in Figure 7.4. The well-developed anodic peak is characteristic of a passivation process. At more positive potentials, the current drops to a low value corresponding to the passive state. Its appearance suggests an active dissolution–passivation transition. The oxidation process is indicative of two processes. First, there is the dissolution of lead and the formation of a soluble lead salt with dodecanoate as the anion. The dissolution of lead in a carboxylate solution can be explained as a series of adsorption reactions involving catalysis by the anion at active surface sites in monatomic steps followed by desorption of the formed soluble salt as follows [4, 30]:

$$Pb^{2+} + C_n^- \rightleftharpoons [Pb(C_n)^+]_{ads}, \tag{7.14a}$$

$$[Pb(C_n)^+]_{ads} + C_n^- \rightleftharpoons [Pb(C_n)_2]_{ads}, \tag{7.14b}$$

$$[Pb(C_n)_2]_{ads} \rightleftharpoons [Pb(C_n)_2]_{aq}. \tag{7.14c}$$

where C_n^- is dodecanoate. Secondly, there is precipitation of a salt film PbL(s) on the electrode surface when the solubility product of the salt is exceeded. This precipitation at the lead electrode blocks the active sites, resulting in an inactivation of the surface with respect to a corrosive medium. The formation of the coating described by the dissolution–precipitation mechanism is controlled by the diffusion of the reacting species. This can be demonstrated by showing that the influence of the scan rate on the peak current obeys the Randles–Sevick equations (see section 7.2.2). Accordingly, the influence of the scan rate on the peak current is shown in Figure 7.7. Both peak current and peak potential increase as a function of scan rate. The inset shows that a linear behavior is observed for I_{A_1} versus $v^{1/2}$, typically for this type of system. As the voltammetric behavior is stable from scan 2, it can be stated that the electrochemical coating process is rather fast. This might be expected because the initial step to deposit the dodecanoate on the lead surface is the oxidation of lead. By cycling the potential during the electrochemical experiment, the lead electrode is brought in this oxidation state followed by a reaction with the dodecanoate. In contrast, for the immersion method, it takes some hours to deposit the dodecanoate film as the lead ions are generated in another way as described in section 7.1.

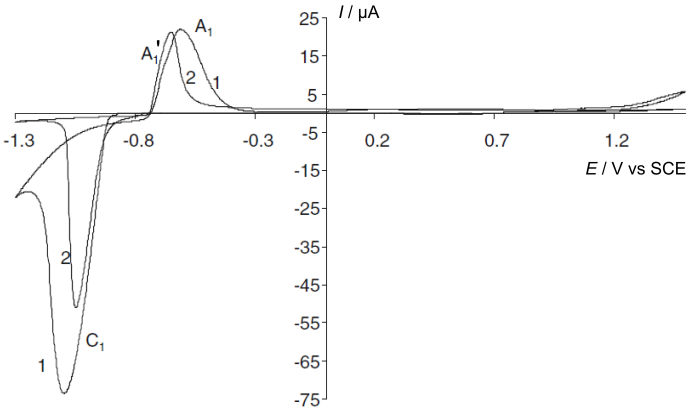


Figure. 7.6 – Current-potential curve recorded at a lead electrode in a 0.025 mol L^{-1} NaC_{12} water solution: scan 1 (1) and scan 2 - 30 (2).

7.4.3 Tafel analysis

The lead corrosion potential after modification by dodecanoate is ca. 120 mV higher than the potential measured at a lead electrode in the absence of dodecanoate at the surface or in the solution. The performance of NaC_{12} for lead protection is investigated by recording potentiodynamic curves. Figure 7.8 represents a Tafel plot of bare lead (curve 1) and coated

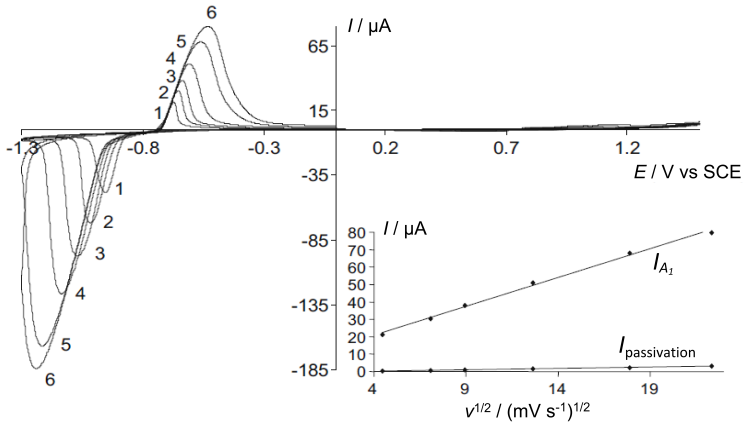


Figure. 7.7 – Current-potential curve recorded at a dodecanoate-coated lead electrode in a 0.025 mol L^{-1} NaC_{12} water solution at different scan rates: 20 (1), 50 (2), 80 (3), 160 (4), 320 (5) and 500 (6) mV s^{-1}. Inset: relationship between the peak current (I) and square root of the scan rate for process A_1 (I_{A_1}) and the passive region ($I_{passivation}$).

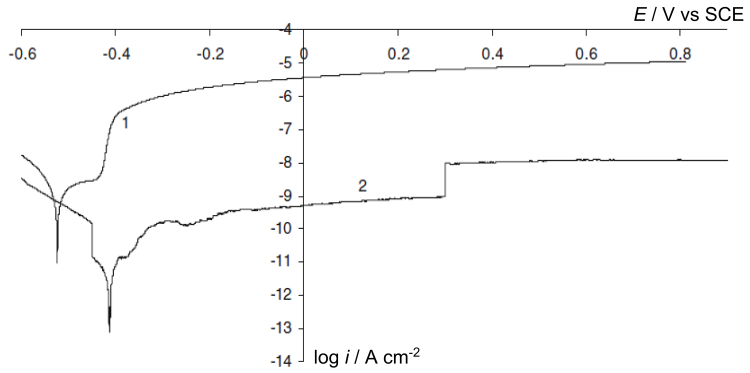


Figure. 7.8 – Potentiodynamic curves of bare lead (1) and coated lead (2) in an ASTM solution.

lead (curve 2) in the ASTM solution. The presence of dodecanoate as inhibitor at the lead electrode induces a decrease of the corrosion current density down to 10^{-11} to 10^{-12} A cm^{-2} and the passivation current density decreases, while the pitting phenomenon is clearly inhibited at the coated electrode.

7.5 Spectroscopic characterization of the dodecanoate film

Figure 7.5 is an optical image of a bare lead electrode (a) and a lead electrode coated with dodecanoate by recording five successive cyclic voltammograms in a potential window from -1.3 to 1.5 V vs SCE with a scan rate of 50 mV s^{-1} (c). A clear difference is observed between both, indicating a deposition. Visually, the coated electrode has a slightly dull view. The infrared spectra in Figure 7.9 were recorded on the following two electrodes: a bare lead electrode (a) and a modified lead electrode with dodecanoate (b). The spectrum of the coated electrode (curve b) shows important characteristic peaks compared with the bare lead electrode (curve a). Table 7.1 sums up the most important infrared peaks. First of all, strong bonds are observed in the vibrational spectra in the region of 1500, 1400 and 930 cm^{-1} corresponding to the vibrations of the carboxylate group, COO^- group [31–33]. More specifically, the adsorptions at 1510, 1415 and 696 cm^{-1} are identified as the antisymmetric mode, ν_{as} COO^-, symmetric stretching mode, ν_s COO^-, and scissoring bending mode, δ_s COO^-. Both ν_{as} and ν_s bands appear as doublets characteristic of long-chain bivalent metal carboxylates [34, 35]. In the enlargement of Figure 7.9, the number of CH_2 wagging progression bands is observed as a set of regularly spaced bands [36]. These bands are characteristic of chains in the all-trans-conformation and their number depends on the number of CH_2 units in

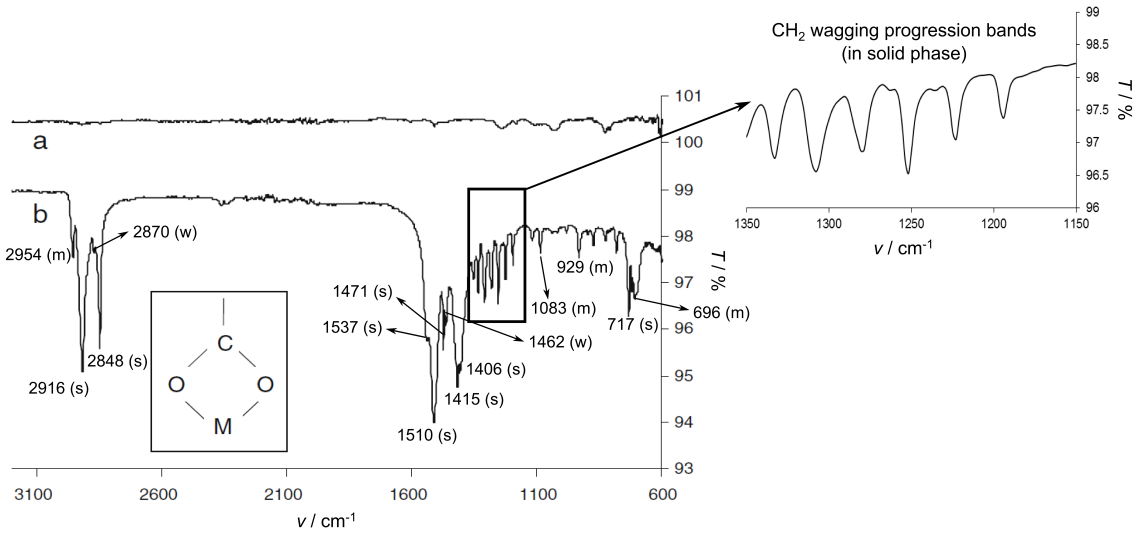


Figure. 7.9 – ATR-IR spectra of a bare lead electrode (a) and a lead electrode coated with dodecanoate (b). Inset: mode of bonding. Enlargement: CH_2 wagging progression bands.

the alkyl chain [37].

ν (cm^{-1})	ν (cm^{-1}) [32, 38]	ASSIGNMENT
2954 (m)	2955	$\nu_{as}(CH_3)$
2916 (s)	2919	$\nu_{as}(CH_2)$
2870 (w)	2870	$\nu_{as}(CH_2)$
2848 (s)	2850	$\nu_{s}(CH_2)$
1537 (w)	1542	$\nu_{as}(COO^-)$
1510 (s)	1512	$\nu_{as}(COO^-)$
1471 (s)	1472	$\delta_{s}(CH_2)$
1462 (w)	1465	$\delta_{s}(CH_2)$
1415 (s)	1420	$\nu_{s}(COO^-)$
1406 (s)	1400	$\nu_{s}(COO^-)$
1350 - 1150 (m)	1350 - 1150	CH_2 wagging progression bands
1083 (m)	1080	$\rho(CH_2)$
929 (m)	920	$\rho(CH_3)$
717 (m)	720	$\rho(CH_2)$
696 (w)	690	$\delta_{s}(COO^-)$

Table 7.1 – Infrared characteristic vibrational wavenumber (in cm^{-1}) observed for lead(II)alkanoates.

The direction of the wavenumber shifts of the ν_{as} and ν_{s} stretching bands of the COO^- relative to those of the free ion depends on the mode of coordination of the carboxyl group with the metal ion and its oxidation state. The four principal modes of coordination are shown in Figure 7.10 [39, 40]. The different coordination geometries are reflected in differences in the carbonyl stretching frequencies[41]. Nakamoto and McCarthy [42] established that for monodentate coordination (structure I) $\nu_{as}(COO^-)$ and $\nu_{s}(COO^-)$ will be shifted to higher and lower frequencies, respectively. Whereas chelating bidentate coordination (structure II) or bridging bidentate coordination (structure III) shifts both the ν_{as} and ν_{s} band of the COO^- in the same direction, because the bond orders would change by the same amount as seen in Table 7.1. Some

authors [39, 43, 44] have used the magnitude of $\Delta\nu$ (compared to the sodium salt), the separation between the ν_{as} and ν_s band of the COO^-, to distinguish different modes of carboxylate coordination to the metal ions,

$$\Delta\nu = \nu_{as}(COO^-) - \nu_s(COO^-) \tag{7.15}$$

The assignment is made using the following guidelines: (i) bidentate chelating coordination occurs when $\Delta\nu(COO^-)$ complex $\ll \Delta\nu(COO^-)$ sodium salt; (ii) the bidentate bridging carboxylate exists when $\Delta\nu(COO^-)$ complex $\leq \Delta\nu(COO^-)$ sodium salt; (ii) monodentate coordination is characterized by $\Delta\nu(COO^-)$ complex $\gg \Delta\nu(COO^-)$ sodium salt [45–49]. The low separation stretch, $\Delta\nu(COO^-)$ complex = 95 cm^{-1} for the lead dodecanoate coating, is an indication of chelating coordination of the carboxylate group since $\Delta\nu(COO^-)$ complex $\gg \Delta\nu(COO^-)$ sodium salt (135 cm^{-1}).

Zeleňák et al. [39] found that high values of $\Delta\nu$, above 180 cm^{-1}, were typical for the monodentate coordination (structure I) because the other types of coordination do not give such high values of $\Delta\nu$. Furthermore, syn-syn bridging coordination (structure III) has $\Delta\nu$ values above 150 cm^{-1}, whereas chelating bidentate (structure II) carboxylate groups normally have $\Delta\nu$ values less than 120 cm^{-1} [40]. However, the syn-anti bridging coordination (structure IV) can yield a separation around this value as well. This means that structures I and III can be ruled out because of their high $\Delta\nu$ values. Analysis of the IR data reported by Ellis et al. [31], showed that there was a non-equivalence of the C-O bonds, hence, the Pb-O bonds were not identical in length, similar to the formate, where ν_{as} stretches were more intense than ν_s; an effect which increases with chain length. Interestingly, $\Delta\nu$ values decrease with decreasing chain length suggesting unsymmetrical chelating bidentate coordination with possible carboxylate bridging, for the shorter chain compounds ($PbC_{8...12}$).

The X-ray diffraction data in Figure 7.11 show the presence of crystalline phases, registered by sharp Bragg peaks, superimposed on an amorphous background, which can be attributed to the epoxy resin in which the sample was mounted. The spectrum is mostly due to lead dodecanoate (pattern reference number 00-0090712 in the 2008 database of the International Centre for Diffraction Data (ICDD)). The two strongest peaks in the diffraction spectrum at 31.26° and 36.26° in 2θ correspond to diffraction from the Pb substrate beneath the thin lead dodecanoate layer. Furthermore, differences in the XRD data resulted in the proposal, that there were differences in the molecular and lattice packing between short and long chain compounds; that is, for $n_c < 12$, a bilayer arrangement of the hydrocarbon chains existed but for $n_c > 12$, a monolayer arrangement was proposed. For example, marked differences in the high angle region, $20° \leq 2\theta \leq 25°$, of the powder diffractograms, associated with reflections from side chains packing interactions were observed [31]. There is evidence for the presence of litharge (PbO) just as we found in the case of the decanoate grown from sodium decanoate solution [29]. This is registered by the peak at 35.60°, which is close to the 002 peak at 35.74° reported for synthetic litharge (reference pattern

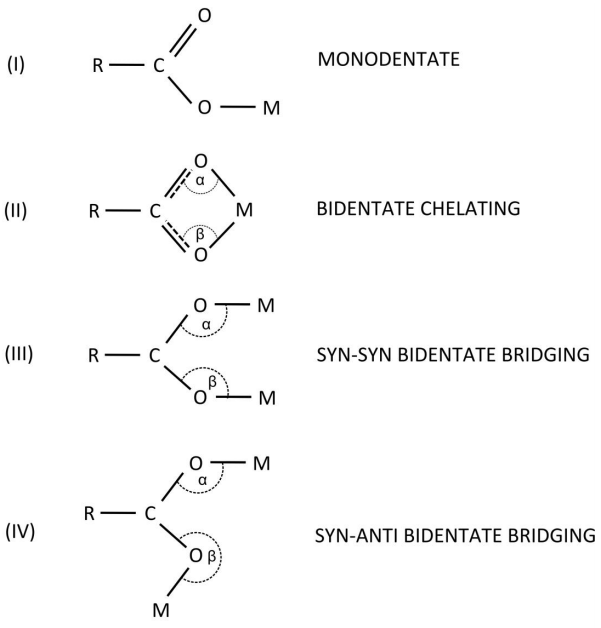


Figure. 7.10 – Four principal modes of coordination for metal carboxylate bonds.

number 00-005-0561 in the ICDD database) and is consistent with the presence of a (001) highly oriented PbO layer. A large degree of (001) orientation in the PbO layer explains the absence of the strongest litharge diffraction peaks at 28.63° and 31.83° in our observed spectrum. These are the 101 and 110 reflections, respectively, which would be in-plane reflections for an (001)-oriented film and are not observable in the Bragg-Brentano reflection geometry of our diffraction experiment. The 0.14° difference in the 2θ angle between the reported litharge peak and our observation can be explained principally by the height error inherent in not having the PbO layer at the half-cut beam position as well as the possible effects of strain in this multilayer system.

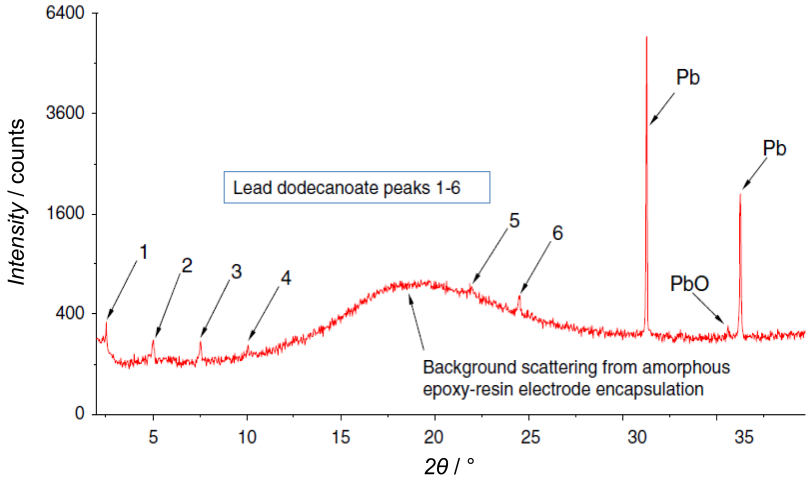


Figure. 7.11 – X-ray diffractogram from an electrode modified with 30 cycles showing the structure of lead dodecanoate overlaid on the lead substrate. Evidence for litharge (PbO) is also found.

7.6 Conclusions

In this work, we have investigated the electrochemical deposition of lead dodecanoate coatings on lead. The advantage of this method over the more commonly immersion treatment is the shortening of the coating process and the control one has over the layer formation. In both cases, however, the carboxylates react with dissolved lead ions formed by lead hydroxide intermediates. The deposition of the carboxylate was successfully achieved by recording successive cyclic voltammetric scans of a lead electrode in a 0.025 mol L^{-1} sodium dodecanoate solution. Results allowed us to reveal the mechanism of the deposition: the first part of the lead surface dissolves and forms a soluble lead salt with dodecanoate as the anion. The latter is followed by the precipitation of a salt film PbL(s) on the electrode surface. The deposition is proven by ATR-IR and X-ray diffraction. Additional Tafel plots of the bare and coated lead electrodes in corrosive environments showed that the presence of dodecanoate induces a decrease of the corrosion current density, while the passivation current density also decreases.

References for Chapter 7

[1] C. CHIAVARI et al., Conservation of organ pipes: protective treatments of lead exposed to acetic acid vapours, in: *Metal 04: Proceedings of the international conference on metals conservation*, ed. by J. ASHTON and D. HALLAM, National Museum of Australia Canberra, 2004, 281–293.

[2] E. ROCCA and J. STEINMETZ, Inhibition of lead corrosion with saturated linear aliphatic chain monocarboxylates of sodium, *Corros. Sci.* **43** (5) (2001), 891–902.

[3] F. LACOUTRE et al., Anhydrous lead(II)heptanoate, *Acta Crystallogr. C* **57** (5) (2001), 530–531.

[4] S. ABD-EL REHIM et al., Electrochemical behavior and corrosion of lead in some carboxylic acid solutions, *J. Chem. Technol. Biotechnol.* **72** (2) (1998), 197–201.

[5] E. ROCCA, C. RAPIN, and F. MIRAMBET, Inhibition treatment of the corrosion of lead artefacts in atmospheric conditions and by acetic acid vapor: use of sodium decanoate, *Corros. Sci.* **46** (3) (2004), 653–665.

[6] R. BROWN, *The design of a potentiostat for electrochemical research*, University of Idaho, 1961, 1–39.

[7] G. CHRISTIAN, *Analytical chemistry*, 5th, John Wiley & Sons, 1994, 385–386.

[8] A. BOND et al., *Electroanalytical methods*, ed. by F. SCHOLZ, 2nd, Springer, 2010, 137.

[9] D. HARRIS, *Voltammetry*, 4th, W.H. Freeman and Company, 1995, chap. 18, 503–505.

[10] A. SEVCIK, Oscillographic polarography with periodical triangular voltage, *Collect. Czech. Chem. Commun.* **13** (1948), 349–377.

[11] J. RANDLES, A cathode ray polarograph. II. The current-voltage curves, *Trans. Faraday Soc.* **44** (1948), 327–338.

[12] D. GOSSER, *Cyclic voltammetry: Simulation and analysis of reaction mechanisms*, 1st, VCH Publishers, 1993, 42–46.

[13] R. COMPTON and C. BANKS, *Cyclic voltammetry at macroelectrodes*, World Scientific, 2007, chap. 4, 107–156.

[14] E. MCCAFFERTY, Validation of corrosion rates measured by the Tafel extrapolation method, *Corros. Sci.* **47** (12) (2005), 3202–3215.

[15] G. BURSTEIN, A hundred years of Tafel's equation: 1905-2005, *Corros. Sci.* **47** (12) (2005), 2858–2870.

[16] M. PERIASSAMY and P. KRISHNASWAMY, Corrosion rate and Tafel slopes from polarization curves, *J. Electroanal. Chem. Interf. Electrochem.* **61** (3) (1975), 349–352.

[17] J. TAFEL, Kathodenpotential und elektrolytische Reduktion in schwefelsaurer Lösung, *Z. Electrochem.* **12** (7) (1906), 112–122.

[18] N. PEREZ, *Electrochemistry and corrosion science*, Springer Science, 2004, 3.

[19] P. RIEGER, *Electrochemistry*, Prentice-Hall International, 1987, 325–327.

[20] W. LORENZ and F. MANSFELD, Determination of corrosion rates by electrochemical DC and AC methods, *Corros. Sci.* **21** (1981), 647–672.

[21] B. SCHOTTE, A study of the electrolytic reduction of corroded lead objects and the application, characterization and testing of a protective lead carboxylate coating, PhD thesis, Ghent University, 2007, 12–13.

[22] D. HAMILTON, U.S. NAVAL HISTORICAL CENTER, and LEGACY RESOURCES MANAGEMENT PROGRAM, *Lead, tin and lead alloys*, U.S. Department of Defense, 1996, 85–87.

[23] AMERICAN SOCIETY FOR TESTING AND MATERIALS, *Standard test method for corrosion test engine coolants in glassware, ASTM standard D1384-87*, American Society for Testing and Materials, ASTM, 1988.

[24] E. ABD EL AAL, S. ABD EL WANEES, and A. ABD EL AAL, Anodic behavior and passivation of a lead electrode in sodium carbonate solutions, *J. Mater. Sci.* **28** (10) (1993), 2607–2614.

[25] S. ABD EL REHIM et al., Potentiodynamic and cyclic voltammetric behaviour of a lead electrode in NaOH solution, *Monatsh. Chem. Chem. Mon.* **128** (3) (1997), 245–254.

[26] K. RAJESHWAR and J. IBANEZ, *Environmental electrochemistry: Fundamentals and applications in pollution sensors and abatement*, 1997, 164.

[27] S. WONG and L. ABRANTES, Lead electrodeposition from very alkaline media, *Electrochim. Acta* **51** (4) (2005), 619–626.

[28] E. MERCK, *Merck index*, 12th, Merck, 1996, 5452.

[29] M. DOWSETT et al., In-situ spectroelectrochemical study of the growth process of a lead decanoate coating as corrosion inhibitor for lead surfaces, *Surf. Interface Anal.* **41** (7) (2009), 565–572.

[30] R. PEREIRA, A. VALENTE, and H. BURROWS, The interaction of long chain sodium carboxylates and sodium dodecylsulfate with Pb(II) ions in aqueous solutions, *J. Colloid Interface Sci.* **414** (2014), 66–72.

[31] H. ELLIS et al., A room temperature structure for anhydrous lead(II) decanoate, *J. Mol. Struct.* **642** (1-3) (2002), 71–76.

[32] A. ARENAS et al., Thermophysical study of lead(II) n-alkanoates by DSC, optical microscopy, FTIR and Raman spectroscopy, *Liq. Cryst.* **18** (3) (1995), 431–441.

[33] C. BAZUIN et al., Thermotropic polymorphism in liquid-crystalline lead(II) alkanoates, *Liq. Cryst.* **3** (12) (1988), 1655–1670.

[34] J. HERMANS et al., The molecular structure of three types of long-chain Zn(II) alkanoates for the study of oil paint degradation, *Polyhedron* **81** (2014), 335–340.

[35] P. TAHERI et al., Molecular interactions of electroadsorbed carboxylic acid and succinic anhydride monomers on zinc surfaces, *J. Phys. Chem. C* **115** (34) (2011), 17054–17067.

[36] F. MARTINEZ CASADO et al., Intermediate rotator phase in Lead(II) alkanoates, *J. Phys. Chem. C* **111** (18) (2007), 6826–6831.

[37] D. CHAPMAN, The polymorphism of glycerides, *Chem. Rev.* **62** (5) (1962), 433–456.

[38] L. ROBINET and M. CORBEIL, The characterization of metal soaps, *Stud. Conserv.* **48** (1) (2003), 23–40.

[39] V. ZELEŇÁK, Z. VARGOVÁ, and K. GYÖRYOVÁ, Correlation of infrared spectra of Zn(II) carboxylates with their structures, *Spectrochim. Acta Mol. Biomol. Spectros.* **66** (2) (2007), 262–272.

[40] P. NELSON and R. TAYLOR, Theories and experimental investigations of the structural and thermotropic mesomorphic phase behaviors of metal carboxylates, *Appl. Petrochem. Res.* **4** (3) (2014), 253–285.

[41] R. KONRADI and J. RÜHE, Interaction of poly(methacrylic acid) brushes with metal ions: An infrared investigation, *Macromolecules* **37** (18) (2004), 6954–6961.

[42] K. NAKAMOTO and P. MCCARTHY, *Infrared spectroscopy*, Wiley, 1968, 216–382.

[43] E. VAN DEN BERGHE, G. VAN DER KELEN, and J. ALBRECHT, Study of the structure of trimethyl-tinhaloacetates by NMR and IR spectroscopy, *Inorg. Chim. Acta* **2** (1968), 89–92.

[44] T. ISHIOKA et al., Vibrational spectra and structures of zinc carboxylates. I. Zinc acetate dihydrate, *Spectrochim. Acta Mol. Biomol. Spectros.* **54** (1998), 1827–1836.

[45] N. ALCOCK, V. TRACY, and T. WADDINGTON, Acetates and acetato-complexes. II. Spectroscopic studies, *J. Chem. Soc., Dalton Trans.* **21** (21) (1976), 2243–2246.

[46] G. DEACON and R. PHILIPS, Relationships between the carbon-oxygen stretching frequencies of carboxylato complexes and the type of carboxylate coordination, *Coord. Chem. Rev.* **33** (1980), 227–250.

[47] W. LEWANDOWSKI et al., The influence of selected metals on the electronic system of biologically important ligands, *Spectrochim. Acta Mol. Biomol. Spectros.* **59** (14) (2003), 3411–3420.

[48] K. NAKAMOTO et al., Infrared spectra of metallic complexes. IV. Comparison of the infrared spectra of unidentate and bidentate metallic complexes, *J. Am. Chem. Soc.* **79** (18) (1957), 4904–4908.

[49] K. PATIL et al., Infrared spectra and thermal decompositions of metal acetates and dicarboxylates, *Can. J. Chem.* **46** (2) (1968), 257–265.

8

Deposition method comparison for a lead dodecanoate coating

Reprinted from Prog. Org. Coat., 74 (1), M. De Keersmaecker, K. De Wael and A. Adriaens, The use of lead dodecanoate as an environmentally friendly coating to inhibit the corrosion of lead objects: comparison of three different deposition methods, 1-7, 2012, with permission from Elsevier.

8.1 Single-sine electrochemical impedance spectroscopy

In this chapter, we report new techniques for the deposition of a coating on lead artifacts starting from a sodium dodecanoate solution. However, instead of using linear polarization (a DC technique) for testing the protective properties of the coating, we started to use single-sine electrochemical impedance spectroscopy (an AC technique). As described in the following part, this technique gives us much more information about the coating's water absorption, the thickness, protective behavior, capacitive and resistive behavior, etc.

8.1.1 Basic concepts

Electrochemical impedance spectroscopy (EIS) is a powerful method for characterizing the electrochemical properties of materials. These special properties can give information about chemical reaction and diffusion coefficients of species through a given medium or at an interface. In the following part, we will present a relatively brief introduction of the technique: its principles, the measurement techniques and the necessity of data validation and the data analysis. For more detailed information on impedance spectroscopy, see Barsoukov and Macdonald [1] or Orazem and Tribollet [2], which both provide a complete overview of the technique.

Basically, a sinusoidally varying potential is applied to the system, often in addition to a constant direct potential (often the OCP). As real world phenomena are represented by the real part of the complex number, the time dependent potential signal can be written as [2]

$$\mathbf{E}(t) = \Delta E \cos(\omega t), \tag{8.1}$$

where $\mathbf{E}(t)$ is the instantaneous value and the ΔE is the amplitude of the applied sinusoidal potential. The angular frequency is $\omega = 2\pi f$, where f is the frequency of the applied signal. The amplitude should be kept small, because then most electrochemical systems behave linearly, i.e. below $\pm$ 10 mV [3] and is usually set between 5 - 10 mV [4]. The current response is usually also a sinusoidal signal, which is written as [5]

$$\mathbf{I}(t) = \Delta I \cos(\omega t + \phi), \tag{8.2}$$

where ΔI is the amplitude and ϕ is the phase difference between the applied voltage and the resulting current. The ratio between the alternating potential and its resulting current is called the impedance expressed as a complex vector [1] as shown in [6]

$$\mathbf{Z} = \frac{\mathbf{E}}{\mathbf{I}} = |\mathbf{Z}| \exp(j\phi) = Z_{\text{real}} + jZ_{\text{imag}}, \tag{8.3}$$

where Z_{real} is the real part, $j = \sqrt{-1}$ is the complex number, Z_{imag} is the imaginary part and $|\mathbf{Z}|$ is the modulus of the impedance with $|\mathbf{Z}| = \sqrt{Z_{\text{real}}^2 + Z_{\text{imag}}^2}$.
An impedance spectrum is measured over a wide range of frequencies [7], which can range from 1 mHz up to 10 MHz [6], and can be recorded at several different steady-state potentials. The data can be plotted in a Nyquist plot and a Bode plot. A Nyquist plot is constructed by placing the real (Z_{real}) and imaginary (-Z_{imag}) parts of the measured impedance values at each frequency in the complex plane. For the Bode plot, both the modulus of the transfer function $|\mathbf{Z}|$ (on a logarithmic scale) and the phase angle are plotted as a function of the logarithm of the frequency [8].

8.1.2 Data validation

Before modeling and fitting the data, it is very important to be able to distinguish between a good and bad data. The Kramers-Kronig relations [9–12] provide a first useful tool to validate impedance data. These relations state that the imaginary part is determined by the dispersion of the real part from 0 to ∞ frequency [13],

$$Z_{\text{imag}}(\omega) = \frac{2\omega}{\pi} \int_0^\infty \frac{Z_{\text{real}}(x) - Z_{\text{real}}(\omega)}{x^2 - \omega^2} \mathrm{d}x. \tag{8.4}$$

Conversely the real part is determined, apart from a constant, R_∞, by the imaginary dispersion [13],

$$Z_{\text{real}}(\omega) = R_\infty + \frac{2}{\pi} \int_0^\infty \frac{xZ_{\text{imag}}(x) - \omega Z_{\text{imag}}(\omega)}{x^2 - \omega^2} \mathrm{d}x. \tag{8.5}$$

These transforms are only valid when the following four conditions are met [14]:

- CAUSALITY: the response must be related to the excitation signal, the noise inherent to the cell and the instrumentation only.
- LINEARITY: the response must scale with the excitation signal; no second harmonics may be present. Hence with inherently non linear systems like electrodes a small excitation voltage must be used in order to stay in a linear regime.
- STATIONARITY: the system may not change with time, i.e. it must be in a steady-state condition or changing at a time scale much larger than the measurement time. The response at time t would be the same response if the measurement would be performed at time $t + \Delta t$.
- FINITE for all frequencies, including $\omega \to 0$ and $\omega \to \infty$.

The two conditions of linearity and stationarity are difficult to satisfy. In practice, EIS measurements are often performed with very small amplitude excitation signals (for reason of linearity) in the stationary regime of the process (for reason of

[1] Since the complex potential is defined as $\mathbf{E} = \Delta E\, \mathrm{e}^{j\omega t}$ and the current as $\mathbf{I} = \Delta I\, \mathrm{e}^{j(\omega t - \phi)}$, it can be calculated that $\mathbf{Z} = \frac{\mathbf{E}}{\mathbf{I}} = \frac{\Delta E}{\Delta I} \frac{e^{j\omega t}}{\mathrm{e}^{j(\omega t - \phi)}} = \frac{\Delta E}{\Delta I} \frac{\mathrm{e}^{j\omega t}}{\mathrm{e}^{j\omega t}\mathrm{e}^{-j\phi}} = \frac{\Delta E}{\Delta I}\mathrm{e}^{j\phi} = |\mathbf{Z}|\mathrm{e}^{j\phi}$.

time-invariance). As a consequence, the measurements can suffer from poor signal-to-noise ratios and will not describe the initial, mostly rapidly evolving, stages of electrochemical phenomena like e.g. corrosion processes [8, 15–17].

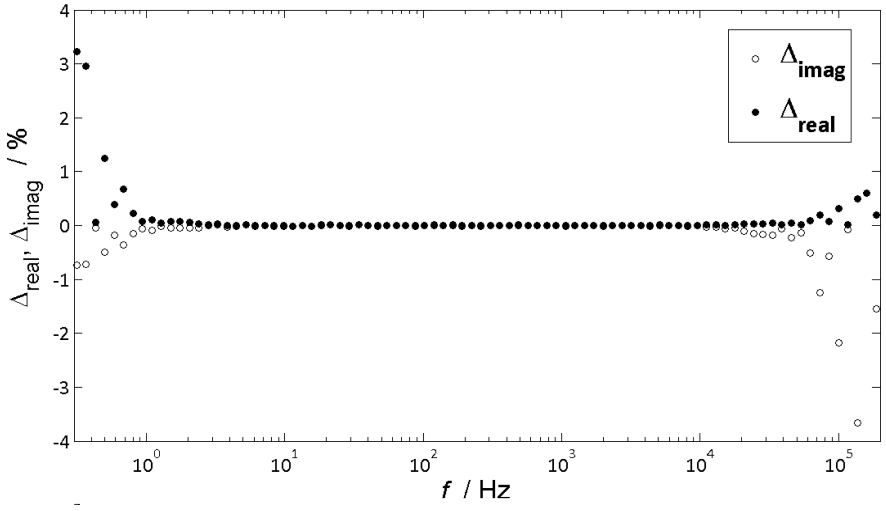


Figure. 8.1 – Residuals plot for the Kramers-Kronig validation of an EIS measurement of a polymer coating on a lead substrate.

To check whether these conditions are fulfilled, different methods are described in literature. Some studies suggest the use of measurement models to evaluate the consistency of the data by means of the previously described Kramers-Kronig relations. When the system changes during the measurement, the transforms will not match with the original data, especially in the low frequency regime. This is easily observed in a so-called residuals graph [18] where the relative differences, Δ_{real} and Δ_{imag}, described by

$$\Delta_{\text{real}}(\omega) = \frac{Z_{\text{real}}(\omega) - \text{KK}_{\text{real}}(\omega)}{|\text{KK}(\omega)|} \tag{8.6a}$$

$$\Delta_{\text{imag}}(\omega) = \frac{Z_{\text{imag}}(\omega) - \text{KK}_{\text{imag}}(\omega)}{|\text{KK}(\omega)|}. \tag{8.6b}$$

are plotted as a function of the frequency. Valid data show a random noise distribution around the frequency axis, where a clear deviation with respect to the frequency axis indicates non-KK behavior. An example is presented in Figure 8.1 where the residual plots are presented for the real and imaginary KK transform fits. It is evident that at the tips of the graph, both transforms show a distinct deviation from the zero error axis [18, 19].

Another faster and much more reliable way of validating EIS data is the use of the Z-HIT transform. This Z-HIT transform is a special form of the Hilbert transform (mathematically equivalent with the KK transform) and calculates the impedance data $Z(\omega)$ from the phase data $\phi(\omega)$ using,

$$\ln\ |H(\omega_0)| \sim C + \frac{2}{\pi}\int_{\omega_s}^{\omega_0} \phi(\omega)\ \mathrm{d}\ln\omega + \gamma \cdot \frac{\mathrm{d}\,\phi(\omega_0)}{\mathrm{d}\ln\omega}. \tag{8.7}$$

where H is the impedance modulus course and ω is the frequency of interest. The result (red line) is plotted in a graph together with the original measurement data (black circles) in Figure 8.2. By comparing the curve and the measurement data visually you are able to decide whether your object was in steady-state during measurement or not. Furthermore, the Z-HIT algorithm allows to recreate impedance data from the phase data in case a measurement was disturbed. Therefore, Z-HIT is a unique function which offers a very reliable tool to judge steady-state and treat steady-state violations in experimental data [20–23].

An alternative approach for the validation of experimental EIS data is also presented by Poprikov and Schindler [14,

24, 25]. In their work, a comparison is made between the response amplitude spectrum and the perturbation spectrum as a diagnostic tool for measurements made by means of a sum of properly defined sine waves. Pilla [26] reported a transient impedance technique in which the time domain response of an arbitrary perturbation is converted to the data in the frequency domain using a Laplace transform.

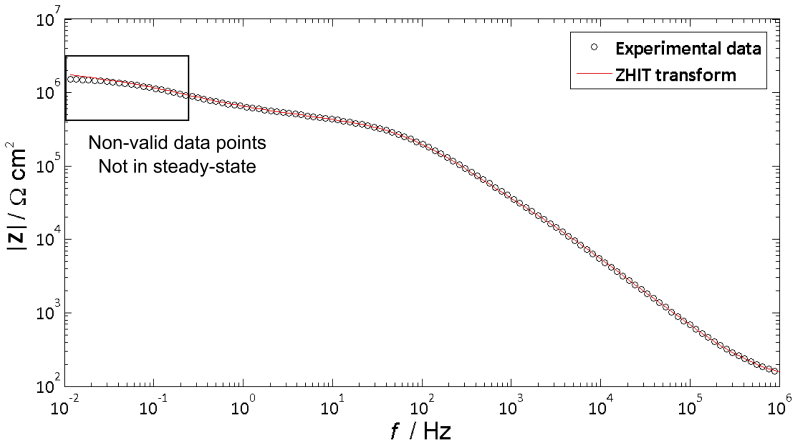


Figure. 8.2 – Z-HIT check of an EIS measurement of a polymer coating on a lead substrate.

Smyrl published a similar approach [27]. Barsoukov et al. [28] recently incorporated this technique into an electrochemical impedance spectrometer by using a variety of excitation signals such as current step, voltage step, current interrupt, and others. In chapter 12, another new approach is given, which is further used in this thesis.

8.1.3 Data modeling

After the data validation, a necessary step in the process of understanding the investigated system is the data modeling. Generally, a mathematical method is developed or an equivalent electrical circuit (EEC) is used. The first method is based on sets of equations and thus requires a profound physical knowledge of the system [29]. The latter approach proposes electrical elements to describe certain physical phenomena in the system. In this approach, experimental impedance data are compared with those stemming from an equivalent electrical circuit. However, there is no one-to-one relation between the equivalent circuit and the impedance curve. One could easily obtain a better fit by increasing the number of electrical elements in the circuit but ending-up with an even more troubling and perhaps (physically) meaningless circuit [30]. With complex systems, the determination of the correct and physical interpretable EEC is not always straightforward. For example, Fletcher [31] has presented a list of different sets of EEC's that can have exact identical dispersions. Furthermore, within the experimental error, different EEC's could yield virtually indistinguishable dispersions. To be able to find a physical interpretable EEC, almost identical systems, where one parameter has been changed such as dimension, grain size, temperature, need to be analyzed. Another way of proposing physical relevant models is the use of complementary techniques.

8.1.3.1 Basic elements

An electrochemical cell can be modeled as an equivalent circuit consisting of a combination of circuit elements like resistances, capacitors or inductances, but also some mathematical components [6]. Basically, we consider the use of an AC voltage source $\mathbf{E} = \Delta E\ \mathrm{e}^{j\omega t}$ driving a current through one of the elements by making a small basic circuit.

Resistor

In the case of a resistor, the current and voltage are related by Ohm's law, so that

$$\mathbf{I} = \frac{\mathbf{E}}{R} = \frac{\Delta E}{R} \mathrm{e}^{j\omega t}. \tag{8.8}$$

Using Ohm's law, we see that

$$\mathbf{I} = \Delta I \ \mathrm{e}^{j\omega t}. \tag{8.9}$$

The current and the potential are in phase ($\phi = 0$) and the resistance of the resistor is equal to its impedance when using an AC source.

Capacitor

A capacitor is described by

$$\mathbf{I} = C \ \frac{\partial \ \mathbf{E}(t)}{\partial t} = j\omega C \Delta E \ \mathrm{e}^{j\omega t}, \tag{8.10}$$

where C is the capacitance, **I** is the complex current and **E** is the voltage [32]. Using Ohm's law, we see that

$$\mathbf{Z} = \frac{1}{j\omega C} = -\frac{j}{\omega C}. \tag{8.11}$$

Taking the Euler representation of complex numbers $j = \mathrm{e}^{j\frac{\pi}{2}}$ we get

$$\mathbf{I} = \omega C \Delta E \ \mathrm{e}^{j(\omega t + \frac{\pi}{2})}, \tag{8.12}$$

which means the phase difference ϕ is $\frac{\pi}{2}$.

Inductor

An inductor, usually in the form of a coil, is described by

$$\mathbf{E} = L \frac{\partial \ \mathbf{I}(t)}{\partial t}, \tag{8.13}$$

exhibits an impedance given by (based on the same calculation as for the capacitor)

$$\mathbf{Z} = j\omega L. \tag{8.14}$$

where L is the inductance. Taking the Euler representation of complex numbers $j = \mathrm{e}^{j\frac{\pi}{2}}$ we get

$$\mathbf{I} = \frac{1}{\omega L} \Delta E \ \mathrm{e}^{j(\omega t - \frac{\pi}{2})}, \tag{8.15}$$

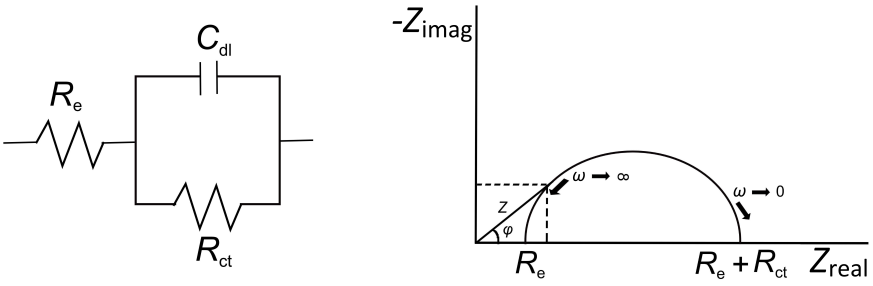
which means the phase difference ϕ is $-\frac{\pi}{2}$.

Example circuit

Most electrochemical systems, however, consist of several circuit elements connected in parallel and/or series. The total impedance of a system is calculated using the same rules as for common resistors connected in a circuit. The total impedance of two impedances in series is calculated from Eq. 8.16a, while the total impedance for two impedances in parallel is found using Eq. 8.16b [33],

$$\mathbf{Z}_{\text{tot}} = \mathbf{Z}_1 + \mathbf{Z}_2, \tag{8.16a}$$

$$\frac{1}{\mathbf{Z}_{\text{tot}}} = \frac{1}{\mathbf{Z}_1} + \frac{1}{\mathbf{Z}_2}. \tag{8.16b}$$



(a) **(b)**

Figure. 8.3 – Equivalent circuit for a simple electron transfer (a) and the corresponding Nyquist diagram (b), which is copied from [34].

As an example, the equivalent circuit for a simple electron transfer reaction is seen in Figure 8.3 (a) [34]. The circuit elements R_{u} and R_{ct} are the resistance of the electrolyte and the charge transfer resistance, respectively. For the studied redox system [2], the charge transfer resistance is coupled to the rate of electron transfer as [3]

$$R_{\text{ct}} = \left(\left. \frac{\partial I}{\partial \eta} \right|_{c_{\text{ox/red},0}} \right)^{-1} \tag{8.17}$$

where the current is determined by Eq. 6.3 as

$$I = FA\left(K_{\text{O}} c_{\text{O}}^0 - K_{\text{R}} c_{\text{R}}^0\right) \tag{8.18}$$

with F = the Faraday constant, A = the surface area, c_{O}^0 and c_{R}^0 = the initial oxidator and reductor concentrations, $K_{\text{O}} = k_{\text{c,0}} \exp \frac{-\alpha_{\text{O}} F \eta}{RT}$ and $K_{\text{R}} = k_{\text{a,0}} \exp \frac{\alpha_{\text{R}} F \eta}{RT}$ and $\eta = E - E_0 - R_{\text{u}} i$ with $R_{\text{u}} i$ being the potential drop in the solution. This leads to the following expression,

$$R_{\text{ct}} = \left(\frac{F^2 A}{RT} \left[K_{\text{O}} \alpha_{\text{O}} c_{\text{O}}^0 - K_{\text{R}} \alpha_{\text{R}} c_{\text{R}}^0 \right] \right)^{-1} \tag{8.19}$$

where R_{ct} is independent of the applied frequency. Furthermore, Figure 8.3a shows the capacitance of the double layer, C_{dl}, measured at the interface [36]. Figure 8.3b shows the Nyquist-diagram in which -Z_{imag} is plotted as a function of Z_{real}. The transfer function represents a semicircle in the complex plane which goes through the origin and has its center at the real axis at $\frac{1}{2}R$. The top of the semicircle is given by the relation $RC\omega_{\text{max}} = 1$, with $\omega_{\text{max}}^{-1} = \tau$ called the relaxation time. The transfer function can be presented as an impedance, modulus or admittance. For example, the admittance (in S or 'Siemens') is just the inverse of the impedance and emphasizes the high frequency spectrum, while the low frequency end is prominent in the impedance representation [2].

In Figure 8.3, diffusion of species is neglected. If this effect is included, the circuit is sketched in Figure 8.4a. The additional parallel element is the Warburg impedance, which comprises a series of resistance and capacitor elements [34].

[2] It has to be remarked that n is equal to 1 and is therefore left out.

[3] More information can be found in the doctoral work of S. Vandeputte [35].

In Figure 8.4b the effect of the Warburg impedance is clearly visible in the low frequency range, marked as the Warburg slope. This Warburg element will be further explained in section 8.1.3.2.

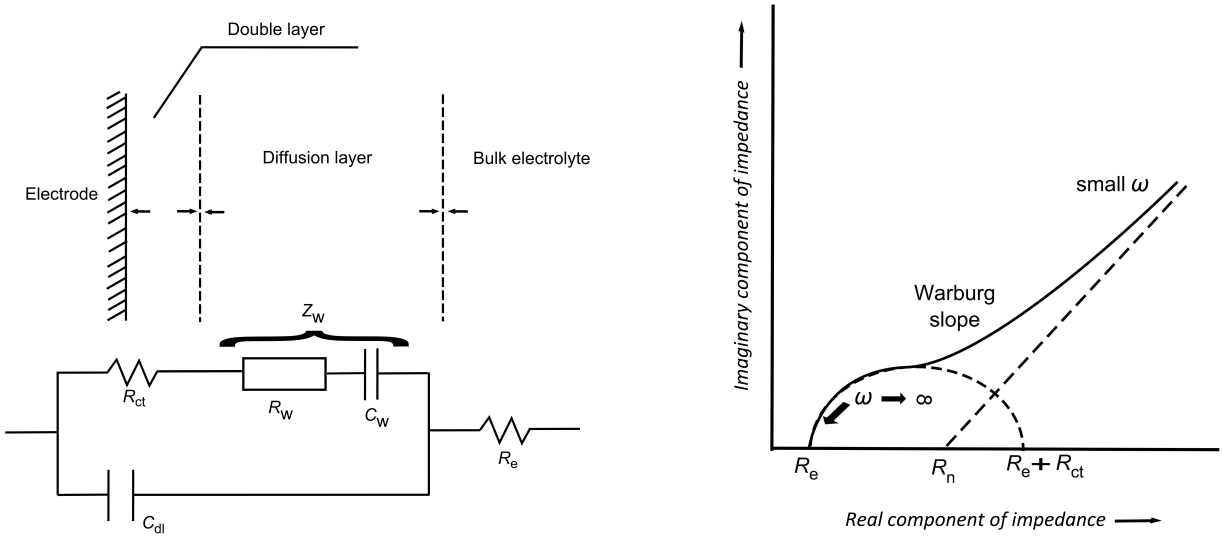


Figure. 8.4 – (a) The EEC with inclusion of diffusion element (b) The Nyquist diagram showing mixed control [34]

8.1.3.2 Diffusion elements

In general, resistances can represent various processes: ionic and electronic conductivity, grain boundary resistance and charge transfer resistance (electrode processes). Capacitive effects result from dielectric displacement, grain boundary capacitance, electrode interface and adsorption effects at electrodes. However, diffusion processes can also occur. The simplest form is the semi-infinite diffusion, where the impedance is derived directly from the Fickian laws. The current due to diffusion is given by the first Fick law in one dimension along the x-axis [38],

$$I(t) = -nFAD_{\mathrm{i}} \left.\frac{\partial\, C_{\mathrm{i}}(x,t)}{\partial x}\right|_{x=0}, \tag{8.20}$$

with F the Faraday constant, n the number of electrons, A the surface area, D_{i} the diffusion coefficient and C_{i} of species i. The second law of Fick gives the relation for planar diffusion in one dimension along the x-axis [38],

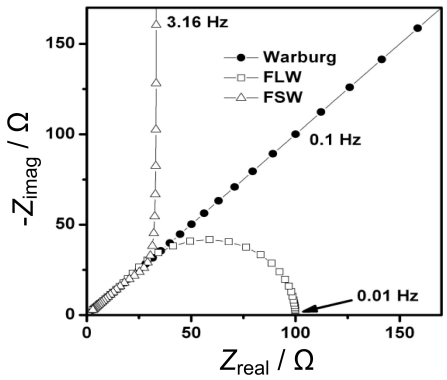


Figure. 8.5 – Impedance representations of the Warburg, Finite Length Warburg (FLW) and Finite Space Warburg (FSW). At high frequency the dispersions overlap with $Z_0 = 100\ \Omega$ for all three. Argument of FLW and FSW: $\frac{d}{\sqrt{D}} = 1$. Figure is copied from [37].

$$\frac{\partial\, C_{\mathrm{i}}(x,t)}{\partial t} = D_{\mathrm{i}} \frac{\partial^2\, C_{\mathrm{i}}(x,t)}{\partial x^2}. \tag{8.21}$$

The boundary condition for $x \to \infty$ is $\lim_{x\to\infty} C_{\mathrm{i}}(x,t) = C_{\mathrm{i}}^0$, where C_{i}^0 is the equilibrium concentration of species i. The concentration of the mobile ion is measured at the electrode/electrolyte interface with respect to a reference electrode using the Nernst equation in Eq. 2.2. When a small perturbation, ΔE, is applied, the deviation from the equilibrium

concentration is used, $\Delta C_{\mathrm{i}}(x,t) = C_{\mathrm{i}}(x,t) - C_{\mathrm{i}}^{0}$. The solution is obtained through a Laplace transformation with s as Laplace variable [5],

$$\Delta I(s) = -nFAD_{\mathrm{i}} \left.\frac{\partial\, C_{\mathrm{i}}(x,s)}{\partial x}\right|_{x=0}, \tag{8.22a}$$

$$\Delta E(s) = \frac{RT}{nFC_{\mathrm{i}}^{0}} \left[\frac{\partial \ln a_{\mathrm{i}}}{\partial \ln C_{\mathrm{i}}}\right] C_{\mathrm{i}}(x,s)|_{x=0}\,, \tag{8.22b}$$

$$s \cdot C_{\mathrm{i}}(x,s) = D_{\mathrm{i}} \frac{\partial^2\, C_{\mathrm{i}}(x,s)}{\partial x^2}, \tag{8.22c}$$

$$C_{\mathrm{i}}(x,s)|_{x\to\infty} = 0. \tag{8.22d}$$

where a is the activity of species i. The solution for the impedance in Laplace space is [5]

$$\mathbf{Z}_{\mathrm{W}}(s) = \frac{\Delta E(s)}{\Delta I(s)} = \frac{RT}{n^2F^2AC_{\mathrm{i}}^{0}\sqrt{sD_{\mathrm{i}}}} \left[\frac{\partial \ln a_{\mathrm{i}}}{\partial \ln C_{\mathrm{i}}}\right]. \tag{8.23}$$

The Laplace variable can be expressed as a complex number: $s = p + j\omega$, where p describes how the system evolves to a steady state (for $p = 0$) and ω the response to an AC-perturbation. Hence, replacing s by $j\omega$ directly yields the impedance expression [5]

$$\mathbf{Z}_{\mathrm{W}}(\omega) = \frac{RT}{n^2F^2AC_{\mathrm{i}}^{0}\sqrt{j\omega D_{\mathrm{i}}}} \left[\frac{\partial \ln a_{\mathrm{i}}}{\partial \ln C_{\mathrm{i}}}\right], \tag{8.24}$$

$$= \frac{A_{\mathrm{W}}}{\sqrt{j\omega}} = \frac{A_{\mathrm{W}}}{\sqrt{2}} \cdot \omega^{-\frac{1}{2}} \left[1 - j\right]. \tag{8.25}$$

This semi-infinite diffusion equation is known as the Warburg impedance and is presented in Figure 8.5. For finite electrochemical diffusion, with thickness d, a similar derivation can be made. The processes at the backside plane, at $x = d$, determine the shape of the transfer function. In case the backplane is impermeable for the mobile species the boundary condition at $x = d$ becomes: $\left.\frac{\partial \Delta C_{\mathrm{i}}(x,t)}{\partial x}\right|_{x=d} = 0$ and the solution is the well-known 'Finite Space Warburg' (FSW) which is typical for insertion electrodes as seen in Figure 8.5 [18],

$$\mathbf{Z}_{\mathrm{FSW}}(\omega) = \frac{A_{\mathrm{W}}}{\sqrt{j\omega}} \coth\left[d\sqrt{\frac{j\omega}{D_{\mathrm{i}}}}\right]. \tag{8.26}$$

When the concentration of the mobile species is fixed at the backside then the boundary condition is given by: $\Delta C_{\mathrm{i}}(x,t)|_{x=d} = 0$, resulting in the 'Finite Length Warburg' (FLW) known from e.g. corrosion impedances as seen in Figure 8.5 [18],

$$\mathbf{Z}_{\mathrm{FLW}}(\omega) = \frac{A_{\mathrm{W}}}{\sqrt{j\omega}} \tanh\left[d\sqrt{\frac{j\omega}{D_{\mathrm{i}}}}\right]. \tag{8.27}$$

8.1.3.3 Constant phase elements

So far the circuit elements have been based on fundamental principles and can be considered as 'ideal' transfer functions. To compensate for the inhomogeneity and the imperfectness of the system and to improve the fitting quality [39], often, a 'constant phase element' (CPE) dispersion function is used. This CPE is presented in the admittance plane by [40]

$$\mathbf{Y}_{\mathrm{CPE}}(\omega) = Y_0(j\omega)^n = (jY_0'\omega)^n = Y_0\omega^n \left[\cos\frac{n\pi}{2} + j\,\sin\frac{n\pi}{2}\right]. \tag{8.28}$$

where Y_0 is the CPE constant and n is the CPE exponent which is used as a surface heterogeneity gauge. The parallel

combination of a CPE (element symbol: Q) with a resistance presents a line with slope $n \cdot \frac{\pi}{2}$ in the admittance plane, or a depressed semicircle in the impedance plane. The CPE is a generic transfer function: for n = 1 it represents a capacitance, for n = 0 a resistance, for n = -1 an inductance and for $n = \frac{1}{2}$ the semi-infinite diffusion or Warburg impedance. Generally, values of n somewhat lower than 1 are considered as non-ideal capacitances. Values around 0.5 are assumed to represent diffusion-related responses. The origin of the CPE is still not well understood, but one should realize that in most applications of EIS, transport processes are one-dimensional where lateral influences are ignored [2]. Afterwards, the CPE values of the experimental fitting can be converted into effective capacitances, C_{eff} (approximated values) using the formula of Brug et al. [41, 42]

$$C_{\text{eff}} = \left[Y_0 R_{\text{u}}^{(1-n)}\right]^{\frac{1}{n}} \tag{8.29}$$

where R_{u} is the solution resistance.

8.1.4 Fitting procedure

In the past mainly simple graphical methods were available for the analysis of impedance or dielectric data [43–46]. However, as more complex systems were studied an increasing need for advanced data analysis methods evolved. Since the 1980s, the complex nonlinear least squares fit algorithm (CNLS) developed in the late 1960s as an extension of nonlinear least squares techniques [47–49]. Weighted CNLS was first applied to impedance data by Macdonald et al. [50, 51]. The concept of weighting is critical for impedance spectroscopy because the impedance is a strong function of frequency [19]. The regression of a complex function $\hat{\mathbf{Z}}$ to complex data $\mathbf{Z}$ can be expressed in a least-squares sense as the minimization of the sum of squares [1],

$$S = \sum_{\text{i}=1}^{N} \left[w'_{\text{i}}[Z'_{\text{i}} - \hat{Z}'_{\text{i}}(\omega_{\text{i}})]^2 + w''_{\text{i}}[Z''_{\text{i}} - \hat{Z}''_{\text{i}}(\omega_{\text{i}})]^2\right] \tag{8.30}$$

where Z'_{i} and Z''_{i} are the real and imaginary parts of the measured impedance at the frequencies ω_{i}, $\hat{Z}'_{\text{i}}(\omega_{\text{i}})$ and $\hat{Z}''_{\text{i}}(\omega_{\text{i}})$ are the values of the real and imaginary parts predicted by the model, w'_{i} and w''_{i} are statistical weights of the data, and the summation runs over all N frequencies used in the experiment.

Besides a proper model function, it is essential to have an appropriate set of starting values for the adjustable parameters. Good starting values will facilitate convergence, and poor starting values may result in convergence to a local minimum that does not represent the physics of the system. A good physical insight is necessary for selection of the initial estimates. A proven method is the so-called partial-fit and subtraction procedure which allows a stepwise deconvolution [18]. In the following part, we describe briefly the basics of the nonlinear least squares fit algorithm.

8.1.5 The complex nonlinear least squares fit algorithm

Consider a general function $f(\mathbf{P}) = 0$ that is nonlinear with respect to parameters P_{k}. Under the assumption that $f(\mathbf{P})$ is twice continuously differentiable, a Taylor-series expansion about a parameter set P_0 yield [52]

$$f(\mathbf{P}) = f(P_0) + \sum_{j}^{N_{\text{p}}} \left.\frac{\partial f}{\partial P_j}\right|_{P_0} \Delta P_j + \frac{1}{2}\sum_{j}^{N_{\text{p}}}\sum_{k}^{N_{\text{p}}} \left.\frac{\partial^2 f}{\partial P_j \partial P_k}\right|_{P_0} \Delta P_j \Delta P_k + ... \tag{8.31}$$

The minimum is found when the sum of the derivatives with respect to the parameter increments ΔP_i is equal to zero; thus

$$\frac{\partial f}{\partial \Delta P_j} = \left.\frac{\partial f}{\partial P_j}\right|_{P_0} + \sum_{k}^{N_\mathrm{p}} \left.\frac{\partial^2 f}{\partial P_j \partial P_k}\right|_{P_0} \Delta P_k = 0. \tag{8.32}$$

Equation 8.32 represents a set of N_P equations of the form [2]

$$\beta_j = \sum_{k}^{N_\mathrm{p}} \alpha_{j,k} \Delta P_k, \tag{8.33}$$

with $\beta_j = -\frac{1}{2} \left.\frac{\partial f}{\partial P_j}\right|_{P_0}$ and $\alpha_{j,k} = \frac{1}{2} \left.\frac{\partial^2 f}{\partial P_j \partial P_k}\right|_{P_0}$. Converting this into a matrix form, this becomes

$$\boldsymbol{\beta} = \boldsymbol{\alpha} \cdot \boldsymbol{\Delta P}. \tag{8.34}$$

The general formation described above can be applied to the nonlinear least squares problem, which involves minimization of the function [52]

$$\chi^2 = \sum_{i=1}^{N_\mathrm{dat}} \frac{\left(Z_i - \hat{Z}(x_i|\mathbf{P})\right)^2}{\sigma_i^2}, \tag{8.35}$$

where Z_i represents the measured values, $\hat{Z}(x_i|\mathbf{P})$ represents the model and σ_i^2 represents the standard deviation of measurement i. Under the understanding that the function f needs to be minimized is given by Eq. 8.35, the gradient of the objective function with respect to parameters **P** is given by [2]

$$\frac{\partial \chi^2}{\partial P_k} = -2 \sum_{i=1}^{N_\mathrm{dat}} \frac{\left(Z_i - \hat{Z}(x_i|\mathbf{P})\right)^2}{\sigma_i^2} \frac{\partial \hat{Z}(x_i|\mathbf{P})}{\partial P_k} = -2\beta_k \tag{8.36}$$

The second derivative of the objective function with respect to the parameters **P** is given by the Hessian matrix [2],

$$\left.\frac{\partial^2 \chi^2}{\partial P_j P_k}\right|_{P_0} = 2 \sum_{i=1}^{N_\mathrm{dat}} \frac{1}{\sigma_i^2} \left[\frac{\partial \hat{Z}(x_i|\mathbf{P})}{\partial P_j} \frac{\partial \hat{Z}(x_i|\mathbf{P})}{\partial P_k} - \left(Z_k - \hat{Z}(x_i|\mathbf{P})\right) \frac{\partial^2 \hat{Z}(x_i|\mathbf{P})}{\partial P_j P_k} \right]. \tag{8.37}$$

The matrix $\boldsymbol{\alpha}$ is equal to one-half of the Hessian matrix. Furthermore, the second derivatives of the Hessian matrix are typically neglected in evaluation of Eq. 8.37, because they are often smaller than the first derivatives. A second reason is that the second derivative term is multiplied by $(y_k - y(x_i|\mathbf{P}))$, a term that, for a successful regression, should be uncorrelated with respect to x_i or to the model $y(x_i|\mathbf{P})$. Accordingly [2],

$$\alpha_{j,k} = \sum_{i=1}^{N_\mathrm{dat}} \frac{1}{\sigma_i^2} \left[\frac{\partial \hat{Z}(x_i|\mathbf{P})}{\partial P_j} \frac{\partial \hat{Z}(x_i|\mathbf{P})}{\partial P_k} \right], \tag{8.38}$$

is used in the nonlinear regression algorithms. Present mathematics, however, describes different methods to solve this nonlinear set of equations. A first method, called the Gauss-Newton method, solves the following matrix [53]

$$\mathbf{P}_{j,l+1} = \mathbf{P}_{j,l} + \boldsymbol{\alpha}^{-1} \cdot \boldsymbol{\beta}, \tag{8.39}$$

where l is the iteration counter, $\boldsymbol{\beta}$ is evaluated following Eq. 8.36, and $\boldsymbol{\alpha}$ is evaluated following Eq. 8.38. The Gauss-Newton method is characterized by quadratic convergence near the solution, but convergence can be very slow far from the solution. Sometimes, the Gauss-Newton method diverges and fails to yield a solution. Most of the times, this method provides the basis for most methods of nonlinear optimization. The method of the steepest descent, on the other hand,

seeks a minimum value of the objective function by following the gradient of the objective function [54, 55], i.e.

$$\mathbf{P}_{j,l+1} = \mathbf{P}_{j,l} + \lambda\boldsymbol{\beta}, \tag{8.40}$$

where l is the iteration counter, $\boldsymbol{\beta}$ is evaluated following Eq. 8.36, and λ is a constant chosen to be sufficiently small as to avoid overrunning the minimum. This method tends to be quite efficient far from the solution, but convergence can be painfully slow near the solution. A last method, called the Levenberg-Marquardt method, represents a compromise between the Gauss-Newton method and the method of the steepest descent. The method of the steepest descent is used far from the converged value, moving smoothly to the Gauss-Newton method as the solution is approached. The critical concepts are the selection of the scaling factor for the method of the steepest descent and an approach for making a smooth transition from one method to the other. The matrix $\boldsymbol{\alpha}$ is replaced by $\boldsymbol{\alpha}'$ such that [56]

$$\boldsymbol{\alpha}'_{jk} = \boldsymbol{\alpha}_{jk}(1+\lambda) \qquad \text{for} \quad j = k, \tag{8.41a}$$

$$\boldsymbol{\alpha}'_{jk} = \boldsymbol{\alpha}_{jk} \qquad \text{for} \quad j \neq k. \tag{8.41b}$$

Using $\boldsymbol{\alpha}'$, Eq. 8.39 is solved, which means that when λ is large, $\boldsymbol{\alpha}'$ is diagonally dominant, and the method approaches that described in Eq. 8.39 and when λ is small, the method approaches Eq. 8.40.

8.2 Deposition techniques

In Rocca et al. [57] and in the PhD thesis of Schotte [58], the deposition is done using the immersion technique. However, this is not the only possible method to produce a coating. In this work, a comparison is made between immersion and electrochemical treatments. Table 8.1 shows the different procedures carried out in a 0.05 mol L^{-1} NaC_{12} solution (see section 7.3.1). The electrochemical treatments are performed using a PGSTAT 100 potentiostat/galvanostat controlled by the GPES 4.9.005 software package (Autolab, The Netherlands) in a three-electrode cell provided with a saturated calomel reference electrode (SCE) containing two compartments (Radiometer Analytical, France), a carbon counter electrode and a polished (see procedure in section 4.2) lead (diameter = 6 mm; purity = $>$ 99.99%; Goodfellow, Cambridge, UK) working electrode embedded in an epoxy resin.

PROCEDURE	METHOD	DESCRIPTION
CV	Cylic voltammetry	Record 5 successive scans in a potential window from -1.3 V to 1.5 V vs SCE with a scan rate of 50 mV s^{-1} [59]
AMP	Amperometry	Record an amperometric scan at 0.2 V during 2,000 s
IMM	Immersion	Hang the lead surface of the electrode in the solution during 2,000 s
AMP-IR	Amperometry with initial reduction step	Run procedure AMP preceded by a cathodic polarization at -1.5 V during 600 s
IMM-IR	Immersion with initial reduction step	Run procedure IMM preceded by a cathodic polarization at -1.5 V during 600 s

Table 8.1 – Description of the different modification procedures used to deposit a lead dodecanoate coating on lead electrode surfaces method.

The initial reduction was used to reduce all lead corrosion products. A reduction potential of -1.5 V vs. SCE was chosen

to avoid hydrogen evolution. The cyclic voltammetry procedure does not need an initial reduction step because the lead surface is already reduced during the first backward scan. The lead dodecanoate coatings were rinsed with distilled water and air-dried before further analysis.

8.3 Electrochemical evaluation of lead dodecanoate coatings

The coatings on lead produced based on the previous described deposition techniques are analyzed using EIS in an ASTM D 1384-87 solution (see section 7.3.1). The EIS spectra were acquired within a 1 MHz - 10 Hz frequency range, applying at the corrosion potential a 10 mV sinusoidal AC perturbation. The frequency range 1 MHz - 1 Hz was distributed logarithmically across the first 120 points in each spectrum and the range 1 - 0.01 Hz across the final 10 points. The impedance measurements were performed using a PGSTAT20 instrument with a FRA2 frequency response analysis module controlled by the GPES/FRA 4.9.005 software package (both ECO Chemie, The Netherlands). In what follows, we present and analyze the inhibition properties of the coatings based on the method used.

8.3.1 Influence of the initial reduction step

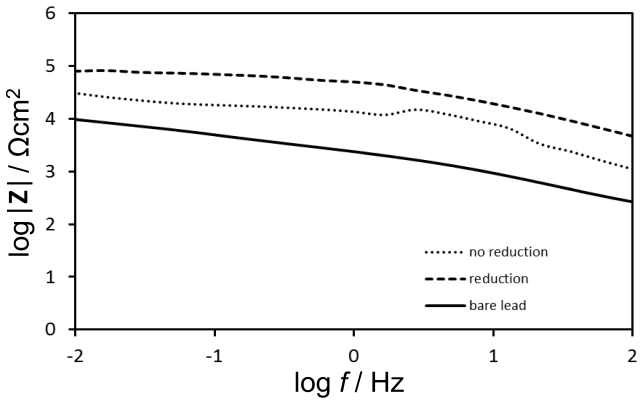


Figure. 8.6 – EIS plots of a lead dodecanoate modified lead surface (AMP) with and without an initial reduction step of the surface at -1.5 V during 600 s recorded in an ASTM D 1384-87 solution.

Figure 8.6 shows the electrochemical impedance measurements of a bare lead and a lead dodecanoate modified lead sample with (AMP-IR) and without (AMP) the initial reduction step. The impedance plot of the coating formed by performing an initial reduction step shows higher absolute impedance values, which indicates an increase of the coating's corrosion resistance. Furthermore, comparing both coated surfaces with the bare lead surface, it is seen that an initial reduction step improves the film's corrosion resistance by a factor 2 as seen in Figure 8.6. Testing the initial reduction using the IMM and IMM-IR procedures, we obtained similar results. The initial reduction step consequently improves the coating's formation and the corrosion resistance.

8.3.2 Fitting of the impedance data

Figure 8.7 shows the impedance modulus plot (a), the phase plot (b) and Nyquist plot (c) of the coated lead electrodes in an ASTM solution. The electrodes were coated using the procedures CV, AMP-IR and IMM-IR in a NaC_{12} solution as described in Table 8.1. For comparison the plot of the bare lead sample is given. Comparing the impedance vs frequency plots in Figure 8.7a, one can conclude that the impedance points for the treated surfaces are higher compared to those of the bare surface. This indicates that the total resistance of the coatings is higher compared to the bare sample, which proves all inhibition treatments worked. Figure 8.7b shows one well-defined time constant in the mid-frequency range

(1 - 10^3 Hz) for the bare sample in the phase angle plot, which defines a capacitive behavior caused by the double-layer. The phase angle diagram of the CV and ATR-IR sample are similar to that of the bare lead surface. The increase (with respect to the frequency axis of the curve) and the broadening and shifting of the capacitive loop, in comparison with to the untreated surface, validates the presence of a coating. The plots of the IMM-IR deposited sample shows a broad phase distribution, which indicates that a more protective barrier is formed.

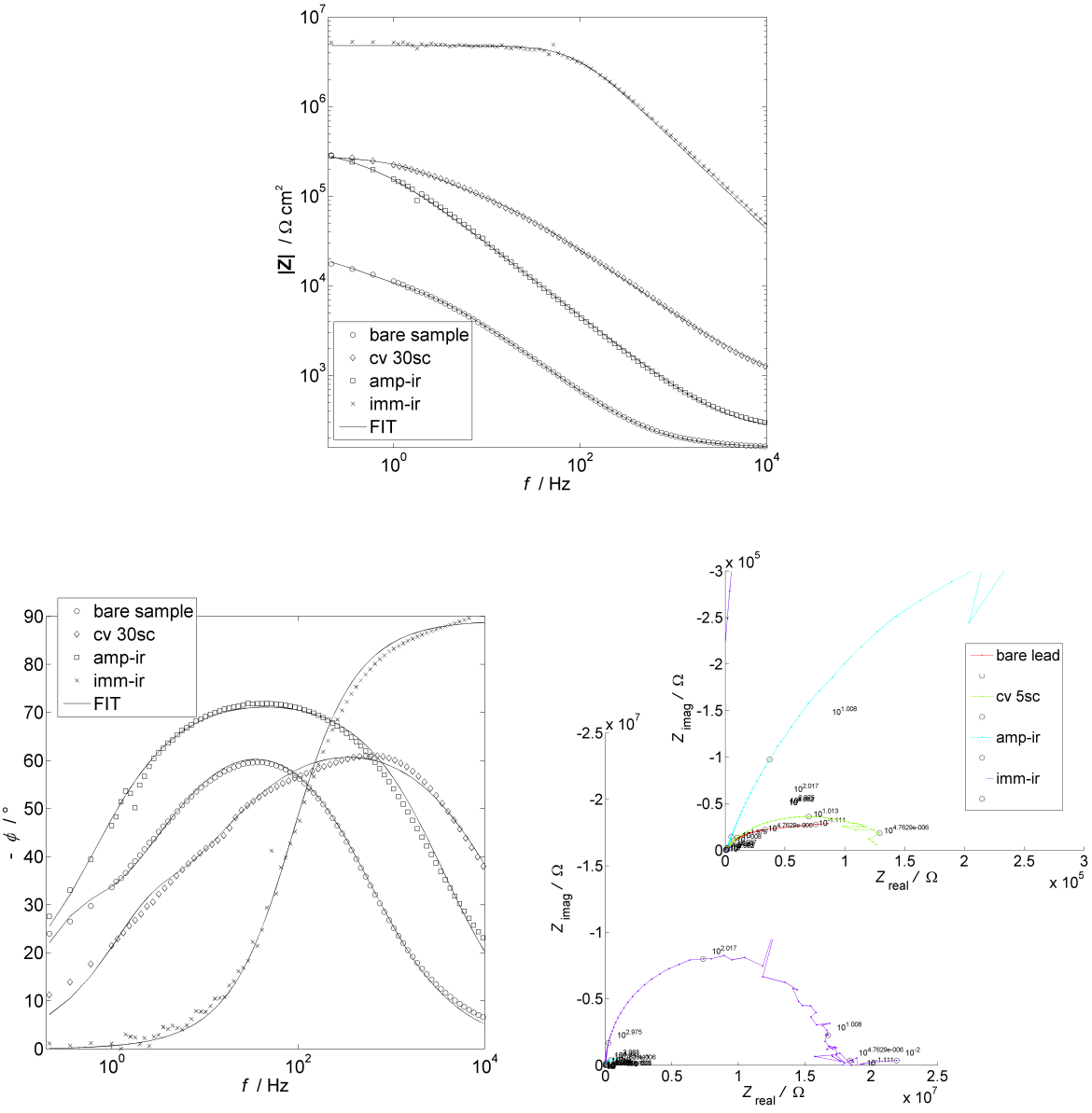


Figure. 8.7 – Electrochemical impedance plots of coated lead electrodes with initial reduction step recorded in ASTM D 1384-87 solution: (a) impedance plot, (b) phase angle plot and (c) Nyquist plot.

All electrochemical impedance measurements recorded in the ASTM solution were simulated using an EEC of four elements, as shown in Figure 8.8. This model includes the solution resistance, R_u, in series with a parallel combination of a CPE for the double-layer capacitance, Q_{dl}, and the charge-transfer resistance, R_{ct} combined with a finite diffusion element caused by the corrosion reaction, W_{corr}. The use of the constant phase elements is described in section 8.1.3.3. Using the fitted R_{ct} values, the inhibition efficiency is calculated using the following relationship [64],

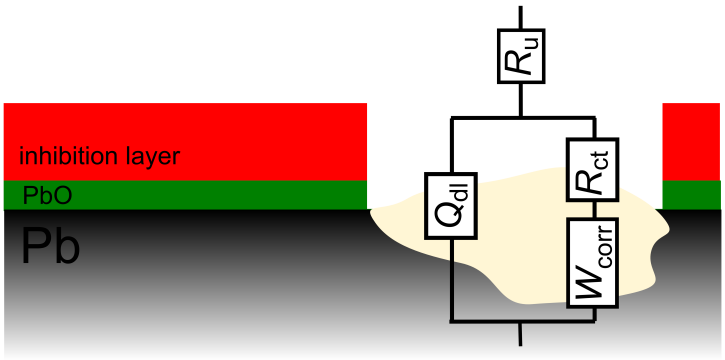


Figure. 8.8 – Electric circuits used to simulate the recorded impedance spectra [60–63].

$$\eta_{IE}(\%) = \frac{R_{ct} - R_{ct}^0}{R_{ct}} \times 100, \tag{8.42}$$

where R_{ct} and R_{ct}^0 are the charge transfer resistances in the presence and absence of the dodecanoate inhibitor, respectively.

METHOD	ELECTROCHEMICAL IMPEDANCE PARAMETERS						
	E_{corr} / V vs SCE	R_u / Ω cm^2	R_{ct} / Ω cm^2	R_W / Ω cm^2	$C_{eff,dl}$ / F cm^{-2}	η_{IE} (%)	χ^2 value
bare lead	-0.558	158 ± 1	11830 ± 80	11200 ± 700	$1.82 \times 10^{-6} \pm 2 \times 10^{-8}$	-	521
CV	-0.498	660 ± 10	159000 ± 900	130000 ± 40000	$1.68 \times 10^{-8} \pm 4 \times 10^{-10}$	92.5 ± 0.5	23772
AMP[1]IR[2]	-0.495	240 ± 6	320000 ± 6000	63489	$1.85 \times 10^{-7} \pm 3 \times 10^{-9}$	96.3 ± 2	28281
IMM[3]IR[2]	-0.490	200 ± 100	$4.8 \times 10^7 \pm 1 \times 10^6$	-	$3.5 \times 10^{-10} \pm 2 \times 10^{-11}$	99.7 ± 2	3.6×10^6

[1] Amperometric deposition at 0.2 V during 2,000 s.

[2] Initial reduction at -1.5 V during 600 s.

[3] Deposition using immersion during 2,000 s.

Table 8.2 – Electrochemical impedance parameters for different lead dodecanoate coatings in an ASTM D 1384-87 solution deposited using different methods in a 0.05 M NaC_{12} solution.

Table 8.2 shows the extracted EIS parameters for the different lead dodecanoate coatings plotted in Figure 8.7. The data show that the deposition method has a big influence on the corrosion resistance. The noise on the IMM-IR impedance data explains the increased goodness-of-fit, χ^2, value. The R_{ct} value increases depending on the method, because a larger area of the surface is blocked by the lead dodecanoate coating. The inhibition efficiencies are significantly different depending on the method. The data reveal that the R_{ct} value and the double layer capacitance, $C_{eff,dl}$, vary in inverse proportion, which is attributed to the formation of a protective film [65]. Following this reasoning, we can conclude the immersion method leads to the most corrosion-resistant layers, followed by amperometry and cyclic voltammetry. The formation of a more corrosion resistant layer using the immersion method compared to cyclic voltammetry and amperometry method can be easily explained, because this method does not force the deposition by applying a certain voltage. The immersion allows the slow formation of lead dodecanoate complexes and the production of well-shaped and ordered crystals on the lead surface [66, 67]. Well-ordered and better formed crystals can protect the bare lead surface much better against corrosion attacks. Cyclic voltammetry and amperometry oxidize the lead surface to form lead ions and forces a fast deposition.

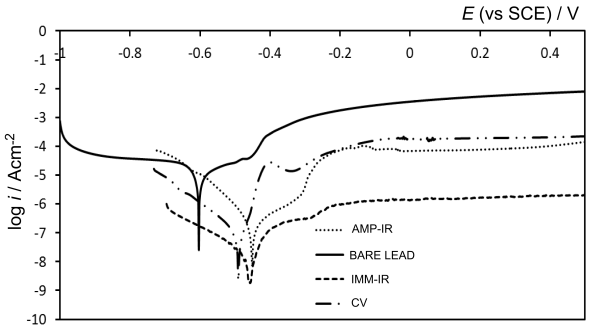


Figure. 8.9 – The potentiodynamic polarization curves of coated lead electrodes with initial reduction step recorded in ASTM D 1384-87 solution.

8.3.3 Evaluation of the potentiodynamic polarization data

Figure 8.9 show the potentiodynamic polarization curves based on section 7.2.3 recorded in a potential window of -0.25 V to 1.3 V vs OCP with a scan rate of 1 mV s^{-1} in an ASTM solution. The plots show a shift of the anodic polarization curve to much lower current density values (more than a factor 10 for CV and IMM-IR) compared to that of the untreated lead. This phenomenon can be explained by the inhibition effect of the lead dodecanoate coating, which influences the dissolution process of the lead [68]. The potentiodynamic polarization curve of the IMM-IR sample shows a lower current density and a higher corrosion resistance compared to the other two, which confirms our EIS measurements. After the dodecanoate modification, we observe that the OCP values in the ASTM solution shift to a more anodic potential compared to the bare lead. This considerable shift of the OCP by ca. 0.068 V to more positive values can be explained by considering a lead dodecanoate film. This dodecanoate anion inhibitor causes a reaction with the lead metal and surface inactivation due to the hydrophobic character of the tail. As a result, a decrease is observed in the corroded surface area in the aqueous ASTM environment [69].

METHOD	POTENTIODYNAMIC POLARIZATION PARAMETERS				
	E_{corr} / V vs SCE	i_{corr} /μA cm^{-2}	β_c / mV	β_a / mV	η_{IE} (%)
bare lead	-0.558	6.91	60	124	-
AMP[1](IR)[2]	-0.516	0.937	114	189	86 ± 3
CV	-0.490	0.523	65	118	92 ± 2
IMM[3](IR)[2]	-0.475	0.00537	81	251	99 ± 1

[1] Amperometric deposition at 0.2 V during 2000 s.

[2] Initial reduction at -1.5 V during 600 s.

[3] Deposition using immersion during 2000 s.

Table 8.3 – Potentiodynamic polarization parameters for different lead dodecanoate coatings in an ASTM D 1384-87 solution deposited using different methods in a 0.05 M NaC_{12} solution.

The electrochemical polarization parameters for the lead dodecanoate coatings deposited using different methods in an ASTM solution are listed in Table 8.3. The parameters include the corrosion potentials E_{corr}, the current densities i_{corr} and the anodic (β_a) and cathodic (β_c) Tafel constants as well as the inhibition efficiencies η_{IE} (%). The inhibition efficiency based on the Tafel measurements is calculated using the following relationship [68],

$$\eta_{\mathrm{IE}}(\%) = \left(1 - \frac{i_{\mathrm{corr}}}{i^0_{\mathrm{corr}}}\right) \times 100. \tag{8.43}$$

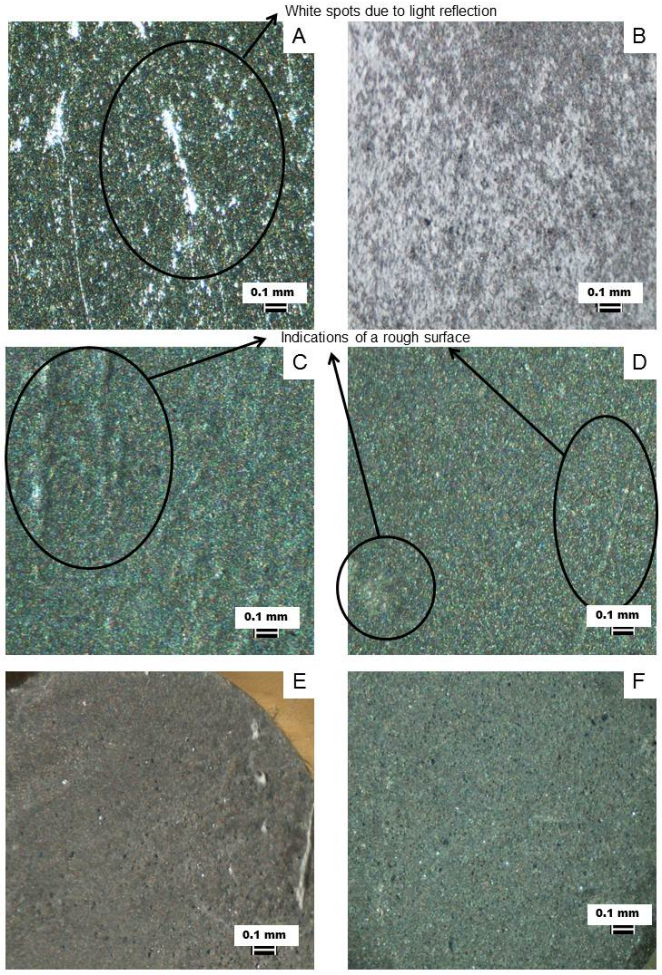


Figure. 8.10 – Optical images obtained from a bare lead electrode (A) and lead dodecanoate modified lead electrodes: (B) cyclic voltammetry (procedure CV), (C) amperometry (procedure AMP), (D) immersion (procedure IMM), (E) amperometry with an initial reduction step (procedure AMP-IR) and (F) immersion with an initial reduction step (procedure IMM-IR).

The corrosion current density, i_{corr}, values, show lower values (ca. a factor 50) for the coated surfaces in comparison to the bare lead. This significant decrease confirms the presence of a protective layer, thereby confirming the EIS measurements. Table 8.3 shows that the anodic Tafel slopes are higher compared to the cathodic Tafel slopes, which means the anodic current increases fast when the potential becomes slightly higher than the OCP. When the lead dodecanoate coating is more protective, this increase will be faster and start at a higher potential. The inhibition efficiency values of the potentiodynamic polarization curves are low compared to the ones obtained by EIS measurements, although they follow the same trend. This could be attributed to the predominant influence of the anodic dissolution process in determining the corrosion rate with Tafel analysis [70].

8.4 Visual comparison of the coatings

Figure 8.10 shows the optical images of a bare lead surface (A) and of lead dodecanoate modified lead surfaces (B - F). The bare lead surface shows big white spots, which are due to the reflection of the light on the bright lead surface. The optical images of the modified surfaces in Figure 8.10B - F show a dull surface covered with small crystals due to the formation of the lead salt. In addition, each modified surface seems to look quite different. Figure 8.10B shows white areas, which means that unreacted sodium carboxylate reagent is present on the coated surface due to precipitation. Figure 8.10C and D shows rough surfaces and very small surface defects covered with a coating. A possible explanation is the fact that our polished lead surfaces are not smooth enough for a homogeneous coverage. Therefore, attention is given to the use of the initial reduction step, i.e. a pretreatment of the surface. Figure 8.10E and F shows the results of this pretreatment. Figure 8.10E, using the AMP-IR procedure, shows a dark lead colored surface, which can be explained by assuming the formation of a smooth and fully covering coating on the lead surface. Figure 8.10F, using the IMM-IR procedure, reveals a smooth surface with almost no defects. The images clearly demonstrate that the surface of the coating is dependent on the deposition method used, which allows us to make assumptions about the corrosion resistance as already predicted by our corrosion measurements.

8.5 Reproducibility of the lead dodecanoate coating

Measuring five other lead dodecanoate films deposited using the IMM-IR method in an ASTM solution using impedance spectroscopy showed us that the inhibition efficiency was 99.7% $\pm$ 0.3. This means that we have a method to produce a reproducible coating. However, in chapter 9, a more profound study is done on the topic of reproducibility. All different lead dodecanoate layers seem to protect and cover the lead surface in a similar way. This means the initial reduction step of the lead surface does not only provide a well-protected surface, but also enhances the reproducibility of our lead dodecanoate coating. We assume the initial reduction step initially levels the lead surface not only due to the reduction of lead corrosion products, but also due to the redistribution of the freshly polished lead metal. The reduction activates the lead surface so that an initial faster adsorption of the lead dodecanoate can take place, which states a faster production of the inhibition layer [59]. The lead dodecanoate layer deposited after the reduction process protects the metal much better because we start with a leveled surface, which makes sure that the coating is less susceptible to defects [71].

8.6 Conclusions

In this work, sodium dodecanoate was deposited as a corrosion protective coating onto a lead surface using three different deposition methods: immobilization of the inhibitor molecules on the lead electrode using cyclic voltammetry, immersion and amperometry. Apart from this, we tested a reduction pretreatment of the lead surface (-1.5 V during 600 s) in order to obtain more reproducible coatings. Results show the reduction of the lead surface before the deposition of the layer improves the corrosion resistance of the coating. The most protective coatings are produced using the immersion method with an initial reduction step (IMM-IR), followed by amperometry (AMP-IR) and cyclic voltammetry (CV). The immersion method does not force the formation of lead ions, which allows the formation of well-ordered lead dodecanoate crystals. This is not the case when depositing the layer using voltammetry (CV) or amperometry (AMP-IR). Here the electrochemical treatment forces the formation of lead complexes not providing time to form ordered crystals. Finally, another advantage of using the initial reduction method is the improvement of the reproducibility of the coatings. The reduction levels the polished surfaces and provides each time almost the same initial surface, which determines, to a large extent, the quality of the deposited lead dodecanoate coating on the lead surface.

References for Chapter 8

[1] E. BARSOUKOV and J. MACDONALD, *Impedance spectroscopy: Theory, experiment, and applications*, Wiley, 2005, 1–608.

[2] M. ORAZEM and B. TRIBOLLET, *Electrochemical impedance spectroscopy*, John Wiley & Sons, 2008, 1–525.

[3] P. BRUCE, *Solid state electrochemistry*, Cambridge University Press, 1997, 267.

[4] S. SUNDE et al., An impedance model for a porous intercalation electrode with mixed conductivity, *J. Electrochem. Soc.* **156** (8) (2009), B927–B937.

[5] D. PLETCHER et al., *AC techniques*, Elsevier, 2001, chap. 8, 251–282.

[6] U. RETTER and H. LOHSE, *Electrochemical impedance spectroscopy*, ed. by F. SCHOLZ, Springer, 2010, chap. II.5, 159–177.

[7] W. SCHMICKLER and E. SANTOS, *Interfacial electrochemistry*, Springer, 2010, 236.

[8] A. ZHELTIKOV, Impedance spectroscopy: Theory, experiment, and applications second edition, *J. Raman Spectrosc.* **38** (1) (2007), 122.

[9] R. DE L. KRONIG, On the theory of dispersion of X-rays, *J. Opt. Soc. Am.* **12** (6) (1926), 547–556.

[10] J. PRINS, Über die Dispersion und Absorption von Röntgenstrahlen, *Z. Phys. Chem.* **47** (7-8) (1928), 479–498.

[11] G. LÁNG, L. KOCSIS, and G. INZELT, Application of the Kramers-Kronig transformation for the data validation of impedance spectra of electroactive polymer films on electrodes, *Electrochim. Acta* **38** (7) (1993), 1047–1049.

[12] A. SADKOWSKI, M. DOLATA, and J. DIARD, Kramers-Kronig transforms as validation of electrochemical immittance data near discontinuity, *J. Electrochem. Soc.* **151** (1) (2004), E20–E31.

[13] D. MACDONALD and M. URQUIDI-MACDONALD, Application of Kramers-Kronig transforms in the analysis of electrochemical systems. I. Polarization resistance, *J. Electrochem. Soc.* **132** (10) (1985), 2316–2319.

[14] G. POPKIROV and R. SCHINDLER, Validation of experimental data in electrochemical impedance spectroscopy, *Electrochim. Acta* **38** (1993), 861–867.

[15] M. DORNBUSCH, The use of modern electrochemical methods in the development of corrosion protective coatings, *Prog. Org. Coat.* **61** (2-4) (2008), 240–244.

[16] X. ZHAO et al., Analysis of deterioration process of organic protective coating using EIS assisted by SOM network, *Electrochem. Comm.* **9** (6) (2007), 1394–1399.

[17] A. LASIA, *Eletrochemical impedance spectroscopy and its applications*, Springer, 2014, 82.

[18] B. BOUKAMP, A linear Kronig-Kramers transform test for immittance data validation, *J. Electrochem. Soc.* **142** (6) (1995), 1885–1894.

[19] M. URQUIDI-MACDONALD, S. REAL, and D. MACDONALD, Applications of Kramers-Kronig transforms in the analysis of electrochemical impedance data. III. Stability and linearity, *Electrochim. Acta* **35** (10) (1990), 1559–1566.

[20] C. SCHILLER et al., Validation and evaluation of electrochemical impedance spectra of systems with states that change with time, *Phys. Chem. Chem. Phys.* **3** (3) (2001), 374–378.

[21] W. STRUNZ, C. SCHILLER, and J. VOGELSANG, The change of dielectric properties of barrier coatings during the initial state of immersion, *Mater. Corros.* **59** (2) (2008), 159–166.

[22] W. STRUNZ et al., *Appearance and reality in impedance spectroscopy validation of experimental data by means of the Z-HIT algorithm*, tech. rep., Zahner Messsysteme, 2008, 1.

[23] N. NAKAJIMA and T. ASAKURA, Two-dimensional phase retrieval using the logarithmic Hilbert transform and the estimation technique of zero information, *J. Phys. D: Appl. Phys.* **19** (1986), 319–331.

[24] G. POPKIROV and R. SCHINDLER, A new approach to the problem of 'good' and 'bad' impedance data in electrochemical impedance spectroscopy, *Electrochim. Acta* **39** (13) (1994), 2025–2030.

[25] G. POPKIROV and R. SCHINDLER, Effect of sample nonlinearity on the performance of time domain electrochemical impedance spectroscopy, *Electrochim. Acta* **40** (15) (1995), 2511–2517.

[26] A. PILLA, A transient impedance technique for the study of electrode kinetics: Application to potentiostatic methods, *J. Electrochem. Soc.* **117** (4) (1970), 467–477.

[27] W. SMYRL, Digital impedance for faradaic analysis. I . Introduction to digital signal analysis and impedance measurements for electrochemical and corrosion systems, *J. Electrochem. Soc.* **132** (7) (1985), 1551–1555.

[28] E. BARSOUKOV, S. RYU, and H. LEE, A novel impedance spectrometer based on carrier function Laplace-transform of the response to arbitrary excitation, *J. Electroanal. Chem.* **536** (1-2) (2002), 109–122.

[29] J. NEWMAN, Resistance for flow of current to a disk, *J. Electrochem. Soc.* **113** (5) (1966), 501–502.

[30] P. GELLINGS and H. BOUWMEESTER, *Handbook of solid state electrochemistry*, CRC Press, 1997, 289.

[31] S. FLETCHER, Tables of degenerate electrical networks for use in the equivalent circuit analysis of electrochemical systems, *J. Electrochem. Soc.* **141** (7) (1994), 1823–1826.

[32] F. MECHEL and L. MUNJAL, *Equivalent netwoks*, Springer, 2008, 59–73.

[33] T. GLISSON, *Introduction to circuit analysis and design*, Springer, 2011, 53–56.

[34] C. HAMANN, A. HAMNETT, and W. VIELSTICH, *Electrochemistry*, Wiley, 2007, 1–532.

[35] S. VANDEPUTTE, Frequency response analysis of electrochemical systems at a rotating disk electrode under sinusoidal potential or flow modulation, PhD thesis, Vrije Universiteit Brussel, 1996.

[36] Z. STOJEK, The electrical double layer and its structure, in: *Electroanalytical methods: Guide to experiments and applications*, ed. by F. SCHOLZ, Springer, 2010, chap. I.1, 3–8.

[37] N. HILDENBRAND, Improving the electrolyte - cathode assembly for mt-SOFC, PhD thesis, University of Twente, The Netherlands, 2011.

[38] P. RIEGER, *Electrochemistry*, Prentice-Hall International, 1987, 325–327.

[39] T. PAJKOSSY, Impedance spectroscopy at interfaces of metals and aqueous solutions - Surface roughness, CPE and related issues, *Solid State Ionics* **176** (25-28) (2005), 1997–2003.

[40] J. JORCIN, M. ORAZEM, and B. TRIBOLLET, CPE analysis by local electrochemical impedance spectroscopy, *Electrochim. Acta* **51** (8-9) (2006), 1473–1479.

[41] G. BRUG et al., The analysis of electrode impedances complicated by the presence of a constant phase element, *J. Electroanal. Chem. Interf. Electrochem.* **176** (1984), 275–295.

[42] C. HSU and F. MANSFELD, Technical note: Concerning the conversion of the constant phase element parameter Y_0 into a capacitance, *Corros.* **57** (2001), 747–748.

[43] K. VETTER, *The theory of overvoltage*, Academic Press, 1967, chap. 2, 104–396.

[44] J. MACDONALD, Binary electrolyte small-signal frequency response, *J. Electroanal. Chem. Interf. Electrochem.* **53** (1) (1974), 1–55.

[45] J. MACDONALD, Simplified impedance/frequency-response results for intrinsically conducting solids and liquids, *J. Chem. Phys.* **61** (10) (1974), 3977–3996.

[46] K. COLE and R. COLE, Dispersion and absorption in dielectrics I. Alternating current characteristics, *J. Chem. Phys.* **9** (4) (1941), 341–351.

[47] R. SHEPPARD, B. JORDAN, and E. GRANT, Least squares analysis of complex data with applications to permittivity measurements, *J. Phys. D* **3** (11) (1970), 1759.

[48] R. SHEPPARD, The least-squares analysis of complex weighted data with dielectric applications, *J. Phys. D* **6** (6) (1973), 790.

[49] J. MACDONALD and W. KENAN, *Impedance spectroscopy: Emphasizing solid materials and systems*, Wiley, 1987, 1–368.

[50] J. MACDONALD, J. SCHOONMAN, and A. LEHNEN, Applicability and power of complex nonlinear least squares for the analysis of impedance and admittance data, *J. Electroanal. Chem. Interf. Electrochem.* **131** (1982), 77–95.

[51] J. MACDONALD and J. GARBER, Analysis of impedance and admittance data for solids and liquids, *J. Electrochem. Soc.* **124** (7) (1977), 1022–1030.

[52] P. BEVINGTON and D. ROBINSON, Testing the fit, in: *Data reduction and error analysis for the physical sciences*, 3rd, McGraw-Hill Book Company, 2003, chap. 11, 194–217.

[53] H. HARTLEY, The modified Gauss-Newton method for the fitting of nonlinear regression functions by least squares, *Technometrics* **3** (2) (1961), 269–280.

[54] R. COURANT, Variational methods for the solution of problems of equilibrium and vibrations, *Bull. Am. Math. Soc.* **49** (1) (1943), 1–23.

[55] H. CURRY, The method of steepest descent for nonlinear minimization problems, *Qu. App. Maths.* **2** (1944), 258–261.

[56] D. MARQUARDT, An algorithm for least-squares estimation of nonlinear parameters, *J. Soc. Indust. Appl. Math.* **11** (2) (1963), 431–441.

[57] E. ROCCA and J. STEINMETZ, Inhibition of lead corrosion with saturated linear aliphatic chain monocarboxylates of sodium, *Corros. Sci.* **43** (5) (2001), 891–902.

[58] B. SCHOTTE, A study of the electrolytic reduction of corroded lead objects and the application, characterization and testing of a protective lead carboxylate coating, PhD thesis, Ghent University, 2007, 12–13.

[59] K. DE WAEL et al., Electrochemical deposition of dodecanoate on lead in view of an environmentally safe corrosion inhibition, *J. Solid State Electrochem.* **14** (3) (2010), 407–413.

[60] W. STRUNZ, Dielectric relaxation in barrier coatings: A square root of time process, *Prog. Org. Coat.* **39** (2000), 49–60.

[61] M. O'DONOGHUE et al., EIS: Testing coatings for rapid immersion service, *Mater. Performance* **28** (2003), 36–41.

[62] Y. J. TAN, S. BAILEY, and B. KINSELLA, An investigation of the formation and destruction of corrosion inhibitor films using electrochemical impedance spectroscopy (EIS), *Corros. Sci.* **38** (9) (1996), 1545–1561.

[63] F. MANSFELD, Use of electrochemical impedance spectroscopy for the study of corrosion protection by polymer coatings, *J. Appl. Electrochem.* **25** (1995), 187–202.

[64] D. LOVEDAY, P. PETERSON, and B. RODGERS, Evaluation of organic coatings with electrochemical impedance spectroscopy, *J. Coat. Technol.* **10** (2004), 88–93.

[65] K. KHALED and M. AMIN, Electrochemical and molecular dynamics simulation studies on the corrosion inhibition of aluminum in molar hydrochloric acid using some imidazole derivatives, *J. Appl. Electrochem.* **39** (12) (2009), 2553–2568.

[66] M. GONZÁLEZ-TEJERA et al., Single crystal growth of Pb(II) n-octa-, n-nona- and n-decanoate, *J. Cryst. Growth* **152** (4) (1995), 330–333.

[67] F. LACOUTRE et al., Anhydrous lead(II)heptanoate, *Acta Crystallogr. C* **57** (5) (2001), 530–531.

[68] S. UMOREN, Y. LI, and F. WANG, Synergistic effect of iodide ion and polyacrylic acid on corrosion inhibition of iron in H_2SO_4 investigated by electrochemical techniques, *Corros. Sci.* **52** (7) (2010), 2422–2429.

[69] M. SHEFFER, A. GROYSMAN, and D. MANDLER, Electrodeposition of sol-gel films on Al for corrosion protection, *Corros. Sci.* **45** (12) (2003), 2893–2904.

[70] E. OGUZIE et al., Corrosion and corrosion inhibition characteristics of bulk nanocrystalline ingot iron in sulfuric acid, *J. Solid State Electrochem.* **12** (6) (2008), 721–728.

[71] E. ABD EL AAL, Cyclic voltammetric behavior of the lead electrode in sodium sulfate solutions, *J. Power Sources* **102** (1–2) (2001), 233–241.

9

Influence of time, method and temperature on the deposition of a $Pb(C_{12})_2$ coating

Reprinted from J. Solid State Electrochem., 17 (5), M. De Keersmaecker, K. De Wael and A. Adriaens, Influence of the deposition method, temperature and deposition time on the corrosion inhibition of lead dodecanoate coatings deposited on lead surfaces, 1259-1269, 2013, with permission from Springer.

9.1 Deposition procedures

In this work, a comparison is made between an immersion and electrochemical treatment at different temperatures. Table 8.1 shows the different procedures carried out in a 0.05 mol L^{-1} NaC_{12} solution (see section 7.3.1). The electrochemical treatments are performed using a PGSTAT 100 potentiostat/galvanostat controlled by the GPES 4.9.005 software package (Autolab, The Netherlands) in a three-electrode 50-mL glass cell provided with a saturated calomel reference electrode (SCE) containing two compartments (Radiometer Analytical, France), a carbon counter electrode and a polished lead (diameter = 6.0 mm) working electrode embedded in an epoxy resin. In order to have the possibility to take SEM images, polished lead coupons (diameter = 12.5 mm) were used together with a holder to fit the substrates for electrochemical measurements. The lead was polished using the procedure in section 4.2.

PROCEDURE	METHOD	DESCRIPTION
CV[1]	Cylic voltammetry	Record 5 successive scans in a potential window from -1.3 V to 1.5 V vs SCE with a scan rate of 50 mV s^{-1} [1]
IMM 2000s[1]	Immersion with initial reduction step	A cathodic polarization at -1.5 V during 600 s followed by hanging the lead sample in the solution during 2,000 s
IMM 17h[1]	Immersion with initial reduction step	A cathodic polarization at -1.5 V during 600 s followed by hanging the lead sample in the solution during 17 h

[1] These deposition methods were tested at two temperatures 25°C and 60°C.

Table 9.1 – Description of the different modification procedures used to deposit a lead dodecanoate coating on lead electrode surfaces method.

The deposition was done using a potenstiostat/galvanostat PGSTAT 100 controlled by the GPES 4.9.005 software package (Autolab, The Netherlands). The lead dodecanoate coatings were rinsed with distilled water and air-dried before further analysis.

9.2 Factorial design approach

Factorial design is a statistical tool used for summarizing information of different variables in a smaller number of independent variables, which are called factors F. The difference from PCA is that for factorial design we use knowledge of the system to propose a model that we will test on the experimental data. In this case, we assume that the inhibition efficiency depends on two factors changed namely the deposition method and the temperature. To check possible interactions between variables, we used a two-way factorial design. The central point in factorial design is represented by a regression model of the form [2]

$$G = \beta_0 + \sum_{i=1}^{k} \beta_i X_i + \sum_{\substack{i=1 \\ j>i}}^{k} \beta_{ij} X_i X_j + \sum_{\substack{i=1 \\ j>i \\ l>j}}^{k} \beta_{ijl} X_i X_j X_l + \cdots + \beta_{1\ldots k}(X_1 \cdots X_k) + \epsilon, \tag{9.1}$$

where β_j is the regression coefficient, X_j represents the different independent variables, ϵ is a random error variable with normal distribution around zero and G is the response of the system. The model equation takes into account both the direct effects and all possible interactions among the different parameters, represented by the terms $X_i X_j$, $X_i X_j X_l$ and other higher order products.

9.3 Electrochemical evaluation of the lead dodecanoate coatings

All electrochemical data in this part of the work are based on performing electrochemical impedance measurements at E_{corr} over a distributed frequency range of 1 MHz - 1 Hz, with a 10 mV amplitude sinusoidal AC perturbation signal. Here, an IM6 impedance and electrochemical measurement system (ZAHNER, Germany) was used. The experimental curves were fitted using the Thales software (ZAHNER). The raw data obtained from the lead dodecanoate coatings were fitted using the two equivalent electric circuits shown in Figure 8.8 using constant phase elements for describing the double-layer instead of capacitances. After the fitting, the inhibition efficiencies of the lead dodecanoate coatings prepared are calculated using Eq. 8.42. In what follows, we evaluate the lead dodecanoate coatings based on the specific circumstances.

9.3.1 Influence of the temperature and the deposition method

The influence of the temperature and the deposition method on the corrosion inhibition of the lead dodecanoate coating was tested using 2^2 factorial design. The system studies both the temperature (X_1) and the deposition method (X_2), each at two levels. The design of the experiment consists of an orthogonal array with 60 runs in total. The matrix, together with the factor definitions, is summarized in Table 9.2. A total of 15 replicate runs for each treatment were performed, which ensures a good estimate of the coating reproducibility.

EXPERIMENT NO.	T (°C) / X_1	DEPOSITION METHOD / X_2
1 - 15	20 / -1	cv10sc / -1
15 - 30	20 / -1	imm2000s / +1
30 - 45	60 / +1	cv10sc / -1
45 - 60	60 / +1	imm2000s / +1

Table 9.2 – Experimental design test matrix (2^2).

Table 9.3 shows the one-way ANOVA data for both responses. The F value for both responses is high (p value < 0.05),

	SS	df	MS	F RATIO	p VALUE
(a) Inhibition efficiency					
Among groups	1032.46	3	344.15		
Within groups	2078.27	56	37.11	9.27	0.000045
Total	3110.72	59			
(b) Charge-transfer resistance					
Among groups	1.52×10^{14}	3	5.06×10^{13}		
Within groups	5.63×10^{14}	56	1.01×10^{13}	5.03	0.0037
Total	7.15×10^{14}	59			

Table 9.3 – One-way ANOVA table for both responses: the inhibition efficiencies and the charge-transfer resistances.

which indicates that at least one of both factors influences the coating's protective characteristics.

MODEL	COEFFICIENT	VALUES	STD. ERROR	t VALUE	p VALUE
Constant	β_0	96.32	0.79	122.39	1.04×10^{-69}
Method	β_1	2.02	0.79	2.58	0.013
Temperature	β_2	-2.96	0.79	-3.77	0.0004
Interaction	β_{12}	2.09	0.79	2.65	0.01

Table 9.4 – Coefficients of the regression analysis using the inhibition efficiency responses.

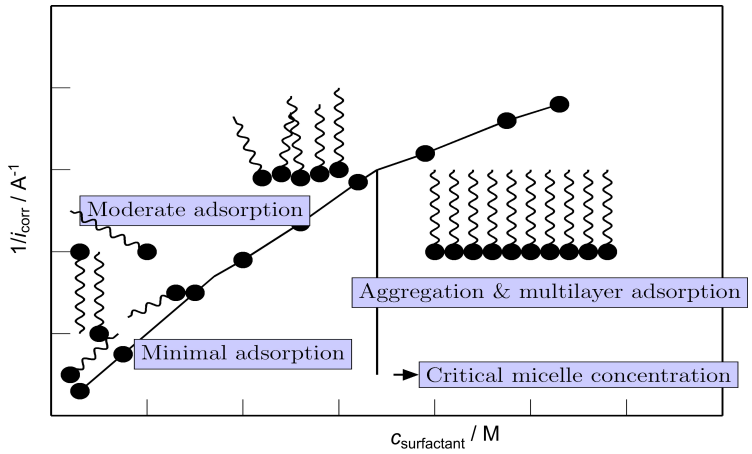


Figure. 9.1 – Effect of the surfactant concentration on the corrosion inhibition

Table 9.4 shows the regression coefficients β using the regression model in Eq. 9.1 with regard to the inhibition efficiencies. The calculated coefficients imply a large influence of the experimental error due to the high β_0 value. The β_2 coefficient (absolute value) is higher than the coefficients of the other parameters, which indicates a bigger influence on the inhibition efficiency. The negative value indicates a considerable decrease of the inhibition efficiency when a higher temperature is used. The two other coefficients (deposition method and interaction) are much lower but nevertheless significant and have almost the same value, which means that they have almost the same influence on the inhibition efficiency. This result is in good agreement with a preliminary set of measurements described in chapter 8, where we stated that the deposition hardly depends on the method in case of CV and IMM 2000 s. The results of the two-way ANOVA analysis on the charge-transfer resistances and the inhibition efficiency are listed in Table 9.5. The F test at the 95% confidence level shows that, in general, the influence of the different factors on the inhibition efficiency response values is higher compared to the ones of the charge-transfer resistance. This can

be clarified by assuming that the inhibition efficiency values can make a better distinction in ineffective and effective coatings. In the following part, we will therefore do the analysis only using the inhibition efficiency values.

SOURCE	SS	df	MS	F RATIO	p VALUE	CR (%)
(a) Inhibition efficiency						
Temperature	525.39	1	525.39	14.16	0.0004	16.88
Method	246.13	1	246.13	6.63	0.0127	7.91
Interaction	260.93	1	260.93	7.03	0.0104	8.39
Error	2078.27	56	37.11			66.81
Total	3110.72	59				100.00
(b) Charge-transfer resistance						
Temperature	1.40×10^{14}	1	1.40×10^{14}	13.95	0.0004	19.65
Method	1.34×10^{12}	1	1.34×10^{12}	0.13	0.72	0.02
Interaction	1.02×10^{13}	1	1.02×10^{13}	0.32	0.32	1.42
Error	5.63×10^{14}	56	1.01×10^{13}			78.90
Total	7.15×10^{14}	59				100.00

Table 9.5 – Two-way ANOVA table for both responses: the inhibition efficiencies and the charge-transfer resistances.

In Table 9.5, the temperature (X_1) has a high contribution ratio (CR) of 16.88%, which means that the temperature factor has an important influence on the deposition of the coating. The coating formed in a NaC_{12} solution at room temperature therefore shows a higher corrosion resistance than a coating formed in the same solution but at a higher temperature. This can be explained by taking into account the critical micellar concentration or c.m.c. of the sodium dodecanoate surfactant. The c.m.c. is a key indicator in determining the effectiveness of surfactants as corrosion inhibitors [3]. Below the c.m.c., individual surfactant molecules tend to adsorb on exposed surfaces, so interfacial aggregation reduces surface tension and is related to the corrosion inhibition (monolayer formation on the surface). Above the c.m.c., the surface becomes covered with more than one monolayer and forms a protective multilayer on the metal surface as seen in Figure 9.1. Surfactant added to the solution above the c.m.c. will form micelles or multiple adsorbed layers on the metal interface. In other words, surfactants with a low c.m.c. are desirable, because they adsorb at lower inhibitor concentrations. The critical micelle concentration of the sodium dodecanoate surfactant is 0.0272 M, which means that, even at low concentrations, aggregation takes place [4]. The tendency of surfactants to aggregate, therefore, depends a lot on the temperature of the solution: an increase in temperature ensures that the solubility of the surfactant increases in the aqueous solvent, which indicates that the c.m.c. increases and surfactant aggregation decreases. The increase in temperature therefore leads to a reduction of the inhibitor

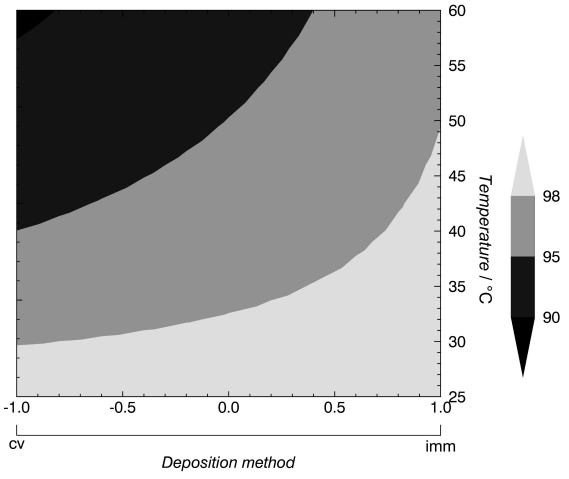


Figure. 9.2 – Response surface for the 2^2 factorial design model

adsorption on the lead surface. The factorial design takes into account the interaction between the deposition method and the temperature, which, in our experiment, is quite low but significant as seen in the CR values in Table 9.5). This means that the temperature has almost no influence on the choice of the deposition method used, but mainly directly on the inhibition efficiency.

Figure 9.2 shows the response surface corresponding to the proposed model. The response surface indicates that using the CV method decreases the probability of producing a better protective coating at higher temperatures. In the case of the IMM 2000s method the protectivity of the coating at higher temperatures stays the same. This phenomenon could be explained by the difference in the deposition process of both methods. Using cyclic voltammetry, the surface is forced to maintain a certain potential using potential cycling and to form a thin protective coating. Because the sodium dodecanoate adsorbs and aggregates much more difficult at higher temperatures as been explained above, less adsorption of the dodecanoate anion takes place and due to the created oxidative conditions and the presence of water, more lead corrosion products will be formed on the surface. The most important observation, however, is that both methods could be used to protect lead objects against corrosion. It is mainly the temperature that has an important influence on the inhibition efficiency of the coating.

9.3.2 Influence of the temperature and the deposition method on the surface structure

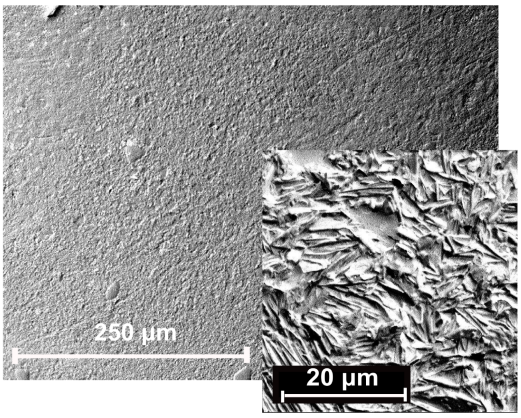


Figure. 9.3 – The SEM images of the coated lead sample before the corrosion test.

The coated lead coupons were corroded using linear sweep voltammetry in the ASTM solution with a potential range from −1 to 1.5 V and with a scan rate of 1 mV s^{-1}. This procedure will be referred to as 'corrosion test'. After this test, the coupons were recorded at low and higher magnification using a Phenom scanning electron microscope (FEI Company, The Netherlands) in topographical mode described in section 4.4.2.7. To be able to compare the coating's surface structure, the samples were measured before the corrosion test in Figure 9.3.

Figure 9.4 shows the electron images of the coated samples using the cyclic voltammetric deposition at 20°C and 60°C, corroded using the corrosion test procedure. In Figure 9.4a, a clear distinction is seen between the surface structure of the coating and of the formed corrosion products. The presence of the coating could be confirmed by comparing the images visually with the ones taken before the corrosion test. At 20°C, these corrosion products are formed around the weak points of the coating as indicated. Figure 9.4b shows that the coating formed using the cyclic voltammetric deposition consists of small crystals which fit in nicely to form an uniform coating. As a result of the fast potential change, small microscopic crystal structures are formed. Because of the small scan rate used during the corrosion test, corrosion products can grow slowly and form big polycrystalline crystal clusters around the weak points of the coating as can be seen in Figure 9.4c. In Figure 9.4d, a more uniform corrosion product layer is formed all over the defective coating deposited at a higher temperature. The formed crystal structures of the corrosion products, using the same corrosion test procedure, seem to be smaller compared to the ones in Figure 9.4c. This phenomenon could be explained by the formation of more corrosion products all over the surface, instead of concentrated in certain surface areas (more weak points). This means that the produced current is not concentrated to one particular area on the surface. The defective coating consisting of

big polycrystalline crystal structures as a consequence of the high temperature allows the formation of small corrosion products. At high temperatures more unprotected areas are present, which makes it easier to form corrosion products. Clearly, the temperature has a considerable effect on the coverage of the coating formed using cyclic voltammetry.

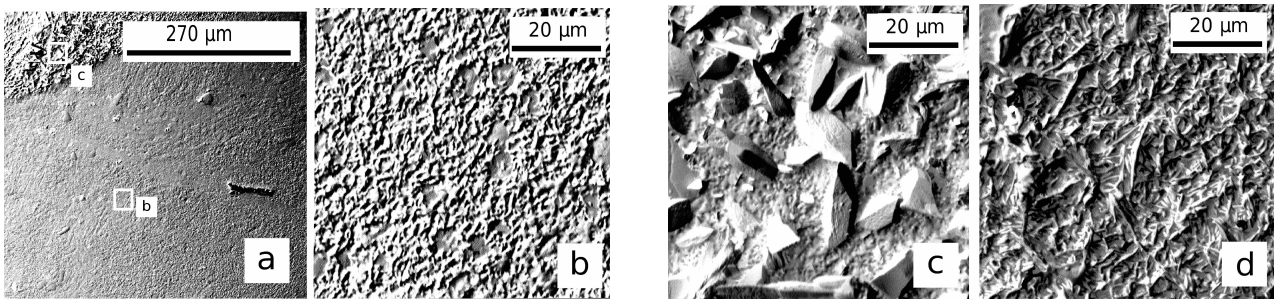


Figure. 9.4 – The SEM images of the corroded lead samples of the cyclic voltammetric deposition: (a) the image of the surface with a deposition at 20 °C (b) the image of a part of the corroded surface with a deposition at 20°C, (c) the image of a part of the coated surface with a deposition at 20°C and (d) the image of the surface with a deposition at 60°C

Figure 9.5 shows the electron images of the coated samples using the immersion technique at 20°C and 60°C, corroded using the corrosion test procedure. Figure 9.5a again shows a distinction between the surface structure of the coating and of the corrosion products by visual comparison with the uncorroded sample. A few macroscopic polycrystalline corrosion crystal clusters are formed around weak points of the coating as indicated. In Figure 9.5b, the coating consists of an ordered and compact layer of crystals which produces an uniform coating. The coating's uniformity causes a higher current to flow through these small corroding regions, which explains the big corrosion crystals seen in Figure 9.5c. The difference with cyclic voltammetry, however, lies in the way the coating is formed. Figure 9.5b, for instance, shows that the polycrystals are better formed and more closely ordered compared to the ones in Figure 9.4b, which means that using immersion provides time for the polycrystals to form a more uniform coating. Indeed, the lead dodecanoate complex molecules arrange more easily according to a lamellar structure, described by Lacoutre et al. [5], in case of an uncontrolled and slower deposition. These more closely ordered crystal clusters protect the surface better against corrosion. Due to the uncontrollable deposition, however, sometimes weak regions are formed in the coating, which can in some cases be bigger and more frequent compared to cyclic voltammetric deposition. At a higher temperature, uniform corrosion is detected, but fewer corrosion products compared to cyclic voltammetry. Figure 9.5d indicates that the formed crystal structures of the corrosion products seem to be smaller compared to the ones using CV in Figure 9.4c, because in this case less corrosion takes place. This uniform corrosion can be explained by the bigger polycrystalline lamellar structures due to the higher temperature and therefore higher entropy of the solution. Bigger lamellar crystals (as seen in Figure 9.5d), however, indicate that small areas in between the lead dodecanoate crystal structures are left unprotected and are therefore more vulnerable to corrosion. Smaller crystals at room temperature protect the bare lead metallic structure better than the bigger crystals at a higher temperature.

9.3.3 Influence of the deposition time on coatings produced using the immersion method

To test the influence of the deposition time, two different time intervals were tested, namely 2,000 seconds (IMM 2000s) and 17 hours (IMM 17h). Figure 9.6 shows the impedance (a) and phase (b) plots of the deposited lead dodecanoate coatings using the IMM procedure with a deposition time of 2,000 s and 17 h compared with the bare lead electrode in an ASTM solution. Figure 9.6a shows that the impedance modulus for the treated surfaces are higher at each frequency compared to the bare lead sample, which means the lead dodecanoate coatings protect the lead surface.

Table 9.6 shows the fitted parameters of the electrochemical impedance curves in Figure 9.6. The spectra were simulated

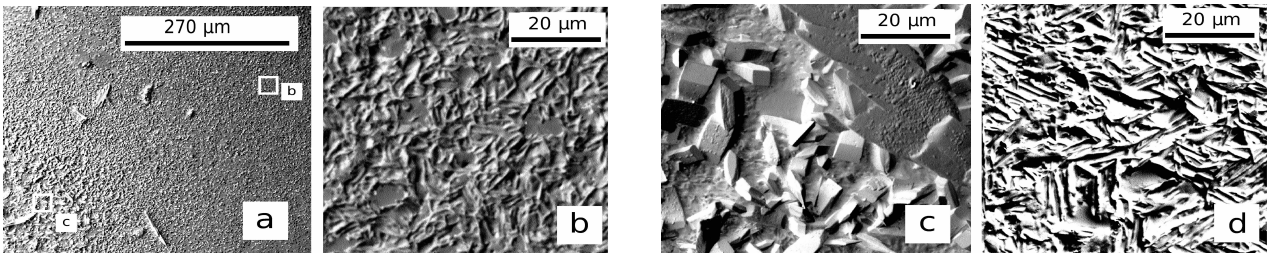
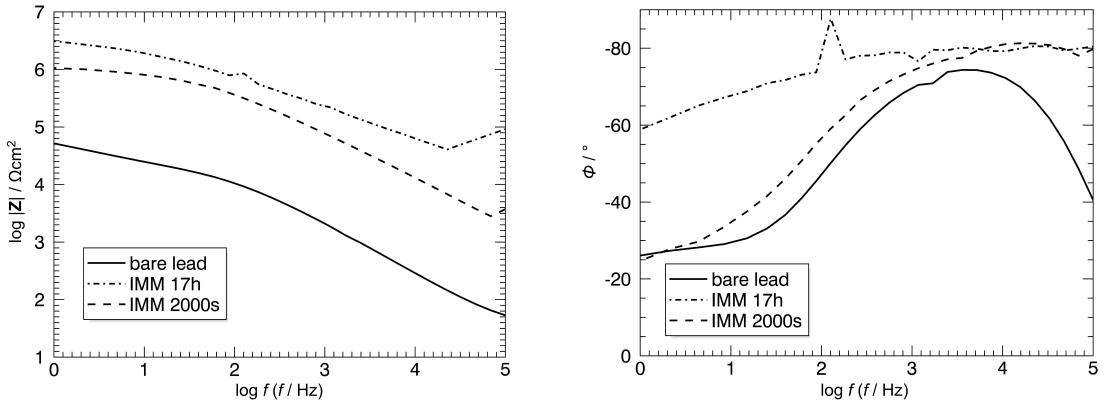


Figure. 9.5 – The SEM images of the corroded lead samples of the immersion deposition: (a) the image of the surface with a deposition at 20°C (b) the image of a part of the corroded surface with a deposition at 20°C, (c) the image of a part of the coated surface with a deposition at 20°C and (d) the image of the surface with a deposition at 60°C



(a) **(b)**

Figure. 9.6 – The impedance (a) and phase (b) plots of lead dodecanoate coatings using the IMM procedure with a deposition time of 2000 s and 17 h (for comparison the bare lead electrode is given)

using the circuit (with and without the diffusion contribution) in Figure 8.8. The charge-transfer resistance value and the inhibition efficiency values of the layer increase depending on the deposition time, because a larger area of the lead surface is blocked. The data show that the charge-transfer resistance and the double-layer capacitance vary in inverse proportion, which can be attributed to the formation of an isolating barrier between the solution and the bare lead surface [9]. A longer deposition time produces more and better ordered crystals, which ensure that the coating protects better against the corrosion of the lead surface [5, 10]. The experiment was repeated four times to examine the reproducibility. Figure 9.7 shows the histogram of the inhibition efficiency values of a set of five lead dodecanoate coatings deposited at room temperature using IMM 17h and IMM 2000s. The relative cumulative distribution clearly shows that 20% and 60% of all investigated coatings have an inhibition efficiency lower than 99.8% in case of respectively the IMM 17h and IMM 2000s method. This means that the IMM 17h technique produces coatings with a slightly higher corrosion inhibition efficiency compared to the IMM 2000s method.

Table 9.7 shows the one-way ANOVA table of the inhibition efficiency response of the lead dodecanoate coatings deposited using IMM 17h and IMM 2000s. The p-values show that the inhibition efficiency values for both methods are not significantly different at a 95% confidence interval. At a 90% confidence interval, however, inhibition efficiencies for both methods are significantly different. This is a consequence of the small inhibition efficiency difference between both methods and the considerable experimental error on the measurements. This small difference of the inhibition efficiencies can be explained by assuming that both methods deposit a lead dodecanoate coating that almost completely covers the lead

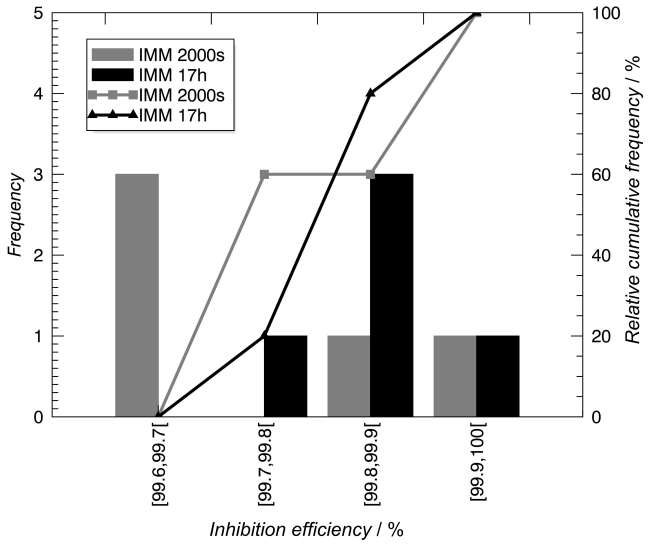


Figure. 9.7 – Histogram and cumulative distribution of inhibition efficiencies of 10 coatings deposited using IMM 2000s and IMM 17h and tested in an ASTM solution

SAMPLE	R_u (Ω cm^2)	R_{ct} (Ω cm^2)	$C_{eff,dl}$ (nF cm^{-2})	η_{IE} (%)
bare lead	3.02	$3.39 \cdot 10^3$	390.87	-
IMM 2000s	4.54	$1.71 \cdot 10^5$	2.18	98.02
IMM 17h	2.94	$1.42 \cdot 10^6$	1.56	99.76

Table 9.6 – Fitted impedance parameters for a bare lead and two coated lead samples. The coating is produced using the immersion technique using a short and a long immersion time

surface and therefore all have an inhibition efficiency close to 100%. A shorter deposition time does not explicitly mean that the protective layer is defective, but a longer deposition definitely provides a longer lifetime and better resistance against aging.

9.3.4 Reproducibility of the coating deposited at room temperature

Figure 9.8 shows a histogram and a cumulative distribution of the inhibition efficiency values of a set of 15 lead dodecanoate coatings deposited at room temperature (20°C) using both CV and IMM 2000s and tested in a standard corrosive ASTM solution. Figure 9.8 shows the histogram and the cumulative distribution of the inhibition efficiency of the different lead dodecanoate coatings. The immersion method produces well-protective coatings with an inhibition efficiency higher than 95%, but shows a higher standard deviation and therefore a poorer reproducibility compared to the CV method. This can be explained by assuming that the immersion method deposits a coating with a variable thickness as a result of the uncontrolled deposition as seen in section 9.3.3. Furthermore, the inhibition efficiency of the immersion method depends on the immersion time. A longer immersion in the inhibitor solution more likely provides a higher coverage, because the probability of creating a full covering coating becomes higher with longer immersion. The CV method, however, with a fast and precise deposition, produces a thin uniform layer with an inhibition efficiency above 98%. The potential and the current flow ensure that the lead surface is positively charged, so that a coating can be deposited all over the surface. The reverse scan provides a reductive current which improves the formation of more ordered crystals due to the potential cyclisation. After the deposition of a thin coating, the same amount of lead dodecanoate is reduced

	SS	df	MS	F RATIO	p VALUE
among groups	0.0462411	1	0.0462411		
within groups	0.0905985	8	0.0113248	4.08	0.0778
total	0.136840	9	-		

Table 9.7 – One-way ANOVA table for the inhibition efficiencies of coatings deposited using the immersion technique using a deposition time of 17 h and 2000 s

and formed meaning that no more lead dodecanoate is deposited. The cumulative distribution indicates that 65% and 50% of the investigated coating layers have an inhibition efficiency lower than 99.4% in the case of cyclic voltammetry and immersion, respectively. This demonstrates that the immersion method more likely produces well-protective layers, but one has to take into account the uncontrolled deposition. For this reason, it is important when using the immersion method to leave the sample for a much longer time in the inhibitor solution. The most important observation is that both deposition methods produce protective and reproducible lead dodecanoate coatings for the bare lead surface at room temperature. Both methods could be used trying to protect lead objects against corrosion. The lead dodecanoate coating is also reversible, because the lead dodecanoate crystals are soluble in ethanol [11, 12].

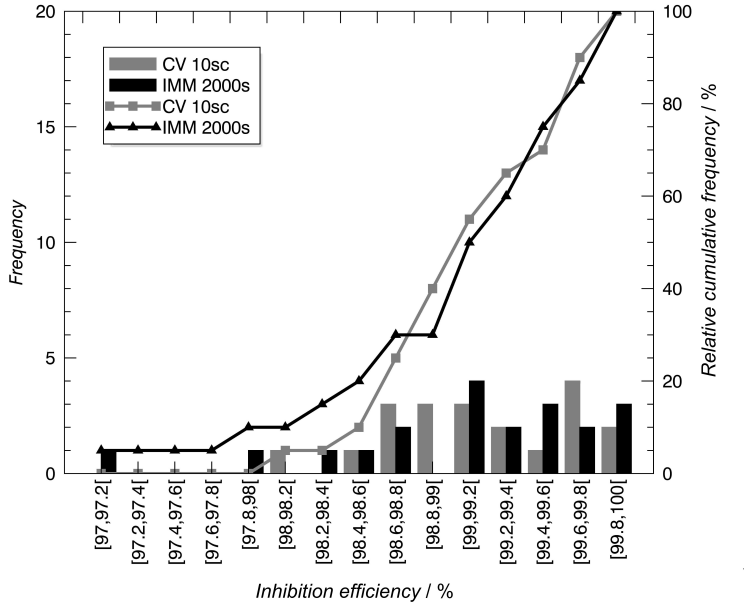


Figure. 9.8 – Histogram and cumulative distribution of IE's of 15 coatings deposited using CV and IMM and tested in an ASTM solution

9.4 Summary and conclusions

In this paper, sodium dodecanoate was used to deposit a lead dodecanoate corrosion protective coating onto a lead surface using two different deposition methods: immobilization using cyclic voltammetry and immersion using a reduction pretreatment. Both deposition methods produce a well-covered and protective coating when working at room temperature. At higher temperatures, the cyclic voltammetric method deposits very defective layers due to the higher solubility and the increase of the c.m.c. of the sodium dodecanoate surfactant. The electrochemical treatment forces the formation of the lead complexes and other products not providing time for adsorption and the formation of ordered lead dodecanoate

crystals. The immersion method, on the other hand, deposits more protective layers compared to the cyclic voltammetric method at higher temperatures, because of the gradual deposition.

The SEM images of the different deposited layers provide a better view on which crystal structures are formed on the surface both during deposition and corrosion. Cyclic voltammetric deposition at room temperature provides a thin protective lead dodecanoate layer on the lead substrate without forming crystal clusters. At a higher temperature, a defective layer is deposited with a lot of defect areas where corrosion products are formed. The type of corrosion crystals can also tell us how protective the coating is. Bigger and well formed crystals are more commonly seen on more protective coatings, while small crystals are seen on defective coatings. The deposition using immersion provides a more ordered and compact lamellar crystal structure on the lead surface, but at a higher temperature the polycrystals seem to be bigger causing some areas on the surface to be less protected.

A longer deposition time produces a more protective coating compared to shorter deposition times, because more and better ordered crystals can be formed, which ensure that the coating protects better against corrosion. A reproducibility measurement, however, nuances this conclusion. It is not proven that the IMM 17h will always produce a more protective layer compared to the IMM 2000s method. Only the chance of depositing a better protecting layer with the IMM 17h method is higher. It is clear that both deposition methods provide protective lead dodecanoate coatings for the bare lead surface, but the reproducibility of the layer depends a lot on the method used and the temperature.

References for Chapter 9

[1] K. DE WAEL et al., Electrochemical deposition of dodecanoate on lead in view of an environmentally safe corrosion inhibition, *J. Solid State Electrochem.* **14** (3) (2010), 407–413.

[2] S. DYSHLOVENKO et al., Experimental design of plasma spraying and laser treatment of hydroxyapatite coatings, *Surf. Coat. Technol.* **201** (5) (2006), 2054–2060.

[3] M. MALIK et al., Anti-corrosion ability of surfactants: A review, *Int. J. Electrochem. Sci.* **6** (2011), 1927–1948.

[4] M. SALIM AKTHER, Effect of acetamide on the cmc of aqueous solutions of some surfactants, *Colloids Surf. A* **121** (1997), 103–109.

[5] F. LACOUTRE et al., Anhydrous lead(II)heptanoate, *Acta Crystallogr. C* **57** (5) (2001), 530–531.

[6] D. LOVEDAY, P. PETERSON, and B. RODGERS, Evaluation of organic coatings with electrochemical impedance spectroscopy, *J. Coat. Technol.* **10** (2004), 88–93.

[7] A. AMURIDIN and D. THIERRY, Application of electrochemical impedance spectroscopy to study the degradation of polymer-coated metals, *Prog. Org. Coat.* **26** (1995), 1–28.

[8] J. MURRAY, Electrochemical test methods for evaluating organic coatings on metals: An update. III. Multiple test parameter measurements, *Prog. Org. Coat.* **31** (1997), 375–391.

[9] S. UMOREN, Y. LI, and F. WANG, Synergistic effect of iodide ion and polyacrylic acid on corrosion inhibition of iron in H_2SO_4 investigated by electrochemical techniques, *Corros. Sci.* **52** (7) (2010), 2422–2429.

[10] H. ELLIS et al., A room temperature structure for anhydrous lead(II) decanoate, *J. Mol. Struct.* **642** (1-3) (2002), 71–76.

[11] A. RALSTON and C. HOERR, The solubilities of the normal saturated fatty acids, *J. Org. Chem.* **7** (6) (1942), 546–555.

[12] A. LI and S. YALKOWSKY, Solubility of organic solutes in ethanol/water mixtures, *J. Pharm. Sci.* **83** (12) (1994), 1735–1740.

10

Electrochemical and surface study of NaC_{12} on lead

Reproduced from J. Electrochem. Soc., 161 (3), M. De Keersmaecker, D. Depla, K. Verbeken and A. Adriaens, Electrochemical and surface study of neutralized dodecanoic acid on a lead substrate, C126-C137, 2014, with permission of The Electrochemical Society.

10.1 Experimental procedures

All electrochemical experiments were performed using a three-electrode system in a 50-mL glass cell. The setup consisted of a saturated calomel reference electrode (SCE) containing two compartments (Radiometer Analytical, France), a carbon counter electrode, and a polished lead working electrode described in section 4.2. All fitted impedance and current values were corrected and normalized versus the electrode surface.

10.1.1 Electrochemical tests

Adsorption tests were carried out using polarization techniques and electrochemical impedance measurements in the ASTM corrosive solution described in section 7.3.1 in the absence and presence of different concentrations (between 1.5 $\times$ 10^{-5} M and 2 $\times$ 10^{-3} M) of sodium dodecanoate test inhibitor. For these experiments, different volumes of a 0.05 M neutralized NaC_{12} solution described in section 7.3.1 were added to 10 mL of the ASTM solution. All experiments were performed at room temperature. First, E_{corr} was monitored for 1,000 s in the different solutions using zero current potentiometry. Next, potentiodynamic polarization curves were recorded in a potential window of -1 V to 0.25 V vs. SCE with a scan rate of 1 mV s^{-1} using a potentiostat (PGSTAT 100, Autolab, Netherlands) controlled by the GPES 4.9.005 software package. The linear Tafel segments of the anodic and cathodic curves were extrapolated to the corrosion potential using the same software to obtain the corrosion current densities, i_{corr}, and the Tafel constants, β_a and β_c. The EIS measurements in the same solutions were recorded at E_{corr}, measured for 1,000 s, over a distributed frequency range of 1 MHz to 10 mHz, with a 10 mV amplitude sinusoidal AC perturbation signal. Here an IM6 impedance and electrochemical measurement system (ZAHNER, Germany) was applied. At the end, the raw data were processed and fitted with the Matlab software release 13.0 (Mathworks, USA).

10.1.2 Surface analysis techniques

The modification of the lead electrode by dodecanoate was done either electrochemically or by immersion in order to form a multilayer of adsorbed lead dodecanoate. The electrochemical deposition was done by cyclic voltammetry (CV) and involved performing 10 consecutive cyclic scans between −1.3 V and 1.5 V vs. SCE with a scan rate of 50 mV s^{-1} in a 0.05 M inhibitor solution. Here a potentiostat (PGSTAT 100, Autolab) controlled by the GPES 4.9.005 software package was used. The immersion method (IMM) consists of a pre-treatment step, which is a cathodic polarization at −1.5 V vs.

SCE for 600 s in the 0.05 M NaC_{12} solution (referred as "initial reduction"), followed by immersing the lead electrode in the same solution for 1 h. This initial reduction was used to reduce all lead corrosion products formed even after polishing. After both treatment methods the lead dodecanoate coatings were rinsed with distilled water and air-dried. The optical microscopical investigations were carried out using a SMZ800 Nikon microscope coupled with a Nikon Digital System (DS Fi1). The micrographs allow investigating the characteristics of the corrosion and coating products and the layer morphology. SEM images of the same samples were recorded using a FEG (Field Emission Gun) SEM Quanta-450 (FEI Company, Netherlands) described in section 4.4.2.7. The EDS spectra are recorded using an EDAX detector and the analysis is done using the TEAM software. The coated lead sample was covered with a thin gold layer to avoid surface charging. XPS measurements were carried out for C 1s, O 1s and Pb 4f spectra based on the instrument described in section 4.6.1.

10.2 Corrosion inhibition study using sodium dodecanoate

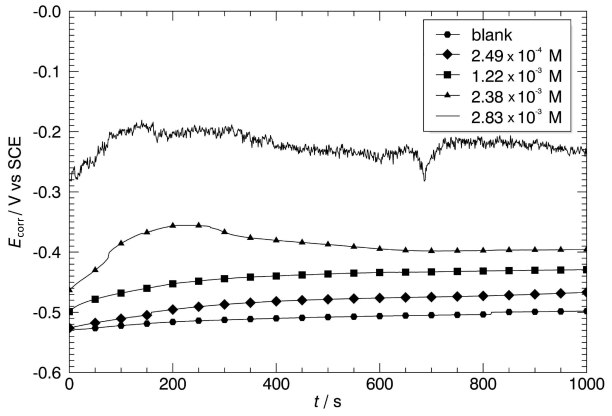


Figure. 10.1 – E_{corr} vs. t plot for lead in the ASTM solution in the absence and the presence of different concentrations of NaC_{12}.

Figure 10.1 presents E_{corr} of a lead electrode in the ASTM solution in the absence of NaC_{12} (blank) and in the presence of 2.49 $\times$ 10^{-4} M, 1.22 $\times$ 10^{-3} M, 2.38 $\times$ 10^{-3} M and 2.83 $\times$ 10^{-3} M NaC_{12}. To avoid the formation of a multilayer, the concentrations were chosen to be lower than the c.m.c. of sodium dodecanoate (0.0272 M). Steady-state values of E_{corr} are achieved after a measuring time of 1000 s. At first (t < 100 s), the value of E_{corr} increases, implying the adsorption of a film on the lead oxide covered lead surface. A higher concentration ensures a larger increase of E_{corr}. Using higher concentrations, around a time of 200 s, the value of E_{corr} starts to drop, and then approaches a steady-state value. The drop indicates that lead dissolution takes place with the formation of slightly soluble $Pb(C_n)_2$ species in solution. The E_{corr} measurements are, however, not sufficient to draw conclusions regarding the inhibitor protection characteristics.

Tafel [1] stated that for hydrogen evolution at a metal electrode the overpotential, η, where (η = $E_{applied}$ - $E_{reversible}$) increased logarithmically with the applied current density $|i|$:

$$\eta = a + b \log |i| \tag{10.1}$$

The recorded current is the sum of the anodic and cathodic components of the corrosion reaction, and the overall polarization curve is the sum of two curves, describing the corrosion reaction between the lead metal and different oxidants present in the solution.

Figure 10.2 shows typical polarization curves of a bare lead sample in the ASTM solution with different inhibitor concentrations. For potentials further from the E_{corr}, the shape of each branch becomes an accurate representation of the kinetics of the anodic and cathodic corrosion reactions. When the overpotential is greater than 50 mV, both branches are assumed to be under activation control and to exhibit linearity in accordance with the known Tafel relationship. The corrosion rate can be calculated by extrapolating the linear Tafel regions back to E_{corr}. For more accurate estimation of

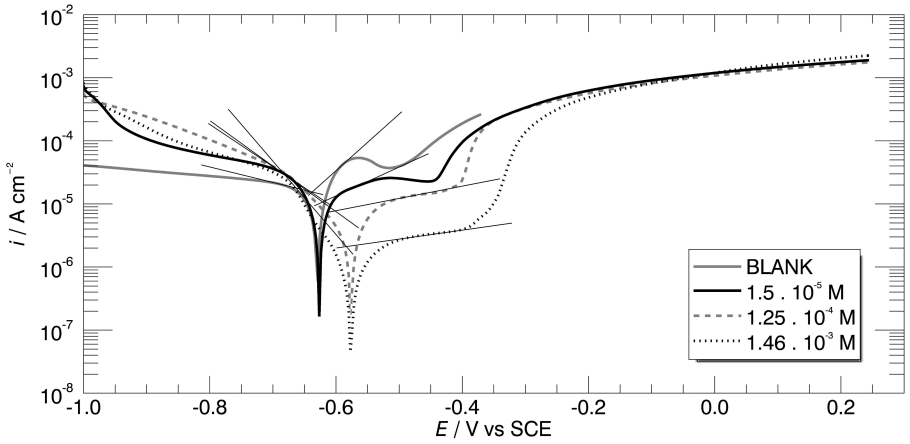


Figure. 10.2 – Current vs. potential plot for lead electrodes in the ASTM solution in the absence and presence of different concentrations of NaC12 with Tafel slope analysis.

the corrosion rate by the Tafel method, the linear parts should extend over about one decade on the log $|i|$ axis. Using our polarization curves this is impossible, so we decided to use the limiting current density region as shown in Figure 10.2 [2]. The anodic and cathodic Tafel slopes were simulated using the linear parts of the log i vs. E plots between the corrosion potential and the current stabilization region. The calculated electrochemical polarization parameters are listed in Table 10.1.

$[NaC_{12}]$ / M	E_{corr} / V vs. SCE	i_{corr} / μA cm^{-2}	β_c / mV	β_a / mV	η_{IE} / %
blank	-0.630	23 ± 3	-300	1200	-
1.50×10^{-5}	-0.622	10 ± 2	-250	200	57
1.25×10^{-4}	-0.601	5.7 ± 0.8	-150	200	75
1.46×10^{-3}	-0.570	1.4 ± 0.7	-200	180	94

Table 10.1 – Fitted potentiodynamic polarization parameters for a bare lead surface in the ASTM D 1384-87 solution in the absence and presence of NaC_{12}.

The parameters include the corrosion potential, E_{corr}, the corrosion current density (with standard deviation), i_{corr}, the anodic and cathodic Tafel constants, β_a and β_c, as well as the inhibition efficiency, η_{IE}. The latter was calculated using the relationship in Eq. 8.43, where i^0_{corr} and i_{corr} are the corrosion current densities in the absence (blank) and the presence of the inhibitor at various concentrations, respectively. The data in Table 10.1 reveal that the increase of the inhibitor concentration shows three effects. First of all, the anodic Tafel slope decreases, which is linked to an anodic effect on the corrosion mechanism. The inhibitor influences the dissolution and the oxidation of the lead metal, implying that the dodecanoate anion is an excellent lead corrosion inhibitor [3]. At potentials above -0.2 V vs. SCE, the current measured in the ASTM solution and in the ASTM solution with inhibitor both overlap, which indicates that the passivation is observable only around E_{corr} observed also in Figure 10.1) [4]. The second effect concerns E_{corr}, which shifts to a higher potential using higher inhibitor concentrations, compared to the bare lead sample. This means that the inhibitor forms a stable film blocking anodic sites on the surface. The fact that the anodic Tafel slope decreases at higher inhibitor concentrations could be related to a better coverage of the film. In other words, low inhibitor concentrations adsorb on the lead oxide covered lead substrate, which explains the decrease in the anodic Tafel slope. This means corrosion decreases without affecting the corrosion mechanism and only cause inactivation of the anodic sites on the lead substrate surface [5].

Higher inhibitor concentrations block more active anodic sites on the metal surface, forcing the E_{corr} to change because the anodic corrosion process has more difficulty initializing and a new corrosion mechanism is set [6, 7]. The third effect involves the calculated inhibition efficiency, which increases with an increase of the inhibitor concentration. A last effect is the decrease of the cathodic Tafel slope. It means the current in the cathodic part of the polarization curve increases when adding more inhibitor. This phenomenon could be related to the reduction of oxides close to the lead surface.

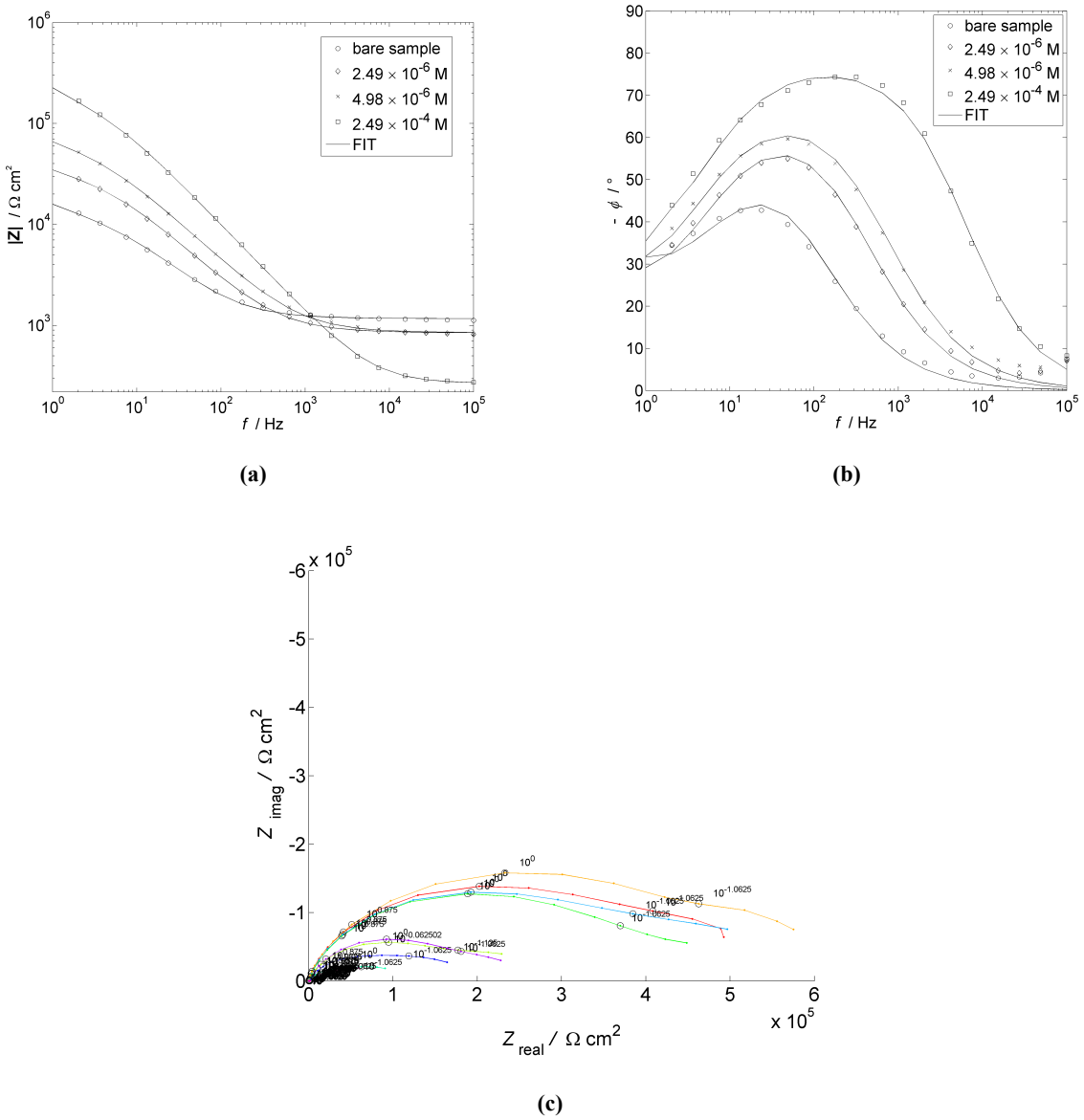


Figure. 10.3 – Electrochemical impedance plots of lead samples in the ASTM solution in the absence and presence of NaC_{12}: (a) impedance plot, (b) phase plot and (c) Nyquist plot.

The magnitude and phase plots for a few of the measured inhibitor concentrations are shown in Figure 10.3. The overall shape of the impedance and phase plots does not change with increasing inhibitor concentration, which implies that the inhibitor does not change the corrosion mechanism, but only the amount of corrosion on the metal surface. The impedance diagrams reveal that an increase in the inhibitor concentration results in an increase in the magnitude of the impedance as seen in Figure 10.3a, due to a higher resistance of the inhibitor film.

In Figure 10.3b, the phase plots at lower inhibitor concentrations consist of one time constant (one capacitive loop) in the

mid-frequency domain (10^1 - 10^3 Hz). This loop could be assigned to the formation of an inhibition layer and therefore the charge-transfer resistance [10–12]. The shape of a wide open capacitive arc in the Nyquist plot in Figure 10.3c is attributed to the finite diffusion process, W_{corr}. Taking into account all these contributions, we use an equivalent circuit of four elements, as shown in Figure 10.4. This circuit was used to analyze and fit the raw data of bare lead in the ASTM solution in the absence and presence of the inhibitor. The model includes the uncompensated resistance, R_{u}, with a series combination of the CPE of the double-layer, Q_{dl}, and the charge-transfer resistance, R_{ct} combined with a finite Warburg element, W_{corr}. As a first approximation, the charge-transfer resistance, R_{ct}, can evaluate the degree of protection of the inhibitor film [13]. In the model, a CPE is used instead of capacitances C to compensate for non-homogeneity using Eq. 8.28. Furthermore, the CPE values of the experimental fitting can be converted into capacitances using the Brug formula in Eq. 8.29. An excellent fit was obtained with the proposed model for all recorded experimental data as observed in Figure 10.3a and b. Table 10.2 shows the fitted impedance parameters and the goodness-of-fit values recorded for a bare lead sample in the ASTM solution for different added inhibitor concentrations at room temperature using the equivalent circuit in Figure 10.4.

Due to the decrease of the defective area ($C \downarrow$ when $A \downarrow$) on the lead oxide covered surface when the inhibitor concentration is increased, the resistance of the passive layer slightly increases because the inhibitor will protect the surface from corroding. At higher inhibitor concentrations the layer capacitance stagnates ($C \uparrow$ when $A \downarrow$ and $t \uparrow$). Secondly, the fitted data indicate that R_{ct} increases with an increase of the inhibitor concentration indicating the protective properties of the inhibitor. This means the R_{ct} value varies in inverse proportion with $C_{\text{eff,dl}}$. The decrease in $C_{\text{eff,dl}}$ ($C \downarrow$ when $A \downarrow$) predicts a decrease in the electro-active area on the metal surface. Together with the increase in R_{ct}, the increase of the inhibitor concentration is attributed to the formation of a protective film. The inhibition efficiency η_{IE} was calculated using the relationship in Eq. 8.42, where R^0_{ct} and R_{ct} are charge-transfer resistances in the blank and in the presence of the inhibitor, respectively.

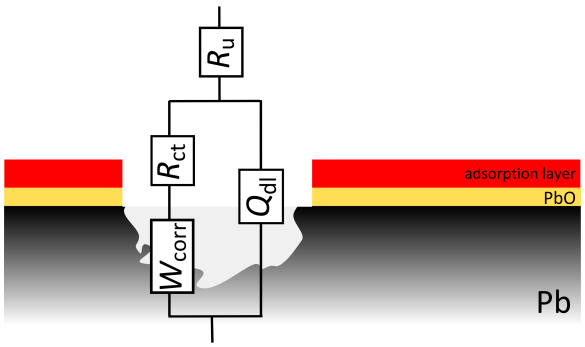


Figure. 10.4 – The EEC used for fitting the experimental EIS spectra.

For the impedance measurements two sources of error must be taken into account: firstly there is the error associated to each individual fitting (mathematical error, related to the equivalent circuit not fully representing the electrochemical system); and secondly there is the experimental error that can be observed by comparing different replicates. The mathematical error from the fitting is much smaller than differences between replicates, as can be estimated by comparing the fitting curves and the experimental data points in Figure 10.3. Table 10.2 shows the errors more clearly. Differences between replicates arise mainly from the lead oxide layer present on the bare lead substrate surface due to atmospheric corrosion and on the sample polishing. The characteristics of this lead oxide layer depend on the temperature, on the relative humidity, and on the reactivity of the sample surface after polishing, among other factors. The magnitude of the error is given for the inhibition efficiency. Taking into account the issue with controlling the oxide layer due to atmospheric corrosion, polishing of the sample, fitting errors, the environment and instrument errors, we can accept the error on the calculated inhibition efficiency. Finally, comparing the values for the inhibition efficiencies from the EIS measurements with the ones calculated using the polarization measurements, it can be seen that the ones using the Tafel

$[NaC_{12}]$ / M	E_{corr} / V vs SCE	$C_{eff,dl}$ / $\mu F\ cm^{-2}$	R_{ct} / $\Omega\ cm^2$	$Z_{W,corr}$ / $\Omega\ s^{-1/2}\ cm^2$	η_{IE} / %	η_{IE} / % (3 replicates)	χ^2 value
blank	-0.508	1.2 ± 0.1	11400 ± 500	25000 ± 3000	-	-	212
2.49×10^{-6}	-0.514	0.45 ± 0.02	31500 ± 600	33000 ± 3000	25 ± 1	26 ± 1	230
4.98×10^{-6}	-0.531	0.25 ± 0.01	65000 ± 1000	57000 ± 5000	57 ± 1	55 ± 3	392
9.90×10^{-6}	-0.493	0.178 ± 0.004	109000 ± 1000	70000 ± 10000	65 ± 1	65 ± 2	577
2.44×10^{-5}	-0.496	0.155 ± 0.004	111000 ± 1000	66000 ± 8000	63 ± 1	63 ± 2	512
2.49×10^{-4}	-0.491	0.094 ± 0.003	180000 ± 1000	170000 ± 30000	86 ± 1	85 ± 2	1978
4.95×10^{-4}	-0.492	0.1082 ± 0.004	152000 ± 3000	200000 ± 30000	88 ± 1	86 ± 4	3690
1.22×10^{-3}	-0.506	0.1066 ± 0.003	173000 ± 3000	210000 ± 30000	88 ± 2	87 ± 4	3083
2.38×10^{-3}	-0.500	0.0856 ± 0.003	149000 ± 3000	280000 ± 40000	91 ± 2	90 ± 4	5330

Table 10.2 – Fitted electrochemical impedance parameters (EIS) for a bare lead surface in the ASTM D 1384-87 solution in the absence and presence of NaC_{12}. The last column indicates the inhibition efficiency value and its deviation using three replicate measurements.

slope analysis technique are lower, although they follow the same trend. The lower values of the inhibition efficiency from the polarization technique could be attributed to the predominant influence of the anodic dissolution process in determining the corrosion rate [14].

10.3 Adsorption study: chemisorption or physisorption?

The surface coverage, θ, can be interpreted as the calculated inhibition efficiency. The relationship between the inhibitor concentration and θ at a constant temperature is known as an adsorption isotherm, and gives insight into the adsorption process of the inhibitor on the metal surface [15, 16]. The degree of surface coverage values for the various concentrations of the inhibitor were evaluated from the impedance measurements using the relationship $\eta_{IE} = \theta \times 100$. This means we assume that the inhibitor efficiency is mainly caused by the blocking effect of the adsorbed species [5]. Two classical monolayer adsorption models, Langmuir and Frumkin, were used to fit the experimental surface coverage values as a function of the inhibitor concentration [17–19]. A monolayer adsorption mechanism can be assumed because all the concentrations used are lower than the c.m.c. of sodium dodecanoate (0.0272 M). The Langmuir isotherm model assumes that the solid surface has a fixed number of adsorption sites where each site holds only one adsorbed species. It concerns monolayer adsorption, and can also be represented by the following relationships [20, 21],

$$q = \frac{K_{ads} q_{max} c}{(1 + K_{ads} c)}, \tag{10.2a}$$

$$\frac{c}{\theta} = \frac{1}{K_{ads}} + c, \tag{10.2b}$$

where q is the number of adsorbed moles per mass unit of absorbent, q_{max} is the upper limit value of q, c is the inhibitor concentration, θ is the degree of surface coverage and K_{ads} is the equilibrium constant of the adsorption process. The Frumkin isotherm, on the other hand, takes into account the interactions between the inhibitor molecules adsorbed onto the metal surface and is represented as follows [22]

$$q = \frac{K_{\text{ads}} q_{\max} c}{\exp\left(\frac{2aq}{q_{\max}} + K_{\text{ads}} c\right)}, \tag{10.3a}$$

$$K_{\text{ads}} + c = \left[\frac{\theta}{1-\theta}\right] \exp(2a\theta), \tag{10.3b}$$

where a is the interaction parameter. A positive value of the Frumkin interaction parameter corresponds to repulsive interactions, whereas a negative corresponds to attractive interactions. The Langmuir isotherm can be regarded as a special case of the Frumkin isotherm obtained for $a = 0$.

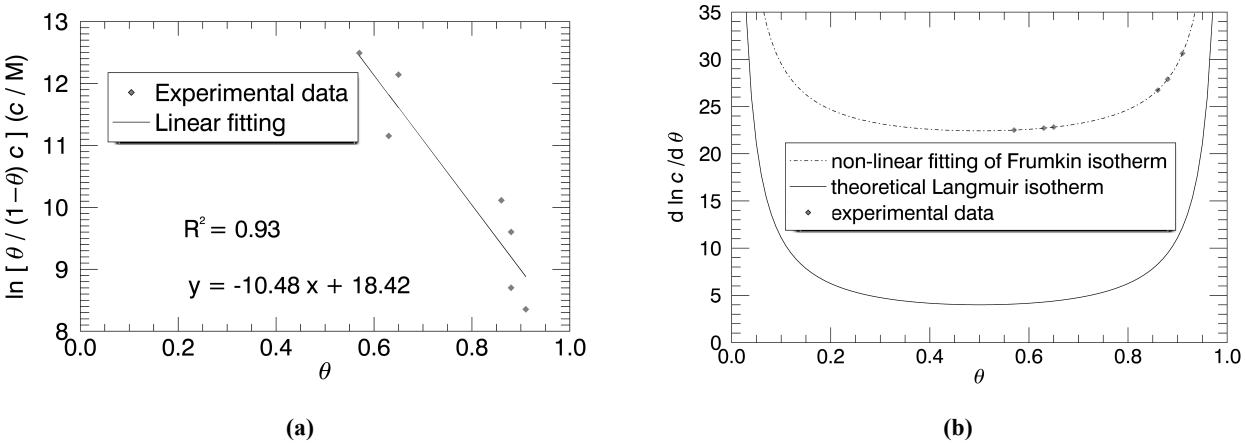


Figure. 10.5 – (a) Langmuir test and (b) Langmuir and Frumkin slope vs. coverage for the sodium dodecanoate inhibitor at room temperature in the ASTM solution.

Langmuirian behavior can be tested in two different ways: (a) the Langmuir test, based on a plot of ln $\left[\frac{\theta}{(1-\theta)c}\right]$ vs. θ or (b) the Langmuir slope, which has a constant value. Figure 10.5a shows the plot of ln $\left[\frac{\theta}{(1-\theta)c}\right]$ vs. θ for the experimentally calculated inhibition efficiencies of the fitted impedance measurements. The Langmuir isotherm would imply a linear plot with a zero slope, which cannot be assumed in this case [22].

A linear plot with a nonzero slope indicates that the use of the Frumkin isotherm is more appropriate. Figure 10.5b shows a plot of the Frumkin slope (see dashed curve) as a function of the coverage θ, where the slope has a constant value, independent of the value of K_{ads}. The term $(1-\theta)\theta$ is a parabolic function with a maximum at $\theta = 0.50$, as would be the case for Langmuirian behavior (see solid curve in Figure 10.5b) [17]. The Frumkin behavior can be identified by comparing the experimentally calculated slopes with the parabolic function of the Langmuirian behavior. In this case, the slope of the isotherm is less steep than that of the Langmuir isotherm, which indicates the presence of repulsive interactions ($a < 0$). Based on Figure 10.5, it is possible to conclude that all experimental values are best fitted using the Frumkin isotherm equation.

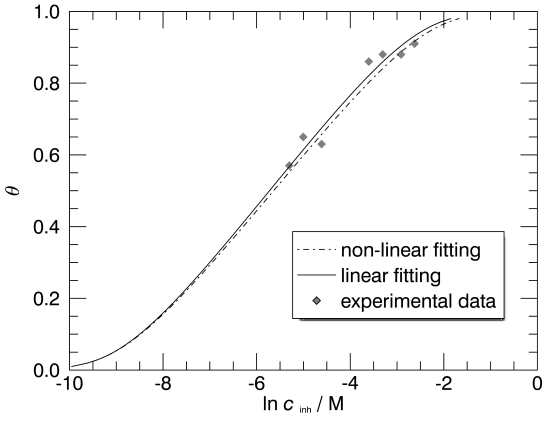


Figure. 10.6 – Frumkin adsorption isotherm for sodium dodecanoate on bare lead electrodes at room temperature in the ASTM solution.

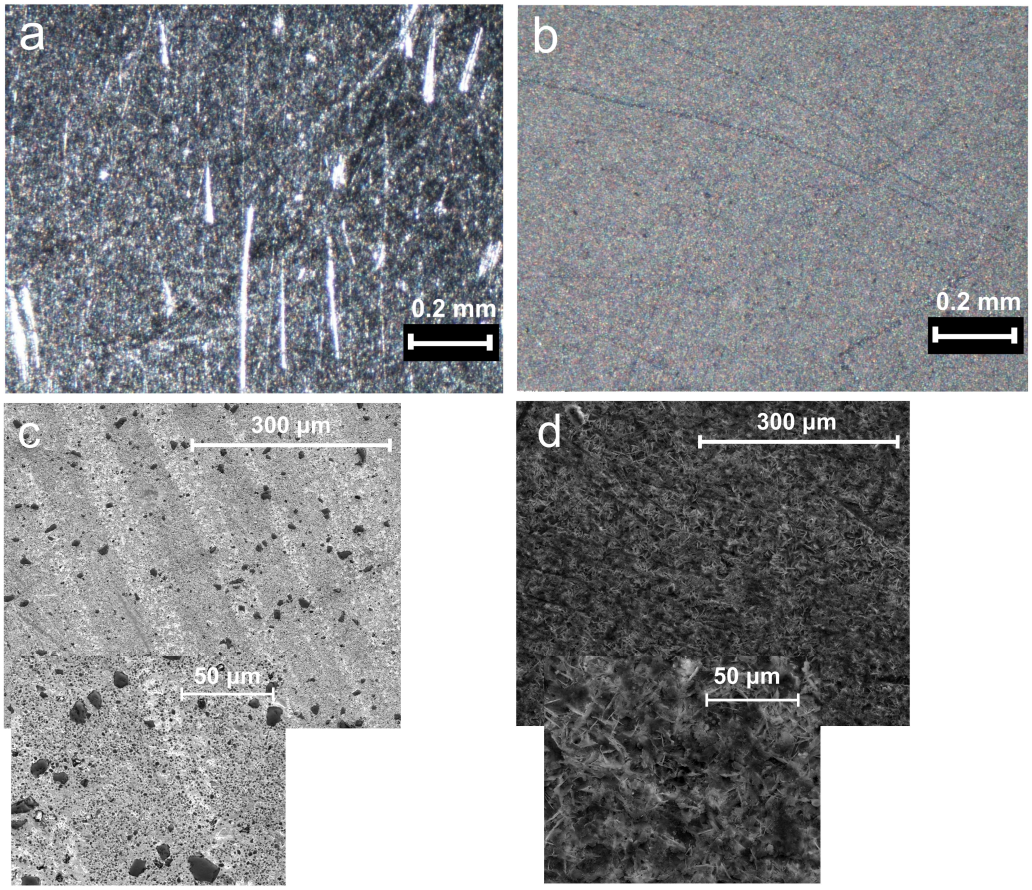


Figure. 10.7 – The optical and secondary electron images of a bare lead polished sample (a and c) and optical and secondary electron images of a lead dodecanoate coated lead sample (b and d).

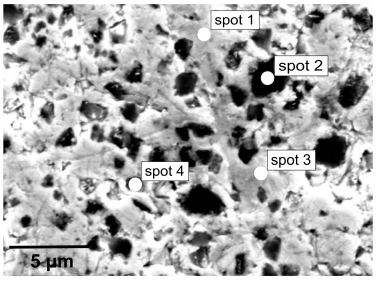
Figure 10.6 shows the Frumkin isotherm obtained by plotting θ as a function of the natural logarithm of the inhibitor concentration. The linear fit provides values of a = -10.48 and ln K_{ads} = 18.4 and the non-linear fitting, a = -10.9 and ln K_{ads} = 18.4. This model assumes that the lead oxide present on the metal surface interact with two dodecanoate anions, and that there are repulsive interactions between the dodecanoate anions in this corrosive medium. Using the Van 't Hoff equation, the standard Gibbs free energy change, ΔG^0_{ads}, of the adsorption reaction is calculated [17] using

$$K_{ads} = \frac{1}{55.5} \exp\left[\frac{-\Delta G^0_{ads}}{RT}\right] \tag{10.4}$$

The standard Gibbs free energy change of the adsorption reaction ΔG^0_{ads} for the inhibition of a lead surface using the sodium dodecanoate inhibitor is -55 $\pm$ 3 kJ mol^{-1}. Values of ΔG^0_{ads} around -20 kJ mol^{-1} or lower are consistent with the electrostatic interaction between the charged organic species and the charged metal surface (physisorption), whilst those around -40 kJ mol^{-1} or higher involve charge sharing or transfer from the inhibitor molecules to the metal surface to form a coordinate bond (chemisorption) [23]. The value of ΔG^0_{ads} obtained for this adsorption reaction is higher than -40 kJ mol^{-1}, which means that the dodecanoate molecules are chemically adsorbed onto the lead oxide covered surface. This chemical reaction ensures the formation of a lead dodecanoate complex, which has been confirmed by X-ray diffraction (XRD), due to the formation of lead carboxylate crystals [24].

10.4 Surface and cross-sectional analysis

The modification of the lead sample by dodecanoate was done by IMM-IR for 1 hour of immersion in order to form a multilayer of adsorbed lead dodecanoate using a 0.05 M inhibitor solution. Figure 10.7 shows the optical and secondary electron images of a bare lead polished sample (a and c) and optical and secondary electron images of a lead dodecanoate coated lead sample (b and d). The optical images in Figure 10.7 show that the surface structure of the bare lead sample is completely changed when coated with a lead dodecanoate coating. In Figure 10.7a, shiny spots are seen due to the polishing of the lead sample. Figure 10.7b, however, shows a dull color due to the immersion in the inhibitor solution. The electron image of the bare polished sample in Figure 10.7c shows the presence of low Z particles in the lead matrix (see EDS for identification). The electron image of the coated sample in Figure 10.7d reveals that a coating layer is formed, because the topography and morphology of the sample surface has changed. The surface is covered with flake-shaped crystals.



spot 1

	w%
C	2.4
O	4.0
Pb	93.6

spot 2

	w%
C	1.8
O	43.2
Pb	29.2
Si	25.8

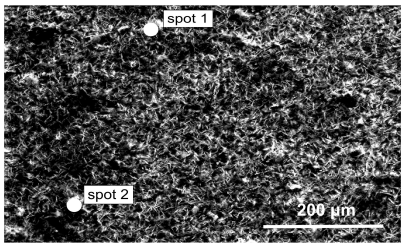
spot 3

	w%
C	0.8
O	2.8
Pb	96.4

spot 4

	w%
C	58.1
O	2.1
Pb	39.7

(a)



spot 1

	w%
C	48.6
O	11.1
Pb	32.2
Si	2.6
Na	2.7
Cl	2.9

spot 2

	w%
C	55.8
O	18.7
Pb	21.4
Si	1.3
Na	1.3
Cl	1.4

(b)

Figure. 10.8 – Secondary electron image and EDS point data of (a) the polished bare lead sample and (b) the coated lead sample.

The point EDS data of the polished lead surface in Figure 10.8a show that the black dots present on the surface are characterized as large SiC particles (see spot 2) and small diamond particles (see spot 4). The white matrix is due to higher Z atoms, in this case, the lead metal. These particles are used for the polishing of the lead surface as described in section 4.2, but due to softness of the lead metal the particles get stuck into the lead metal matrix. The point EDS data of the coated sample shown in Figure 10.8b show a high contribution of O- and C-atoms due to the reaction between the aliphatic carboxylate group and the lead oxide. A hydrophobic lead soap is formed with a two-dimensional crystal structure, which is characterized by a lamellar building of sheets as seen in the SEM image [25]. The Si atoms are related to the polishing. The Na ions are present because of the use of neutralized carboxylate groups and the use of NaOH for the saponification.

Figure 10.9 shows a cross-sectional image of the coated lead sample together with its EDS map. The image shows the lead sample with the lead dodecanoate coating as demonstrated by the EDS maps. The C contribution is completely attributed to the coating due to carbon chains of the fatty acid. The oxygen is related to the atmospheric corrosion of the lead sample and the presence of the carboxylate group in the coating. It is clear that the lead concentration reduces going to the top of the coating, which indicates the presence of lead complexes within the coating. The thickness of the coating is determined to be between 10 - 20 µm. The thickness is, however, not the same along the sample surface.

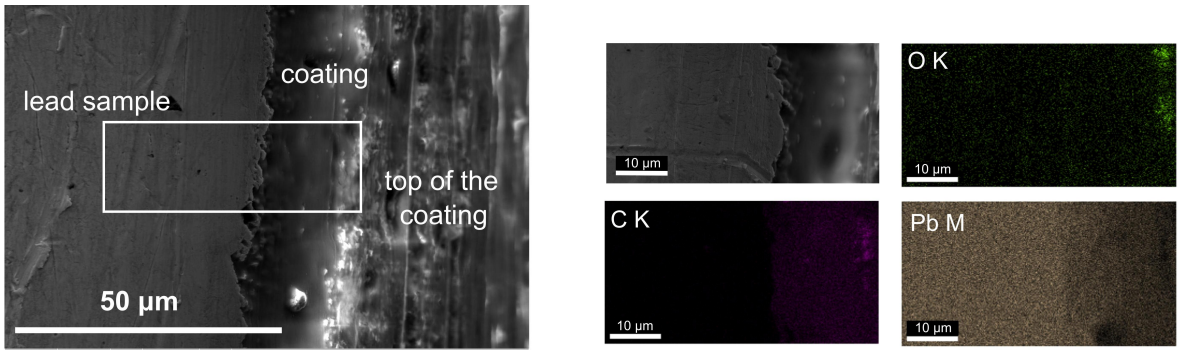


Figure. 10.9 – Secondary electron image of the cross-section of the coated lead sample with EDS-mapping.

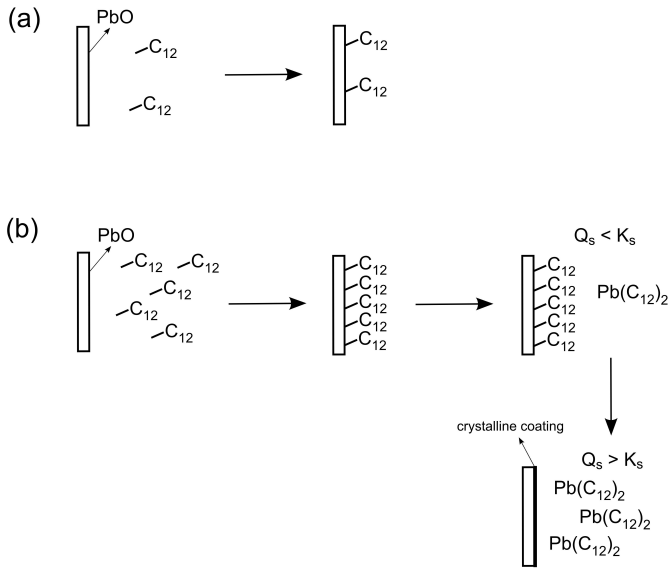


Figure. 10.10 – Schematic representation of the mechanistic model for inhibitor concentrations: (a) below c.m.c. and (b) above c.m.c.

10.5 Mechanistic model of the deposition of the lead dodecanoate coating

To summarize, at inhibitor concentrations below the c.m.c. shown in Figure 10.10a, a dodecanoate monolayer film adsorbs to the lead oxide covered lead surface. The chemisorption of the dodecanoate molecules on the lead oxide film ensures the formation of a protective film. Higher inhibitor concentrations below the c.m.c. result in a wider coverage of the film on the lead surface. An increase of the inhibitor concentration is linked to a wider coverage of the film. At inhibitor concentrations above the c.m.c. (Figure 10.10b), there is the formation of the soluble lead salt at the lead oxide film due to monolayer chemisorption in reactions eqs. (7.14a) to (7.14c). Secondly, there is a precipitation and crystallization of the salt film $Pb(C_{12})_2$ (s) on the lead surface when the solubility product of the salt in the aqueous solvent is exceeded [24, 26]. The precipitation of the salt film blocks the active sites, passivating the surface. This principle is called a dissolution-precipitation mechanism, which is controlled by the diffusion of the reacting species. The higher inhibitor concentration and longer immersion times result in multilayer formation and a crystalline layer on the lead metal surface as described in chapter 9.

10.6 XPS analysis of the corrosion and passive layers

10.6.1 Analysis of an atmospherically corroded lead sample

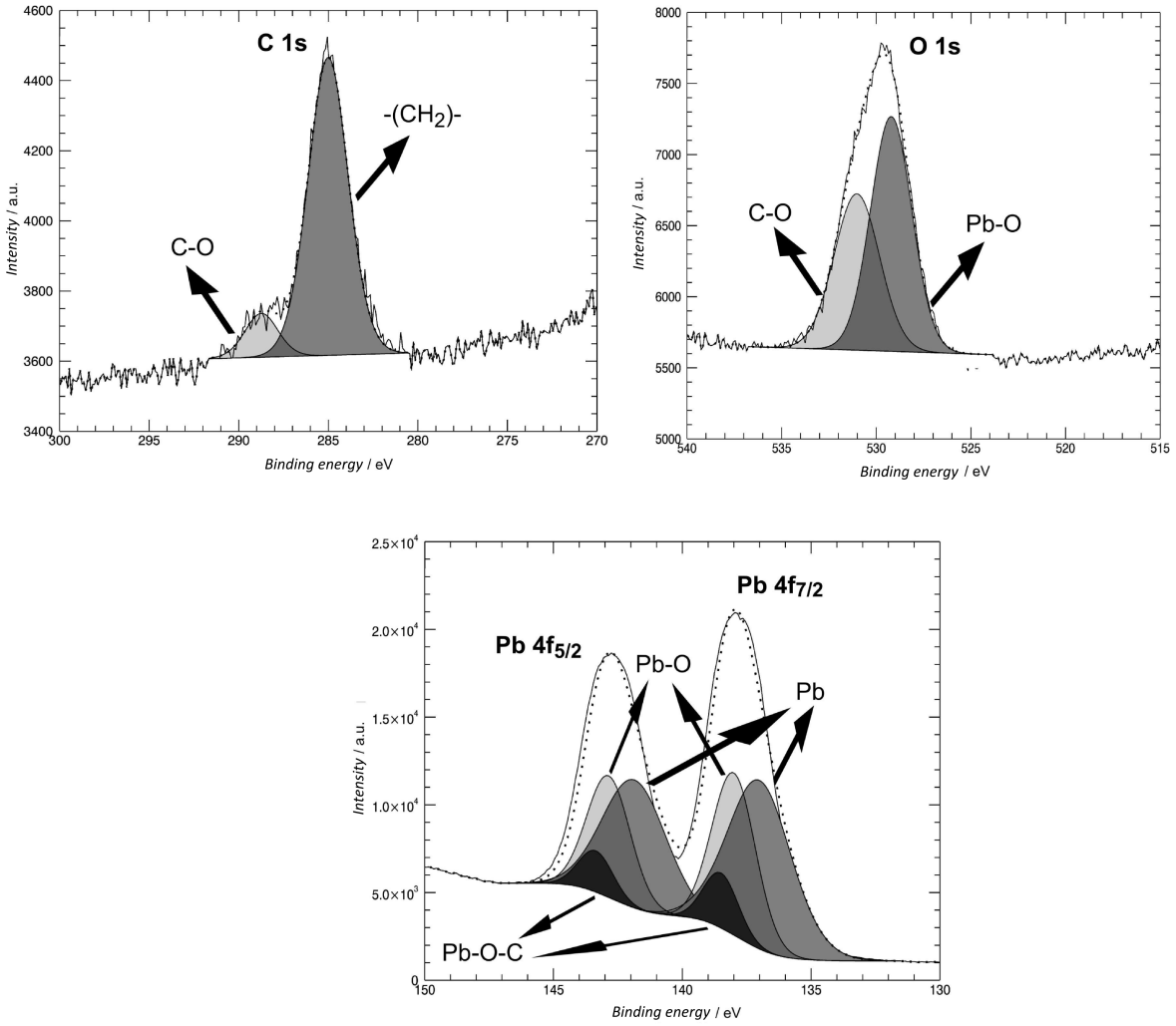


Figure. 10.11 – XPS core level spectra of the C 1s, O 1s and Pb $4f_{7/2}$ levels of the bare corroded lead metal samples with components determined by curve fitting analysis and background subtraction.

Figure 10.11 shows the XPS core level spectra of the C 1s, O 1s and Pb $4f_{7/2}$ levels of the corroded bare lead metal samples with all values corrected for C 1s to appear at 285.0 eV, which is due to contamination of the sample. The Pb $4f_{7/2}$ spectrum reveals three peaks with binding energies of 137.0, 138.0 and 138.5 eV which are associated with two different oxidation states of lead: metallic lead Pb(0) and a mixture of Pb(II) corrosion products as described in Table 10.3. The higher elemental concentration (25%) for metallic lead is a consequence of the detection of the metallic lead under a very thin corrosion layer on the lead surface, because of the low humidity of the atmospheric air and therefore limited corrosion. The curve fitting analysis of the C 1s and O 1s core level spectra predicts the formation of lead carbonates with a binding energy of 288.7 eV for O 1s and a binding energy of 531.4 eV and lead oxides with a binding energy of 529.2 eV as lead corrosion products [27–29]. These lead corrosion products are formed due to the reaction of the lead metal with carbon dioxide and oxygen in the atmosphere. The formation of lead oxide can be confirmed by using the elemental concentrations of the Pb $4f_{7/2}$ and the O 1s core electron contributions. Taking into account the

RSFs for the different elements, an atomic ratio of $PbO_{1.001}$ is calculated, which explains the presence of lead(II)oxide. Table 10.3 indicates that the concentration of the PbO is higher than the concentration of the lead carbonate compounds based on the elemental concentrations of both compounds. This can indeed be explained by the chemical reactions of the formation of lead carbonate compounds like cerussite ($PbCO_3$), hydrocerussite ($2\,PbCO_3 \cdot Pb(OH)_2$) and plumbonacrite ($Pb_{10}O(OH)_6(CO_3)_6$). First, the metallic lead on the surface is oxidized to PbO due to the presence of oxygen gas in the solution as described in reaction 2.5b. The formation of bicarbonate and carbonate ions due to the presence of carbon dioxide gas and water on the surface can lead to a reaction with the initially formed lead oxide to form all different lead carbonate compounds as described in reactions eqs. (2.6a), (2.6b) and (2.7) [31, 32] and also

$$3Pb^{2+}(aq) + 2{CO_3}^{2-}(aq) + 2OH^-(aq) \rightleftharpoons Pb_3(OH)_2(CO_3)_2(s), \tag{10.5a}$$

$$Pb_3(OH)_2(CO_3)_2(s) + H_2CO_3(aq) \rightleftharpoons 2H_2O + 3PbCO_3(s). \tag{10.5b}$$

Therefore, the concentration of these lead carbonate compounds depends on the presence of carbon dioxide in the atmospheric air (0.03%), which has a lower atmospheric presence than oxygen (20.95%), which is needed for the formation of lead oxide. To determine the nature of the lead carbonate compounds formed, an experimental composition of the lead carbonate is calculated. The experimentally determined composition PbC_1O_3 indicates the presence of hydrocerussite and plumbonacrite and not pure lead carbonate as seen in Table 10.3. This can be explained by the limited formation of bicarbonate ions compared to the presence of hydroxide ions.

10.6.2 Analysis of a coated lead sample using the cyclic voltammetry (CV) procedure

Figure 10.12 shows the XPS core level spectra of the C 1s, O 1s and Pb $4f_{7/2}$ levels of a coated lead sample using CV for 10 consecutive scans with all values corrected for C 1s to appear at 285.0 eV. The Pb $4f_{7/2}$ peak reveals three peaks with a binding energy of 136.7, 137.7 and 138.8 eV which are associated with again two different oxidation states of lead: metallic lead Pb(0) and a mixture of Pb(II) products as observed in Table 10.3. The elemental concentration of the metallic lead is much lower compared to the bare corroded sample, which is due to the formation of a thicker coating on the lead sample. The latter attenuates the signal of the metallic lead more strongly. The curve fitting analysis of the C 1s XPS spectrum of the treated sample shows three peaks at 285.0 eV, 283.1 eV and 288.3 eV. The first big peak at 285.0 eV can be assigned to the contamination of aliphatic carbon, but more importantly to the carbon atoms in the saturated aliphatic chains of the carboxylate anion in the lead dodecanoate complex. The small peak at 288.3 eV is attributed to the carbon atom of the carboxyl group of the lead complex. No specific reference was found for this complex, but the binding energy values can be compared with those of lead acetate (another lead carboxylate), which has a similar structure around the lead atom of the molecule [35, 36]. The longer linear aliphatic carbon chain has indeed almost no influence on the binding energy of the Pb $4f_{7/2}$ core level electron. The aliphatic carbon / carboxylic carbon atomic ratio from the C 1s (285.0 eV) / C 1s (288.2 eV) intensity ratios is approximately 13. This ratio predicts the number of carbon atoms in the aliphatic carbon chain of the proposed complex, which should be close to 11 for lead dodecanoate compounds. The last small peak at 283.1 eV is attributed to the formation of lead-carbon bonds similar in energy to carbide-like species on metals ($\pm$ 283 eV) suggesting that the carboxylates react with the lead substrate [34, 38]. This reaction is possibly due to reductive processes at the lead electrode, which form carbide-like species with a direct lead-carbon bond. One of the possible reactions is the formation of a metal-alkonyl bond using the carboxyl-group described in Figure 10.13. The reduction of a metal surface can indeed lead to a very reactive metal and the formation of a lead-carbon bond as in case of electrografting [39]. In the supplementary information, additional measurements are supplied to confirm the hypothesis on the influence of the reduction process on the lead carboxylate film formation.

COMPOUND	ELECTRON	FWHM	B.E. / eV[a]	REF.	B.E. / eV[a]	ELEM. CONC.[b]	COMPOSITION EXP.	COMPOSITION THEOR.[c]
(a) corroded bare lead sample in Figure 10.11								
metallic lead	Pb $4f_{7/2}$	2.903	137.0	[27]	136.7 - 137	25	-	-
aliphatic carbon	C 1s	2.627	285.0	[33]	285.0	23	-	-
lead oxide	Pb $4f_{7/2}$	1.986	138.0	[27]	137.8 - 138.3	16	PbO_1	PbO_1
(PbO)	O 1s	2.565	529.2	[28]	529.3 - 529.7	16		
hydrocerussite	Pb $4f_{7/2}$	1.582	138.5		138.4	5		PbC_1O_3
plumbonacrite	C 1s	2.165	288.7	[27]	288.9	3	PbC_1O_3	PbC_1O_3[d]
cerussite	O 1s	2.822	531.0		531.1	12		PbC_1O_3
(b) CV treated lead sample in Figure 10.12								
metallic lead	Pb$4f_{7/2}$	1.961	136.7	-	136.7 - 137	2	-	-
aliphatic carbon	C 1s	1.927	285.0	-	285.0	69	-	-
lead-carbon	C 1s	2.005	283.1	[34]	283.0 - 283.2	10	-	-
	Pb $4f_{7/2}$	1.961	138.8	[35]	138.5 - 138.9	3		
lead dodecanoate	C 1s	1.851	288.2	[36]	288.5	4	$PbC_{1.5}O_{3.4}$	PbC_2O_4[e]
	O 1s	2.454	531.2	[27]	531.2	10		
lead oxide	Pb $4f_{7/2}$	1.961	137.7	[28]	137.5 - 137.7	1	$PbO_{1.5}$	$PbO_{1.5}$
(PbO_2)	O 1s	2.158	529.0	[30]	527.7 - 529.0	1		
(b) IMM treated lead sample in Figure 10.14								
metallic lead	Pb $4f_{7/2}$	2.248	136.7		136.7 - 137	1	-	-
aliphatic carbon	C 1s	2.510	285.0		285.0	67	-	-
lead-carbon	C 1s	2.510	283.1		283.0 - 283.2	15	-	-
	Pb $4f_{7/2}$	2.248	138.8		138.5 - 138.9	2	PbC_2O_4	PbC_2O_4[e]
lead dodecanoate	C 1s	2.510	288.2		288.5	4		
	O 1s	2.606	531.3		531.2	7		
lead oxide	Pb $4f_{7/2}$	2.248	137.7		137.5 - 137.7	2	PbO_1	PbO_1
(PbO_2)	O 1s	2.606	529.0		527.7 - 529.0	2		PbO_1

[a] Taking into account the correction that aliphatic C 1s needs to appear at 285.0 eV.

[b] Elemental analysis and composition calculated using the area sensitivity factors with relative variations within 2.0 % [37].

[c] The theoretical compositions are measured by Taylor and Perry [27].

[d] Calculated using the plumbonacrite chemical formula: $Pb_{10}O(OH)_6(CO_3)_6$.

[e] Calculated using the lead dodecanoate chemical formula: $Pb(CH_3(CH_2)_{10}COO)_2$.

Table 10.3 – List of the results of the curve fitting analysis on the C 1s, O 1s and Pb $4f_{7/2}$ photoelectron spectra (the values are corrected for C 1s to appear at 285.0 eV).

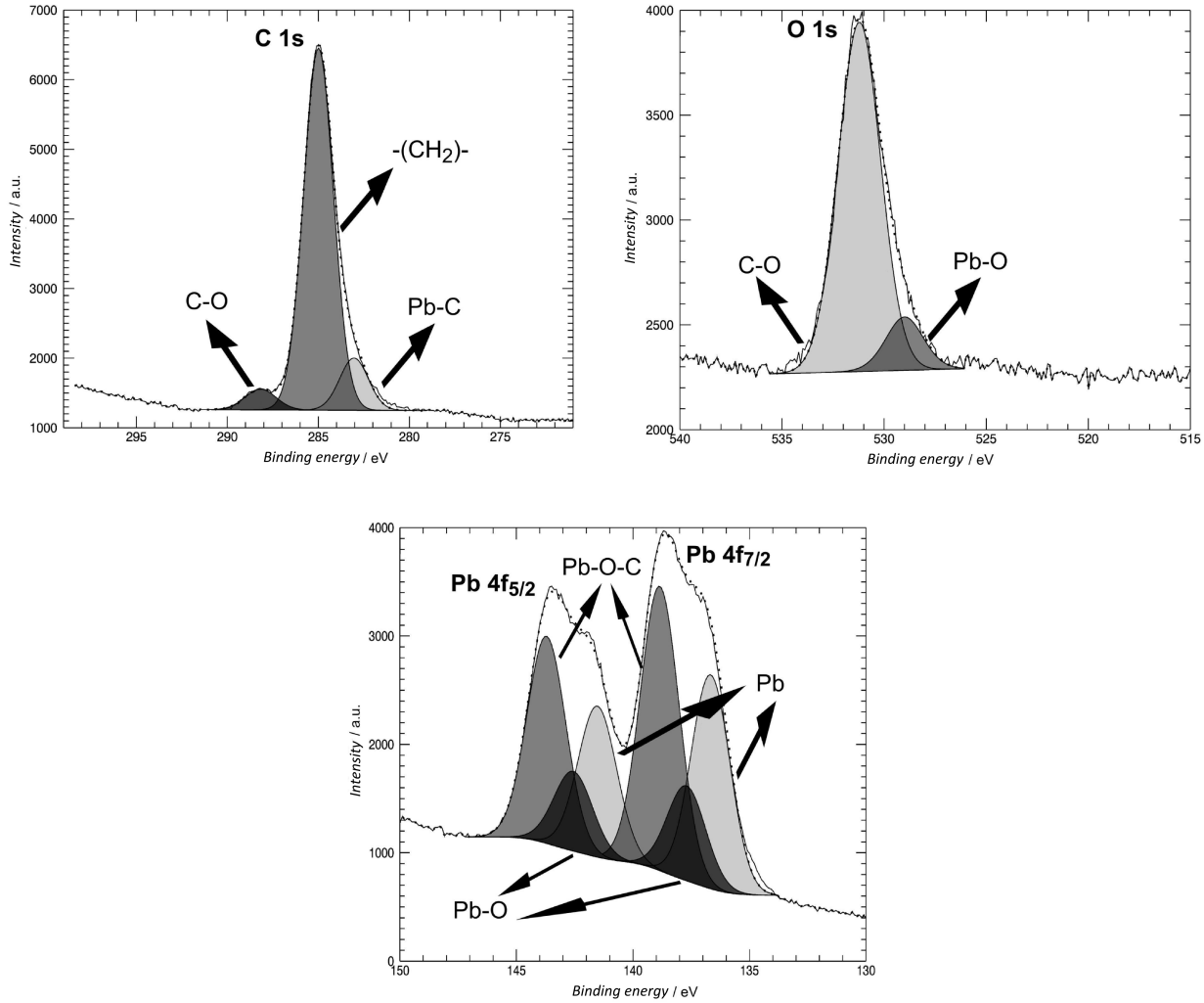


Figure. 10.12 – XPS core level spectra of the C 1s, O 1s and Pb $4f_{7/2}$ level of the with lead dodecanoate coated lead metal samples using cyclic voltammetry with components determined by the curve fitting analysis and background subtraction.

To confirm the formation of a lead dodecanoate complex on the lead electrode the high peak at 531.2 eV in the O 1s spectrum is assigned to a carbonate or carboxyl group. The atomic ratio calculated for the lead dodecanoate complexes is $PbC_{1.5}O_{3.4}$ described in Table 10.3 could be related to the proposed complex; for each lead atom there should be 2 carbon atoms and 4 oxygen atoms. The oxygen / carbon (not including the aliphatic carbons in the hydrophobic chain) atomic ratio, however, is approximately 2.3 for the adsorbed species on lead from the O 1s (531.2 eV) / C 1s (288.2 eV) intensity ratios by comparing with the results for the dodecanoic acid (which should be 2). This higher value may suggest the presence of very small amounts of other corrosion products like hydrocerussite and plumbonacrite. A larger contribution of these corrosion products will result in a higher atomic ratio value. The slightly lower atomic ratio calculated for the lead dodecanoate complex is probably a consequence of a mixture of mainly lead dodecanoate, but also some formed corrosion products.

The other small peak at 529.0 eV refers to presence of lead oxides at the surface, but in this case probably $Pb(IV)O_2$ because of the lower binding energy value. Considering different references as described in Table 10.3, we can conclude that as the oxidation of the lead and the number of oxygen atoms increases, the binding energy values tend to decrease. Due to the use of CV and high potentials up to 1.5 V vs. SCE, the lead metal is oxidized and it becomes easier to form

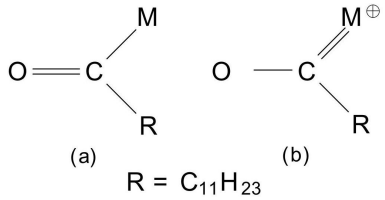


Figure. 10.13 – Chemical structure of (a) metal-alkonyl bond and (b) carbide formation.

lead corrosion products in the presence of hydroxide ions and water. These anions are present in small concentrations in the sodium dodecanoate solution from the NaOH used to neutralize the acid. Because of the high potential and the conclusions deduced from the O 1s spectrum, it is acceptable to state that predominantly PbO_2 will be present, which can be confirmed by the trend of Pb 4f core level binding energy values of PbO phases exhibiting higher values than PbO_2 and Pb_3O_4 phases, literature reports [40], theoretical predictions [41] and the atomic ratio of $PbO_{1.5}$ [27]. This oxidation of lead(II)oxides to lead(IV)oxides can be explained by the reactions in reactions eqs. (7.12a) and (7.12b).

10.6.3 Analysis of a coated lead sample using the IMM procedure

Figure 10.14 shows the XPS core level spectra of the C 1s, O 1s and Pb $4f_{7/2}$ levels of a coated lead sample using the IMM-IR technique for 1 hour immersion with all values corrected for C 1s to appear at 285.0 eV. The Pb $4f_{7/2}$ peak reveals three peaks with a binding energy of 136.7, 137.7 and 138.8 eV which are associated with again two different oxidation states of lead: metallic lead Pb(0) and, a mixture of Pb(II)products as observed in Table 10.3. As in the case of cyclic voltammetric deposition, the elemental concentration for the metallic lead is very low indicating the formation of a film containing Pb(II)compounds. The C 1s photoelectron spectrum of this treated sample shows three peaks at 285.0 eV, 283.1 eV and 288.2 eV. After curve fitting analysis, the O 1s XPS spectrum shows two peaks at 531.3 eV and 529.0 eV. The C 1s, O 1s and Pb 4f peaks could be explained the same way as the ones from the cyclic volammetrically deposited lead dodecanoate coating. The most important conclusions are based on the differences of the intensities of the peaks. The experimental composition for the lead dodecanoate complexes is calculated to be $PbC_{2.1}O_{4.0}$ as shown in Table 10.3. This agrees with the proposed complex: for each lead atom there should be 2 carbon atoms and 4 oxygen atoms. This perfect fit assumes that no other corrosion products containing carbon atoms are formed. The aliphatic carbon / carboxylic carbon atomic ratio from the C 1s (285 eV) / C 1s (288.2 eV) intensity ratios is estimated to be 18. This ratio predicts the number of carbon atoms in the aliphatic carbon chain of the proposed complex, which should be close to 11.0 for lead dodecanoate compounds. The higher contamination is caused by the longer and more uncontrollable deposition of the lead dodecanoate complex, which could also explain the higher elemental concentration of the carbide-like bond. The oxygen / carbon (not including the aliphatic carbons in the hydrophobic chain) atomic ratio, however, is estimated to be approximately 2 for the adsorbed species on lead from the O 1s (531.3 eV) / C1s (288.2 eV) intensity ratios by comparing with the results for the dodecanoic acid (which should be 2). This value also predicts the presence of only lead dodecanoate complexes containing carbon atoms on the surface. The Pb 4f (137.7 eV) / O 1s (529.0 eV) atomic ratio predicts the presence of a PbO_1 compound. This indicates that both PbO and PbO_2 species are present on the surface, which is probably a consequence of the lower oxidative conditions. If the intensity of the C 1s core electron spectra from the aliphatic carbon and the carbon from the lead carboxylate for both techniques are compared, one can see that twice the amount of carboxylates is deposited using CV compared to IMM. Nevertheless, the corrosion protective properties of both techniques are almost the same as already established in chapter 8.2. This means the protection using immersion is much more effective considering the formation of more protective crystal clusters instead of forming small packed

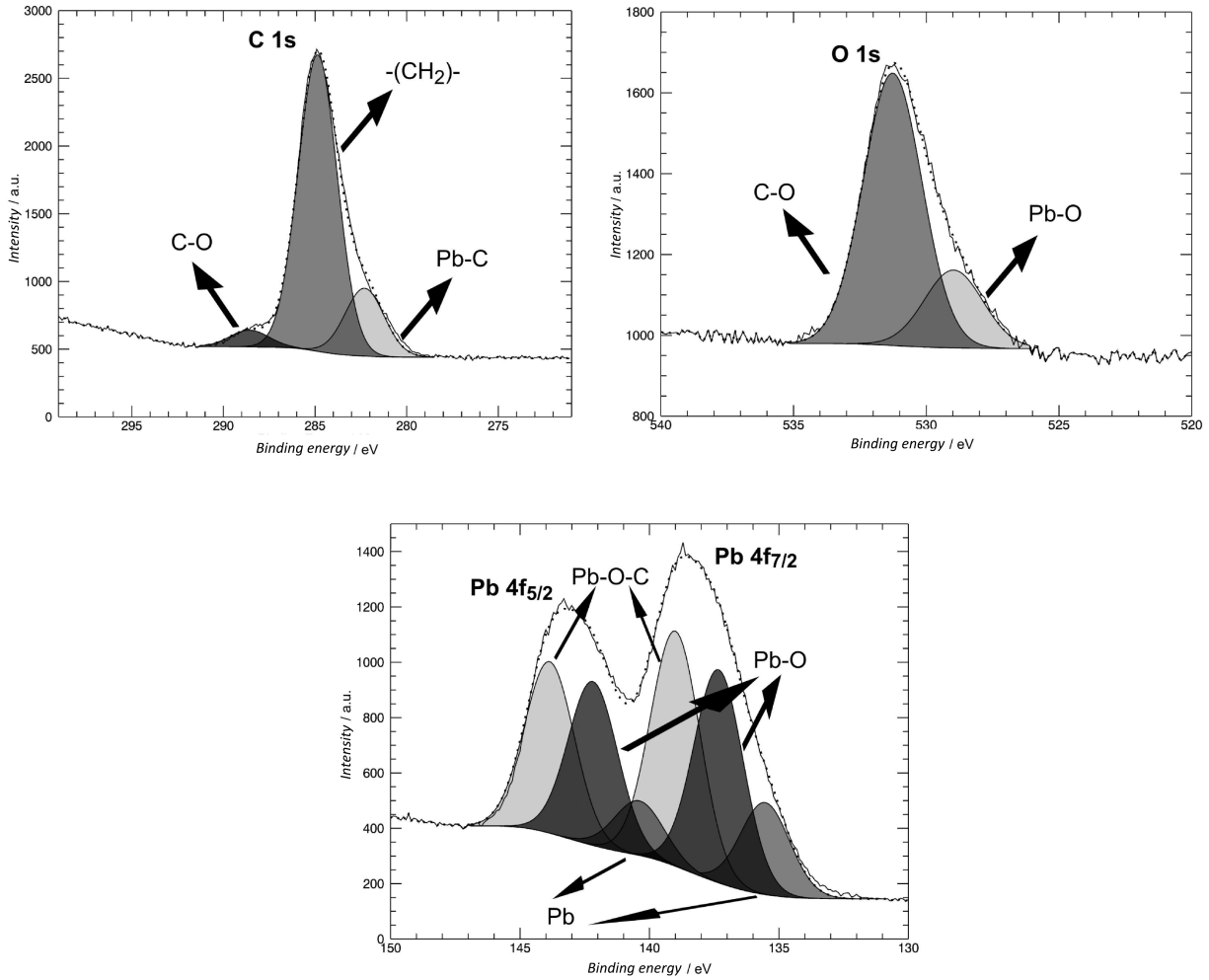


Figure. 10.14 – XPS core level spectra of the C 1s, O 1s and Pb $4f_{7/2}$ level of the with lead dodecanoate coated lead metal samples using the immersion technique with components determined by curve fitting analysis and background subtraction.

crystals.

10.6.4 Influence of reduction step on the XPS data

In Figure 10.15, the C 1s core level spectrum of a lead dodecanoate coated lead sample without the use of an initial reduction step is shown. A comparison of Figures 10.12a and 10.14a with Figure 10.15a shows that the use of the initial reduction step has increased the amount of lead-carbide species formed on the lead surface. The reductive process makes the lead metal atoms at the surface more reactive and permits them to react directly with the carbon atoms with the formation of metal-carbonyl functional groups. In Figure 10.15b, where the C 1s core level spectrum of a lead sample corroded in the atmosphere after an initial reduction is depicted, no lead-carbon bonds are seen. This means that even with an initial reduction step the atmosphere does not provide an environment to grow lead carbide species, probably because in this case no carboxylate solution is used. As a conclusion, we can state that a carboxylate solution is needed to provide metal-carbon bonds and that a reduction treatment provides a more reactive surface to produce more metal-carbon bonds.

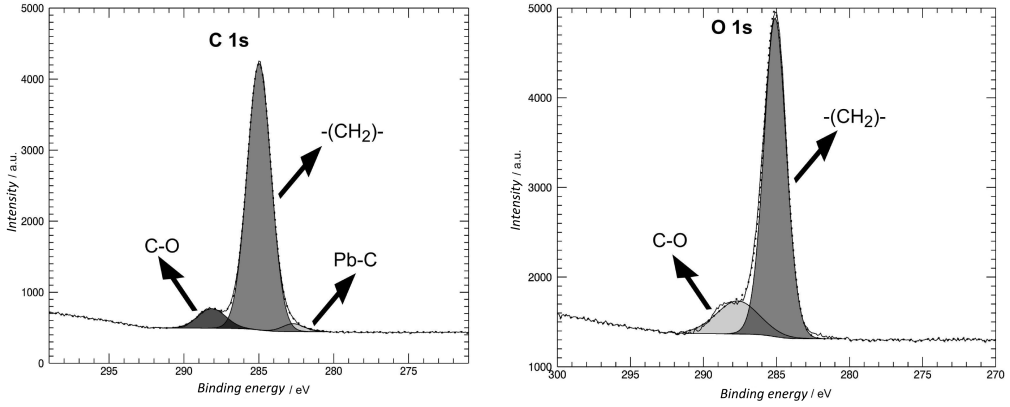


Figure. 10.15 – XPS core level spectra of the C 1s spectrum of (a) a lead sample coated with a lead dodecanoate coating without the use of the initial reduction and (b) a lead sample corroded in the atmosphere after an initial reduction in the sodium dodecanoate with components determined by curve fitting analysis and background subtraction.

10.7 Summary and conclusions

The adsorption of sodium dodecanoate inhibitor was tested in the ASTM solution on a polished lead substrate in order to study the adsorption and inhibition behavior. The impedance and potentiodynamic polarization results show that a higher inhibitor concentration causes an increase of the total resistance and a decrease of the corrosion current density. Using lower inhibitor concentrations (lower than the c.m.c.), the inhibitor covers a part of the lead surface protecting against anodic corrosion. In this case, monolayer adsorption can be assumed. Higher inhibitor concentrations (higher than the c.m.c.) cover a larger area of the surface, produce $Pb(C_{12})_2$ species and form a lead dodecanoate coating.

By applying the Frumkin adsorption theory on the impedance measurements, we assume that the lead oxide covered surface has a fixed number of adsorption sites where each site holds only one adsorbed species considering interactions between the adsorbing inhibitor species. From the fitting of the impedance measurements, protection due to lead corrosion products is observed. The inhibitor forms a hydrophobic film, which repels water, one of the primary malefactors for corrosion. The calculated standard Gibbs free energy change of the adsorption confirms that the metal surface forms a coordinate bond with dodecanoate anions to form a new lead dodecanoate complex upon chemisorption.

The SEM-EDS measurements of the polished sample show particles used for the polishing, which are stuck into the lead matrix due to softness of the lead metal. It concerns large SiC and small diamond particles. The coated sample shows the formation of a hydrophobic lead soap with a two-dimensional crystal structure, which is characterized by a lamellar building of sheets. The cross-sectional image predicts a thickness of the lead dodecanoate coating between 10 - 20 μm.

The XPS study of the atmospherically corroded lead sample shows a thin layer (a few nanometers thick) of lead corrosion products consisting of particularly lead(II)oxide and, to a lesser extent, hydrocerussite and plumbonacrite, which forms from a reaction with atmospheric carbon dioxide. The XPS measurement of the treated lead sample using CV indicated the formation of a lead carboxylate complex. In addition to the coating, lead(IV)oxides are also formed on the surface, which indicates the presence of gaseous oxygen or hydroxide-ions in the solution and the polarization of the surface to a high potential. The XPS measurements show that the immersion method results in the formation of a smaller amount of lead dodecanoate complexes, but produces a less contaminated surface. This explains the high inhibition efficiency even with the formation of a smaller amount of lead dodecanoate complexes, which can, in this case, form perfectly ordered crystals on the lead surface.

Finally, we conclude that the lead dodecanoate coatings are contaminated with small amounts of lead corrosion products. However, despite this contamination, lead dodecanoate coatings protect the lead surface very well and are easily formed using both electrochemical and immersion techniques.

References for Chapter 10

[1] J. TAFEL, Kathodenpotential und elektrolytische Reduktion in schwefelsaurer Lösung, *Z. Electrochem.* **12** (7) (1906), 112–122.

[2] M. ZHELUDKEVICH et al., Triazole and thiazole derivatives as corrosion inhibitors for AA2024 aluminum alloy, *Corros. Sci.* **47** (12) (2005), 3368–3383.

[3] M. ABDALLAH, Rhodanine azosulpha drugs as corrosion inhibitors for corrosion of 304 stainless steel in hydrochloric acid solution, *Corros. Sci.* **44** (4) (2002), 717–728.

[4] A. GEWIRTH and S. THORUM, Electroreduction of dioxygen for fuel-cell applications: Materials and challenges, *Inorg. Chem.* **49** (8) (2010), 3557–3566.

[5] S. UMOREN, Y. LI, and F. WANG, Synergistic effect of iodide ion and polyacrylic acid on corrosion inhibition of iron in H_2SO_4 investigated by electrochemical techniques, *Corros. Sci.* **52** (7) (2010), 2422–2429.

[6] E. ROCCA and J. STEINMETZ, Inhibition of lead corrosion with saturated linear aliphatic chain monocarboxylates of sodium, *Corros. Sci.* **43** (5) (2001), 891–902.

[7] E. ROCCA, C. RAPIN, and F. MIRAMBET, Inhibition treatment of the corrosion of lead artefacts in atmospheric conditions and by acetic acid vapor: use of sodium decanoate, *Corros. Sci.* **46** (3) (2004), 653–665.

[8] D. LOVEDAY, P. PETERSON, and B. RODGERS, Evaluation of organic coatings with electrochemical impedance spectroscopy, *J. Coat. Technol.* **10** (2004), 88–93.

[9] J. GRANDLE and S. TAYLOR, Electrochemical impedance spectroscopy of coated aluminum beverage containers. I. Determination of an optimal parameter for large sample evaluation, *Corros.* **50** (10) (1994), 792–803.

[10] M. KENDIG, F. MANSFELD, and S. TSAI, Determination of the long term behavior of coated steel with AC impedance measurements, *Corros. Sci.* **23** (4) (1983), 317–329.

[11] F. MANSFELD, M. KENDIG, and S. TSAI, Evaluation of corrosion behavior of coated metals with AC impedance measurements, *Corros.* **38** (1982), 478–485.

[12] B. FASTRUP and A. SAARNAK, AC impedance of painted and scribed steel panels under atmospheric exposure, *Prog. Org. Coat.* **16** (3) (1988), 277–290.

[13] P. BONORA, F. DEFLORIAN, and L. FEDRIZZI, Electrochemical impedance spectroscopy as a tool for investigating underpaint corrosion, *Electrochim. Acta* **41** (7-8) (1996), 1073–1082.

[14] E. OGUZIE et al., Corrosion and corrosion inhibition characteristics of bulk nanocrystalline ingot iron in sulfuric acid, *J. Solid State Electrochem.* **12** (6) (2008), 721–728.

[15] C. GILES, D. SMITH, and A. HUITSON, A general treatment and classification of the solute adsorption isotherm. I. Theoretical, *J. Colloid Interface Sci.* **47** (3) (1974), 755–765.

[16] C. GILES, A. D'SILVA, and I. EASTON, A general treatment and classification of the solute adsorption isotherm part. II. Experimental interpretation, *J. Colloid Interface Sci.* **47** (3) (1974), 766–778.

[17] L. NARVÁEZ, E. CANO, and D. BASTIDAS, 3-hydroxybenzoic acid as AISI 316L stainless steel corrosion inhibitor in a H_2SO_4-HF-H_2O_2 pickling solution, *J. Appl. Electrochem.* **35** (5) (2005), 499–506.

[18] I. LANGMUIR, The adsorption of gases on plane surfaces of glass, mica and platinum, *J. Am. Chem. Soc.* **40** (9) (1918), 1361–1403.

[19] A. FRUMKIN, Electrocapillary curve of higher aliphatic acids and the state equation of the surface layer, *Z. Phys. Chem.* **116** (1925), 466–484.

[20] S. SOHN and D. KIM, Modification of Langmuir isotherm in solution systems-definition and utilization of concentration dependent factor, *Chemosphere* **58** (1) (2005), 115–123.

[21] K. KOLEV et al., Comparison of the van der Waals and Frumkin adsorption isotherms for sodium dodecyl sulfate at various salt concentrations, *Langmuir* **18** (2002), 9106–9109.

[22] E. CASTELLINI et al., Thermodynamic aspects of the adsorption of cytochrome c and its mutants on kaolinite, *Langmuir* **25** (12) (2009), 6849–6855.

[23] H. KELEŞ et al., Adsorption and inhibitive properties of aminobiphenyl and its Schiff base on mild steel corrosion in 0.5M HCl medium, *Colloids Surf. A* **320** (1-3) (2008), 138–145.

[24] K. DE WAEL et al., Electrochemical deposition of dodecanoate on lead in view of an environmentally safe corrosion inhibition, *J. Solid State Electrochem.* **14** (3) (2010), 407–413.

[25] F. LACOUTRE et al., Anhydrous lead(II)heptanoate, *Acta Crystallogr. C* **57** (5) (2001), 530–531.

[26] R. PEREIRA, A. VALENTE, and H. BURROWS, The interaction of long chain sodium carboxylates and sodium dodecylsulfate with Pb(II) ions in aqueous solutions, *J. Colloid Interface Sci.* **414** (2014), 66–72.

[27] J. TAYLOR and D. PERRY, An X-ray photoelectron and electron energy loss study of the oxidation of lead, *J. Vac. Sci. Technol. A* **2** (2) (1984), 771–774.

[28] K. KIM, T. O'LEARY, and N. WINOGRAD, X-ray photoelectron spectra of lead oxides, *Anal. Chem.* **45** (13) (1973), 2214–2218.

[29] C. COZZA et al., An X-ray photoelectron spectroscopy study of the interaction of mercapto-benzo-thiazole with cerussite, *Int. J. Miner. Process.* **34** (1–2) (1992), 23–32.

[30] P. VELUCHAMY and H. MINOURA, Surface analysis of anodic lead oxide films prepared in hot alkaline solutions, *Appl. Surf. Sci.* **126** (1998), 241–245.

[31] E. KIM and J. HERRERA, Characteristics of lead corrosion scales formed during drinking water distribution and their potential influence on the release of Lead and Other Contaminants, *Environ. Sci. Technol.* **44** (2010), 6054–6061.

[32] A. NIKLASSON, L. JOHANSSON, and J. SVENSSON, Influence of acetic acid vapor on the atmospheric corrosion of lead, *J. Electrochem. Soc.* **152** (12) (2005), B519–B525.

[33] T. TAKAHAGI and A. ISHITANI, XPS study on the surface structure of carbon fibers using chemical modification and C1s line shape analysis, *Carbon* **26** (3) (1988), 389–395.

[34] K. KISHI and M. ROBERTS, Mechanism of the interaction of hydrogen sulphide with adsorbed oxygen on lead studied by X-ray induced photoelectron spectroscopy, *J. Chem. Soc., Faraday Trans. 1* **71** (1975), 1721–1726.

[35] P. BERTRAND and P. FLEISCHAUER, X-ray photoelectron spectroscopy study of the surface adsorption of lead naphthenate, *J. Vac. Sci. Technol. A* **17** (6) (1980), 1309–1314.

[36] J. GAO et al., Synthesis and characterization of adsorbent for Pb(II) - capture by using glow discharge electrolysis plasma, *Bull. Korean Chem. Soc.* **31** (2) (2010), 406–414.

[37] C. WAGNER et al., Empirical atomic sensitivity factors for quantitative-analysis by electron-spectroscopy for chemical-analysis, *Surf. Interface Anal.* **3** (1981), 211–225.

[38] K. KISHI and S. IKEDA, X-ray photoelectron spectroscopic study for the adsorption of acetic acid and ethylenediamine on iron and nickel, *Appl. Surf. Sci.* **5** (1) (1980), 7–20.

[39] G. DENIAU et al., Carbon-to-metal bonds: Electrochemical reduction of 2-butenenitrile, *Surf. Sci.* **600** (3) (2006), 675–684.

[40] P. VELUCHAMY and H. MINOURA, Selective formation of α-PbO and β-PbO films on Pb electrodes by potentiostatic anodisation in alkaline solutions, *J. Electroanal. Chem.* **396** (1995), 211–217.

[41] J. THOMAS and M. TRICKER, Electronic structure of the oxides of lead. II. An XPS study of bulk rhombic PbO, tetragonal PbO, β-PbO_2 and Pb_3O_4, *J. Chem. Soc., Faraday Trans. 2* **71** (1975), 329–336.

11

Lead dodecanoate coatings for the protection of organ samples

Reprinted from Appl. Surf. Sci., 292, M. De Keersmaecker, K. Verbeken and A. Adriaens, Lead dodecanoate coatings for the protection of lead and lead-tin alloy artifacts: two examples, 149-160, 2014, with permission from Elsevier.

11.1 Description and treatment of the organ samples

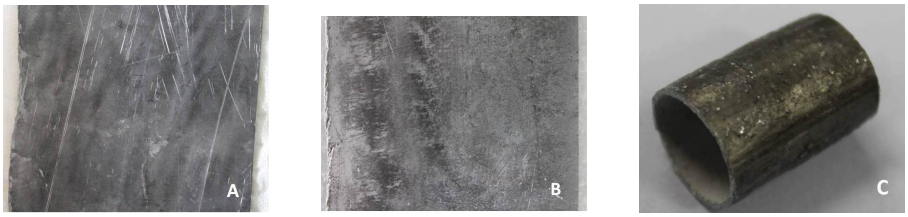


Figure. 11.1 – Photograph of the investigated organ samples: (a) sample 1, (b) sample 2 and (c) sample 3.

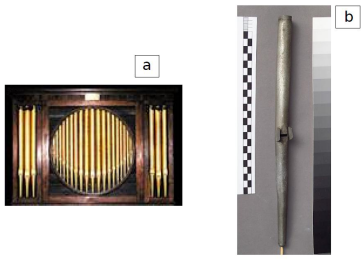


Figure. 11.2 – Photograph of (a) the organ in St. Mary the Virgin Parish Church (Edith Weston, Rutland, UK) © Amphion Recordings and (b) the studied organ pipe © P. Storme.

All organ samples are shown in Figure 11.1. The first (sample 1) and second (sample 2) samples are two sheets (with dimensions 20 cm $\times$ 10 cm) of organ metal, which consist of a mixture of lead and tin. The two metal sheet samples were pre-treated by hammering and painting. To produce the organ pipe, the pipe maker simply needs to cut the sheet to the right size, roll it around a cylinder to shape it, and solder the seam closed. The third sample (sample 3) is a piece of a real organ pipe (measuring 2 $\times$ 1.5 cm $\times$ 1.5 cm) originating from the principal part of the organ in St. Mary the Virgin Parish Church (Edith Weston, Rutland, UK), which was built by Samuel Green of London in 1787 (English Baroque) for an unknown residence in the capital (Figure 11.2). The organ was sold in 1842 to the Rev. C.H. Lucas, who was vicar of the church, and transported by rail to Edith Weston where it was placed in Edith Weston Hall. The brass plate on the organ bears the inscription: ”This organ is presented to the inhabitants of Edith Weston by Richard Lucus (1867)”. It is presumed that Porrit of Leicester installed the present swell front in 1873. An electric blower was installed in 1971, and the organ was restored in 1981 by M. Goetze and D. Gwynne [1]. Using X-ray fluorescence, the research

group of P. Storme (Artesis, Antwerp, Belgium), observed that the organ's corpus contains a large amount of tin, and that the organ's foot consists mainly of lead [2].

11.2 Experimental procedures

11.2.1 Deposition procedure

The organ samples were not pretreated, and were used as received. Two deposition procedures were used to apply a lead dodecanoate coating on the sample surface: the 'controlled' CV method using 30 scans (cv 30sc) and the 'uncontrolled' IMM-IR method with a 24 hour immersion (IMM 24h) in Table 8.1 and Table 9.1 described in chapter 7. The voltammetric deposition was done using a potentiostat/galvanostat PGSTAT 100 controlled by the GPES 4.9.005 software package (ECO Chemie (Autolab), The Netherlands). Both were carried out in a neutralized 0.05 mol L^{-1} sodium dodecanoate solution described in section 7.3.1. Finally, the lead dodecanoate coatings are rinsed in distilled water and air-dried.

11.2.2 Corrosion test procedure

The electrochemical experiments were performed using a three-electrode system in a 500 mL glass beaker filled with 100 mL electrolyte consisting of 5 μg L^{-1} acetic acid (98 - 99%, Merck, USA) and 0.1 M tetrabutylammonium bromide (TBAB) (> 99%, Sigma Aldrich, USA)[1] as a supporting electrolyte[2]. The setup consisted of a saturated calomel reference electrode (SCE), a platinum mesh counter electrode, and the organ sample as a working electrode. The corrosion resistance of the coated samples was recorded using electrochemical impedance spectroscopy, at E_{corr} measured during 1,000 s, over a distributed frequency range of 100 kHz - 1 Hz, with a 10 mV amplitude sinusoidal AC perturbation signal. The total contact time with the acetic acid electrolyte was 20 min. To record the AC impedance plots, an IM6 impedance and electrochemical measurement system controlled by the Thales software (ZAHNER, Germany) was used. At the end, the raw data were processed and fitted with the Matlab software release 13.0 (Mathworks, USA).

11.2.3 Surface analysis techniques

Scanning electron microscope (SEM) micrographs and energy dispersive X-ray spectroscopy (EDS) spectra of selected specimens were obtained using a SEM XL30 (Philips, The Netherlands) with a tungsten filament, equipped with both a secondary electron and backscattered electron detector. The electron beam source was operated at 20 kV. SEM images were taken of all three organ samples using both secondary and backscattered electrons. The morphology and composition of the alloy, the coating, and the corrosion layers were characterized using EDS. The instrument is described in section 4.4.2.7.

X-ray diffraction data were obtained from the bare and coated samples using a Siemens D5000 X-ray diffractometer equipped with a germanium focusing monochromator to produce Mo $K_{\alpha 1}$ radiation. Data were collected by means of a conventional θ-2θ scan in the 2θ range 2°– 40° with a step size of 0.05°, and measuring each point for 5 s. Figures 11.7 and 11.8 show the XRD data of the bare and coated sample 1 and sample 2. This procedure is explained in section 4.5.1.

[1] Different supporting electrolyte solutions were tested, but all of them reacted with the lead ions forming lead precipitates. Trying to exclude the influence of the supporting electrolyte as much as possible, the measurements were carried out in TBAB. Furthermore, the presence of the bromide ions was taken into account in the overall discussion of the results.

[2] The electrode surface will either be positively or negatively charged, depending on the applied potential, and this surface charge will either repulse or attract the ion diffusing to the electrode surface. This will cause an increase or decrease in the limiting current, which is called the migration current. The migration current can be prevented by adding a high concentration, at least 100-fold greater than the test substance, of an inert supporting electrolyte. The high concentration of inert ions eliminates the attraction or repulsion forces between the electrode and the analyte, and the inert ions are attracted or repulsed instead. These inert ions are not electrolyzed, however. A second reason for adding a supporting electrolyte is to decrease the iR drop of the cell. For this reason, at least 0.1 M supporting electrolyte is commonly added [3–5].

11.3 Microscopic examination

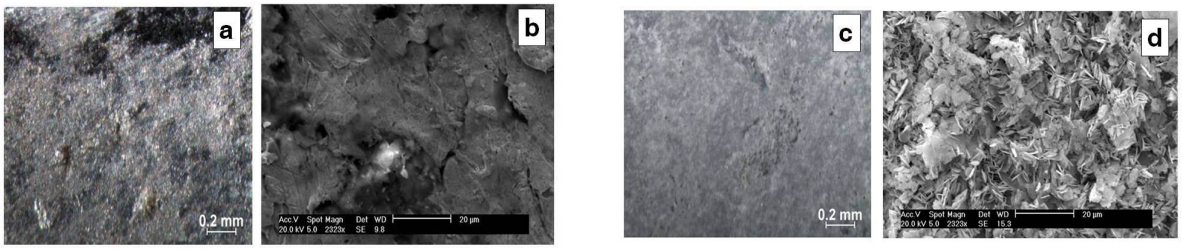


Figure. 11.3 – The untreated and treated first metal sheet pipe organ sample using the IMM method: optical observation (a and c) and SEM image (b and d).

The characterization of the surfaces by optical and scanning electron microscopy was carried out without any pretreatment. Optical and SEM micrographs of the untreated and treated surfaces of both metal sheets are shown in Figures 11.3-11.5. The surface pattern of both untreated organ samples appears to be heterogeneous and disparate at first sight. The organ samples show color changes on the metal surface, which indicates the presence of a thin layer of different atmospheric corrosion products as shown in Figures 11.3a, 11.4a and 11.5a. The pretreatment and the hammering of the organ metal causes the metal sheets to form cracks or fissures and results in a very rough surface topography. The rough surface complicates the construction of a coating without irregularities and pinholes as shown in Figures 11.3b, 11.4b, and 11.5b.

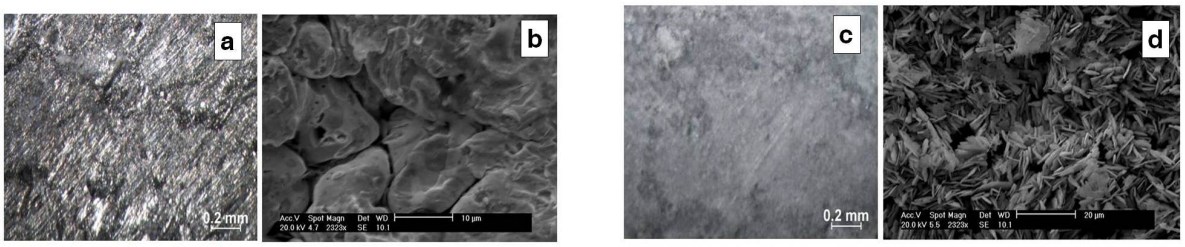


Figure. 11.4 – The untreated and treated second metal sheet pipe organ sample using the IMM method: optical observation (a and c) and SEM image (b and d).

The treated lead-tin organ samples, after immersion for 24 h in a solution containing 0.05 mol L^{-1} of NaC_{12} were also visualized. After this inhibition treatment, the optical view of the organ sample surface changes to a light gray color due to the coating deposition as shown in Figures 11.3c, 11.4c, and 11.5c). In Figures 11.3d, 11.4d and 11.5d, show that the pipe material's surface morphology totally changed. The SEM observations reveal that the surface of both organ samples is well covered by flake-shaped crystals [6]. These are formed during the reaction between the aliphatic carboxylate group and the surface of the organ metal. A hydrophobic lead soap is formed with a two-dimensional crystal structure, which is characterized by a lamellar building of carboxylate units containing a middle metallic plane from which the aliphatic chains are perpendicularly arranged. The lead atoms are disposed on a zigzag chain in these planes, and are coordinated to six oxygen anions in a very distorted polyhedron by analogy with the lead heptanoate crystal structure [7] based on the morphological similarity. The tin metal present does not interfere with the reaction between the lead and the dodecanoate anions. The images of the treated organ metal surface show good coverage by the lead dodecanoate layer. The lead soap crystals form close-packed hydrophobic clusters, which hinder the progress of corrosion processes. A small irregularity or hole in the coating could, however, rapidly decrease the protective behavior of the deposited lead dodecanoate coating.

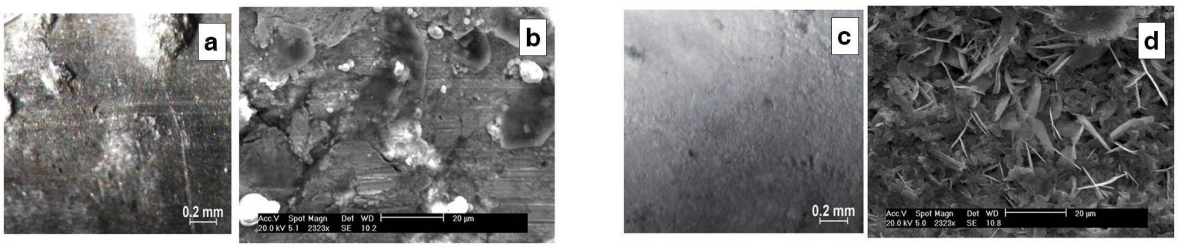


Figure. 11.5 – The untreated and treated pipe organ sample using the IMM method: optical observation (a and c) and SEM image (b and d).

11.4 EDS-analysis

Six sample fragments, three untreated and three treated, were analyzed using SEM-EDS. EDS microanalysis was done on the same area where the SEM image was taken. The EDS spectra were used to determine the chemical composition of the metal organ samples before and after exposure to the dodecanoate inhibitor solution. Three measurements were taken on different places on the surface of the samples. The composition of the sample is defined as the average of the individual compositions calculated using a standard less method. Table 11.1 shows the calculated elemental compositions for the three untreated metal organ samples. The results indicate, as expected, the presence of two main alloy elements, namely lead and tin. The distribution remains approximately the same from one area to another, which means that tin is homogeneously distributed in the bulk lead material. In addition to the lead-tin alloy bulk material, it is possible to find small iron and copper inclusions on the sample surface. Table 11.1 demonstrates that the tin content of the different organ samples changes considerably. The tin concentration influences the sound of the organ pipe, which means that it is possible that the organ pipe builder changes the lead-tin alloy composition depending on the sound it needs to produce.

	SAMPLE 1		SAMPLE 2		SAMPLE 3	
	SnL	PbL	SnL	PbL	SnL	PbL
1	8	92	15	85	28	72
2	14	86	15	85	28	73
3	9	90	15	85	26	72
average	11	89	15	85	28	72

Table 11.1 – The calculated elemental compositions for the untreated different metal organ samples (normalized, in wt%).

Figure 11.6 shows the EDS spectra of sample 3 both before and after the 24 h inhibition treatment. The spectrum of the untreated surface in Figure 11.6a indicates the presence of other elements, apart from lead and tin, such as C and O, which originate from anions such as carbonates and oxides, which are produced by atmospheric corrosion and ionic exchange processes. The very low intensities of these elements are caused by the high intensities of the bulk material, especially from the lead metal, and the fact that these are both low atomic number elements. For the lead, which is a high atomic number atom, it is usually not difficult to get a higher precision, because of the higher sensitivity of the method for this element. The higher sensitivity ensures, in this case, that the signals for the lower Z elements are reduced. In most organ samples, regardless of the macroscopic corrosion morphology, the dominant corrosion products are lead corrosion products such as hydrocerussite, cerussite and plumbonacrite [8]. The presence of these corrosion products can explain the oxygen and carbon peaks. The presence of the Na peak indicates lead corrosion in the presence of sodium chloride

(NaCl), which strongly enhances the atmospheric corrosion of lead at high relative humidity. The relatively intense Na peak indicates a high relative humidity and high salt concentration in the church atmosphere.

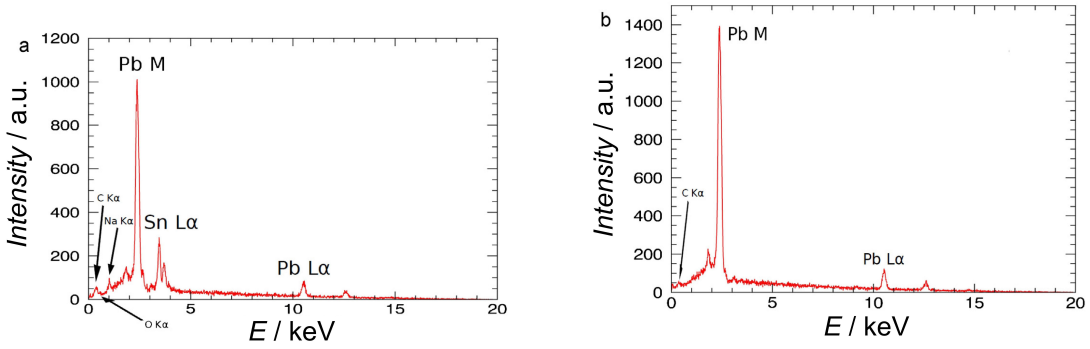


Figure. 11.6 – The EDS spectra of the pipe organ sample (sample 3): a) untreated sample and b) treated sample.

After the inhibition treatment shown in Figure 11.6b, the tin peak in the EDS spectrum disappears. The only possible hypothesis for this result is the formation of a thick film which does not contain tin compounds. This means that the dodecanoate anion only reacts with lead, and forms a thick lead dodecanoate crystal film, which is the only metal compound which can be detected after immersion. After deposition, C and O elements are detected. In this case, however, it is not due to the lead corrosion products, but due to the presence of the organic dodecanoate compound. The formation of a protective film of inhibitor on the lead-tin alloy surface was also confirmed in the previous paragraph by the SEM observations in Figure 11.5.

11.5 XRD-analysis

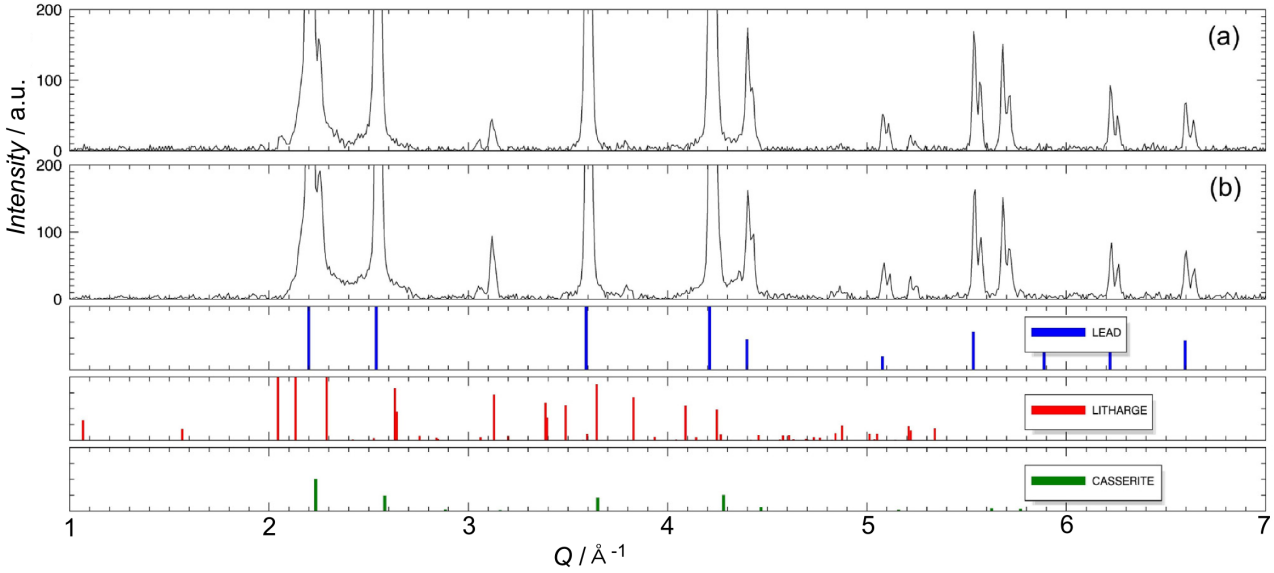


Figure. 11.7 – X-ray diffractogram from uncoated Pb/Sn sample 1 (a) and uncoated Pb/Sn sample 2 (b).

The presence of crystalline phases is demonstrated by sharp Bragg peaks. Figure 11.7 shows the diffraction peaks of the bare organ sample containing very intense and sharp peaks. The four strongest peaks in the diffraction spectrum, at Q values of 2.19 $Å^{-1}$, 2.53 $Å^{-1}$, 3.58 $Å^{-1}$ and 4.20 $Å^{-1}$ and correspond to diffraction peaks from the lead substrate (pattern reference number 03-065-2873 in the PDF-2 database (2012) of the International Centre for Diffraction Data (ICDD)).

On sample 1, there is also evidence of the presence of a small concentration of litharge(PbO), just as we found in the case of decanoate growth from a sodium decanoate solution [9]. This is demonstrated by the peak at 2.04 $Å^{-1}$, which is the (111) peak at 2.04 $Å^{-1}$ reported for synthetic litharge (pattern reference number 03-065-1471 in the PDF-2 ICDD database (2012)). Most of the other important diffraction peaks of litharge are masked by the very intense lead peaks. The difference in the angle between the reported and the observed litharge peak can be explained by strain effects in the top oxide layer. All tin seems to be present as tin dioxide (casserite), which shows important peaks, at 2.23 $Å^{-1}$, 2.56 $Å^{-1}$, 3.63 $Å^{-1}$ and 4.27 $Å^{-1}$ (pattern reference number 00-050-1429 in the PDF-2 ICDD database (2012)). The diffraction peaks of this tin corrosion product seem a lot sharper and more intense in Figure 11.7b compared to the peaks in Figure 11.7a. This is explained by the higher tin concentration in the second sample, which has already been suggested by the EDS analysis. The higher tin concentration in sample 2 also explains the absence of a clear litharge peak, because less lead corrosion can take place at the sample surface. Furthermore, small contributions of lead carbonates (cerussite and hydrocerussite) and lead oxides (minium and plattnerite).

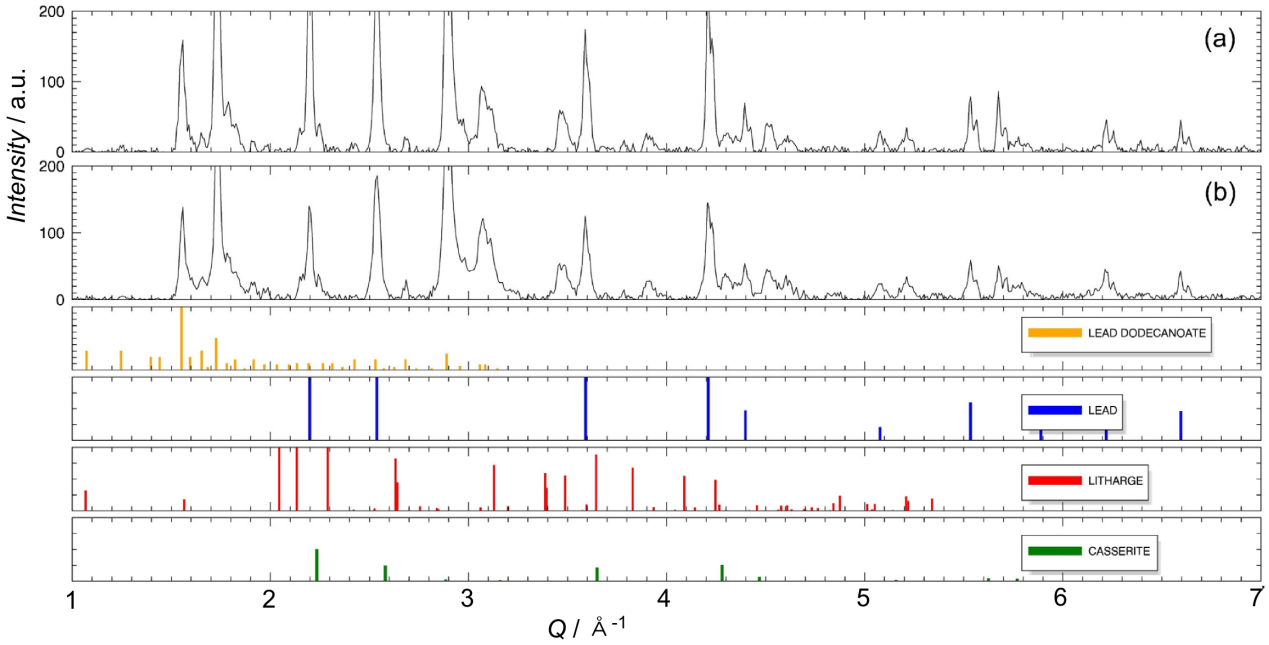


Figure. 11.8 – X-ray diffractogram from coated Pb/Sn sample 1 (a) and coated Pb/Sn sample 2 (b).

Figure 11.8 shows the XRD data of the coated sample 1 and sample 2. These spectra indicate the presence of lead dodecanoate crystals (pattern reference number 00-009-0712 in the ICDD database). This is demonstrated by strong diffraction peaks at 1.5514 $Å^{-1}$, 1.65 $Å^{-1}$, 1.73 $Å^{-1}$ and 2.89 $Å^{-1}$. The litharge peaks are mostly masked by the lead dodecanoate diffraction peaks. The intensities of all lead substrate diffraction peaks are lowered due to the presence of the thin lead dodecanoate layer on the sample surface. The intensities of the tin diffraction peaks, however, show no decrease, which indicates that tin itself does not take part in the reaction with the dodecanoate inhibitor. Also, for the coated samples, sample 2 has more intense tin diffraction peaks. Tin forms a thin layer of tin dioxide (casserite) on the lead–tin alloy surface, as a result of atmospheric corrosion and the deposition in a slightly basic solution. The two most intense casserite diffraction peaks, at 2.23 $Å^{-1}$ and 4.28 $Å^{-1}$, are clearly seen in the diffraction spectra of the coated samples The intensity, however, is somewhat lower, which means a slightly thicker layer is formed due to the deposition in the basic inhibitor solution. The presence of this tin dioxide layer on the surface decreases the active corrosion of lead in the presence of acetic acid vapor [10].

11.6 Corrosion testing

In the following section, we will test the coated organ samples for their corrosion protective properties.

11.6.1 Organ plate samples

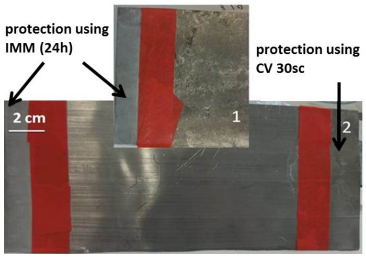
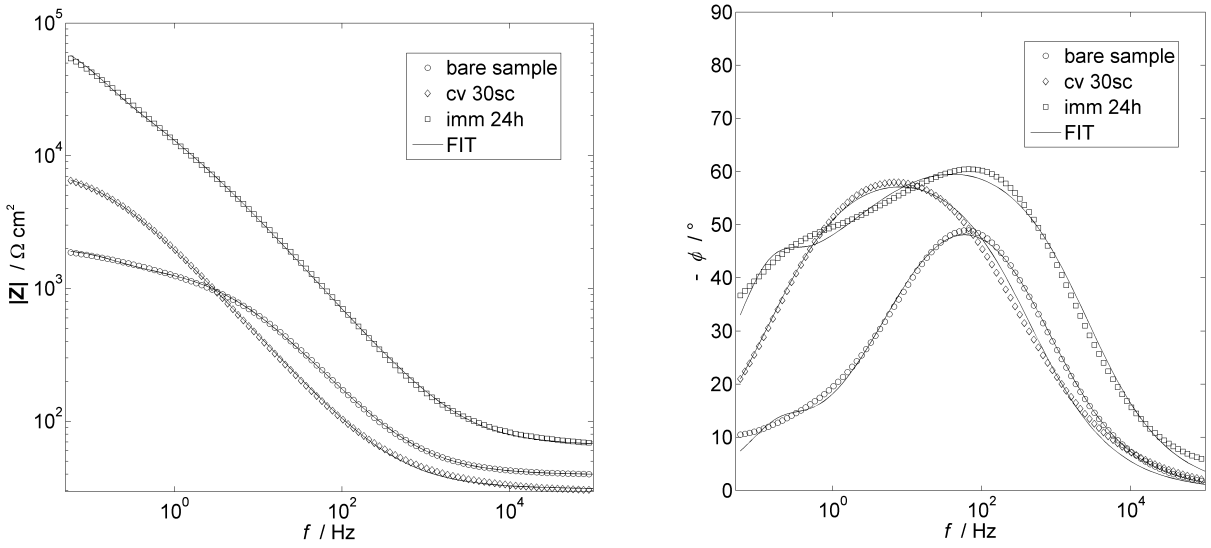


Figure. 11.9 – Photograph of two partly coated organ samples. The samples have been coated with lead dodecanoate using IMM (on the left) and CV (only sample 2, on the right)

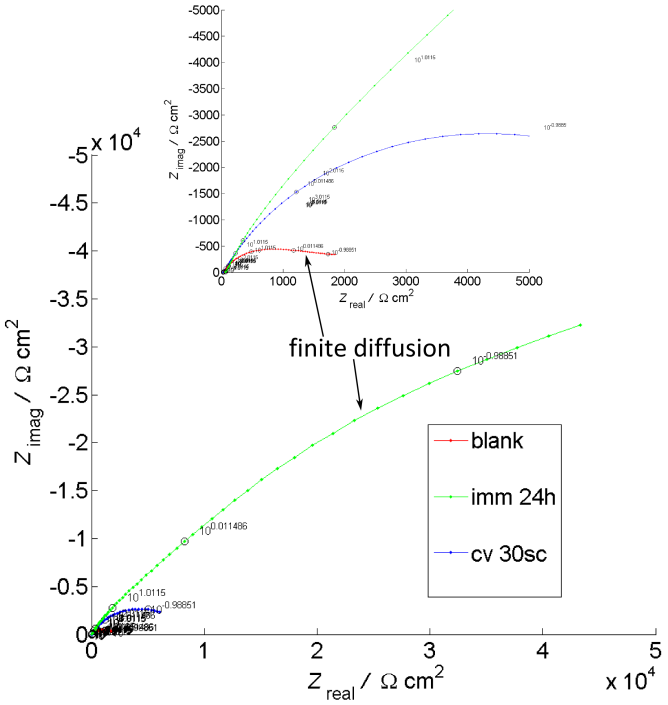
Figure 11.9 shows the two metal organ plate samples (sample 1 and 2), which have been partly coated with a lead dodecanoate coating using the IMM method. The other side of sample 2 was coated using CV. Figure 11.10 shows the imdedance modulus (a), phase angle (b) and Nyquist (c) plot of the lead dodecanoate coated organ sample (sample 2) recorded in an acetic acid corrosive solution, using both CV 30sc and the IMM 24h. For comparison, the plot of the bare sample is also shown.

The phase angle versus frequency plot for the CV deposition looks very similar to that of the bare surface. The increase (with respect to the x-axis or frequency axis of the curve), the shift and broadening of the loop, in comparison to the untreated surface, indicate a slightly higher corrosion resistance of the CV treated surface compared to the bare organ sample [13]. Sekine et al. [14] observed a linear relationship between the frequency at the maximum phase angle and the coating resistance. This indicates that a more protective coating is formed using the IMM method. It is also observed that the shapes of the impedance and phase diagrams do not depend on the deposition method, suggesting that similar mechanisms for metal dissolution are taking place during the corrosion measurement. All electrochemical impedance measurements recorded in the acetic acid corrosive solution were simulated using an equivalent electric circuit model of four elements, as shown in Figure 11.11. This model includes the solution resistance, R_{u}, in series with a parallel combination of a CPE for the double-layer, Q_{dl}, and the charge-transfer resistance, R_{ct}. The use of the constant phase elements is described in section 8.1.3.3. A Warburg element is added to take into account finite diffusion or mass transfer behavior of ionic species in the corrosive solution as indicated in Figure 11.10c.

Table 11.2 shows the extracted electrochemical impedance parameters for the bare and coated (CV 30 scans and IMM 24h) lead dodecanoate coatings plotted in Figure 11.10. The data show that the deposition method has an important influence on the corrosion resistance. The R_{ct} value increases depending on the method, because some of the reactive sites on the bare surface are blocked by the lead dodecanoate coating, so we can conclude that the IMM method generates the most corrosion-resistant layer. The inhibition efficiency of the coatings is calculated in Table 11.2 based on the fitted parameters using Eq. 8.42. The inhibition efficiency values suggest that the the CV method provides a poor protection of the organ sample. An explanation could be found in the controlled deposition process, which can only deposit a thin coating layer and therefore cannot generate sufficient protection for the rough surface. Smoothing the surfaces of the organ samples using several polishing methods could improve the protective properties of the deposited lead dodecanoate coatings. The CV technique ensures that the top layer changes (no finite diffusion contribution) as a consequence of the reverse reduction reaction. Furthermore, it causes an increase in the double-layer capacitance, which means the covered surface area decreases. The CV deposition shows a small increase in the charge-transfer resistance with respect to the bare organ sample, because the thin film prevents some of the electrolyte from reaching the surface. Because of the



(a) (b)



(c)

Figure. 11.10 – The imdedance modulus (a), phase angle (b) and Nyquist (c) plot of the lead dodecanoate coated (using both CV 30sc and IMM 24h) and bare organ sample (sample 2) recorded in an acetic acid corrosive solution.

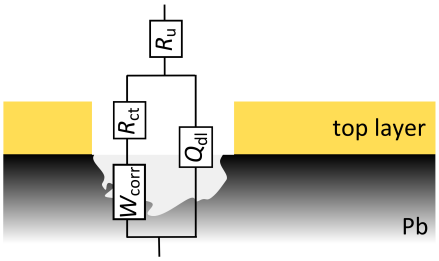


Figure. 11.11 – The EEC used for the simulation of the raw impedance data.

very rough surface of the original organ samples (caused by the hammering of the metal), it is very difficult to form a protective coating to prevent corrosion of this sample. This is the reason why a long immersion (24 h) is necessary to provide a better protection of the lead dodecanoate coating. The long immersion (24 h) clearly provides a more powerful tool to deposit a protective coating on a rough surface. This means that the IMM method provides the best protection for the organ sample. Table 11.2 shows that the sample treated with the IMM method is better protected against acetic acid corrosion, which is due to the uncontrolled deposition on a more reactive reduced lead surface (due to the use of the initial reduction procedure). This method increases the possibility of better deposition on the rough parts of the surface. The chance of protecting the sample better against corrosion and therefore getting higher inhibition efficiencies increases with immersion time.

SAMPLE	E_{corr} / V vs. SCE	R_u / Ω cm^2	R_{ct} / Ω cm^2	$C_{eff,dl}$ / F cm^{-2}	$Z_{W,corr}$ / Ω s$^{-1/2}$	η_{IE} / %	χ^2 value
bare	-0.482	40.7	1043	9.0×10^{-6}	780	-	33
		$\pm$ 0.3	$\pm$ 7	$\pm 2 \times 10^{-7}$	$\pm$ 80		
cv 30sc	-0.437	30.9	8700	4.7×10^{-5}	-	88	21
		$\pm$ 0.1	$\pm$ 100	1×10^{-6}	-	$\pm$ 1	
imm 24h	-0.454	65.7	21500	3.7×10^{-6}	67000	95	1290
		$\pm$ 0.8	$\pm$ 500	1×10^{-7}	$\pm$ 3000	$\pm$ 2	

Table 11.2 – Fitted EIS parameters for bare and coated (CV and IMM) sample 2 in a corrosive solution.

The CPE exponent n_{dl}, which is a gauge for the surface roughness, should normally have a value between 0.8 - 1. In Table 11.2, the values for the CPE exponent are lower indicating a very rough surface, which is explained by a thick, rough and inhomogeneous dielectric corrosion layer on the organ sample.

11.6.2 English organ sample

Figure 11.12 shows two photographs of the protected organ sample coated with a lead dodecanoate coating using the IMM 24h method. This lead dodecanoate coating was locally analyzed using electrochemical impedance data at the E_{corr} at room temperature. The The impedance modulus (a) and phase angle (b) plots of the coating at different positions on the sample in an acetic acid corrosive solution is shown in Figure 11.13. For comparison, the plot of the bare sample is also depicted. As established in section 11.6.1, the long immersion clearly provides a powerful tool to produce a protective coating on a rough organ sample surface. The results show that the points of the impedance plots for the treated surface are higher at each frequency compared to the bare sample.

The long immersion of the sample in the inhibitor solution indeed provides a protective coating, even in the case of a

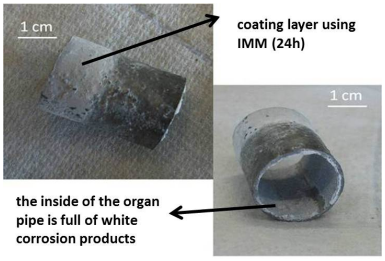
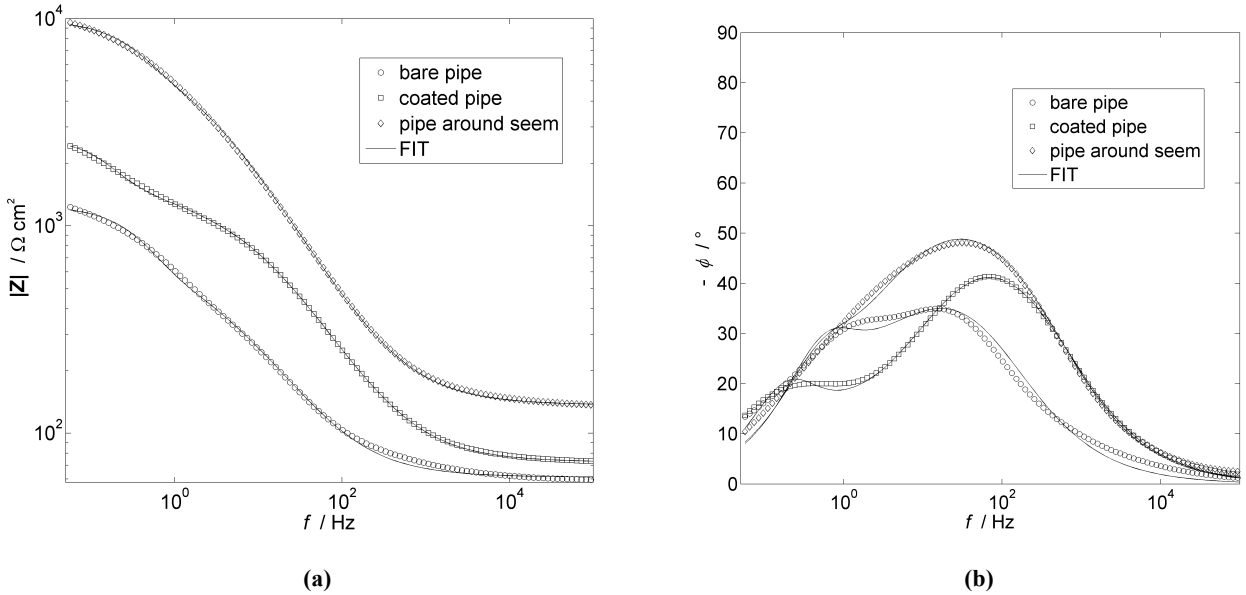


Figure. 11.12 – Photographs of partly treated piece of the organ pipe.



(a) **(b)**

Figure. 11.13 – The impedance modulus (a) and phase angle (b) plots of the bare and coated English organ sample at different positions recorded in an acetic acid corrosive solution.

bent piece of organ pipe. Therefore, it can be suggested that the shape of the object has no effect on the deposition of the lead dodecanoate coating. Table 11.3 shows the inhibition efficiencies calculated using Eq. 8.42 and the extracted electrochemical impedance parameters from the simulation using the model in Figure 11.11. It is clear that not every sample location shows the same protective behavior of the coating. The problem is that R_{ct} decreases when measuring closer to the soldered seam of the English organ sample. A reason for this decrease could be that the composition of the seam is different or another crystal structure of the metal substrate.

11.7 Conclusions

We have studied the influence of the deposition of lead dodecanoate protective coatings on lead-based organ metal samples using CV and IMM deposition methods. Optical and SEM micrographs allowed to identify the changing colors and the very rough topography of lead alloy organ sample, characterized by the presence of different corrosion products, fissures and cracks. These are most probably caused by atmospheric corrosion and the hammering pretreatment, respectively. After the inhibition treatment, the surface turns light gray and the surface morphology changes drastically. In light of the conservation ethics, this change of appearance could be a problem which means further experimentation is certainly needed. The SEM images reveal that the surface of both coated samples is well covered by more or less tangled flake-shaped crystals. The good surface coverage and the close-packed hydrophobic crystal clusters slow down corrosion

SAMPLE	E_{corr} / V vs. SCE	R_u / Ω cm^2	R_{ct} / Ω cm^2	$C_{eff,dl}$ / F cm^{-2}	$Z_{W,corr}$ / Ω s$^{-1/2}$	η_{IE} / %	χ^2 value
bare	-0.482	61.2	441	2.7×10^{-5}	760	-	96
		$\pm$ 0.9	$\pm$ 7	$\pm 1 \times 10^{-6}$	$\pm$ 80		
pipe	-0.437	136	5630	2.52×10^{-6}	4300	92.2	228
		$\pm$ 1	$\pm$ 40	4×10^{-8}	400	$\pm$ 0.6	
pipe around seem	-0.454	72.5	1143	4.3×10^{-6}	1400	61.4	38
		$\pm$ 0.3	$\pm$ 3	5×10^{-8}	$\pm$ 20	$\pm$ 0.2	

Table 11.3 – Fitted EIS parameters for bare and coated English organ sample in a corrosive solution.

processes on the samples. EDS analysis indicates that the organ samples are made of a lead-tin alloy, where lead is the main element. The presence of oxygen and carbon, as minor elements, indicates that lead and tin are oxidized at the surface by atmospheric corrosion using the air oxygen and carbon dioxide. The thin top layer is composed of different corrosion compounds, such as oxides, carbonates, and hydroxides of lead and tin. The XRD spectra of the bare samples clearly show the most important lead and tin diffraction peaks (for lead $2\theta = 14.29°$, $16.51°$, $23.43°$ and $27.56°$ and for tin $2\theta = 19.90°$ and $20.35°$). Furthermore, we see evidence of litharge (PbO). The XRD analysis explains the higher tin concentration in the second sample. The intensities of all diffraction peaks on the coated samples are lower compared to the bare samples except the tin compound diffraction peaks because the alloy contains pure tin phases which are not covered by the lead carboxylate coating. After the deposition, a thin layer of tin dioxide is formed on the lead-tin alloy surface due to the presence of hydroxides in a slightly basic solution. The electrochemical impedance measurements of metal organ plates in the corrosive acetic acid solution suggest that the layer deposited using CV 30sc does not protect the organ sample. Controlled deposition cannot protect such a rough surface. The IMM method provides a more powerful tool to deposit a protective coating at a rough surface. The impedance measurements allow to measure the protection provided by different lead corrosion products present on the surface. To increase the protective properties of the lead dodecanoate coating, it is possible to extend the initial reduction because of the presence of more corrosion products or to extend the immersion time to produce a thicker coating. The use of the lead dodecanoate coating on the English organ pipe using the IMM method protects the metal very well. The problem is that the coating offers lower protection close to the soldered seam of the lead-tin alloy organ sample. The protection decreases even more when measured on the seam itself.

References for Chapter 11

[1] M. MONKMAN, Vocal and historic compact discs, in: *Amphion recordings*, Amphion Recordings, 2008.

[2] P. STORME, *Personal communication*, Antwerp, 2012.

[3] E. DAHMEN, *Electroanalysis: Theory and applications in aqueous and non-aqueous media*, Elsevier, 1986, 129.

[4] G. CHRISTIAN, P. DASGUPTA, and K. SCHUG, Voltammetry and electrochemical sensors, in: *Analytical Chemistry*, 7th, John Wiley & Sons, 2014, chap. 15, 466–467.

[5] E. PASCIAK and S. HOCHSTELLER, Electrochemical reduction of phthalide at carbon cathodes in dimethylformamide: Effects of supporting electrolyte and gas chromatographic injector-port chemistry on the product distribution, *Electrochim. Acta* **113** (2013), 557–563.

[6] E. ROCCA and J. STEINMETZ, Inhibition of lead corrosion with saturated linear aliphatic chain monocarboxylates of sodium, *Corros. Sci.* **43** (5) (2001), 891–902.

[7] F. LACOUTRE et al., Anhydrous lead(II)heptanoate, *Acta Crystallogr. C* **57** (5) (2001), 530–531.

[8] C. CHIAVARI et al., Conservation of organ pipes: protective treatments of lead exposed to acetic acid vapours, in: *Metal 04: Proceedings of the international conference on metals conservation*, ed. by J. ASHTON and D. HALLAM, National Museum of Australia Canberra, 2004, 281–293.

[9] M. DOWSETT et al., In-situ spectroelectrochemical study of the growth process of a lead decanoate coating as corrosion inhibitor for lead surfaces, *Surf. Interface Anal.* **41** (7) (2009), 565–572.

[10] L. SELWYN and CANADIAN CONSERVATION INSTITUTE, *Metals and corrosion: A handbook for the conservation professional*, Canadian Conservation Institute, 2004, 223.

[11] D. LOVEDAY, P. PETERSON, and B. RODGERS, Evaluation of organic coatings with electrochemical impedance spectroscopy, *J. Coat. Technol.* **10** (2004), 88–93.

[12] J. GRANDLE and S. TAYLOR, Electrochemical impedance spectroscopy of coated aluminum beverage containers. I. Determination of an optimal parameter for large sample evaluation, *Corros.* **50** (10) (1994), 792–803.

[13] A. FRIGNANI et al., Mono-carboxylate conversion coatings for AZ31 Mg alloy protection, *Mater. Corros.* **62** (11) (2011), 995–1002.

[14] I. SEKINE, K. SAKAGUCHI, and M. YUASA, Estimation and prediction of degradation of coating films by frequency at maximum phase angle, *J. Coat. Technol.* **64** (1992), 449–485.

[15] K. KHALED and M. AMIN, Electrochemical and molecular dynamics simulation studies on the corrosion inhibition of aluminum in molar hydrochloric acid using some imidazole derivatives, *J. Appl. Electrochem.* **39** (12) (2009), 2553–2568.

PART III

TIME LAPSE STUDIES

12

Time-lapse multisine impedance study of lead in acetic acid

This chapter is based on a unpublished article: M. De Keersmaecker, T. Hauffman, T. Muselle, K. Verbeken, A. Hubin and A. Adriaens, Time-lapse multisine impedance study of lead substrates in a corrosive acetic acid solution.

12.1 Odd random phase electrochemical impedance spectroscopy

In the research group of the Electrochemical and Surface Engineering (SURF) of the Materials and Chemistry (MACH) department at the Vrije Universiteit Brussel (VUB), an integrated measuring and modeling methodology for EIS based on an odd random phase multisine excitation signal (ORP-EIS). This technique allows us to determine and quantify the level of disturbing noise, the level of the non-linear distortions and the level of the non-stationary behavior. The group published a number of papers on this methodology: the theoretical background can be found [1, 2] and the advantages of the methodology are demonstrated on an electrical circuit [3] and on a coated metal [4]. The use of a random phase multisine signal containing only odd harmonics was already introduced by Creason [5] and others [6, 7]. An overview of the construction of the excitation signal of the ORP-EIS technique and its properties are given in the next paragraphs. For a more detailed description of the method, we refer the reader to the work of J. Schoukens and R. Pintelon [8–10].
Using single-sine electrochemical impedance spectroscopy, a sinusoidal potential $U(t)$ is applied to the working electrode and its current response $I(t)$ is monitored as explained in chapter 8.1. The potential of the working electrode is kept constant with respect to a reference electrode in the cell (most of the time the OCP potential). As in single-sine EIS, $U(t)$ and $I(t)$ are related to each other in the frequency domain by the impedance $\mathbf{Z}$, with $\mathbf{Z}$ a frequency dependent complex number [11].

12.1.1 The excitation signal

The excitation signal that is used in this work is an odd random phase multisine. This periodic input signal consists of the sum of N harmonically related sine waves with amplitude $u(k)$, maximum frequency $f_{\max}$ and random phases ϕ_k [8, 12]. In the time domain, this signal is defined as [13]

$$\mathbf{U}(t) = \sum_{k=-N}^{N} \frac{u(k)}{2} \mathrm{e}^{j\left(\frac{2\pi f_{\max} k t}{N} + \phi_k\right)}, \tag{12.1a}$$

$$= \sum_{k=1}^{N} u(k) \cos\left(2\pi f_k t + \phi_k\right), \tag{12.1b}$$

where $k \in \mathbb{K}_{\text{exc}}$ is the user-defined discrete set of excited frequency bins and the root-mean-square value of $u(k)$ is independent of N. For this reason, $u(k)$ decreases as $\frac{1}{\sqrt{N}}$. For the excitation signal, the random phases ϕ_k are chosen

between [0; 2π] such that $\epsilon[e^{j\phi_k}] = 0$ (with $\epsilon[]$ the expected value) [12]. On top of that, only the odd harmonics in equation 12.1b are excited ($u(k) = 0$ for $k = 2n$ with $n \in \mathbb{N}$) and per group of 3 consecutive odd harmonics, one is randomly omitted. This creates an odd random phase multisine with a random harmonic grid which has a logarithmic distribution for this study. The resulting excited harmonics may look like: 1, 5, 9, 11, 13, 15, 21, 23,... . The lowest frequency in the signal is called the fundamental frequency [13].

The excitation signal in the time domain is illustrated in Figure 12.1. Higher frequencies are excited many times more than in the case of a classical single-sine experiment. A chosen number of consecutive periods of this excitation signal is measured.

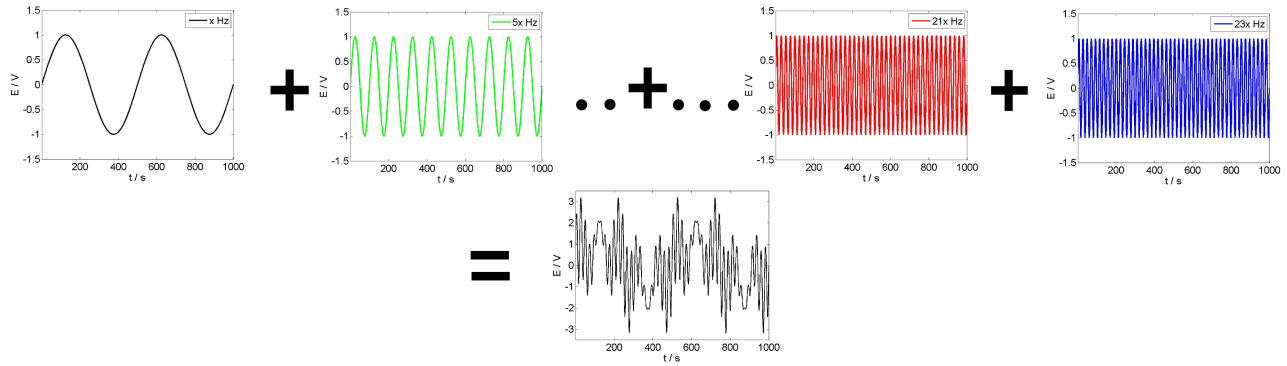


Figure. 12.1 – Schematic representation of one period of an odd random phase multisine in the time domain. The plus sign denotes that the signals are applied simultaneously. x represents the fundamental frequency [14].

In the frequency domain, the Fourier transform of a single cosine with a frequency of f Hz results in two spikes: one at -f and the other at f Hz. For the multisine, this Fourier spectrum is the sum of the Fourier transforms of the individual cosine waves and is given by [13]

$$\mathbf{U}_{\text{multi}}(j\omega) = \sum_k \sqcap(k)\delta(\omega - \omega_k), \tag{12.2}$$

with ω being the angular frequency, $\delta()$ the Dirac delta function and the complex, discrete function $\sqcap(k)$ defined as [4] [1]

$$\sqcap(k) \equiv \begin{cases} u(\mathrm{k})\pi e^{(j\phi_k)} & k > 0 \\ u(\mathrm{k})\pi e^{(-j\phi_k)} & k < 0 \end{cases} \tag{12.3}$$

In Figure 12.2 the signal of Figure 12.1 is illustrated in the frequency domain. As can be seen, only 2 out of 3 odd harmonics are randomly retained in the excitation signal. The fundamental frequency will determine the measurement time and is selected depending on the phenomena that are studied and the capabilities of the measurement system. For measurement quality reasons, a quasi-logarithmic frequency distribution is used in order to obtain frequencies that are integer multiples of the fundamental frequency. This is done to avoid leakage errors during the measurements [8].

12.1.2 Data analysis

An important advantage of this perturbation signal is that it is possible to determine the noise level, the contribution of non-linearities and non-stationarities at each frequency level [1, 14]. The background of this data analysis is explained

[1] From the Fourier spectrum of a complex exponential $\mathcal{F}(e^{j\omega_k t}) = 2\pi\delta(\omega - \omega_k)$ and $\cos(\omega_k t + \phi_k) = \left[e^{j(\omega_k t + \phi_k)} + e^{-j(\omega_k t + \phi_k)}\right] / 2$, the linearity of the Fourier transform yields: $\mathcal{F}\left(\sum_k \cos(\omega_k t + \phi_k)\right) = \pi \sum_k \delta\left[(\omega - \omega_k)e^{j\phi_k} + \delta(\omega - \omega_k)e^{-j\phi_k}\right]$. Substituting this equation in Eqs. 12.3 and 12.1b yields Eq. 12.2.

below.

12.1.2.1 Noise level

For an experiment, $P + 1$ consecutive periods of the chosen signal were measured. Before processing the recorded spectra, the first period was omitted to eliminate possible transients. All calculations were performed using the results of the other P periods. These periods are used to calculate the standard deviation on the non-excited frequencies, which makes a good estimate for the noise level of the system.

12.1.2.2 Non-stationary behavior

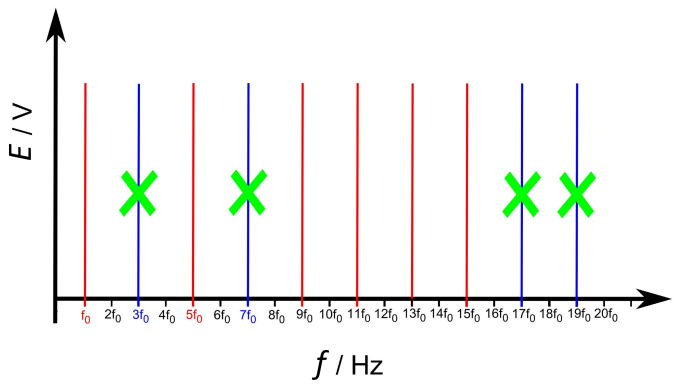


Figure. 12.2 – Illustration of the odd random phase multisine excitation signal of Figure 12.1 represented in the frequency domain after a Fourier transform operation.

The standard deviation on the excited frequencies over P periods is used to determine the system's non-stationary behavior. When the calculated standard deviation values at all frequencies coincide with the noise level of the system, the system is behaving in a stationary manner. In the other case, a large part coincides with the noise level but the value increases suddenly at each excited frequency. To be able to fit the data, the variance of the measurement noise should be a smooth function of the frequency. This is not the case because of the non-stationary behavior. Indeed, the calculated standard deviation value at the excited frequencies contains information of the system's noise and its non-stationary behavior. Furthermore, it can be mathematically proven that the magnitude of the excitation peak influences the non-stationary modulation [8]. Therefore, the contribution of the non-stationary behavior will be less pronounced at the non-excited frequencies. For this reason, the standard deviation at the non-excited frequencies will mainly contain information on the noise level, while at the excited frequencies also non-stationary effects are considered. To summarize, a difference between both standard deviations indicates the presence of non-stationary effects. The quantification of this non-stationary behavior will be further elucidated in this chapter.

12.1.2.3 Non-linear behavior

Next to the noise level and the non-stationary behavior, the linearity of the system is studied. The total impedance $\mathbf{Z}$ can be theoretically split into different contributions depending on the angular frequency ω_k [15],

$$\mathbf{Z}(\omega_k) = \mathbf{Z}_{\mathrm{L}}(\omega_k) + \mathbf{Z}_{\mathrm{S}}(\omega_k) + \mathbf{Z}_{\mathrm{N}}(\omega_k) + \mathbf{Z}_{\mathrm{NS}}(\omega_k), \tag{12.4}$$

with $\mathbf{Z}_{\mathrm{L}}(\omega_k)$ the best linear approximation to the real non-linear system, $\mathbf{Z}_{\mathrm{S}}(\omega_k)$ the stochastic non-linear distortions, $\mathbf{Z}_{\mathrm{N}}(\omega_k)$ the measurement noise and $\mathbf{Z}_{\mathrm{NS}}(\omega_k)$ the non-stationary contributions. The $\mathbf{Z}_{\mathrm{L}}(\omega_k)$ is build-up of [16],

$$\mathbf{Z}_{\mathrm{L}}(\omega_k) = \mathbf{Z}_0(\omega_k) + \mathbf{Z}_{\mathrm{B}}(\omega_k), \tag{12.5}$$

where $\mathbf{Z}_0(\omega_k)$ is the response function of the true underlying linear system and $\mathbf{Z}_{\mathrm{B}}(\omega_k)$ stands for the bias non-linear contributions, which are a consequence of the non-linear distortions that are in phase with the excitation signal. These distortions depend on the system and the power of the excitation signal. The fact that this term $\mathbf{Z}_{\mathrm{B}}(\omega_k)$ is independent

of the phase realization of the excitation signal, means that its value will not decrease by averaging over all periods or by using several phase realizations of the multisine. The stochastic non-linear contributions $\mathbf{Z}_S(\omega_k)$ are defined as the non-linear distortions not in phase with the multisine signal. This means that its expected value $\epsilon[Z_S]$ will become zero since this value depends upon the phase realization [13]. The non-linearities, $\mathbf{Z}_B(\omega_k)$ and $\mathbf{Z}_S(\omega_k)$, do not disappear if the number of excited frequencies increases. The non-linear distortions depend only upon the system's non-linearity. This is either even, odd or a combination of both. This response to a sine excitation is illustrated in Figure 12.3.

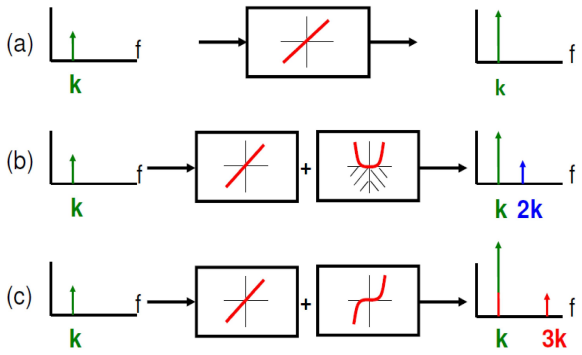


Figure. 12.3 – Illustration of (a) a perfectly linear system, (b) an even non-linear system and (c) an odd non-linear system to a sinusoidal perturbation at frequency k [1].

Using ORP-EIS, only the odd frequencies are excited, allowing one to distinguish between even and odd linearities originating from the system. This way the even non-linear contributions are easily detected at the non-excited even frequencies of the response signal, since these harmonics are not excited initially. However, also the detection of the odd non-linear distortions is necessary. This is possible when the input signal is divided into groups of 3 consecutive odd frequencies so that in each of these groups one frequency can be randomly omitted as shown in Figure 12.2).

To be able to calculate the non-linear contribution, the output spectrum is first corrected for non-linearities that might be caused by the signal generator and/or by the non-linear interaction between the electrochemical process and the signal. It is assumed that, since the investigated system is dominantly linear, the non-linearities in the excitation signal will be transformed mainly linearly at the non-excited harmonics in the output spectrum [9]. Therefore, a first order corrected output spectrum is obtained by subtracting the linear transformation of the non-linear input from the response spectrum at the non-excited frequencies [1]

$$\mathbf{I}_c^{[P]}(\omega_k) = \begin{cases} \mathbf{I}_{meas}^{[P]}(\omega_{k_e}) & \text{at } \omega_{k_e} \\ \mathbf{I}_{meas}^{[P]}(\omega_{k_{ne}}) - \frac{1}{\mathbf{Z}^{[P]}(\omega_{k_{ne}})}\mathbf{U}^{[P]}(\omega_{k_{ne}}) & \text{at } \omega_{k_{ne}} \end{cases}, \tag{12.6}$$

with $\mathbf{I}_c^{[P]}$ the corrected response and $\mathbf{I}_{meas}^{[P]}$ the measured response for the P^{th} period. The ω_{k_e} are the excited frequencies and $\omega_{k_{ne}}$ are the non-excited frequencies. $\mathbf{Z}^{[P]}(\omega_{k_{ne}})$ is obtained through a linear interpolation of the impedance values at the excited frequencies. Afterwards, the mean of the corrected output spectrum $\hat{\mathbf{I}}_c$ and its variance $\sigma^2_{\hat{\mathbf{I}}_c}$ are calculated over P periods[2] [17],

$$\hat{\mathbf{I}}_c(\omega_k) = \frac{1}{P}\sum_{p=1}^{P}\mathbf{I}_c^{[P]}(\omega_k), \tag{12.7a}$$

$$\sigma^2_{\hat{\mathbf{I}}_c}(\omega_k) = \sum_{p=1}^{P}\frac{\left|\mathbf{I}_c^{[P]}(\omega_k) - \hat{\mathbf{I}}_c(\omega_k)\right|^2}{P(P-1)}. \tag{12.7b}$$

Next, the level of even and odd non-linear distortions in the response spectrum is calculated from the difference between the magnitude of respectively $\hat{\mathbf{I}}_c(\omega_{k_{ne,even}})$ and $\hat{\mathbf{I}}_c(\omega_{k_{ne,odd}})$ with the uncertainty at the non-excited frequencies $\sigma_{\mathbf{I}_c}(\omega_{k_{ne}})$ [9]. Linear interpolation of the values of $\hat{\mathbf{I}}_c(\omega_{k_{ne,odd}})$ at the odd non-excited frequencies towards the excited frequencies,

[2] In this work, P equals 4

results in the quantity $\hat{\mathbf{I}}_{\text{distort}}(\omega_{k_e})$ defined as the non-linear behavior at the excited frequencies. Indeed, due to the random harmonic grid of the excitation, the level of the stochastic non-linear distortions at the non-excited harmonics equals that at the excited harmonics [18]. Division of $\hat{\mathbf{I}}_{\text{distort}}(\omega_{k_e})$ by the input signal $\mathbf{U}(\omega_{k_e})$ at the excited frequencies results in the stochastic non-linear distortion on the admittance[3] at the excited harmonics [9]

$$\mathbf{Y}_{\text{S}}(\omega_{k_e}) = \frac{\hat{\mathbf{I}}_{\text{distort}}(\omega_{k_e})}{\mathbf{U}(\omega_{k_e})} \tag{12.8}$$

In practice, the inverse value $\mathbf{Z}_{\text{S}}$ (the total variance of the system) of this total distortion $\mathbf{Y}_{\text{S}}$ will be plotted at each angular frequency ω_{k} together with the standard deviation $\sigma_{\mathbf{I}_{\text{c}}}(\omega_{k_{\text{ne}}})$ at the non-excited frequencies. As explained, the $\mathbf{Z}_{\text{S}}$ contains not only the level of non-linear distortions but also the noise level. When both curves coincide, the system behaves linearly. In the other case, the system behaves non-linearly.

12.1.2.4 Non-linear behavior in the presence of strong non-stationary behavior

One must be careful detecting the non-linear behavior in the presence of a strong non-stationary behavior, which changes the output response over the P measured periods. Since the total variance $\mathbf{Z}_{\text{S}}$ is calculated over these P periods, this non-stationary behavior contributes to this value. Obviously, even if the system behaves linearly, the calculated total variance differs from the noise level. To determine the system's linearity, one should look at the obtained output spectrum of the current. The most clear indication of a strong non-stationary behavior is found at the excited frequencies together with contributions at the non-excited frequencies. Using a Fourier transform operation, clear skirt-like contributions are formed around the excited frequencies [13]. The faster the system's time-variance, the stronger the non-stationary behavior and the higher the formed skirts, which could lead to an erroneous interpretation of the noise.

12.1.2.5 Fitting procedure

For the fitting of the measurements, the procedure is slightly different compared to classical SS-EIS as described in section 8.1.4. If the contributions of non-linear and non-stationary behavior cannot be avoided, their presence and influence should be considered when modeling. As mentioned, non-linear and/or non-stationary data points cannot be modeled. Therefore, the different data points chosen to be fitted can be weighted considering their reliability. Weighting factors like unity, amplitude, noise level or non-linearities can be selected [14]. For example, by using the noise level as a weighting factor, the high-quality data points are considered more important for the fitting. By using the total variance of the system, more importance will be given to high-quality data points with a linear behavior and a low noise level.

12.1.2.6 Statistical evaluation

Instead of using a data validation as in section 8.1.2, we use the measurement noise to evaluate our raw data. The appropriateness of a model is often judged by a graphical comparison between experiment and model. However, a more correct approach is to compare the difference between model and experiment with the noise level. To validate an appropriate model, the residuals between model and experiment will be plotted and compared. When these residuals coincide with the measurement noise, the model is accepted [13]. When the model cannot completely describe the experimental results, it should be decided whether the differences between the residual curve and the noise level are small enough to accept the model. If this evaluation points out that model errors are too large, a new model should be proposed and the previous step should be restarted.

[3] $\mathbf{Y}_{\text{S}}(\omega_{k_e})$ is the frequency response function (FRF) of the system. It is the inverse value of $\mathbf{Z}_{\text{S}}(\omega_{k_e})$. This value is then given by $\mathbf{Z}_{\text{S}}(\omega_{k_e}) = \frac{\mathbf{Y}_{\text{S}}(\omega_{k_e})}{\left|(\hat{\mathbf{Y}}_{\text{S}}(\omega_{k_e}))^2\right|}$ with $\hat{\mathbf{Y}}(\omega_{k_e}) = \frac{1}{P}\sum_{p=1}^{P}\mathbf{Y}^{[P]}(\omega_{k_e})$.

12.2 ORP-EIS: A case study on lead immersed in acetic acid

12.2.1 Experimental procedures

All the electrochemical experiments were performed using a three-electrode system in a 250 mL glass beaker filled with 100 mL electrolyte consisting of 5 μg L^{-1} acetic acid (98 - 99%, Merck, USA) and 0.1 M tetrabutylammonium bromide (TBAB) (> 99%, Sigma Aldrich, USA) as a supporting electrolyte. The setup consisted of a saturated double-compartment calomel electrode (SCE), a platinum mesh, and a working electrode holder filled with a bare polished lead sample (diameter = 12.6 mm, Goodfellow, purity 99.99%) as described in section 4.2. The surface area of the lead samples in the holder exposed to the corrosive solution was 1 cm^2.

12.2.1.1 Electrochemical test

The measuring device is an EG&G Princeton Applied Research potentiostat (PAR model 2273) with a National Instruments PCI-4451 DAQ-card which is provided with an anti-aliasing filter. The odd random phase multisine with random logarithmic harmonic grid was digitally composed with Matlab software release 12.1 from Mathworks Inc. This signal was sent to the potentiostat, which superimposed the excitation signal on the OCP and the resultant was then sent to the system. With the potentiostat, the voltage and the related current in the test setup were measured and these data were sent to the DAQ-card. This last one was operated using the Labview software package version 5.0 from National Instruments. At the end, the raw data were processed with Matlab software release 13.0. The perturbation signal contained respectively excited frequencies situated between 50 mHz and 20 kHz. The amplitude of the excitation signals was set to 1 mV_{RMS}. Five consecutive periods of the excitation signals were measured. Before, the processing of the recorded spectra, the first measured period was omitted to eliminate possible transients. All calculations were thus performed using the results of 4 multisine periods. The set-up is explained further in section 11.2.2. The fitting of the impedance data to the proposed model was done in two ways. One method is using the Zview software. The alternative is a self-written procedure in Matlab, using a Gauss-Newton algorithm followed by a Levemberg-Marquard minimization scheme [3]. Using noise weighting, it is possible to deduce the reliability of the parameters based on the experimental data.

12.2.1.2 Surface analysis techniques

Scanning electron images of the samples were recorded using a FEG SEM Quanta-450 (FEI, The Netherlands). The EDS-spectra are recorded using an EDAX detector and the analysis is done using the TEAM software (EDAX, USA). The coated lead sample was first coated with a thin gold layer to avoid charging of the surface.

12.2.2 Time-lapse impedance study

Figure 12.4 shows the magnitude Bode plot (‘full red line’), non-stationarities (‘full blue line’), non-linearities (‘full black line’) and the noise level (‘∗’) of the measurement of a polished bare lead sample corroded in an acetic acid solution. An evolution throughout the first 20 hours of immersion is observed.

Since the noise level (‘∗’) differs significantly from the standard deviation at the excited frequencies (‘full blue line’), non-stationary behavior is assumed [13]. The system’s non-stationarities are explained by the extensive ongoing ‘active’ corrosion of the lead substrate surface in the acetic acid solution. The measurements show also non-linear behavior because the total variance at the odd non-excited frequencies (‘full black line’) does not coincide with the noise level (‘∗’). Both curves for the non-stationary and non-linear behavior follow the same trend in a large part of the chosen frequency range, indicating that the so called non-linear behavior is a consequence of the large non-stationary behavior due to the corrosion processes. This behavior alters the output response over the periods that are measured. Since the total

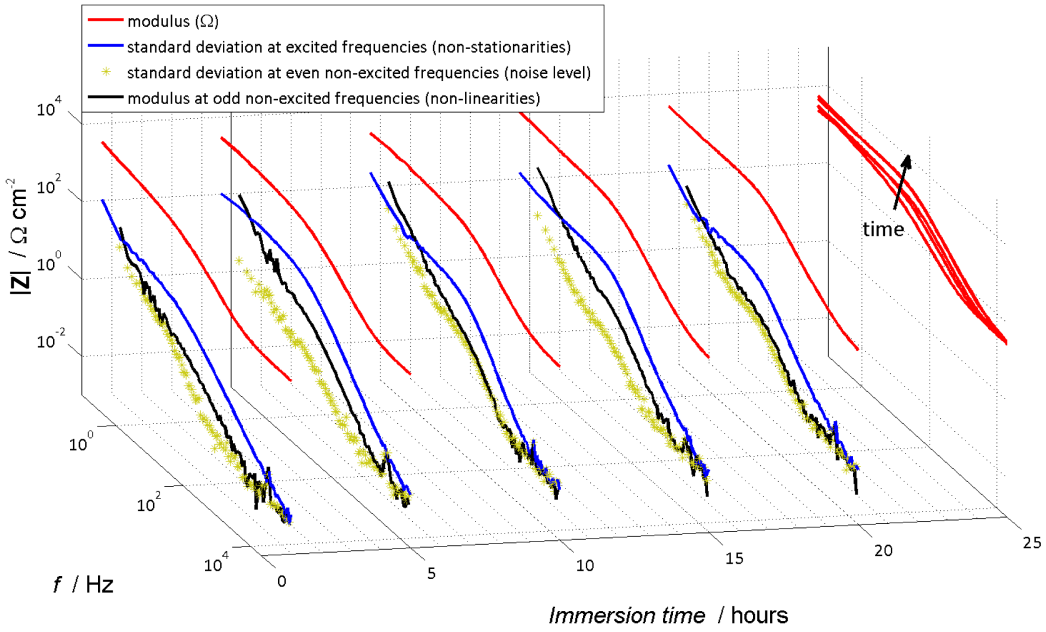


Figure. 12.4 – Magnitude Bode plot, non-stationarities, non-linearities and the noise level of the measurement of a polished bare lead sample corroded in an acetic acid solution during the first 20 hours of immersion (hours of immersion are shown).

variance is calculated over these periods, the non-stationary behavior might contribute to the total variance of the system as explained in section 12.1.2.4. This means that the total variance from the system can differ from the noise level even if the system behaves linearly. In order to determine whether the system is linear or not, one should look at the obtained output spectrum of the current [13].

The impedance modulus (a), phase (b) plot in Figure 12.6 of a bare lead sample in an acetic acid solution show a continuous increase of the impedance modulus together with a shift of the phase loop to higher frequencies. In the first 15 hours, the amplitude of the impedance increases drastically in the same frequency region from 1500 Ω to 2500 Ω as seen in Figure 12.6a. Figure 12.6b shows a negative phase angle loop, predicting capacitive behavior. In order to visualize the possible mass transfer processes, the Nyquist plots are shown in Figure 12.6c. An important diffusion process is noticed in the lower frequency region (lower than 0.5 Hz) during the first 10 hours of the immersion. This behavior suggests an aggressive corrosion process with the diffusion of newly corroded species from the surface to the solution. After 15 hours, the corrosion layer crust ensures the presence of only a semicircle. The diffusion of corroded species is not measured using the selected frequency range. Additional information about the occurring phenomena is obtained from complimentary surface analysis techniques.

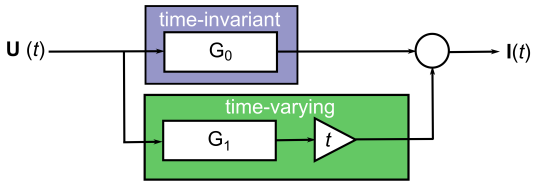


Figure. 12.5 – Equivalent block schematic of a linearly in time varying system.

12.2.3 Instantaneous impedance values

The occurrence of this detected non-stationary behavior is in contradiction with the necessary conditions to obtain reliable EIS data. To study the corrosion protection mechanism by modeling the EIS spectra, one should tackle this problem. A first important step is the shortening of the measurement time. If less time is needed to record an impedance spectrum,

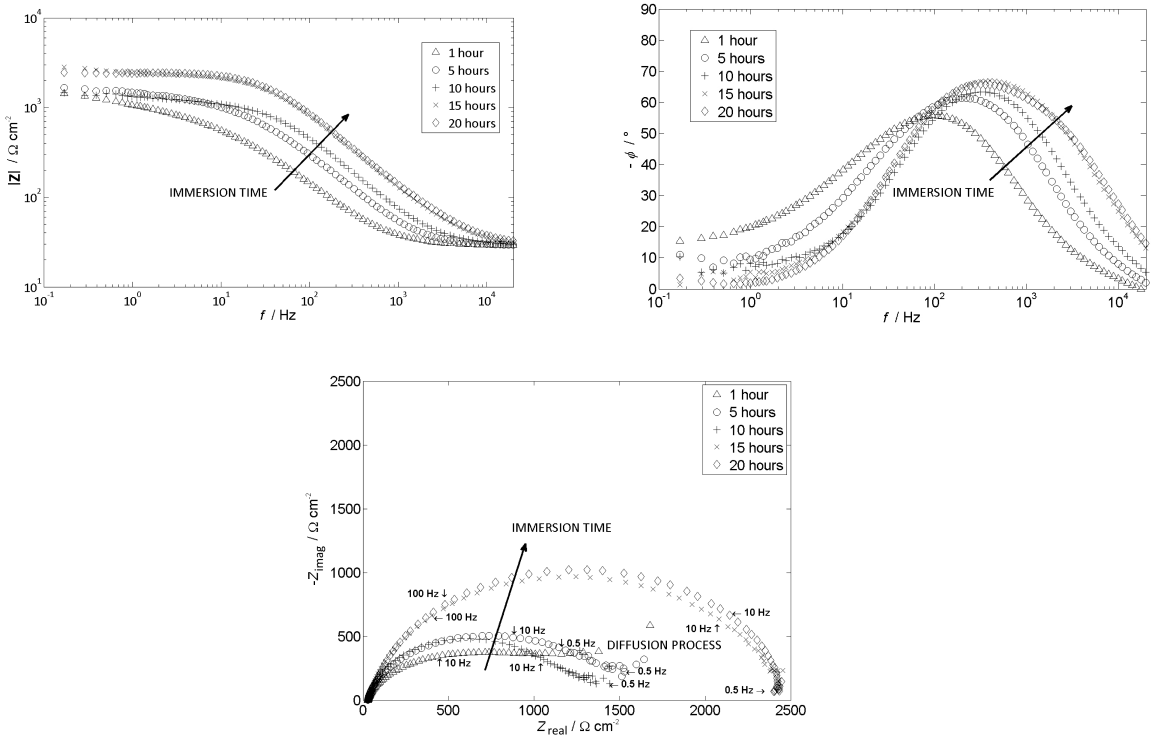


Figure. 12.6 – Magnitude of the impedance (a), phase (b) plots and Nyquist diagram (c) for the lead corrosion in an acetic acid solution as a function of immersion time.

the contributions of non-stationary behavior will become smaller. Clearly, this is a major advantage of the ORP-EIS method. By using a broadband multisine, all frequencies are superimposed and measured at the same time so that the measurement time is reduced considerably. In what follows, we try a different approach by assuming the possibility of calculating instantaneous impedance values depending on the non-stationary behavior signal.

12.2.3.1 Intuitive approach

When a multisine signal is applied to a linear and time-invariant system, the output is another multisine with the phases and amplitudes shaped by the system's transfer function. In the noiseless case, no signal is expected between any two excited harmonics as seen in Figure. For linear, slowly time-varying systems, extra contributions are measured. The excited frequencies still contain the most important contributions of the applied multisine. The unexcited frequencies, on the other hand, consist of a deterministic part of the signal due to time variation [4].

First, it is assumed that the time-varying contributions are only varying linearly with time. A block schematic of such a system is illustrated in Figure 12.5. In this scheme, G_0 and G_1 are defined as two (non-zero) linear time-invariant systems, so that when excited the output of both systems are multisines. However, the multisine at the output of G_1 is now multiplied by a linearly increasing gain. As shown in Figure 12.7, the Fourier transform of this linear gain in the time domain is a hyperbolic curve ('skirts') in the frequency domain. As it is possible to define a clear difference of the time-invariant and the time-variant part of an output multisine, we can deconvolve the raw data. Convolving the skirt with the spectrum of the multisine (i.e. a series of Dirac delta functions), means that the skirt is scaled, phase-shifted and copied around each excited line. These skirt-like contributions are formed around each excited frequency of the multisine. This convolution is shown using the black lines in Figure 12.7. To be able to use this effect, many harmonics are left unexcited between the excited frequencies. The time-varying part of the system (i.e. the signal branch through G_1) is responsible for a small contribution at the excited lines and for the skirts at the unexcited harmonics in the output

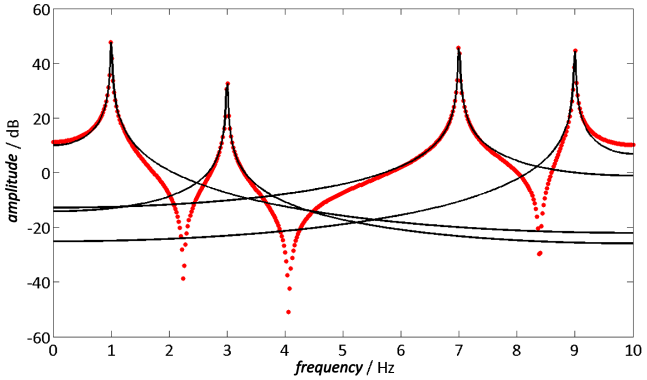


Figure. 12.7 – Illustration of the convolution of the skirts with the multisine. The skirts around each frequency are plotted separately in (black lines) and the result of their convolution is plotted (blue dotted) [19].

spectrum. The signal branch through G_0 is the 'time-invariant part' of the system and is only responsible for (the major part of) the level at the excited lines. This clear distinction made between the excited and the non-excited lines allows us to extract the evolving instantaneous impedance spectra. An instantaneous system is a system obtained when holding up the dynamic system at a chosen time instant. To be able to create an evolution of these instantaneous systems provides a interesting insight into the electrochemical process. The mathematical method developed for this work is described in the PhD thesis of J. Lataire [19]. More information about the method can be found in the article of E. Louarroudi [20]. A short outline of the mathematical method is given in the following section.

12.2.3.2 Mathematical background

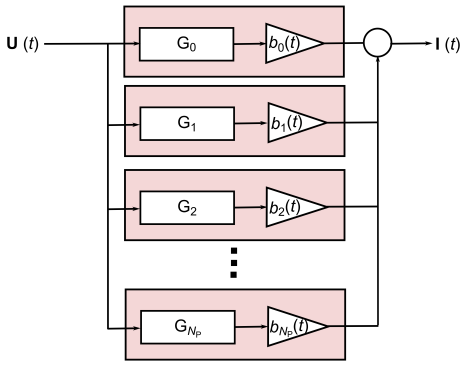


Figure. 12.8 – Considered general system model of a higher order in t: combination of linear time-invariant systems, followed by time-varying gains.

The model considered for a more general time evolution is given in Figure 12.8. It consists of a parallel connection of linear time-invariant systems transfer functions (G_0, G_1, G_2, ...) followed by gains varying as basis functions in time ($b_0(t)$, $b_1(t)$, $b_2(t)$, ...). The time domain input/output relation is then given by

$$\mathbf{I}(t) = \sum_{p=0}^{N_P} \mathrm{G}_p\{u(t)\} b_p(t). \tag{12.9}$$

The choice of basis functions $b_p(t)$ is application dependent. In this work, the following basis functions are considered

$$b_p(t) = P_p\left(\frac{2t}{T} - 1\right). \tag{12.10}$$

where $P_p(t)$ is the pth order Legendre polynomial. T is the length of the measured time record which equals, in this work, P times the period of one multisine. The motivation to use these Legendre polynomials can be found in the work of J. Lataire [19]. In Figure 12.9a, the Legendre polynomials can be seen as smooth functions of time, yielding discrete Fourier transform spectra with the highest levels concentrated around the origin. The spectrum of the first Legendre basis function has a single non-zero value at the origin. As mentioned before, the amplitudes of the other basis functions are shaped like skirts trying to fit the raw non-stationary data. In the frequency domain, the Fourier transform of these

Legendre polynomials are defined at discrete frequencies ω_k as shown in Figure 12.9b.

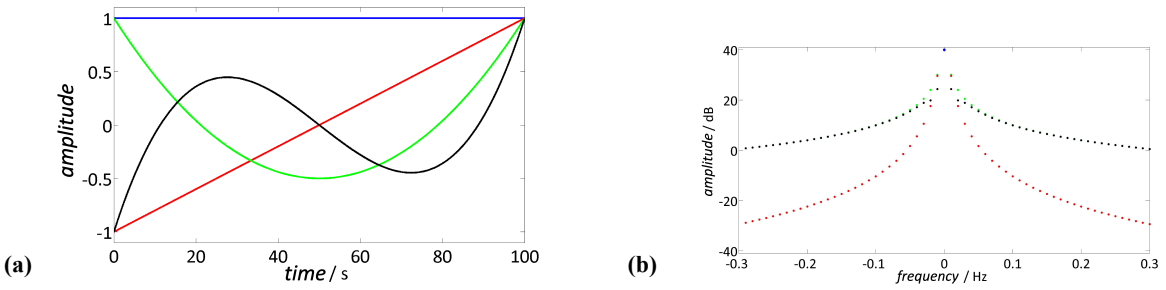


Figure. 12.9 – First 4 time-scaled and shifted Legendre polynomials in the time domain based on the basis function for time-varying gains $b_p(t) = P_p\left(\frac{2t}{T} - 1\right)$ (a) and the amplitude (b) in the frequency domain

To extract the instantaneous values, the concept of an instantaneous Frequency Response Function (FRF) is introduced. The system is based on the model in Eq. 12.9 at a particular time instant $t^\star$ obtained by freezing the time-varying basis functions $b_p(t)$ in Eq. 12.9 at time $t^\star$. In the frequency domain the function is defined as

$$\mathrm{FRF}_{\mathrm{inst}}(j\omega, t^\star) = \sum_{p=0}^{N_\mathrm{p}} \mathrm{G}_p(j\omega) b_p(t^\star). \tag{12.11}$$

The corresponding block schematic is obtained by replacing all t's by $t^\star$'s in the time-varying gains. Also very important is that the definition of an instantaneous system is associated with a certain model structure [19]. Although the previous intuitive explanation is restricted to steady-state measurements, the formalization can handle transient data too. First, in practice, a digital processing apparatus has only limited amounts of memory, so that sampling is performed over a limited amount of time. To do this, the multisine is multiplied by a rectangular window, which is called windowing. In practice, this means convolving the multisine with the Fourier transform of a sinc function so that [21]

$$\mathbf{U}_{\mathrm{multi},T}(j\omega_k) = \begin{cases} \frac{T}{2\pi}\sqcap(k) & \forall k = k_\mathrm{e} \\ 0 & \forall k = k_\mathrm{ne} \end{cases}, \tag{12.12}$$

where subscript T stands for a windowed, transient response. The Fourier transform of the windowed response of $\mathrm{G}_p(t)$ excited by the multisine is

$$\mathbf{Y}_{\mathrm{G}_p,T}(j\omega_k) = \mathbf{Y}_{\mathrm{G}_p}(j\omega_k) + \mathbf{T}_{\mathrm{G}_p}(j\omega_k), \tag{12.13}$$

where $\mathbf{T}_{\mathrm{G}_p}(j\omega_k)$ is equal to zero if the system attained a steady-state. $\mathbf{Y}_{\mathrm{G}_p}(j\omega_k) = \mathrm{G}_p(j\omega_k) + \mathbf{U}_{\mathrm{multi},T}(j\omega_k)$ is the spectrum of the windowed steady-state response of the system to the multisine. The windowed response of the P^{th} branch is the following convolution

$$\mathbf{Y}_{p,T}(j\omega_k) = \left[\mathbf{Y}_{\mathrm{G}_p,T}(j\omega)\right] \cdot \left[TB_p(j\omega)\right]|_{\omega=\omega_k} = \mathbf{Y}_p(j\omega_k) + \mathbf{T}_{\mathbf{Y},p}(j\omega_k), \tag{12.14}$$

with $\mathbf{Y}_p(j\omega_k) = \left[\mathrm{G}_p(j\omega_k)\mathbf{U}_{\mathrm{multi},T}(j\omega)\right] \cdot \left[TB_p(j\omega)\right]|_{\omega=\omega_k}$, $\mathbf{T}(j\omega_k)$ is a rational form in $j\omega_k$ and the normalized Fourier transforms of the windowed basis functions $B_p(j\omega) = \frac{1}{T}\int_0^T b_p(t)\mathrm{e}^{-j\omega t}\,\mathrm{d}t$ so that $\mathbf{U}_{\mathrm{multi},T}(j\omega)$ can be replaced with $\mathbf{U}_{\mathrm{multi}}(j\omega)$. This results in [4]

[4] This is based on the definition of convolving with a Dirac function. The convolution of two functions f(t) and g(t) is written as f · g and is defined as: $(\mathrm{f}\cdot\mathrm{g})(t) = \int_{-\infty}^{\infty} \mathrm{f}(t')\mathrm{g}(t-t')\,\mathrm{d}t'$. In case function f is a Dirac function (f(t) = $\delta(t\text{-}t_\mathrm{e})$), the convolution yields: $\delta(t\text{-}t_\mathrm{e}) \cdot \mathrm{g}(t) = \mathrm{g}(t\text{-}t_\mathrm{e})$.

$$\mathbf{Y}_p(j\omega_k) = \frac{T}{2\pi}\int_{-\infty}^{\infty} B_p(j\omega_k - j\omega')\mathrm{G}_p(j\omega')\mathbf{U}_{\text{multi}}(j\omega')\,\mathrm{d}\omega', \tag{12.15a}$$

$$= \frac{T}{2\pi}\sum_{k_\mathrm{e}} \mathbf{U}(k_\mathrm{e})\mathrm{G}_p(j\omega_{k_\mathrm{e}})B_p j\omega_{k-k_\mathrm{e}}). \tag{12.15b}$$

Since $\mathbf{Y}(j\omega_k) = \sum_{p=0}^{N_p}\mathbf{Y}_p(j\omega_k)$, the equation can be changed to

$$\mathbf{Y}(j\omega_k) = \sum_{p=0}^{N_p}\sum_{k_\mathrm{e}} \theta_{p,k_\mathrm{e}} B_p\left(j\omega_{k-k_\mathrm{e}}\right) + \mathbf{T}_\mathrm{Y}(j\omega_k), \tag{12.16}$$

with

$$\theta_{p,k_\mathrm{e}} = \frac{T}{2\pi}\mathbf{U}(k_\mathrm{e})\mathrm{G}_p(j\omega_{k_\mathrm{e}}) \tag{12.17a}$$

$$\mathbf{T}(j\omega_k) = \sum_{p=0}^{N_p}\mathbf{T}_{\mathrm{Y,p}}(j\omega_k) \tag{12.17b}$$

When plugged in Eq. 12.9,

$$\mathrm{FRF}_{\text{inst}}(j\omega_{k_\mathrm{e}}, t^\star) = \sum_{p=0}^{N_p}\frac{\theta_{p,k_\mathrm{e}}}{\mathbf{U}_{\text{multi,T}}(j\omega_{k_\mathrm{e}})} b_p(t^\star). \tag{12.18}$$

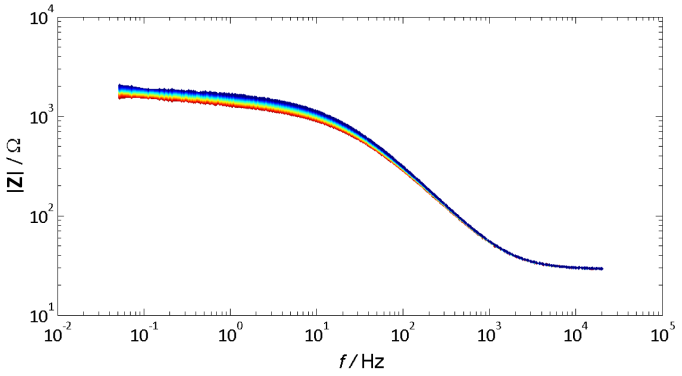


Figure. 12.10 – Calculated instantaneous impedance values on the measurement after 5 hours of immersion.

Note that the described model in Eq. 12.16 is linear-in-the-parameters θ_{p,k_e}, meaning the estimation of the weights of these skirts (which are the θ_{p,k_e} parameters) can be extracted from the output spectrum using a simple Linear Least Squares (LLS) algorithm. In practice, first some assumptions are made concerning the noise and the error. Then the LLS algorithm is used for estimating θ_{p,k_e} by limiting the output spectrum to the DFT bins in $\mathbb{K}_{k_\mathrm{e}}$. Then, the parameters θ_{p,k_e}, $\theta_{p,k_\mathrm{e}^-}$ and $\theta_{p,k_\mathrm{e}^+}$ are estimated to put into the regression matrix. In practice, the LLS algorithm is computationally expensive due to the huge size of the regression matrix. In addition, if the output signal is corrupted by colored noise, the LLS estimator is inefficient. Because of these two drawbacks, the LLS estimator is slightly altered. More concrete, θ_{p,k_e} is estimated by limiting the output spectrum to the first 100 discrete frequencies left and the first 100 discrete frequencies right of each excited frequency. The parameter θ_{p,k_e} is then estimated as the minimizer of the cost function. This estimate is nonparametric in the frequency domain and parametric in the time domain. This means that, at each user-defined excited frequency, the evolution of the impedance is provided as a polynomial in time within the measured time range. The complete background is not explained in this work. For an explanation of the complete procedure, we refer to [19].

12.2.3.3 The resulting instantaneous impedance value

In this work, the total measurement time (i.e. the 7 minutes needed to perform one ORP-EIS measurement) is divided into 100 equal time steps. For each of those 100 instant times $t^\star$, the instantaneous impedance is plotted in Figure 12.10. The

calculated instantaneous impedance values show the time-evolution of the corrosion process during one measurement. Each estimated linear and stationary instantaneous impedance curve at a certain time instant $t^\star$ can be fitted using an equivalent electric circuit (EEC) model.

12.2.4 Impedance model

The Bode magnitude and phase plots, in Figure 12.6a and b, clearly show that more than one time constant is needed to fit the experimental data. With complementary techniques and some literature research [22–27] we could distinguish two processes, i.e. the deterioration of the natural lead oxide layer and the formation of a new corrosion product layer. Both time constants are related to the phenomena at the surface interface. Therefore, we propose a model using two time constants. The EEC is depicted in Figure 12.11. Its ability to describe the system is discussed further in the text. The noise of the system will be used as a weighing factor in the fitting procedure.

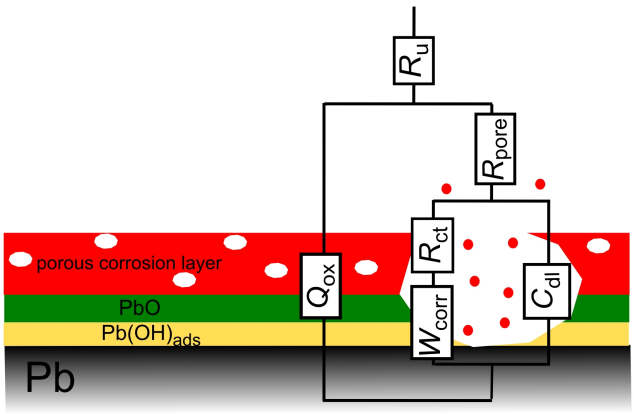


Figure. 12.11 – Equivalent electric circuit model for the fitting of the raw ORP-EIS data.

Figure 12.12 presents the magnitude Bode plot, modeled curve, residual curve and the different noise levels (noise on the excited frequencies and noise at the non-excited frequencies) at the last calculated time instant of the measurement at 5 hours of immersion. It should be remarked that all instantaneous impedance curves are by definition stationary and can be fitted with the proposed model. Using the technique described by T. Breugelmans et al. [4], it can be demonstrated the system is linear. The complex residual is the difference between the modeled data and the raw data. An excellent fit was obtained with the proposed model (‘gray line’) for the bare lead sample recorded experimental data (‘.’). A good fit implies that the residual curve (‘–’) is situated within the non-stationary level of the measurement. Furthermore, it is observed that the residual relative error is always less than 1.3% (except for the points at the lowest frequencies, where the residual relative error is less than 4.3%). Because the residual error is small enough, it is feasible to accept the proposed EEC model.

12.2.5 Fitting results

In the following subsections, the fitted parameters are shown and compared. In the Figures figs. 12.13 to 12.15, the parameter values with their deviations (calculated based on the 100 fitted instantaneous impedance values and their deviations) are given. Furthermore, for each parameter, figures show the fitted instantaneous impedance values with their standard deviations for randomly chosen times.

12.2.5.1 Electrolyte resistance

In Figure 12.13, it is observed that the electrolyte resistance can be considered constant throughout the total immersion time (all fitted values are in between 28 and 30 Ω cm^2). The relative error is below 1% for all instantaneous impedances

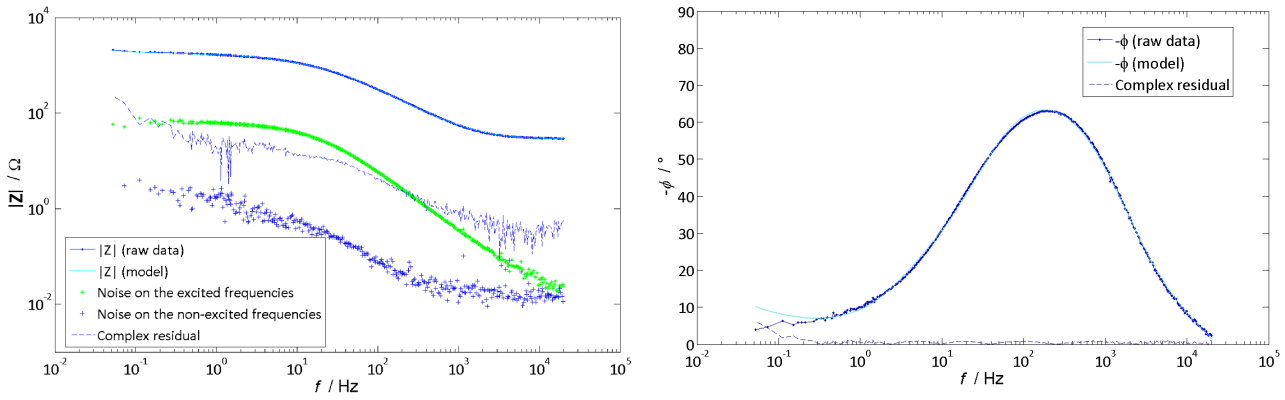


Figure. 12.12 – Magnitude plot, modeled curve, residual curve, noise on the excited frequencies and noise on the non-excited frequencies at the last calculated time instant of the measurement at 5 hours of immersion.

during the whole measurement.

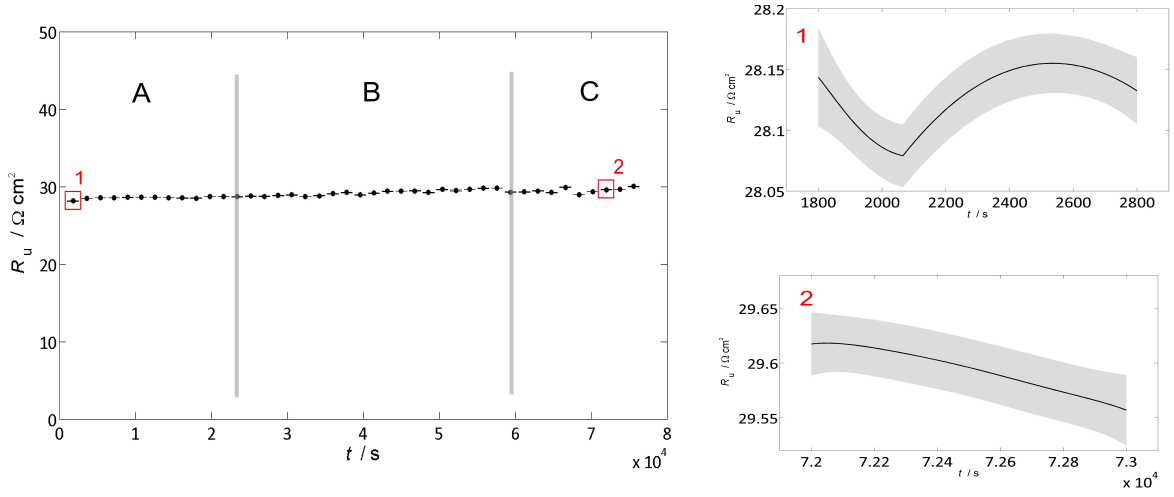


Figure. 12.13 – Electrolyte resistance of the instantaneous impedances as a function of immersion time.

12.2.5.2 Oxide layer parameters

Before submersion, the polished lead metal is corroded in the air to form a 3-6 nm-thick native PbO layer (mainly litharge) following the chemical reaction 2.5b. The constant phase element representing the protective properties of the oxide layer, is recalculated to a pseudo-capacitance, using the formula of Brug in section 8.1.3.3 an plotted in Figure 12.14a. This pseudo-capacitance, $C_{\text{eff,ox}}$, decreases during 6 hours. After that, the pseudo-capacitance starts to drop more slowly. At the end of the measurement we measure a stable value. For the first 5 hours the R_{pore} stays stable, but shows a very low value. Afterwards, it has been seen that the pore resistance increases slowly. After the deterioration of the initial lead oxide layer, a sudden drop in the pore resistance occurs.

12.2.5.3 Corrosion reaction parameters

In Figure 12.15a, the double layer capacitance exhibits a stable behavior for 5 hours. The lead oxide dissolution process starts to induce instability in the C_{dl} value because of the change around the oxide/metal interface. When the lead substrate is 6 hours in the corrosive solution, the capacitance increases because the lead metal close to the oxide/metal interface starts to corrode and dissolve. At first, the charge-transfer resistance R_{ct}, decreases slightly as a consequence of the lead

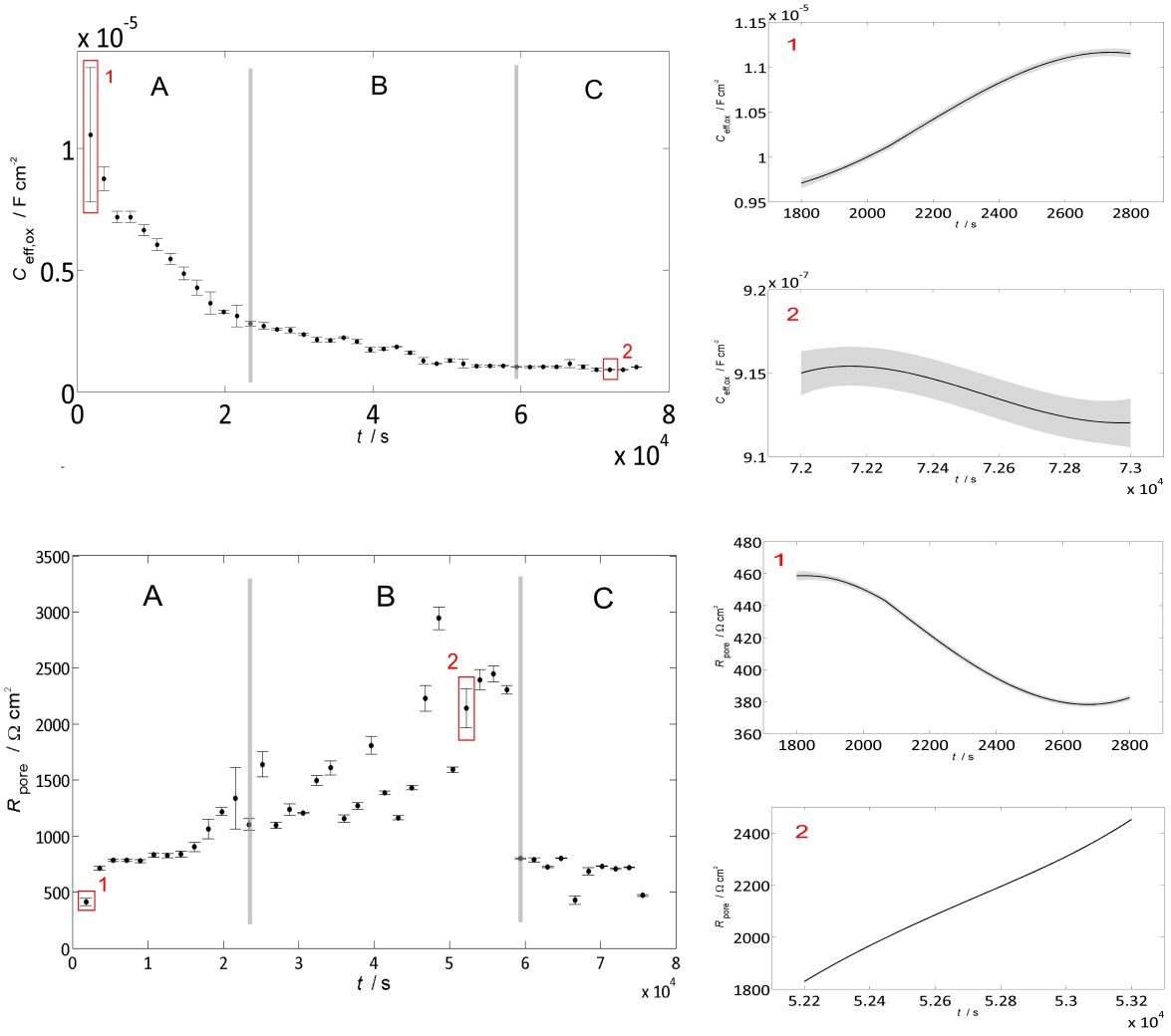


Figure. 12.14 – Oxide layer parameters of the instantaneous impedances as a function of immersion time.

oxide dissolution process (Figure 12.15b). After 16 hours, the R_{ct} value starts to increase, indicating that, after an initial fast formation of the solid corrosion products, an equilibrium is set in the dissolution-precipitation mechanism of the corrosion process. For the corrosion reaction, there is a resistance coupled with the Warburg element connected to the corrosion. In Figure 12.16, the influence of the electron transfer resistance with respect to the mass transfer resistance is compared for three immersion times: 1 hour, 5 hours and 10 hours of immersion. A discussion of all the parameters will be given in the following section.

12.2.6 Scanning electron images

Figure 12.17 shows SEM images taken before the lead substrate was brought in contact with the acetic acid environment and after 20 hours of immersion. Figure 12.17a shows a smooth lead oxide layer with black spots due to the presence of silicon carbide polishing particles (see Figure 12.17b in the Si K_α EDS spectrum). The sample exposed to the air is covered by a corrosion product layer consisting of mainly litharge so thin (3 - 6 nm) that scratches from the polishing are still visible. Figure 12.17b shows a surface that is covered by a thick layer of corrosion products. The surface exhibits small cauliflower-like corrosion products. A. Niklasson et al. [28] identifies these corrosion products as lead hydrocarbonates and lead acetate oxide hydrates. Next to the corrosion products rod-shaped lead bromides are seen due to the high concentration of TBAB. Figure 12.17b shows the EDS maps measured on the same area of the corroded

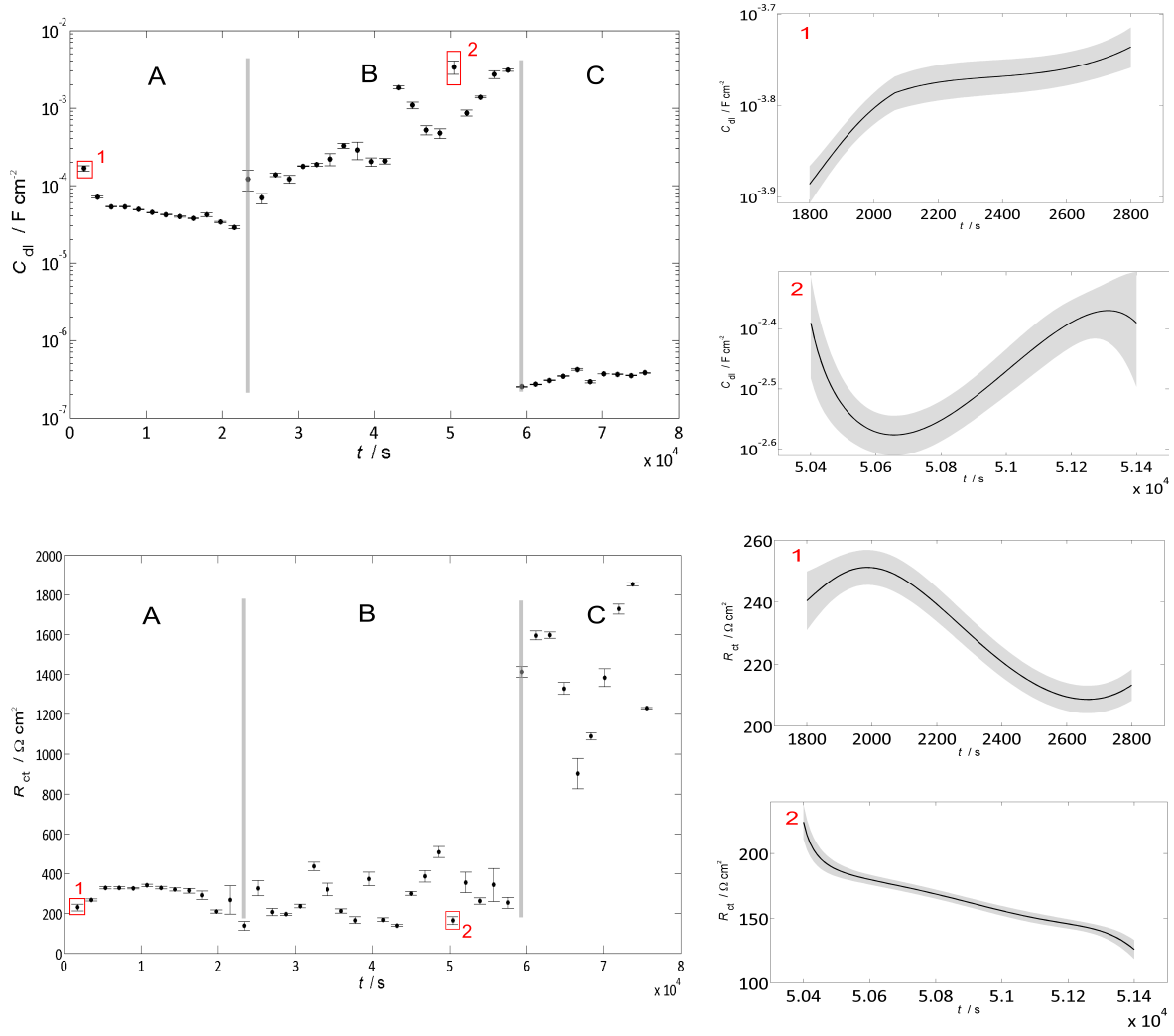


Figure. 12.15 – Charge-transfer parameters of the instantaneous impedances as a function of immersion time.

lead substrate as the SEM image. The Si K_α map shows local concentrated intensities as a consequence of the silicon carbide polishing particles, which are stuck into the lead matrix due to the soft nature of the metal. The cauliflower-like structures consist of carbon, oxygen and lead atoms confirming the presence of lead corrosion products like lead acetate oxide hydrate and plumbonacrite [23]. The SEM-EDS images show us that the initial lead oxide layer is deteriorated by the presence of the acetic acid. Compared to the reference sample (see Figure 12.17c) immersed only in TBAB supporting electrolyte, however, fewer lead bromide compounds are formed when acetic acid is added (see wt% Br). This indicates that the acetic acid, although present in a low concentration (5 ppb), has a more important influence on the corrosion of the lead sample compared to the bromide ions. Certainly in the first hours of the experiment acetic acid starts to adsorb on the lead sample attacking the surface very fast. The EDS maps of the reference sample shows only Br and O indicating the presence of lead bromides and lead oxides. It is clear that the acetic acid even in low concentrations influences the corrosion process considerably.

12.2.7 Discussion using fitted parameters

In this section, we discuss the electrochemical processes using the different fitted parameters. It is clear from section 12.2.5 that three important time frames are considered: from 0 to 6 hours (referred to as the lead oxide dissolution time frame), from 6 to 16 hours (referred to as the corrosion time frame) and from 16 to the end of the measurement (referred

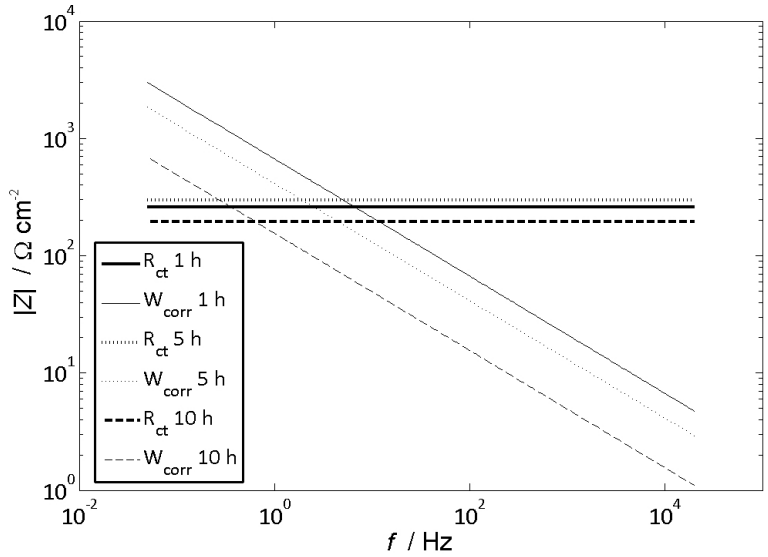


Figure. 12.16 – Comparison of the charge-transfer resistance R_{ct} with the mass transfer resistance (W_{corr}) for different immersion times.

to as the porous corrosion layer time frame).

12.2.7.1 Lead oxide dissolution time frame

In this time frame, the change in the parameter values is small but meaningful taking into account all instantaneous impedances. The pseudo-capacitance representing the barrier properties of the oxide layer ($C_{\text{eff,ox}}$) starts to drop very fast, which indicates that the oxide layer is removed, indicating that the area of the lead metal covered by lead oxide decreases ($C \downarrow\sim \frac{A\downarrow}{d}$). The basic PbO layer is dissolved by the adsorbed acetic acid because of fast adsorption of the acetic acid on the surface [29], which is described by a simple acid-base reaction in 2.10. The presence of this lead oxide layer is confirmed by analyzing its capacitance, which is associated with the formed oxide layer expressed as [30]

$$C_{\text{eff,ox}} = \frac{\epsilon_{\text{r}}\epsilon_0 A}{d} \tag{12.19}$$

where ϵ_{r} is the relative permittivity for the dielectric oxide (25.6), ϵ_0 is the permittivity of the vacuum (i.e. 8.8542×10^{-12} F m^{-1}), A is the surface area and d is the thickness of the oxide layer. After 2 hours of immersion, before severe corrosion, the thickness of the lead oxide layer is calculated to be 3.2 nm using Eq. 12.19. Graedel et al. [31] predicted a native lead oxide (mainly litharge) layer on lead of 3 to 6 nm thick. The presence of this lead oxide layer on the lead substrate is confirmed by XPS analysis in another scientific publication of our group [32]. When submersed in an aqueous solution, the lead metal is continuously oxidized to PbO using different electrochemical steps in reactions eqs. (7.10a), (7.10b), (7.11a) and (7.11b). The production and dissolution of PbO shown in reaction 2.10 provide continuously lead and acetate ions for the production of lead corrosion products like lead acetate oxide hydrate described in reaction 2.11, plumbonacrite described in reaction 2.7 [33] and in this case also lead bromide crystals because of the electrolyte described in reaction

$$\text{Pb}^{2+}(\text{aq}) + 2\text{Br}^{-}(\text{aq}) \leftrightharpoons \text{PbBr}_2(\text{s}). \tag{12.20}$$

The formed products are crystalline solids and start to precipitate when its solubility products are exceeded. It means a layer of corrosion products is formed explaining the fast drop of $C_{\text{eff,ox}}$ ($C \downarrow\sim \frac{A}{d\uparrow}$). In Figure 12.14b, R_{pore} has been interpreted as the pore resistance of a layer resulting from the penetration of the electrolyte [34–36] through pores [37].

During the formation of the corrosion products, the pores of the oxide layer are gradually filled blocking the electrolyte, so that the R_{pore} value exhibits a small global increasing tendency. However, the value stays very low because of extensive electrolyte penetration in the layer.

In this time frame, the metal interface is not changing as seen in Figure 12.15a. The Helmholtz double-layer capacitance ranges from 30 to 50 μF cm^{-2}. Values around 40 μF cm^{-2} predict a solution side formed by anions, indicating the lead metal is positively charged as a result of the oxidation process [38]. Furthermore, using the Helmholtz model, the thickness of the electric double layer is calculated to be 1 - 2 Å, which is explained by a monolayer of bromide (r_{Br^-} = 1.96 Å [39]) and acetate (r_{Ac^-} = 1.62 Å [40]) anions. The small decreasing tendency of the resistance against corrosion, R_{ct}, is because of the dissolution in the upper oxide layer described by the small drop in Figure 12.15b. Overall, the R_{ct} values are very low suggesting an easy exchange of electrons between the solution and the metal.

In Figure 12.16, the Warburg element connected to the corrosion reaction at the lead oxide surface demonstrates that the Warburg resistance is dominant. Indeed, the dissolution process going on at the surface shows an important mass transfer process. The formed lead ions diffuse away from the surface to the corrosive solution. At the same time, these lead ions start to react with anions (also bromides) in the solution and precipitate on the surface. Also, the non-stationary system explains the constant corrosion processes. In this time frame, mass transfer plays a dominant role starting from the mid-frequency region (starting from 101 Hz).

12.2.7.2 Corrosion time frame

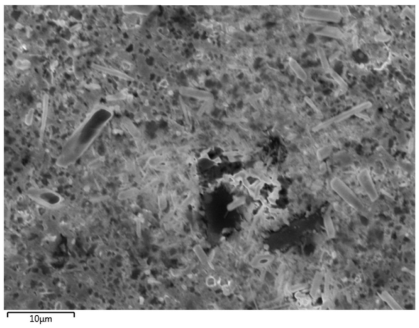
In the corrosion time frame, the acetic acid reaches the bulk metal through the formed pathways in the lead oxide layer (almost completely dissolved) [41]. As a result, a strong corrosion process starts, which ensures that the corrosion product layer grows slowly, so that the pseudo-capacitance, $C_{\text{eff,ox}}$, in Figure 12.14a decreases slowly. These porous insoluble corrosion products (also lead bromides) precipitate and cover up the underlying lead oxide layer blocking the initially formed electrolyte pathways and filling the pores [42]. The blocking of the corrosive solution from reaching the metal/oxide interface, which changes very fast due to the corrosion of the lead metal, explains the increasing unstable R_{pore} values in Figure 12.14b). In the previous time frame, only local corrosion systems exist, while now the corrosion reaction has spread out over the entire surface indicated by the larger variations of the different parameters. A sudden increase in the C_{dl} at the lead metal/oxide interface as seen in Figure 12.15a is ascribed to the start of lead metal corrosion. The strong increase of C_{dl} indicates that the lead metal under the initial oxide layer is now corroded to form PbO using reactions eqs. (7.10a), (7.10b), (7.11a) and (7.11b) (afterwards it is dissolved in reaction 2.10) so that the area of the metal/oxide interface increases due to pits in the metal ($C \uparrow\sim \frac{A\uparrow}{d}$). The unstable values explain the continuous corrosion ensuring a change of the area of the pits in the metal surface. Furthermore, the R_{ct} values are very low explaining the strong corrosion process. However, the R_{ct} values become very unstable, which is attributed to the sudden changes around the metal interface due to the dissolution process (decreasing the resistance) and the formation of corrosion products (increasing the resistance). In the corrosion time frame, the Warburg modulus of the corrosion reaction in Figure 12.16 decreases substantially (at 10 hours). The formed porous corrosion product clusters (growth of the layer slows down as explained by $C_{\text{eff,ox}}$) in the pores and the lack of lead oxides at the surface confirms the slowing down of the ongoing diffusion process.

12.2.7.3 Porous corrosion layer time frame

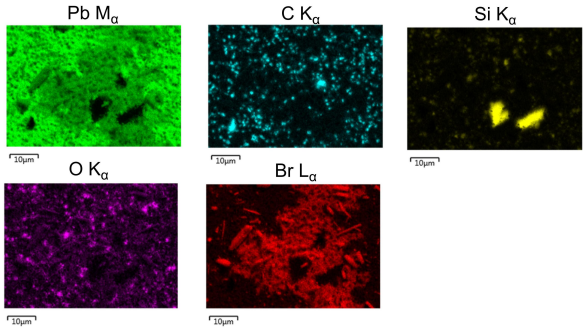
At the end of the process in Figure 12.14, the sudden decrease of the R_{pore} value assumes the complete deterioration of the atmospherically formed oxide layer. A continuous corrosion process starts to produce soluble ions, which precipitate as a layer of porous clusters on the lead surface as described in reactions eqs. (2.7), (2.11) and (12.20)), making it easier for the



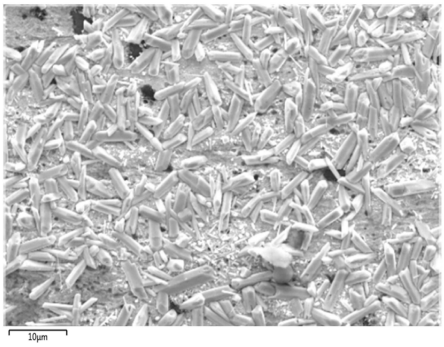
(a)



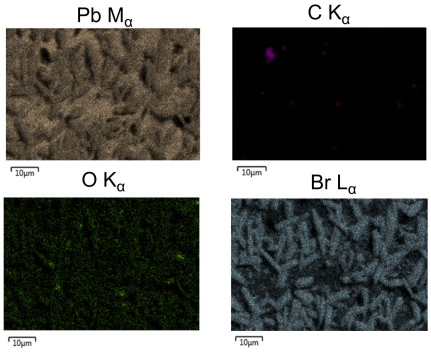
	w%
Pb	57
C	28
O	6
Br	6
Si	3



(b)



	w%
Pb	69
C	3
O	9
Br	19



(c)

Figure. 12.17 – SEM images of a blank (a) and corroded lead substrate in (b) TBAB + acetic acid and (c) TBAB.

electrolyte to reach the lead metal. The R_{pore} is now related only to the porous corrosion product layer explaining the low and stable value. The low stable $C_{\text{eff,ox}}$ values indicate the presence of the thick layer of corrosion product clusters on the surface providing new barrier properties [22–24]. Furthermore, the stable value explains a slow corrosion process where an equilibrium is created between the oxide layer being dissolved and new corrosion products precipitate. However, this indicates that the corrosion process is not finished.

The formation of a new corrosion product layer explains why the capacitive behavior close to the interface is suddenly decreasing and stabilizing. The porous corrosion products fill up the pits very fast. As a result, the exposed area of the metal/oxide interface to the corrosive solution suddenly decreases ($C \downarrow\sim \frac{A\downarrow}{d}$). The more stable values of C_{dl} and the increase of the R_{ct} values are ascribed to a slower corrosion process due to the corrosion product layer and to the dissolution-precipitation mechanism. Indeed, it is more difficult for the acetic acid to reach the lead oxide present at the metal/oxide interface due to the precipitated compounds. The unstable increased R_{ct} values clearly show that the system is trying to reach an equilibrium state between the dissolution and precipitation process. Another explanation for the instability of the R_{ct} value is the constant change of the corrosion layer during immersion. A loss of corrosion products in the layer could increase the corrosion reaction rate ensuring a drop in the R_{ct} value.

In this time frame, no more Warburg modulus is measured in the frequency range used, explaining the slowing down of the diffusion process. Corrosion processes are still going on, but an equilibrium is created between the corrosion reaction and the precipitation of the solid corrosion products. The slower corrosion process is also confirmed by the more stationary behavior. Two processes exist in all time frames namely dissolution and precipitation. In the lead oxide dissolution time frame, the initial lead oxide layer dissolves and precipitation starts. In the corrosion time frame, the dissolution of the lead metal is dominant. In the last time frame, an equilibrium exists between the dissolution of the lead and the precipitation of lead corrosion products, explaining the slower corrosion process.

12.2.7.4 Mechanism for the active corrosion of lead in acetic acid

The scheme, presented in Figure 12.18, exhibits what is happening during the three defined time frames, based on the SEM-EDS images and statistical analysis of the EIS data using the proposed model. The fact that the parameter trends and the instantaneous impedance fittings for each measurement are explained by the different physical processes, established the validity of the model. This corrosion mechanism is an interesting continuation of the experiments conducted by the E. Rocca et al. [25] and A. Niklasson et al. [23]. In these papers, a mechanism was suggested to explain the formation of certain corrosion products measured on top of the lead substrate after immersion in an acetic acid environment. This paper, however, starts from an electrochemical point of view, trying to understand the fundamental physical processes taking place at the surface of the lead substrate. Using odd random phase electrochemical impedance spectroscopy, an in-situ measurement technique, the active corrosion mechanism for lead substrates in an acetic acid medium is studied. This novel technique allows us to measure a large frequency range in a very short time, enabling us to perform time lapse studies on different electrochemical systems. Furthermore, using instantaneous impedances, dynamic systems are considered stationary.

The model representing the corrosion mechanism of lead substrates in an acetic acid environment was proven to be correct based on the valid parameter trends. The corrosion mechanism is split in three time frames. At the start, the atmospherically formed oxide layer is dissolved with the simultaneous precipitation of lead corrosion products. The acetic acid attacks the basic lead oxide layer. Secondly, the electrolyte reaches the metal/oxide interface and induces metal corrosion with the formation of pits in the metal. The formed porous hydrophobic corrosion products pile up on top of the lead oxide layer slowing down the metal corrosion. These corrosion products, however, form porous crystal

clusters, leaving corrosion processes to go on slowly.

In this work, a mechanism is suggested to explain the active corrosion of lead in an acetic acid environment. This paper states that two processes exist during the measurement namely dissolution and precipitation. In the lead oxide dissolution time frame, the initial lead oxide layer dissolves and precipitation starts. In the corrosion time frame, the dissolution of the lead metal is dominant. In the last time frame, an equilibrium exists between the dissolution of the lead and the precipitation of lead corrosion products, explaining the slower corrosion process.

This electrochemical impedance test gives us a detailed view on the corrosion process in a diluted acetic acid environment. However, for conservation purposes, only the corrosion process of acetic acid in air is interesting. In general, vapor phase corrosion is more severe compared to liquid phase corrosion. For example, acids in crude oil cause more severe corrosion to the steel pipes on condensation from the vapor phase back to the liquid phase [43]. However, in food technology, the diluted acetic acid attack on the aluminum cans is stronger in the liquid phase [44].

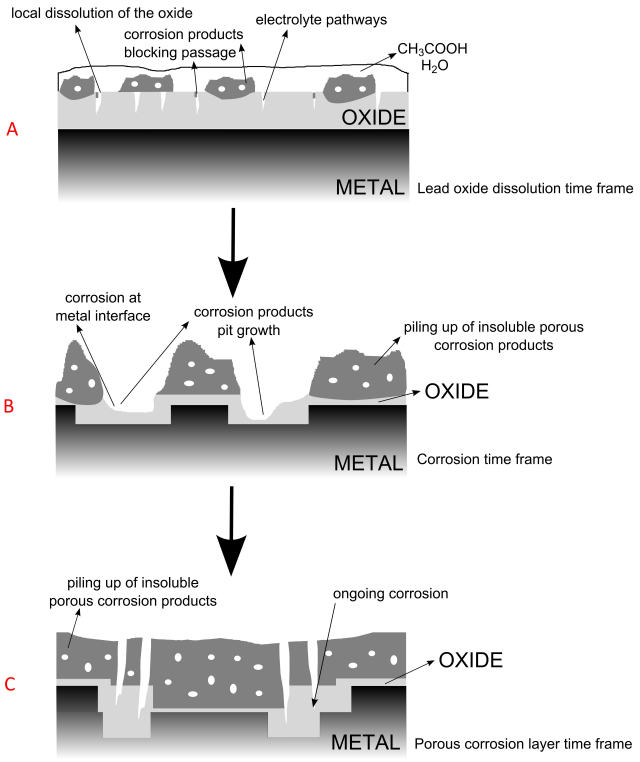


Figure. 12.18 – Physical representation of the active corrosion of a lead substrate in an acetic acid environment.

Clearly, the state of matter of the corrosive species has an influence on the corrosion speed, but this depends on the corrosion process which depends on the corrosive species, the substrate, the presence of water, the environment, etc.

12.3 Conclusions

This work explains, using odd random phase electrochemical impedance spectroscopy, an in-situ measurement technique, the active corrosion mechanism for lead substrates in an acetic acid medium. This novel technique measures a large frequency range in a very short time, enabling us to perform time lapse studies on different electrochemical systems. Furthermore, using instantaneous impedances, dynamic electrochemical systems are considered linear and stationary using different time steps.

The model representing the corrosion mechanism of lead substrates in an acetic acid environment was proven to be correct based on the valid parameter trends. The corrosion mechanism is split in three time frames. At the start, the atmospherically formed oxide layer is dissolved with the simultaneous precipitation of lead corrosion products. The acetic acid attacks the basic lead oxide layer. Secondly, the electrolyte reaches the metal/oxide interface and induces metal corrosion with the formation of pits in the metal. The formed porous hydrophobic corrosion products pile up on top of the lead oxide layer slowing down the metal corrosion. These corrosion products, however, form porous crystal clusters, leaving corrosion processes to go on slowly.

In this work, a mechanism is suggested to explain the active lead corrosion in a diluted acetic acid environment. This paper states that two processes exist during the measurement namely dissolution and precipitation. In the lead oxide

dissolution time frame, the initial lead oxide layer dissolves and precipitation starts. In the corrosion time frame, the dissolution of the lead metal is dominant. In the last time frame, an equilibrium exists between the dissolution of the lead and the precipitation of lead corrosion products, explaining the slower corrosion process. When considering lead corrosion in air, it is difficult to predict how the corrosion process will change. Much of this corrosion process depends on important factors such as the corrosive species, the substrate, the presence of water, the environment, etc.

References for Chapter 12

[1] E. VAN GHEEM et al., Electrochemical impedance spectroscopy in the presence of non-linear distortions and non-stationary behavior. I. Theory and validation, *Electrochim. Acta* **49** (26) (2004), 4753–4762.

[2] O. BLAJIEV, R. PINTELON, and A. HUBIN, Detection and evaluation of measurement noise and stochastic non-linear distortions in electrochemical impedance measurements by a model based on a broadband periodic excitation, *J. Electroanal. Chem.* **576** (1) (2005), 65–72.

[3] Y. VAN INGELGEM et al., Advantages of odd random phase multisine electrochemical impedance measurements, *Electroanalysis* **21** (6) (2009), 730–739.

[4] T. BRUEGELMANS et al., Odd random phase multisine EIS for organic coating analysis, *Prog. Org. Coat.* **69** (2010), 215–218.

[5] S. CREASON, J. HAYES, and D. SMITH, Fourier transform faradaic admittance measurements III. Comparison of measurement efficiency for various test signal waveforms, *J. Electroanal. Chem. Interf. Electrochem.* **47** (1) (1973), 9–46.

[6] K. DAROWICKI, J. ORLIKOWSKI, and G. LENTKA, Instantaneous impedance spectra of a non-stationary model electrical system, *J. Electroanal. Chem.* **486** (2) (2000), 106–110.

[7] R. SCHWALL et al., High speed synchronous data generation and sampler system: Application to on-line fast Fourier transform faradaic admittance measurements, *Anal. Chem.* **49** (12) (1977), 1797–1805.

[8] R. PINTELON and J. SCHOUKENS, *System identification: A frequency domain approach*, 2nd, Wiley, 2012, 1–788.

[9] R. PINTELON et al., Experimental characterization of operational amplifiers: A system identification approach. I. Theory and simulations, *IEEE Trans. Instrum. Meas.* **53** (3) (2004), 854–862.

[10] J. SCHOUKENS, R. PINTELON, and Y. ROLAIN, Broadband versus stepped sine FRF measurements, *IEEE Trans. Instrum. Meas.* **49** (2) (2000), 275–278.

[11] M. URQUIDI-MACDONALD, S. REAL, and D. MACDONALD, Applications of Kramers-Kronig transforms in the analysis of electrochemical impedance data. III. Stability and linearity, *Electrochim. Acta* **35** (10) (1990), 1559–1566.

[12] J. SCHOUKENS, R. PINTELON, and T. DOBROWIECKI, Linear modelling in the presence of nonlinear distortions, in: *Proceedings of the 18th IEEE Instrumentation and Measurement Technology Conference*, **2**, 2001, 1332–1338.

[13] T. BRUEGELMANS, An identification approach as a prerequisite for quantitative electrochemical studies, PhD thesis, Vrije Universiteit Brussel, 2010.

[14] Y. VAN INGELGEM, Implementation of multisine EIS in a toolbox for electrochemical studies, PhD thesis, Vrije Universiteit Brussel, 2009.

[15] J. SCHOUKENS, T. DOBROWIECKI, and R. PINTELON, Parametric and nonparametric identification of linear systems in the presence of nonlinear distortions - a frequency domain approach, *IEEE Trans. Autom. Control* **43** (2) (1998), 176–190.

[16] C. EVANS and D. REES, Nonlinear distortions and multisine signals. I. Measuring the best linear approximation, *IEEE Trans. Instrum. Meas.* **49** (3) (2000), 602–609.

[17] E. VAN GHEEM, A new methodology for electrochemical impedance spectroscopy in the presence of non-linear and non-stationary behavior: Application to pitting corrosion of aluminum, PhD thesis, Vrije Universiteit Brussel, 2005.

[18] K. VANHOENACKER, T. DOBROWIECKI, and J. SCHOUKENS, Design of multisine excitations to characterize the nonlinear distortions during FRF-measurements, *IEEE Trans. Instrum. Meas.* **50** (2001), 1097–1102.

[19] J. LATAIRE, Frequency domain measurement and identification of linear, time-varying systems, PhD thesis, Vrije Universiteit Brussel, 2011.

[20] E. LOUARROUDI, J. LATAIRE, and R. PINTELON, Nonparametric tracking of the time-varying dynamics of weakly nonlinear periodically time-varying systems using periodic inputs, *IEEE Trans. Instrum. Meas.* **61** (5) (2012), 1384–1394.

[21] A. OPPENHEIM, A. WILLSKY, and I. YOUNG, *Signal and systems*, Prentice-Hall International, 1983, 195.

[22] A. NIKLASSON, L. JOHANSSON, and J. SVENSSON, Atmospheric corrosion of lead: The influence of formic acid and acetic acid vapors, *J. Electrochem. Soc.* **154** (11) (2007), C618–C625.

[23] A. NIKLASSON, L. JOHANSSON, and J. SVENSSON, Influence of acetic acid vapor on the atmospheric corrosion of lead, *J. Electrochem. Soc.* **152** (12) (2005), B519–B525.

[24] A. NIKLASSON, L. JOHANSSON, and J. SVENSSON, The influence of relative humidity and temperature on the acetic acid vapor-induced atmospheric corrosion of lead, *Corros. Sci.* **50** (11) (2008), 3031–3037.

[25] E. ROCCA, C. RAPIN, and F. MIRAMBET, Inhibition treatment of the corrosion of lead artefacts in atmospheric conditions and by acetic acid vapor: use of sodium decanoate, *Corros. Sci.* **46** (3) (2004), 653–665.

[26] K. DE WAEL et al., Electrochemical deposition of dodecanoate on lead in view of an environmentally safe corrosion inhibition, *J. Solid State Electrochem.* **14** (3) (2010), 407–413.

[27] R. GRAYBURN et al., Time-lapse synchrotron X-ray diffraction to monitor conservation coatings for heritage lead in atmospheres polluted with oak-emitted volatile organic compounds, *Corros. Sci.* **82** (2014), 280–289.

[28] A. NIKLASSON, Atmospheric corrosion of historic lead organ pipes, PhD thesis, Chalmers University of Technology, 2007.

[29] R. JURCZAKOWSKI, Impedance of porous Au based electrodes, *J. Electroanal. Chem.* **572** (2004), 355–366.

[30] M. ORAZEM and B. TRIBOLLET, *Electrochemical impedance spectroscopy*, John Wiley & Sons, 2008, 1–525.

[31] T. GRAEDEL, Chemical mechanisms for the atmospheric corrosion of lead, *J. Electrochem. Soc.* **141** (4) (1994), 922–927.

[32] M. DE KEERSMAECKER et al., Electrochemical and surface study of neutralized dodecanoic acid on a lead substrate, *J. Electrochem. Soc.* **161** (3) (2014), C126–C137.

[33] C. BERGSTEN et al., *The Collapse project: Corrosion of organ pipes - causes and recommendations*, University of Gothenburg, Göteborg Organ Art Center, 2011, 136–140.

[34] B. FASTRUP and A. SAARNAK, AC impedance of painted and scribed steel panels under atmospheric exposure, *Prog. Org. Coat.* **16** (3) (1988), 277–290.

[35] M. KENDIG, F. MANSFELD, and S. TSAI, Determination of the long term behavior of coated steel with AC impedance measurements, *Corros. Sci.* **23** (4) (1983), 317–329.

[36] F. MANSFELD, M. KENDIG, and S. TSAI, Evaluation of corrosion behavior of coated metals with AC impedance measurements, *Corros.* **38** (1982), 478–485.

[37] M. KENDIG and H. LEIDHEISER, The electrical properties of protective polymer coatings as related to corrosion of the substrate, *J. Electrochem. Soc.* **123** (1976), 982–989.

[38] V. BAGOTSKY, Structure and properties of surface layers, in: *Fundamentels of electrochemistry*, John Wiley & Sons, 2006, 147–180.

[39] R. SHANNON, Revised effective ionic radii and systematic studies of interatomic distances in halides and chalcogenides, *Acta Crystallogr. A* **32** (1976), 751–767.

[40] G. MANKU, Ionic radii, in: *Theoretical principles of inorganic chemistry*, McGraw-Hill Book Company, 1980, 98–105.

[41] P. LI, T. TAN, and J. LEE, Corrosion protection of mild steel by electroactive polyaniline coatings, *Synthetic Metals* **88** (1997), 237–242.

[42] F. MANSFELD and M. KENDIG, Evaluation of anodized aluminum surfaces with electrochemical impedance spectroscopy, *J. Electrochem. Soc.* **135** (1988), 828–833.

[43] J. SPEIGHT, *The refinery of the future*, Elsevier, 2011, 7.

[44] M. SCHÜTZE, D. WIESER, and R. BENDER, eds., *Corrosion resistance of aluminium and aluminium alloys*, Wiley, 2010, 10–11.

13

Spectroelectrochemical characterization of a $Pb(C_{12})_2$ coating

Reprinted from Talanta, 132, M. De Keersmaecker, M. Dowsett, R. Grayburn, D. Banerjee and A. Adriaens, In-situ spectroelectrochemical characterization of the electrochemical growth and breakdown of a lead dodecanoate coating on a lead substrate, 760-768, 2015, with permission from Elsevier.

13.1 In-situ X-ray diffraction measurements

The real-time growth and breakdown of a lead dodecanoate ($Pb(C_{12})_2$) coating was studied on the Belgian-Dutch CRG beamline DUBBLE (BM26A) at the ESRF with specifications described in section 4.5.2.1 in order to confirm coating growth and breakdown during electrochemical treatments. The setup and the instrumentation of the SR-XRD experiments on DUBBLE using the equipment described in section 4.5.3. In what follows, we describe the electrochemical / environmental cell (eCell) and the sample holder.

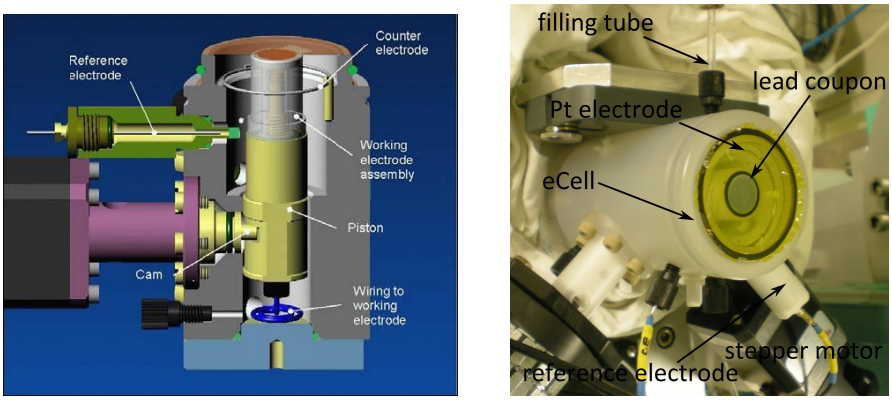


Figure. 13.1 – (a) Cross section of the eCell (b) A view of the experimental set-up at station BM26A

For the experiments, an eCell Mk IV was used, shown in Figure 13.1a, of which the prototype has been published in Analytical Chemistry by M. Dowsett and A. Adriaens [1]. Earlier cell designs were already proposed by Robinson et al. [2, 3]. The improved eCell is a cell consisting of a 40 mL polychlorotrifluoroethylene (PCTFE) cup, with inner and outer diameters of 30 and 44 mm, respectively, configured to take electrodes or coupons with a diameter of 12.6 mm in a holder from which they can easily be demounted from the piston (known as the working electrode holder). The piston is driven by a variable-speed motor (Portescap stepper motor type 17H218D05B, USA) in the vertical direction, using remote control from outside the X-ray hutch. This mechanism allows that the sample to be deep in the solution (in the low position) for a certain time so that the chemical processes can continue undisturbed. Afterwards, the electrode can go

to the high position to be able to take a proper X-ray image. This process is continuously repeated during the complete time of deposition. The cell is filled with a solution for a particular (electro)chemical treatment, while at the same time the metal surface is analyzed through a thin electrolyte layer using the XRD spectroscopic technique. To insert liquids in the eCell, a tube is attached, which is connected to a syringe. The syringe driven by a stepper motor allows the filling of the eCell from the control room and the detection of the first changes on the surface of the substrate.

A sequence of surface powder diffraction images was recorded through a 6 mm Kapton window (polyimide film made by Dupont) and approximately 100 μm of the electrolyte solution (should not be higher than 200 μm). Also when the electrode is too close to the 7 μm Kapton window, ensures a more difficult access of the decanoate ions for the progress of the chemical process and more impurities in the coating layer [4]. Using the window, the conditions in the environment can be adjusted depending on the experiment. The eCell allows the analysis of the lead substrate surface during the deposition of lead decanoate [5]. In Figure 13.1b, the Ag/AgCl reference and counter electrode are indicated. During the growth sequence (ca. 1 h), the sample was automatically moved between the analysis position (close to the window) and deeper (1 cm down) in the solution by the eCell control system. Data collection was synchronized with this movement: actual collection time was 5 s per image, time in between images was 35 s. For the corrosion test experiment a collection time of 10 s per image and the time between the images was 50 s. Figure 13.1b shows a view of the eCell in the experimental set-up.

13.2 Growth of a coating on lead using cyclic voltammetry

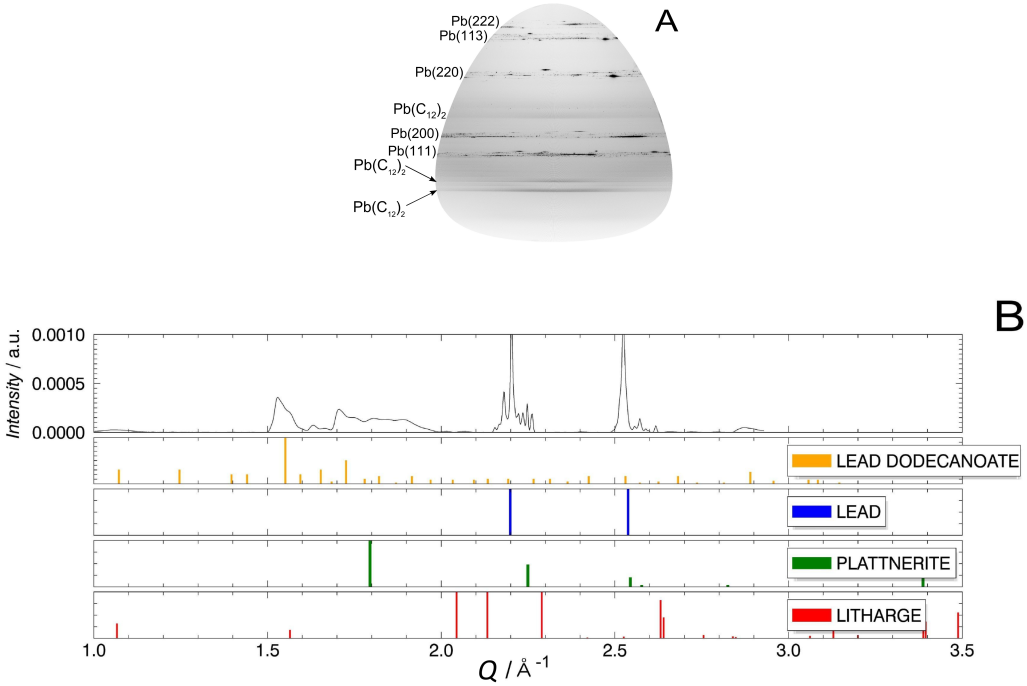


Figure. 13.2 – (A) Reprojected image of a Mar SR-XRD diffraction pattern from a lead dodecanoate coated lead coupon acquired on the DUBBLE beamline at the ESRF. The acquisition time was 10 s. (B) The XRD pattern of the lead dodecanoate coated lead sample calculated using integration.

For the growth experiment, the eCell is filled with a NaC_{12} solution as described in section 7.3.1. A lead coupon is put into the working electrode holder and immersed in the solution. Afterwards, 10 consecutive cyclic voltammetric scans are carried out in-situ between -1.3 and 1.5 V vs. SCE at a scan rate of 20 mV s^{-1} to produce the coating based on the procedure explained in chapter 7. During the electrochemical treatment, XRD spectra are taken.

Figure 13.2a shows a reprojected Mar diffractogram from a lead dodecanoate coated coupon. The acquisition time was 10 s. The two bottom rings in the images refer to Q = 1.55 Å^{-1} and 1.73 Å^{-1} from the lead dodecanoate coating (pattern reference number 00-009-0712 for lead dodecanoate in the ICDD database). The coarse polycrystallinity of the lead substrate is demonstrated by the streaky nature of the lead rings. On the other hand, the evenly spaced rings which represent the lead dodecanoate are smooth and homogeneous. This tells us that the coating is formed from small and random poly crystals [6]. The lead dodecanoate rings demonstrate the c-axis alignment of the coating from the localization of the intensity to the center of the image. By integrating the different image rows as a function of the diffraction angle θ, a one-dimensional pattern is constructed as shown in Figure 13.2b. The 1D diffraction pattern shows us clearly the diffraction peaks of the formed lead dodecanoate coating between 1.5 Å^{-1} and 2.0 Å^{-1}. The (111) and (200) lead diffraction peaks, however, form an intense narrow peak at higher Q-space values around 2.19 Å^{-1} and 2.53 Å^{-1} (pattern reference number 03-065-2873 in the PDF-2 ICDD database (2012)). Due to atmospheric corrosion and electrochemical oxidation of the lead substrate, lead(II)oxide is detected. At 2.04 Å^{-1}, a small (101) lead(II)oxide diffraction peak is detected (pattern reference number 03-065-1471 in the PDF-2 ICDD database (2012)). This is in agreement with previous findings in our research group [5, 7]. The presence of small concentrations of OH^--ions in the aqueous solution ensures the formation of PbO (litharge) [8, 9],

$$\mathrm{Pb(s) + 2OH^-(aq) \rightleftharpoons PbO(s) + H_2O + 2e^-} \qquad E_0 = -0.002 \text{ V vs. SCE} \tag{13.1}$$

In addition to the formation of lead(II)oxide, due the high oxidation potentials, lead(IV)oxide (PbO_2, plattnerite) is produced. The (110), (101) and (200) plattnerite diffraction peaks at 1.7952 Å^{-1}, 2.22 Å^{-1} and 2.54 Å^{-1} are clearly detected (pattern reference number 00-025-0447 in the PDF-2 ICDD database (2012)). The first oxidative scan to 1.5 V provides together with the presence of OH^--ions an ideal environment for the production of PbO_2 [9, 10],

$$\mathrm{PbO(s) + 2OH^-(aq) \rightleftharpoons PbO_2(s) + H_2O + 2e^-} \qquad E_0 = +0.860 \text{ V vs. SCE} \tag{13.2}$$

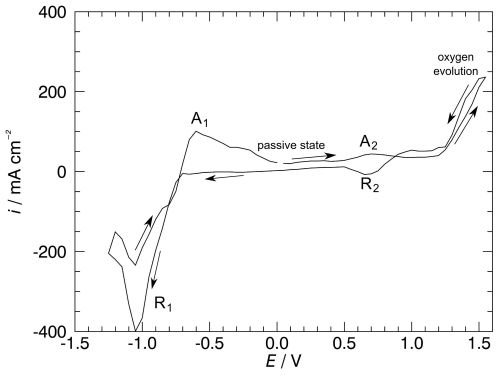


Figure. 13.3 – The first voltammetric scan of the deposition of the lead dodecanoate coating with a scan rate of 20 mVs^{-1}.

Figure 13.3 shows the first voltammetric scan of the deposition of the lead dodecanoate coating with a scan rate of 20 mV s^{-1} using the eCell system. This voltammetric scan explains the formation of all the products mentioned in Figure 13.2b. The anodic peak, A_1, is characteristic for a passivation process, because the current drops to a low value corresponding to the passive state. This process can be explained using two consecutive steps. At the start, lead dissolves and forms a soluble lead salt with dodecanoate as anion explained by a series of adsorption reactions in reactions eqs. (7.14a) to (7.14c). After that, there is a precipitation of a crystalline salt film $Pb(C_{12})_2$ (s) on the electrode surface when the solubility product of the salt is exceeded. The formation is described by the dissolution-precipitation mechanism [11]. After precipitation, as a consequence of crystallization, the film stays on top of the surface without dissolving during the cathodic process. After the third scan, only lead dodecanoate compounds present in the solution are reduced and oxidized. This oxidation process ensures the lead dodecanoate coating is formed rapidly. Above

0.5 V, the current forms a second oxidation peak, A_2, which represents the production of lead(IV)oxides. This initially formed oxidative layer is then partly reduced in two steps (R_2 and R_1) to form lead metal. Table 13.1 shows the calculation of the potential of the peaks measured in the cylic voltammogram based on the Pourbaix diagram of lead-water and the solubility product of lead dodecanoate.

peak	reaction	Ecalculation
$\mathbf{A}_1$	$Pb(s) + 2OH^-(aq) \leftrightharpoons PbO(s) + H_2O + 2e^-$	$E_{A_1} = E_{0,A_1} - 0.059$ pH
		= -0.533 V vs. SCE
$\mathbf{R}_1$	$Pb(C_{12})_2(s) + 2e^- \leftrightharpoons Pb(s) + 2C_{12}^-(aq)$	$E_{R_1} = E_{0,A_1} - 0.059$ pH $+ 0.0295 \log \frac{K_{sp}}{[C_{12}^-]^2}$
		= -0.929 V vs. SCE
		with $K_{sp}[Pb(C_{10})_2] = 8.91 \times 10^{-17}$ [12]
$\mathbf{A}_2$	$Pb^{2+}(aq) + 4OH^-(aq) \leftrightharpoons PbO_2(s) + H_2O + 2e^-$	$E_{A_2} = E_{R_2} = E_{0,A_2} - 0.059$ pH $- 0.0295 \log \frac{K_{sp}}{[C_{12}^-]^2}$
$\mathbf{R}_2$		= 0.722 V vs. SCE

Table 13.1 – Thermodynamic analysis based on the Pourbaix diagram of lead-water and the solubility product of lead dodecanoate.

Figure 13.4 shows the pattern set image of all diffraction patterns recorded during the progressive growth process of the lead dodecanoate coating on a bare lead coupon using cyclic voltammetry with a scan rate of 20 mV s^{-1} in a 0.05 mol L^{-1} aqueous NaC_{12} solution as a function of time. The total length of the experiment is 46 min. In addition, the relevant diffraction lines are indicated, obtained from the reference spectra present in the ICCD database. All diffraction peaks of the lead dodecanoate coating clearly increase during the cyclic voltammetric measurement up to a maximum intensity due to complete coverage of the lead substrate surface. The reduction of the surface during the reverse scan in the cyclic voltammetric procedure stimulates the formation of metallic lead, which allows the intensity of the lead diffraction peaks to range around a stable value. All the Q-values of the lead diffraction peaks seem to be shifted to a more positive value (+ 0.08 $Å^{-1}$). A possible explanation is the strain in the upper lead crystal structure due to the fast oxidation processes. The diffraction peaks of the lead(IV)oxide show an increase after the start of the time lapse measurement, but stabilize very quickly to a maximum value.

Figure 13.5 shows the peak areas extracted from the diffraction patterns of the change in surface composition in real time using 10 consecutive cyclic voltammetric scans with a potential range from -1.3 V to 1.5 V and a scan rate of 20 mV s^{-1}. Figure 13.5a shows the peak area of the lead dodecanoate peaks at 1.55 $Å^{-1}$, 1.72 $Å^{-1}$ and 2.89 $Å^{-1}$ extracted from a stack of recorded two-dimensional SR-XRD patterns. The observed growth in peak area of all three curves is due to the progressive formation of the lead dodecanoate coating during the different voltammetric scans. The experimental graphs for all peak areas calculated at three different Q-space values are fitted to an exponential growth curve based on the following equation,

$$I = I_m(1 - e^{-\frac{t}{\tau}}), \tag{13.3}$$

with τ is the time constant and I_m is the intensity for $t \to \infty$. The fitted values are presented in Table 13.2. The fitted time constant τ, in seconds, gives some idea as to the relative speed of the lead dodecanoate coating growth. The low time constant given by the exponential fit of the peak area of the diffraction peak at 1.55 $Å^{-1}$, indicates a fast growth of this peak due the growth of the lead dodecanoate layer. After 10 consecutive cycles, a steady state value is measured,

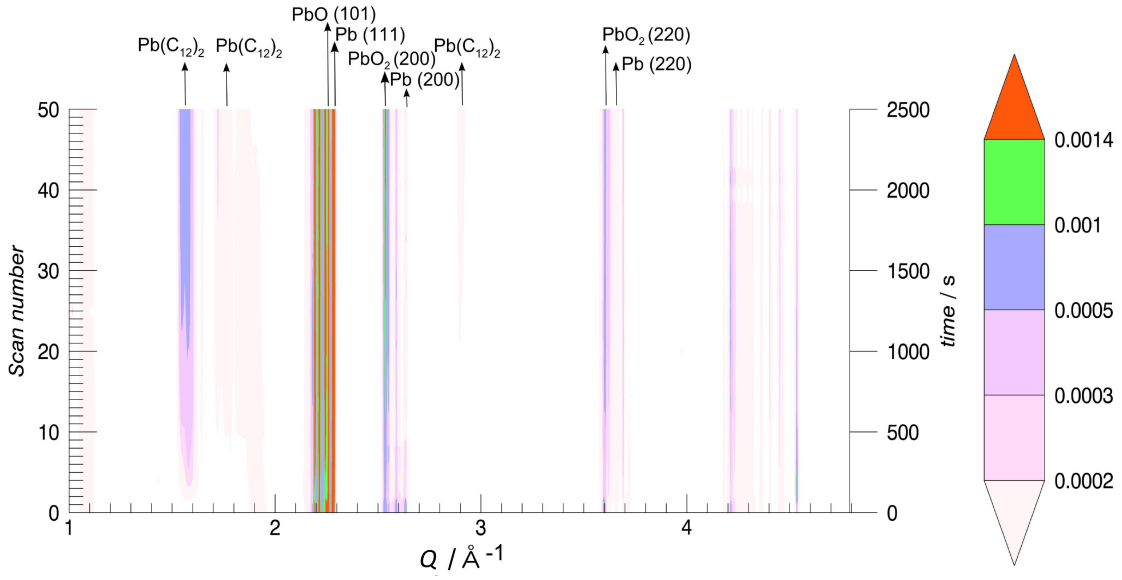


Figure. 13.4 – A pattern set image of all diffraction patterns recorded during the growth process of the lead dodecanoate coating on a bare lead coupon using cyclic voltammetry with a scan rate of 20 mV s^{-1} in a 0.05 M aqueous sodium dodecanoate solution (as a function of time).

because of the saturation of all binding sites on the lead substrate.

Figure 13.5b shows the small change of the (101) peak area of lead(II)oxide over time. The lead(II)oxide growth results from the direct contact of the lead surface with the NaC_{12} solution. For the fitting of the lead(II)oxide signal, however, the fact of a native oxide layer due to atmospheric corrosion should be taken into account using the following equation,

$$I = I_0 + I_m(1 - e^{-\frac{t}{\tau}}), \tag{13.4}$$

with I_0 the peak area of the diffraction peak at the start of the exponential growth. The diffraction peak of lead(II)oxide keeps growing very slowly, which is due to the oxidative treatment and the presence of OH^--ions in the NaC_{12} inhibitor solution as described in reaction 13.1. In Figure 13.5b, the peak area of the diffraction peak of lead(II)oxide seems to change continuously, which can be explained by the quick change of oxidation and reduction processes (due to the CV procedure) taking place at the lead surface.

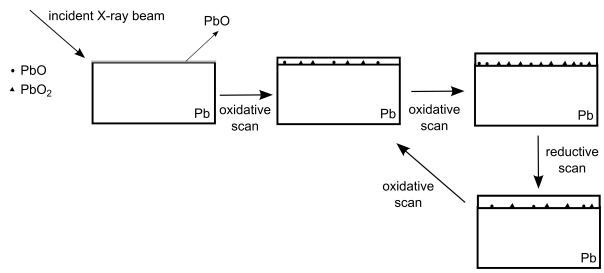


Figure. 13.6 – A hypothetical scheme for growth of the lead dodecanoate coating on a bare lead sample.

Figure 13.5c shows the area of the (110) and (200) plattnerite diffraction peaks at 1.79 $Å^{-1}$ and 2.54 $Å^{-1}$. The lead(IV)oxide growth results from the direct contact with OH^--ions in the inhibitor solution and the presence of a lead(II)oxide corrosion layer as described in reaction 13.2. The most sensitive diffraction peak at 2.5398 $Å^{-1}$ shows small fluctuations in the calculated peak area, which are related to the alternating oxidation and reduction process due to the cyclic voltammetric deposition procedure (see second x-axis representing the number of CV cycles). At the start, lead(IV)oxide grows very

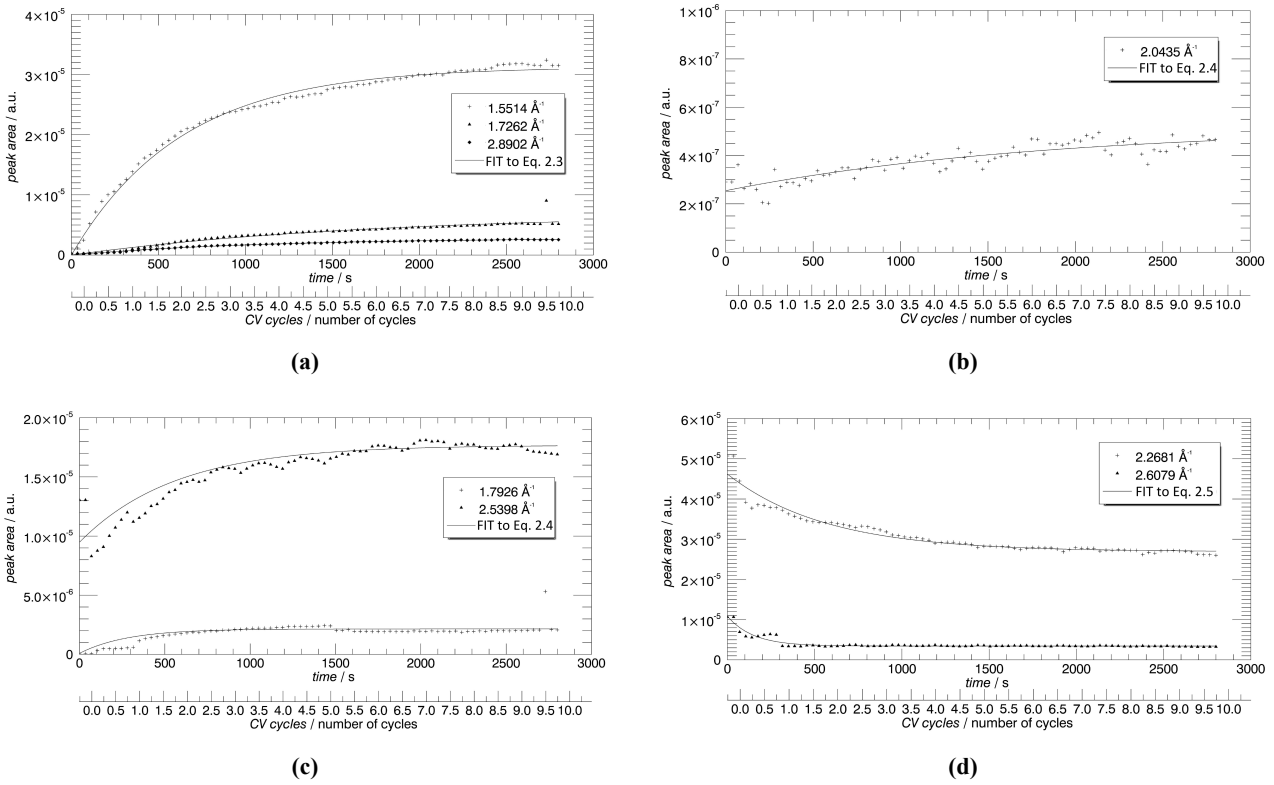


Figure. 13.5 – The peak areas extracted from the diffraction patterns of the growth of the lead dodecanoate coating in real time using 10 consecutive cyclic voltammetric scans with a range from -1.3 V to 1.5 V and a scan rate of 20 mV s^{-1}. The peak areas were extracted from (a) lead dodecanoate at 1.55 $Å^{-1}$, 1.73 $Å^{-1}$ and 2.89 $Å^{-1}$, (b) litharge at 2.04 $Å^{-1}$, (c) plattnerite at 1.80 $Å^{-1}$ and 2.54 $Å^{-1}$ and (d) lead at 2.27 $Å^{-1}$ and 2.61 $Å^{-1}$ (taking into account the 0.08 shift of the peaks).

fast due to the high vertex potential (1.5 V). The peak area reaches a maximum due to saturation of the surface.

Figure 13.5d shows the peak area of the (111) and (200) lead peaks at 2.27 $Å^{-1}$ and 2.61 $Å^{-1}$ (taking into account the 0.08 shift of the peaks) extracted from the consecutive diffraction patterns. The observed decrease in peak area is due to surface coverage by the lead dodecanoate coating or by some corrosion products, which reduces the interaction of X-rays with the lead bulk metal. The formation of this coating layer reduces the peak area of the lead diffraction peaks. This information proves that a layer is continuously covering the lead surface of the substrate. The intensity of the lead characteristic peaks drops rapidly at the starting point and stagnates after the first two scans, which demonstrates the formation of a lead dodecanoate coating layer during the first voltammetric scan. An explanation of the changing of the peak shapes could be the reorientation of the lead crystals. The exponential fit of the lead peak is given by

$$I = I_0 + I_{\mathrm{m}} \mathrm{e}^{-\frac{t}{\tau}}, \tag{13.5}$$

The small oscillations in the calculated peak area of the peak at 2.27 $Å^{-1}$ are related to the alternating oxidative and reductive process due to the cyclic voltammetric deposition procedure. All above-mentioned products have been identified using XPS, as reported in a previous communication of our group [13]. Furthermore, a hypothetical scheme is drafted in Figure 13.6 for the lead dodecanoate growth on a lead sample. This hypothetical scheme shows the atmospheric corrosion of the bare substrate forming an initial lead monoxide layer. The first oxidative scan in the inhibitor solution produces a lead dodecanoate coating on the lead substrate together with the formation of lead(II)oxide and lead(IV)oxide.

	Q / Å^{-1}	I_m / a.u.	τ / s	I_0 / a.u.
$Pb(CH_3(CH_2)_{10}COO)_2$	1.5514	$3.13 \times 10^{-5} \pm 0.5\%$	$630 \pm 2.5\%$	
	1.7262	$6.9 \times 10^{-6} \pm 6\%$	$1700 \pm 15\%$	
	2.8902	$2.83 \times 10^{-6} \pm 0.9\%$	$1110 \pm 2.9\%$	
PbO	2.0435	$2.6 \times 10^{-7} \pm 13.9\%$	$1800 \pm 45\%$	$2.5 \times 10^{-7} \pm 4.9\%$
PbO_2	1.7926	$2.0 \times 10^{-6} \pm 12.9\%$	$390 \pm 21.7\%$	$8.9 \times 10^{-8} \pm 10.5\%$
	2.5398	$8.2 \times 10^{-6} \pm 2.0\%$	$780 \pm 4.7\%$	$9.5 \times 10^{-6} \pm 2.0\%$
Pb	2.2681	$1.93 \times 10^{-5} \pm 3.1\%$	$570 \pm 9.2\%$	$2.69 \times 10^{-5} \pm 1.0\%$
	2.6079	$8.7 \times 10^{-6} \pm 3.8\%$	$220 \pm 7.4\%$	$1.90 \times 10^{-6} \pm 2.8\%$

Table 13.2 – List of the values of the exponential fit of the growth process of the lead dodecanoate coating using cyclic voltammetry with a scan rate of 20 mV s^{-1}.

During the reductive scan, these lead oxides are reduced to form lead metal. The consecutive cyclic voltammetry scans ensure the formation of a thicker lead dodecanoate coating up to surface saturation.

Using the decay of the peak area of the most intense (111) lead peak, we can calculate the lead dodecanoate coating thickness. Consider we have a coating of thickness d on the lead substrate surface, the incoming X-ray beam will be attenuated on its way through the surface, and then the fraction scattered into the peak will be attenuated some more on the way out. The total attenuation of the lead peak will therefore depend on the total path length on the coating as a function of time following the Beer-Lambert law [14],

$$\ln\left(\frac{A_k(t)}{A_0}\right) = -\left(\frac{\mu}{\rho}\right) d(t), \tag{13.6}$$

where $A_k\ (t)$ is the peak area of the lead (111) peak at immersion time k (time dependent), A_0 is the peak area of the lead peak for no attenuation, $d(t)$ is the mean mass thickness (mass per unit area or g cm^{-2}) of the lead dodecanoate layer and $\frac{\mu}{\rho}$ is the mean mass attenuation coefficient for the lead dodecanoate layer at 8 keV (= 122.3 cm^2 g^{-1} [15]). This quantification gives us information on the thickness of the lead dodecanoate layer by simply dividing the mass thickness results by the density of lead acetate (comparable for lead dodecanoate), 3.25 g cm^{-3}.

This total path length is written as a function of the thickness of the coating. If we consider a X-ray beam incident at θ_i to the surface and scattered at $2\theta_s$ into the diffraction peak, the length of the inward path will be $\frac{d}{\sin(\theta_i)}$ and the length of the outgoing path $\frac{d}{\sin(2\theta_s - \theta_i)}$. The total path length t will therefore be [14],

$$t = d\left[\frac{1}{\sin(\theta_i)} + \frac{1}{\sin(2\theta_s - \theta_i)}\right]. \tag{13.7}$$

To calculate the thickness d from the total path length, the equation is rewritten as follows

$$d = t\left[\frac{\sin(\theta_i)\cdot\sin(2\theta_s - \theta_i)}{\sin(\theta_i) + \sin(2\theta_s - \theta_i)}\right], \tag{13.8}$$

where θ_i is the incident angle (= 10°) and $2\theta_s$ is the two-theta angle for the Pb (111) peak.

Figure 13.7 shows the calculated thickness of the lead dodecanoate coating as a function of immersion time. The error lines are based on the fitting error on the measured peak areas of the lead (111) peak. After 1 h, the thickness of the lead dodecanoate layer is around 1.5 μm. The fast deposition is related to the fast oxidation of the lead metal in the solution due to the use of cyclic voltammetry. The reduction processes in the backward scan do not allow the lead dodecanoate

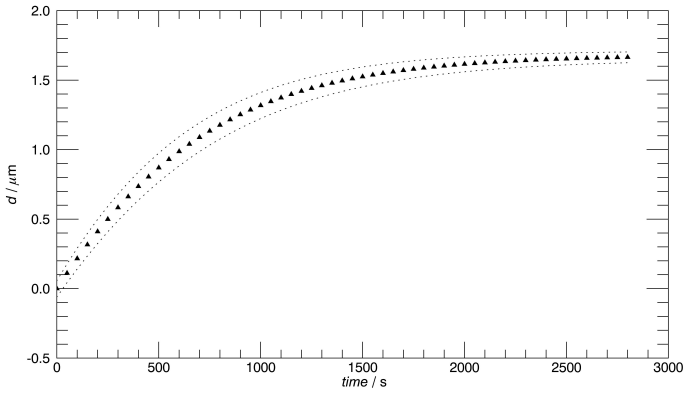


Figure. 13.7 – The calculated thickness (d) of the lead dodecanoate coating as a function of immersion time.

film to form a thick layer. As predicted by the graph in Figure 13.7, the thickness of the lead dodecanoate layer tends towards asymptotic behavior due to the passivation of the surface by the protective layer.

Table 13.2 shows statistically different time constants from the fitting implying different growth rates for the different compounds. The different τ values for the lead dodecanoate show that one peak grows faster than the other. This suggests an anisotropic growth of the lead dodecanoate crystal structure from a sodium dodecanoate aqueous solution. Probably due to the fact of the lamellar structure of the crystal, one layer is formed faster than another in the crystal [16]. Another explanation is the anisotropic formation of a lower temperature mesophase involving increased lateral disorder [17].

13.3 Corrosion test of the lead dodecanoate coated lead coupon

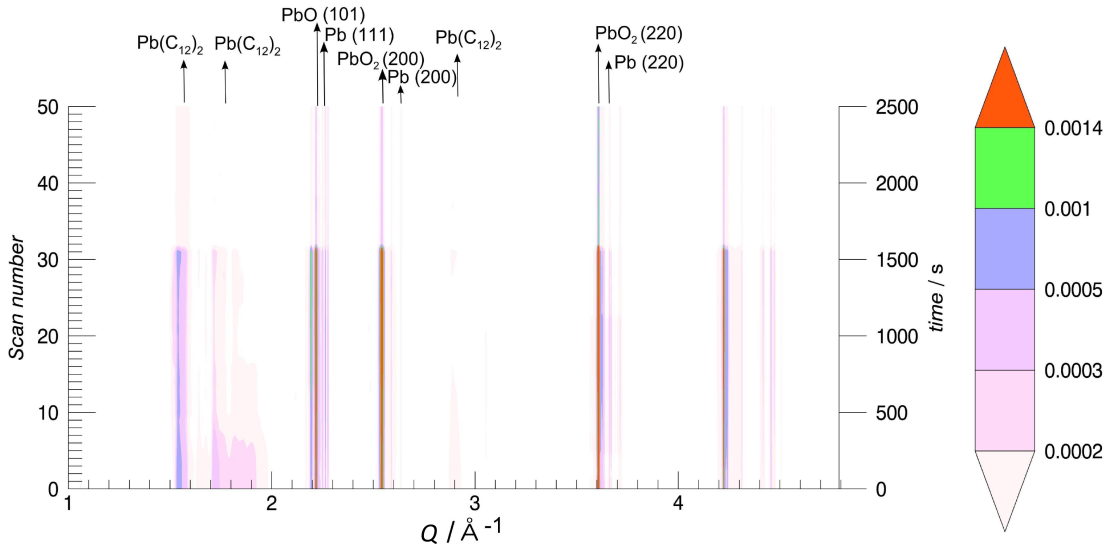


Figure. 13.8 – A pattern set image of all diffraction patterns recorded during the corrosion test process of the lead dodecanoate coated lead coupon using LSV in an acetic acid solution (as a function of time).

For the corrosion experiment, the deposited coating of the previous experiment was air-dried and put into the working electrode holder of the eCell. Then, the coated sample is corroded using LSV in a 5 mg L^{-1} acetic acid solution with a potential range from -1 V to 1.5 V and a scan rate of 1 mV s^{-1}. During the electrochemical treatment again XRD spectra are taken.

Figure 13.8 shows the pattern set images of the corrosion of the lead dodecanoate coated lead sample in real time using a

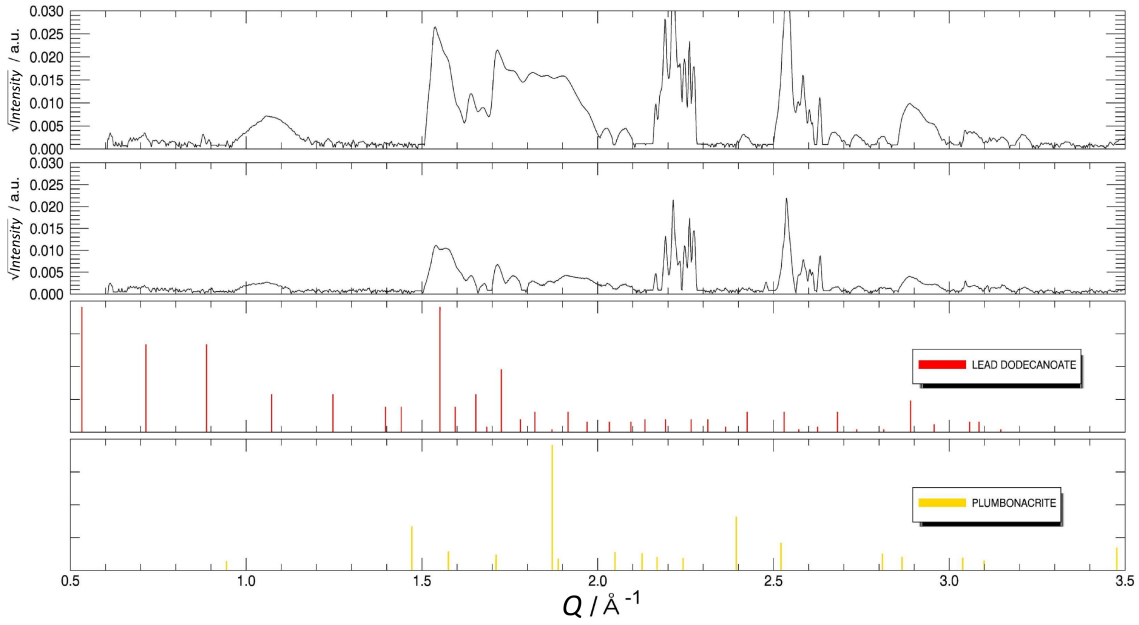


Figure. 13.9 – The first and last diffraction pattern of the corrosion test process of the lead dodecanoate using integration. The reference diffraction peaks of lead dodecanoate and plumbonacrite.

LSV scan with a potential range from -1 V to 1.5 V and a scan rate of 1 mV s^{-1} in an acetic acid solution. The total length of the experiment is 41 min. The image shows the relevant *Q*-space values, obtained from the reference spectra present in the ICCD database, of the most important corrosion products. The initial coated sample shows diffraction lines between a q-value of 1 and 2 $Å^{-1}$. These peaks originate from the well-ordered lamellar lead dodecanoate crystals as described by Lacoutre et al. [18]. Drying the sample in air ensures that the formed complexes reorganize and form less distorted lamellar crystal structures. Figure 13.9 shows that the most important corrosion product is a lead carbonate compound (plumbonacrite). Due to presence of CO_2 in the ambient air during drying, hydrogen carbonate is formed in the aqueous solution, which reacts with the PbO at the surface to form carbonates following the reactions eqs. (2.6a) and (2.7).

Figure 13.10 shows the peak areas extracted from the corrosion of the lead dodecanoate coated lead sample in real time using a LSV scan with a potential range from -1 V to 1.5 V and a scan rate of 1 mV s^{-1} in an acetic acid solution. This figure shows that next to the lead dodecanoate coating and plumbonacrite, lead(II)oxide and lead(IV)oxide are present due to the high oxidation potential during deposition. During the cathodic polarization (up to -0.5 V), Figure 13.10a-b shows that the lead dodecanoate complexes and lead(II)oxide corrosion products are reduced to form metallic lead. Figure 13.10c clearly shows that the lead(IV)oxide is reduced at a higher rate. The cathodic current ensures a big loss of lead corrosion products, but does not destroy the deposited lead dodecanoate coating. Due to these reduction reactions, metallic lead is formed as seen in Figure 13.10d extracted from the (200) lead diffraction peak at 2.5376 $Å^{-1}$.

After -0.5 V, the anodic polarization starts. It is noticeable that peak areas of all compounds shown in Figure 13.10 stagnate from -0.5 V to 0.5 V. This is explained by supposing a protective region (and corrosion inhibition) for the lead dodecanoate coating present on the lead sample. In this region, no corrosion takes place due to the fact that no extra crystalline corrosion products are being formed. The SR-XRD patterns recorded at these potentials do not change as a function of time.

Around the potential of 0.5 V, major changes occur on top of the coated lead sample. A sudden drop in the peak area of the lead dodecanoate diffraction peaks explains the cracking and destruction of the lead dodecanoate coating so that the acetic acid starts to attack the lead sample as seen in Figure 13.10a. This implies that a small amount of acetic acid in

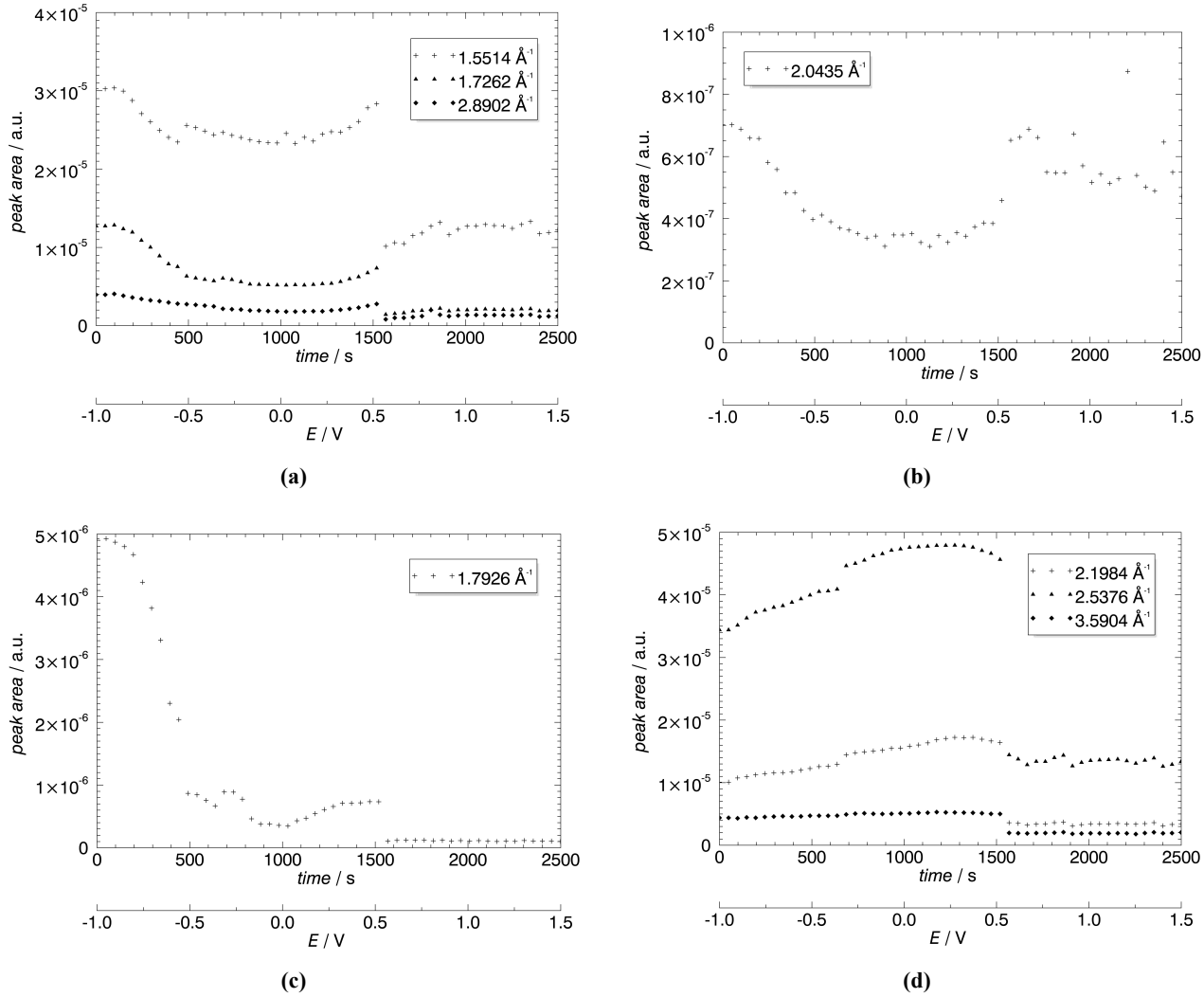


Figure. 13.10 – The peak areas extracted from the diffraction patterns of the corrosion test of the lead dodecanoate coated lead sample in real time using a LSV scan with a range from -1 V to 1.5 V and a scan rate of 1 mV s^{-1}: (a) lead dodecanoate at 1.5514 $Å^{-1}$, 1.7262 $Å^{-1}$ and 2.8902 $Å^{-1}$, (b) litharge at 2.0435 $Å^{-1}$, (c) plattnerite at 1.7926 $Å^{-1}$ and (d) lead at 2.1984 $Å^{-1}$, 2.5376 $Å^{-1}$ and 3.5904 $Å^{-1}$.

the aqueous solution attacks and decomposes the hydrophobic lead dodecanoate crystal layer due to its acidic character. The presence of acetic acid ensures the start of a very fast 'active' corrosion process forming new lead acetate complexes starting with the acidification of the surface resulting in lead(II)oxide dissolution [19].

Figure 13.10b shows that higher potentials induce the production of lead(II)oxide. Due to the reaction with acetic acid, these water soluble lead acetate complexes will associate with these formed lead(II)oxides present on the surface as in described in reaction 2.11. The formed water insoluble lead acetate oxide hydrate cannot be identified due to the fact that the range of our measurements did not extend to 0 - 0.5 $Å^{-1}$. The main lead acetate peak appears around 0.3 $Å^{-1}$. The formation of lead(IV)species, however, is unlikely at these lower oxidative potentials and without the presence of basic hydroxide species (see Figure 13.10c). Figure 13.10d shows that the peak area of the diffraction peak of lead drops suddenly together with the accumulation of corrosion products on the lead surface. Next to the production of lead hydroxy carbonates and lead acetate oxide hydrate, the formation of dodecanoic acid on the surface explains the decrease of the lead peak area. Acids attack the hydrophobic lead dodecanoate coating re-converting the lead complexes into lead ions and dodecanoic acid [20],

$$Pb(C_{12})_2 + 2H^{2+} \rightleftharpoons Pb^{2+} + 2HC_{12}. \tag{13.9}$$

The formation of dodecanoic acid could not be confirmed using XRD, as it is not a crystalline compound (could be verified using Raman spectroscopy) under these circumstances. In any case, the scattering from the hydrocarbon chain is very weak in comparison with that from the lead planes in the lead dodecanoate. One must keep in mind that this corrosion process is enormously accelerated when using LSV. Real time corrosion processes would proceed much more slowly. Furthermore, a hypothetical scheme is drafted in Figure 13.11 for the corrosion test measurement of a lead dodecanoate coated lead sample based on the SR-XRD patterns.

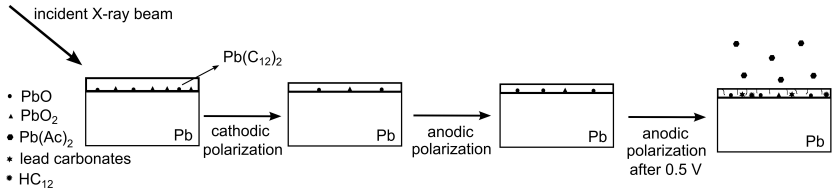


Figure. 13.11 – A hypothetical scheme for the progress of the corrosion test measurement of a lead dodecanoate coated lead sample based on the recorded SR-XRD patterns.

To be able to compare a reference on the acetic acid corrosion on lead, the same corrosion test procedure was applied on a bare lead coupon during 41 min. During the measurement, the only visible diffraction peaks are the ones of the bare lead substrate. Afterwards, the coupon was dried in air and a diffraction pattern was recorded as seen in Figure 13.12. Most of the formed lead corrosion products are soluble in the acidic water making it impossible to detect them during the in-situ growth [21]. First of all, the (111) and (200) lead diffraction lines form intense narrow peaks. Close to the lead diffraction lines, the (110), (101) and (200) plattnerite diffraction peaks are detected. The low intensity peaks between q-space values of 1 - 1.5 $Å^{-1}$ evidence the presence of a lead carboxylate complex. The presence of acetic acid in the corrosive solution results in the formation of insoluble lead acetate oxide hydrate using reaction 2.11. The lead acetate complexes can be converted to lead hydroxy carbonates following reactions eqs. (2.6a) and (2.6b). The formation of lead hydroxy carbonates is confirmed by the presence of the (115) plumbonacrite diffraction peak. Compared to the protected sample, the bare sample starts to corrode at lower potentials, which explains the higher relative intensities of these diffraction peaks associated with the active acetic acid corrosion. The lower relative intensities of the diffraction peaks predict a protective behavior of the lead dodecanoate coating on the lead samples.

As mentioned previously in section 12.2.7.4, only the corrosion process of acetic acid in air is interesting from a conservationist's point of view. The inhibition of the corrosion process depends on the corrosive species, the substrate, the presence of water, the environment, but also and most importantly on the nature of the inhibitor. In some cases, specific inhibitors are used for vapor phase corrosion [22]. An interesting example is the use of benzotriazole for the protection of copper antiques which is effective as a vapor phase inhibitor, an ingredient in lacquers and a complex compound on the surface [23]. The lead carboxylate coating provides protection when the acetic acid is diluted, but also when vapor phase acetic acid is present in the atmospheric air. In order to understand to what extent the protective behavior is different in both cases more research is needed using in-situ vapor phase experiments combined with XRD analysis as proposed by [14, 24].

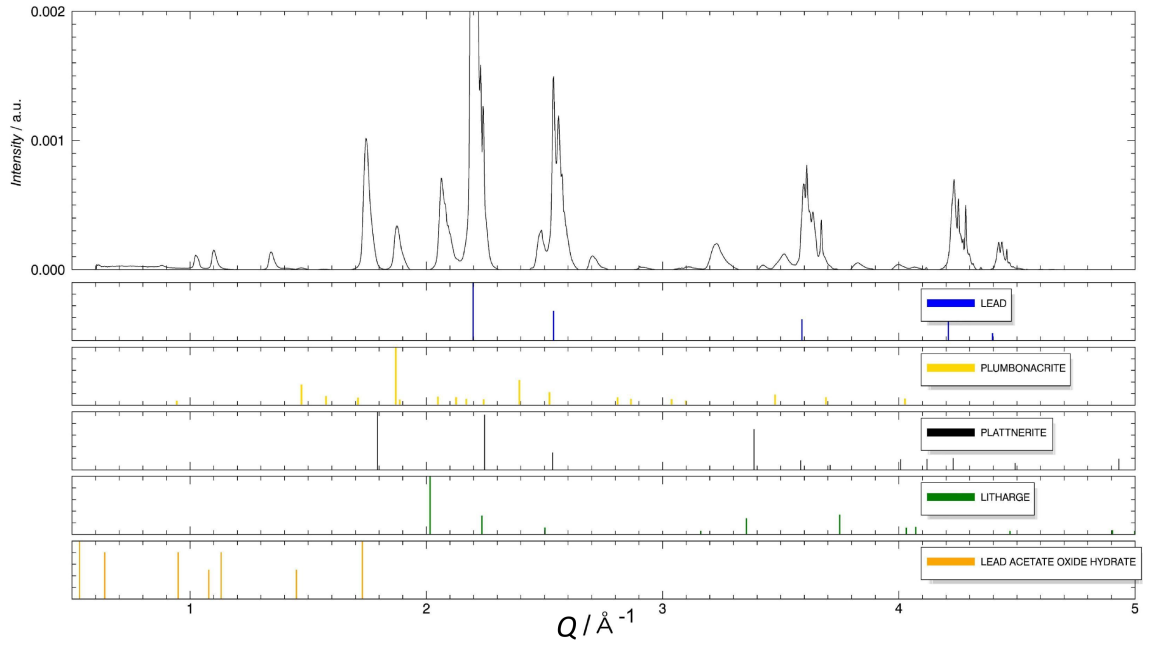


Figure. 13.12 – The last pattern of the corrosion test procedure applied on a bare polished lead coupon.

13.4 Summary and conclusions

In-situ spectroelectrochemical measurements have demonstrated that a crystalline lead dodecanoate coating immediately forms at the start of the experiment using cyclic voltammetry. Later on, during the drying process the formed complexes reorganize and lead hydroxy carbonates are formed. In addition to the lead dodecanoate coating, small quantities of other lead corrosion products are detected, which are explained by the oxidation of the surface and atmospheric corrosion. During the reductive scan, these lead corrosion products are reduced to form lead metal. The consecutive cyclic voltammetry scans ensure the formation of a lead dodecanoate coating up to the saturation of the surface. The fast and thin layer deposition, however, is related to the oxidation of the lead metal using cyclic voltammetry. The reduction processes do not allow the lead dodecanoate film to form a thick layer.

An accelerated 'active' corrosion test in acetic acid has been conducted on a bare and a lead dodecanoate coated lead coupon. In both cases, lead acetate oxide hydrate is formed due to the formation of lead oxides and lead acetates in the aqueous corrosive acetic acid solution. The bare sample formed much more corrosion products compared to the coated sample, which indicates the inhibitive properties of the coating.

Not only is the electrochemical coating method in an aqueous solvent quick and inexpensive (the materials are all cheap substances mass produced for industrial applications), but the deposited layers of lead dodecanoate are considerably hydrophobic and therefore potentially more protective. The method may be extended to using cotton drenched or a spray can filled with the inhibitor solution to apply the lead dodecanoate coating, increasing the range of possible applications in archeaometry and conservation.

References for Chapter 13

[1] M. DOWSETT and A. ADRIAENS, Cell for simultaneous synchrotron radiation X-ray and electrochemical corrosion measurements on cultural heritage metals and other materials, *Anal. Chem.* **78** (10) (2006), 3360–3365.

[2] M. FLEISCHMANN, A. OLIVER, and J. ROBINSON, In Situ X-ray diffraction studies of electrode solution interfaces, *Electrochim. Acta* **31** (8) (1986), 899–906.

[3] J. ROBINSON, In situ synchrotron radiation X-ray techniques for studies of corrosion and protection, *Corros. Sci.* **35** (1993), 791–800.

[4] M. HAND et al., A new method for coating heritage lead observed in real-time using synchrotron techniques, in: *Diamond Synchrotron User Meeting 2010*, 2010, 1.

[5] M. DOWSETT et al., In-situ spectroelectrochemical study of the growth process of a lead decanoate coating as corrosion inhibitor for lead surfaces, *Surf. Interface Anal.* **41** (7) (2009), 565–572.

[6] A. ADRIAENS, *Corrosie*, Leuven: Acco, 2008.

[7] M. DOWSETT et al., Real time spectroelectrochemical growth and corrosion resistance monitoring of lead carboxylate coatings in an environmental cell (eCell), *Metal 07* **3** (2007), 26–31.

[8] C. LEYGRAF and T. GRAEDEL, *Atmospheric corrosion*, 1st, New York: Wiley, 2000.

[9] P. DELAHAY, M. POURBAIX, and P. VAN RYSSELBERGHE, Potential-pH diagram of lead and its applications to the study of lead corrosion and to the lead storage battery, *J. Electrochem. Soc.* **98** (2) (1951), 57–64.

[10] P. RÜETSCHI and B. CAHAN, Anodic corrosion and hydrogen and oxygen overvoltage on lead and lead antimony alloys, *J. Electrochem. Soc.* **104** (7) (1957), 406–413.

[11] K. DE WAEL et al., Electrochemical deposition of dodecanoate on lead in view of an environmentally safe corrosion inhibition, *J. Solid State Electrochem.* **14** (3) (2010), 407–413.

[12] S. MAUCHAUFFÉE and E. MEUX, Use of sodium decanoate for selective precipitation of metals contained in industrial wastewater, *Chemosphere* **69** (5) (2007), 763–768.

[13] M. DE KEERSMAECKER et al., Electrochemical and surface study of neutralized dodecanoic acid on a lead substrate, *J. Electrochem. Soc.* **161** (3) (2014), C126–C137.

[14] R. GRAYBURN et al., Time-lapse synchrotron X-ray diffraction to monitor conservation coatings for heritage lead in atmospheres polluted with oak-emitted volatile organic compounds, *Corros. Sci.* **82** (2014), 280–289.

[15] C. CHANTLER et al., *X-ray form factor, attenuation and scattering tables, detailed tabulation of atomic form factors, photoelectric absorption and scattering cross section, and mass attenuation coefficients for Z = 1 - 92 from E = 1 - 10 eV to E = 0.4 - 1.0 MeV*, NIST, Physical Measurement Laboratory, U.S. Department of Commerce, 2001.

[16] T. HASHIMOTO and N. SAKAMOTO, Nucleation and anisotropic growth of lamellar microdomains in block copolymers, *Macromolecules* **28** (13) (1995), 4779–4781.

[17] A. AMORIM DA COSTA et al., Mesophase formation in lead(II) decanoate, *Liq. Cryst.* **1** (3) (1986), 215–226.

[18] F. LACOUTRE et al., Anhydrous lead(II)heptanoate, *Acta Crystallogr. C* **57** (5) (2001), 530–531.

[19] S. GOBOM, On the complex formation of Sn(II) and Pb(II) with acetate ions, PhD thesis, Göteborg University, 1977.

[20] E. ROCCA, C. RAPIN, and F. MIRAMBET, Inhibition treatment of the corrosion of lead artefacts in atmospheric conditions and by acetic acid vapor: use of sodium decanoate, *Corros. Sci.* **46** (3) (2004), 653–665.

[21] R. LIETH, *The influence of relative humidity and temperature on the acetic acid vapor induced atmospheric corrosion of lead*, Reidel Publishing Company, 1977, 263.

[22] A. SUBRAMANIAN et al., An overview: Vapor phase corrosion inhibitors, *Corros.* **56** (2) (2000), 144–155.

[23] R. WALKER, Benzotriazole a corrosion inhibitor for antiques, *J. Chem. Educ.* **57** (11) (1980), 789–791.

[24] V. FLEXER et al., A new strategy for corrosion inhibition coatings for lead heritage metal objects, *Electrochim. Acta* (2015).

PART IV

POLYMER COATINGS

14

Hydrogenated dimer acids as a coating for lead substrates

Reproduced from J. Electrochem. Soc., 162 (4), M. De Keersmaecker, O. van den Berg, K. Verbeken, D. Depla and A. Adriaens, Hydrogenated dimer acid as a corrosion inhibitor for lead metal substrates in acetic acid, C167-C179, 2015, with permission of The Electrochemical Society.

14.1 Experimental

14.1.1 Oligomer analysis

The mixture of different carboxylic acids was first analyzed by ^{1}H NMR (300 MHz, $CDCl_3$) on an Avance 300 spectrometer (Bruker, Germany). The mixture was characterized by signals appearing at 0.75 ppm (m, 1H, -CH_3), 1.2 ppm (m, cyclic and backbone -CH_2-), 1.6 ppm (m, 2H, -CH_2 - CH_2 - COOH) and 2.3 ppm (t, 2H, -CH_2 - COOH). Thermogravimetric analysis (TGA) was performed with a TGA/SDTA851e instrument (Mettler-Toledo, USA) under nitrogen at a heating rate of 10°C min^{-1} from 25 to 800°C. Differential scanning calorimetry (DSC) was performed with a DSC 7 (Perkin Elmer, USA) under nitrogen at a heating rate of 10°C min^{-1} starting from -50°C to near the onset temperature. Earlier studies have shown that a heating rate of 10°C min^{-1} can yield good information about the thermal behavior of fatty acids [1–3].

14.1.2 Neutralization of the hydrogenated dimer acid

The carboxylic acid functional groups of the hydrogenated commercially available dimer acid (98%, Sigma Aldrich, USA) were neutralized using one equivalent of dimer acid (DA), two equivalents of NaOH (> 97%, Merck, USA) and seven equivalents of ethanol (> 99%, VWR, USA). To ensure a high reaction yield, a 1 M NaOH solution was used. The solution was heated to temperatures between 85 and 95°C for 30 min. To separate the solvent, a saturated NaCl solution was added to allow the solid soap to be filtered off. This separation method avoided the presence of hydroxide ions in the solution, which would have formed lead corrosion products on the lead substrate. After filtration, the hard sodium soap, NaDA, was air-dried. The amount of neutralized COOH functional groups was calculated to be 0.0027 mol COONa g^{-1}.

14.1.3 Inhibitor solutions

A 10 g L^{-1} inhibitor solution was prepared by dispersing DA (1.000 g) in absolute ethanol (100 mL). The solution was stirred for 30 min to allow complete dissolution. The corresponding 10 g L^{-1} inhibitor solution of the completely neutralized acid was prepared by dispersing NaDA (1.000 g) in deionized water (100 mL). Neutralizing the acid ensured its good solubility in water. To accelerate the dissolution, the inhibitor solution was heated to 45 - 50°C and stirred for 30 min. The pH of the solution after stirring and dissolution had an average value around 9.

14.1.4 Electrochemical procedure

Electrochemical experiments were performed using a three-electrode system in a 250 mL glass cell. The set-up consisted of a saturated calomel reference electrode (SCE) containing two compartments (Radiometer Analytical, France), a counter platinum mesh and a lead working electrode. The working electrodes were lead coupons 12.6 min diameter (99.99%, Goodfellow, UK), which were designed to fit in a special holder for the electrochemical measurements. The exposed surface area of the lead coupons in the holder was 1 cm^2. All fitted impedance and current values were corrected and normalized related to the surface. The coupons were pre-treated using the procedure described in section 4.2.

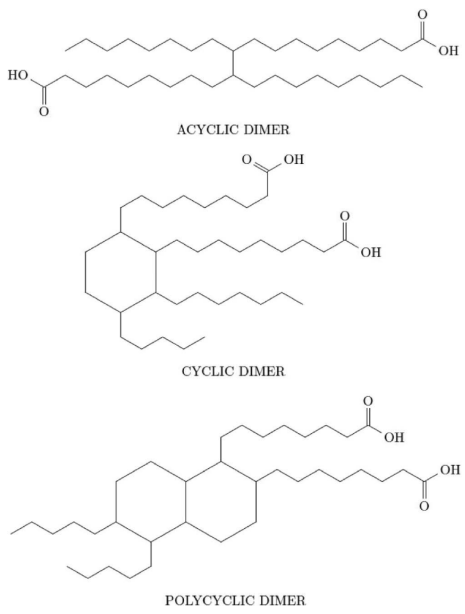


Figure. 14.1 – Representative Lewis structures of fatty acid dimer mixture. Many geometric isomers of these structures are also present in the mixture.

The corrosion resistance of the bare and coated samples was analyzed through EIS measurements in a corrosive solution containing 5 $upmu$g L^{-1} acetic acid at the corrosion potential, E_{corr}, over a distributed frequency range of 100 kHz - 50 mHz, with a 10 mV amplitude sinusoidal AC perturbation signal. Plots were recorded using an IM6 impedance and electrochemical measurement system controlled by the Thales software package (ZAHNER, Germany). The raw data were processed using the Z-HIT algorithm in the Thales software, before being further processed and fitted with Matlab release 13.0 (Mathworks, USA). Next to the EIS measurements, potentiodynamic polarization measurements were performed for both the bare and coated samples. First, the OCP was determined. Next, the potentiodynamic polarization curves were recorded in a potential window of −0.2 V to 1.5 V vs. the OCP value with a scan rate of 0.5 mV s^{-1} using also the IM6 system. The linear Tafel segments were extrapolated using the Thales software package.

14.1.5 Deposition techniques

The lead samples were modified through immersion. DA-treated samples were immersed in DA inhibitor solution for several days before being sintered at 80°C for 2 h. Sintering appeared to cause the dimer acid to react with the lead oxide to form a solid layer because of a hardening process. Other samples were immersed in NaDA inhibitor solution at 60°C for 6 h, 1 d or 4 d; they were then rinsed with deionized water and air-dried.

14.1.6 Surface analysis techniques

A JSM-7600F field emission scanning electron microscope (JEOL, USA) was used for scanning electron microscopy (SEM) measurements with the electron beam source operating at 20 kV. The instrument is described in section 4.4.2.7. It was used together with energy-dispersive spectroscopy (EDS) using an X-MAX^N (OXFORD instruments, UK) silicon drift detector controlled by AZTEC software (OXFORD instruments, UK), which was used to determine the elemental composition of the sample. For the SEM examinations, the treated lead-coated samples were coated with a very thin gold layer to avoid surface charging using a sputter coater. Attenuated total reflectance (ATR) spectra were acquired using a Spectrum 1000 FTIR Infrared spectrometer (Perkin Elmer, USA) equipped with a Spectrum 100 Series' Universal ATR

accessory, which was fitted using a diamond crystal as described in section 4.7.3. The coating of the lead substrate was measured directly by pressing the lead substrate against the ATR crystal. Spectra were recorded over a wavenumber range of 4000 – 600 cm^{-1} and averaged over 4 scans. XPS measurements were carried out for C 1s, O 1s and Pb 4f spectra based on the instrument described in section 4.6.1.

14.2 Thermal properties of DA and NaDA

The thermal stability is described by thermal parameters such as the onset temperature, T_0, of decomposition, the temperature of maximum decomposition rate, $T_{d,max}$, and the percentage of residue at 800°C, which are listed in Table 14.1. The TGA curve for NaDA shows a small endotherm around 100°C, most likely caused by solvent evaporation. Table 14.1 shows that NaDA was more thermally stable compared to DA, corroborating previous findings [4]. The principal thermal degradation occurred in two distinct steps for DA, probably due to anhydride formation, and in a single continuous step for NaDA. The thermal decomposition of DA involved the breakdown of the oxygenated hydrocarbon into volatile lower-molecular hydrocarbons, carbon dioxide, and carbon monoxide [5]. The two distinct steps resulted from the presence of different structural isomers in the DA mixture as shown in Figure 14.1. The formation of these volatile compounds explains the low residue percentage. The thermal decomposition of NaDA formed more residue because of the oxidation of metal carboxylates to metal carbonates at higher temperatures [6]. The mechanisms have been discussed in the literature [7].

	T_0 (°C)	$T_{d,max}$ (°C)	RESIDUE (%)
DA	315	450	0.5
NaDA	420	480	13.8

Table 14.1 – Onset temperature, T_0, temperature of maximum decomposition rate, $T_{d,max}$, and percentage of residue at 800°C from TGA.

A clear melting peak was found at a very low temperature interval, which is explained by the low pour point of the amorphous hydrogenated dimer acid that acts as an oily substance [8]. At room temperature, DA is a viscous amorphous liquid. NaDA showed different melting peaks around much higher temperatures. In carboxylic acid salts, the strong electrostatic forces holding the ions in the lattice are only overcome at high temperatures [9]. The temperature required for melting was measured to be around 240°C. The sample was amorphous with some crystalline structures, which is consistent with the presence of large carbon chains and different isomers. The close related melting peaks are explained by the three isomer types present in the soap sample, as seen in Figure 14.1. During cooling, the crystallization peaks are measured.

14.3 SEM-EDS analysis

Three sample fragments, one untreated and two treated using DA or NaDA inhibitor solutions, were analyzed using SEM-EDS. EDS microanalysis was performed on the same areas as captured in the SEM images. The composition was calculated by a standardless method using the AZTEC software. The SEM images and EDS maps are shown in Figure 14.2. Table 14.2 indicates the local presence of silicon and carbon because of silicon carbide and diamond particles of the polishing process. On the bare lead sample, atmospheric corrosion with atmospheric oxygen led to the formation of lead oxides (black dots on the white background of the lead metal substrate in Figure 14.2a) [10]. The oxygen signal of

LABEL	SPEC 1 (%)	SPEC 2 (%)	AVERAGE (%)	SPEC 1 (%)	SPEC 2 (%)	AVERAGE (%)
	a) bare lead metal coupon					
O	11	6	9			
Si	8	1	4			
Pb	81	93	87			
	b) lead coupon treated with DA			c) lead coupon treated with NaDA		
C	48	50	49	42	49	46
O	5	6	5	11	11	11
Si	4	2	3	3	1	2
Pb	43	43	43	44	39	42

Table 14.2 – Composition analysis of (a) bare, (b) DA-treated and (c) NaDA-treated lead coupons based on a standardless analysis of the EDS-spectra.

the EDS-map is indeed concentrated around the black spots seen in the SEM image.

In Figure 14.2b, the lead coupon treated with DA shows a complete surface layer of oxygen and carbon because of the presence of a DA coating. The coating seems to form a layer on the lead surface [11]. In Figure 14.2c, The lead coupon treated with NaDA showed the presence of lead dicarboxylate clusters as demonstrated in the C K_α spectrum. The carbon chains and the oxygen of the carboxyl functional group from the DA and NaDA inhibitor were measured in the EDS-maps [12–14]. These hydrophobic clusters protect the underlying lead substrate. Some of the oxygen measured on the sample resulted from the corrosion of the lead substrate. The total lead signal measured on the coated samples was lower than that measured on the bare lead sample because of the presence of the inhibitor compounds.

14.4 ATR-IR analysis

Figure 14.3 shows the recorded infrared spectra for three coupons. The spectra of the two coated samples (curves b and c) show important characteristic peaks compared with that of the bare lead sample (curve a). Table 14.3 shows the characteristic infrared frequencies for both coatings and the NaDA powder sample. Adsorption peaks around 2919 and 2850 cm^{-1} correspond to the antisymmetric stretch, ν_{as}, and the symmetric stretch, ν_s, of -CH_2 - in the aliphatic chains of the inhibitor [15]. Other strong absorptions were observed in the regions around 1500, 1400, and 700 cm^{-1}, corresponding to the common vibrations of the carboxyl, COO^-, group [16]. More specifically, these peaks were identified as the anti-symmetric stretching mode, the symmetric stretching mode and the scissoring bending mode, δ_s, of COO^-. Both ν_{as} and ν_s bands appear in the spectrum, which is expected for bivalent metal carboxylates [17–19]. Small peaks around 1700 cm^{-1} corresponds to the C-O stretching vibration of the carboxylic acid [20]. The absorption peak explains the presence of non-reacted carboxylic acid functional groups (see also XPS measurements). The absorption peak around 720 cm^{-1} was assigned to the rocking vibrations of the -$(CH_2)_n$- chains [21].

The direction of the wavenumber shifts of the ν_{as} (COO^-) and ν_s (COO^-) stretching bands relative to those of the free ion depends on the mode of coordination of the carboxyl group with the metal ion and its oxidation state. The four principal modes of coordination are shown in Figure 7.10 [23, 24]. Based on the separation between ν_{as} and ν_s band of COO^- described in section 7.5, we try to find the coordination mode. The low separation stretch, $\Delta\nu\ (COO^-)_{complex}$ = 114.1 cm^{-1} for NaDA and 118.6 cm^{-1} for DA, is an indication of chelating coordination of the carboxylate group since $\Delta\nu\ (COO^-)_{complex} \ll \Delta\nu\ (COO^-)_{sodium\ salt}$ (142.9 cm^{-1}). Zeleňák et al. [24] found that syn-syn bridging coordination

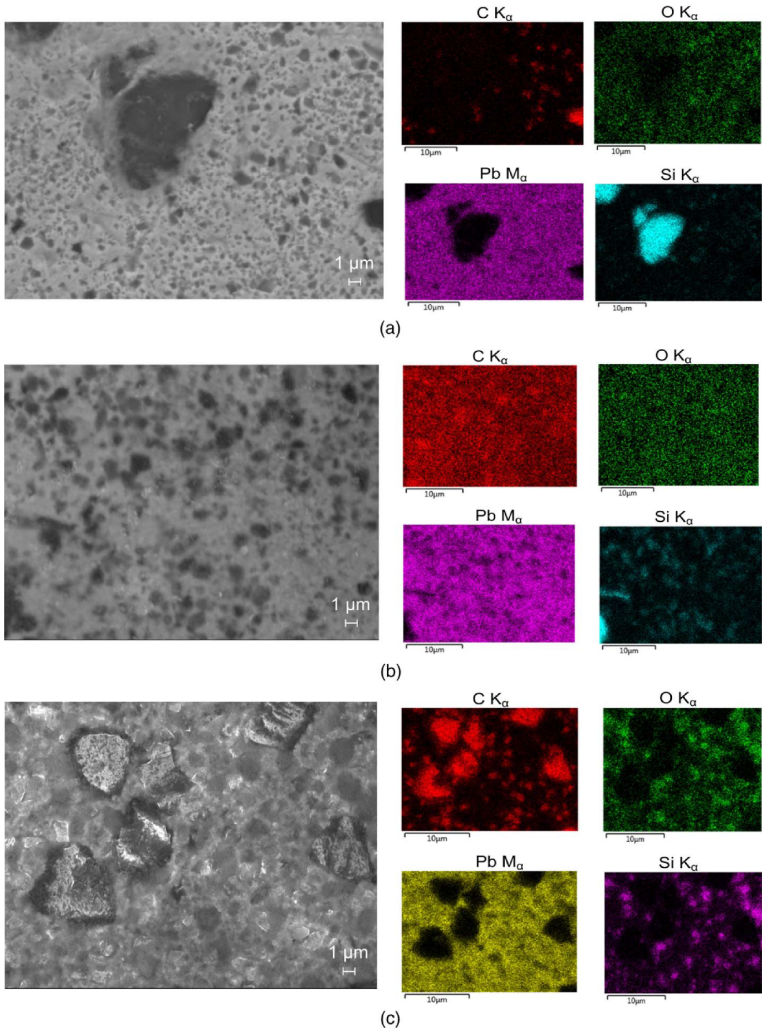


Figure. 14.2 – SEM images and EDS maps of the (a) untreated lead metal coupons and of those treated with (b) DA and (c) NaDA.

(structure III) has $\Delta\nu$ values above 150 cm^{-1}, whereas chelating bidentate (structure II) carboxylate groups normally have $\Delta\nu$ values less than 120 cm^{-1} [23]. However, the syn-anti bridging coordination (structure IV) can yield a separation around this value as well. This means that structures I and III can be ruled out because of their high $\Delta\nu$ values. In a paper of Ishioka et al. [25], the importance of the rocking frequency of the COO^- group is proposed. They found a difference in wavenumber in the rocking vibration of about 50 cm^{-1} between the two compounds (structure II and IV). The observation of an absorption peak around 470 cm^{-1} suggests a chelating bidentate structure (structure II) for both coatings (see Table 14.3). The coordination of the lead carboxylate compound is defined as an asymmetric covalent chelating bidentate bond [17], which has been seen in other lead carboxylate structures using dicarboxylic acids such as azelaic acid.

The ATR-IR spectra in Figure 14.3 are strongly correlated to the spectrum for lead(II) azelate given in literature [22]. The characteristic infrared wavenumbers for the lead(II)azelate in the 4000 – 600 cm^{-1} region seem to agree to those for both coated lead samples (see Table 14.3). Both carboxylate groups of the inhibitor are involved in the bonding with the lead metal ions at the surface of the sample in the inhibitor solution, leading to the formation of a hydrophobic polymer that has lead atoms acting as linkers. The wagging modes of the aliphatic chain show regularly spaced bands in lead(II)n-alkanoates because of the chains being in the all-trans-conformation [21, 26]. However, in this case, no regular pattern is observed, indicating that no solid crystal phase is formed because of the inhibitor's structure. From these facts, it must be concluded that because of the inhibitor's structure a more disordered solid (the all-trans carbon planes start to rotate),

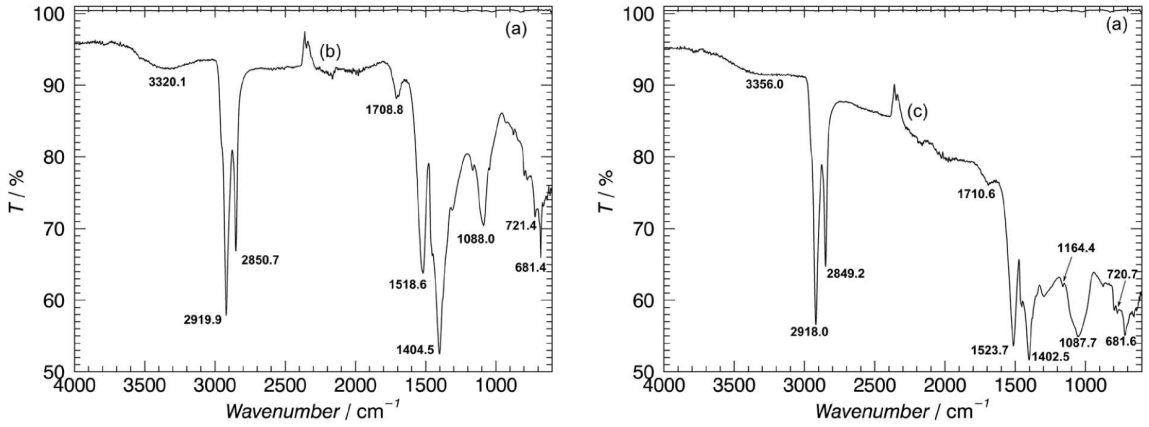


Figure. 14.3 – ATR-IR measurements of the surfaces of lead substrates treated using 10 g L^{-1} inhibitor solutions of (a) NaDA in water and (b) DA in ethanol

called the mesophase, has formed. In addition, weak bands ascribed to localized gtg (kink) sequences around 1306 cm^{-1} can be observed [27–29]. The same can be concluded for the rocking modes.

14.5 XPS analysis

Figure 14.4 shows XPS core level spectra of the C 1s, O 1s, and Pb $4f_{7/2}$ levels of (a) DA-coated lead and (b) NaDA-coated lead, with components determined by curve fitting analysis and background subtraction. All values have been corrected for aliphatic C 1s to appear at 285.0 eV. Figure 14.4a shows that the Pb $4f_{7/2}$ peak reveals two peaks with binding energies (B.E.) of 137.0 and 139.0 eV, which are associated with two different oxidation states of lead: metallic lead Pb(0) and Pb(II) products (see Table 14.4 and Refs. [30] and [31]). Curve fitting analysis of the C 1s XPS spectrum of the treated sample shows two peaks at 285.0 and 288.4 eV. The first big peak at 285.0 eV was assigned to the carbon atoms in the saturated aliphatic chains of the dicarboxylic acid [32]. The small peak at 288.5 eV was attributed to the carbon atom of the carboxylic groups of the DA [33]. No specific reference was found for the lead-dimer complex, but the B.E. values are comparable to those of lead acetate (another lead carboxylate), which has a similar structure around the lead atom of the complex [34]. The longer linear aliphatic carbon chain had indeed almost no influence on the B.E. of the Pb $4f_{7/2}$ core level electron. The aliphatic carbon/carboxylic carbon atomic ratio from the ratio of the C 1s (285.0 eV)/C 1s (288.7 eV) intensities was approximately 17. This ratio predicts that the number of carbon atoms in the aliphatic carbon chain of the proposed complex should be close to 17 for lead-dimer compounds (see Figure 14.1). To confirm the formation of a lead-dimer complex on the lead substrate, the large peak at 531.5 eV in the O 1s spectrum was assigned to the oxygen atoms of the carboxyl group [35]. The atomic ratio calculated from the XPS measurements for the lead-dimer complex was PbC_1O_3 (see Table 14.4). On average, one lead ion reacts with one carboxylic acid group from the inhibitor, which means that the precipitated acid reacts only partly with the lead metal close to the surface during heating. Therefore, sintering is essential for the production of the coating.

The Pb $4f_{7/2}$ peak for the NaDA-coated sample reveals two peaks, in Figure 14.4b, similar to those shown by the DA-coated sample in Figure 14.4a. Curve fitting analysis of the C 1s XPS spectrum of the treated sample shows two peaks at 285.0 and 288.4 eV. The aliphatic carbon/carboxylic carbon atomic ratio from the ratio of C 1s (285.0 eV) / C 1s (288.4 eV) intensities is 24, although it should be close to 17. This overestimation may rise from the formation of oxidation products or contamination. To confirm the formation of a lead-dimer complex on the lead substrate, the large peak at 531.7 eV in the O 1s spectrum was assigned to the oxygen atoms of the carboxyl group.

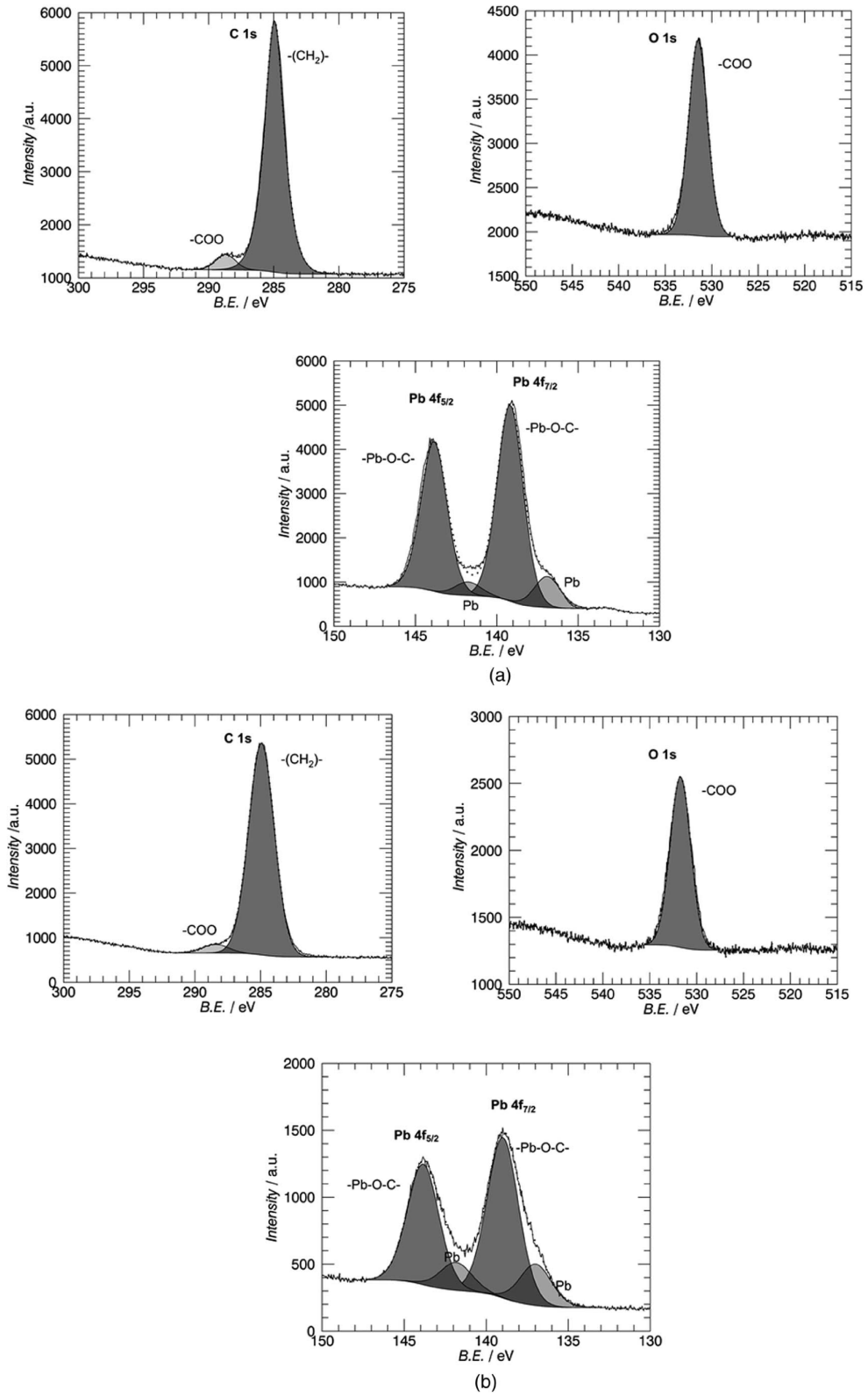


Figure. 14.4 – XPS core level spectra of the C 1s, O 1s, and Pb $4f_{7/2}$ levels of (a) DA-coated lead and (b) NaDA-coated lead, with components determined by curve fitting analysis and background subtraction.

ASSIGNMENT	REF	NaDA POWDER	DA LAYER	NaDA LAYER	[22]
ν_{as} (C-H)$_{alph}$ of -CH_2-	2919	2919.5 (s)	2919.4 (s)	2919.9 (s)	2931 (s)
ν_s (C-H)$_{alph}$ of -CH_2-	2850	2850.7 (s)	2850.3 (s)	2850.7 (s)	2854 (s)
ν (C-O) of -COOH	1725 – 1700	1701.9 (m)	1708.0 (w)	1708.8 (m)	-
δ_s (C-H)$_{alph}$ of -CH_2-	1435 – 1465	1443.1 (m)	1455.9 (m)	1446.0 (w)	1444 (s)
ν_{as} (COO^-)[a]	1610 – 1500[a]	1562.0 (s)	1514.6 (s)	1518.6 (s)	1517 (s)
ν_s (COO^-)[a]	1420 – 1300[a]	1419.1 (s)	1396.0 (s)	1404.5 (s)	1403 (s)
ω (C-H) of -CH_2- wagging [b]	1350 – 1150	-	1303.0 (m)	1310.0 (w)	-
ρ (C-H) of -CH_b- rocking [b]	1100 – 700	-	1075.2 (m)	1088.0 (m)	-
δ_s (C-H) of -CH_3	1380	1376.4 (m)	-	-	-
ρ (C-H) of -CH_3	925	925.4 (m)	-	-	-
ρ (C-H) of -$(CH_2)_n$- with n > 3	720	721.6 (m)	721.3 (m)	721.4 (m)	722 (m)
δ_s (COO^-)[a]	690	697.9 (m)	698.0 (w), 653.9 (w)	681.4 (m)	-
ω (COO^-)[a]	540	547.6 (w)	541.8 (w)	538.2 (w)	-
ρ (COO^-)[a]	470	-	469.1 (w)	472.6 (w)	-

[a] carboxylate binding dependent wavenumber.

[b] temperature and phase dependent wavenumber(s).

Table 14.3 – Characteristic vibrational wavenumbers (ν / cm^{-1}) in the 4000 – 400 cm^{-1} region for the spectra of a lead sample coated with DA or NaDA and of a NaDA reference powder sample.

The atomic ratio calculated for the lead-dimer complexes was PbC_2O_5 (see Table 14.4). This ratio is related to the formation of a lead(II)complex; on average each lead ion reacts with two carboxylic acid groups from the inhibitor. The complex formation is possible due to the higher reactivity of the neutralized dimer acid molecules. The high oxygen content could be explained by the presence of lead corrosion products such as lead carbonates, which have a different O 1s (531.7 eV) / C 1s (288.4 eV) intensity ratio [30]. This XPS measurement predicts an overall coordination number of 4 of the complex, similar to that of the lead(II)acetate structure [34]. The formation of this complex can be described by the dissolution-precipitation mechanism [37]. The difference in coordination between both inhibitor compounds is explained by both the reaction mechanism and the reactivity of each inhibitor. The reaction mechanism also depends on the solvent. PbO precursors for the formation of the lead carboxylate coating are more easily formed in water than in ethanol.

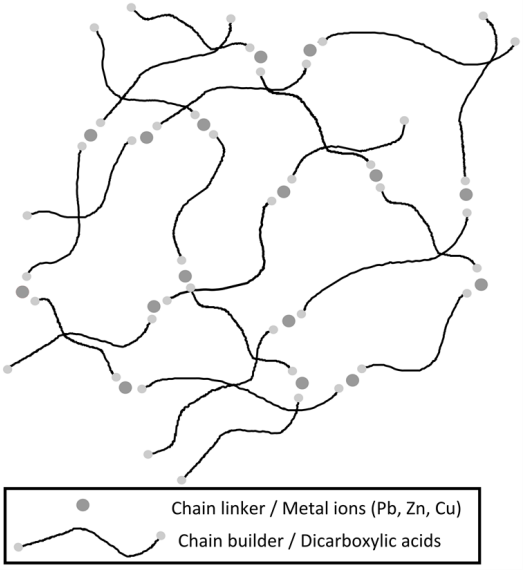


Figure. 14.5 – Proposed structure of metal-coordinated carboxylates, in which diacids form a 3D structure when coordinated by lead. A simplified 2D model is shown.

Figure 14.5 shows a proposed structure of the metal carboxylates, in which diacids form a relatively stable metal-

COMPOUND	ELECTRON	FWHM	B.E. / eV[a]	REF.	B.E. / eV[a]	ELEM. CONC.[b]	COMPOSITION EXP.	COMPOSITION THEOR.[c]
(a) DA-treated sample in Figure 14.4a								
metallic lead	Pb4f$_{7/2}$	1.89	137.0	[30]	136.7 - 137.0	0.6	-	-
aliphatic carbon	C 1s	1.76	285.0	[32]	285.0	49.9	-	-
	Pb 4f$_{7/2}$	1.89	139.2	[31]	138.5 - 139.0	3.6		
lead dicarboxylate	C 1s	1.76	288.7	[33]	288.4 - 289.5	2.8	PbC_1O_3	PbC_1O_2
	O 1s	2.39	531.5	[35]	531.2	9.7		
(b) NaDA-treated sample in Figure 14.4b								
metallic lead	Pb 4f$_{7/2}$	2.26	137.0		136.7 - 137.0	0.3	-	-
aliphatic carbon	C 1s	2.20	285.0		285.0	59.9	-	-
	Pb 4f$_{7/2}$	2.26	139.0		138.5 - 139.0	1.2		
lead dicarboxylate	C 1s	2.20	288.4		288.4 - 289.5	2.4	PbC_2O_5	PbC_2O_4[d]
	O 1s	2.60	531.7		531.2	6.1		

[a] Taking into account the correction that aliphatic C 1s needs to appear at 285.0 eV.

[b] Elemental analysis and composition calculated using the area sensitivity factors with relative variations within 2.0% [36].

[c] The theoretical compositions are measured by Taylor and Perry [30].

[d] Calculated using the lead(II) carboxylate structure with two carboxylic acid groups per lead ion [34].

Table 14.4 – Curve fitting results for C 1s, O 1s and Pb 4f$_{7/2}$ photoelectron spectra; values are corrected for C 1s to appear at 285.0 eV.

coordinated polymer because of their ability to build chains [38]. This is supported by the previous XPS and ATR-IR measurements. This model implies that the lead ions form links between the carboxylic groups of the dimer acid in a metal-coordinated physical network [39, 40]. If the polymer is composed of acids from environmental sources or of anions that compete with relatively weak fatty acid carboxyl groups, the coordination of the diacid structure could be locally lost temporarily. Although a diacid might re-establish its coordination through the remaining metal carboxylate group still attached to the polymer, monocarboxylic acids may lose their bond to the metal [38]. This suggests that this physical network has intrinsic self-healing properties.

14.6 Electrochemical impedance spectroscopy

In this section, we describe and fit the impedance data from a bare lead sample, a DA-coated sample and a NaDA-coated sample in the acetic acid corrosive medium.

14.6.1 Bare lead sample

Figure 14.6 shows the Nyquist plot of the bare lead sample immersed in the corrosive solution at the start and after 25 hours of immersion. The Nyquist plot forms a depressed semi-circle (○, Figure 14.6), suggesting capacitive behavior due to the formation of an oxide layer on the bare lead surface. After longer immersion, two time constants emerge owing to the diffusion of corrosion products close to the surface (×, Figure 14.6), suggesting corrosion and the formation of a corrosion layer [41].

A detailed mechanism for the acetic acid corrosion in the active dissolution region involves a connected network of

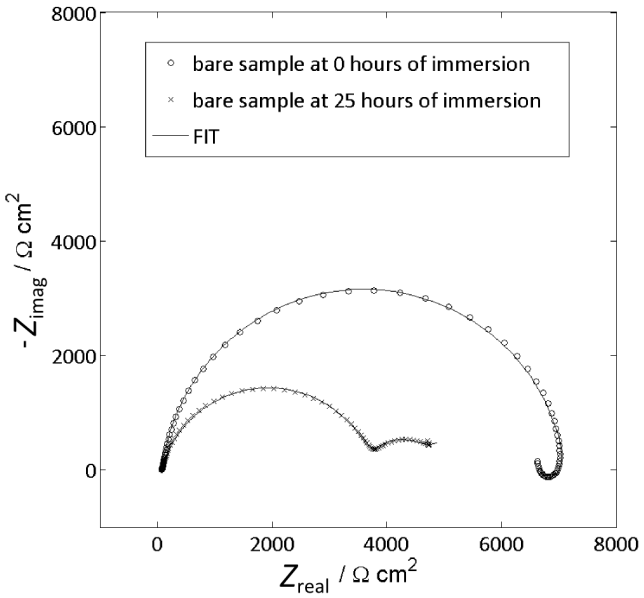


Figure. 14.6 – The Nyquist plot of bare lead in acetic acid at the start and after 25 hours of immersion.

reactions. The following reactions eqs. (14.1a) to (14.1c), however, describe the impedance functions that are consistent with the experimental observations with $Pb(OH)_{ads}$ as a categorical representation of Pb(I) adsorbed reaction intermediates [42, 43],

$$Pb + OH^-(aq) \underset{k_{b1}}{\overset{k_{f1}}{\rightleftharpoons}} PbOH_{ads} + e^-, \tag{14.1a}$$

$$PbOH_{ads} + OH^-(aq) \underset{k_{b2}}{\overset{k_{f2}}{\rightleftharpoons}} PbO^-_{ads} + H_2O, \tag{14.1b}$$

$$PbO^-_{ads} \overset{k_{f3}}{\rightarrow} PbO(s) + e^-. \tag{14.1c}$$

$$PbO(s) + 2CH_3COOH(aq) \overset{k_{f4}}{\rightarrow} Pb^{2+}(aq) + 2CH_3COO^-(aq) + H_2O \tag{14.1d}$$

Within the high-frequency limit, the inductive contribution is insignificant, which indicates that the Nyquist plot (○, Figure 14.6) of the impedance is a semicircle characteristic of the parallel arrangement of the CPE for the dielectric contribution of the double layer and charge-transfer resistance. The contribution at low frequency range comes mainly from the charge-transfer resistance and the inductive component in parallel explaining the formation of a semicircular arc in the fourth quadrant. This inductor arises from adsorption effects (the DC resistance is smaller than the AC impedance) due to the formation of $Pb(OH)_{ads}$ species [44]; this process at the start of the measurement is the rate-determining step. The inductor is defined as [45]

$$L_{ads} = R_{ads} \cdot \tau, \tag{14.2}$$

where τ is the time constant of the adsorption reaction. The experimental impedance plots show a slow evolution of the inductive behavior into capacitive behavior in the low-frequency region with an anodically increasing polarization potential (×, Figure 14.6). Such transitions have been attributed to the increase in surface coverage of an intermediate species formed during metal dissolution. At potentials close to the corrosion potential where metal dissolution is comparatively moderate, most of the $Pb(OH)_{ads}$ formed is consumed by reaction 14.1c and the adverse effect of its

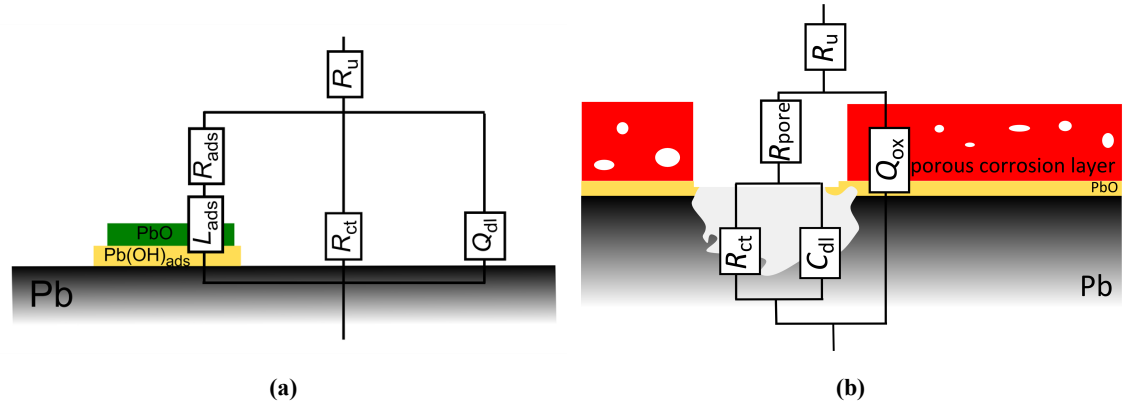


Figure. 14.7 – Electrochemical equivalent circuit used for the simulation of the experimental impedance spectra: (a) bare lead immersed for 0 h in the corrosive solution [45] and (b) bare lead immersed for 25 h.

coverage on reaction 14.1a is not sensed ($K > 0$) [45]. Based on this mechanism, the bare lead sample recorded in the corrosive solution was simulated using the equivalent electric circuit (EEC) of five elements shown in Figure 14.7a. This circuit includes the solution resistance, R_u, in series with a parallel combination of a constant phase element (CPE), Q_{dl}, for the capacitive behavior of the double layer, the charge-transfer resistance, R_{ct}, and the charge-transfer resistance of the adsorption reaction, R_{ads}, in series with the inductance for the adsorption reaction, L_{ads} [45]. The CPE element is explained in section 8.1.3.3.

During immersion, the consumption of PbO or the corrosion process becomes the rate-determining step, where the presence of acetic acid in reaction 14.1d leads to metal dissolution caused by the formation of water-soluble lead corrosion products such as lead acetates. The formation of a corrosion layer is described by a new Voigt element with a resistance, R_{ox}, and a CPE, Q_{ox}. The composition of this corrosion layer is described in detail by Niklasson et al. [46]. The equivalent circuit for the impedance plot after longer immersion is given in Figure 14.7b. In this case, the high-frequency range is dominated by the charge-transfer resistance and the double layer CPE. The low-frequency region is described by a parallel RC circuit of the corrosion layer forming a second semicircular arc in the Nyquist plot [45]. The impedance spectrum consists of two semicircles of different RC time constants. The two different models describe the different behaviors at different times: initially, the lead oxide layer grows and covers the whole surface, and after longer immersion the produced lead oxide reacts with the acetic acid to form new 'active' corrosion products.

	E_{corr}	R_u	R_{ads}	$C_{eff,dl}$	R_{ct}	L_{ads}	R_{ox}	$C_{eff,ox}$	χ^2 value
TIME	/ V vs. SCE	/ Ω cm^2	/ Ω cm^2	/ μF cm^{-2}	/ Ω cm^2	/ H cm^2	/ Ω cm^2	/ μF cm^{-2}	
0 hours	-0.499	83	7042	1.32	1.1×10^5	1.19×10^5	-	-	120
		± 3	± 7	± 0.01	± 0.02	± 0.09			
25 hours	-0.489	77.9	-	2000	3730	-	1050	1.17	108
		± 0.3		± 254	± 10		± 20	± 0.01	

Table 14.5 – Fitted impedance parameters of a bare lead sample immersed in a corrosive acetic acid solution for 0 h and 25 h.

Table 14.5 shows the extracted impedance parameters of the bare lead sample. The proposed models provide an excellent fit for all the recorded experimental data. Note that the potential, E_{OCP}, for the bare lead sample shifts to a more positive potential, introducing the new capacitive loop. This shift indicates the occurrence of other corrosion reactions at the

time of the measurement; this is also suggested by the different shape of the Nyquist plot. Furthermore, the drop in the charge-transfer resistance (a smaller semi-circle) over time indicates that increasing amounts of electrons are exchanged with the solution, thus forming new corrosion products. The resistance of the corrosion layer, R_{ox}, is very low, suggesting that almost no protection is offered by this new corrosion layer.

14.6.2 DA-coated sample

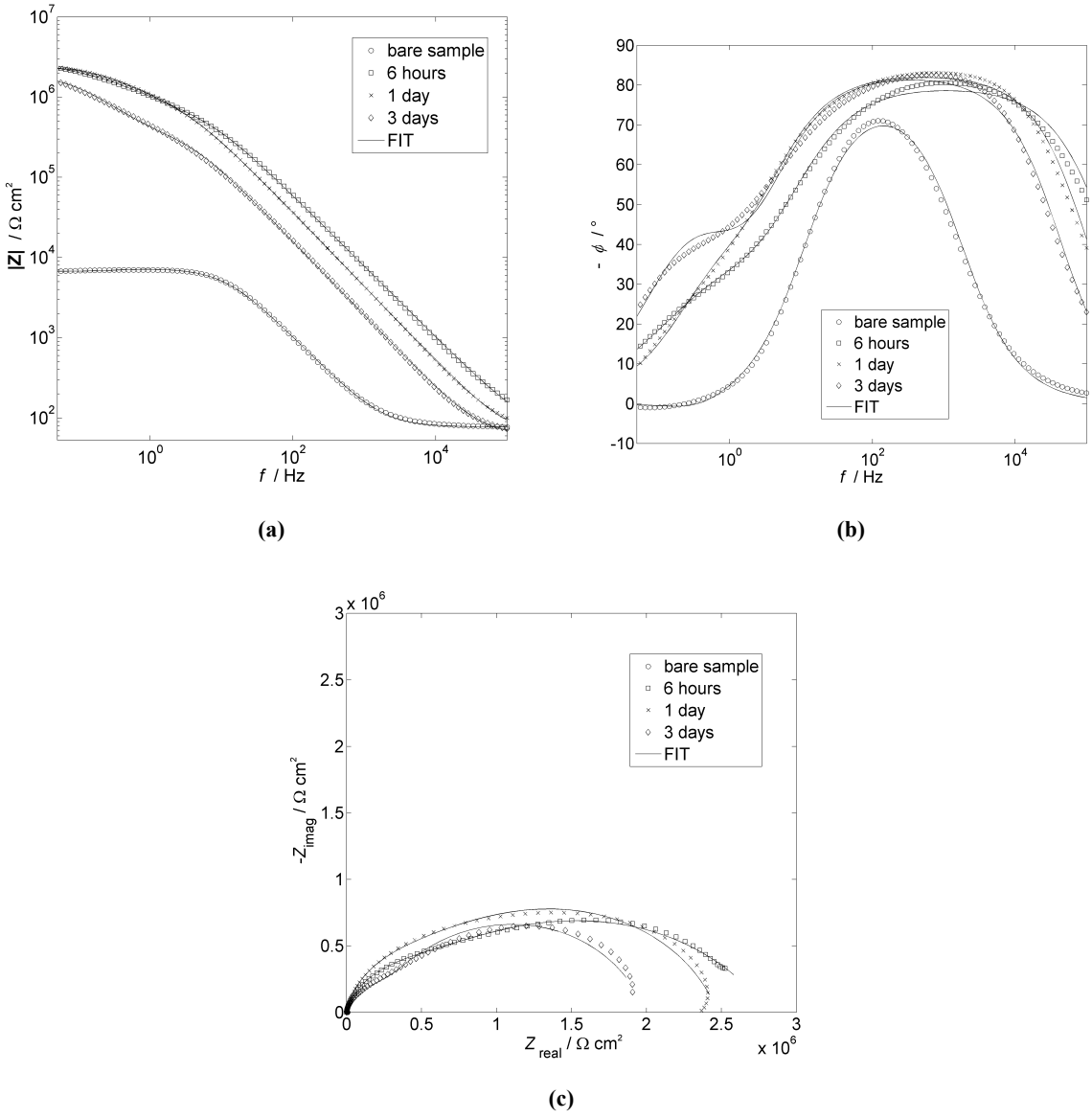


Figure. 14.8 – (a) Modulus, (b) phase and (c) Nyquist plot of DA-coated lead samples recorded in the acetic acid corrosive environment.

Figure 14.8 shows the (a) impedance magnitude, (b) phase and (c) Nyquist plot of DA-coated lead samples recorded in the acetic acid corrosive environment. The coatings were deposited by immersing the lead samples in ethanol DA solution for different durations (6 h, 1 d, and 3 d). The plot of the bare sample (shown in Figure 14.6) is shown for comparison. In Figure 14.8a, the coatings show a continuous increase over a large frequency range, which implies a high total resistance [47]. The large phase loops for the coated samples in Figure 14.8b indicate clear capacitive behavior.

The EIS measurement for the DA-coated lead sample recorded in the corrosive solution was simulated by an EEC of five elements as described in Figure 14.9. This circuit includes the solution resistance, R_u, in series with a parallel

TIME	E_{corr} / V vs. SCE	R_u / Ω cm^2	R_{pore} / Ω cm^2	$C_{eff,coat}$ / nF cm^{-2}	R_{ct} / Ω cm^2	$C_{eff,dl}$ / nF cm^{-2}	η_{IE} / %	χ^2 value
6 hours	-0.443	69	733000	10.2	2.08×10^6	40	94	69061
		± 2	± 7000	± 0.5	± 6×10^4	± 10	± 1	
1 day	-0.452	63	982000	25.3	1.49×10^6	30	92	106096
		± 2	± 9000	± 0.6	± 6×10^4	± 10	± 4	
3 days	-0.455	63	404000	61	1.58×10^6	60	90	63101
		± 1	± 4000	± 1	± 3×10^4	± 30	± 2	

Table 14.6 – Fitted impedance parameters of a bare lead and lead surfaces immersed in an ethanol DA solution for different durations recorded in a corrosive acetic acid solution.

combination of a CPE, Q_{coat}, for the capacitive behavior of the coating, and the pore resistance, R_{pore}, in series with a parallel combination of the charge-transfer resistance, R_{ct}, and a CPE for the double-layer capacitance, Q_{dl} [48].

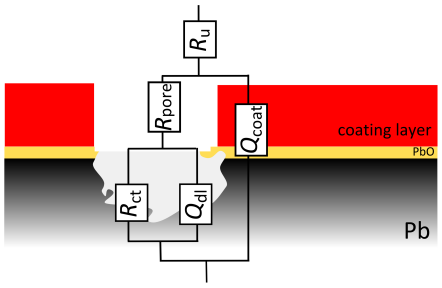


Figure. 14.9 – Electrochemical equivalent circuit used for the simulation of the experimental impedance spectra of the coated lead samples.

Table 14.6 lists the extracted impedance parameters of the DA-coated lead samples. The proposed circuit (Figure 14.9) was used to fit all the recorded experimental data successfully as seen in Figure 14.8. Note that the potential, E_{OCP}, for the coated samples shifts to a more positive potential, which indicates that the acetic acid reacts very slowly because of the high charge-transfer resistance. The coating covers the lead oxide layer during the immersion, although the polymer only forms during sintering as described in section 14.1.5. The electrolyte penetrates through microscopic pores in regions of the polymer with lower degree of entanglement. All the DA-coated samples show comparable R_{pore} values, indicating that each display equally dense coating layers with similar levels of linking. The thickness of the film can be predicted from $C_{eff,coat}$ following the Helmholtz model of the electrical double-layer [49],

$$C_{eff,coat} = \frac{\epsilon_r \epsilon_0 A_{eff}}{d}, \tag{14.3}$$

where d is the thickness and ϵ_r is the dielectric constant of the coating, ϵ_0 is the vacuum permittivity ($\epsilon_0 = 8.854 \times 10^{-12}$ F m^{-1}), and A_{eff} is the effective surface area of the sample. This model, using the fitted parameters (and with $\epsilon_{r(polymer)} = 3$ [50]) predicts a 0.1 - 0.25 µm thick coating. Water uptake by the coating, will cause the $C_{eff,coat}$ values to increase ($\epsilon_r \uparrow$ due to the water uptake). To verify the protective behavior of the coatings, their inhibition efficiencies η_{IE} were calculated using the relationship in Eq. 8.42. The calculated values, listed in the last column of Table 14.6, are between 90% and 95%, indicating that the bulk metal was protected by the DA coating.

14.6.3 NaDA-coated sample

The NaDA coatings produced too much noise during the impedance measurement making it impossible to fit the recorded impedance data. Trying to compare both coatings, we used the potentiodynamic polarization measurements.

14.7 Potentiodynamic polarization curves

In this section, we describe and the polarization curves from a bare lead sample, a DA-coated sample and a NaDA-coated sample in the acetic acid corrosive medium.

14.7.1 Bare lead sample

In the case of lead corrosion, the electron transfer takes place around the same potential E and only a single peak is noticed in Figure 14.10. As postulated before in Eq. eqs. (14.1a) to (14.1d), we suppose a multistep charge transfer composed of two one-electron transfer steps with an intermediate deprotonation step. To explain the kinetics of the corrosion process, it is assumed that one step, called the rate determining step (rds), is much slower than all the other steps using the quasi-equilibrium treatment. The first part of the Tafel plot (between –0.740 V and –0.655 V) is characterized by water reduction. This process is explained using the following mechanism [51],

$$\mathrm{Pb} + \mathrm{H^+} + \mathrm{e^-} \rightleftharpoons \mathrm{Pb{-}H} \tag{14.4a}$$

$$\mathrm{Pb{-}H} + \mathrm{H^+} + \mathrm{e^-} \rightleftharpoons \mathrm{Pb} + \mathrm{H_2} \tag{14.4b}$$

When we assume that Eq. 14.4a is the rate-determining step, the current potential response is identical to a simple single electron transfer and independent of the surface coverage. Single electron transfers are characterized by a Tafel slope of

$$\left(\frac{\partial E}{\partial \log i}\right)_{C_{\mathrm{H^+}}} = -\frac{0.059}{\alpha}\ \mathrm{V} = -120\ \mathrm{mV}, \tag{14.5}$$

with symmetry factor described in section 6.2, which is generally around 0.5. Looking at all (uncoated and coated samples) potentiodynamic curves in Figure 14.10 (short thick lines), the first part of the Tafel plots is explained by this Tafel slope. Table 14.7 shows the potentiodynamic polarization parameters of the bare and the coated lead samples. The corrosion mechanism is based on the reduction and oxidation of lead in an aqueous solution. In what follows, the bare lead Tafel plot in Figure 14.10 is explained based on the postulated (oxidation) mechanism. We assume that the rate is determined by the second electron transfer where the adsorbed intermediate species react to form the end-product. This means that the surface coverage of the adsorbed intermediate becomes an important factor as we look to the rate expression (for the oxidation) [52],

$$v = k_{\mathrm{f3}}^{0} \cdot \theta \cdot \exp(-\alpha f E) \tag{14.6}$$

with

$$\frac{\theta}{1-\theta} = K \cdot C_{\mathrm{OH^-}}^{2} \cdot \exp(fE) \tag{14.7}$$

for Langmuir adsorption. If the surface coverage is low ($\theta \approx 0$), the Tafel slope is 40 mV ($\alpha_{\mathrm{a}} = 1.5$). The same reasoning is valid for the reduction reaction. Experimentally, we get higher Tafel slopes around –47 mV and 50 mV, which are often considered to be due to lateral repulsive interactions of the adsorbed intermediates and a higher surface coverage ($\theta \approx 0.5$) [53].

The last part of the Tafel plot (between 0 V and +1.4 V) is characterized by a constant anodic current i independent of potential E. This occurs when the reaction 14.1c is very slow (due to low OH^- concentrations in reaction 14.1b) and θ becomes almost 1, because there would be no surface sites for further reaction on increasing the electrode potential. This

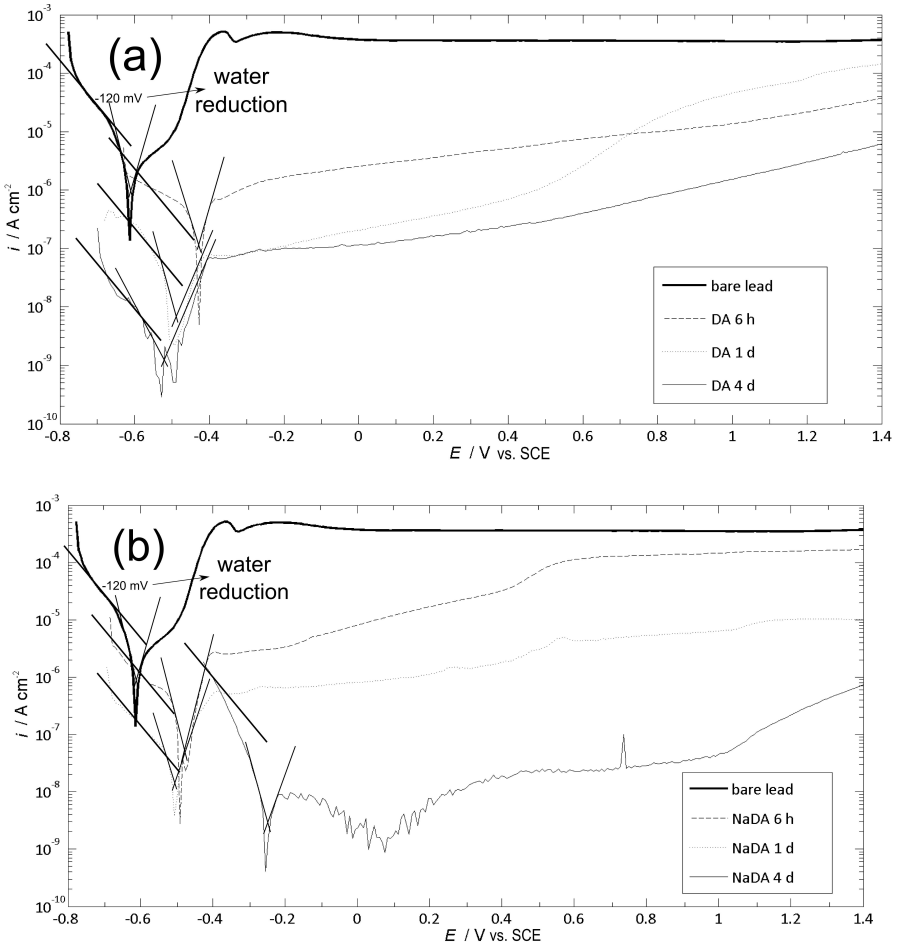


Figure. 14.10 – Current vs. potential plot for lead, (a) DA coated electrodes and (b) NaDA coated electrodes in the acetic acid corrosive environment.

means the current is controlled by the migration and diffusion of OH^- ions through the micropores of the corrosion layer from the bulk solution toward the metal surface for the growth of the PbO layer (the Pb^{2+} ion must migrate and diffuse in the opposite direction) [54]. The PbO layer is needed to initiate acetic acid corrosion in reaction 14.1d. The same process takes place at potentials between -0.588 V and -0.518 V during the PbO layer formation. Because of the lower potential, the OH^- concentration is too low causing reaction 14.1c to slow down.

14.7.2 Coatings

First of all, the data for all coated samples in Table 14.7 reveal a considerable decrease of the measured current over the whole potential range compared to the bare sample. At the corrosion potential E_{corr}, the corrosion current density, i_{corr}, is lower than for the bare sample. This indicates that the coatings block possible reaction sites of the lead metal sample at low overpotentials. Furthermore, the coatings have an inhibiting influence even at very high overpotentials, which proves the protection of the coatings even in more corrosive environments. A second effect concerns E_{corr}, which shifts to a more positive potential in the presence of a coating compared to the bare sample. The corrosion reaction starts at a more positive potential because of the blocked anodic corrosion sites on the surface. A third effect involves the calculated inhibition efficiency using Eq. 8.43. The inhibition efficiency increases with an increase of the immersion time for both the DA and NaDA-coated samples. This indicates that the immersion time has an influence on the deposition of the coating. An increase of the immersion time suggests an increase of the amount of deposited inhibitor on the sample surface. A last effect is the small increase of the anodic and cathodic Tafel slopes of the coated samples compared to the

	E_{corr} / mV vs. SCE	i_{corr} / A cm^{-1}	β_c / mV	β_a / mV	η_{IE} (%) (3 ×)
bare lead	-607	9.83×10^{-7}	-47	50	-
DA 6 h	-426	1.68×10^{-7}	-85	58	81 ± 3
DA 1 d	-477	1.25×10^{-8}	-94	83	99 ± 2
DA 4 d	-526	9.07×10^{-10}	-66	66	100 ± 1
NaDA 6 h	-474	3.73×10^{-8}	-68	45	90 ± 3
NaDA 1 d	-505	1.41×10^{-8}	-44	51	99 ± 2
NaDA 4 d	-244	3.17×10^{-9}	-51	55	100 ± 1

Table 14.7 – Fitted impedance parameters of a bare lead sample immersed in a corrosive acetic acid solution for 0 h and 25 h.

bare sample, indicating that the coating has a small influence on the kinetics of the corrosion process. The increased Tafel slope, values suggest that the surface coverage of adsorbed intermediates drops because of the presence of the coating.

14.8 Conclusions

The inhibitor molecules chemically react with lead metal ions present at the lead substrate surface. These Pb-O bonds form a polymer with lead atoms acting as linkers. The coordination of the carboxylate groups around the lead metal atom is defined as an asymmetric chelating bidentate bond. The DA inhibitor forms a coating during sintering, whereas the NaDA inhibitor reacts with the substrate to form clusters. XPS measurements of the DA-deposited coating show that the inhibitor only reacts partly with the lead metal during sintering. The NaDA coatings, however, form lead(II)complexes described by a dissolution-precipitation mechanism. In short, the different appearance of both coatings is explained by both the reaction mechanism, the inhibitor reactivity and the solvent used.

The coating blocks possible anodic reaction sites even at high overpotentials. The inhibition efficiencies of the DA and NaDA coatings depend on the immersion time, suggesting a constant deposition. An increase of the immersion time suggests an increase of the amount of deposited inhibitor on the sample surface. However, the deposition is uncontrolled so deviations are possible. All DA coatings show comparable R_{pore} values, indicating equally dense layers with similar levels of polymer entanglement. For NaDA coated samples a link is established between the immersion time, the coating thickness, the rate of water uptake and the degree of polymer entanglements.

From the electrochemical tests, we conclude that the NaDA coating (especially during a longer immersion) provides a better barrier against corrosion and water uptake than the DA coating considering the potentiodynamic curves. Therefore, use of water-soluble carboxylate soaps is preferred over the use of carboxylic acid dissolved in ethanol. However, more experiments comparing the corrosion protection offered by both coatings over longer periods would constitute an interesting extension to this work.

References for Chapter 14

[1] J. DWECK and C. SAMPAIO, Analysis of the thermal decomposition of commercial vegetable oils in air by simultaneous TG/DTA, *J. Therm. Anal. Calorim.* **75** (2) (2004), 385–391.

[2] J. SANTOS et al., Thermal stability and kinetic study on thermal decomposition of commercial edible oils by thermogravimetry, *J. Food Sci.* **67** (4) (2002), 1393–1398.

[3] J. SANTOS et al., Thermoanalytical, kinetic and rheological parameters of commercial edible vegetable oils, *J. Therm. Anal. Calorim.* **75** (2) (2004), 419–428.

[4] A. SHEPHERD, A mechanistic analysis of naphthenate and carboxylate soap-forming systems in oilfield exploration and production, PhD thesis, Heriot-Watt University, 2008, 105–109.

[5] N. JAYADAS and K. NAIR, Coconut oil as base oil for industrial lubricants-evaluation and modification of thermal, oxidative and low temperature properties, *Tribol. Int.* **39** (9) (2006), 873–878.

[6] E. RUFINO and E. MONTEIRO, Characterisation of lithium and sodium salts of poly(methacrylic acid) by FTIR and thermal analyses, *Polymer* **41** (11) (2000), 4213–4222.

[7] I. MCNEILL and M. ZULFIQAR, Thermal degradation of ammonium polymethacrylate and polymethacrylamide, *J. Polym. Sci. A* **16** (10) (2003), 2465–2474.

[8] G. KNOTHE and R. O. DUNN, A comprehensive evaluation of the melting points of fatty acids and esters determined by DSC, *J. Am. Oil Chem. Soc.* **86** (2009), 843–856.

[9] A. VALOR et al., Thermal decomposition of the calcium salts of several carboxylic acids, *Thermochim. Acta* **389** (1-2) (2002), 133–139.

[10] M. CRUZ et al., Spray pyrolysis as a method for preparing PbO coatings amenable to use in lead-acid batteries, *J. Power Sources* **108** (1-2) (2002), 35–40.

[11] D. BURG and R. KLEIMAN, Preparation of meadowfoam dimer acids and dimer esters, and their use as lubricants, *J. Am. Oil Chem. Soc.* **68** (8) (1991), 600–603.

[12] M. DE KEERSMAECKER, K. VERBEKEN, and A. ADRIAENS, Lead dodecanoate coatings for the protection of lead and lead-tin alloy artifacts: Two examples, *Appl. Surf. Sci.* **292** (2014), 149–160.

[13] M. FOREMAN, M. PLATER, and J. SKAKLE, Synthesis and characterisation of polymeric and oligomeric lead(II) carboxylates, *J. Chem. Soc., Dalton Trans.* (12) (2001), 1897–1903.

[14] J. YANG et al., Supporting information organic acid effect on the structures of a series of lead (II) complexes, *Inorg. Chem.* **46** (2007), 6542–6555.

[15] J. COATES, Interpretation of infrared spectra: A practical approach, in: *Encyclopedia of Analytical Chemistry*, ed. by R. MEYERS, John Wiley & Sons, 2000, 10815–10837.

[16] H. ELLIS et al., A room temperature structure for anhydrous lead(II) decanoate, *J. Mol. Struct.* **642** (1-3) (2002), 71–76.

[17] M. MESUBI, An infrared study of zinc, cadmium, and lead salts of some fatty acids, *J. Mol. Struct.* **81** (1982), 61–71.

[18] M. GASGNIER, IR spectra of some potassium carboxylates, *J. Mater. Sci. Lett.* **20** (13) (2001), 1259–1262.

[19] K. PATIL et al., Infrared spectra and thermal decompositions of metal acetates and dicarboxylates, *Can. J. Chem.* **46** (2) (1968), 257–265.

[20] E. PALACIOS and A. MONHEMIUS, Infrared spectroscopy of metal carboxylates: I. Determination of free acid in solution, *Hydrometallurgy* **62** (3) (2001), 135–143.

[21] J. HERMANS et al., The molecular structure of three types of long-chain Zn(II) alkanoates for the study of oil paint degradation, *Polyhedron* **81** (2014), 335–340.

[22] C. HIGGITT, M. SPRING, and D. SAUNDERS, Pigment-medium interactions in oil paint films containing lead-based pigments, *Newsletter (Western Association for Art Conservation)* **27** (2) (2005), 12–16.

[23] P. NELSON and R. TAYLOR, Theories and experimental investigations of the structural and thermotropic mesomorphic phase behaviors of metal carboxylates, *Appl. Petrochem. Res.* **4** (3) (2014), 253–285.

[24] V. ZELEŇÁK, Z. VARGOVÁ, and K. GYÖRYOVÁ, Correlation of infrared spectra of Zn(II) carboxylates with their structures, *Spectrochim. Acta Mol. Biomol. Spectros.* **66** (2) (2007), 262–272.

[25] T. ISHIOKA et al., Vibrational spectra and structures of zinc carboxylates. I. Zinc acetate dihydrate, *Spectrochim. Acta Mol. Biomol. Spectros.* **54** (1998), 1827–1836.

[26] C. BAZUIN et al., Thermotropic polymorphism in liquid-crystalline lead(II) alkanoates, *Liq. Cryst.* **3** (12) (1988), 1655–1670.

[27] A. ARENAS et al., Thermophysical study of lead(II) n-alkanoates by DSC, optical microscopy, FTIR and Raman spectroscopy, *Liq. Cryst.* **18** (3) (1995), 431–441.

[28] F. MARTINEZ CASADO et al., Intermediate rotator phase in Lead(II) alkanoates, *J. Phys. Chem. C* **111** (18) (2007), 6826–6831.

[29] M. MARONCELLI et al., Nonplanar conformers and the phase behavior of solid n-alkanes, *J. Am. Chem. Soc.* **104** (23) (1982), 6237–6247.

[30] J. TAYLOR and D. PERRY, An X-ray photoelectron and electron energy loss study of the oxidation of lead, *J. Vac. Sci. Technol. A* **2** (2) (1984), 771–774.

[31] A. P. TERZYK, The influence of activated carbon surface chemical composition on the adsorption of acetaminophen (paracetamol) in vitro. Part II. TG, FTIR, and XPS analysis of carbons and the temperature dependence of adsorption kinetics at the neutral pH, *Colloids Surf. A* **177** (1) (2001), 23–45.

[32] T. TAKAHAGI and A. ISHITANI, XPS study on the surface structure of carbon fibers using chemical modification and C1s line shape analysis, *Carbon* **26** (3) (1988), 389–395.

[33] E. JOHANSSON and L. NYBORG, XPS study of carboxylic acid layers on oxidized metals with reference to particulate materials, *Surf. Interface Anal.* **35** (4) (2003), 375–381.

[34] R. DAVIDOVICH et al., Stereochemistry of lead(II) complexes with oxygen donor ligands, *Coord. Chem. Rev.* **253** (9-10) (2009), 1316–1352.

[35] G. BEAMSON and D. BRIGGS, High resolution XPS of organic polymers: The Scienta ESCA300 database, *J. Chem. Educ.* **70** (1) (1993), A25.

[36] C. WAGNER et al., Empirical atomic sensitivity factors for quantitative-analysis by electron-spectroscopy for chemical-analysis, *Surf. Interface Anal.* **3** (1981), 211–225.

[37] M. DE KEERSMAECKER et al., Electrochemical and surface study of neutralized dodecanoic acid on a lead substrate, *J. Electrochem. Soc.* **161** (3) (2014), C126–C137.

[38] J. BOON, F. HOOGLAND, and K. KEUNE, Chemical processes in aged oil paints affecting metal soap migration and aggregation, in: *AIC paintings specialty group postprints: 34th annual meeting of the AIC of Historic and Artistic Works providence*, ed. by H. PARKIN, AIC, 2006, 16–23.

[39] R. CORKERY, Metal organic framework (MOF) liquid crystals. 1D, 2D and 3D ionic coordination polymer structures in the thermotropic mesophases of metal soaps, including alkaline earth, transition metal and lanthanide soaps, *Curr. Opin. Colloid Interface Sci.* **13** (4) (2008), 288–302.

[40] M. JOHN PLATER et al., The characterisation of lead fatty acid soaps in protrusions in aged traditional oil paint, *Polyhedron* **22** (24) (2003), 3171–3179.

[41] S. CHUNG et al., EIS behavior of anodized zinc in chloride environments, *Corros. Sci.* **42** (7) (2000), 1249–1268.

[42] E. ABD EL AAL, S. ABD EL WANEES, and A. ABD EL AAL, Anodic behavior and passivation of a lead electrode in sodium carbonate solutions, *J. Mater. Sci.* **28** (10) (1993), 2607–2614.

[43] S. ABD EL REHIM et al., Potentiodynamic and cyclic voltammetric behaviour of a lead electrode in NaOH solution, *Monatsh. Chem. Chem. Mon.* **128** (3) (1997), 245–254.

[44] M. MIGAHED et al., Effectiveness of some non ionic surfactants as corrosion inhibitors for carbon steel pipelines in oil fields, *Electrochim. Acta* **50** (24) (2005), 4683–4689.

[45] P. LI, T. TAN, and J. LEE, Impedance spectra of the anodic dissolution of mild steel in sulfuric acid, *Corros. Sci.* **38** (11) (1996), 1935–1955.

[46] A. NIKLASSON, L. JOHANSSON, and J. SVENSSON, Influence of acetic acid vapor on the atmospheric corrosion of lead, *J. Electrochem. Soc.* **152** (12) (2005), B519–B525.

[47] J. MCINTYRE and H. PHAM, Electrochemical impedance spectroscopy; a tool for organic coatings optimizations, *Prog. Org. Coat.* **27** (1996), 201–207.

[48] P. BONORA, F. DEFLORIAN, and L. FEDRIZZI, Electrochemical impedance spectroscopy as a tool for investigating underpaint corrosion, *Electrochim. Acta* **41** (7-8) (1996), 1073–1082.

[49] F. DEFLORIAN et al., Organic coating capacitance measurement by EIS: ideal and actual trends, *Electrochim. Acta* **44** (24) (1999), 4243–4249.

[50] Y. REN and D. LAM, Properties and microstructures of low-temperature-processable ultralow-dielectric porous polyimide films, *J. Elec. Mater.* **37** (7) (2008), 955–961.

[51] Y. MENG et al., The hydrogen evolution reaction in a room temperature ionic liquid: mechanism and electrocatalyst trendsNo Title, *Phys. Chem. Chem. Phys.* **14** (2012), 5222–5228.

[52] D. PLETCHER and F. WALSH, Adsorption, in: *Industrial electrochemistry*, Springer, 1990, chap. 1.4, 32–38.

[53] J. BOCKRIS and S. KHAN, Phenomenological electrode kinetics, in: *Surface electrochemistry: A molecular level approach*, Springer US, 1993, chap. 3, 211–407.

[54] Y. GUO, Kinetics of Oxidation Processes on Lead Electrode in H_2SO_4, *J. Electrochem. Soc.* **142** (10) (1995), 3378–3382.

15

Acrylate-based coatings to protect lead substrates

15.1 Polymer preparation

In this section, we explain the preparation of the different acrylate-based copolymers used as a coating on lead substrates.

15.1.1 Synthesis of 1-ethoxyethyl acrylate

The monomer, 1-ethoxyethyl acrylate (EEA), was synthesized by the acid catalyzed addition reaction of acrylic acid to ethyl vinyl ether as seen in the synthesis mechanism in Figure 15.1.

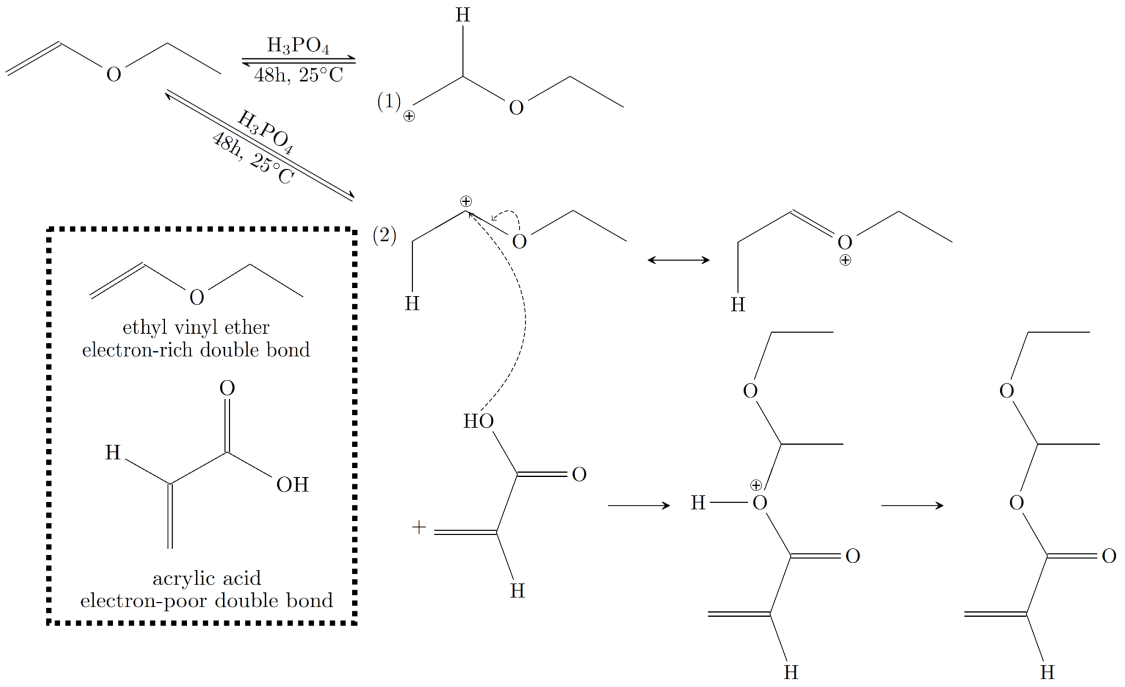


Figure. 15.1 – Reaction mechanism for the synthesis of 1-ethoxyethyl acrylate (EEA) [1].

The synthesis for both compounds is completely or partly bio-based [2]. This procedure is previously described by different authors [3–5]. Based on the electron-rich double bond position of the ethyl vinyl ether, it is possible to add the acidic proton on two positions. However, as seen in Figure 15.1, addition to position (2) is more favorable due to the existence of two stabilizing resonance structures. A simple nucleophilic attack of the acrylic acid to the formed carbocation, followed by a proton transfer, forms the proposed monomer. Electrophilic addition to acrylic acid does not occur because of the electron-poor character of the double bond as described in the Figure 15.1. The monomer synthesis

can be performed on a large scale with a yield of about 90% [1]. Afterwards, the monomer is purified using a high vacuum distillation. The exact synthesis protocol is described in different works [6]. The monomer was characterized by ^{1}H NMR signals at 1.07 (3H, t, -OCH_2CH_3), 1.30 (3H, d, -$COOCH(CH_3)$), 3.40 - 3.63 (2H, m, -OCH_2-), 5.73 (1H, d, CH_2=CH-), 5.90 (1H, q, -$COOCH(CH_3)$), 6.00 (1H, dd, CH_2=CH-), 6.30 (1H, d, CH_2=CH-) [1].

15.1.2 Synthesis of the RAFT reagent

The RAFT reagent, 2-[(butylsulfanyl)carbonothioyl]sulfanyl]propanoic acid (BuPAT), was synthesized using a procedure found in an article of Ferguson et al. [7]. First, a 50% NaOH solution was added to a stirring mixture of butane thiol ($pK_a \approx 10$). Using this strong base ($pK_a \approx 16$), the thiol is easily deprotonated to form the sodium salt. Afterwards, the mixture is treated with carbon disulfide to give an orange solution. After the nucleophilic addition reaction, the mixture is cooled down to 10°C. Finally, 2-bromopropanoic acid was added, followed by 50% NaOH, at such a rate that the temperature did not exceed 30°C. This nucleophilic substitution (S_N2) reaction is performed in an ice bath because of its exothermal character [8]. This trithiocarbonate molecule is characterized by a carboxylic acid at the α-end, which makes the RAFT agent interesting to form bonds with lead substrate.

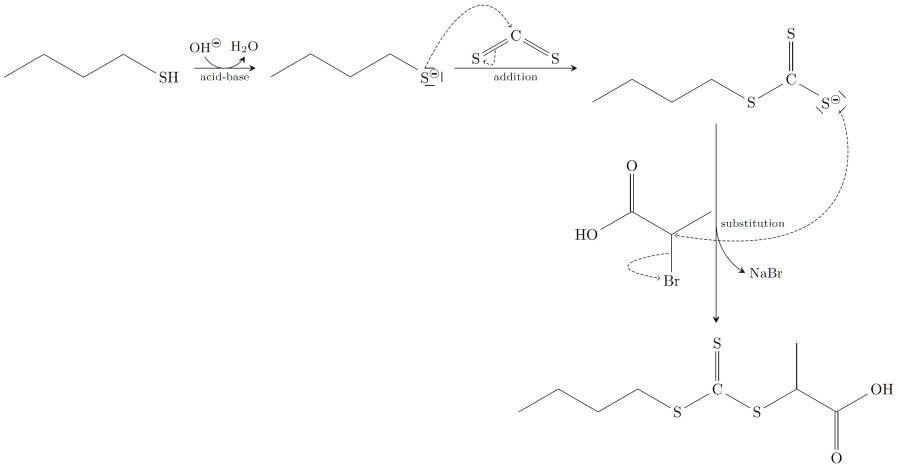


Figure. 15.2 – Reaction mechanism for the synthesis of RAFT reagent.

The RAFT agent was characterized by ^{1}H NMR signals at 10.6 (br, 1H, CO_2H), 4.87 (q, 1H, SCH), 3.37 (t, 2H, CH_2S), 1.69 (q, 2H, CH_2CH_2S), 1.63 (d, 3H, $SCHCH_3$), 1.44 (se, 2H, $CH_3CH_22CH_2$), 0.94 (t, 3H, CH_33CH_2) [1, 7, 9].

15.1.3 Synthesis of the acrylate copolymers: RAFT polymerization

The reversible addition fragmentation chain transfer (RAFT) polymerization is one of several kinds of reversible-deactivation controlled radical polymerizations (CRP) discovered by Rizzardo et al. [10]. The control over the generated molecular weight (MW) and polydispersity (Đ) during free-radical polymerization is achieved by establishing a dynamic equilibrium between a dormant polymeric RAFT agent and the free polymeric radicals as depicted in Figure 15.3. The equilibrium is a consequence of addition and fragmentation steps achieved by the use of a chain transfer agent in the form of a thiocarbonylthio compound. The equilibrium controls the free radical concentration, the polymerization speed and determines the chain termination and chain transfer probability. When appropriate conditions are applied, control can be obtained by reducing the termination reactions to a minimum. As all polymer chains have a (dormant) radical chain end, all polymer chains will grow with similar rates resulting in a narrow molecular weight (= low polydispersity). This controlled polymerization method allows the synthesis of well-defined random, gradient and block copolymers [11–13]. Recent investigations of Lingier [6] revealed an optimal RAFT to initiator ratio 1:0.1 for the polymerization of acrylates

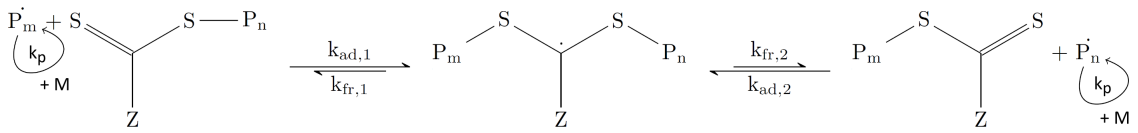


Figure. 15.3 – Mechanism for the RAFT polymerization [10].

utilizing BuPAT as RAFT agent and azobisisobutyronitrile (AIBN) as initiator in toluene. Using this ratio, we obtained higher molecular weights and more narrow dispersities. Therefore, the current work on the RAFT copolymerization of EEA with 2-ethylhexylacrylate (EHA) with BuPAT and AIBN in toluene was conducted at this optimal RAFT to initiator ratio of 1:0.1 [6]. A schematic of the complete co-polymerization reaction is given in Figure 15.4 together with the end-product taking into account the attachment of the RAFT reagent based on the mechanism given in Figure 15.3.

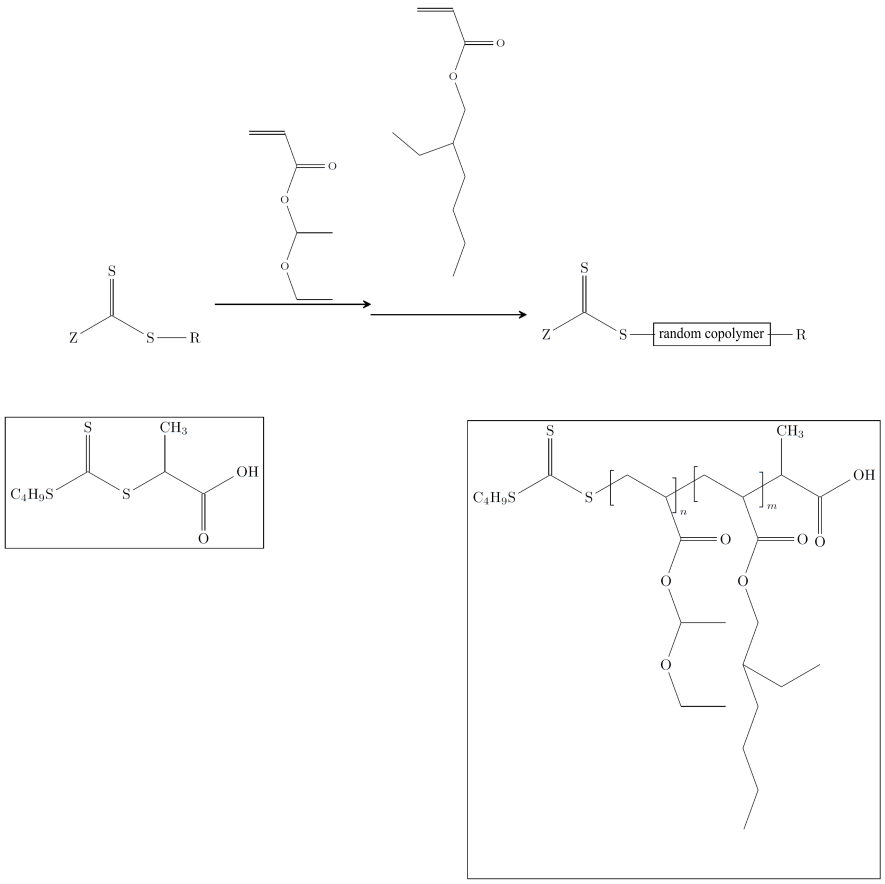


Figure. 15.4 – Mechanism for the RAFT co-polymerization with monomers EEA and EHA, AIBN as initiator and BuPAT as RAFT reagent [10].

Experimental - First of all, the monomers were purified by passing over basic alumina to remove the stabilizators. Then, for the preparation of a copolymer with 5% carboxylic groups and a molecular weight of 15,000 g mol^{-1} (= copolymer 2 in Table 15.1), a Schlenk flask was filled with AIBN (16.4 mg, 0.1 mmol), BuPAT (238.4 mg, 1 mmol), 1-ethoxyethylacrylate (1.5 g, 10.4 mmol), 2-ethylhexylacrylate (14.3 g, 77.3 mmol) and toluene so that the monomer concentration was 3 M. For other copolymer compositions the amount of 1-ethoxyethylacrylate and 2-ethylhexylacrylate was recalculated as done in Table 15.1. To remove the oxygen in the flask, the liquid mixture was degassed

using the freeze-vacuum-thaw procedure with nitrogen gas. The reaction mixture was put into an oil bath at 70°C for 6 hours. After reaction, the formed polymer was precipitated dropwise in cold methanol (cooled with liquid nitrogen) resulting in a solid product. The precipitate was decanted and put into the vacuum oven overnight to remove the solvents.

No.	%[EEA]$_0$	MW / kDa	n_{EEA} / mmol	n_{EHA} / mmol
1	5	10	6.9	51.6
2	5	15	10.4	77.3
3	5	20	13.9	103.1
4	10	10	13.8	48.8
5	10	15	20.8	73.3
6	10	20	27.8	97.7

Table 15.1 – Composition of the different random copolymers used as a lead coating.

Based on the described procedure, we make random copolymers with different compositions as described in Table 15.1. On one hand, the coating needs to be as hydrophobic as possible to protect the metal against the humidity, but, on the other hand, the polymer needs to have sufficient built-in carboxylic groups to react with the oxidized lead metal. Trying to make a compromise between both requirements, we choose to work with 5% and 10% built-in carboxylic groups. Another important property of the polymer is the molecular weight. Indeed, Wicks et al. [14] postulates that "molecular weight is often a critical factor controlling the strength of films that are not cross-linked". A high weight results in polymer precipitation during immersion of the lead sample and low weights do not provide enough protection against corrosion. Clearly, one needs to make a compromise between the film and viscosity properties [14]. Therefore, we start by making polymers with a molecular weight of 10,000 to 20,000 kDa.

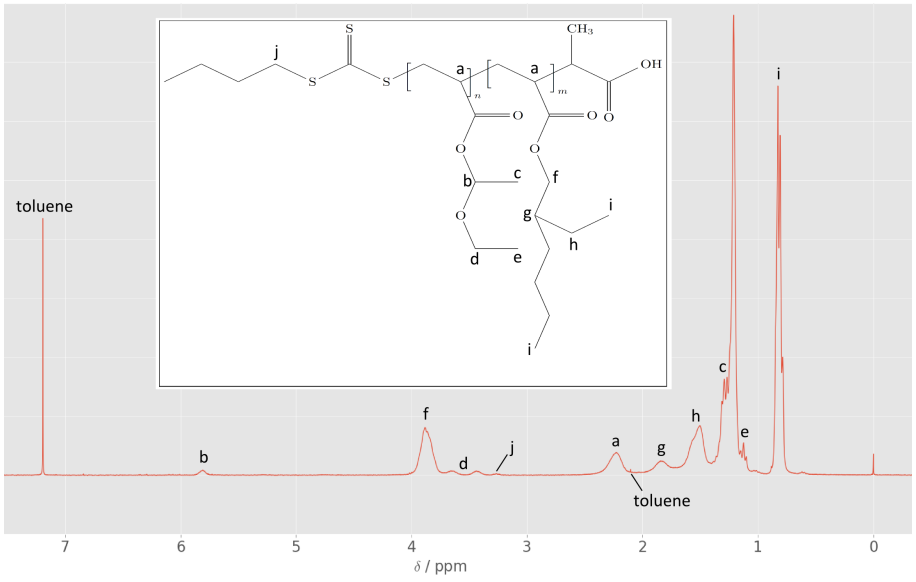


Figure. 15.5 – ^{1}H NMR spectrum of the RAFT copolymer with EEA and EHA building blocks ($CDCl_3$, 300 MHz).

The ^{1}H NMR spectrum of the RAFT copolymer with EEA and EHA building blocks is shown in Figure 15.5. It is the ^{1}H NMR spectrum for copolymer 2. First of all, the broadening of the signals explains the polymer formation. The signals

are identified in Figure 15.5.

No.	%[EEA]$_0$	wt% of EEA	wt% of EHA	Average number of repeating units per chain[a]	Average number of COOH groups per chain[a]	calculated M_n / Da[b]
1	5	9.22	90.78	32.5	3.7	6072
2	5	7.21	92.79	86.6	7.8	15854
3	5	8.04	91.96	102.3	10.3	18650
4	10	15.81	84.19	49.1	9.5	8898
5	10	14.46	85.54	79.9	14.2	14363
6	10	15.81	84.19	86.0	16.6	15388

[a] Calculation based on ^{1}H NMR signals at 5.8 ppm, 0.8 ppm and 3.25 ppm.

[b] The number average molar mass

Table 15.2 – The calculated compositions of the different random copolymers based on the ^{1}H NMR signals.

Using the integration of the ^{1}H NMR signals, we could calculate the relative composition of the formed random copolymer, but not the total number of built-in monomers. Table 15.2 sums up the calculated compositions of the different polymers used as a lead coating using the integration of the NMR signal at 5.8 ppm (b) and at 0.8 ppm (i) representing six hydrogens. Using the ^{1}H NMR signal at 3.25 ppm (j), which represents two hydrogen atom in the RAFT end-group, we are able to calculate the number of repeating units in the copolymer based on the signal at 5.8 ppm (b) and at 0.8 ppm (i). The calculations are based on the polymer molecular weight analysis executed by Izunobi and Higginbotham [15]. Furthermore, the signal at 5.8 ppm (b) represents only the 1-ethoxyethylacrylate building blocks, which means we can calculate the number of carboxylic groups per chain after deprotection as seen in Table 15.2. This number of carboxylic groups is very important because it represents the probability of a reaction with the lead sample during immersion. An increase in the number of carboxylic groups ensures a higher reaction probability.

No.	%[EEA]$_0$	[M]$_0$/[CTA]$_0$[a]/[I]$_0$[b]	M_n / Da	Đ
1	5	58.5/1/0.1	6507	1.12
2	5	87.7/1/0.1	13900	1.12
3	5	117.0/1/0.1	18000	1.15
4	10	62.7/1/0.1	10600	1.09
5	10	94.0/1/0.1	14800	1.13
6	10	125.4/1/0.1	19100	1.15

[a] The amount of equivalents chain transfer reagent (BuPAT)

[b] The amount of equivalents AIBN initiator

Table 15.3 – Results of RAFT co-polymerization of EEA and EHA at 70°C after a reaction time of 6 hours in 3 M toluene measured with a THF-GPC

In Table 15.3, the GPC results for the co-polymerization with EEA and EHA are given after 6 hours reaction time. It is clear that for the purified samples, in most cases, the targeted molecular weights are reached. The GPC results also clearly show that small dispersities are easily obtained. Comparing the calculated molecular weight based on the number of repeating units calculated using the ^{1}H NMR data and the GPC data, a clear similarity is seen between the weights. This proves that the ^{1}H NMR signals have been successfully identified.

15.1.4 Deprotection of the acrylate polymer

When the formed copolymer is exposed to heat, all the 1-ethoxyethyl groups in the polymer backbone will transform into carboxylic acid groups with the loss of gaseous ethyl vinyl ether (boiling point: 33°C) [4, 5, 16]. The fact that a simple temperature increase can deprotect the polymer, is the main advantage of using 1-ethoxyethyl as a protecting group rather than using tert-butyl or benzyl protecting groups. The easiest way to perform the deprotection in bulk is to reflux the protected polymer in a chosen solvent. Furthermore, no purification steps are necessary [1]. The deprotection step is schematically depicted in Figure 15.6. One has to be careful at high temperatures for anhydride formation, which results in partial cross-linking as depicted in Figure 15.7.

Experimental - The deprotection of the acrylic acid was done by refluxing a polymer solution [17]. Indeed, for large quantities this was the best method. In this case, we choose THF as a solvent. The oil bath temperature was set at 70 - 80°C. After 3 hours, the deprotection was completed. After the reaction, the solvent in the polymer mixture was removed using a rotary evaporator. The remaining polymer in the flask was removed using aceton. A night in the vacuum oven completed the deprotection step.

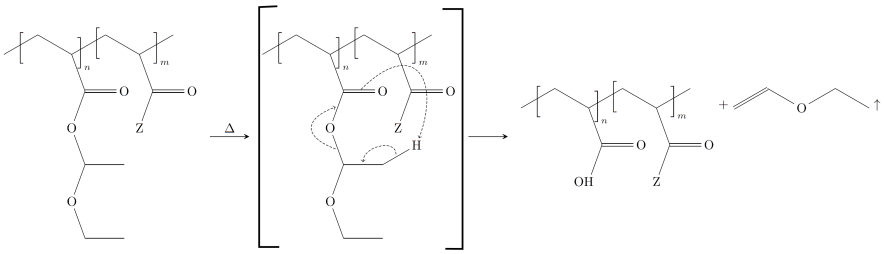


Figure. 15.6 – Mechanism for the deprotection step of the RAFT copolymer [1].

A ^{1}H NMR experiment, using copolymer 2, confirms the deprotection by looking at the disappearing characteristic PEEA peaks at 5.7 - 5.9 ppm (peak a) and 3.3 - 3.7 ppm (peak b) in $CDCl_3$. After the heating process, 3 hours at 66°C, the spectrum showed small peaks explaining the presence of small amounts of ethyl vinyl ether and the formation of anhydride functional groups. These peaks justify the deprotection mechanism shown in Figure 15.6. However, we see no peak at 10 - 12 ppm for the proton of the carboxylic acid group. This is explained by the difficulty to see protons directly bonded to heteroatoms in proton NMR, which is due to the interaction with the $CDCl_3$ solvent [18]. The measured IR data, in the following section, clearly confirm the deprotection with a clear absorption band.

15.2 Experimental

15.2.1 Inhibitor solutions

All deprotected random copolymers were dissolved in 100 mL of an organic solvent/water mixture. The organic solvent is used for the dissolution of the polymer and the water is used for the oxidation of the lead sample to lead oxides. These oxides are necessary to provide a reaction of the carboxylic acid groups with the lead sample. First, 0.25 g of all polymers was dissolved in the organic solvent (ethanol and THF) using an ultrasonic bath. When completely dissolved, water was added to get a turbid solution. When using THF, we needed 30 mL water and for ethanol we used 10 mL water. The lead samples were modified through immersion for 4 days in the solutions and then, the samples were rinsed and air-dried. The solvent, however, did not have an effect on the coating's protective properties.

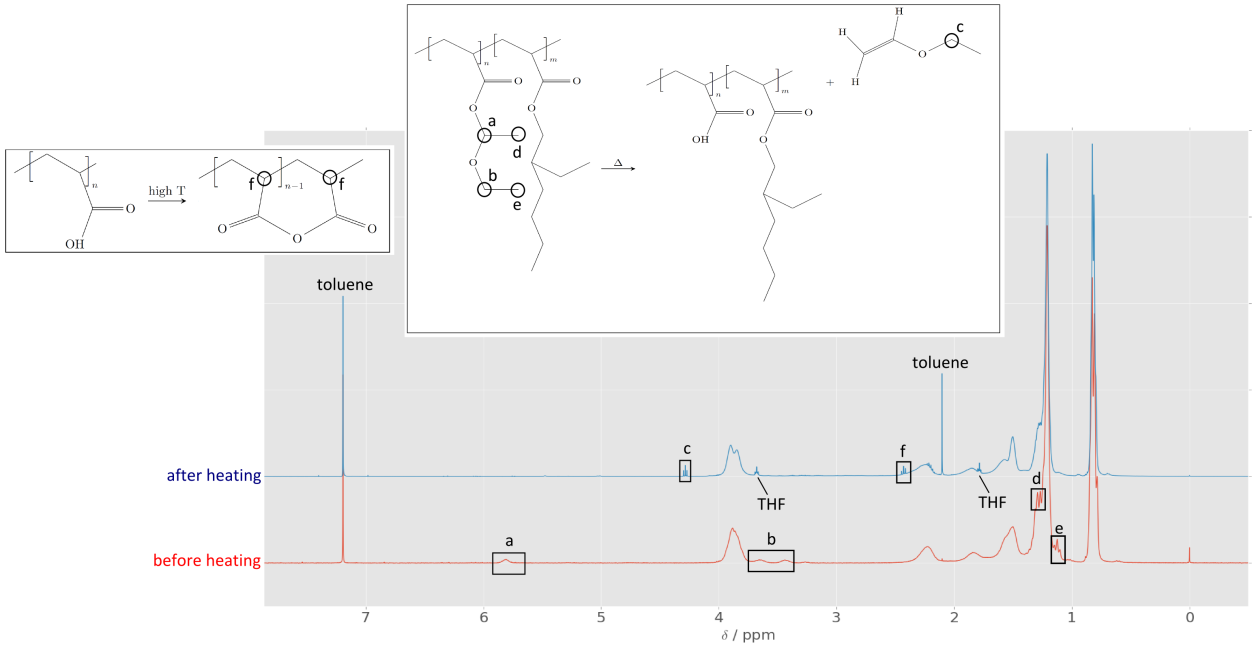


Figure. 15.7 – ^{1}H NMR spectra of a sample of copolymer 2 before heating (in $CDCl_3$, 500 MHz) and after heating.

15.2.2 Surface analysis techniques

Attenuated total reflectance (ATR) spectra were acquired using a Spectrum 1000 FTIR Infrared spectrometer (Perkin Elmer, USA) equipped with a Spectrum 100 Series' Universal ATR accessory, which was fitted using a diamond crystal as described in section 4.7.3. The coating of the lead substrate was measured directly by pressing the lead substrate against the ATR crystal. Spectra were recorded over a wavenumber range of 4000 – 600 cm^{-1} and averaged over 16 scans. SEM images are recorded using the FEG SEM Quanta-450 (FEI, The Netherlands) with a FEG source operated at a voltage of 5 kV. The EDS data were taken using a voltage of 15 kV with a built-in EDAX SDD detector (EDAX, USA). The instrument is described in section 4.4.2.7.

15.3 Infrared analysis

Figure 15.8 shows the recorded infrared spectra for (a) a bare lead surface, (b) the copolymer 2 and (c) a lead sample coated with copolymer 2. The spectra of the polymer and the coated sample (curves b and c) show important characteristic peaks compared to the bare lead sample (curve a). Table 15.4 shows the characteristic infrared frequencies for the polymer and the coating. Adsorption peaks around 2927 and 2860 cm^{-1} correspond to the antisymmetric stretch, ν_{as}, and the symmetric stretch, ν_s, of -CH_2- in the aliphatic chains of the copolymer [19]. The peaks at 2957 and 2872 cm^{-1} are the antisymmetric stretch, ν_{as}, and the symmetric stretch, ν_s, of -CH_3 of the aliphatic chains [20]. In the 2500 - 3500 cm^{-1} range, the baseline of the infrared spectrum of the copolymer shifted to a lower transmission, explaining the ν_s (O-H) of the carboxylic acid groups. The shift is small, because of the low percentage of carboxylic acid groups in the copolymer [21]. Only the small peak at 2360 cm^{-1} shows clear evidence of the ν_s (O-H). Indeed, copolymer 5 with 10% carboxylic acid groups shows a slightly bigger peak (not shown). Other strong absorptions were observed in the regions around 1730, 1246, and 1160 cm^{-1}, corresponding to the common vibrations of the -COOH [22] and the -C=S group [23]. More specifically, these peaks were identified as the symmetric stretches of the carboxyl and the thiocarbonyl group. The infrared spectrum of the lead sample coated with copolymer 2 shows new broad peaks around 1560 cm^{-1}, 1395 cm^{-1} and 682 cm^{-1}, which were identified as the antisymmetric stretch, symmetric stretch and scissoring vibrations of the carbonyl group of bivalent

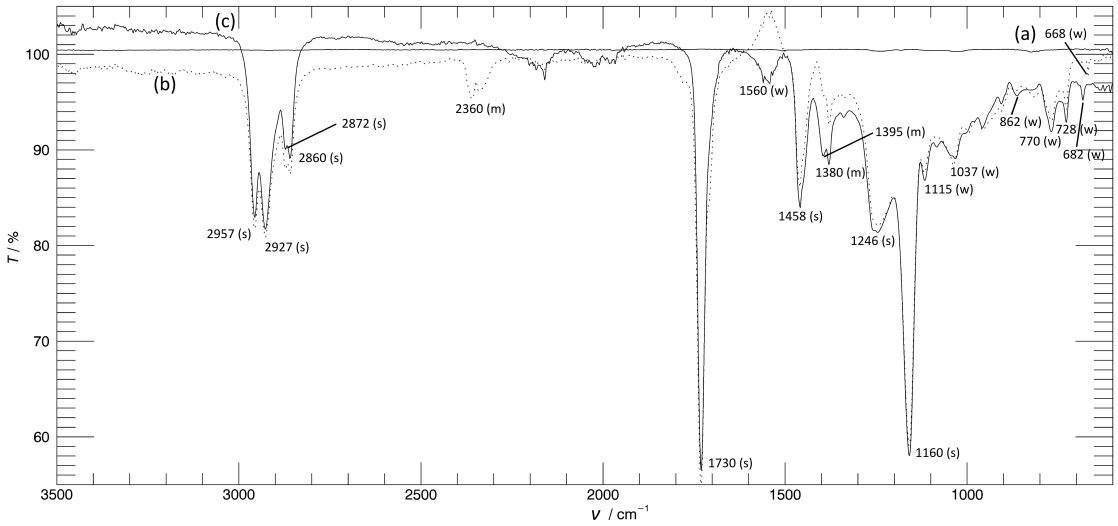


Figure. 15.8 – ATR-IR measurements of (a) a bare lead surface, (b) the copolymer 2 and (c) a lead sample coated with copolymer 2.

metal carboxylates, respectively [24–26]. This indicates that some of the available carboxylic acid functional groups undergo chemisorption on the lead oxide surface [27]. Indeed, lead(II)complexes are easily formed with polyacrylic acid compounds [28]. Moreover, the ν_s (O-H) of the carboxylic acid groups disappears, which means the carboxylic acid groups are involved in the reaction with the lead substrate. Most of the weak adsorption peaks between 1120 cm^{-1} and 700 cm^{-1} can be explained by rocking and scissoring vibrations of the 2-ethylhexyl acrylate groups of the copolymer as calculated by Belaidi et al. [29]. Analyzing the data made clear that most of the rocking and scissoring vibrations of the C-O bonds of the copolymer are influenced by the reaction with the lead substrate.

ASSIGNMENT	REF [29–31]	POLYMER	COATING	ASSIGNMENT	REF [29–31]	POLYMER	COATING
ν_{as} (C-H) of -CH_3	2955	2957 (s)	2957 (s)	ρ (C-H) of -CH_2-CH-	1116	1115 (w)	1115 (w)
ν_{as} (C-H)$_{alph}$ of -CH_2-	2919	2927 (s)	2927 (s)	δ_s (C-C) of -CH_2-CH-CH_2-	1079- 1089	1084	1084
ν_s (C-H) of -CH_3	2870	2872 (s)	2872 (s)	ν (C-C) of hexylgroup	1032 - 1040	1037 (w)	1032 (w)
ν_s (C-H)$_{alph}$ of -CH_2-	2850	2860 (s)	2860 (s)	δ_s (C-O) of -CH-CH_2-O-	984	995 (w)	-
ν_s (O-H) of -COOH	3400 - 2400	2360 (m)	-	ρ (C-O) of -CH_2-O-CH-	962	954 (w)	954 (w)
ν_s (C=O) of -COOH	1725 – 1700	1730 (s)	1730 (s)	ρ (C-C) of ethylgroup	909	904 (w)	904 (w)
ν_{as} (COO^-)[a]	1610 – 1500[a]	-	1560 (m) and 1542 (m)	ν (C-C) of ethylgroup	852	862 (w)	868 (w)
δ_s (C-H)$_{alph}$ of -CH_2-	1435 – 1465	1458 (s)	1458 (s)	ρ (C-H) of -O-CH_2	811	814 (w)	-
ν_s (COO^-)[a]	1420 – 1300[a]	-	1395 (m) and 1380 (m)	ρ (C-H) of -CH_2-CH-CH_2-	770	770 (w)	770 (w)
δ_s (C-H) of -CH_3	1380	1380 (m)	1380 (m)	ρ (C-H) of -CH_2-CH-CH_2-	770	770 (w)	770 (w)
ν_s (C-O) of -COOH	1320 - 1210	1246 (s)	1246 (s)	δ_s (COO^-)[a]	690	-	682 (w)
ν_s (C-S) of -C=S	1160	1160 (s)	1160 (s)	ν (C-S) of -S-C=S	674 (m)	668 (w)	-

[a] carboxylate binding dependent wavenumber.

[b] temperature and phase dependent wavenumber(s).

Table 15.4 – Characteristic vibrational wavenumbers (ν / cm^{-1}) in the 3500 – 600 cm^{-1} region for the spectra of the polymer sample and the lead sample coated with the polymer.

Based on the separation between ν_{as} and ν_s band of COO^- described in section 7.5, we can try to find the coordination mode of the carboxyl group with the metal ion. For this, we take into account the four principal modes of coordination shown in Figure 7.10 [32–34]. As described in Table 15.4, two bands due to ν_{as} (COO^-) were observed in the spectrum at 1560 and 1542 cm^{-1}. The symmetric ν_s (COO^-) stretches were observed at 1396 and 1380 cm^{-1}. The $\Delta\nu$ values, calculated using Eq. 7.15, are 180 and 146 cm^{-1}. First, we need a comparable $\Delta\nu$ (COO^-)$_{sodium\ salt}$ value. In previous

chapters 7 and 14, this value was calculated to be 136 cm^{-1} (for the lead dodecanoate) and 143 cm^{-1} (for the dimer acid). Additionally, several other authors [26, 33, 35] calculated the $\Delta\nu\ (COO^-)_{\text{sodium salt}}$ for other related compounds, which was often in the range of 136 - 164 cm^{-1}. Following the guidelines described in section 7.5, the $\Delta\nu\ (COO^-)_{\text{copolymer 2}}$ value of 180 $cm^{-1} > 164\ cm^{-1}$ suggests a monodentate carboxylate coordination in the formed complex. The second $\Delta\nu\ (COO^-)_{\text{copolymer 2}}$ value of 146 cm^{-1} clearly falls in the range of the salts indicating that an ionic group exists.

As suggested by Deacon et al. [33], acetate-like metal ion complexes show different coordination geometries including two of particular significance: the chelating bidentate and the bridging bidentate coordination as shown in Figure 7.10. From studies of crystalline metal acetates, several authors have claimed that an increase in $\nu_{as}(COO^-)$ relative to the sodium salt is indicative of bridging whereas a decrease in $\nu_{as}(COO^-)$ is indicative of chelation [33]. Taheri et al. [20] agrees by saying that "a higher energy level is required to stretch the group because of the bonding force directly opposing the charge." Moreover, Pomogailo et al. [36] claims that $\nu_{as}\ (COO^-)$ = 1580 cm^{-1} for non-bridging structures and $\nu_{as}\ (COO^-)$ = 1520 - 1560 cm^{-1} for bridging structures. Based on these statements and the calculated $\Delta\nu\ (COO^-)_{\text{copolymer 2}}$ values, it is more likely that polymer adsorption on the lead sample covered with lead oxide forms a bridging bidendate coordination between the lead substrate and the carboxylate groups. From this point of view, we assume that both vibrations originate from two non-equivalent *syn-syn* carboxylate bridges. As the $\Delta\nu$ values depend on the 'symmetry' of the bidentate carboxylate coordination, Zeleňák et al. [35] defined a parameter describing the 'deformation of the bidentate bond' as

$$\sum = |240 - (\alpha + \beta)| \tag{15.1}$$

where α and β are M-O-C angles as depicted in Figure 7.10. They concluded that as the parameter $\sum$ increases, the magnitude of the separation $\Delta\nu$ decreases. For an ideally symmetric coordination $\alpha = \beta = 120°$ and $\sum = 0$, the separation $\Delta\nu$ is highest. In our case, values for α and β for one bridge are predicted close to 120° as in the ideal case, the other bridge is more deformed with angle values further from the ideal 120°.

15.4 Corrosion protection of acrylate coatings

In this section, we look at the corrosion protective properties of the polymer-coated lead samples.

15.4.1 Corrosion experiment

All the electrochemical experiments were performed using a three-electrode system in a 250 mL glass beaker filled with 100 mL electrolyte consisting of 5 µg L^{-1} acetic acid (98 - 99%, Merck, USA) and 0.1 M tetrabutylammonium bromide (TBAB) (> 99%, Sigma Aldrich, USA) as a supporting electrolyte. The setup consisted of a saturated double-compartment calomel electrode (SCE), a platinum mesh, and a working electrode holder filled with a polymer-coated lead sample. The surface area of the samples in the holder exposed to the corrosive solution was 1 cm^2. The same set-up and instrument were used as described in section 12.2.1.1. The perturbation signal used contained respectively excited frequencies situated between 50 mHz and 20 kHz. The amplitude of the excitation signals was set to 1 mV_{RMS}. Five consecutive periods of the excitation signals were measured.

15.4.2 Bare lead sample

An ORP-EIS study of a bare lead sample in 100 mL electrolyte consisting of 5 µg L^{-1} acetic acid and 0.1 M TBAB was already performed in chapter 12.2. We will use these data to compare them with the coated samples. To be able to compare the bare and coated sample, we will use the inhibition efficiency value as described in Eq. 8.42. For the R_{ct}^0

value, we will use the R_{ct} values of the first EIS measurements during the lead oxide dissolution time frame. These values represent the protective properties of the native lead oxide layer. This way we compare the protective properties of the coating with the native protection of the bare lead sample.

15.4.3 Time lapse EIS study of the polymer coatings

In this section, we describe and fit the consecutive odd random phase impedance data from a sample coated with copolymer 2, copolymer 3 and copolymer 5 in the acetic acid corrosive medium.

15.4.3.1 Sample coated with copolymer 2

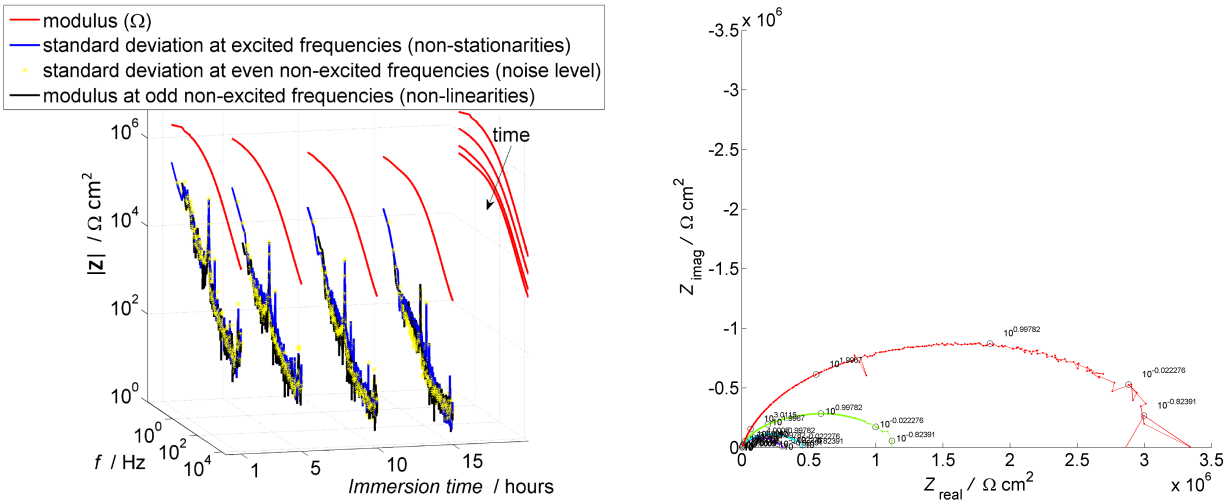


Figure. 15.9 – (a) Magnitude Bode plot ('full red line'), non-stationarities ('full blue line'), non-linearities ('full black line') and the noise level ('∗') and (b) Nyquist plots of the measurement of a coated lead sample with copolymer 2 corroded in an acetic acid solution during the first 16 hours of immersion (hours of immersion are shown).

Figure 15.9a shows the magnitude Bode plot ('full red line'), non-stationarities ('full blue line'), non-linearities ('full black line') and the noise level ('∗') of the measurement of a lead sample coated with copolymer 2 corroded in an acetic acid solution. An evolution throughout the first 16 hours of immersion is observed. Since the noise level ('∗') coincides with the standard deviation at the excited frequencies ('full blue line') and the odd non-excited frequencies ('full black line'), a stationary and linear behavior is assumed [37]. The spikes at 50 Hz are a consequence of the power line frequency. In order to visualize the mass transfer processes of species involved in the corrosion process, the Nyquist plots are shown in Figure 15.9b.

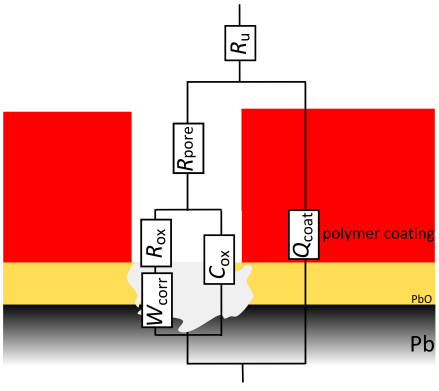


Figure. 15.10 – The EEC used for the simulation of the experimental impedance spectra of the damaged polymer coating.

The EIS measurements for the lead sample coated with copolymer 2 recorded in the corrosive solution are simulated using the model shown in Figure 15.10. This model includes the solution resistance, R_u, in series with a parallel combination of the CPE of the coating, Q_{coat}, and the pore resistance of the coating, R_{pore}, in series with a parallel combination of the capacitance, C_{ox}, and the resistance of the oxide layer, R_{ox} combined with the mass transfer process of ionic species in the coating's pores corroding the metal, W_{corr}. To consider the non-ideal behavior of the organic coating, the contribution of the capacitive element of the organic layer to the total impedance is generally obtained by using a CPE [38] as described in section 8.1.3.3. The non-ideal CPE behavior is characteristic for the film properties: variable thickness, inhomogeneity and overall changing penetration depths [39]. During the fitting procedure, the measured noise is used as a weighing factor.

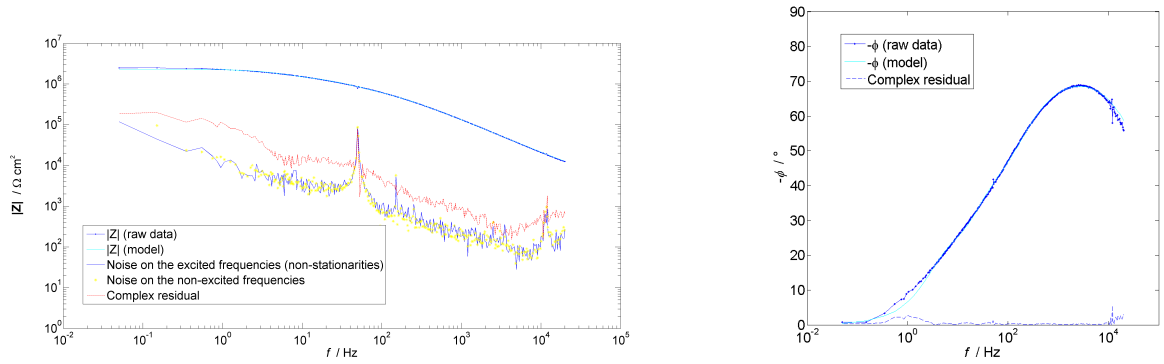


Figure. 15.11 – Magnitude plot, modeled curve, residual curve, noise on the excited frequencies and noise on the non-excited frequencies at the last calculated time instant of the measurement at 2 hours of immersion.

Figure 15.11 presents the magnitude Bode plot, modeled curve, residual curve and the different noise levels (noise on the excited frequencies and noise at the non-excited frequencies at 2 hours of immersion. Because the raw data show a stationary and linear behavior, the data can be directly fitted using the proposed model. Visually, an excellent fit was obtained with the proposed model ('cyan line') for the recorded experimental data ('.'). To have a better idea on the model fit, we take a look at the complex residual, which is the calculated difference between the modeled data and the raw data. A good fit implies that this complex residual plot ('broken red line') is situated close to the measurement's noise level. Furthermore, it is observed that the residual relative error is less than 2% (except for the points at the lowest frequencies, where the residual relative error is less than 15%). Because the residual error is small enough, it is feasible to accept the proposed EEC model. The quick water uptake, the coating's inhomogeneity and the diffusion of ionic species into the coating explain the higher relative errors at the lowest frequencies. In the following subsections, the important fitted parameters with standard deviations are shown and discussed.

Corrosion parameters

Figure 15.12 shows the evolution of the corrosion parameters of the lead oxide layer. The R_{ox} parameter, coupled with the oxide layer below the coating, exhibits a decreasing trend. The corrosion reaction has an influence on the EIS data from the beginning of the measurement, which means some damaged areas are present on the coated sample from the start. In the beginning, these R_{ox} values are highly unstable, which is attributed to the sudden changes around the oxide interface due to the dissolution process (decreasing the resistance) and the formation of new precipitated corrosion products (increasing the resistance) [40]. Close to the end of the measurement a dissolution-precipitation equilibrium is set, explaining the decreasing errors. Overall, the R_{ox} values are high compared to the bare sample as described in section 15.4.2 suggesting a difficult exchange of electrons between the solution and the metal caused by the coating's inhibition properties. After

15 hours of immersion, R_{ox} value is close to 0 Ωcm^2, which indicates that the oxide layer is completely dissolved.

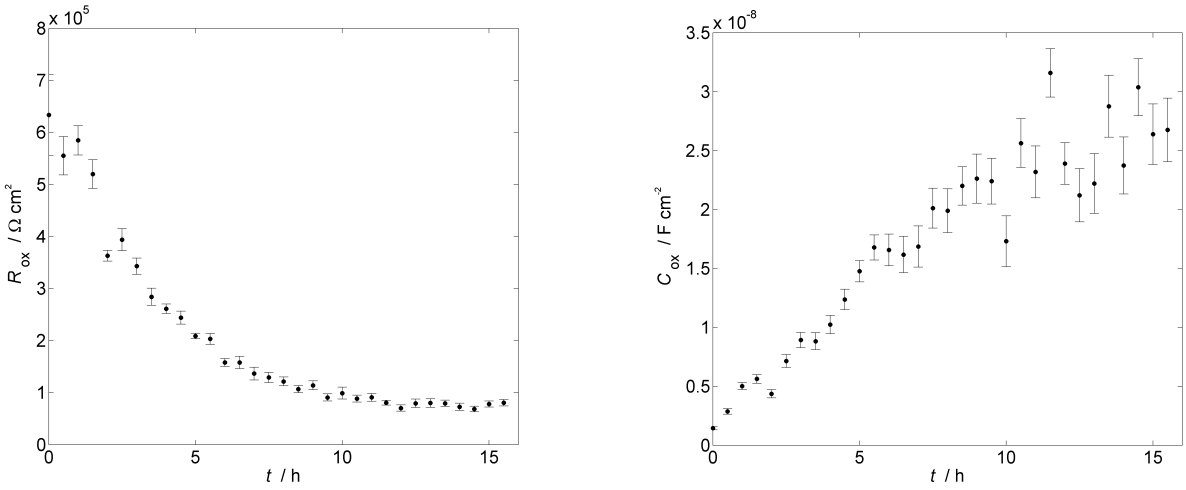


Figure. 15.12 – Evolution of (a) the resistance of the oxide and (b) the capacitance of the oxide layer vs the time.

The C_{ox} values show an increasing trend indicating that the area of the lead metal/oxide interface increases due to the delamination of the coating and the formation of small pits in the metal ($C \uparrow \approx A \uparrow / d$). The unstable values explain the continuous corrosion ensuring a constant change around the sample's corroded area during the immersion. After 10 hours of immersion, a semi-infinite diffusion process connected to the corrosion reaction at the lead oxide surface starts to appear. This means there are holes in the coating layer, due to delamination, allowing the formation of corrosion products around damaged areas on the sample. Indeed, the dissolution process going on at the surface shows an important mass transfer process. The formed lead ions diffuse away from the surface to the corrosive solution. Looking at the SEM-EDS data in Figure 15.18A, corrosion reactions at the lead oxide are only seen around weak points in the coating. To compare the R_{ox} value of the coating with the R_{ct} value of the bare sample, we calculate the inhibition efficiency at the end of the immersion. The η_{IE} value is 99%, which means still a large area of the sample is protected. The SEM image in Figure 15.18A confirms this statement.

Coating thickness and water uptake

Figure 15.13a, R_{pore} has been interpreted as the resistance against the penetration of the electrolyte [42–44] through small pores in the coating [45]. The coating's pores are gradually filled with the corrosive electrolyte, so that the R_{pore} value exhibits a small global decreasing tendency. At the end of the measurement, the water uptake process proceeds slower explained by the stabilizing value.

In Table 15.5, the coating thickness was measured using the Eddy current coating thickness probe DCXX-3000PRO (Checkline Europe, The Netherlands) with a precision, in the thickness range of the studied coatings, of $\pm$ 2 µm. The thickness results are the mean and standard deviation value of 30 measurements. Using the ORP-EIS measurements at t = 0, the $C_{eff,coat}$ value gives us information about the coating's thickness and dielectric behavior. First, the CPE of the coating representing the coating's protective properties, is recalculated to a pseudo-capacitance, using the formula of Brug [46] as described in section 8.1.3.3. Using the simplified Helmholtz model given by Eq. 12.19, the coating thickness can be calculated using the relative permittivity value of a non-electroactive polymer (ϵ_r = 2.0 - 3.5 [41] - we used a value of 2.5) as seen in Table 15.5. During the immersion, the C_{coat} value changes due to the water uptake of the coating.

All coatings in Table 15.5 present a different thickness, which is the consequence of the deposition method. Precipitation happens faster, when the polymer chains have a higher molecular weight and/or have a higher acrylic acid content. The

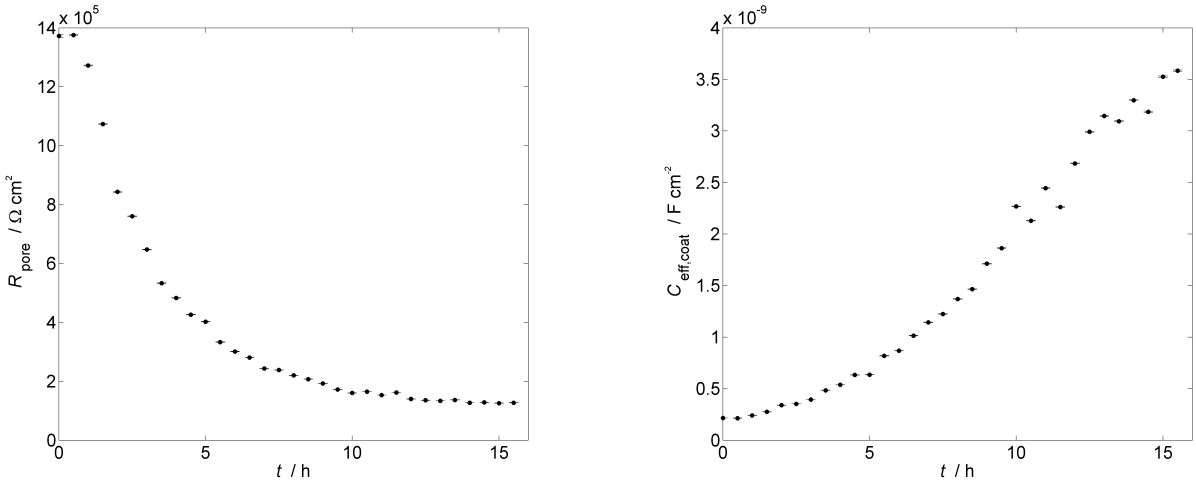


Figure. 15.13 – Evolution of (a) the pore resistance and (b) the effective capacitance of the copolymer 2 coating vs the time.

	copolymer 2	copolymer 3	copolymer 5
Eddy current probe	8 ± 2	5 ± 3	13 ± 1
Impedance data	10.5 ± 0.3	19.5 ± 0.3	16.7 ± 0.3

Table 15.5 – Coating thickness values (in μm)

higher acid content ensures a faster reaction with the lead oxide present on the surface and thus a faster deposition of the polymer on the sample.

In what follows, we discuss the water uptake of the coating, which results in the swelling of the hydrophobic polymer. Figure 15.13b shows the evolution of the coating's effective capacitance vs the time. The acrylic coating's pseudo-capacitance increases during the complete immersion time, but close to the end, we measure a stagnating value as shown in Figure 15.13b. The increase is easily explained by the introduction of water in the polymer film. As known from section 12.2.7.1, the $C_{\text{eff,coat}}$ can be expressed by the Helmholtz model described in Eq. 12.19 for a homogeneous coating. This model shows that $C_{\text{eff,coat}}$ can be considered proportional with the dielectric constant when the geometrical parameters are constant. Taking into account this assumption, the relative permittivity is calculated by using the measured capacitance from the EIS measurements as seen in Figure 15.14a. The increase in the relative permittivity ϵ_r (relative dielectric constant) of the material is a result of an increase of the polarisability as a consequence of the water uptake of the film. Naturally, the assumption of a constant thickness is not always true considering the swelling of the coating's polymeric matrix. However, Figure 15.14a gives us a good approximation.

Knowledge on the dielectric properties of the coating, makes it possible to calculate of the amount of water absorbed by the polymer coating. In most cases, water is heterogeneously distributed in the polymer matrix explained by the presence of pigments, defects, holes and areas with different chemical composition or curing [38]. Actually, Deflorian [38] says that "[t]he polymeric matrix is saturated after the beginning of the water accumulation in specific weak points of the coating." These saturated weak points can be interpreted as the cause of the local corrosion reactions as described in section 15.4.3.1. However, as an approximation, we can consider a homogeneous distribution of water in the film. Brasher and Kinsbury [47] proposed an empirical relation between the coating capacitance and the volume fraction of water in the coating described by [48],

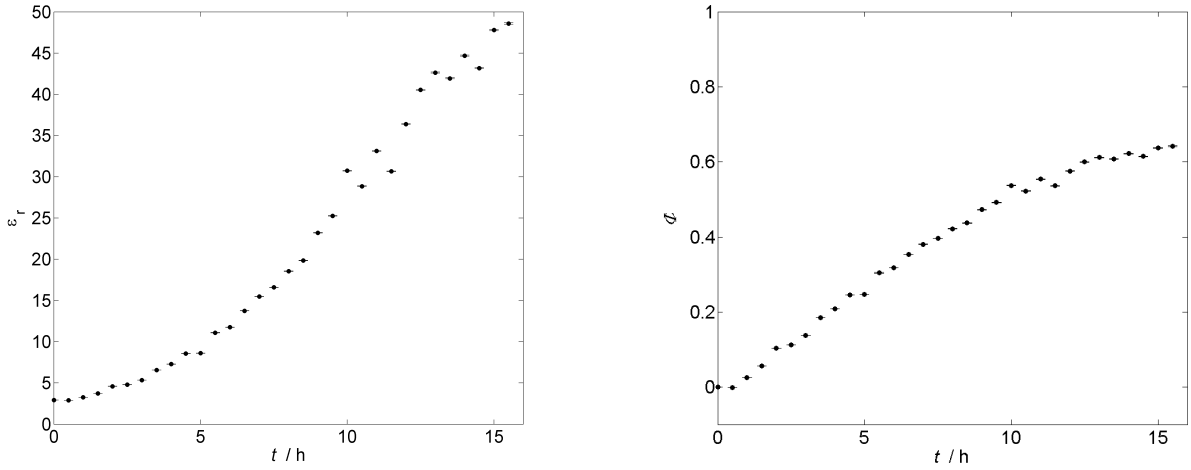


Figure. 15.14 – Evolution of (a) the dielectric constant and (b) the volume fraction of water of the copolymer 2 coating vs the time.

$$\Phi = \frac{\log\left(C_t/C_0\right)}{\log 80}, \tag{15.2}$$

where Φ is the volume fraction of water in the coating, C_t is the capacitance of the film at time t, C_0 is the capacitance of the film at time t = 0, and 80 is the relative permittivity of water at T = 20°C. For a homogeneous distribution of water in the film, the evolution of the volume fraction of water is given in Figure 15.14b. The theory predicts a gradual filling of the polymer coating with water till the volume fraction of water in the coating is around 65%. At that moment, the coating is completely saturated with water.

Furthermore, the determination of the water uptake of a polymer film that is immersed in water can also be performed by using the weight gain as described by Crank and Park for a constant exterior concentration, an initially dry film, and the assumption of ideal Fickian diffusion [49] using

$$\frac{M_t}{M_\infty} = 1 - \left(\frac{8}{\pi^2}\right)\sum_{i=0}^{\infty}\frac{1}{(2i+1)^2}\exp\left[-\frac{(2i+1)^2\pi^2 Dt}{d^2}\right], \tag{15.3}$$

where i = 0,1,2,$\cdots$,M_t is the absorbed or desorbed mass at time t (kg), M_s is the absorbed or desorbed mass at infinite time (kg) and d is the thickness of polymer film (m). As an approximation, the quotient $\frac{M_t}{M_\infty}$ can be replaced by $\frac{V_t}{V_\infty}$, where V_t and V_∞ represent the volume of water absorbed by the coating, respectively at time t = 0 and $t = \infty$. Taking the approximation,

$$\frac{V_t}{V_c + V_t} \approx \frac{V_t}{V_c} = \Phi, \tag{15.4}$$

where V_c denotes the coating volume, which means we assume that no swelling occurs. The ratio $\frac{V_t}{V_c}$ is equal to the volume fraction of water taken up by the coating, which is Φ from Brasher's formula in Eq. 15.2.

Based on Eq. 15.3, a nonlinear least squares fitting algorithm can be introduced using only the first two exponential terms of the expansion as described by [48]

$$Y = P1\left(1 - \frac{8}{\pi^2}\exp\left(-\pi^2 P2t\right) - \frac{8}{9\pi^2}\exp\left(-9\pi^2 P2t\right)\right) + P3 \tag{15.5}$$

where $P1$, $P2$, $P3$ are the fitting parameters, $P1 = \log(\frac{C_\infty}{C_0})$; $P2 = \frac{D}{l^2}$; $P3 = \log(C_0)$; t is the independent variable (exposure time, s); Y is the dependent variable $\log(C_t)$, C_0 is the capacitance at $t = 0$ and C_∞ is the capacitance at infinite time. In Figure 15.15, the fitting results are shown. Based on the fitting parameters, C_∞ is predicted to be 4.6 nF. Using the diffusion coefficient of bromine ions in water (1.18×10^{-9} m^2s^{-1}), the film thickness of 11.02 µm is calculated using the fitting parameters. The deviation at low immersion times is explained by the approximation due to the fact that the theory assumes a homogeneous distribution, which is not the case at the start of the measurement as the coating is still filling with electrolyte.

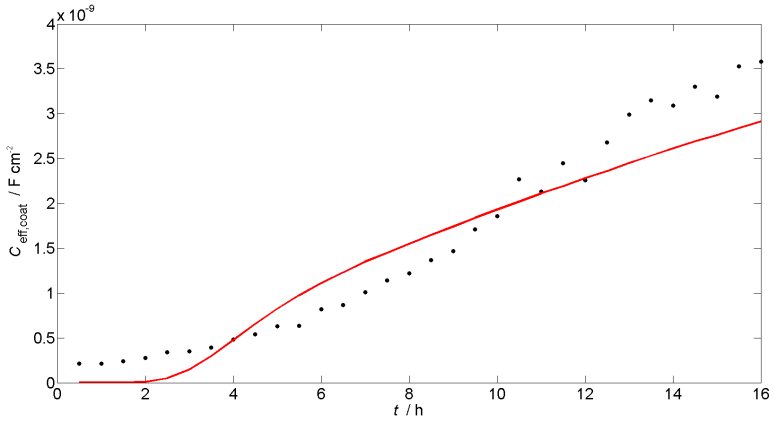


Figure. 15.15 – Fit results on the curve of the measured capacitance increase as function of time during water uptake.

Pore diffusion

Orazem and Tribollet [50] stated that "[p]orous nonreacting layers covering reacting metallic interfaces may slow down the mass transfer of diffusing species." This means that the diffusion processes detected using impedance spectroscopy provide valuable information about the diffusion and conductance in polymers [51, 52]. A schematic representation of the system under investigation is depicted in Figure 15.16. In this case, the total concentration gradient is divided between the electrolyte and the porous film.

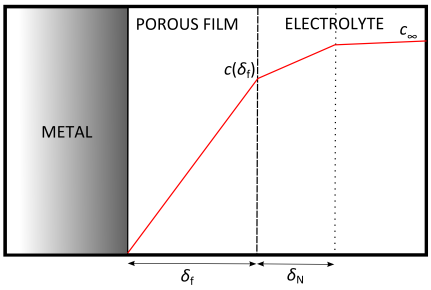


Figure. 15.16 – Schematic representation of a sample surface covered with a porous film with film thickness ,δ_f, Nernst diffusion layer, δ_N, and the concentration of the electroactive species which reacts at the interface and diffuses through the film [50].

By converting the second Fickian law for planar diffusion in Eq. 8.21 to the Laplace domain with variable s, we get [53]

$$sC(x,s) = D\frac{\partial^2 C(x,s)}{\partial x^2}. \tag{15.6}$$

With the aid of the complex number $\lambda = \left(\frac{\omega_d}{s}\right)^{1/2} L$, we can rewrite Eq. 15.6 to [54]

$$\frac{\partial^2 C(x,s)}{\partial x^2} - \frac{1}{\lambda^2} C(x,s) = 0, \tag{15.7}$$

with the diffusion time constant $\omega_{\mathrm{d}} = \frac{D}{\delta^2}$ where δ is the thickness of the diffusion layer, which, in the case of a coated system, can be treated as the coating thickness [50, 55, 56].

At the metal/coating interface (x = 0), both the potential and the current are related to the oscillating concentration [54] as described by the semi-infinite Warburg impedance. However, at the coating/electrolyte interface ($x = \delta_{\mathrm{f}}$), the polymer coating is characterized by a totally absorbing boundary condition for the small ac oscillating described as

$$(C = 0)_{x=L} \tag{15.8}$$

Using the same reasoning as in section 8.1.3.2 and the proposed boundary conditions, one gets,

$$\mathbf{Z} = \frac{\mathbf{Z}_{\mathrm{W}}}{\sqrt{j\omega}} \tanh\left[\left(\sqrt{\frac{j\omega}{\omega_{\mathrm{d}}}}\right)\right]. \tag{15.9}$$

Based on this equation, two regimes of the diffusion behavior are separated by the frequency ω_{d}. For $\omega \gg \omega_{\mathrm{d}}$, the particles will not sense the boundary at $x = \delta_{\mathrm{f}}$, so that the system will behave as for semi-infinite diffusion. At low frequencies $\omega \ll \omega_{\mathrm{d}}$, the admittance is given by [54]

$$\mathbf{Y} = \frac{1}{\mathbf{Z}_{\mathrm{W}}} + \frac{1}{3} j\omega C_{\mathrm{f}} \tag{15.10}$$

where C_{f} is the diffusion capacitance.

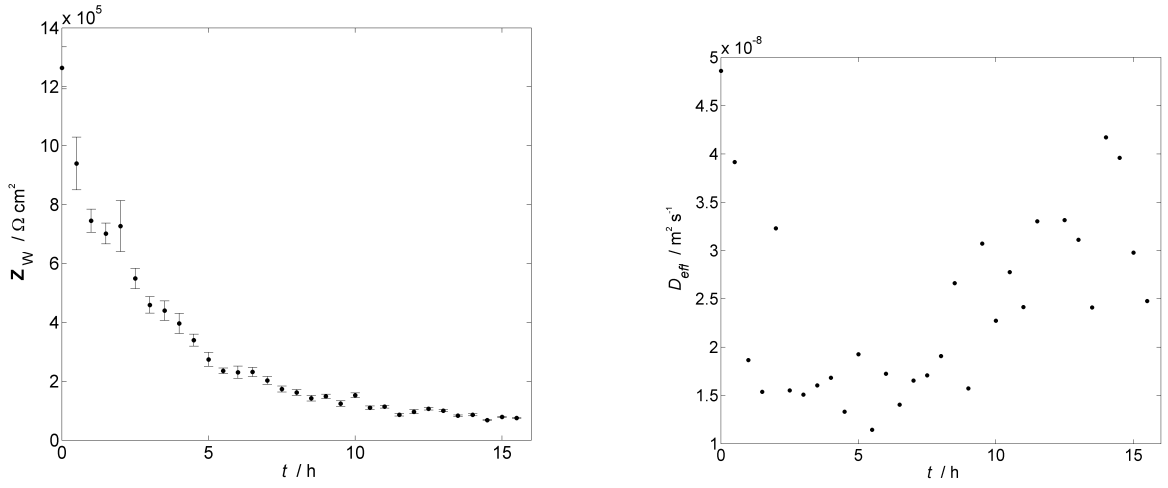


Figure. 15.17 – Evolution of (a) the diffusion impedance and (b) the effective diffusion coefficient as a function of immersion time for the copolymer 2 coating.

Fitting the raw data with the impedance for finite diffusion in Eq. 15.9 for the Warburg element, W_{corr} in Figure 15.10, we can calculate the diffusion impedance, $\mathbf{Z}_{\mathrm{W}}$, and, using the diffusion time constant, ω_{d}, the effective diffusion coefficient, D_{eff}, which was introduced to describe the through-pore diffusion and expressed as [57]

$$D_{\mathrm{eff}} = \frac{D\epsilon_{\mathrm{t}} c}{\tau} \tag{15.11}$$

where ϵ_{t} is the porosity available for transport, c is the constrictivity and τ is the tortuosity. This D_{eff} value tells us how

fast the ions diffuse in the porous medium from a high to a low concentration. Eq. 15.11 stipulates a clear relationship between the number of pores or void fractions and the corresponding effective diffusion coefficient through the coating [58].

In Figure 15.17 the evolution of the diffusion impedance and the effective diffusion coefficient is shown using the fitted parameters of the EIS data. Figure 15.17a shows an exponential drop of the diffusion impedance as a function of the immersion time. From the start of the immersion, water enters the coating's pores, increasing diffusion through the coating and, therefore, decreasing the resistance against diffusion. This means the water uptake of the coating shows an exponential profile. The water uptake starts to enter the coating very fast in the beginning, going much slower towards the end when the coating is saturated with the electrolyte. The D_{eff} values, in Figure 15.17, show a constant value around the start of the immersion. When the coating is saturated, the effective diffusion coefficient increases due to the formation of new conductive pathways in the coating. To summarize, the filling of pores leads to the decrease of the Warburg diffusion impedance and the formation of new pores leads to a higher effective diffusion coefficient. Furthermore, the coating thickness and the porosity of the coating have a direct influence on the $\mathbf{Z}_{\text{W}}$ and the D_{eff} value.

15.5 SEM-EDS analysis

Figure 15.18 shows the SEM images and the EDS spectra of the coated lead samples using (a) copolymer 2, (b) copolymer 3 and (c) copolymer 5. These pictures are compared to the bare sample in Figure 12.17a. First of all, comparing the coated samples with the bare sample, we see no direct evidence of diamond and silicon particles due to the polishing in the EDS maps. Furthermore, as for all previous coatings, the SEM images display no polishing scratches indicating a coating has been deposited. The EDS maps indicate the formation of a homogeneous coating. The SEM images, however, exhibit the presence of particles and/or clusters, which can be explained by two hypotheses: (1) the coating covers the polishing particles and/or (2) the reaction of the copolymer forms clusters on the surface. Based on previous experience, it is more likely the coating covered the particles.

Figure 15.18a shows that parts of the sample are not covered with a coating especially in the magnification of the specific area indicated by white rectangle. The inhomogeneous coverage of the surface is a consequence of the uncontrollable deposition of the dissolved copolymer. Moreover, the EDS map shows specific areas with elevated bromine concentrations, which indicates lead corrosion due to the formation of insoluble lead bromide crystals. The SEM image clearly exhibits cracks at weak points in the coating around the area where the elevated bromine concentrations are observed. Indeed, the extra Voigt element in the EEC circuit for the fitting of the raw impedance data as described in section 15.4.3 and in Figure 15.10b explains the presence of damaged areas on the surface. The EDS maps of the other elements show a homogeneous distribution throughout the surface indicating the formation of an uninterrupted homogeneous coating. The coatings in Figure 15.18b and c show no evidence of corrosion. In this case, the coating is clearly not crystalline, because to regular shapes are recognized scanning the coated surface as seen for the lead dodecanoate coatings in Figure 9.5.

Next to EDS maps, the total wt% of the different elements calculated using a standardless method contains valuable information. The total wt% of lead, measured using EDS, gives us a relative indication of the coating thickness. The lowest lead concentration characterizes the thickest coating due to the attenuation of the lead signal. This means copolymer 3 and 5 produce a thicker coating compared to copolymer 2. Based on the acrylic acid content in the copolymer, calculated using the ^{1}H NMR data in Table 15.2, it is possible to calculate the theoretical C / O ratio of all coated copolymers. For all copolymers, we calculated the C / O ratio, using the atom's molecular weights to be 4. As seen from the EDS maps, the C / O ratios based on the wt% are calculated to be 4, which means we can prove that the

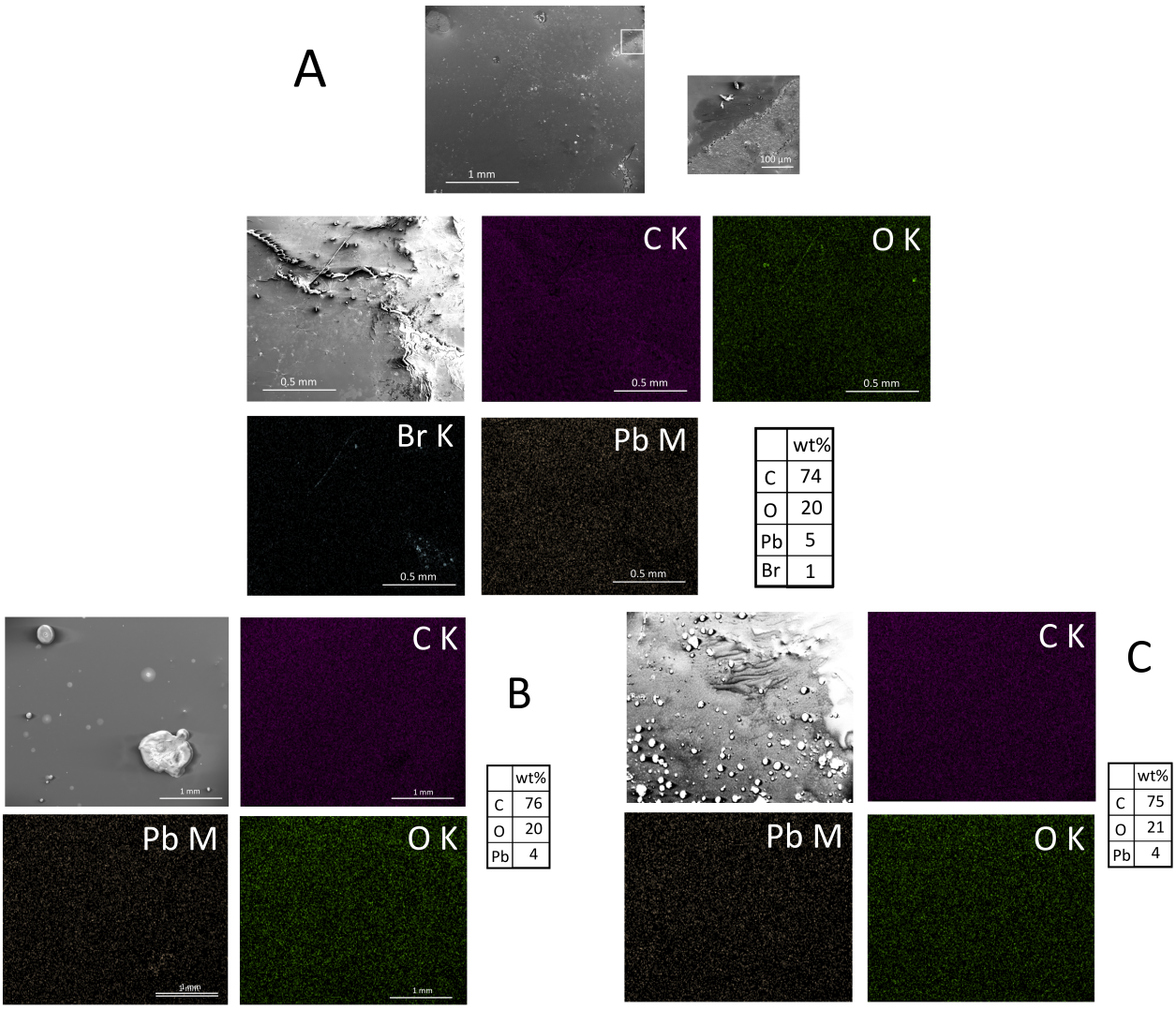


Figure. 15.18 – The SEM images and the EDS spectra of the coated lead samples using (a) copolymer 2, (b) copolymer 3 and (c) copolymer 5 after the corrosion test.

proposed coating is present.

15.5.0.1 Sample coated with copolymer 3 and 5

Figure 15.19a shows the magnitude Bode plot ('full red line'), non-stationarities ('full blue line'), non-linearities ('full black line') and the noise level ('$*$') of the measurement of a lead sample coated with copolymer 5 corroded in an acetic acid solution. An evolution throughout the first 16 hours of immersion is observed. Since the noise level ('$*$') coincides with the standard deviation at the excited frequencies ('full blue line') and the odd non-excited frequencies ('full black line'), a stationary and linear behavior is assumed [37]. In order to visualize the mass transfer processes of species involved in the corrosion process, the Nyquist plots are shown in Figure 15.19b. An important finite diffusion process is noticed in the low (< 1 Hz) frequency region during the immersion.

The EIS measurements for the lead sample coated with copolymer 3 and 5 recorded in the corrosive solution are simulated using the model shown in Figure 15.10. This model includes the solution resistance, R_{u}, in series with a parallel combination of a coating capacitance, Q_{coat}, and the pore resistance of the coating, R_{pore}, which in series with the capacitance C_{ox} and resistance of the oxide layer, R_{ox}, combined with a mass transfer process due to corrosion W_{corr}. This suggests that the already formed lead oxide layer reacts with the solution so that mass transfer processes start.

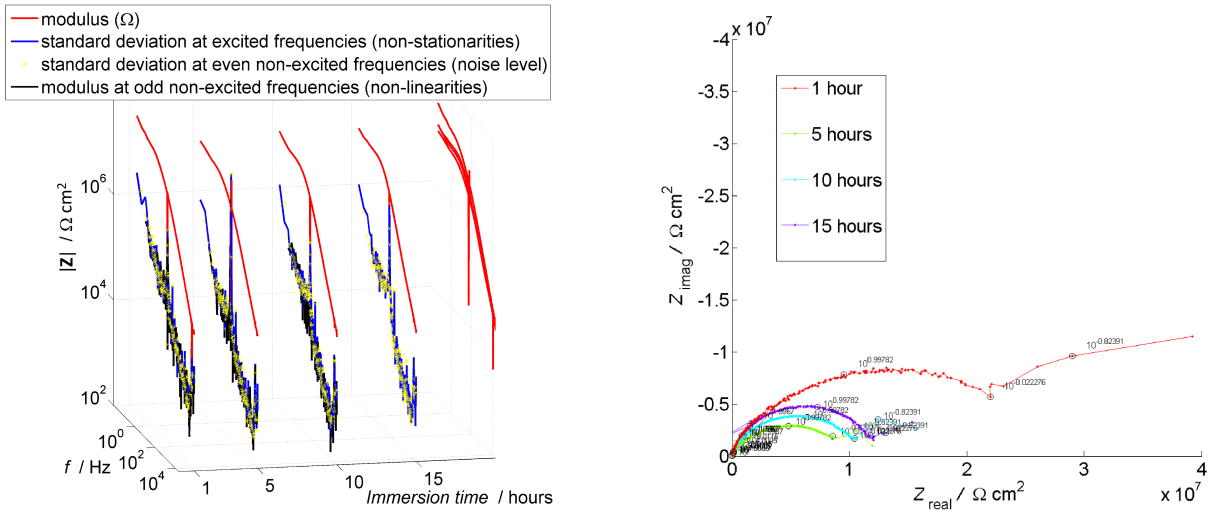


Figure. 15.19 – (a) Magnitude Bode plot ('full red line'), non-stationarities ('full blue line'), non-linearities ('full black line') and the noise level ('∗') and (b) Nyquist plots of the measurement of a coated lead sample with copolymer 5 corroded in an acetic acid solution during the first 16 hours of immersion (hours of immersion are shown).

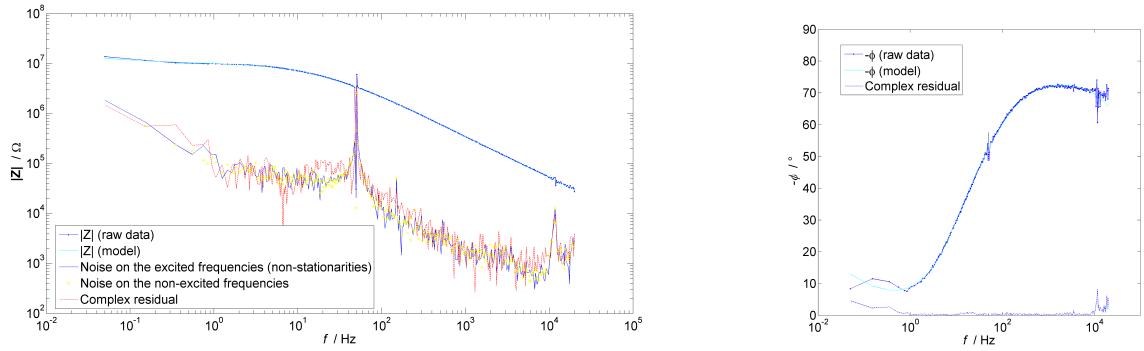


Figure. 15.20 – Magnitude plot, modeled curve, residual curve, noise on the excited frequencies and noise on the non-excited frequencies at the last calculated time instant of the measurement at 15 hours of immersion.

Figure 15.20 presents the magnitude Bode plot, modeled curve, residual curve and the different noise levels (noise on the excited frequencies and noise at the non-excited frequencies) at 15 hours of immersion. Because the raw data show a stationary and linear behavior, the data can be directly fitted using the proposed model. Visually, an excellent fit was obtained with the proposed model ('cyan line') for the recorded experimental data ('.'). To have a better idea on the model fit, we take a look at the complex residual, which is the calculated difference between the modeled data and the raw data. A good fit implies that this complex residual plot ('broken red line') is clearly situated within the measurement's noise level. Furthermore, it is observed that the residual relative error is less than 2% (except for the points at the lowest ($<$ 1 Hz) frequencies, where the residual relative error is less than 20%). The deviations of the raw data at low ($<$ 1 Hz) frequencies are a consequence of the reactions in the oxide layer. In the following subsections, the important fitted parameters with standard deviations are shown and discussed for the copolymer 5 coating. The results for the copolymer 3 coating are comparable.

Electrolyte uptake

In Figure 15.21a, at the start of the measurement, it is seen that the coating's pores are gradually filled with the corrosive electrolyte, so that the R_{pore} value exhibits a decreasing tendency. Due to the thicker coating, the R_{pore} value is higher compared to the copolymer 2 coating. Some deterioration of the coating (pore formation - no delamination) is seen in the

SEM images in Figure 15.18c. The R_{pore} value drops much faster compared to the copolymer 2 coating, which means a faster formation of pores in the coating. In this case, no uncoated areas are present at the start of the measurement, which means all the electrolyte has to pass through the coating before corrosion can take place. Therefore, all corrosion products are formed in the coating's pores. After 3 hours of immersion, the R_{pore} value increases due to the formation of corrosion products within the coating's pores so that they are partly blocked. The spots in the SEM image in Figure 15.18c could explain the local formation of corrosion products. At the end of the measurement, the coating's pores are completely filled with corrosive products explained by the stabilizing R_{pore} value.

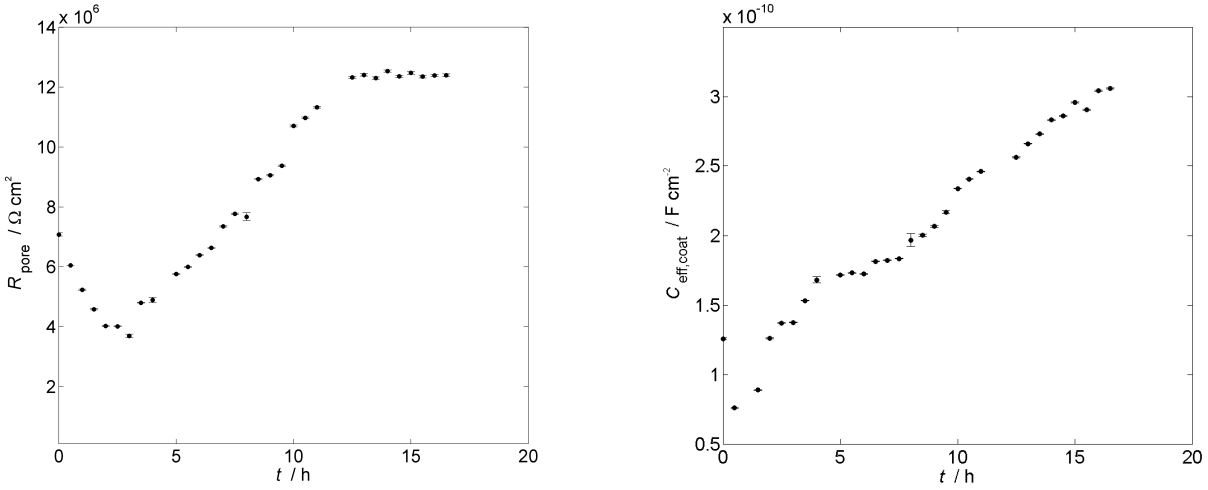


Figure. 15.21 – Evolution of (a) the pore resistance and (b) the effective capacitance of the copolymer 5 coating vs the time.

Corrosion parameters

Figure 15.22 shows the evolution of the corrosion parameters of the lead oxide layer. The R_{ox} parameter, coupled with the oxide layer below the coating protected by the coating, exhibits a slow decreasing trend. In the beginning, these R_{ox} values are stable, which is attributed to the stable oxide layer. After 10 hours of immersion, the oxide layer is damaged indicating a corrosion process explaining the unstable values. The increase of the R_{pore} values does not stop the surface from corroding. Overall, the R_{ox} values are high compared to the bare sample as described in section 15.4.2 suggesting a difficult exchange of electrons between the solution and the metal caused by the coating's inhibition properties. After 12 hours of immersion, R_{ox} value is close to 0 Ωcm^2, which indicates that the oxide layer is completely dissolved.

The C_{ox} values show an unchanging trend indicating that the oxide layer is stable. The unstable values around 10 hours of immersion explain the start of the corrosion process. This means there are pores in the coating layer allowing the formation of corrosion products around damaged areas under the coating. To compare the R_{ox} value of the coating with the R_{ct} value of the bare sample, we calculate the inhibition efficiency at the end of the immersion. The η_{IE} value is 99%, which means still a large area of the sample is protected. The SEM image in Figure 15.18c confirms this statement.

Diffusion process

Figure 15.23 shows that the Warburg element connected to the corrosion reaction at the lead oxide surface is dominant starting from 10 Hz. Indeed, the dissolution process going on at the surface shows an important mass transfer process. The formed lead ions diffuse away from the surface to the corrosive solution. After 15 hours of immersion, the Warburg contribution is not detected. At that moment, lead corrosion products have formed (also bromides) in the solution and precipitate on the surface blocking partly the pores in the coating slowing down the diffusion process.

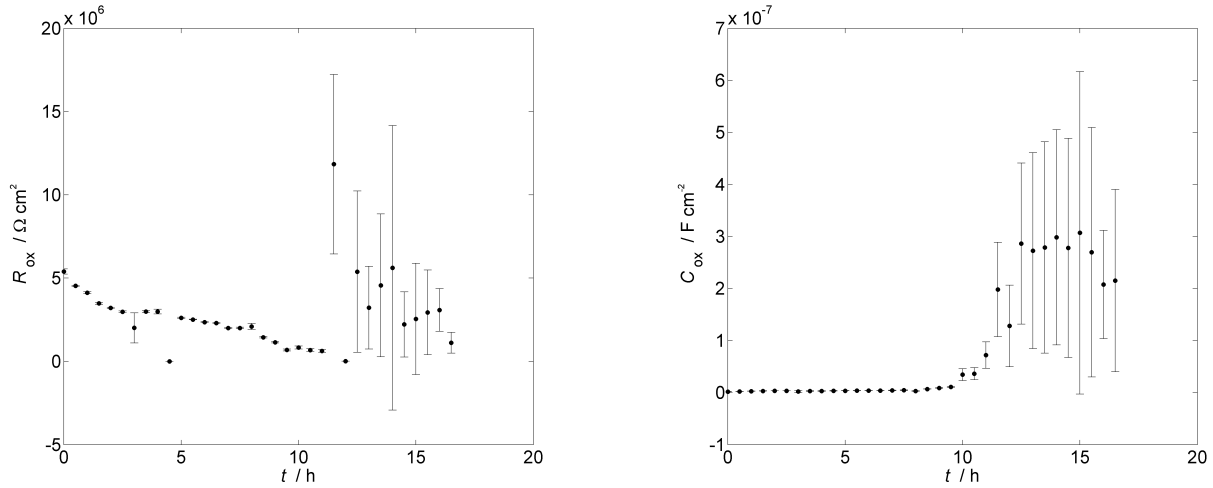


Figure. 15.22 – Evolution of (a) the resistance of the oxide and (b) the capacitance of the oxide layer vs the time.

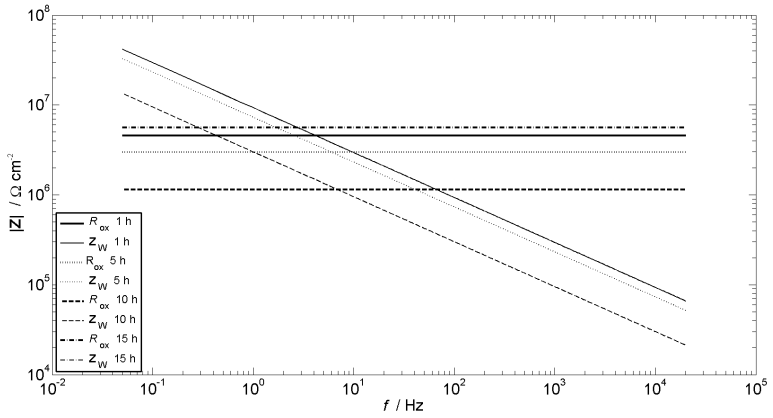


Figure. 15.23 – The EEC used for the simulation of the experimental impedance spectra of the protecting polymer coating.

15.6 Conclusions

The polymer molecules partly chemically react with lead metal ions present at the lead substrate surface. It is clear that not all carboxylic acid groups present in the polymer chain react with lead sample surface. The formed Pb-O bonds act as linkers between two chains making it more likely the formed compounds will precipitate on the surface to from a coating. The coordination of the carboxylate groups around the lead metal atom is defined as an asymmetric bridging bidentate bond. In this case, no sintering process is needed to produce a non-sticky surface. However, a sintering process could provide some modifications to the coating, which could have a beneficial effect on the coating. Furthermore, the organic solvent has no influence on the protective properties of the coating.

Electrochemical impedance spectroscopy seems to very useful for the study of coating degradation mechanisms. This technique has the advantage to look at and identify various processes such as water uptake, formation of conductive pathways, start of corrosion processes, diffusion processes in the coating, $\cdots$ The use of fast multisine measurements gives us the opportunity to get valuable mechanistic information of the coating. Comparing the identified processes with sources in literature, opens the possibility to verify the proposed model. However, the construction and fitting of the EEC model has to be done with care.

The shapes of all the raw ORP-EIS plots do not vary with the presence of other coatings explaining similar processes going

on in the coating and at the metal/coating interface. Indeed, the models predict the same processes for all the coatings. The EIS and SEM data clearly indicate a homogeneous damaged coating and the start of delamination processes around the unprotected areas. Furthermore, semi-infinite diffusion processes due to corrosion are identified.

The thickness of the coating depends on the molecular weight and the acrylic acid content of the polymer. All coatings show an exponential profile for the water uptake. At the start of the measurement, water uptake goes very fast until the coating is completely saturated with water. The saturation point and the speed of the water uptake depend on the acrylic acid content.

The diffusion profile of the copolymer 2 coating clearly shows that the diffusion coefficient is constant around the start of the immersion during the water uptake process. When the coating is saturated, the effective diffusion coefficient increases due to the formation of new conductive pathways in the coating. The profile of the thicker protective coatings are characterized by an increase as a consequence of the filling of the pores of the coating. Afterwards, the coating defects are clogged with corrosion products, so that the diffusion processes in the coating are slowed down.

References for Chapter 15

[1] W. VAN CAMP, Novel routes for the design of poly ((meth)acrylic acid) containing polymer structures by controlled radical polymerization, PhD thesis, Ghent University, 2007, 79–118.

[2] W. BAO et al., Acetylene from the co-pyrolysis of biomass and waste tires or coal in the H_2/Ar plasma, *Energ. Source Part A* **37** (2008), 609–614.

[3] Y. NAKANE, M. ISHIDOYA, and T. ENDO, Synthesis and thermal dissociation of polymers having hemiacetal ester moieties, *J. Polym. Sci. A* **37** (1999), 609–614.

[4] P. ESCALÉ et al., Highly structured pH-responsive honeycomb films by a combination of a breath figure process and in situ thermolysis of a polystyrene-block-poly(ethoxy ethyl acrylate) precursor, *Polym. Chem.* **4** (2013), 4710–4717.

[5] W. VAN CAMP, F. DU PREZ, and S. BON, Atom transfer radical polymerization of 1-ethoxyethyl (meth)acrylate: Facile route toward near-monodisperse poly((meth) acrylic acid), *Macromolecules* **37** (18) (2004), 6673–6675.

[6] S. LINGIER, Synthese van amfifiele graftcopolymeren op basis van hernieuwbare grondstoffen, PhD thesis, Ghent University, 2013, 46–72.

[7] C. FERGUSON et al., Ab initio emulsion polymerization by RAFT-controlled self-assembly?, *Macromolecules* **38** (6) (2005), 2191–2204.

[8] J. HYSLOP et al., RAFT polymerized nanoparticles: Influences of shell and core chemistries on performance for electrokinetic chromatography, *Electrophoresis* **35** (5) (2014), 728–735.

[9] S. VAN DE WALLE, Hypervertakte glycopolymeren gebruikmakende van gecontroleerde radicalaire polymerisatietechnieken, PhD thesis, Ghent University, 2014, 38.

[10] J. CHIEFARI et al., Living Free-Radical Polymerization by Reversible Addition−Fragmentation Chain Transfer: The RAFT Process, *Macromolecules* **31** (1998), 5559–5562.

[11] K. DAVIS and K. MATYJASZEWSKI, Statistical, gradient, block and graft copolymers by controlled/living radical polymerizations, in: *Statistical, gradient, block and graft copolymers by controlled/living radical polymerizations*, Springer, 2002, chap. 1, 1–13.

[12] M. SAVE et al., Synthesis by RAFT of amphiphilic block and comblike cationic copolymers and their use in emulsion polymerization for the electrosteric stabilization of latexes, *Macromolecules* **38** (2) (2005), 280–289.

[13] E. RIZZARDO et al., Tailored polymers by free radical processes, *Macromol. Symp.* **143** (1) (1999), 291–307.

[14] Z. WICKS et al., Polymerization and film formation, in: *Organic coatings*, 3rd, Wiley, 2007, chap. 2, 7–41.

[15] J. IZUNOBI and C. HIGGINBOTHAM, Polymer molecular weight analysis by ^{1}H NMR spectroscopy, *J. Chem. Educ.* **88** (8) (2011), 1098–1104.

[16] R. HOOGENBOOM et al., RAFT polymerization of 1-ethoxyethyl acrylate: A novel route toward near-monodisperse poly(acrylic acid) and derived block copolymer structures, *Macromolecules* **38** (18) (2005), 7653–7659.

[17] S. DE SMET, S. LINGIER, and F. DU PREZ, MacroRAFT agents from renewable resources and their use as polymeric scaffolds in a grafting from approach, *Polym. Chem.* **5** (9) (2014), 3163–3169.

[18] R. ABRAHAM et al., ^{1}H chemical shifts in NMR: Part 23, the effect of dimethyl sulphoxide versus chloroform solvent on ^{1}H chemical shifts, *Mag. Reson. Chem.* **44** (5) (2006), 491–509.

[19] J. COATES, Interpretation of infrared spectra: A practical approach, in: *Encyclopedia of Analytical Chemistry*, ed. by R. MEYERS, John Wiley & Sons, 2000, 10815–10837.

[20] P. TAHERI et al., Molecular interactions of electroadsorbed carboxylic acid and succinic anhydride monomers on zinc surfaces, *J. Phys. Chem. C* **115** (34) (2011), 17054–17067.

[21] W. POTTS, The use of infrared spectroscopy in characterization of polymer structure, in: *International symposium on plastics testing and standardization*, ASTM, 1959, 225–241.

[22] E. PALACIOS and A. MONHEMIUS, Infrared spectroscopy of metal carboxylates: I. Determination of free acid in solution, *Hydrometallurgy* **62** (3) (2001), 135–143.

[23] C. RAO and R. VENKATARAGHAVAN, The C=S stretching frequency and the "−N−C=S bands" in the infrared, *Spectrochim. Acta Mol. Biomol. Spectros.* **45** (1958) (1989), 299–305.

[24] M. MESUBI, An infrared study of zinc, cadmium, and lead salts of some fatty acids, *J. Mol. Struct.* **81** (1982), 61–71.

[25] M. GASGNIER, IR spectra of some potassium carboxylates, *J. Mater. Sci. Lett.* **20** (13) (2001), 1259–1262.

[26] K. PATIL et al., Infrared spectra and thermal decompositions of metal acetates and dicarboxylates, *Can. J. Chem.* **46** (2) (1968), 257–265.

[27] G. SHUSTAK, A. DOMB, and D. MANDLER, Preparation and characterization of n-alkanoic acid self-assembled monolayers adsorbed on 316L stainless steel, *Langmuir* **20** (18) (2004), 7499–7506.

[28] C. MORLAY et al., Potentiometric study of Cd (II) and Pb (II) complexation with two high molecular weight poly (acrylic acids); comparison with Cu (II) and Ni (II), *Talanta* **48** (1999), 1159–1166.

[29] O. BELAIDI, T. BOUCHAOUR, and U. MASCHKE, Molecular structure and vibrational spectra of 2-ethylhexyl acrylate by density functional theory calculations, *Org. Chem. Int.* **2013** (2013), 1–14.

[30] A. ARENAS et al., Thermophysical study of lead(II) n-alkanoates by DSC, optical microscopy, FTIR and Raman spectroscopy, *Liq. Cryst.* **18** (3) (1995), 431–441.

[31] D. LIN-VIEN et al., Organic sulfur compounds, in: *Infrared and Raman characteristic frequencies of organic molecules*, Academic Press, 1991, chap. 14, 225–251.

[32] P. NELSON and R. TAYLOR, Theories and experimental investigations of the structural and thermotropic mesomorphic phase behaviors of metal carboxylates, *Appl. Petrochem. Res.* **4** (3) (2014), 253–285.

[33] G. DEACON and R. PHILIPS, Relationships between the carbon-oxygen stretching frequencies of carboxylato complexes and the type of carboxylate coordination, *Coord. Chem. Rev.* **33** (1980), 227–250.

[34] R. KONRADI and J. RÜHE, Interaction of poly(methacrylic acid) brushes with metal ions: An infrared investigation, *Macromolecules* **37** (18) (2004), 6954–6961.

[35] V. ZELEŇÁK, Z. VARGOVÁ, and K. GYÖRYOVÁ, Correlation of infrared spectra of Zn(II) carboxylates with their structures, *Spectrochim. Acta Mol. Biomol. Spectros.* **66** (2) (2007), 262–272.

[36] A. POMOGAILO, G. DZHARDIMALIEVA, and V. KESTELMAN, *Macromolecular metal carboxylates and their nanocomposites*, Springer, 2010, 156.

[37] T. BRUEGELMANS, An identification approach as a prerequisite for quantitative electrochemical studies, PhD thesis, Vrije Universiteit Brussel, 2010.

[38] F. DEFLORIAN et al., Organic coating capacitance measurement by EIS: ideal and actual trends, *Electrochim. Acta* **44** (24) (1999), 4243–4249.

[39] C. SCHILLER et al., Validation and evaluation of electrochemical impedance spectra of systems with states that change with time, *Phys. Chem. Chem. Phys.* **3** (3) (2001), 374–378.

[40] T. HAUFFMAN et al., Dynamic, in situ study of self-assembling organic phosphonic acid monolayers from ethanolic solutions on aluminium oxides by means of odd random phase multisine electrochemical impedance spectroscopy, *Electrochim. Acta* **106** (2013), 342–350.

[41] Z. AHMAD, Polymeric Dielectric Materials, in: *Dielectric Material*, ed. by M. SILAGHI, 2012, chap. 1, 3–26.

[42] B. FASTRUP and A. SAARNAK, AC impedance of painted and scribed steel panels under atmospheric exposure, *Prog. Org. Coat.* **16** (3) (1988), 277–290.

[43] M. KENDIG, F. MANSFELD, and S. TSAI, Determination of the long term behavior of coated steel with AC impedance measurements, *Corros. Sci.* **23** (4) (1983), 317–329.

[44] F. MANSFELD, M. KENDIG, and S. TSAI, Evaluation of corrosion behavior of coated metals with AC impedance measurements, *Corros.* **38** (1982), 478–485.

[45] M. KENDIG and H. LEIDHEISER, The electrical properties of protective polymer coatings as related to corrosion of the substrate, *J. Electrochem. Soc.* **123** (1976), 982–989.

[46] G. BRUG et al., The analysis of electrode impedances complicated by the presence of a constant phase element, *J. Electroanal. Chem. Interf. Electrochem.* **176** (1984), 275–295.

[47] D. BRASHER and A. KINGSBURY, Electrical measurements in the study of immersed paint coatings on metal. I. Comparison between capacitance and gravimetric methods of estimating water uptake, *J. Appl. Chem.* **4** (2) (2007), 49–96.

[48] E. van WESTING, G. FERRARI, and J. de WIT, The determination of coating performance with impedance measurements II. Water uptake of coatings, *Corros. Sci.* **36** (6) (1994), 957–977.

[49] J. CRANK, *The mathematics of diffusion*, Oxford University Press, 1967.

[50] M. ORAZEM and B. TRIBOLLET, *Electrochemical impedance spectroscopy*, John Wiley & Sons, 2008, 1–525.

[51] K. KREUER et al., Proton and water transport in nano-separated polymer membranes, *J. Phys. IV* **10** (P7) (2000), 279–281.

[52] I. RUBINSTEIN, An AC-impedance Study of electrochemical processes at nafion-coated electrodes, *J. Electrochem. Soc.* **133** (4) (1986), 729.

[53] J. BISQUERT et al., Theoretical models for ac impedance of diffusion layers exhibiting low frequency dispersion, *J. Electroanal. Chem.* **475** (1999), 152.

[54] J. BISQUERT, Theory of the impedance of electron diffusion and recombination in a thin layer, *J. Phys. Chem. B* **106** (2) (2002), 325–333.

[55] V. FREGER, Diffusion impedance and equivalent circuit of a multilayer film, *Electrochem. Comm.* **7** (9) (2005), 957–961.

[56] V. WILLIAM GRIPS et al., Electrochemical behavior of single layer CrN, TiN, TiAlN coatings and nanolayered TiAlN/CrN multilayer coatings prepared by reactive direct current magnetron sputtering, *Thin Solid Films* **514** (1-2) (2006), 204–211.

[57] F. HO and W. STRIENDER, A variational calculation of the effective surface diffusion coefficient and tortuosity, *Chem. Eng. Sci.* **36** (2) (1981), 253–258.

[58] M. TATLER and A. ERDEM-ŞENATALAR, Estimation of the effective diffusion coefficients in open zeolite coatings, *Chem. Eng. J.* **102** (3) (2004), 209–216.

PART V

CONCLUSIONS AND FUTURE WORK

16

Summary of the results and conclusions

During my work, the main goal was to prevent the corrosion of lead and lead alloy artifacts. As previously established, the research concerning the protection of objects proceeds in two directions: (1) try to reduce the corrosive substances in the nearby environment and/or (2) perform a surface protection treatment. Based on the second pathway, the search towards a protective organic coating which is stable, reproducible, reversible, corrosion resistant and aesthetically justified is continued. The research started with experiments considering hydrophobic organic coatings with carboxylic groups, which react with lead, forming lead carboxylate complexes. It is important to form a hydrophobic film, which repels water, one of the primary malefactors for any form of corrosion. In this work, all coatings contain (neutralized) carboxylic acid groups to make use of this lead carboxylate reaction to form hydrophobic organic coatings on lead substrates. To pursue this goal, four steps are considered, starting with the study of bare lead in two different electrolytes (step (i)), the use of non-toxic linear sodium monocarboxylates (step (ii)) and (neutralized) dimer acids (step (iii)) and ending with the production and testing of a new polymer coating (step (iv)). In those steps, the lead substrate-coating system's stability, the reproducibility and the protectivity of the coating are studied. In the different case studies a lot of important issues, like adsorption behavior of the carboxylic groups, mechanism of coating deposition, electrochemical deposition, characterization of the coating, corrosion resistance, etc., will be addressed.

To prevent lead corrosion, different surface analysis and electrochemical techniques are used to determine the stability, reproducibility and protectivity of three types of organic coatings, each characterized by an increasing amount of carboxylic groups: studies using non-toxic linear sodium monocarboxylates (part II and III) and a dicarboxylic acid and polymer coating (part IV).

16.1 Lead carboxylate coatings

To summarize the properties of the hydrophobic coatings using non-toxic linear sodium monocarboxylates, the importance of each of the important reaction conditions is listed below. Their properties are evidenced based on the results of surface analysis and electrochemical techniques.

16.1.1 Influence of the deposition method and reduction treatment

For the deposition of a lead dodecanoate coating starting from an aqueous sodium dodecanoate solution, three different deposition methods are considered: (1) cyclic voltammetry, (2) immersion and (3) amperometry. Furthermore, a reduction pretreatment is tested for method (2) and (3) in order to obtain more reproducible coatings. This reduction pretreatment improves the corrosion resistance and reproducibility of the coating and 'cleans' the initial surface, which determines, to a large extent, the quality of the deposited lead dodecanoate coating on the lead surface. Indeed, a corroded lead surface

is covered with lead corrosion products consisting of particularly lead(II)oxide and, to a lesser extent, hydrocerussite and plumbonacrite, which forms from a reaction with atmospheric carbon dioxide. We assume these corrosion products have a big influence on the produced coating.

The advantage of cyclic voltammetry is the shortening of the coating process and deposition control. The deposition mechanism indicates that a soluble lead salt with dodecanoate as anion is formed, followed by the precipitation of a salt film, which is proven using ATR-IR spectroscopy and XRD. The presence of the lead dodecanoate coating induces a decrease of the corrosion current density, while the passivation current density also decreases. The electrochemical treatment, however, forces the formation of lead complexes not providing time to form ordered crystals. Furthermore, in-situ spectroelectrochemical measurements have demonstrated that a crystalline lead dodecanoate coating immediately forms at the start of the experiment. During the drying process, the formed lead complex crystals reorganize and lead hydroxy carbonates are formed. The electrochemical force induces the formation of lead(IV)oxides during the oxidative scan, which indicates the presence of gaseous oxygen or hydroxide-ions in the solution. During the reductive scan, these lead corrosion products are reduced to form lead metal. The consecutive cyclic voltammetry scans ensure the formation of a lead dodecanoate coating up to the saturation of the lead sample surface. The reduction processes also do not allow the lead dodecanoate film to form a 1.5 μm-thick layer. Not only is the electrochemical coating method in an aqueous solvent quick and inexpensive (the materials are all cheap substances mass produced for industrial applications), but also the lead dodecanoate coatings are considerably hydrophobic and therefore potentially more protective. The method may be extended to using cotton drenched or a spray can filled with the inhibitor solution to apply the lead dodecanoate coating, increasing the range of possible applications in archeaometry and conservation.

Using another electrochemical technique, amperometry, we tried to deposit a lead dodecanoate coating on a lead sample. This technique, however, always produced defective coatings probably explained by the constant anodic electrochemical force and the absence of any reductive scan during the deposition.

Using the immersion method, no electrochemical force is used. Therefore, well-ordered lead dodecanoate crystals are formed using a dissolution-precipitation mechanism, producing the most protective coatings. The immersion method produces a film composed of a hydrophobic lead soap with a three-dimensional crystal structure, which is characterized by a lamellar building of sheets. The cross-sectional image of the coating produced using the immersion technique has a thickness in the 10 to 20 μm range. The most important disadvantage of this technique is the slower deposition of lead dodecanoate complexes. However, the smaller amount of lead dodecanoate complexes forms perfectly ordered crystals on the lead surface and produces a less contaminated surface, explaining the higher inhibition efficiencies.

Finally, we conclude that, using both electrochemical and immersion techniques, the lead dodecanoate coatings are contaminated with small amounts of lead corrosion products. However, despite this contamination, lead dodecanoate coatings protect the lead surface very well and are easily produced.

16.1.2 Influence of the deposition temperature

At room temperature, deposition methods (1) and (2) produce a thin, well-covered and protective coating. At higher temperatures, less protective coatings are deposited as a consequence of the higher solubility and the increase of the critical micelle concentration of the sodium dodecanoate surfactant. In these conditions, the sodium dodecanoate adsorbs and aggregates more difficult on the surface. Therefore, a slower deposition method such as immersion method should provide a more protective coating. Indeed, the electrochemical treatment forces the reaction not providing time for the formation of ordered crystals. Basically, bigger and well-formed crystals are more commonly seen on better protective coatings, while small crystals are seen on defective coatings. At room temperature, the immersion method forms a more

ordered and compact lamellar crystal layer, but at higher temperatures larger polycrystals are formed indicating some areas are not fully protected.

16.1.3 Influence of the deposition time

A longer deposition time produces a somewhat better protective coating compared to shorter deposition times, because more and better ordered crystals can be formed, which ensure that the coating protects better against corrosion. A reproducibility measurement, however, nuances this conclusion. It is not proven that the longer immersion times will always produce a more protective layer, however, the chance of depositing a better protecting coating is higher.

16.1.4 Adsorption considerations

In order to study the adsorption and inhibition behavior, the sodium dodecanoate inhibitor was tested in the ASTM solution using electrochemical measurements. Increasing the inhibitor concentration causes an increase of the total resistance and a decrease of the corrosion current density. Using low inhibitor concentrations (lower than the c.m.c.), the inhibitor partly covers the surface protecting against anodic corrosion. In this case, monolayer adsorption is assumed. Only high inhibitor concentrations (higher than the c.m.c.) cover the whole surface forming an actual coating. Applying the Frumkin theory, we assume that the lead oxide covered surface has a fixed number of adsorption sites where each site holds only one adsorbed species considering interactions between the adsorbing inhibitor species. The calculated standard Gibbs free energy change of the adsorption confirms that the metal surface forms a coordinate bond, defined as an asymmetric chelating bidentate bond, with dodecanoate anions (chemisorption) to form a new lead dodecanoate complex.

16.1.5 Lead corrosion in an acetic acid environment

Using odd random phase electrochemical impedance spectroscopy, an in-situ measurement technique, the corrosion mechanism for lead substrates in an acetic acid medium is studied, which is important to know for testing the deposited coatings. This novel technique measures a large frequency range in a very short time, enabling us to perform time lapse studies on different electrochemical systems. Furthermore, using instantaneous impedances, dynamic electrochemical systems are considered linear and stationary using different time steps. The model representing the corrosion mechanism of lead substrates in an acetic acid environment was proven to be correct based on the valid parameter trends. The corrosion mechanism is split in three time frames. At the start, the atmospherically formed oxide layer is dissolved with the simultaneous precipitation of lead corrosion products. The acetic acid attacks the basic lead oxide layer. Secondly, the electrolyte reaches the metal/oxide interface and induces metal corrosion with the formation of pits in the metal. The formed porous hydrophobic corrosion products pile up on top of the lead oxide layer slowing down the metal corrosion. These corrosion products, however, form porous crystal clusters, leaving corrosion processes to go on slowly. The study states that two processes exist during the corrosion process namely dissolution and precipitation. In the lead oxide dissolution time frame, the initial lead oxide layer dissolves and precipitation starts. In the corrosion time frame, the dissolution of the lead metal is dominant. In the last time frame, an equilibrium exists between the dissolution of the lead and the precipitation of lead corrosion products, explaining the slower corrosion process.

16.2 Polymer coatings

In what follows the properties of the hydrophobic coatings using compounds with more than one carboxylic acid group are summarized.

16.2.1 Dimer acid coatings

The inhibitor molecules with two carboxylic acid groups react chemically with lead oxide layer present on the surface. It is found that these Pb-O bonds, defined as an asymmetric chelating bidentate bond, form a polymer with lead atoms acting as linkers. The DA inhibitor forms a coating during sintering, whereas the neutralized DA inhibitor reacts with the substrate to form clusters. The DA-deposited coating only reacts partly with the lead metal during sintering. The neutralized DA coatings, however, form lead complexes following the dissolution-precipitation mechanism. In short, the different appearance of both coatings is explained by both the reaction mechanism, the inhibitor reactivity and the solvent used. All coated samples undergo similar corrosion reactions in the corrosive acetic acid environment, which means the coating blocks possible anodic reaction sites, but have no influence on the corrosion reactions itself. It is established that the inhibition efficiencies of both coatings depend on the immersion time, suggesting a constant deposition. An increase of the immersion time suggests an increase of the amount of deposited inhibitor on the sample surface. However, it concerns an uncontrolled deposition, which means deviations are possible. All DA coatings have equally dense layers with similar levels of polymer entanglement. The neutralized DA-coated samples predict a more impenetrable layer compared to the DA-coated samples. Moreover, for the neutralized DA coated samples a link is established between the immersion time, the coating thickness, the rate of water uptake and the degree of polymer entanglements. We conclude that the neutralized DA coating provides a better barrier against corrosion and water uptake than the DA coating.

16.2.2 Acrylate-based coatings

The polymer molecules partly chemically react with lead metal ions present at the lead substrate surface. The formed Pb-O bonds act as linkers between two chains making it more likely the formed compounds will precipitate on the surface to form a coating. The coordination of the carboxylate groups around the lead metal atom is defined as an asymmetric bridging bidentate bond. All polymer coatings are produced using this precipitation mechanism. The copolymer 2 coating shows some damage and delamination around the unprotected areas characterized by a semi-infinite diffusion process and an extra Voigt element. The other coating from a completely covering layer. The thickness of the coatings depends on the molecular weight and the acrylic acid content of the polymer as described by the precipitation mechanism. At the start of the measurement, water uptake goes very fast until the coating is completed saturated with water. The saturation point and the speed of the water uptake depend on the acrylic acid content. The damaged coating clearly shows a different diffusion profile compared to the protective coatings. The diffusion coefficient is constant around the start of the immersion during the water uptake process. When the coating is saturated, the effective diffusion coefficient increases due to the formation of new conductive pathways in the coating. The profile of the thicker protective coatings is characterized by an increase as a consequence of the filling of the pores of the coating. Afterwards, the coating defects are clogged with corrosion products, so that the diffusion processes in the coating are slowed down. From these results we conclude that a higher acrylic acid content provides a more stable, thicker and more protective coating. Moreover, the use of polymers with a higher molecular mass also provides a more protective coating.

16.3 General summary

Table 16.1 tries to give a general summary of the qualitative estimate of the efficacy of the different coatings analyzed in this thesis.

method	reduction treatment	deposition time / h	compound	solvent	substrate	coating quality
cyclic voltammetry	no	-	neutralized dodecanoic acid	water	lead	+
amperometry	yes	-	neutralized dodecanoic acid	water	lead	-
immersion	no	17	neutralized dodecanoic acid	water	lead	-
immersion	yes	0.5	neutralized dodecanoic acid	water	lead	+
immersion	yes	17	neutralized dodecanoic acid	water	lead	+++
cyclic voltammetry	no	-	neutralized dodecanoic acid	water	lead-tin alloy	-
immersion	yes	24	neutralized dodecanoic acid	water	lead-tin alloy	+
immersion	yes	24	neutralized dodecanoic acid	water	organ sample	-
immersion	no	6	dimer acid	ethanol	lead	+
immersion	no	24	dimer acid	ethanol	lead	+
immersion	no	96	dimer acid	ethanol	lead	+
immersion	no	6	neutralized dimer acid	water	lead	++
immersion	no	24	neutralized dimer acid	water	lead	+++
immersion	no	96	neutralized dimer acid	water	lead	+++
immersion	no	96	acrylate copolymer 2[1]	water - THF water - ethanol	lead	++
immersion	no	96	acrylate copolymer 3[2]	water - THF water - ethanol	lead	+++
immersion	no	96	acrylate copolymer 5[3]	water - THF water - ethanol	lead	+++

[1] A copolymer with 5% carboxylic groups and a molecular weight of 15 kDa

[2] A copolymer with 5% carboxylic groups and a molecular weight of 20 kDa

[3] A copolymer with 10% carboxylic groups and a molecular weight of 15 kDa

Table 16.1 – A qualitative estimate of the efficacy of the coatings and deposition methods described in this thesis

16.4 Perspectives

The future perspectives of this work can be divided into improvements on the techniques and the development of new organic coatings and methods

16.4.1 Future improvements

In order to tackle some of the drawbacks encountered in this work, the following future improvements are presented:

1. It is clear that the LSV and EIS data measured using both corrosive environments for testing the organic coatings and the bare lead sample are different. This means that the corrosive environment has an important influence on the coating's inhibition properties. In this case, we did a thorough study on the acetic acid corrosion of lead in an electrolyte containing TBAB, which is necessary to provide information on the coatings. However, I think the coating's protective behavior should be tested in more representative situations. For example, wear tests in controlled humidity cabinets using ASTM standard methods.

2. To do research on organic coatings, often single-sine electrochemical impedance spectroscopy is used. However, in this work, a new method is put forward using odd random phase multisine electrochemical spectroscopy. This type of impedance spectroscopy, developed by the SURF group at the VUB, gives us much more information about the raw data of the measurement making it easier to draw conclusions concerning the fitting parameters. Furthermore, it provides important information about the linearity and stationarity of the measurement system. In the future, it would be more interesting to use multisine measurements for in-depth studies of rapidly changing systems.
   These conclusions do not mean the single-sine measurements reported in this thesis are invalid. A profound data analysis is possible based on a general statistical error analysis of multiple consecutive single-sine impedance measurements and/or on a validation procedure using the Z-HIT transform equation. It is, however, not possible to differentiate between non-linear and non-stationary distortions. Furthermore, at this moment, the basic single-sine technique is the only commercially available EIS instrumentation and can be used for quality control purposes. In the light of these conclusions, the earlier results using single-sine measurements should be regarded with more caution compared to the multisine data.

3. To start the fitting of the impedance data the initial values need to be in close proximity to the best-fit values to obtain convergence. Actually, the choice of the starting values becomes critical because, using the Gauss-Newton and the Levenberg-Marquardt minimization algorithms, the risk of getting trapped in a local minimum is quite high. However, the scientist has rarely enough information to choose suitable initial values. Other algorithms, such as genetic algorithms, could help to provide a first estimation of the best-fit values, while the Gauss-Newton and the Levenberg-Marquardt minimization algorithms should be used for the fine-tuning of the parameters.

4. The in-situ measurements presented in the manuscript provide the most valuable information concerning the organic coating's properties. Therefore, it is important to keep updating and renewing these techniques and its software to provide more information. In case of the spectroelectrochemical measurements, I think it would be interesting to keep upgrading the eCell to be able to do more advanced experiments.

5. The state of matter has an influence on the corrosion speed. In this thesis, we decided to work with a dilute acetic acid solution whereas the corrosion process of acetic acid in air is more interesting from a conservationist's point of view. When considering lead corrosion in air, it is difficult to predict how the established corrosion process will change. Much of this corrosion process depends on important factors such as the corrosive species, the substrate, the presence of water, the environment, nature of the inhibitor, etc. In order to understand to what extent the protective behavior is different in both cases more research is needed using in-situ vapor phase experiments combined with XRD analysis.

16.4.2 Future tests

Before applying the suggested coatings on real artifacts, other important tests need to be preformed:

1. All coatings have been tested using impedance spectroscopy in standard corrosive and an acetic acid containing environment. These measurements provide valuable information but do not simulate real atmospheric conditions. Therefore, tests in weathering cabinets need to be preformed to have a better view on the corrosion mechanism when the sample is placed in museum-like conditions.

2. Long-term experiments provide information about the corrosion protection of the coatings over longer periods. When used as a coating in cultural heritage, these coatings need to provide protection for at least a few years.

3. When applying the coatings, pure lead samples were used. As most of the artifacts are alloyed samples, it is necessary to test the coating deposition on lead alloyed samples. These tests could give us valuable information on the influence of inclusions and grain boundaries on the coating deposition.

4. To provide an easier way of applying the coating on large objects, we need to test the use of spray cans filled with the inhibitor solutions.

5. A significant amount of investigation into the development of lead carboxylate coatings has been carried out by ESA group members (UGent). The work in this thesis continues this research by investigating the aqueous lead carboxylate coating mechanism, the influence of the temperature and deposition method, the effectiveness of the coating and the surface structure. Trying to develop new coating strategies, new molecules with carboxylic acid functional groups are used to coat lead samples. However, there is no summary or review available, which makes a comparison between the different deposition methods for lead carboxylates (use of aqueous and ethanolic solutions, melted carboxylates, micro-emulsions).

6. As seen in chapter 11, encouraging results were obtained when using the lead carboxylate coating on pre-corroded and untreated lead alloyed artifacts. However, some problems are identified: the coating's white color, the unprotected inner part of the organ sample, the less protected seam and the formation of an inhomogeneous coating. In order to understand the use of this coating on real artifacts, the reactivity of a range of lead corrosion products with carboxylic acids to produce lead carboxylates could be tested. Furthermore, it would be interesting to know the influence of the metal crystal structure on the coating formation. The seam and the hammered body of the organ sample clearly show a different crystal structure.

7. An interesting study would be a continuation on the study which uses acrylate polymers to protect lead surfaces. It is clear that the molecular mass and the acrylic acid content of the polymer have an important influence on the coating properties such as the diffusion and water uptake processes. Based on these results, a study can be done for finding the optimal acrylic acid content and the optimal molecular mass.

16.4.3 Final remarks

The ongoing study towards the development of coatings is an important branch in conservation science and is vital for the long-term survival of valuable cultural heritage artifacts. In this work, new conservation strategies for lead objects are suggested based on the use of inhibitors with carboxylic acid groups. Using surface analysis and electrochemical techniques, valuable information is given about the coating's protective properties, stability, deposition mechanism and structure. Based on the results, the carboxylate coatings need more testing on actual heritage objects, but I am sure they could be an interesting alternative for the wax treatment. The polymer coatings also provide good results, but need much more testing before applying these on real artifacts. However, these transparent coatings provide a very good barrier against corrosion, which seems promising for future developments.

Furthermore, two interesting and valuable techniques have been used, namely in-situ XRD and ORP-EIS. The in-situ XRD instrumentation is an interesting tool, which can be used in a wide range of studies to explore changing crystal structures. The ORP-EIS technique is difficult to learn, but contains a wealth of information about the electrochemical system one is measuring. In the case of coating studies, it is possible to study the level of non-stationary and non-linear behavior of the system, the diffusion processes, the protective properties, the water uptake, $\cdots$ Of course, both techniques are certainly not restricted to corrosion studies in a cultural heritage context.

List of Tables

2.1 Important physical properties of the lead metal [1, 5, 6]. . . . 19
2.2 Standard electrode potential in H_2O at 25°C (298 K) [46]. . . . 22
2.3 Wood types harmful for lead metal artifacts [80–84]. . . . 25
2.4 Different properties of acetic acid and formic acid: comparative study [91]. . . . 26
2.5 Paints, glues and other materials destructive to lead metal artifacts [80–82, 126]. . . . 29
2.6 Characteristics of the lead corrosion products. . . . 31
2.7 Summary of the presented electrochemical treatments [3]. . . . 35
2.8 Summary of the presented corrosion inhibitors on lead and lead alloys. . . . 36
2.9 Summary of coatings used on lead and lead alloys. . . . 37

4.1 List of the chemicals used. . . . 50
4.2 Instructions for the use of the Mimimet 1000 Grinder-Polisher (Buehler, USA) to polish lead substrates. 51
4.3 Spin-orbit splitting intensities [87]. . . . 66
4.4 Degrees of freedom for polyatomic molecules. . . . 69

7.1 Infrared characteristic vibrational wavenumber (in cm^{-1}) observed for lead(II)alkanoates. . . . 100

8.1 Description of the different modification procedures used to deposit a lead dodecanoate coating on lead electrode surfaces method. . . . 115
8.2 Electrochemical impedance parameters for different lead dodecanoate coatings in an ASTM D 1384-87 solution deposited using different methods in a 0.05 M NaC_{12} solution. . . . 118
8.3 Potentiodynamic polarization parameters for different lead dodecanoate coatings in an ASTM D 1384-87 solution deposited using different methods in a 0.05 M NaC_{12} solution. . . . 119

9.1 Description of the different modification procedures used to deposit a lead dodecanoate coating on lead electrode surfaces method. . . . 125
9.2 Experimental design test matrix (2^2). . . . 126
9.3 One-way ANOVA table for both responses: the inhibition efficiencies and the charge-transfer resistances. 127
9.4 Coefficients of the regression analysis using the inhibition efficiency responses. . . . 127
9.5 Two-way ANOVA table for both responses: the inhibition efficiencies and the charge-transfer resistances. 128

9.6 Fitted impedance parameters for a bare lead and two coated lead samples. The coating is produced using the immersion technique using a short and a long immersion time 132
9.7 One-way ANOVA table for the inhibition efficiencies of coatings deposited using the immersion technique using a deposition time of 17 h and 2000 s 133

10.1 Fitted potentiodynamic polarization parameters for a bare lead surface in the ASTM D 1384-87 solution in the absence and presence of NaC_{12}. 137
10.2 Fitted electrochemical impedance parameters (EIS) for a bare lead surface in the ASTM D 1384-87 solution in the absence and presence of NaC_{12}. The last column indicates the inhibition efficiency value and its deviation using three replicate measurements. 140
10.3 List of the results of the curve fitting analysis on the C 1s, O 1s and Pb $4f_{7/2}$ photoelectron spectra (the values are corrected for C 1s to appear at 285.0 eV). 147

11.1 The calculated elemental compositions for the untreated different metal organ samples (normalized, in wt%). 158
11.2 Fitted EIS parameters for bare and coated (CV and IMM) sample 2 in a corrosive solution. 163
11.3 Fitted EIS parameters for bare and coated English organ sample in a corrosive solution. 165

13.1 Thermodynamic analysis based on the Pourbaix diagram of lead-water and the solubility product of lead dodecanoate. 194
13.2 List of the values of the exponential fit of the growth process of the lead dodecanoate coating using cyclic voltammetry with a scan rate of 20 mV s^{-1}. 197

14.1 Onset temperature, T_0, temperature of maximum decomposition rate, $T_{d,max}$, and percentage of residue at 800°C from TGA. 209
14.2 Composition analysis of (a) bare, (b) DA-treated and (c) NaDA-treated lead coupons based on a standardless analysis of the EDS-spectra. 210
14.3 Characteristic vibrational wavenumbers (ν / cm^{-1}) in the 4000 – 400 cm^{-1} region for the spectra of a lead sample coated with DA or NaDA and of a NaDA reference powder sample. 214
14.4 Curve fitting results for C 1s, O 1s and Pb $4f_{7/2}$ photoelectron spectra; values are corrected for C 1s to appear at 285.0 eV. 215
14.5 Fitted impedance parameters of a bare lead sample immersed in a corrosive acetic acid solution for 0 h and 25 h. 217
14.6 Fitted impedance parameters of a bare lead and lead surfaces immersed in an ethanol DA solution for different durations recorded in a corrosive acetic acid solution. 219
14.7 Fitted impedance parameters of a bare lead sample immersed in a corrosive acetic acid solution for 0 h and 25 h. 222

15.1 Composition of the different random copolymers used as a lead coating. 228
15.2 The calculated compositions of the different random copolymers based on the ^1H NMR signals. 229
15.3 Results of RAFT co-polymerization of EEA and EHA at 70°C after a reaction time of 6 hours in 3 M toluene measured with a THF-GPC 229

15.4 Characteristic vibrational wavenumbers (ν / cm^{-1}) in the 3500 – 600 cm^{-1} region for the spectra of the polymer sample and the lead sample coated with the polymer. 232
15.5 Coating thickness values (in μm) 237

16.1 A qualitative estimate of the efficacy of the coatings and deposition methods described in this thesis . . 255

List of Figures

1.1 Overview of the periods and events from 6500 B.C. to 1000 B.C. 3
1.2 Overview of the periods, events and people from the Greek and Roman period 6
1.3 The roof of the Pantheon in Rome is made out of lead sheets. © M. De Keersmaecker 8
1.4 The lead glass window of the Ste Croix Cathedral in Orléans. © M. De Keersmaecker 9
1.5 Overview of the periods and events starting from the begin of the Middle Ages. 10
1.6 Wall paintings from the Bibliotheca Apostolica Vaticana in Rome. © M. De Keersmaecker 10
1.7 The romantic grand Cavaillé-Coll organ in the Ste Croix Cathedral of Orléans. © M. De Keersmaecker 11
1.8 Mechanism of flue and reed pipe. © Cavasant Frères 12
1.9 Different end uses of lead. ©Gravita Engineering & Technology 12

2.1 Distribution of lead artifacts according to lead content based on Figure in [3]. Three compositional groups: (a) high lead content, the structure of which consists of a lead-rich matrix (α) with precipitates of a second phase, minor-element-rich (β); (b) intermediate lead content, corresponding to low melting-point alloys, used in the as-cast condition, revealing lead-rich (α) dendrites in an eutectic matrix ($\alpha + \beta$); (c) low lead content, exemplified by copper-based leaded alloys, where lead is segregated in the form of fine globules. 20
2.2 Phase diagram of lead and tin based on Figure in [12]. 20
2.3 A schematic representation of the atmospheric corrosion processes on lead involved in the formation of carbon containing compounds based on Figure in [61]. 24
2.4 The rate of lead solubility as a function of different inorganic acids and hydroxides from Figure in [3]. . 24
2.5 Scheme of the hydrolysis of hemicelluloses 25
2.6 A schematic representation of the atmospheric corrosion processes on lead in moist air containing acetic acid vapor based on Figure in [65]. 27
2.7 Lead corrosion of the foot of the organ pipe ©Lapon. 28
2.8 (a) Intergranular corrosion and (b) Copper inclusion in lead matrix. ©M. De Keersmaecker. 28
2.9 Active pit on a passive metal surface. ©M. De Keersmaecker. 30
2.10 Schematic mechanism of 'active' lead corrosion in the proximity of organic acids based on Figure in [65]. 31

4.1 (a) Optical image (6.3 x) and (b) electron image (500 μm x 500 μm) of an ideally polished lead sample. 51

4.2 The relative appearance of (a) a traditional thermionic electron gun and (b) a thermal field emission gun. The suppressor is negatively biased with respect to the cathode, while the extractor is positively biased. These figures are based on [7] . . . 52
4.3 Schematic diagram of an SEM set-up [16]. . . . 53
4.4 The interaction volume at the sample illuminated with the incident electron beam. The schematic process for the production of secondary and backscattered electrons is shown as well [27]. . . . 54
4.5 Schematic representation of the Phenom detection system for the detection of backscattered electrons for (a) information about the composition of the sample and (b) information about the topography of the sample [30]. . . . 55
4.6 Schematic representation of the X-ray formation [37]. . . . 56
4.7 Energies of major X-ray emission lines observed below 10 keV [27, 41]. . . . 56
4.8 (a) A primitive unit cell described by lattice parameters (**a**,**b**,**c**) and (α,β,γ). (b) An example of the determination of Miller indices (hkl) of a crystal plane (210). The black dots represent the basis. This figure is based on [54]. . . . 58
4.9 Bragg's reflections [54]. . . . 58
4.10 Diffraction from the (001) planes of (a) base-centered and (b) body-centered orthorhombic unit cells . . 59
4.11 Schematic of a (a) Bragg-Brentano geometry, (b) modern X-ray tube and (c) scintillation detector [54]. . 60
4.12 A schematic of the most important components of a third generation synchrotron source [68]. . . . 62
4.13 Bending magnet spectrum of the DUBBLE BM26A beamline. . . . 62
4.14 X-ray optics: (a) Basic geometry of the double-crystal monochromator and (b) Schematic of the X-ray optical system at DUBBLE [75]. . . . 63
4.15 The setup and geometry of the experiment at BM26A (DUBBLE) for time-lapse XRD measurements ©Mark Dowsett. . . . 64
4.16 Schematic representation of (a) the photoelectron emission process and (b) the Auger de-excitation process [90]. . . . 65
4.17 Schematic of the XPS instrument with a magnification of the hemispherical electron analyzer [87]. . . . 66
4.18 Chemical shifts for the C 1s levels in ethyl trifluoroacetate. The chemical shifts are related to the electronegativity differences: The known [107] electronegativity differences (ΔE) are C - H: 0.4; C - O: 1.0; C - F: 1.5, which rationalize the chemical shifts in ethylfluoroacetate [108]. . . . 67
4.19 Total reflection of an infrared beam in an ATR-crystal [131]. . . . 70
4.20 Schematic of (a) the (ATR-)FTIR spectrometer and (b) the Michelson interferometer [135]. . . . 71

5.1 The nuclear spin energy levels of a spin-$\frac{1}{2}$ nucleus in a magnetic field. Resonance occurs when the energy separation of the levels matches the energy of the photons in the electromagnetic field [2]. μ is the magnetic moment. . . . 77
5.2 (a) The effect of spin-spin coupling on an AX spectrum. (b) The origin of the 1:2:1 triplet in the A resonance of an AX_2 species. (c) Pascal's triangle [2]. . . . 79

6.1 Schematic energy profile for activation polarization (a) at equilibrium and (b) at an anodic overpotential η [2, 3]. . . . 83

6.2 Representation of the electron transfer, without movement of the nuclei, according to the Born-Oppenheimer approximation. λ is the solvent reorganization energy. 85

6.3 Schematic representation of the positions of the ion and counterion in the double layer [12]. 86

6.4 Current-potential curve of the corrosion behavior starting from the partial Butler-Volmer curves of M and EA. The corrosion potential E_{corr} is presented [25]. 88

7.1 General set-up for voltammetric measurements. 92

7.2 (a) Potential waveform in cyclic volammetry [9]. (b) Effect of the heterogenous rate constants on the process reversibility. The transfer coefficient are set to 0.5 [12]. 93

7.3 The extrapolation of the two Tafel slopes for the determination of the corrosion current i_{corr} 94

7.4 Current-potential curves recorded at a lead electrode in a 0.025 mol L^{-1} NaOH solution in the absence of dodecanoic acid at a scan rate of 50 mV s^{-1} and a temperature of 298 K as a function of scan number. The first four scans are shown (scan 1: solid line, scan 2: broken line, scan 3: dotted line and scan 4: dash-and-dot line). 96

7.5 Optical images of a bare lead electrode (a), a lead electrode after potential cycling in an alkaline reference solution (b) and a lead electrode coated with dodecanoate (c). 97

7.6 Current-potential curve recorded at a lead electrode in a 0.025 mol L^{-1} NaC_{12} water solution: scan 1 (1) and scan 2 - 30 (2). 98

7.7 Current-potential curve recorded at a dodecanoate-coated lead electrode in a 0.025 mol L^{-1} NaC_{12} water solution at different scan rates: 20 (1), 50 (2), 80 (3), 160 (4), 320 (5) and 500 (6) mV s^{-1}. Inset: relationship between the peak current (I) and square root of the scan rate for process A_1 (I_{A_1}) and the passive region ($I_{\text{passivation}}$). 99

7.8 Potentiodynamic curves of bare lead (1) and coated lead (2) in an ASTM solution. 99

7.9 ATR-IR spectra of a bare lead electrode (a) and a lead electrode coated with dodecanoate (b). Inset: mode of bonding. Enlargement: CH_2 wagging progression bands. 100

7.10 Four principal modes of coordination for metal carboxylate bonds. 101

7.11 X-ray diffractogram from an electrode modified with 30 cycles showing the structure of lead dodecanoate overlaid on the lead substrate. Evidence for litharge (PbO) is also found. 102

8.1 Residuals plot for the Kramers-Kronig validation of an EIS measurement of a polymer coating on a lead substrate. 107

8.2 Z-HIT check of an EIS measurement of a polymer coating on a lead substrate. 108

8.3 Equivalent circuit for a simple electron transfer (a) and the corresponding Nyquist diagram (b), which is copied from [34]. 110

8.4 (a) The EEC with inclusion of diffusion element (b) The Nyquist diagram showing mixed control [34] . 111

8.5 Impedance representations of the Warburg, Finite Length Warburg (FLW) and Finite Space Warburg (FSW). At high frequency the dispersions overlap with $Z_0 = 100\ \Omega$ for all three. Argument of FLW and FSW: $\frac{d}{\sqrt{D}} = 1$. Figure is copied from [37]. 111

8.6 EIS plots of a lead dodecanoate modified lead surface (AMP) with and without an initial reduction step of the surface at -1.5 V during 600 s recorded in an ASTM D 1384-87 solution. 116

8.7 Electrochemical impedance plots of coated lead electrodes with initial reduction step recorded in ASTM D 1384-87 solution: (a) impedance plot, (b) phase angle plot and (c) Nyquist plot. 117
8.8 Electric circuits used to simulate the recorded impedance spectra [60–63]. 118
8.9 The potentiodynamic polarization curves of coated lead electrodes with initial reduction step recorded in ASTM D 1384-87 solution. 119
8.10 Optical images obtained from a bare lead electrode (A) and lead dodecanoate modified lead electrodes: (B) cyclic voltammetry (procedure CV), (C) amperometry (procedure AMP), (D) immersion (procedure IMM), (E) amperometry with an initial reduction step (procedure AMP-IR) and (F) immersion with an initial reduction step (procedure IMM-IR). 120

9.1 Effect of the surfactant concentration on the corrosion inhibition 127
9.2 Response surface for the 2^2 factorial design model 128
9.3 The SEM images of the coated lead sample before the corrosion test. 129
9.4 The SEM images of the corroded lead samples of the cyclic voltammetric deposition: (a) the image of the surface with a deposition at 20 °C (b) the image of a part of the corroded surface with a deposition at 20°C, (c) the image of a part of the coated surface with a deposition at 20°C and (d) the image of the surface with a deposition at 60°C 130
9.5 The SEM images of the corroded lead samples of the immersion deposition: (a) the image of the surface with a deposition at 20°C (b) the image of a part of the corroded surface with a deposition at 20°C, (c) the image of a part of the coated surface with a deposition at 20°C and (d) the image of the surface with a deposition at 60°C 131
9.6 The impedance (a) and phase (b) plots of lead dodecanoate coatings using the IMM procedure with a deposition time of 2000 s and 17 h (for comparison the bare lead electrode is given) 131
9.7 Histogram and cumulative distribution of inhibition efficiencies of 10 coatings deposited using IMM 2000s and IMM 17h and tested in an ASTM solution 132
9.8 Histogram and cumulative distribution of IE's of 15 coatings deposited using CV and IMM and tested in an ASTM solution 133

10.1 E_{corr} vs. t plot for lead in the ASTM solution in the absence and the presence of different concentrations of NaC_{12}. 136
10.2 Current vs. potential plot for lead electrodes in the ASTM solution in the absence and presence of different concentrations of NaC12 with Tafel slope analysis. 137
10.3 Electrochemical impedance plots of lead samples in the ASTM solution in the absence and presence of NaC_{12}: (a) impedance plot, (b) phase plot and (c) Nyquist plot. 138
10.4 The EEC used for fitting the experimental EIS spectra. 139
10.5 (a) Langmuir test and (b) Langmuir and Frumkin slope vs. coverage for the sodium dodecanoate inhibitor at room temperature in the ASTM solution. 141
10.6 Frumkin adsorption isotherm for sodium dodecanoate on bare lead electrodes at room temperature in the ASTM solution. 141
10.7 The optical and secondary electron images of a bare lead polished sample (a and c) and optical and secondary electron images of a lead dodecanoate coated lead sample (b and d). 142

10.8 Secondary electron image and EDS point data of (a) the polished bare lead sample and (b) the coated lead sample. 143

10.9 Secondary electron image of the cross-section of the coated lead sample with EDS-mapping. 144

10.10 Schematic representation of the mechanistic model for inhibitor concentrations: (a) below c.m.c. and (b) above c.m.c. 144

10.11 XPS core level spectra of the C 1s, O 1s and Pb $4f_{7/2}$ levels of the bare corroded lead metal samples with components determined by curve fitting analysis and background subtraction. 145

10.12 XPS core level spectra of the C 1s, O 1s and Pb $4f_{7/2}$ level of the with lead dodecanoate coated lead metal samples using cyclic voltammetry with components determined by the curve fitting analysis and background subtraction. 148

10.13 Chemical structure of (a) metal-alkonyl bond and (b) carbide formation. 149

10.14 XPS core level spectra of the C 1s, O 1s and Pb $4f_{7/2}$ level of the with lead dodecanoate coated lead metal samples using the immersion technique with components determined by curve fitting analysis and background subtraction. 150

10.15 XPS core level spectra of the C 1s spectrum of (a) a lead sample coated with a lead dodecanoate coating without the use of the initial reduction and (b) a lead sample corroded in the atmosphere after an initial reduction in the sodium dodecanoate with components determined by curve fitting analysis and background subtraction. 151

11.1 Photograph of the investigated organ samples: (a) sample 1, (b) sample 2 and (c) sample 3. 155

11.2 Photograph of (a) the organ in St. Mary the Virgin Parish Church (Edith Weston, Rutland, UK) © Amphion Recordings and (b) the studied organ pipe © P. Storme. 155

11.3 The untreated and treated first metal sheet pipe organ sample using the IMM method: optical observation (a and c) and SEM image (b and d). 157

11.4 The untreated and treated second metal sheet pipe organ sample using the IMM method: optical observation (a and c) and SEM image (b and d). 157

11.5 The untreated and treated pipe organ sample using the IMM method: optical observation (a and c) and SEM image (b and d). 158

11.6 The EDS spectra of the pipe organ sample (sample 3): a) untreated sample and b) treated sample. 159

11.7 X-ray diffractogram from uncoated Pb/Sn sample 1 (a) and uncoated Pb/Sn sample 2 (b). 159

11.8 X-ray diffractogram from coated Pb/Sn sample 1 (a) and coated Pb/Sn sample 2 (b). 160

11.9 Photograph of two partly coated organ samples. The samples have been coated with lead dodecanoate using IMM (on the left) and CV (only sample 2, on the right) 161

11.10 The imdedance modulus (a), phase angle (b) and Nyquist (c) plot of the lead dodecanoate coated (using both CV 30sc and IMM 24h) and bare organ sample (sample 2) recorded in an acetic acid corrosive solution. 162

11.11 The EEC used for the simulation of the raw impedance data. 163

11.12 Photographs of partly treated piece of the organ pipe. 164

11.13 The impedance modulus (a) and phase angle (b) plots of the bare and coated English organ sample at different positions recorded in an acetic acid corrosive solution. 164

12.1 Schematic representation of one period of an odd random phase multisine in the time domain. The plus sign denotes that the signals are applied simultaneously. x represents the fundamental frequency [14]. . 170

12.2 Illustration of the odd random phase multisine excitation signal of Figure 12.1 represented in the frequency domain after a Fourier transform operation. 171

12.3 Illustration of (a) a perfectly linear system, (b) an even non-linear system and (c) an odd non-linear system to a sinusoidal perturbation at frequency k [1]. 172

12.4 Magnitude Bode plot, non-stationarities, non-linearities and the noise level of the measurement of a polished bare lead sample corroded in an acetic acid solution during the first 20 hours of immersion (hours of immersion are shown). 175

12.5 Equivalent block schematic of a linearly in time varying system. 175

12.6 Magnitude of the impedance (a), phase (b) plots and Nyquist diagram (c) for the lead corrosion in an acetic acid solution as a function of immersion time. 176

12.7 Illustration of the convolution of the skirts with the multisine. The skirts around each frequency are plotted separately in (black lines) and the result of their convolution is plotted (blue dotted) [19]. 177

12.8 Considered general system model of a higher order in t: combination of linear time-invariant systems, followed by time-varying gains. 177

12.9 First 4 time-scaled and shifted Legendre polynomials in the time domain based on the basis function for time-varying gains $b_p(t) = P_p\left(\frac{2t}{T} - 1\right)$ (a) and the amplitude (b) in the frequency domain 178

12.10 Calculated instantaneous impedance values on the measurement after 5 hours of immersion. 179

12.11 Equivalent electric circuit model for the fitting of the raw ORP-EIS data. 180

12.12 Magnitude plot, modeled curve, residual curve, noise on the excited frequencies and noise on the non-excited frequencies at the last calculated time instant of the measurement at 5 hours of immersion. . . . 181

12.13 Electrolyte resistance of the instantaneous impedances as a function of immersion time. 181

12.14 Oxide layer parameters of the instantaneous impedances as a function of immersion time. 182

12.15 Charge-transfer parameters of the instantaneous impedances as a function of immersion time. 183

12.16 Comparison of the charge-transfer resistance R_{ct} with the mass transfer resistance (W_{corr}) for different immersion times. 184

12.17 SEM images of a blank (a) and corroded lead substrate in (b) TBAB + acetic acid and (c) TBAB. 186

12.18 Physical representation of the active corrosion of a lead substrate in an acetic acid environment. 188

13.1 (a) Cross section of the eCell (b) A view of the experimental set-up at station BM26A 191

13.2 (A) Reprojected image of a Mar SR-XRD diffraction pattern from a lead dodecanoate coated lead coupon acquired on the DUBBLE beamline at the ESRF. The acquisition time was 10 s. (B) The XRD pattern of the lead dodecanoate coated lead sample calculated using integration. 192

13.3 The first voltammetric scan of the deposition of the lead dodecanoate coating with a scan rate of 20 mVs^{-1}. 193

13.4 A pattern set image of all diffraction patterns recorded during the growth process of the lead dodecanoate coating on a bare lead coupon using cyclic voltammetry with a scan rate of 20 mV s^{-1} in a 0.05 M aqueous sodium dodecanoate solution (as a function of time). 195

13.6 A hypothetical scheme for growth of the lead dodecanoate coating on a bare lead sample. 195

13.5 The peak areas extracted from the diffraction patterns of the growth of the lead dodecanoate coating in real time using 10 consecutive cyclic voltammetric scans with a range from -1.3 V to 1.5 V and a scan rate of 20 mV s^{-1}. The peak areas were extracted from (a) lead dodecanoate at 1.55 $Å^{-1}$, 1.73 $Å^{-1}$ and 2.89 $Å^{-1}$, (b) litharge at 2.04 $Å^{-1}$, (c) plattnerite at 1.80 $Å^{-1}$ and 2.54 $Å^{-1}$ and (d) lead at 2.27 $Å^{-1}$ and 2.61 $Å^{-1}$ (taking into account the 0.08 shift of the peaks). 196

13.7 The calculated thickness (d) of the lead dodecanoate coating as a function of immersion time. 198

13.8 A pattern set image of all diffraction patterns recorded during the corrosion test process of the lead dodecanoate coated lead coupon using LSV in an acetic acid solution (as a function of time). 198

13.9 The first and last diffraction pattern of the corrosion test process of the lead dodecanoate using integration. The reference diffraction peaks of lead dodecanoate and plumbonacrite. 199

13.10 The peak areas extracted from the diffraction patterns of the corrosion test of the lead dodecanoate coated lead sample in real time using a LSV scan with a range from -1 V to 1.5 V and a scan rate of 1 mV s^{-1}: (a) lead dodecanoate at 1.5514 $Å^{-1}$, 1.7262 $Å^{-1}$ and 2.8902 $Å^{-1}$, (b) litharge at 2.0435 $Å^{-1}$, (c) plattnerite at 1.7926 $Å^{-1}$ and (d) lead at 2.1984 $Å^{-1}$, 2.5376 $Å^{-1}$ and 3.5904 $Å^{-1}$. 200

13.11 A hypothetical scheme for the progress of the corrosion test measurement of a lead dodecanoate coated lead sample based on the recorded SR-XRD patterns. 201

13.12 The last pattern of the corrosion test procedure applied on a bare polished lead coupon. 202

14.1 Representative Lewis structures of fatty acid dimer mixture. Many geometric isomers of these structures are also present in the mixture. 208

14.2 SEM images and EDS maps of the (a) untreated lead metal coupons and of those treated with (b) DA and (c) NaDA. 211

14.3 ATR-IR measurements of the surfaces of lead substrates treated using 10 g L^{-1} inhibitor solutions of (a) NaDA in water and (b) DA in ethanol 212

14.4 XPS core level spectra of the C 1s, O 1s, and Pb $4f_{7/2}$ levels of (a) DA-coated lead and (b) NaDA-coated lead, with components determined by curve fitting analysis and background subtraction. 213

14.5 Proposed structure of metal-coordinated carboxylates, in which diacids form a 3D structure when coordinated by lead. A simplified 2D model is shown. 214

14.6 The Nyquist plot of bare lead in acetic acid at the start and after 25 hours of immersion. 216

14.7 Electrochemical equivalent circuit used for the simulation of the experimental impedance spectra: (a) bare lead immersed for 0 h in the corrosive solution [45] and (b) bare lead immersed for 25 h. 217

14.8 (a) Modulus, (b) phase and (c) Nyquist plot of DA-coated lead samples recorded in the acetic acid corrosive environment. 218

14.9 Electrochemical equivalent circuit used for the simulation of the experimental impedance spectra of the coated lead samples. 219

14.10 Current vs. potential plot for lead, (a) DA coated electrodes and (b) NaDA coated electrodes in the acetic acid corrosive environment. 221

15.1 Reaction mechanism for the synthesis of 1-ethoxyethyl acrylate (EEA) [1]. 225

15.2 Reaction mechanism for the synthesis of RAFT reagent. 226

15.3 Mechanism for the RAFT polymerization [10]. 227

15.4 Mechanism for the RAFT co-polymerization with monomers EEA and EHA, AIBN as initiator and BuPAT as RAFT reagent [10]. 227
15.5 ^{1}H NMR spectrum of the RAFT copolymer with EEA and EHA building blocks ($CDCl_3$, 300 MHz). . . 228
15.6 Mechanism for the deprotection step of the RAFT copolymer [1]. 230
15.7 ^{1}H NMR spectra of a sample of copolymer 2 before heating (in $CDCl_3$, 500 MHz) and after heating. . . 231
15.8 ATR-IR measurements of (a) a bare lead surface, (b) the copolymer 2 and (c) a lead sample coated with copolymer 2. 232
15.9 (a) Magnitude Bode plot (‘full red line’), non-stationarities (‘full blue line’), non-linearities (‘full black line’) and the noise level (‘$*$’) and (b) Nyquist plots of the measurement of a coated lead sample with copolymer 2 corroded in an acetic acid solution during the first 16 hours of immersion (hours of immersion are shown). 234
15.10 The EEC used for the simulation of the experimental impedance spectra of the damaged polymer coating. 234
15.11 Magnitude plot, modeled curve, residual curve, noise on the excited frequencies and noise on the non-excited frequencies at the last calculated time instant of the measurement at 2 hours of immersion. . . . 235
15.12 Evolution of (a) the resistance of the oxide and (b) the capacitance of the oxide layer vs the time. 236
15.13 Evolution of (a) the pore resistance and (b) the effective capacitance of the copolymer 2 coating vs the time. 237
15.14 Evolution of (a) the dielectric constant and (b) the volume fraction of water of the copolymer 2 coating vs the time. 238
15.15 Fit results on the curve of the measured capacitance increase as function of time during water uptake. . 239
15.16 Schematic representation of a sample surface covered with a porous film with film thickness ,δ_f, Nernst diffusion layer, δ_N, and the concentration of the electroactive species which reacts at the interface and diffuses through the film [50]. 239
15.17 Evolution of (a) the diffusion impedance and (b) the effective diffusion coefficient as a function of immersion time for the copolymer 2 coating. 240
15.18 The SEM images and the EDS spectra of the coated lead samples using (a) copolymer 2, (b) copolymer 3 and (c) copolymer 5 after the corrosion test. 242
15.19 (a) Magnitude Bode plot (‘full red line’), non-stationarities (‘full blue line’), non-linearities (‘full black line’) and the noise level (‘$*$’) and (b) Nyquist plots of the measurement of a coated lead sample with copolymer 5 corroded in an acetic acid solution during the first 16 hours of immersion (hours of immersion are shown). 243
15.20 Magnitude plot, modeled curve, residual curve, noise on the excited frequencies and noise on the non-excited frequencies at the last calculated time instant of the measurement at 15 hours of immersion. . . 243
15.21 Evolution of (a) the pore resistance and (b) the effective capacitance of the copolymer 5 coating vs the time. 244
15.22 Evolution of (a) the resistance of the oxide and (b) the capacitance of the oxide layer vs the time. 245
15.23 The EEC used for the simulation of the experimental impedance spectra of the protecting polymer coating. 245

16.5 Publications in international peer-reviewed journals

I. Pieter-Jan Sabbe, Mark Dowsett, **Michel De Keersmaecker**, Matthew Hand, Paul Thompson and Annemie Adriaens, Synthesis and surface characterization of a patterned cuprite sample: preparatory step in the evaluation scheme of an X-ray-excited optical microscopy system, APPLIED SURFACE SCIENCE 332 (2015) 657-664.

II. **Michel De Keersmaecker**, Otto van den Berg, Kim Verbeken, Diederik Depla and Annemie Adriaens, Hydrogenated dimer acid as a corrosion inhibitor for lead metal substrates in acetic acid, JOURNAL OF THE ELECTROCHEMICAL SOCIETY 162 (4) (2015) C167-C179.

III. Roohangiz Zandi Zand, Victoria Flexer, **Michel De Keersmaecker**, Kim Verbeken and Annemie Adriaens, Effects of activated ceria and zirconia nanoparticles on the protective behavior of silane coatings in chloride solutions, INTERNATIONAL JOURNAL OF ELECTROCHEMICAL SCIENCE 10 (2015) 997-1014.

IV. **Michel De Keersmaecker**, Mark Dowsett, Rosie Grayburn, Dipanjan Banerjee and Annemie Adriaens, In-situ spectroelectrochemical characterization of the electrochemical growth and breakdown of a lead dodecanoate coating on a lead substrate, TALANTA 132 (2015) 760-768.

V. Rosie Grayburn, Mark Dowsett, **Michel De Keersmaecker**, Dipanjan Banerjee, Simon Brown and Annemie Adriaens, Towards a new method for coating heritage lead, HERITAGE SCIENCE 2 (2014) 1-9.

VI. Rosie Grayburn, Mark Dowsett, **Michel De Keersmaecker**, Eric Westenbrink, James A Covington, James B Crawford, Matthew Hand, David Walker, Pamela A Thomas and Dipanjan Banerjee, Annemie Adriaens, Time-lapse synchrotron X-ray diffraction to monitor conservation coatings for heritage lead in atmospheres polluted with oak-emitted volatile organic compounds, CORROSION SCIENCE 82 (2014) 280-289.

VII. **Michel De Keersmaecker**, Kim Verbeken and Annemie Adriaens, Lead dodecanoate coatings for the protection of lead and lead-tin alloy artifacts: two examples, APPLIED SURFACE SCIENCE 292 (2014) 149-160.

VIII. **Michel De Keersmaecker**, Diederik Depla, Kim Verbeken and Annemie Adriaens, Electrochemical and surface study of neutralized dodecanoic acid on a lead substrate, JOURNAL OF THE ELECTROCHEMICAL SOCIETY 161 (3) (2014) C126-C137.

IX. **Michel De Keersmaecker**, Karolien De Wael and Annemie Adriaens, Influence of the deposition method, temperature and deposition time on the corrosion inhibition of lead dodecanoate coatings deposited on lead surfaces, JOURNAL OF SOLID STATE ELECTROCHEMISTRY 17 (5) (2013) 1259-1269.

X. Koodlur Sannegowda Lokesh, **Michel De Keersmaecker**, Alice Elia, Diederik Depla, Peter Dubruel, Peter Vandenabeele, Sandra Van Vlierberghe and Annemie Adriaens, Adsorption of cobalt (II) 5,10,15,20-tetrakis(2-aminophenyl)-porphyrin onto copper substrates: characterization and impedance studies for corrosion inhibition, CORROSION SCIENCE 62 (2012) 73-82.

XI. Koodlur Sannegowda Lokesh, **Michel De Keersmaecker** and Annemie Adriaens, Self assembled films of porphyrins with amine groups at different positions: influence of their orientation on the corrosion inhibition and the electrocatalytic activity, MOLECULES 17 (7) (2012) 7824-7842.

XII. Michel De Keersmaecker, Karolien De Wael and Annemie Adriaens, The use of lead dodecanoate as an environmentally friendly coating to inhibit the corrosion of lead objects: comparison of three different deposition methods, PROGRESS IN ORGANIC COATINGS 74 (1) (2012) 1-7.

XIII. Karolien De Wael, Michel De Keersmaecker, Mark Dowsett, David Walker, Pamela Thomas and Annemie Adriaens, Electrochemical deposition of dodecanoate on lead in view of an environmentally safe corrosion inhibition, JOURNAL OF SOLID STATE ELECTROCHEMISTRY 14 (3) (2010) 449-451.

16.6 Oral and poster presentations on national and international conferences

I. **Michel De Keersmaecker**, Otto Van Den Berg, Tom Hauffman, Diederik Depla, Kim Verbeken, Filip Du Prez, Annick Hubin, Annemie Adriaens, The protective behavior of organic coatings containing carboxylic functional groups on lead metal substrates, Chemistry conference for Young Scientists 2014, Koninklijke Vlaamse Chemische Vereniging, Blankenberge, Belgium, 27/02/2014 - 28/02/2014.

II. **Michel De Keersmaecker**, Otto van den Berg, Tom Hauffman, Diederik Depla, Kim Verbeken, Filip Du Prez, Annick Hubin and Annemie Adriaens, The protective behavior of organic coatings containing carboxylic functional groups on lead metal substrates, 3rd International Congress on Chemistry for Cultural Heritage, Academy of Fine Arts, Vienna, Austria, 01/07/2014 - 05/07/2014.

III. **Michel De Keersmaecker** and Annemie Adriaens, The study of a coating based on carboxylate compounds as protection for lead or lead alloyed metal objects, European Corrosion Congress 2013, European Federation of Corrosion, Estoril, Portugal, 01/09/2013 - 05/09/2013.

IV. **Michel De Keersmaecker**, Karolien De Wael and Annemie Adriaens, Deposition of a lead dodecanoate coating on a lead or lead alloy metal surface, 3rd International meeting Youth for the Conservation of Cultural Heritage, Italian Association of Conservation Scientists, Antwerp, Belgium, 18/06/2012 - 20/06/2012.

V. **Michel De Keersmaecker**, Karolien De Wael and Annemie Adriaens, Deposition of a lead dodecanoate coating on a lead or lead alloy metal surface, 2nd International Congress of Chemistry for Cultural Heritage, Turkish Chemical Society, Istanbul, Turkey, 09/07/2012 - 11/07/2012.

VI. **Michel De Keersmaecker** and Annemie Adriaens, Characterization of lead dodecanoate coatings, Chemistry conference for Young Scientists 2012, Koninklijke Vlaamse Chemische Vereniging, Blankenberge, Belgium, 01/03/2012 - 02/03/2012.

16.7 European search reports

I. Annemie Adriaens, **Michel De Keersmaecker**, Annelies Verstraete, Jan Garrevoet, Lien Van de Voorde and Laszlo Vincze, Scanning X-ray micro-fluorescence study of hydrogels as a matrix for the immobilization of redox enzymes, Photon Science 2011: highlights and Hasylab annual report: author contributions, Deutsches Elektronen-Synchrotron (DESY) and Hamburger Synchrotronstrahlungslabor (HASYLAB) (2012).

II. Annelies Verstraete, Tom Schoonjans, Karolien De Wael, Lien Van de Voorde, **Michel De Keersmaecker**, Laszlo Vincze and Annemie Adriaens, Scanning X-ray micro-fluorescence study of gelatin as a matrix for the immobilization of redox enzymes, Photon Science 2010: highlights and Hasylab annual report: author contributions, Deutsches Elektronen-Synchrotron (DESY) and Hamburger Synchrotronstrahlungslabor (HASYLAB) (2011).